

Copyright is owned by the Author of the thesis. Permission is given for a copy to be downloaded by an individual for the purpose of research and private study only. The thesis may not be reproduced elsewhere without the permission of the Author.

# Quantum description of dark solitons in one-dimensional quantum gases

A thesis presented in partial fulfilment of the  
requirements for the degree of

Doctor of Philosophy  
in  
Physics

at Massey University, Albany,  
New Zealand.

Sophie S. Shamailov

2017

# Abstract

The main objective of this thesis is to explain, from the quantum-mechanical point of view, the nature of dark solitons in one-dimensional cold-atom systems. Models of bosons and fermions with contact interactions on a ring are exactly solvable via the Bethe ansatz, and support so-called type-II elementary excitations. These have long been associated with dark solitons of the Gross-Pitaevskii equation due to the similarity of the dispersion relation, despite the completely different physical properties of the states. Fully understanding this connection is our primary aim.

We begin by reviewing the Gross-Pitaevskii equation and its dark soliton solutions. Next, we solve the mean-field problem of two coupled one-dimensional Bose-Einstein condensates, with special emphasis on Josephson vortices and their dispersion relation. Predictions are given for possible experimental detection. Then we give a derivation that justifies a method for the extraction of the so-called *missing particle number* from the dispersion relation of solitonic excitations.

A derivation of the finite Bethe ansatz equations for the Lieb-Liniger and Yang-Gaudin models follows. These describe a single species of bosons and two component fermions, respectively. We review the elementary excitations of the Lieb-Liniger model, and carry out a comprehensive study of the (much richer) excitations of the Yang-Gaudin model. The thermodynamic limit Bethe ansatz equations for all states of interest in both models are derived, and the missing particle number and the closely-related *phase-step* are extracted from the dispersion relations. Next, we develop a method for approximating the finite-system dispersion relation of solitonic excitations from the thermodynamic limit results.

Finally, we show that the single particle density and phase profiles of appropriately-formed superpositions of type-II states with different momenta exhibit solitonic features. Through this idea, the missing particle number and phase step extracted from the dispersion relation gain physical meaning. Moreover, we use a convolution model to extract the fundamental quantum dark soliton length scale across the range of interactions and momenta. The insight gained in the bosonic case is used to make inferences about dark solitons in the fermionic case. Furthermore, we study the Hess-Fairbank effect in the repulsive Yang-Gaudin model and the fermionic super Tonks-Girardeau regime.

# Acknowledgements

I would very much like to thank my supervisor, Prof. Joachim Brand, for taking me on as a student and putting up with me ever since =) Quite honestly, you have been the best advisor one could ever hope for. I've greatly enjoyed working with you and found our research truly exciting and fascinating. Thanks for all the wonderful ideas, advice and constant help with everything =) It's been great fun – THANKS!

I'd also like to thank all the profs, post-docs and students at the CTCP and NZIAS – and Vesna, of course! – for making our little department such a warm and pleasant place. I've rarely seen a group of people who are, without exception, so lovely and friendly. Thank-you and all the best to everyone! :)

A huge thank-you to my examiners (especially Josh!!), who invested an enormous amount of time and effort into reading this beastie and providing feedback. I am sincerely grateful for your input, and am forever in your debt :-)

# Contents

<b>1</b>	<b>Introduction</b>	<b>1</b>
1.1	Thesis Overview . . . . .	6
<b>2</b>	<b>Gross-Pitaevskii Dark Solitons</b>	<b>12</b>
2.1	Bose-Einstein Condensation . . . . .	12
2.1.1	No Condensation in One Dimension . . . . .	14
2.2	Hartree-Fock in One Dimension . . . . .	16
2.2.1	Dark Soliton Solutions . . . . .	18
2.2.1.1	Local Density Approximation . . . . .	22
	<b>Appendices</b>	<b>25</b>
2.A	Exact Dark Solitons on Finite Rings . . . . .	25
<b>3</b>	<b>The Coupled Bose-Einstein Condensates System</b>	<b>28</b>
3.1	Introduction . . . . .	28
3.2	The Model . . . . .	31
3.3	Analytical Solutions . . . . .	32
3.3.1	The Manakov Case . . . . .	32
3.4	Useful Observables . . . . .	33
3.4.1	Analytical Expressions for Dark Solitons . . . . .	35
3.4.2	Analytical Expressions for Manakov Solutions . . . . .	35
3.4.3	Variational Calculation for Josephson Vortices . . . . .	36
3.5	Numerical Methods . . . . .	37
3.6	Visual Inspection of Numerical Solutions . . . . .	38
3.7	Dispersion Relation and Other Observables . . . . .	41
3.8	Parameter Regimes, Types of Excitations and Their Stability . . . . .	43
3.9	Inertial Mass and Missing Particle Number . . . . .	47
3.10	The Sine-Gordon Equation . . . . .	49
3.11	Relativistic Behaviour . . . . .	52
3.12	Discussion and Conclusions . . . . .	54
	<b>Appendices</b>	<b>57</b>
3.A	Stability Calculation . . . . .	57
3.A.1	Analytical Stability Calculation for Dark Solitons . . . . .	59
3.B	Derivation of the Sine-Gordon Equation . . . . .	61

<b>4</b>	<b>Detecting Josephson Vortices</b>	<b>64</b>
4.1	Introduction . . . . .	64
4.2	The Model . . . . .	65
4.3	The Fringe Pattern . . . . .	66
4.4	Trajectory in a Trap . . . . .	68
4.5	Local Density Approximation . . . . .	70
<b>5</b>	<b>Missing Particle Number</b>	<b>73</b>
5.1	Introduction . . . . .	73
5.2	The SGR Formula . . . . .	75
5.3	Main Derivation . . . . .	76
5.3.1	Canonical Ensemble . . . . .	80
5.4	SDPS-SGR Equivalence . . . . .	81
5.4.1	Analytical Examples . . . . .	82
5.4.2	Numerical Examples . . . . .	85
5.5	Discussion and Conclusions . . . . .	88
	<b>Appendices</b>	<b>91</b>
5.A	Hellmann-Feynman Theorem . . . . .	91
<b>6</b>	<b>The Bethe Ansatz</b>	<b>92</b>
6.1	The Bethe Ansatz Wavefunction . . . . .	92
6.2	Spatial Part of the Bethe Ansatz . . . . .	95
6.3	Spin Part of the Bethe Ansatz . . . . .	99
6.3.1	Statement of Results . . . . .	100
6.3.2	Outline of Proof . . . . .	102
6.4	Exponential to Logarithmic Form . . . . .	103
6.4.1	Final Remarks . . . . .	104
	<b>Appendices</b>	<b>106</b>
6.A	M=1 . . . . .	106
6.B	M=2 . . . . .	110
<b>7</b>	<b>Lieb-Liniger Model</b>	<b>120</b>
7.1	Introduction . . . . .	120
7.2	The Model . . . . .	121
7.3	Ground State . . . . .	122
7.4	Elementary Excitations . . . . .	122
7.4.1	Comparison to Dark Solitons . . . . .	126
7.5	Attractive Regime . . . . .	127

<b>8</b>	<b>Yang-Gaudin Model</b>	<b>129</b>
8.1	Introduction . . . . .	129
8.2	The Model . . . . .	131
8.2.1	Free Case . . . . .	131
8.2.2	Interacting Case . . . . .	132
8.3	Ground State . . . . .	133
8.3.1	Exact . . . . .	133
8.3.2	String Hypothesis for $\gamma < 0$ . . . . .	134
8.3.3	Overview . . . . .	136
8.4	Single Fermion Holes . . . . .	138
8.4.1	Exact . . . . .	138
8.4.2	String Hypothesis for $\gamma < 0$ . . . . .	141
8.4.3	String Hypothesis for $\gamma > 0$ . . . . .	141
8.4.4	Overview . . . . .	144
8.5	Double Fermion Holes . . . . .	146
8.5.1	Exact . . . . .	146
8.5.1.1	Compliment . . . . .	149
8.5.2	String Hypothesis for $\gamma < 0$ . . . . .	149
8.5.2.1	Compliment . . . . .	150
8.5.3	Overview . . . . .	150
8.6	Spin-Flip Excitations . . . . .	153
8.6.1	Exact . . . . .	153
8.6.2	String Hypothesis for $\gamma < 0$ . . . . .	154
8.6.3	Overview . . . . .	154
8.6.4	$c \rightarrow \infty$ limit . . . . .	156
8.7	Discussion and Conclusions . . . . .	159
	<b>Appendices</b>	<b>160</b>
8.A	Technical Details . . . . .	160
<b>9</b>	<b>Thermodynamic Limit</b>	<b>163</b>
9.1	Introduction . . . . .	163
9.2	Thermodynamic Limit Equations . . . . .	164
9.2.1	Repulsive Lieb-Liniger . . . . .	165
9.2.1.1	Ground State . . . . .	165
9.2.1.2	Single Boson Holes . . . . .	167
9.2.2	Attractive Yang-Gaudin . . . . .	169
9.2.2.1	Ground State . . . . .	170
9.2.2.2	Single and Double Fermion Holes . . . . .	172
9.2.2.3	Spin-Flip Excitations . . . . .	173

9.2.3	Repulsive Yang-Gaudin . . . . .	175
9.2.3.1	Ground State . . . . .	176
9.2.3.2	Single Fermion Holes . . . . .	178
9.2.3.3	Double Fermion Holes . . . . .	179
9.2.3.4	Spin-Flip Excitations . . . . .	181
<b>Appendices</b>		<b>183</b>
9.A	Thermodynamic Limit Equations: Outline of Derivation . . . . .	183
<b>10 Extracting Solitonic Properties from the Bethe Ansatz</b>		<b>187</b>
10.1	Introduction . . . . .	188
10.2	Missing Particle Number and Phase Step . . . . .	189
10.2.1	Repulsive Lieb-Liniger . . . . .	191
10.2.1.1	Single Boson Holes . . . . .	191
10.2.2	Yang-Gaudin Model . . . . .	193
10.2.2.1	Single Fermion Holes (Attractive) . . . . .	195
10.2.2.2	Double Fermion Holes (Attractive) . . . . .	197
10.2.2.3	Spin-Flip Excitations (Attractive) . . . . .	197
10.2.2.4	Single Fermion Holes (Repulsive) . . . . .	199
10.2.2.5	Double Fermion Holes (Repulsive) . . . . .	201
10.2.2.6	Spin-Flip Excitations (Repulsive) . . . . .	201
10.3	Physical and Inertial Masses . . . . .	201
10.4	Discussion and Conclusions . . . . .	204
<b>Appendices</b>		<b>209</b>
10.A	Approximate Analytical Solutions . . . . .	209
10.A.1	Repulsive Lieb-Liniger Model . . . . .	209
10.A.2	Attractive Yang-Gaudin Model . . . . .	212
10.A.3	Repulsive Yang-Gaudin Model . . . . .	214
<b>11 Finite-System Approximation</b>		<b>215</b>
11.1	Introduction . . . . .	215
11.2	The Derivation . . . . .	216
11.3	Gross-Pitaevskii Dark Solitons . . . . .	221
11.4	Lieb-Liniger Type-II Excitations . . . . .	224
11.5	Discussion and Conclusions . . . . .	230
<b>12 Quantum Dark Solitons</b>		<b>232</b>
12.1	Introduction . . . . .	232
12.2	Lieb-Liniger Model . . . . .	235
12.3	Superpositions of Type-II States . . . . .	236

12.3.1	Algebraic Bethe Ansatz . . . . .	238
12.3.2	Gaussian Momentum Distribution . . . . .	239
12.3.2.1	Tonks-Girardeau Limit . . . . .	240
12.3.3	Momentum Distribution of Gross-Pitaevskii Dark Solitons . . . . .	241
12.4	Physical Properties of Superposition States . . . . .	245
12.5	Length Scale of the Quantum Dark Soliton . . . . .	257
12.6	Discussion and Conclusions . . . . .	263
<b>13</b>	<b>Physics of the Yang-Gaudin Model</b>	<b>266</b>
13.1	Dark Solitons . . . . .	266
13.1.1	Dimer Super Tonks-Girardeau . . . . .	269
13.2	Spin Waves . . . . .	269
13.3	Hess-Fairbank Effect . . . . .	272
13.3.1	Introduction . . . . .	272
13.3.2	The Model . . . . .	273
13.3.3	Results . . . . .	274
13.4	Fermionic Super Tonks-Girardeau . . . . .	279
13.5	Conclusion . . . . .	280
<b>Appendices</b>		<b>281</b>
13.A	Finite-System Approximate Dispersion Relations . . . . .	281
13.B	Repulsive Two-Component Bose Gas . . . . .	285
13.C	Box Boundary Conditions . . . . .	286
<b>14</b>	<b>Summary, Conclusions &amp; Outlook</b>	<b>289</b>
14.1	Future Work . . . . .	292

# Chapter 1

## Introduction

The purpose of this chapter is to give a very broad overview of the field and an outline of the thesis. More specific introductions are to be found at the start of each chapter to come.

### A Gentle Introduction

This thesis belongs to the field of ultra-cold atom physics, which is concerned with what happens to atoms when they are cooled down so much that thermal fluctuations are essentially suppressed and zero-temperature quantum mechanics chiefly determines the behaviour. In particular, under such circumstances one usually witnesses *condensation* – the gas of atoms falls down into the lowest energy state available to it, which is a single, coherent quantum state involving a macroscopic number of atoms. The total spin of the atoms determines their quantum statistics – the particles can either be bosons (integer spin, symmetric wavefunctions) or fermions (half-integer spin, anti-symmetric wavefunctions). These two types of particles behave fundamentally differently: bosons can all occupy one quantum state, and therefore a non-interacting Bose-Einstein condensate sees all the atoms in the zero-momentum mode, while no two identical fermions can occupy the same quantum state, so fermionic condensates are limited by Fermi pressure, a term referring to the Pauli exclusion principle.

Condensation in cold atomic gases is extremely closely-linked to superfluidity and superconductivity, dissipationless flow quantum phenomena that largely dominated twentieth-century condensed matter physics. Leading scientists from all over the world participated in the quest to explain these fascinating phenomena, building up our current understanding of interacting quantum fluids. The astounding properties of superfluid Helium-4, easily visible with the naked eye, continue to capture the imagination to this day. More recently, cold atom physics has allowed us to take the exploration of such effects further than was possible in condensed matter physics, because the experimental setting is so highly controllable. One has direct control over the dimensionality of the system, the number of particles (and spin-components) present, the strength of interaction, and many other parameters. Precision metrology, which has now reached the single-atom level [1], makes detection incredibly

accurate.

Returning to the question of dimensionality, it is possible to produce quasi-one-dimensional systems with cold atoms by using trapping potentials of different “aspect ratios” (traps of different widths along the different directions). In practice, the resulting gas cloud is cigar-shaped, but its radial width can be tuned relative to its length, so an effective one-dimensional regime can certainly be reached. Many-body physics in one dimension is fundamentally different compared to two- and three-dimensions, because quantum fluctuations are stronger. Intuitively, particles cannot pass each other without interacting – they cannot go “around” each other, as a one-dimensional line has zero width. For example, it is well-known that a true Bose-Einstein condensate is not possible in one dimension even at zero temperature [2], as we do not have true off-diagonal long range order<sup>1</sup>. On the other hand, one-dimensional systems are advantageous because they are clearly easier to treat theoretically. Moreover, the full many-body problems are often exactly-solvable – a luxury which is almost non-existent in higher dimensions.

Whenever a model is not exactly-solvable, one always seeks approximate approaches to extract useful information about the physics. One such method is mean-field theory, which reduces the many-body quantum problem to an effective classical field model. Often, this model is in the form of nonlinear differential equations that (hopefully) capture the leading order physics in the weakly interacting regime. The solutions to these differential equations describe the behaviour of the entire fluid, and can therefore be considered “collective”, in the sense that they involve all the individual particles. Nonlinear wave solutions are particularly curious, since the interplay between nonlinear interactions and dispersion can produce very stable, localized objects that retain their shape as a function of time and only translate at some speed. The most basic example of such excitations are solitons, which often arise as solutions to weakly nonlinear dispersive partial differential equations. The key feature is a localized density peak (for bright solitons) or a trough (for dark solitons) which moves at constant velocity without changing shape. Moreover, when two solitons collide, they pass through each other, unaffected by their interaction apart from a phase shift. Solitons can exist in one- and higher-dimensional systems.

The other common type of collective nonlinear excitation is a vortex. Vortices exist in many exciting forms, some of which are encountered in nature very often. Tornadoes and waterspouts are funnel-shaped vortices, as are ocean maelstroms and the smaller whirlpools created in our coffee cups after stirring. Dolphins and whales create and play with ring vortices under water, in the same way as some people are able to blow smoke rings (curiously, vortex ring guns and cannons also exist).

---

<sup>1</sup>Off-diagonal long range order means that the largest eigenvalue of the single particle density matrix scales as the number of particles in the system.

The novel aspect in vortices compared to solitons is the rotation – the angular momentum. In order to rotate, one usually needs more than one dimension, so conventional vortices usually exist in two or more dimensions<sup>2</sup>.

Now, in one-dimensional bosonic systems (with contact interactions) both an exact solution and the mean-field one are easily available. The mean-field equations support dark solitons, which have even been repeatedly observed experimentally, but such solutions are absent in the exact quantum model. Instead, the exact quantum system has a low-energy excitation branch which resembles dark solitons in some ways, and yet is distinctly different in others. Understanding the connection between these two types of excitations, and explaining the nature of these nonlinear waves from the quantum-mechanical point of view, is our primary goal.

### Landmark Theories and Experiments

In 1924-1925, Bose and Einstein [3, 4] worked out the theory of non-interacting quantum particles with Bose statistics. They predicted the condensed state of matter such particles fall into when they are cooled (so that they are all in the ground state of the system), known today as the Bose-Einstein condensate. The first experimental observation of this new state of matter came in 1938 with superfluid Helium-4 [5, 6], and in 1941 was phenomenologically explained by Landau’s two-fluid model [7]. A closely-related phenomenon to superfluidity (usually observed with bosons) is superconductivity (occurs in systems of electrons, which are fermions). Superconductivity was experimentally discovered in 1911 by Onnes (see [8] and references therein) and phenomenologically described in 1950 by Ginzburg and Landau [9], with the seminal Bardeen-Cooper-Schrieffer microscopic theory following closely after in 1957 [10, 11].

More recently, in 1995, experimentalists have succeeded for the first time to create a Bose-Einstein condensate of cold atoms [12, 13] (fermionic condensation was achieved in 2004 [14, 15]). This was a huge breakthrough as it allowed for very precise experiments with high levels of control. In 1999 the first quasi-one-dimensional Bose-Einstein condensate was created in the laboratory [16]. These thin cigar-shaped clouds can be approximately described by the one-dimensional Gross-Pitaevskii equation [17, 18], which is a mean-field description of the problem. However, for truly one-dimensional systems, mean-field theories are questionable (as mentioned above), motivating the need for more sophisticated techniques. Thus, the theoretical description of a one-dimensional strongly-interacting gas is non-trivial, much like its experimental realisation. Nevertheless, the Gross-Pitaevskii equation supports dark soliton solutions [19, 20], which were observed in quasi-one-dimensional

---

<sup>2</sup>However, we will see that a special kind of vortex can exist in a system of two parallel, linear Bose-Einstein condensate strands, in which case “rotation” becomes a flow of matter between these two one-dimensional lines.

Bose-Einstein condensates at the turn of the 21<sup>st</sup> century [16, 21, 22]. Explaining the existence of these “classical” collective excitations from the perspective of the fully-quantized exact models is therefore both interesting and challenging.

Likewise, quantum vortices in three dimensions – originally predicted by Onsager in 1947 [23], theoretically explained by Feynman in 1955 [24], and extended to superconductors by Abrikosov in 1957 [25] – have been experimentally detected in cold-atom systems [26–28]. Such quantum vortices have originally been observed in superfluid Helium-4 [29] and in type-II superconductors [30–32]. Josephson vortices [33] (which will be of particular interest to us) have been first studied in the context of a superconducting Josephson junction [34]. Currently, they are on the verge of being observed in Bose-Einstein condensates [35], with many theoretical proposals (e.g. [36]) to complement the experimental progress.

Historically, bright solitons were discovered experimentally by J.S. Russell in 1844 when he saw a soliton in a water canal in Scotland and then reproduced it in a water tank [37]. The Korteweg-de Vries equation describing the phenomenon was derived in 1895 [38], in 1965 the first computer simulations were performed [39], and in 1967 an analytical solution to the water-waves equation was obtained [40]. Over the last two decades, the utilisation of solitons for optocommunication [41] – using them to send light pulses in optical fibres – has been a major research theme because solitons are intrinsically stable against dispersion. However, today this method is only used sparingly for transmitting data because of the narrow bandwidth associated with solitons, which limits the transmission capacity severely.

As for exactly solvable one-dimensional quantum many-body systems, we shall be making extensive use of the so-called Bethe ansatz technique to go well beyond mean-field predictions, applicable to integrable models where the many-body interaction is equivalent to a sequence of two-body scattering events. It was introduced in 1931 by Bethe [42] to solve the antiferromagnetic Heisenberg model. Rapid progress of direct relevance to our work has been made in the 1960’s, aided by the pioneering work of Girardeau at the turn of that decade [43]. He showed that infinitely-repulsive bosons with contact interactions, known as the Tonks-Girardeau gas, were mappable on to free fermions. The Bethe ansatz was then first applied to continuous systems by McGuire in 1964-1965 when he considered the attractive bosonic case [44] and repulsive spin-1/2 fermionic case with a single spin-down particle [45].

In parallel, Lieb and Liniger solved the repulsive Bose gas with arbitrary contact interactions in 1964 [46, 47], which has come to be known as the Lieb-Liniger model. They were soon followed by Yang [48] and Gaudin [49, 50] in 1967 who solved the general spin-1/2 fermion system with contact interactions by the nested Bethe ansatz, a somewhat more difficult task. Similarly, this model is referred to as the Yang-Gaudin model. Only a year later, Sutherland [51] generalized the solution to

an arbitrary number of spin-components of either symmetry. Other important steps in the development of the coordinate Bethe ansatz, as the original formulation came to be known later, are outlined in [52], section 1.7.

The quantum inverse scattering method was initiated in 1978 (see the introduction to chapter two of [53]), and starting from 1989, it was applied to one-dimensional integrable models, creating the algebraic Bethe ansatz [54]. The algebraic Bethe ansatz reproduces all the results of the coordinate Bethe ansatz using an alternative method, but it can go much further – it allows for the calculation of correlation functions. Except for very special cases, this involves very heavy and complicated numerical procedures [55].

### **Our Objective**

We will be primarily concerned with the Lieb-Liniger and Yang-Gaudin models, describing spin-0 bosons and spin-1/2 fermions with contact interactions on a ring. These models are presently within reach of experimental realization in cold-atom systems (e.g. [56, 57]), which has naturally renewed interest in them.

In the weakly-interacting regime with many particles (i.e. the mean-field regime), the one-dimensional Gross-Pitaevskii equation captures the physics of the full Lieb-Liniger model correctly [58]. Now, the Gross-Pitaevskii equation has dark soliton solutions [59], which are the lowest energy excitations at given momentum and are dynamically stable. The Lieb-Liniger model, on the other hand, clearly cannot have dark soliton solutions since it is a linear quantum system. The lowest energy excitations at a given value of the momentum of the Lieb-Liniger model are so-called type-II states [47], which happen to resemble dark solitons in certain ways while strongly differing from them in other important aspects. In particular, the dispersion relation (the excitation energy versus momentum) is strikingly similar [60], while the single-particle density profile is completely different (the soliton has a density dip while type-II states are uniform).

Our goal is to understand the connection between dark solitons and type-II states in the Lieb-Liniger model. Where are the solitons in the Lieb-Liniger model in the Gross-Pitaevskii regime? What happens to the solitons as we increase interactions and enter the Tonks-Girardeau limit? Note that there have been no experimental studies of dark solitons in one dimension outside of the mean-field regime (i.e. with few particles and/or strong interactions), so little is known about quantum dark solitons experimentally. Considerable theoretical work has been done on this question (see the introduction to chapter 12), but most studies are inconclusive, providing only indirect evidence. One group of papers [61–66], however, contains some very insightful work and we will see that our ideas and results are completely consistent with these articles, the two approaches complimenting each other.

As for solitons in a one-dimensional Fermi gas, since there is no adequate mean-field description of this system (see discussion in [67]), even though some predictions are available from such an approach [68], they are unreliable. Furthermore, solitons in one-dimensional fermionic condensates have not been observed experimentally to date, so very little is known about them. On the other hand, considering that we will show in great detail which properties of the bosonic Bethe ansatz type-II excitations are shared by the dark solitons they relate to, we will be able to use the Bethe ansatz to predict the properties of dark solitons in the Fermi gas.

## Experimental Relevance

The theoretical questions posed above are more relevant now than ever before due to the fact that in recent years, the Lieb-Liniger & Yang-Gaudin models have become experimentally accessible, as they can be directly realized in the laboratory with cold-atom systems. Bose-Einstein condensates [12, 13] and fermionic condensates [14, 15] are prepared routinely and have a remarkably low noise level and fine control over many parameters in a wide range. Moreover, quasi-one-dimensional condensates can be prepared [69], perhaps soon in ring geometry, made possible by toroidal traps [70, 71]. In addition, the contact potential is a good first order approximation to the interaction between the atoms [59], and the interaction strength is widely tunable through a Feshbach resonance [72, 73].

Now, condensates with weak interactions and a large number of atoms have been experimentally accessible for some time, but recently, experiments have begun work on the few-particle and strongly-interacting gases, preparing the Tonks-Girardeau limit of the Lieb-Liniger model [74, 75], probing elementary excitations of the Lieb-Liniger gas [56], realizing the few-fermion Yang-Gaudin model [57, 76–78], and even a generalized model with several spin components [79].

Therefore, understanding the nature and predicting the properties of the lowest energy excitations in one-dimensional Bose and Fermi gases across the range of interactions is of vital importance.

## 1.1 Thesis Overview

The thesis opens with an exposition on the Gross-Pitaevskii equation, the work-horse of theoretical cold-atom physics. In chapter 2, we briefly review condensation and the importance of dimensionality. Next, we show how the Gross-Pitaevskii equation may be obtained in one dimension from the Hartree-Fock method, and discuss the regime of its applicability. Then we present the exact dark soliton solutions on an infinite (and finite) ring, which we will use in chapters 3, 5, 11 & 12, as dark solitons are a central theme in our work. Practically all key mean-field concepts encountered throughout the thesis are introduced in this chapter, using the dark soliton as an

example. Most-importantly, we familiarize ourselves with the dispersion relation of dark solitons, as well as the missing particle number – the number of particles that had to be removed from the uniform background to create the solitonic density dip, and the phase step across the soliton.

In chapter 3 we consider the slightly more complicated case of two coupled Gross-Pitaevskii equations, modelling two strands of one-dimensional Bose-Einstein condensates that are coherently coupled. In addition to dark solitons, this system supports Josephson vortex solutions, which in general cannot be written down analytically – the exception is a stationary vortex. Therefore, we numerically extend the zero-velocity Josephson vortex to non-zero velocities, thus obtaining the full dispersion relation. We find that there is a special tunnelling strength at which the dispersion relation changes concavity at its central point, which causes the inertial mass to diverge<sup>3</sup>. This implies that by tuning the coupling strength about this critical point, a large range of inertial masses is accessible. Moreover, we compare the full Gross-Pitaevskii equations at small coupling to the analytically-solvable sine-Gordon model, as it is often claimed that the former reduces to the latter in this regime. We show that while the two models do have the same limit, there exist significant differences at finite tunnelling. Finally, in a certain parameter regime, we find a new excitation branch which is always dynamically unstable while, in its presence, dark solitons and Josephson vortices are bistable.

Apart from discovering interesting physics, the motivation for solving this problem is to gain “hands-on” experience with the Gross-Pitaevskii equation (both time-independent and time-dependent – see chapter 4) and the mean-field formalism. Moreover, the solutions we find here will be used in chapter 5 as a test-case for a particular formula.

In chapter 4 we consider two possible experiments via which Josephson vortices of the coupled Bose-Einstein condensates system may be detected and show explicit simulations of the expected observations. In particular, we demonstrate that Josephson vortices may be identified from the fringe pattern which results upon recombination of the two atomic Bose-Einstein condensate strands. Furthermore, we solve the time-dependent Gross-Pitaevskii equations for the harmonically-trapped system and predict an exotic trajectory for the Josephson vortex, arising from the rich structure of its dispersion relation. This behaviour is explained in the framework of the local density approximation, which only requires the uniformly-translating, untrapped results of chapter 3. Needless to say, we use the solutions found in the previous chapter to initiate the time-dependent simulations, as well as to predict the fringe-pattern.

---

<sup>3</sup>The inertial mass can be expressed as a derivative of the dispersion relation, and quantifies the resistance of the quasi-particle to being moved by applied forces.

In the course of reviewing the quasi-particle equation of motion under the local density approximation in chapter 2, we find an expression for the so-called physical mass of the solitonic excitation which, in the hydrodynamic analogy, would correspond to the mass of an air bubble under water, giving rise to the buoyancy force. For two years it was believed that this expression gave the *actual* physical mass of a solitonic excitation, that is, the missing particle number times the mass of each particle. However, soon a competing formula for the missing particle number appeared in the literature, but its origins were somewhat obscure. In chapter 5 we derive this second formula for a superfluid, Lagrangian system based on the Hellmann-Feynman theorem for functionals in a clear and transparent manner. We will apply this formula later in chapter 10 to compute the missing particle number for various excitation branches in the Lieb-Liniger & Yang-Gaudin models.

Moreover, we compare and discuss the relation between the actual missing particle number (as defined above) and the “effective” one, which is proportional to the physical mass, relevant for the motion of the solitonic excitation in a harmonic trap. In general, these two quantities are different and only become equal for stationary excitations, but in many cases they are equivalent at all velocities – we give several simple examples of both possibilities (using results from chapters 2 and 3, among others). Furthermore, in chapter 4 we confirm that it is in fact the effective, and not the actual, missing particle number that enters the quasi-particle equation of motion, by explicitly computing the exact Gross-Pitaevskii trajectory and the local density approximation trajectories with both options in turn.

Next, in chapter 6 we provide a derivation of the Bethe ansatz equations for the Lieb-Liniger & Yang-Gaudin models. The spatial part of the ansatz is independent of the number and type of the spin-components, which only influence the spin part. There exist several approaches to handle the latter – we choose the Bethe-Yang hypothesis, also known as the nested Bethe ansatz. The advantage of this method is that it is quite explicit and conceptually clear. The disadvantage is that a general proof of the final results is very hard, and usually one simply demonstrates that everything is consistent in the two simplest cases, as shall we. The equations derived here will be solved in chapters 7 & 8, and some of the details of the derivation will illuminate interesting questions considered in chapter 13.

Thus, chapter 7 reviews the Lieb-Liniger model for a finite number of particles, examining the ground state and the elementary type-I (particle) and type-II (hole) excitations. The similarity of the (finite-system) type-II dispersion relation to that of dark solitons (chapter 2) is highlighted and tested quantitatively. We also briefly discuss the attractive regime and the super Tonks-Girardeau gas.

The well-understood Lieb-Liniger case helps to develop intuition for such systems, which is then applied to the Yang-Gaudin model in chapter 8, where we

study the ground state and three type-II excitation branches across the full range of interactions, from infinitely-attractive to infinitely-repulsive. These excitations are classified according to their nature in the free system: a single fermion hole, a double fermion hole and a spin-flip. We find that in the infinitely-attractive and infinitely-repulsive regimes (respectively) the three branches (in the order listed) become: a single dimer hole and a system translation, a double dimer hole and a single fermion hole, a spin-flip and a system translation. We solve the exact exponential Bethe ansatz equations where-ever possible. In the strongly-attractive regime and for the single fermion holes in the strongly-repulsive regime, we derive approximate, string-hypothesis equations, appropriate when some of the variables become complex and the interaction is sufficiently strong. In addition, we show that the infinitely-repulsive system is not a true Tonks-Girardeau gas, in the sense that a lower energy excitation is possible than a one fermion hole: the classical translation parabola is accessible for all values of the quantized total momentum of the system.

The finite-system results of chapters 7 & 8 are then used in chapter 9 to derive the thermodynamic limit equations describing the same states. We take the opportunity to compare the dispersion relations of Lieb-Liniger type-II states and dark solitons in the thermodynamic limit and find good agreement in the weakly-interacting regime. Results on the finite Lieb-Liniger model (chapter 7) are also directly used later in chapters 11 & 12 in relation to dark solitons. Our understanding of the finite and infinite Yang-Gaudin model directly contributes to the discussion of the physics predicted in the system (chapter 13). The thermodynamic limit results of chapter 9 also come in useful for explaining some of the properties of the quantum dark soliton (chapter 12) and are simply vital for chapters 10 & 11.

Chapter 10 is dedicated to computing the missing particle number and the phase step from the thermodynamic limit dispersion relations of chapter 9 according to the formula derived in chapter 5. The physical meaning of the results is discussed, relating to both the nature of the excitations in finite systems in various limits and the solitonic interpretation of type-II excitations. In fact, we show that in the Gross-Pitaevskii regime of the Lieb-Liniger model, not only the thermodynamic limit dispersion relation but also the missing particle number and phase step of type-II excitations match those of Gross-Pitaevskii dark solitons. Finally, we extract the physical and inertial masses of the quasi-particles associated with each branch as a function of coupling strength and compute the ratio of the two, which determines the dynamics of such excitations in harmonic traps.

Knowledge of the missing particle number and phase step of type-II excitations for the Lieb-Liniger model contributes strongly to the arguments of chapter 12, and is a key component in the calculation of chapter 11. The corresponding quantities for the Yang-Gaudin model are likewise helpful for interpreting the physics in chapter

13.

Next, in chapter 11 we derive an approximation to the dispersion relation of soliton-like excitations in finite systems based on thermodynamic limit results. The derivation is performed for a superfluid gas in one dimension, and hinges upon Galilean invariance and the assumption that the excitation is well localized in the system. In the course of the derivation, we pass through three different stages of approximate expressions for the dispersion relation, each building further on the previous one. We illustrate the various approximations using two examples: dark solitons in the one-dimensional Gross-Pitaevskii equation (chapter 2), and type-II excitations in the Lieb-Liniger model (chapters 7, 9 & 10). The quality of the approximation can tell us about the validity of the assumptions, and as such, constitutes a useful tool for characterizing the various type-II excitations, both of the Lieb-Liniger model (in chapter 12) and the Yang-Gaudin model (in chapter 13).

Finally, in chapter 12 we tackle the main research question of this dissertation. We show that with weak repulsion, dark solitons can be constructed as appropriate superpositions of type-II eigenstates, and explicitly compute the expansion coefficients. The algebraic form of the Bethe ansatz allows us to obtain the single particle density of any superposition state, as well as a quantity which may be associated with the phase of the order parameter in mean-field theory. Next we perform a numerical survey of various Gaussian superpositions (across the range of interactions) and explore their properties, in the course of which we are able to physically interpret the missing particle number and phase step of type-II states (which can be calculated starting from the dispersion relation) as the limiting values in the case of an infinitesimally thin Gaussian superposition.

Then, we hypothesise that the single-particle density of Gaussian superpositions of type-II states is given by a convolution of a fundamental quantum solitonic density with a Gaussian center-of-mass of the missing particles density. Such a model implies that the variance of the single-particle density is the sum of the variances of the convolutants. This allows us to predict a simple formula for the total variance, where the center-of-mass variance obeys single-particle dynamics. We find that the numerical data follows the hypothesised equations very well. From this, the length scale of the underlining fundamental quantum dark soliton is readily extracted and analysed.

The understanding of the connection between type-II excitations and dark solitons in the Lieb-Liniger model is directly applicable to two of the excitation branches in the attractive Yang-Gaudin model and one in the repulsive. The solitonic interpretation of these branches is discussed in chapter 13. A non-trivial result is that our calculations predict dark-soliton like excitations in the repulsive Fermi gas as well, where pairing and superfluidity are at best hypothesized. Largely, the rest of

that chapter is dedicated to understanding spin-waves in the Yang-Gaudin model.

We begin by considering the physical nature of the translatory excitations in the infinitely-repulsive Yang-Gaudin model (found in chapter 8). We confirm that these exist in the bosonic counter-part of the Yang-Gaudin model also, and analyse the effect of boundary conditions. We point out the connection of the translatory excitations to the Luttinger-Liquid theory prediction that the spin-sector becomes soft – that is, the speed of sound vanishes. According to Luttinger liquid theory, a two-component gas has two decoupled excitation sectors, charge and spin, corresponding to waves travelling at different speeds in the total and relative (bosonized) densities, respectively. Thus, spin-flips and single fermion holes correspond to spin-waves, while the double fermion holes are charge excitations.

Next, we simulate the Hess-Fairbank experiment, where the ring trap is externally rotated and the angular momentum of the ground state of the rotating gas is measured. Since superfluids have a non-classical rotational inertia, the fluid does not rotate with the container, allowing one to witness the quantization of circulation. This is particularly interesting for the repulsive Yang-Gaudin model where the lowest energy excitations change from the convex-up solitonic shape to the concave-up translation parabola. We find several distinct phases in the Hess-Fairbank diagrams, separated by linear phase boundaries. At weak to intermediate repulsion, a half-vortex ground state circulation becomes accessible. The length of the corresponding plateau in the Hess-Fairbank diagram is carefully analysed: the number of particles can be effectively scaled out and analytical formulae are given to capture the limiting behaviour in the weak and strong interaction regimes. The next phase is a discontinuous rotation regime, where some, but not all, fractional values of the unit angular momentum are possible in rotational equilibrium. For stronger repulsion, the system enters the continuous non-classical rotation phase, where previously-forbidden angular momentum fractions are now accessible. Eventually, at infinite repulsion, classical rotation is recovered.

Finally, we venture out of the repulsive regime: when the interaction strength is taken to infinity, the Lieb-Liniger and Yang-Gaudin systems can be smoothly followed in one-over the coupling strength to negative infinity – this regime is called the super Tonks-Girardeau gas. We follow the ground state of the Yang-Gaudin model to the super Tonks-Girardeau regime and beyond: we track it from  $+\infty$  to  $-\infty$ , then to  $0^-$ , crossing over to  $0^+$ , then back to  $+\infty$ , and find exotic states where the momentum distribution of the particles has empty slots, or holes.

A summary of all the research presented in the thesis is given in chapter 14, as well as key conclusions and some possible directions for future work.

# Chapter 2

## Gross-Pitaevskii Dark Solitons

In this chapter we will briefly review three-dimensional Bose-Einstein condensates and derive the three-dimensional Gross-Pitaevskii equation from the second-quantized Hamiltonian. Next, we will heuristically motivate the fact that condensation does not occur in lower than three dimensions, deriving the one-dimensional Gross-Pitaevskii equation from the Hartree-Fock ansatz instead. Finally, we discuss the fact that the one-dimensional Gross-Pitaevskii equation provides the correct mean-field description of the system and review the analytically-known dark soliton solutions.

### 2.1 Bose-Einstein Condensation

We begin this chapter with an introductory discussion of Bose-Einstein condensates [59, 80]. First consider a non-interacting three-dimensional Bose gas at some finite temperature. Clearly the many-body Hamiltonian is a sum of all the single-particle Hamiltonians (as there is no interaction). A many-body state can then be described by the occupation numbers  $n_j$ , indicating how many bosons are in each of the single-particle states with energies  $E_j$ . The Bose-Einstein distribution then gives us the average (over all the possible states) occupation numbers as

$$\bar{n}_j = \left[ \exp\left(\frac{E_j - \mu}{k_B T}\right) - 1 \right]^{-1}, \quad (2.1)$$

where  $\mu$  is the chemical potential, determined from  $\sum_j \bar{n}_j = N$ , and  $N$  is the number of particles. The chemical potential is large and negative at high temperatures. Let  $E_0$  be the single-particle ground state energy. As  $T$  decreases, if there exists a  $T_c$  at which  $\mu \rightarrow E_0$  from below, then at that critical temperature,  $\bar{n}_0 \rightarrow N_0$ , where  $N_0$  is some number of order  $N$ . This is the critical temperature at which  $N_0$  bosons condense into the ground state (while the rest,  $N_T = N - N_0$ , remain thermal); below  $T_c$ , the chemical potential vanishes. Conceptually, condensation occurs when the mean interparticle distance becomes comparable to the thermal de-Broglie wavelength.

At zero temperature, the existence of a Bose-Einstein condensate is directly con-

ditioned on the existence of off-diagonal long range order. The single-particle density matrix is given by

$$\begin{aligned} n^{(1)}(\mathbf{r}, \mathbf{r}') &= \langle \hat{\Psi}^\dagger(\mathbf{r}) \hat{\Psi}(\mathbf{r}') \rangle = N \int d\mathbf{r}_2 \dots \mathbf{r}_N \Psi^*(\mathbf{r}, \mathbf{r}_2, \dots, \mathbf{r}_N) \Psi(\mathbf{r}', \mathbf{r}_2, \dots, \mathbf{r}_N) \\ &= \sum_j n_j \phi_j^*(\mathbf{r}) \phi_j(\mathbf{r}'), \end{aligned} \quad (2.2)$$

where  $\hat{\Psi}(\mathbf{r})$  is the bosonic field operator,  $\Psi(\mathbf{r}_1, \mathbf{r}_2, \dots, \mathbf{r}_N)$  the many-body wavefunction,  $\phi_j(\mathbf{r})$  the eigenfunctions of the single-particle density matrix, known as the natural orbitals, and  $n_j$  the eigenvalues, or the natural occupations. Clearly  $\sum_j n_j = N$ . Off-diagonal long range order exists when  $n_0 = N_0 = \mathcal{O}(N)$  is the largest eigenvalue and the rest are independent of system size<sup>1</sup>. The order parameter (the condensate wavefunction) is then simply  $\psi = \sqrt{N} \phi_0$ .

Next, let us include weak interactions between the particles. The Hamiltonian in second quantization and in the grand canonical ensemble takes the form

$$\begin{aligned} \hat{H} &= \int d\mathbf{r} \hat{\Psi}^\dagger(\mathbf{r}) \left[ -\frac{\hbar^2}{2m} \nabla^2 + V_0(\mathbf{r}) - \mu \right] \hat{\Psi}(\mathbf{r}) \\ &+ \frac{1}{2} \int d\mathbf{r} \int d\mathbf{r}' \hat{\Psi}^\dagger(\mathbf{r}) \hat{\Psi}^\dagger(\mathbf{r}') V(\mathbf{r} - \mathbf{r}') \hat{\Psi}(\mathbf{r}') \hat{\Psi}(\mathbf{r}). \end{aligned} \quad (2.3)$$

The first term is simply the kinetic energy and the second is some external potential to which all particles are subject.  $\mu$  is the chemical potential which is included to constrain the number of particles. The last term represents two-body interactions. If the gas is very dilute, collisions are rare<sup>2</sup>, elastic, and low-energy. Any potential  $V$  can then be replaced by  $g_{3D} \delta(\mathbf{r} - \mathbf{r}')$ , with  $g_{3D} = \frac{4\pi\hbar^2 a_{3D}}{m}$  where  $m$  is the mass of the particles and  $a_{3D}$  is the three-dimensional scattering length, which can be both measured experimentally and calculated theoretically. In fact, collisions can be pictured as hard-sphere, and  $a_{3D}$  is twice the radius of the hard-sphere.

Writing out the Heisenberg equation of motion for the field operator,  $i\hbar\partial_t \hat{\Psi}(\mathbf{r}, t) = [\hat{\Psi}(\mathbf{r}, t), \hat{H}]$ , and using the bosonic commutation relations,  $[\hat{\Psi}(\mathbf{r}), \hat{\Psi}^\dagger(\mathbf{r}')] = \delta(\mathbf{r} - \mathbf{r}')$  and  $[\hat{\Psi}(\mathbf{r}), \hat{\Psi}(\mathbf{r}')] = 0$ , we arrive at

$$i\hbar\partial_t \hat{\Psi}(\mathbf{r}, t) = \left[ -\frac{\hbar^2}{2m} \nabla^2 + V_0(\mathbf{r}) - \mu + g_{3D} \hat{\Psi}^\dagger(\mathbf{r}, t) \hat{\Psi}(\mathbf{r}, t) \right] \hat{\Psi}(\mathbf{r}, t). \quad (2.4)$$

We can now replace the field operator by its expectation value,  $\hat{\Psi}(\mathbf{r}, t) \rightarrow \langle \hat{\Psi}(\mathbf{r}, t) \rangle =$

---

<sup>1</sup>If two or more natural occupations are  $\mathcal{O}(N)$ , the Bose-Einstein condensate is said to be “fragmented”.

<sup>2</sup>Three-body collisions are therefore highly unlikely, which prevents the gas from forming a solid.

$\psi(\mathbf{r}, t)$ , the mean-field order parameter, and immediately arrive at the three-dimensional Gross-Pitaevskii equation. In doing so, we neglect the quantum fluctuations of the field operator, and break the symmetry of the Hamiltonian: all the terms in  $\hat{H}$  are invariant under global transformations of the phase of the field operator, but we select a single complex field with a well-defined phase. This phase symmetry breaking inevitably leads to non-conservation of the particle number, as the two are canonically-conjugate variables. This is permissible if the number of particles in the condensate is sufficiently large, so that  $N_0 + 1 \approx N_0$  [81]. The condition for the validity of the Gross-Pitaevskii equation is  $\frac{N}{V}|a_{3D}|^3 \ll 1$  (where  $V$  is the volume of the system), i.e. the range of interactions is much smaller than the average interparticle distance.

We remark that in the ultra-cold atom experimental realization of this system, the scattering length  $a_{3D}$  can be positive or negative (corresponding to repulsive or attractive interactions) and is widely tunable via Feshbach resonances [80].

In the case when the gas is confined in a three-dimensional harmonic trap with  $\omega_x = \omega_y \equiv \omega_r$ , and  $\omega_z/\omega_r \ll 1$ , we enter the quasi-one-dimensional regime [80]. Define  $a_r = \sqrt{\hbar/m\omega_r}$ , the length-scale associated with the transverse confinement, and the healing length of the condensate,  $\xi_{3D} = \sqrt{8\pi a_{3D}N/V}$ , the length-scale over which deformations of the density “heal”. The quasi-one-dimensional regime is attained when  $a_r < \xi_{3D}$ . Under this condition, we can factorize the order parameter into a transverse component times a longitudinal component. The former satisfies the linear Schrödinger equation with a harmonic potential, and is assumed to remain in the Gaussian ground state. Knowing the radial wavefunction, the transverse directions can be integrated out, yielding a Gross-Pitaevskii equation for the longitudinal component with a new, effective interaction strength:  $g_{1D} = \frac{g_{3D}}{2\pi a_r^2} = 2a_{3D}\hbar\omega_r$ , which can be tuned via a so-called confinement-induced resonance [82].

### 2.1.1 No Condensation in One Dimension

It is well known that there cannot be true condensation in two dimensions (unless  $T = 0$ ) and in one dimension (even at  $T = 0$ ). To see why, let us consider the following two arguments [83] (section 16.7).

The first is based on testing the stability of the system against long-wavelength fluctuations, i.e. Goldstone excitations. Briefly, macroscopic systems lose a symmetry when the temperature is decreased – this is known as symmetry breaking. There are many equivalent ground states, transformable into one another by some symmetry operation. For example, when we associate an order parameter with a Bose-Einstein condensate, it is only defined up to some arbitrary constant phase factor, amounting to  $U(1)$  symmetry. When the gas/fluid is cooled below  $T_c$ , one phase is chosen at random, and the inherent mathematical symmetry of the system is not

reflected in the ground state. Nature chooses one particular realization because it cannot use a quantum superposition of all the equivalent ground states, since they belong to isolated sub-Hilbert spaces. An operator which would transform one state into the other would need to act on all particles at once, and in the thermodynamic limit, such an operator does not exist. A Goldstone mode is an excited state where the local ground state changes very gradually over space. Such a state is orthogonal to all the uniform ground states and its excitation energy tends to zero as the wavelength tends to infinity.

Let our system be translationally-invariant in  $d$ -dimensions with volume  $V \rightarrow \infty$ , and  $u(\mathbf{x})$  denote the deviation of the particles from their equilibrium position at  $\mathbf{x}$ . Assume we are in a symmetry-broken ground state, and decompose  $u(\mathbf{x})$  as a superposition over all the normal modes of the system. The energy content of each mode can be written down assuming we know its dispersion relation. Using the equipartition theorem of statistical mechanics, the mean-square of  $u(\mathbf{x})$  can be found. Among the normal modes there will be a Goldstone mode, the energy of which vanishes as the wavevector  $\mathbf{k}$  vanishes, presumably linearly. It will be the primary contributor to  $\langle u(\mathbf{x}) \rangle^2$  in the short-wavelength regime. In fact, the final result shows that the mean-square of the displacement goes as  $\int dk k^{d-3}$ , which is divergent for  $d \leq 2$ .

The second approach tests the stability of off-diagonal long range order against domain walls – these are phase boundaries, separating regions in space where the order parameter has a different value. The Helmholtz free energy is defined as  $A = U - TS$ , where  $U$  is the internal energy and  $S$  the entropy; it is minimized at equilibrium for systems at constant  $T$  &  $V$ . To minimize  $A$ , we must minimize  $U$  and maximize  $S$ . Since entropy is a measure of disorder, it grows with the number of domains – the question is how much does the creation of these domains cost in energy.

Consider an otherwise-uniform system with one domain of volume  $\ell^d$ . The two ground states only interact on the surface of the domain (which increases the energy), the area of which scales as  $\ell^{d-1}$ . Thus in  $d \leq 1$ , the energy is independent of the domain size. Creating  $\mathcal{N}$  domains costs  $\mathcal{O}(\mathcal{N})$  energy but  $S \propto \log(\mathcal{N}!)$ , which grows faster than  $\mathcal{N}$ . Therefore, minimizing  $A$  favours the creation of domains, and off-diagonal long range order will be destroyed.

In higher dimensions, the argument goes as follows. A domain wall will have some characteristic length-scale over which the order parameter changes, say  $\ell$ . The contribution of the domain to the kinetic energy can be estimated from  $\int_{\text{domain}} d\mathbf{x} \left| \vec{\nabla} \psi(\mathbf{x}) \right|^2$ , but  $\left| \vec{\nabla} \psi(\mathbf{x}) \right| \sim 1/\ell$  as it is the only relevant length scale, so after integrating over the volume of the domain, the energy is proportional to  $\ell^{d-2}$ . Therefore, domains

will be favoured in  $d \leq 2$  dimensions.

The arguments above are simply meant to give one intuition as to why condensation does not occur in lower dimensions at  $T > 0$ . The original rigorous proofs are due to Mermin & Wagner [84], Hohenberg [85], and Kane & Kadanoff [86], with the works of Coleman [87] and Schwartz [88] coming a few years later. Following closely after, Haldane [89] used his one-dimensional fluid theory to predict the power-law behaviour of the single-particle density matrix. In parallel to the general rigorous proofs, Lenard [90] specifically addressed the Tonks-Girardeau gas while Yang & Yang [91] showed that all thermodynamic properties of the Lieb-Liniger model at arbitrary coupling (and  $T > 0$ ) are analytic, and therefore a phase transition is impossible.

Moreover, it has been established on a general basis that at  $T = 0$  no condensation takes place in one dimension [2, 92], as well as being specifically shown analytically for the Tonks-Girardeau gas [93–95], and numerically for the Lieb-Liniger model [96–99].

Note that all of the above studies focus on uniform systems (the case of direct relevance to us), as opposed to harmonically trapped, where much work has also been done, e.g. [100–102].

## 2.2 Hartree-Fock in One Dimension

In the previous section, we have seen that there cannot be a true Bose-Einstein condensate in one dimension, only a so-called quasi-condensate. Nevertheless, the Gross-Pitaevskii equation is the correct weak-coupling limit of the Lieb-Liniger model, as can be seen by solving the Lieb-Liniger thermodynamic limit equations directly (chapter 9). In fact, it can be derived without assuming a Bose-Einstein condensate with a symmetry-broken order parameter in the following way. The Hamiltonian in first quantisation (and in the grand canonical ensemble) is give by

$$H = -\frac{\hbar^2}{2m} \sum_{j=1}^N \frac{d^2}{dx_j^2} + \sum_{j=1}^N V_0(x_j) - \mu N + g \sum_{\langle i,j \rangle} \delta(x_i - x_j), \quad (2.5)$$

where the sum in the last term runs over all pairs counted once. The interaction strength  $g$  (we drop the “1D” subscript from now on) can be written as  $g = \frac{\hbar^2}{m} c$  where  $c = -\frac{2}{a_{1D}}$  and  $a_{1D}$  is the one-dimensional scattering length [103, 104]. Also, introduce the dimensionless interaction parameter

$$\gamma = \frac{c}{n_0} = \frac{mg}{\hbar^2 n_0}, \quad (2.6)$$

where  $n_0 = N/L$  is the one-dimensional density and  $L$  is the length of the system.

If the interactions are weak ( $\gamma \ll 1$ ), we may employ the Hartree-Fock ansatz (see [59], section 5.1) whereby one assumes that all the particles are in the same single-particle state and the many-body wavefunction is simply a product of these. Thus, we expand the many-body wavefunction as

$$\Psi(\{x_j\}, t) = \prod_{j=1}^N \phi(x_j, t), \quad (2.7)$$

with  $\|\Psi\|^2 = \|\phi\|^2 = 1$ . Next, calculate the expectation value of the Hamiltonian in this state

$$W = \int dx_1 \dots dx_N \Psi^*(\{x_j\}, t) H \Psi(\{x_j\}, t). \quad (2.8)$$

The first three terms in  $H$  only involve single-body operators, so their contribution to  $W$  is trivial:

$$N \int dx \phi^*(x) \left[ -\frac{\hbar^2}{2m} \frac{d^2}{dx^2} + V_0(x) - \mu \right] \phi(x). \quad (2.9)$$

As for the interaction term, it is easy to verify that the number of  $\delta$ -functions in the double sum is  $\binom{N}{2} = \frac{N(N-1)}{2}$ , so the contribution to  $W$  is

$$\frac{N(N-1)}{2} \int dx_i dx_j g \delta(x_i - x_j) |\phi(x_i)|^2 |\phi(x_j)|^2 = \frac{N(N-1)}{2} \int dx g |\phi(x)|^4. \quad (2.10)$$

If  $N \gg 1$ ,  $N-1 \approx N$ , so we may define the order parameter as  $\psi(x, t) = \sqrt{N} \phi(x, t)$ , and rewrite the energy functional as

$$W = \int dx \psi^*(x, t) \left[ -\frac{\hbar^2}{2m} \frac{d^2}{dx^2} + V_0(x) - \mu + \frac{g}{2} |\psi(x, t)|^2 \right] \psi(x, t). \quad (2.11)$$

Using the product rule on the first term on the right-hand side, and the assumption that either the wavefunction or its first derivative vanish at the boundary, we arrive at

$$W = \int dx \frac{\hbar^2}{2m} |\partial_x \psi(x, t)|^2 + V_0(x) |\psi(x, t)|^2 - \mu |\psi(x, t)|^2 + \frac{g}{2} |\psi(x, t)|^4. \quad (2.12)$$

The Lagrangian density is then given by

$$\begin{aligned} \mathcal{L} = & \frac{i\hbar}{2} [\psi^*(x, t) \partial_t \psi(x, t) - \psi(x, t) \partial_t \psi^*(x, t)] \\ & - \left[ \frac{\hbar^2}{2m} |\partial_x \psi(x, t)|^2 + V_0(x) |\psi(x, t)|^2 - \mu |\psi(x, t)|^2 + \frac{g}{2} |\psi(x, t)|^4 \right], \end{aligned} \quad (2.13)$$

the Lagrangian is  $\mathcal{L} = \int dx \mathcal{L}$  and the action is  $S = \int dx \int dt \mathcal{L}$ . According to the action principle, the system will follow the path that minimizes  $S$ , i.e. variations of

$S$  need to vanish. The Euler-Lagrange equations then read

$$\frac{\delta S}{\delta \psi} = \frac{\partial \mathcal{L}}{\partial \psi} - \frac{\partial}{\partial x} \frac{\partial \mathcal{L}}{\partial (\partial_x \psi)} - \frac{\partial}{\partial t} \frac{\partial \mathcal{L}}{\partial (\partial_t \psi)} = 0, \quad (2.14)$$

and similarly for  $\psi^*$ . Performing the functional derivatives, we arrive at the Gross-Pitaevskii equation

$$i\hbar \partial_t \psi(x, t) = \left[ -\frac{\hbar^2}{2m} \partial_{xx} + V_0(x) - \mu + g |\psi(x, t)|^2 \right] \psi(x, t). \quad (2.15)$$

As mentioned previously, this mean-field description is valid in the limit of weak interactions, when the Hartree-Fock method is justifiable. It is also possible to directly confirm that the Gross-Pitaevskii equation correctly describes the physics of the full quantum model in this regime. If we work in the canonical ensemble (that is, remove the  $\mu$  term from the Hamiltonian), and consider an untrapped gas (so  $V_0 = 0$ ), the Hamiltonian reduces to that of the Lieb-Liniger model [46, 47], which is solvable exactly by the Bethe ansatz. In their original papers, the authors have demonstrated that the  $\gamma \rightarrow 0$  limit recovers Gross-Pitaevskii results. When an external potential is added, translational symmetry is broken and the Bethe ansatz fails. Nevertheless, Lieb *et al.* have carefully considered the more general case of a trapped gas in a series of recent papers which are reviewed in [58] (see chapter 8), and have succeeded in rigorously showing that the Gross-Pitaevskii equation is still applicable in the appropriate regime.

### 2.2.1 Dark Soliton Solutions

In the homogeneous case of  $V_0 = 0$ , and in the thermodynamic limit when  $N, L \rightarrow \infty$  with  $n_0$  remaining finite, several analytical solutions of the one-dimensional Gross-Pitaevskii equation are known. First, we search for a constant solution, independent of  $x$  and  $t$  – we shall refer to this as the background solution. Clearly, it must satisfy  $\mu = g |\psi|^2 = gn_0$ , with the phase of the background state some arbitrary constant. Second, the Gross-Pitaevskii equation supports dark soliton solutions. Recall that dark solitons are nonlinear waves that travel at constant speed without changing shape. Let  $v_s$  denote the speed of the soliton, then we can transform to a co-moving frame by defining  $z = x - v_s t$ , and rewrite the Gross-Pitaevskii equation as

$$-i\hbar v_s \partial_z \psi(z) = \left[ -\frac{\hbar^2}{2m} \partial_{zz} - \mu + g |\psi(z)|^2 \right] \psi(z). \quad (2.16)$$

The dark soliton solution is then given by

$$\psi_s(z) = \sqrt{n_0} \left[ i s + \sqrt{1 - s^2} \tanh \left( \sqrt{\gamma n_0} \sqrt{1 - s^2} z \right) \right], \quad (2.17)$$

where  $s = \sqrt{\frac{m}{\mu}}v_s$  is the velocity scaled by the speed of sound,  $v_c = \sqrt{\gamma n_0 \hbar}/m$ . Notice that we have substituted  $\mu = gn_0 = \gamma \hbar^2 n_0^2/m$  and expressed everything in terms of  $\gamma, n_0, \hbar$  and  $m$ , to facilitate comparison to the Lieb-Liniger model later on. Examples of the density and phase profiles are shown in Fig. 2.1, demonstrating that a dark soliton is characterised by a localized density dip and a phase step across it. For a stationary soliton, the density vanishes at the soliton's position, and the phase step is exactly  $\pi$ . For moving solitons, the minimum of the density is non-zero and the phase step is smaller than  $\pi$ . When the soliton moves at the speed of sound ( $s = 1$ ), the density dip and phase step disappear and we are left with the background solution.

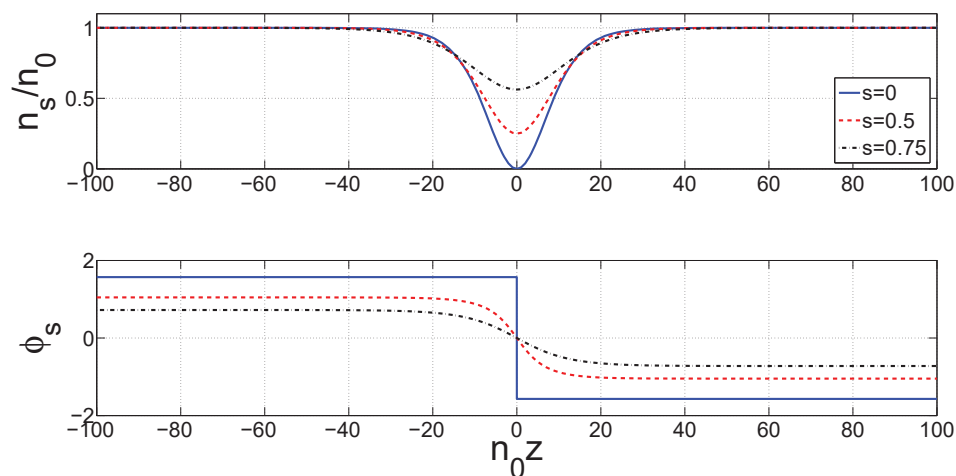


Figure 2.1: The density (top panel) and phase (bottom panel) profiles of a Gross-Pitaevskii dark soliton with open boundary conditions, in an infinite system with  $\gamma = 0.01$ , and  $s = 0$  (blue solid line),  $s = 0.5$  (red dashed line),  $s = 0.75$  (black dash-dotted line).

Notice that the wavefunction (2.17) has open boundary conditions, meaning that the solution must stop changing far from the position of the soliton. Indeed, while the density in the soliton state tends to the same value ( $n_0$ ) as  $z \rightarrow \pm\infty$ , the phase certainly does not: there is a phase jump of  $\Delta\phi = \phi(-\infty) - \phi(\infty) = 2\cos^{-1}(s)$  across the soliton. In practice, one is often interested in solutions with periodic boundary conditions. The dark soliton solution above can be multiplied by a factor of  $\exp[i\Delta\phi z/L]$  which serves to linearly connect the phase in any given finite system, as illustrated in Fig. 2.2. Physically, it corresponds to inducing a so-called “counterflow” (or “backflow”): the entire gas flows at velocity  $v_{cf} = \frac{\hbar\Delta\phi}{mL}$ . As  $L \rightarrow \infty$ , the counterflow velocity clearly vanishes, but the *momentum* associated with this flow does not, as the mass of the entire fluid is  $mN$  and  $N/L$  remains finite in the

thermodynamic limit. It is simple to check, however, that this prefactor does not give a finite contribution to the energy of the state in the thermodynamic limit.

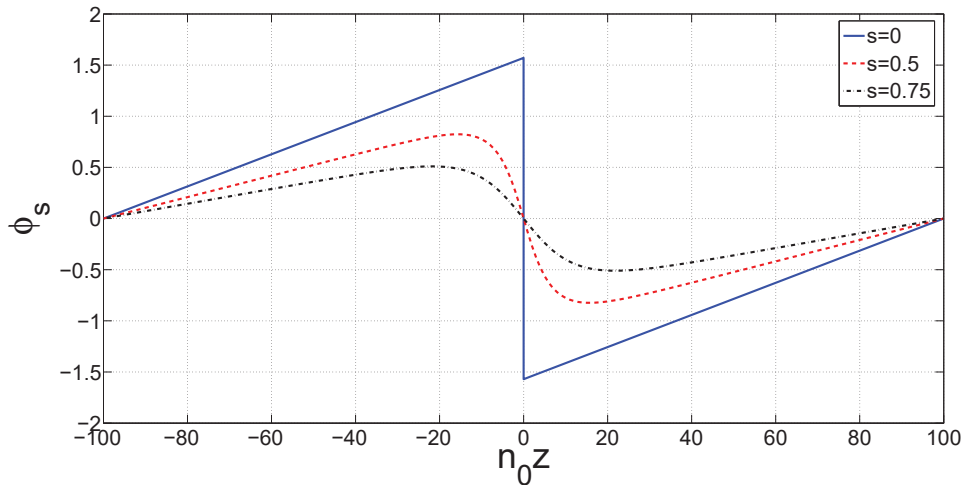


Figure 2.2: The phase profiles of the Gross-Pitaevskii dark soliton with periodic boundary conditions, in a finite system with  $N = 200$ ,  $\gamma = 0.01$ , and  $s = 0$  (blue solid line),  $s = 0.5$  (red dashed line),  $s = 0.75$  (black dash-dotted line).

Thus, defining the momentum operator as

$$P = \int dz -\frac{i\hbar}{2} [\psi^*(z)\partial_z\psi(z) - \psi(z)\partial_z\psi^*(z)], \quad (2.18)$$

the excitation energy and the total (also known as the “canonical”) momentum of the dark soliton are

$$E_s = \frac{4}{3}\sqrt{\gamma}\frac{\hbar^2 n_0^2}{m}(1-s^2)^{3/2}, \quad (2.19)$$

$$P_c = 2\hbar n_0 \left[ \cos^{-1}(s) - s\sqrt{1-s^2} \right] = P_{cf} + P_s. \quad (2.20)$$

In the expression for  $P_c$ , the first term arises from the counterflow and is thus denoted  $P_{cf}$ , while the second term is the contribution of the soliton,  $P_s$ . The dispersion relation – that is, the excitation energy versus momentum – is depicted in the top panel of Fig. 2.3, featuring the typical concave-down shape associated with dark solitons.

We can also define the missing particle number as

$$N_d = \int dz n_s(z) - n_0, \quad (2.21)$$

where  $n_s(z) = |\psi_s(z)|^2$  is the density of the dark soliton. Thus, the missing particle number is the number of particles that had to be removed from the background

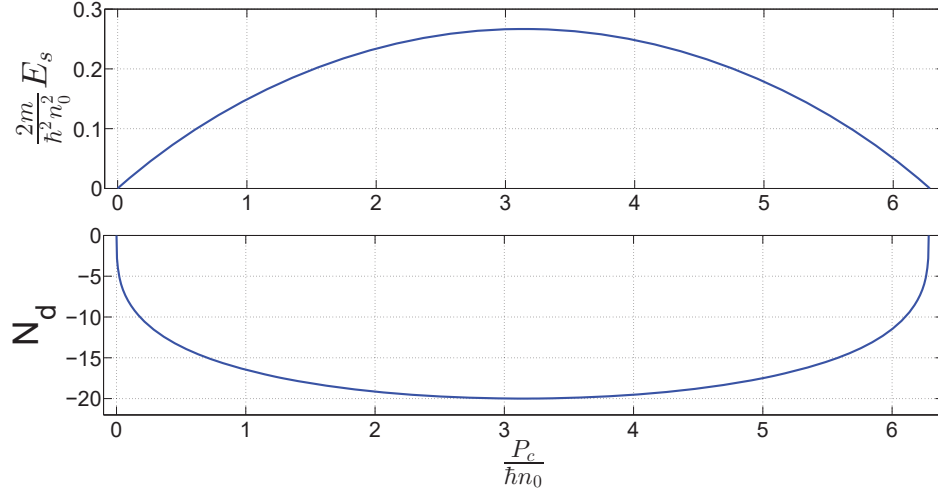


Figure 2.3: The dispersion relation (top panel) and missing particle number (bottom panel) of a Gross-Pitaevskii dark soliton with  $\gamma = 0.01$ .

state to produce the soliton. For the Gross-Pitaevskii dark soliton, it is given by

$$N_d = -\frac{2}{\sqrt{\gamma}} \sqrt{1 - s^2}, \quad (2.22)$$

plotted in the bottom panel of Fig. 2.3. It is clear that the missing particle number is always negative, as is to be expected for a dark soliton. It is minimal for a stationary soliton and vanishes at the edges of the dispersion relation where  $s = \pm 1$ . The mass of the missing particles is then simply  $mN_d$ . On the other hand, the *inertial* mass which determines the response of the quasi-particle to applied forces is given by

$$m_I = \frac{dP_c}{dv_s} = 2 \frac{dE_s}{d(v_s^2)} = \left( \frac{d^2 E_s}{dP_c^2} \right)^{-1}, \quad (2.23)$$

where the derivatives should be evaluated at the extrema of the dispersion relation. For the dark soliton, there is only one global maximum in the dispersion relation, corresponding to a stationary soliton, and we find

$$m_I = -\left. \frac{4m}{\sqrt{\gamma}} \sqrt{1 - s^2} \right|_{v_s=0} = -\frac{4m}{\sqrt{\gamma}}. \quad (2.24)$$

Exact analytical dark soliton solutions on finite rings are also known [105–108], and one of the two equivalent formulations described in these articles is reviewed in appendix 2.A. Using the exact solutions, we can plot the dispersion relation of a dark soliton on a finite ring, as shown in Fig. 2.4. The dispersion relation consists of smooth segments (“wings”) that connect to each other at undifferentiable cusps.

Each wing of the dispersion relation represents dark solitons with velocity in the range  $s \in [-1, 1]$ . At the cusps, the soliton disappears as it reaches the speed of sound, and the non-zero excitation energy is due only to the backflow of the superfluid. Thus, the cusps are simply quantized supercurrent states, and as such, they fall on the system translation parabola,  $E = P^2/2mN$ , also shown on Fig. 2.4. As we approach the thermodynamic limit, the mass of the system diverges, and all the cusps fall down to zero energy. In the thermodynamic limit, we recover fully periodic and symmetric wings, the first of which is shown in Fig. 2.3. Moreover, all the information about dark solitons is fully contained in each wing (which differ only in the counterflow), which justifies restricting our attention to the first wing.

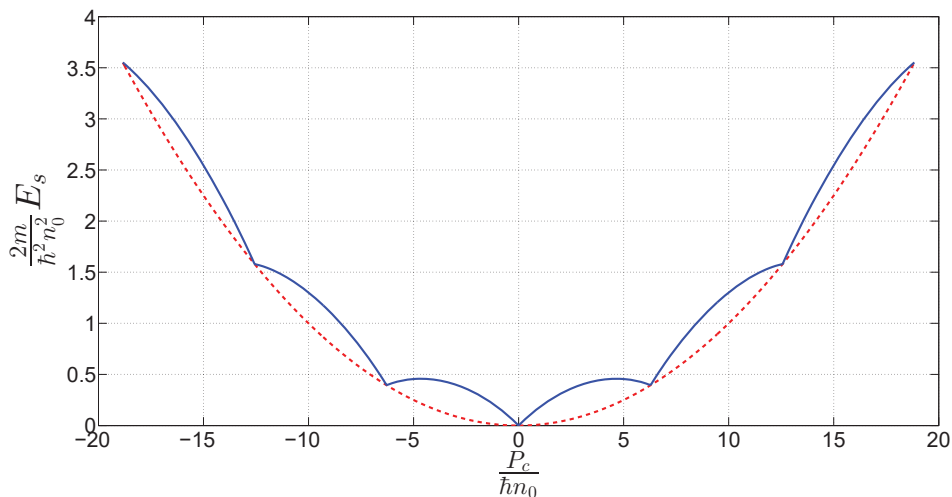


Figure 2.4: The dispersion relation of a Gross-Pitaevskii dark soliton (blue solid line) on a finite ring with  $\gamma = 0.01$ ,  $N = 100$ , showing six cycles, each corresponding to a different quantized supercurrent (backflow) state. The red dashed line shows the translation parabola of the entire gas,  $E = P^2/2mN$ .

### 2.2.1.1 Local Density Approximation

Finally, we note that dark solitons have been observed experimentally in quasi-one-dimensional Bose gases [16, 21, 22] and the results are in agreement with Gross-Pitaevskii predictions. However, most experimental realisations feature a harmonic trapping potential for the quasi-condensate, and therefore the theory presented above for a dark soliton on an otherwise-uniform infinite ring must be modified in order to account for the observations. One way to approach the modelling is to solve the time-dependent Gross-Pitaevskii equation numerically, explicitly including the trapping potential. Alternatively, if the soliton is fairly small compared to the trapped gas cloud, one can think of the dynamics in the trap as of a free soliton moving on a landscape with a changing chemical potential – this is the so-called

local density approximation.

In fact, a simple equation of motion for the quasi-particle can be derived [67, 109, 110]). The argument proceeds as follows. We assume that the dark soliton does not radiate energy, so that  $E_s$  is conserved.  $E_s$  can be thought of as a function of two parameters:  $\mu$  and  $v_s$ <sup>3</sup>, where  $\mu$  must now be replaced by  $\mu(X) = \mu_0 - \frac{1}{2}m\omega^2 X^2$ ,  $X$  being the position coordinate of the excitation. If the energy is a constant of the motion,

$$\frac{dE_s}{dt} = \frac{dE_s}{d\mu} \frac{d\mu}{dX} \frac{dX}{dt} + \frac{dE_s}{dv_s} \frac{dv_s}{dX} \frac{dX}{dt} = 0. \quad (2.25)$$

Since

$$\frac{dv_s}{dX} = \frac{dt}{dX} \frac{dv_s}{dt} = \frac{1}{v_s} \frac{dv_s}{dt} = \frac{1}{v_s} \frac{d^2 X}{dt^2}, \quad (2.26)$$

the right-hand side of (2.25) can be replaced by

$$\left( \frac{dE_s}{d\mu} \frac{d\mu}{dX} + \frac{dE_s}{dv_s} \frac{1}{v_s} \frac{d^2 X}{dt^2} \right) \frac{dX}{dt}, \quad (2.27)$$

and the terms in the brackets must then cancel. We further notice that

$$\frac{1}{v_s} \frac{dE_s}{dv_s} = 2 \frac{dE_s}{dv_s} \frac{1}{2v_s} = 2 \frac{dE_s}{dv_s} \frac{dv_s}{d(v_s^2)} = 2 \frac{dE_s}{d(v_s^2)} = m_I, \quad (2.28)$$

and that

$$\frac{d\mu}{dX} = -m\omega^2 X, \quad (2.29)$$

which leads to the requirement

$$-m\omega^2 X \frac{dE_s}{d\mu} + m_I \frac{d^2 X}{dt^2} = 0. \quad (2.30)$$

Define the physical mass as

$$m_P = -m \left. \frac{dE_s}{d\mu} \right|_{v_s} \equiv m N_s, \quad (2.31)$$

where we have introduced  $N_s$ , the effective missing particle number, defined as the ratio of the physical mass  $m_P$  to the mass of a single particle  $m$ , in analogy to the buoyancy force on an air bubble in liquid. The resultant equation of motion reads

$$m_I \ddot{X} = -m_P \omega^2 X. \quad (2.32)$$

For small amplitude oscillations about an extremum of the dispersion relation, one may approximately take the inertial and physical masses as constant throughout the motion, and compute them at the extremum. Furthermore, if  $m_I$  and  $m_P$  have

---

<sup>3</sup>In the equations that follow, derivatives with respect to  $\mu$  keep  $v_s$  constant and vice versa.

the same sign, the quasi-particle will oscillate in simple harmonic motion about the trap center. For the Gross-Pitaevskii dark soliton, it so happens that  $N_s = N_d$  at all velocities (see chapter 5), so

$$m_p = -m \frac{2}{\sqrt{\gamma}}, \quad (2.33)$$

and so one expects to see the soliton oscillating in the trap, as was indeed observed experimentally [111, 112]. Moreover, expressing the oscillation period of the soliton  $T_s$  in terms of the parameters in the equation of motion, we find

$$\frac{m_I}{m_P} = \left( \frac{T_s}{T_t} \right)^2, \quad (2.34)$$

where  $T_t = 2\pi/\omega$  is the trap period.

Thus, by computing  $m_I$  and  $m_P$  it is possible to predict the dynamics of dark solitons in a harmonic trap. In fact, the theory is equally applicable to other kinds of collective nonlinear excitations that involve a localized density depletion.

# Appendix

## 2.A Exact Dark Solitons on Finite Rings

The first exact solutions of the one-dimensional Gross-Pitaevskii equation in a finite system (with box and periodic boundary conditions) were found by Carr *et al.* [113]. Subsequently, more detailed results for dark soliton solutions on a finite ring were presented by Ueda *et al.* [107, 108] and Jackson *et al.* [105, 106]. We have implemented both of these formulations and checked that they are equivalent, so here we shall only review the first version.

Define

$$\lambda = \frac{2M gNL}{\hbar^2 4\pi^2}, \quad (2.35)$$

the relevant dimensionless interaction strength. Note that in this appendix only,  $M$  is used for the mass (instead of  $m$ ). Now, the approach taken by Ueda *et al.* is to search for dark solitons of various momenta by externally rotating the system and looking for the ground state at every value of the rotation frequency. This is a valid procedure because dark solitons are the lowest energy excitations at any given momentum value, so if we specify the momentum and look for the lowest energy state we indeed find the dark soliton.

Thus, in addition to the usual parameters of the Hamiltonian, we have the driving frequency of the system,  $\Omega$ . There is a quantum number associated with  $\Omega$ : if  $\Omega < 1/2$ ,  $J = 1$  and if  $\Omega \geq 1/2$ ,  $J = 0$ . The bounds for  $\Omega$  at any given  $\lambda$  value are:  $\Omega_{max} = \sqrt{\frac{\lambda+1/2}{2}}$ ,  $\Omega_{min} = 1 - \Omega_{max}$ .

For each  $\Omega$  value we must do the following calculations. Define  $S = 1$  if  $\Omega \geq J$  and  $S = -1$  if  $\Omega < J$ . Now we must solve a highly non-linear equation. Let  $m \in [0, 1]$  be the *elliptic module*, related to the *elliptic modulus*  $k$  by  $m = k^2$ . Let  $K(m)$  and  $E(m)$  be the complete elliptic integrals of the first and second kind, respectively. We may now drop the explicit  $m$  dependence of  $K$ ,  $E$ , with the understanding that it is implied. Define three useful functions:

$$f = \pi^2\lambda - 2K^2 + 2KE, \quad (2.36)$$

$$g = f + 2K^2, \quad (2.37)$$

$$h = f + 2mK^2. \quad (2.38)$$

Further, define

$$\epsilon = \sin^{-1} \left( \sqrt{f/h} \right). \quad (2.39)$$

Solving the equation mentioned above amounts to minimizing the **absolute value** of  $A(m)$  with respect to  $m$ , where

$$A = 2(1-m)K^2 \sqrt{\frac{2f}{gh}} + \sqrt{\frac{2fh}{g}} + \pi (1 - \Lambda_0(\epsilon, m)) - 2\pi |\Omega - J|. \quad (2.40)$$

The function  $\Lambda_0$  involves complete and incomplete elliptic integrals. To avoid confusion,  $K(m)$  and  $E(m)$  continue to denote the complete integrals,  $F(\phi, m)$  and  $E(\phi, m)$  are the incomplete elliptic integrals of the 1<sup>st</sup> and 2<sup>nd</sup> kinds ( $\phi$  is the integral bound and can in general be complex). So, with these definitions,

$$\Lambda_0(\epsilon, m) = \frac{2}{\pi} \{K(m)E(\epsilon, 1-m) - [K(m) - E(m)]F(\epsilon, 1-m)\}. \quad (2.41)$$

If a minimum of  $|A|$  exists for  $m \in [0, 1]$ , then a soliton solution exists. The search for the minimum is performed in Matlab, using the `fminbnd.m` function (implementing a golden section search algorithm), setting the absolute and relative tolerances to  $10^{-10}$ .

Thus, for each  $\Omega$  value in our range, we find the  $m$  that minimizes  $|A|$ , and calculate the functions  $f(m)$ ,  $g(m)$ ,  $h(m)$  defined above. Then we calculate the dimensionless momentum and energy of the excited soliton state (in the rotating frame):

$$\tilde{P} = N \left\{ \Omega - \frac{S}{\lambda\pi^3} \sqrt{\frac{fgh}{2}} \right\}, \quad (2.42)$$

$$\begin{aligned} \tilde{E} = N \left\{ \lambda + \frac{1}{\pi^2} (3KE - (2-m)K^2) \right. \\ \left. + \frac{2K^2}{3\lambda\pi^4} [3E^2 - 2(2-m)KE + (1-m)K^2] \right\}. \end{aligned} \quad (2.43)$$

Once this is done for all  $\Omega$ 's, we can transform the energy into a frame which is stationary:

$$\bar{E} = \tilde{E} + 2\Omega\tilde{P} - \Omega^2 N. \quad (2.44)$$

Note that the momentum does not need to be transformed, i.e.  $\bar{P} = \tilde{P}$ . Finally, we must rescale  $\bar{P}$  and  $\bar{E}$  (reinstating full units):

$$P = \hbar \frac{2\pi}{L} \bar{P}, \quad (2.45)$$

$$E = \frac{\hbar^2}{2M} \left( \frac{2\pi}{L} \right)^2 \bar{E}. \quad (2.46)$$

It remains to calculate the ground state (homogeneous background) energy and momentum to be subtracted ( $E_s$  and  $P_c$  are respectively the difference in energy and momentum between the soliton and background states). The plane-wave solution with  $J = 0$  (for any  $\Omega$ ) plays the part of the ground state. For the plane wave solutions, the dimensionless momentum and energy in the rotating frame are

$$\tilde{P} = NJ, \quad (2.47)$$

$$\tilde{E} = N \left\{ (\Omega - J)^2 + \frac{\lambda}{2} \right\}. \quad (2.48)$$

Again we must transform to the stationary frame:  $\bar{E} = \tilde{E} + 2\Omega\tilde{P} - \Omega^2N$ ,  $\bar{P} = \tilde{P}$ , and rescale:  $P = \hbar\frac{2\pi}{L}\bar{P}$  and  $E = \frac{\hbar^2}{2M} \left(\frac{2\pi}{L}\right)^2 \bar{E}$ .

At any given  $\Omega$  value, having solved for the correct  $m$ , we can calculate the density as a function of  $z$ . Define

$$\eta = -2K^2(m)/g(m), \quad (2.49)$$

$$\mathcal{N} = \frac{K(m)}{K + \eta E}, \quad (2.50)$$

and introduce the Jacobi  $\text{dn}(U, m)$  function: the first argument is the phase and the second the elliptic module. The density is given by

$$n(z) = \mathcal{N} \left[ 1 + \eta \text{dn}^2 \left( \frac{2K(m)z}{L}, m \right) \right]. \quad (2.51)$$

To calculate the phase, we need to know  $\Omega$  &  $S$ , solve for the correct  $m$  value, calculate the functions  $f(m)$ ,  $g(m)$ ,  $h(m)$  and from these find

$$\xi = -\frac{2mK(m)^2}{f(m)}. \quad (2.52)$$

We also need the Jacobi amplitude,  $\text{am}(U, m)$ , with the first argument being the phase and the second the elliptic module, as before, and the incomplete elliptic integral of the third kind:  $\Pi(U, m, t)$ , where  $U$  and  $m$  have the same meaning, and  $t$  is the additional parameter required by this function. The phase is given by

$$\phi(z) = \Omega \frac{2\pi}{L} z - \frac{S}{K(m)} \sqrt{\frac{g(m)h(m)}{2f(m)}} \Pi \left[ \text{am} \left( \frac{2K(m)z}{L}, m \right), m, \xi \right]. \quad (2.53)$$

# Chapter 3

## The Coupled Bose-Einstein Condensates System

Having understood the spinless one-dimensional Bose gas with contact repulsion in the mean-field regime, we proceed to the next level of complexity: two coherently-coupled one-dimensional Bose-Einstein condensate strands, modelled by two coupled, time-independent Gross-Pitaevskii equations. While not directly relevant to the objective of the thesis, this problem provides us with practical experience with mean-field collective excitations and their properties. The solutions we find will also be used later as test-cases in chapter 5.

### 3.1 Introduction

As briefly mentioned at the end of the previous chapter, the concept of effective (or inertial) mass [59] is commonly used in condensed matter physics: it captures the response of a collective excitation in an interacting system to an applied force, as if it were a classical particle obeying Newton's second law. Atomic Bose-Einstein condensates [12, 13] provide a platform for the realization of many quantum-mechanical systems in highly controllable conditions (e.g. see [80, 114]). The possibility of adjusting the effective mass of localized excitations in Bose-Einstein condensates by tuning experimental parameters could potentially open the way to many interesting applications. Quasi-one-dimensional Bose-Einstein condensates have been prepared experimentally almost two decades ago [16], and more recently, two coherently-coupled one-dimensional Bose-Einstein condensates have been demonstrated [115–118]. Dark solitons [59] have been created and observed in one-dimensional Bose-Einstein condensate systems [16, 21, 22], as have been vortices [26–28]. Josephson vortices in particular [33] (which have all the properties of solitons plus a supercurrent circulation between the two Bose-Einstein condensate strands), usually studied in the context of Josephson junctions [34], will also hopefully be soon realized in a cold atoms setting [119].

The model studied here comprises two long, linear, parallel, coupled Bose-Einstein condensates. It describes two different physical realizations: a spinor Bose-Einstein

condensate with two spin components and coherent coupling achieved through radio-frequency or microwave radiation driving a hyperfine transition [120], or a single-component Bose-Einstein condensate in a double-well potential [121–125]. Both options are illustrated in Fig. 3.1. Previous theoretical considerations ranged from testing the Kibble-Zurek mechanism in a ring geometry [125], to modelling the decay of an unstable vacuum to a universe with structure [124, 126], to metastable domain walls [120, 121], to dynamical response to periodic modulation [122] and tunnelling quenches leading to breather modes forming out of quantum fluctuations [123]. Out of these studies, Refs. [120, 122–124] reduced the model to the integrable sine-Gordon case (applicable in the small tunnelling limit) in order to obtain their main results. Testing the validity of this approximation is part of the work presented in the current chapter.

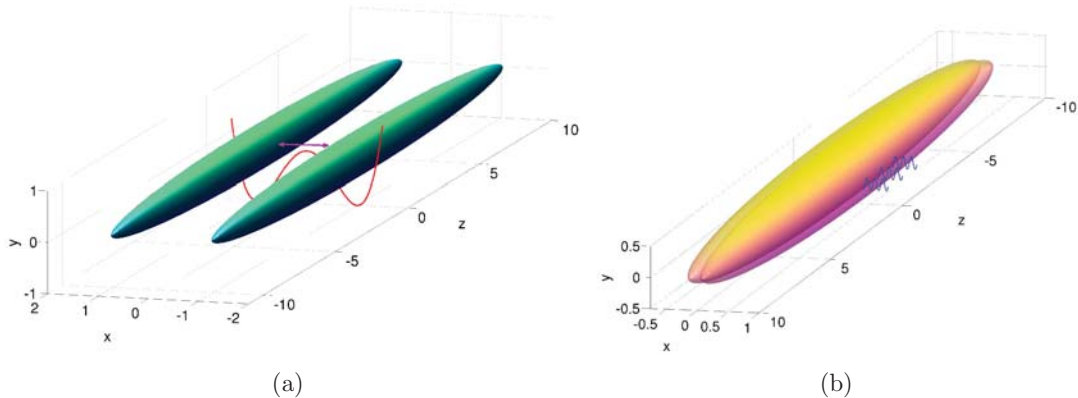


Figure 3.1: A conceptual illustration of two possible realizations of the system studied. (a) Two elongated, cigar-shaped Bose-Einstein condensates, confined in a double-well potential (shown as a red line), with atom tunnelling yielding the coherent coupling between the strands (shown as a purple arrow). In this case, there is no cross non-linear interaction. (b) An atomic condensate in two different pseudo-spin states in a cigar-shaped trap. The two components are slightly off-shifted for clarity. They are coherently coupled by radio-frequency radiation, shown as blue incoming waves. In this case, the cross non-linearity is of the same order as the self non-linearity.

The model of interest was first introduced in [120], where the authors studied domain walls of the relative phase. Later, it was solved by Kaurov and Kuklov in [127, 128], who found analytical stationary Josephson vortex and dark soliton solutions and discussed the bifurcation of one from the other. Qadir *et al.* [129] then expanded on the stability analysis of [127, 128], demonstrating that dark solitons are unstable whenever Josephson vortices and dark solitons coexist. They also gave approximate expressions for slow-moving Josephson vortices, as did [128].

Thus, the model has two kinds of known solutions: dark solitons and Josephson vortices. Exact analytical solutions have been found for translating dark solitons

[59] and for stationary Josephson vortices [127]. Exact moving Josephson vortex solutions have not been obtained to date, though some approximate results were derived in [129]. Here we present numerical solutions of the model (used in [130] to simulate collisions of Josephson vortices), with particular emphasis on the inertial mass of the Josephson vortex excitation in the center of the dispersion relation, the relativistic behaviour of Josephson vortices in the small tunnelling limit, and the existence of a bistable region for dark solitons and Josephson vortices.

We show that there exists a critical tunnelling value at which the Josephson vortex dispersion relation changes from having a single maximum to having three (local) extrema: maximum, minimum and another maximum. At this point the inertial mass of the Josephson vortex at the center of the dispersion relation changes sign and diverges to  $\pm\infty$  on either side of the bifurcation.

In the small coupling limit, we test whether the Gross-Pitaevskii Josephson vortex dispersion relation around the center of the dispersion relation approaches the sine-Gordon dispersion relation. The latter can be described by only two parameters – the “mass” and the “speed of light”. The inertial mass of the Josephson vortex approaches the sine-Gordon mass parameter smoothly<sup>1</sup> as the tunnelling is decreased, but the speed of light does not – the approach to the common value at zero tunnelling occurs at completely different rates.

We extend the stability analysis of [129] to all excitation branches and velocities, finding that for zero cross non-linearity, dark solitons are unstable whenever they co-exist with Josephson vortices, which are, in turn, stable. When the two Bose-Einstein condensate components have a finite non-linear interaction, we discover a new excitation branch with energy between the dark soliton and Josephson vortex dispersion relations which, like dark solitons, has zero angular momentum. These new excited states replace dark solitons as the transition states from left-handed Josephson vortices to right-handed ones (and *vice versa*). In the region where these new excitations exist, dark solitons and Josephson vortices are both stable, separated (in energy) by these new unstable excitations.

The chapter is structured as follows. Section 3.2 introduces the equations, 3.3 summarizes known analytical solutions, 3.4 defines useful observables for characterizing the solutions, 3.5 explains how we numerically obtain solutions, and 3.6 allows one to visualize them. Section 3.7 presents plots of some useful, characteristic quantities for the solutions, which are described (including a discussion of the region of bistability) in section 3.8. Next, section 3.9 addresses the inertial mass and missing particle number of Josephson vortices (identifying the critical point), 3.10 summarizes some key results regarding the sine-Gordon equation, and 3.11 examines the validity of approximating the Gross-Pitaevskii model with the sine-Gordon model.

---

<sup>1</sup>Meaning that the first derivatives, as well as the masses themselves, tend to the same values.

Discussion and conclusions are given in 3.12. Appendix 3.A gives details of how we perform the stability calculation and appendix 3.B derives the sine-Gordon equation from the Gross-Pitaevskii model, thus enabling a direct comparison of the two.

## 3.2 The Model

Consider two coupled quasi-one-dimensional Bose gases, with linear coupling achieved either via a double-well potential for a scalar Bose-Einstein condensate, or a pseudo spin-1/2 Bose-Einstein condensate with radio-frequency coupling of the spin components [126]. In quasi-one-dimensional geometry (when the ratio of chemical potential to transverse trap energy is small,  $\frac{\mu}{\hbar\omega_r} \ll 1$ ), and when  $\gamma$  of equation (2.6) is small, the physical system of interest can be modelled by two coupled Gross-Pitaevskii equations:

$$\begin{aligned} i\hbar\partial_t\Psi_1 &= -\frac{\hbar^2}{2m}\partial_{xx}\Psi_1 - \mu\Psi_1 + g|\Psi_1|^2\Psi_1 + g_c|\Psi_2|^2\Psi_1 - J\Psi_2, \\ i\hbar\partial_t\Psi_2 &= -\frac{\hbar^2}{2m}\partial_{xx}\Psi_2 - \mu\Psi_2 + g|\Psi_2|^2\Psi_2 + g_c|\Psi_1|^2\Psi_2 - J\Psi_1, \end{aligned} \quad (3.1)$$

where  $\mu$  is the chemical potential,  $g$  and  $g_c$  are self- and cross- non-linearity strengths and  $J > 0$  is the tunnelling/coupling strength (in general, if  $J$  is complex, its phase can be absorbed into the definitions of the wavefunctions). We can define dimensionless quantities:

$$\begin{aligned} \xi &= \frac{\sqrt{m\mu}}{\hbar}x, \quad \tau = \frac{\mu}{\hbar}t, \quad v_s = \sqrt{\frac{m}{\mu}}V_s, \quad z = \xi - v_s\tau, \\ \psi &= \sqrt{\frac{g+g_c}{\mu}}\Psi, \quad \nu = \frac{J}{\mu}, \quad \Gamma = \frac{g-g_c}{g+g_c}, \end{aligned} \quad (3.2)$$

where we have introduced  $V_s$ , the translation velocity of localized solutions (such as dark solitons and Josephson vortices). Here we shall only be interested in such uniformly translating solutions that depend only on  $z$ . Ultimately, we will compute properties of solutions with periodic boundary conditions by first solving the problem with open boundary conditions and then accounting for the counterflow, present in a ring geometry. Thus, the dimensionless equations in a frame moving at  $v_s$  are

$$\begin{aligned} -iv_s\partial_z\psi_1 &= -\frac{1}{2}\partial_{zz}\psi_1 - \psi_1 + \frac{1}{2}(1+\Gamma)|\psi_1|^2\psi_1 + \frac{1}{2}(1-\Gamma)|\psi_2|^2\psi_1 - \nu\psi_2, \\ -iv_s\partial_z\psi_2 &= -\frac{1}{2}\partial_{zz}\psi_2 - \psi_2 + \frac{1}{2}(1+\Gamma)|\psi_2|^2\psi_2 + \frac{1}{2}(1-\Gamma)|\psi_1|^2\psi_2 - \nu\psi_1. \end{aligned} \quad (3.3)$$

### 3.3 Analytical Solutions

Several exact solutions of (3.3) are known. The lowest-energy constant solution is  $\psi_1 = \psi_2 = \sqrt{1 + \nu}$ , which we shall refer to as the background. Dark-soliton solutions satisfy  $\psi = \psi_1 = \psi_2$  and are given by [59]

$$\psi = \sqrt{1 + \nu - v_s^2} \tanh \left[ \sqrt{1 + \nu - v_s^2} z \right] + i v_s. \quad (3.4)$$

This corresponds to an identical soliton in each of the strands. The maximal velocity at which a dark soliton can travel is the Bogoliubov speed of sound,  $v_B = \sqrt{1 + \nu}$ .

Zero-velocity Josephson vortices exist for  $0 < \nu < 1/3$  and satisfy  $\psi_1 = \psi_2^* = \psi$ , where

$$\psi = \sqrt{1 + \nu} \tanh(2\sqrt{\nu}z) + i\sqrt{1 - 3\nu} \operatorname{sech}(2\sqrt{\nu}z). \quad (3.5)$$

At  $\nu = 1/3$  the Josephson vortex bifurcates from the dark soliton excitation. The antivortex, possessing opposite circulation to (3.5), is obtained by taking the complex-conjugate of  $\psi$ .

The vortex nature of this solution can be seen by examining the phase profiles along the two strands (for convenience, we will imagine the two components separated in space, as in the double-well potential scenario of Fig. 3.1). Defining  $\psi_k = \sqrt{n_k(z)} \exp i\phi_k(z)$ , if one traces a closed loop around the center of the system (lying at  $z = 0$  and half way between the two strands), at the position of the vortex core, the phase continuously changes from 0 to  $2\pi$ , as can be seen in Fig. 3.2 (b). Nevertheless, the phases of both strands are equal far away from the excitation. The distinctive features of this stationary vortex are an equal dip in the density and an equal-but-opposite phase step in each component.

Note that both the analytical dark soliton & Josephson vortex solutions given above are independent of  $\Gamma$ .

#### 3.3.1 The Manakov Case

In the case when  $\Gamma = 0$ , one can transform the Gross-Pitaevskii equations to an integrable model known as the Manakov system. In this limit, a whole family of solutions can be found analytically [131] – we shall refer to these as the Manakov solutions, as they are related to Manakov's, but are somewhat different due to a non-zero  $\nu$ . This is achieved as follows. Defining  $\chi_{1,2} = \frac{1}{\sqrt{2}}(\psi_2 \pm \psi_1)$ , we rewrite equations (3.3) for the new variables:

$$-i v_s \partial_z \chi_k = -\frac{1}{2} \partial_{zz} \chi_k - (1 \pm \nu) \chi_k + \frac{1}{2} (|\chi_1|^2 + |\chi_2|^2) \chi_k, \quad (3.6)$$

where the two different signs in front of  $\nu$  are to be taken with the two different indices,  $k = 1, 2$ . We take a trial solution of the form found in [131] (all parameters are assumed to be real),

$$\chi_1 = \alpha i + \beta \tanh(\eta z), \quad \chi_2 = \delta \operatorname{sech}(\eta z) e^{i\varepsilon z}, \quad (3.7)$$

substitute it into (3.6) and solve the resulting non-linear equations for the unknown parameters:

$$\begin{aligned} \alpha &= \sqrt{\frac{1+\nu}{2\nu}} v_s, \\ \beta &= \sqrt{\frac{(4\nu - v_s^2)(1+\nu)}{2\nu}}, \\ \eta &= \sqrt{4\nu - v_s^2}, \\ \delta &= \sqrt{\frac{(4\nu - v_s^2)(1-3\nu)}{2\nu}}, \\ \varepsilon &= v_s. \end{aligned} \quad (3.8)$$

In fact,  $\chi_2$  may be multiplied by an arbitrary phase factor,  $e^{i\theta}$ , and the resulting solution still satisfies the differential equations. Transforming back to the  $\psi$ -variables gives

$$\psi_{1,2} = \frac{1}{\sqrt{2}} (\alpha i + \beta \tanh(\eta z) \pm e^{i\theta} \delta \operatorname{sech}(\eta z) e^{i\varepsilon z}). \quad (3.9)$$

Notice that for the parameters in (3.8) to be real (and the solution to be non-trivial) we need  $\nu < 1/3$  and  $v_s^2 < 4\nu$ .

All three analytical solutions presented above are illustrated in Fig. 3.2.

### 3.4 Useful Observables

Let us now define several useful quantities that shall be evaluated later on for the numerical solutions. Energy (scaled by  $\frac{\hbar\mu^2}{\sqrt{\mu m}(g+g_c)}$  in our dimensionless units) is given by

$$\begin{aligned} E &= \int_{-L}^L dz \sum_{k=1,2} \left\{ \frac{1}{2} |\partial_z \psi_k|^2 - |\psi_k|^2 - \nu \psi_k^* \psi_{3-k} + \frac{1}{4} (1+\Gamma) |\psi_k|^4 \right\} \\ &\quad + \frac{1}{2} (1-\Gamma) |\psi_1|^2 |\psi_2|^2. \end{aligned} \quad (3.10)$$

The excitation energy is then  $E_s = E_x - E_0$ , where  $E_x$  is the energy of the excited state and  $E_0 = -2L(1+\nu)^2$  is the background energy. Momentum is scaled by  $\frac{\hbar\mu}{g+g_c}$ ,

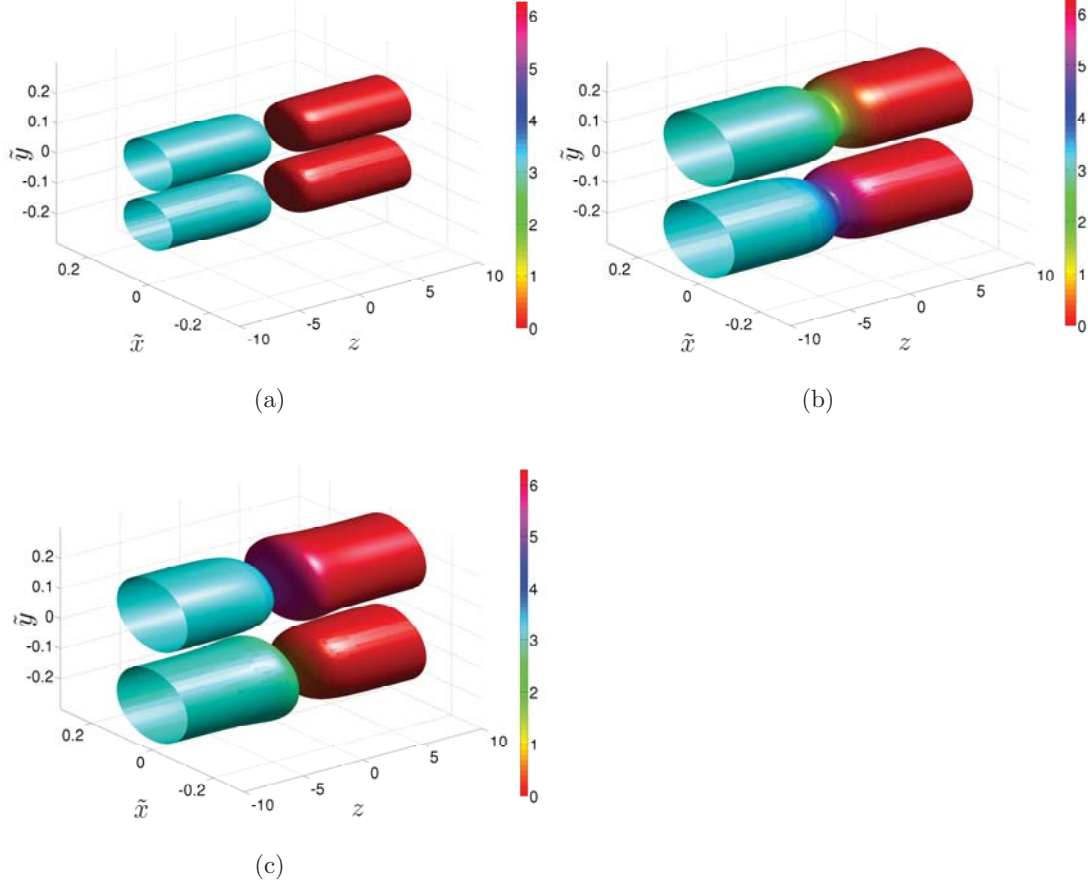


Figure 3.2: The density (related to the width of the tubes) and phase (encoded as a colour map) of three analytical solutions with various parameters. The two densities  $n_{1,2}$  are taken to be functions of  $z$ , and we define  $N_k = n_k(z) \exp[-\frac{(\tilde{y} \pm 0.15)^2 + \tilde{x}^2}{0.1^2}]$ . The plots show isosurfaces of  $N_k$  at the function value of 0.3. (a) stationary dark soliton:  $\Gamma = 1, \nu = 0.15, P_c = 2\pi(1 + \nu)$ , (b) stationary Josephson vortex:  $\Gamma = 1, \nu = 0.15, P_c = 2\pi(1 + \nu)$ , (c) stationary Manakov solution:  $\Gamma = 0, \nu = 0.15, P_c = 2\pi(1 + \nu)$ , with  $\theta = -\pi/4$ .

and

$$\begin{aligned}
 \Delta P &= \int_{-L}^L (p_1 - p_2) dz, \\
 P_s &= \int_{-L}^L (p_1 + p_2) dz, \\
 p_k &= -\frac{i}{2} \left[ \psi_k^* \frac{d\psi_k}{dz} - \psi_k \frac{d\psi_k^*}{dz} \right], \\
 \Delta\phi &= \phi_1(-L) - \phi_1(L) = \phi_2(-L) - \phi_2(L), \\
 P_{cf} &= 2(1 + \nu)\Delta\phi, \\
 P_c &= P_s + P_{cf},
 \end{aligned} \tag{3.11}$$

where  $\Delta P$  is the angular momentum,  $P_s$  is the physical momentum of the soliton (or vortex),  $p_k$  is the momentum density of each field,  $\Delta\phi$  is the phase step across the excitation,  $P_{cf}$  is the counter-flow momentum (present because we are interested in the periodic boundary condition case), and  $P_c$  is the canonical momentum. In addition, the missing particle number (scaled by  $\frac{\hbar\mu}{\sqrt{\mu m}(g+g_c)}$ ) in the excitation is

$$N_d = \int_{-L}^L n_1(z) + n_2(z) dz - 4(1 + \nu)L, \quad (3.12)$$

where  $n_k(z) = |\psi_k(z)|^2$  are the particle densities in the two Bose-Einstein condensate strands. Another property of quasi-particles that can be defined at extrema of the dispersion relation is the inertial mass, given by equation (2.23).

### 3.4.1 Analytical Expressions for Dark Solitons

We can calculate the defined observables for dark solitons analytically: the excitation energy, angular momentum, phase step, canonical momentum, and missing particle number are

$$\begin{aligned} E_s &= \frac{8}{3} (1 + \nu - v_s^2)^{3/2}, \\ \Delta\phi &= \pi - 2 \tan^{-1} \left[ \frac{v_s}{\sqrt{1 + \nu - v_s^2}} \right], \\ P_c &= 2\pi(1 + \nu) - 4v_s \sqrt{1 + \nu - v_s^2} - 4(1 + \nu) \tan^{-1} \left( \frac{v_s}{\sqrt{1 + \nu - v_s^2}} \right), \\ N_d &= -4\sqrt{1 + \nu - v_s^2}. \end{aligned} \quad (3.13)$$

The excitation energy and missing particle number vanish when the soliton reaches the Bogoliubov speed  $v_B$ . The phase step is  $\pi$  for a stationary dark soliton and reaches the extremal values of  $0, 2\pi$  at  $v_s = \pm v_B$ . The limits of  $P_c$  are  $P_c = 0, 4\pi(1 + \nu)$ . Clearly, the angular momentum is zero, and the inertial mass is found to be  $m_I = -8\sqrt{1 + \nu}$ .

### 3.4.2 Analytical Expressions for Manakov Solutions

Likewise, it is possible to calculate all the quantities of interest for the  $\Gamma = 0$  analytical Manakov solutions: the excitation energy, phase step, canonical momentum,

and missing particle number are

$$\begin{aligned}
E_s &= 4\sqrt{4\nu - v_s^2} \left[ \frac{2}{3}(4\nu - v_s^2) - (3\nu - 1) \right], \\
\Delta P &= 2\pi\sqrt{1+\nu}\sqrt{1-3\nu} \operatorname{sech} \left( \frac{\pi v_s}{2\sqrt{4\nu - v_s^2}} \right) \sin \theta, \\
\Delta\phi &= \pi - 2 \tan^{-1} \left[ \frac{v_s}{\sqrt{4\nu - v_s^2}} \right], \\
P_c &= 2\pi(1+\nu) - 4 \left\{ v_s \sqrt{4\nu - v_s^2} + (1+\nu) \tan^{-1} \left[ \frac{v_s}{\sqrt{4\nu - v_s^2}} \right] \right\}, \\
N_d &= -4\sqrt{4\nu - v_s^2}.
\end{aligned} \tag{3.14}$$

The inertial mass evaluates to  $m_I = -2\frac{5\nu+1}{\sqrt{\nu}}$ . Note that the limits of  $P_c$  are  $P_c = 0, 4\pi(1+\nu)$ , the same as for dark solitons.

### 3.4.3 Variational Calculation for Josephson Vortices

It is possible to find a variational approximation for Josephson vortices near  $v_s = 0, P_c = 2\pi(1+\nu)$ , i.e. in the immediate vicinity of the known analytical solution (3.5). We take the variational ansatz

$$\psi_{1,2} = \sqrt{1+\nu} \left\{ i \sin(\alpha) + \cos(\alpha) \tanh(Az) \pm i B_{1,2} \operatorname{sech}(Az) e^{iz\varepsilon} \right\}, \tag{3.15}$$

a form general enough to capture dark solitons, zero-velocity Josephson vortices and Manakov solitons. One then has to evaluate  $\mathcal{L} = E_s - v_s P_c$  for this variational guess and take away  $\mathcal{L}$  for the background state, resulting in the difference,  $\Delta\mathcal{L}$ . Differentiating  $\Delta\mathcal{L}$  with respect to all five variational parameters  $(A, \alpha, B_1, B_2, \varepsilon)$  and setting the resulting expressions to zero, we obtain a system of five coupled non-linear equations. These are quite complicated, and a direct solution is impractical. Instead, we linearise the equations in  $v_s$ : we set  $A = A_0 + v_s \tilde{A}$ ,  $\varepsilon = \varepsilon_0 + v_s \tilde{\varepsilon}$ ,  $\alpha = \alpha_0 + v_s \tilde{\alpha}$ ,  $B_{1,2} = B_0 + v_s \tilde{B}_{1,2}$ , where the zeroth order parameters are chosen to correspond with the solution (3.5):  $A_0 = 2\sqrt{\nu}$ ,  $B_0 = \sqrt{\frac{1-3\nu}{1+\nu}}$ ,  $\varepsilon_0 = \alpha_0 = 0$ . The zeroth-order terms in the linearised equations thus cancel, and it remains to set the first order terms (in  $v_s$ ) to zero. Introducing  $\tilde{B}_\pm = \tilde{B}_1 \pm \tilde{B}_2$ , we replace the equations resulting from  $d\Delta\mathcal{L}/dB_{1,2} = 0$  by the sum and difference of these two equations. The five equations we must now solve decouple into two sets: two- and three-coupled

equations. The solutions are:  $\tilde{A} = \tilde{B}_+ = 0$ , and

$$\begin{aligned}\Omega &= -48 \left\{ -\Gamma^2 + 2(\Gamma - 2)\Gamma\nu + \nu^2 [24 + \Gamma(44 + 3\Gamma)] \right\} [3\nu + \Gamma(6\nu - 2)] \\ &\quad - 4\pi^2 [2\nu + \Gamma(3\nu - 1)] [3\Gamma\nu(7 - 29\nu) - 54\nu^2 + 5\Gamma^2(1 + \nu)(3\nu - 1)] \\ &\quad + 3\Gamma\pi^4(1 + \nu)(\Gamma - 2\nu - 3\Gamma\nu)^2, \end{aligned} \quad (3.16)$$

$$\begin{aligned}\tilde{\alpha} &= \sqrt{\nu} \left\{ 216\nu^2(\pi^2 - 8) + 6\Gamma\nu [168 - 888\nu + 4\pi^2(19\nu - 5) + \pi^4(1 + \nu)] \right. \\ &\quad \left. + \Gamma^2(3\nu - 1) [-96(1 + 13\nu) + 4\pi^2(13\nu - 5) + 3(1 + \nu)\pi^4] \right\} / \Omega, \end{aligned} \quad (3.17)$$

$$\tilde{\varepsilon} = 72(1 + 2\Gamma)\nu^2 [6\nu(\pi^2 - 8) + \Gamma(3\nu - 1)(3\pi^2 - 32)] / \Omega, \quad (3.18)$$

$$\tilde{B}_- = 144\Gamma(1 + 2\Gamma)\nu^{3/2}\pi(3\nu - 1) / \Omega. \quad (3.19)$$

Linearising the variational equations in  $v_s$  is an approximation that is of the same order as keeping terms up to  $\mathcal{O}(v_s^2)$  in  $E_s$  (the excitation energy) and  $\mathcal{O}(v_s)$  in  $P_c$  (the total momentum). Making such an expansion we can calculate the inertial mass  $m_I = 2 \frac{dE_s}{d(v_s^2)}$ , to obtain

$$\begin{aligned}m_I &= 8\sqrt{\nu} \left\{ 48 [\Gamma + 2\nu(3 + \Gamma) + \nu^2(30 + 49\Gamma)] [3\nu + \Gamma(6\nu - 2)] \right. \\ &\quad - 3\Gamma(1 + \nu)^2\pi^4(2\nu + \Gamma\pi^4(3\nu - 1)) - 4\pi^2 [27\nu^2(1 + 5\nu) + 3\Gamma\nu(\nu(137\nu - 14) - 7) \\ &\quad \left. + \Gamma^2(5 + \nu(\nu(309\nu - 133) - 5))] \right\} / \Omega, \end{aligned} \quad (3.20)$$

which is plotted in Fig. 3.11 alongside the numerical results. Using the zero-velocity solution (3.5), we can compute the excitation energy and the missing particle number at  $v_s = 0$  as  $E_s = \frac{8}{3}(3 - \nu)\sqrt{\nu}$  and  $N_d = -8\sqrt{\nu}$ , and extract the speed of light (see later) as  $c = \sqrt{\frac{E_s}{m_I}}$ ;  $N_d/m_I$  from this calculation is added to Fig. 3.13 and  $c$  to Figs. 3.15 and 3.16. Note that Ref. [129] predicted  $N_d/m_I = (5\nu - 1)/(1 + \nu)$ , which is also added to Fig. 3.13 for comparison.

### 3.5 Numerical Methods

We work in the MATLAB environment, making use of the boundary value problem solver `bvp5c.m` (a finite difference algorithm). We would like to numerically solve the case of open boundary conditions where  $z \in (-\infty, \infty)$ . Necessarily, the system is truncated to a finite size,  $z \in [-L, L]$ , where  $L$  is large enough for the solutions to settle in to the constant background. The equations are written as a first order system, separating out the real and complex parts. As boundary conditions, we require zero first derivatives at  $\pm L$  for both fields. The absolute and relative tolerances of the solver are set to  $10^{-8}$ ; if this accuracy cannot be reached with the chosen system size,  $L$  is increased. After a solution is obtained, we check that the densities  $n_k$  at  $\pm L$  are within 0.01 of the background density and that the phases of the two fields satisfy  $|\phi_k(\pm L) - \phi_{3-k}(\pm L)| \leq 0.01$ . If either condition is not fulfilled,  $L$  is increased

and the solver is called again.

In order to find a solution, one needs to provide the solver with a guess for the wavefunctions. An obvious way to find translating Josephson vortices is to start from the known zero velocity Josephson vortices and slowly increase velocity, using each subsequent solution as a guess for the next (so-called *continuation* in velocity). Although this method works in general, below the critical coupling (in the region where the dispersion relation has three extrema) we find that numerically, the solver is unable to follow the solution past the maxima of the dispersion relation, located on either side of the zero-velocity minimum. The rest of the dispersion relation can be found by first continuing the stationary solution in velocity at some tunnelling value *above* the critical point (to obtain a full dispersion relation), and then continuing each point on this dispersion relation down in coupling strength. This process is explained further in section 3.6. Except for this particular case, solutions can be followed in any parameter with no difficulty, as described in detail below.

In addition, we found that out of the entire  $\theta$ -spectrum of analytic Manakov solutions at  $\Gamma = 0$ , only the  $\theta = 0, \pm\pi$  and  $\theta = \pm\pi/2$  solutions extend to positive, finite  $\Gamma$ . When  $\Gamma = 0$ , the stationary Manakov solution is identical to the zero-velocity Josephson vortex solution if  $\theta = -\pi/2$ . Indeed, following the  $\theta = -\pi/2$  solution from  $\Gamma = 0$  to  $\Gamma > 0$  yields the Josephson vortex branch obtained by following Josephson vortices from  $\Gamma = 1$  to  $\Gamma < 1$ . On the other hand, following the  $\theta = 0$  solution from  $\Gamma = 0$  to  $\Gamma > 0$  gives an entirely new branch, which we shall refer to as *staggered solitons*, due to the fact that the density minima (and the associated positions of the phase jumps) are off-shifted from each other along the strands (see Fig. 3.3 (e)).

### 3.6 Visual Inspection of Numerical Solutions

In order to visualize the solutions, we show surface plots similar to those of Fig. 3.2, where the width of the two cylinders is related to the density of the two fields (see the caption of Fig. 3.3) and the phase is encoded as a colour map. We choose representative examples that illustrate the different solutions in all distinct regions of parameter space.

Figure 3.3 (a) shows a moving Josephson vortex for  $\Gamma = 1, \nu = 0.15$ . In all cases for  $\Gamma = 1, \nu \geq 0.15$  the solutions were obtained by starting from the known zero-velocity Josephson vortices (3.5) and increasing velocity at a fixed  $\nu$ . With reference to Fig. 3.5, we followed the corresponding Josephson vortex solution (blue dashed lines) from the origin out to positive velocities until the branch terminated.

Figure 3.3 (b) shows a stationary Josephson vortex at the maximum of the dispersion relation for  $\Gamma = 1, \nu = 0.005$  and panel (c) shows a moving Josephson vortex for

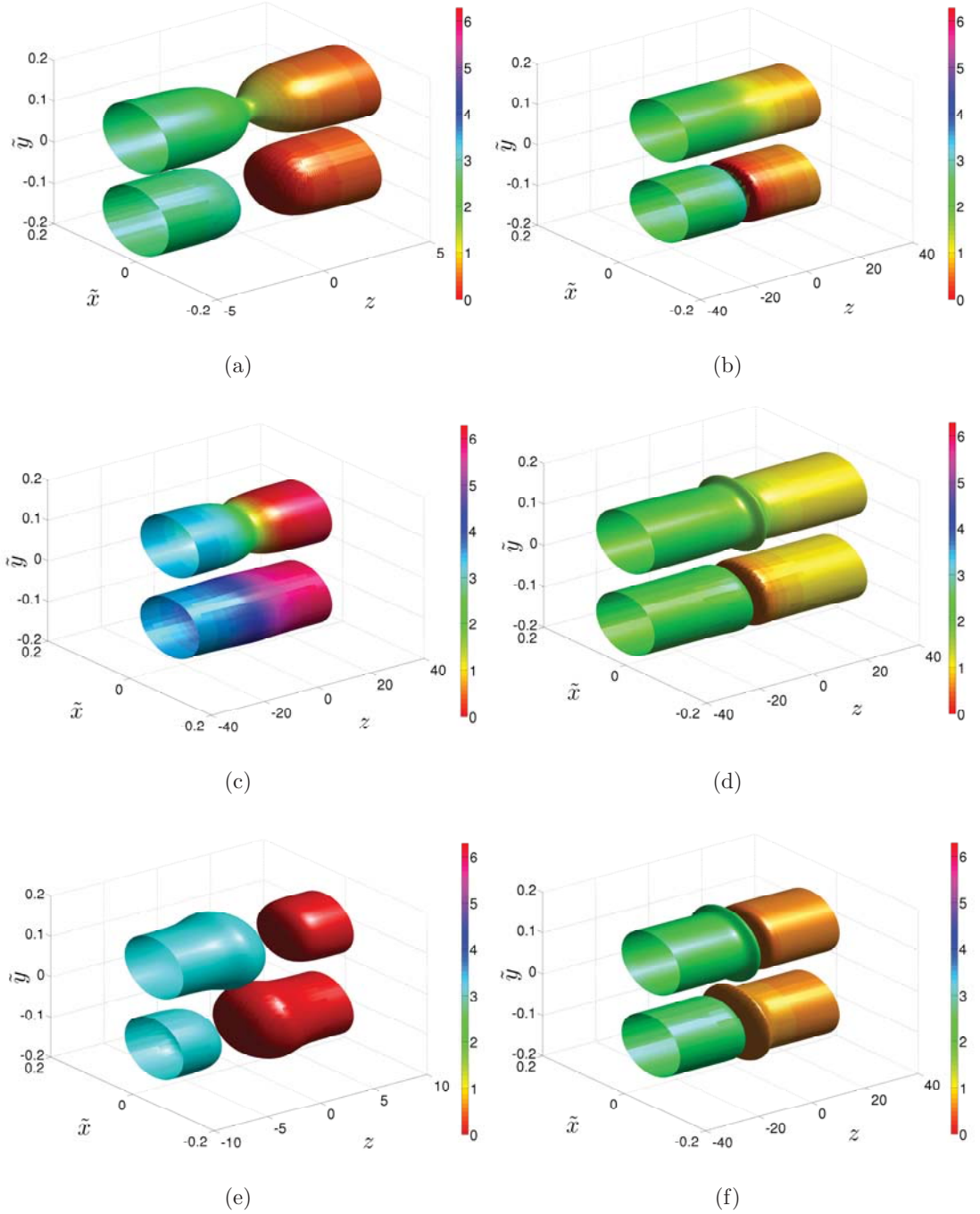


Figure 3.3: The density (related to the width of the tubes) and phase (encoded as a colour map) of six numerical solutions with various parameters. The two densities  $n_{1,2}$  are taken to be functions of  $z$ , and we define  $N_k = n_k(z) \exp[-\frac{(\tilde{y} \pm 0.1)^2 + \tilde{x}^2}{0.1^2}]$ . The plots show isosurfaces of  $N_k$  at the function value of 0.6. (a) moving Josephson vortex:  $\Gamma = 1, \nu = 0.15, P_c = 1.34\pi$ , (b) stationary Josephson vortex maximum:  $\Gamma = 1, \nu = 0.005, P_c = 1.05\pi$ , (c) moving Josephson vortex:  $\Gamma = 1, \nu = 0.005, P_c = 2.17\pi$ , (d) moving Josephson vortex:  $\Gamma = 0.5, \nu = 0.005, P_c = 0.49\pi$ , (e) stationary staggered soliton:  $\Gamma = 0.5, \nu = 0.005, P_c = 2\pi(1 + \nu)$ , (f) moving staggered soliton:  $\Gamma = 0.5, \nu = 0.005, P_c = 0.86\pi$ .

the same  $\Gamma$  and  $\nu$ . The solutions for  $\Gamma = 1, \nu < 0.15$  were obtained by starting from the previously-calculated wavefunctions at  $\nu = 0.15$ , and at each velocity gradually decreasing  $\nu$ . With reference to Fig. 3.6, the relevant Josephson vortex curves are plotted as dashed lines. Continuing the Josephson vortex branch down in  $\nu$  from  $\nu = 0.15$  gave us the sections plotted in blue. Then, at a given  $\nu$ , we continued the blue Josephson vortex segment to negative  $v_s$ , thus obtaining the black parts of the curves. Separately, at a fixed  $\nu$ , we also started from the zero-velocity Josephson vortex (3.5) and increased  $v_s$ , which yielded the green segments of the curves.

Note that, as shown in Fig. 3.4 (a), as  $\nu$  goes to zero, the Josephson vortex dispersion relation is “split in half” as  $E_s(P_c = 2\pi(1 + \nu))$  drops to zero. At  $\nu = 0$  each “wing” of the dispersion relation corresponds to a dark soliton in one of the two Bose-Einstein condensate strands and the uniform background solution in the other. This can be seen clearly in Fig. 3.3 (b) where the density of one condensate is practically flat and the other has a strong dip. We therefore refer to the quasi-particles around the maxima of the Josephson vortex dispersion relation as “Josephson vortex maxima”, and interpret them as single-strand dark solitons. Conversely, the dark soliton dispersion relation consists of a dark soliton in each of the Bose-Einstein condensate strands and the Josephson vortex dispersion relation merges with it as  $\nu \rightarrow 1/3$ .

Physically, at the maxima of the dispersion relation, the vortex core can be thought of as exactly crossing one of the Bose-Einstein condensate strands as it moves out (perpendicularly to the Bose-Einstein condensates) from in between the two strands.

Figure 3.3 (d) shows an example of a moving Josephson vortex for  $\Gamma = 0.5, \nu = 0.005$ . The solutions for  $\nu = 0.005, \Gamma < 1$  were obtained by starting from the previously-calculated wavefunctions at  $\nu = 0.005, \Gamma = 1$ , and at each velocity gradually decreasing  $\Gamma$ . Once part of the dispersion relation was available at each  $\Gamma$  value, if necessary, we could complete it by following in  $v_s$ . In Fig. 3.7, the relevant Josephson vortex curves are plotted as dashed lines.

Figure 3.3 (e) shows a stationary staggered soliton for  $\Gamma = 0.5, \nu = 0.005$  and panel (f) shows a moving staggered soliton for the same  $\Gamma$  and  $\nu$ . These solutions were obtained by starting from the analytical Manakov wavefunctions at  $\nu = 0.005, \Gamma = 0$ , and at each velocity gradually increasing  $\Gamma$ . This gave us the central part of the dispersion relation at all  $\Gamma$  values, which we then extended in  $v_s$  at each constant  $\Gamma$ . In Fig. 3.7, the relevant curves are plotted as dash-dotted lines.

### 3.7 Dispersion Relation and Other Observables

Figure 3.4 panels (a), (c), (e) show the dispersion relations of dark solitons, Josephson vortices and of the staggered solitons, the latter only for  $\Gamma < 1$ . This is because the staggered solitons branch completely merges with dark solitons at about  $\Gamma = 0.975$ . Likewise, the Josephson vortex dispersion relation overlaps with the dark soliton dispersion relation at  $\nu = 1/3$ . From panel (a) it is clear that for  $\Gamma = 1$ , the Josephson vortex dispersion relation changes concavity at  $P_c = 2\pi(1 + \nu)$  at around  $\nu \approx 0.14 - 0.15$ . The same process is observed in reverse as  $\Gamma \rightarrow 0^+$  with  $\nu \leq 0.14$ , as we move from panel (c) to (e). At  $\Gamma = 0$ , the equations reduce to the Manakov case, which is solved analytically in sections 3.3.1 and 3.4.2, and indeed the Manakov solitons have a dispersion relation with a single central maximum.

In Fig. 3.4 panels (b), (d), (f) we compare the energy of dark solitons, Josephson vortices, Josephson vortex maxima and staggered solitons at the extrema of the dispersion relations (which necessarily implies at zero velocity) as a function of  $\nu$ . In (b), for  $\Gamma = 1$ , the Josephson vortex and Josephson vortex maximum lines merge at around  $\nu \approx 0.14 - 0.15$ . It may be expected that this bifurcation point depends on  $\Gamma$ , and this is indeed found to be the case. Panel (d) shows that at  $\Gamma = 0.5$ , the bifurcation point has now moved from  $\nu = 0.1413$  to around  $\nu = 0.1$ . Finally, at  $\Gamma = 0$  in panel (f), only the dark soliton-Josephson vortex bifurcation remains: Josephson vortices join the dark soliton line at  $\nu = 1/3$ , which is independent of  $\Gamma$ .

Note that in (d), both the Josephson vortex and the Josephson vortex maximum solutions are stable, but the Josephson vortex maxima have  $P_c \neq 2\pi(1 + \nu)$ , unlike all other solutions shown. The staggered soliton solutions only exist below about  $\nu = 0.125$  where they are unstable, while the higher energy dark solitons are stable. For  $\nu > 0.125$ , staggered solitons disappear and dark solitons become unstable.

The energy, missing particle number, angular momentum and phase step are plotted as a function of velocity in Figs. 3.5-3.7 for the three parameter sets that were used in Fig. 3.3. The colour code refers to how the solutions were obtained (also see section 3.6): segments in blue, black, light-green and dark-green were calculated from solutions found by the solver, and segments in cyan, red, magenta and purple are reflections of the first four data sets. Note that we assumed the dispersion relation was symmetric, as in the thermodynamic limit there is nothing to break left-right symmetry, and thus the same excitation translating in either direction would cost the same amount of energy. The change in concavity of the Josephson vortex branch as  $\nu$  goes down through  $\nu \approx 0.14 - 0.15$  in Fig. 3.4 (a) is seen as the development of a loop in velocity-energy plots (compare panels (a) of Figs. 3.5 and 3.6).

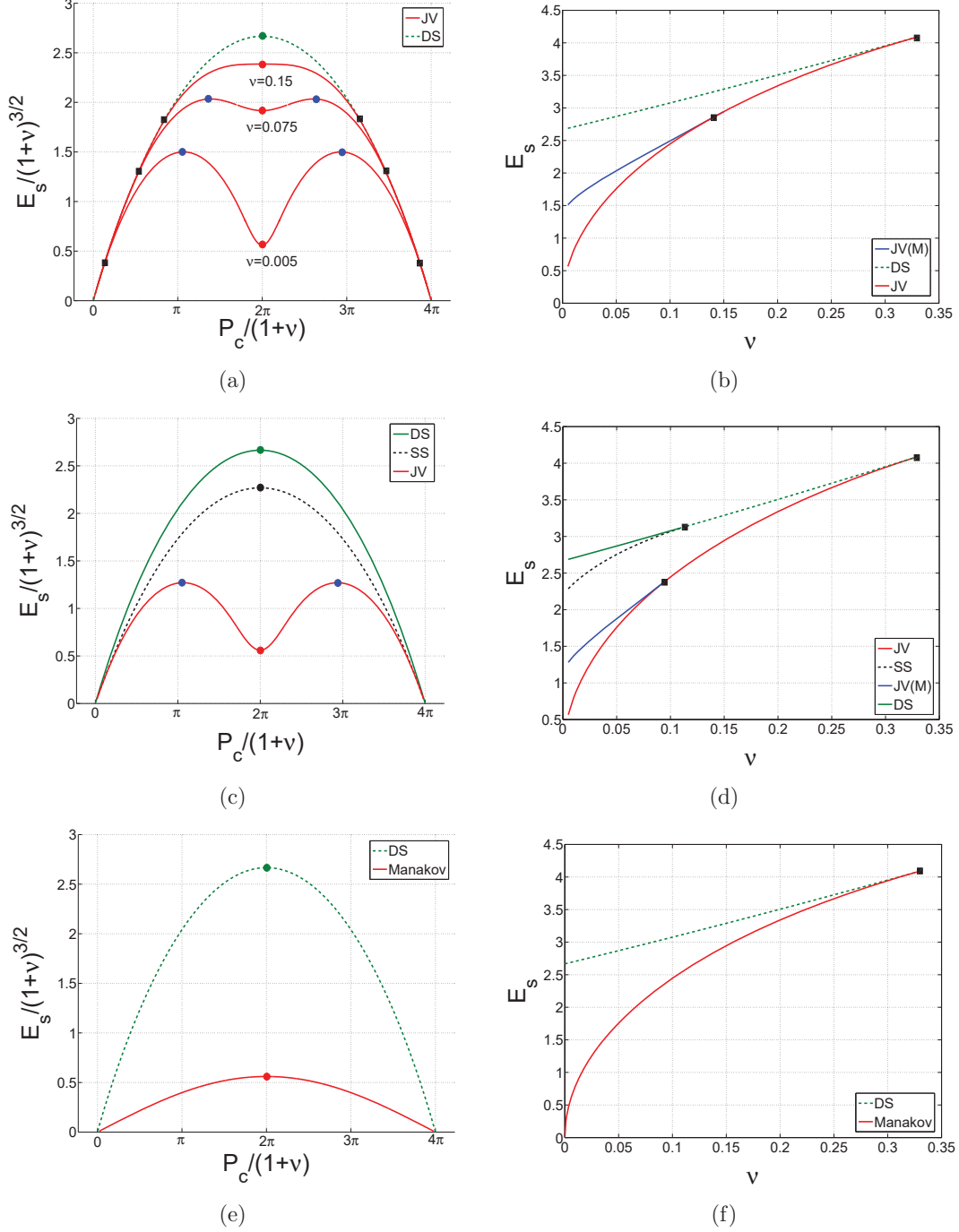


Figure 3.4: Dispersion relations showing all found solutions (a, c, e) and energy at the extrema of the dispersion relations as a function of  $\nu$  (b, d, f). The green curve is the dark soliton (labelled “DS”) branch, Josephson vortex (labelled “JV”) solutions are plotted in red, Josephson vortex maximum (labelled “JV(M)”) in blue and the staggered solitons (labelled “SS”) branch in black. Solid lines indicate stable solutions and dashed lines indicate unstable. Circular markers show the extreme points of the dispersion relations while square markers indicate bifurcation points. (a)  $\Gamma = 1$ . The three red lines show the Josephson vortex branch for different  $\nu$  values, as indicated next to each curve. (b)  $\Gamma = 1, v_s = 0$ . (c)  $\Gamma = 0.5, \nu = 0.005$ . (d)  $\Gamma = 0.5, v_s = 0$ . (e)  $\Gamma = 0, \nu = 0.005$ . (f)  $\Gamma = 0, v_s = 0$ . In the last two panels, the red line is the analytical Manakov branch (numerical Josephson vortices and staggered solitons at  $\Gamma = 0$  overlap with this curve).

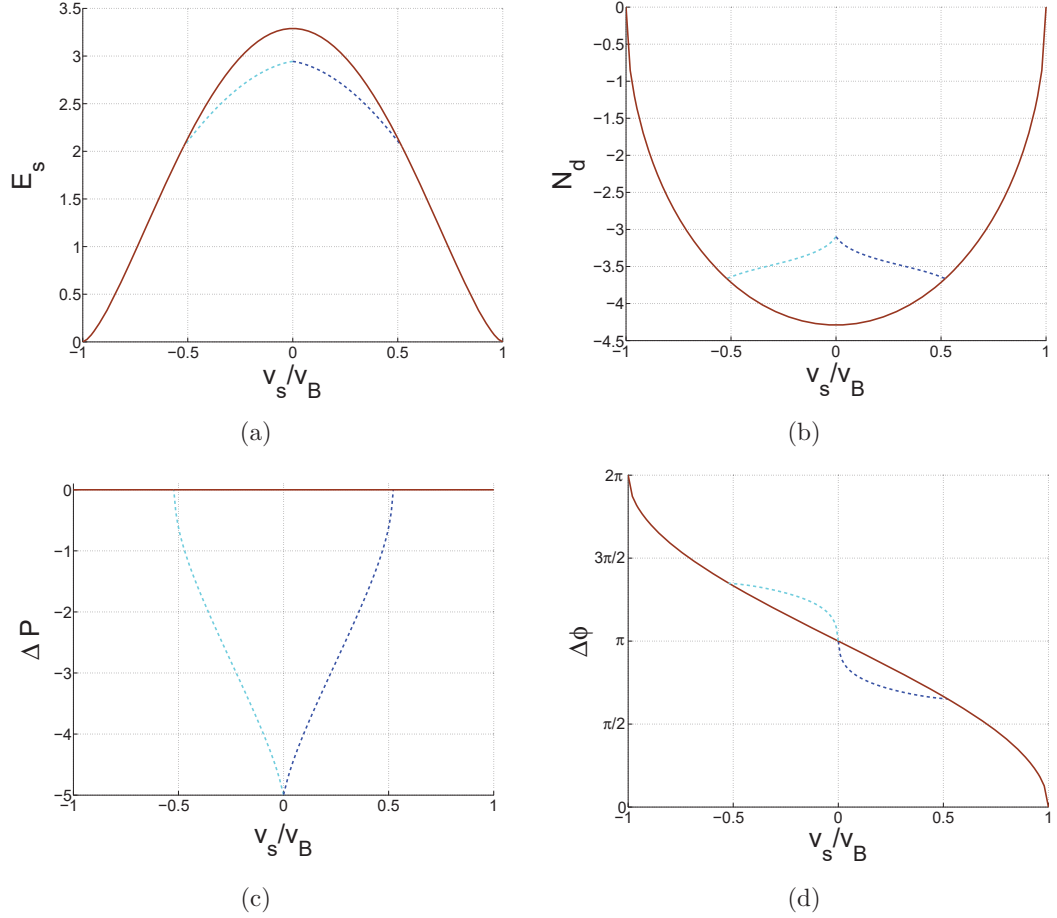


Figure 3.5: Energy (a), missing particle number (b), angular momentum (c) and phase step (d) as a function of velocity for  $\Gamma = 1, \nu = 0.15$ . Dashed line – Josephson vortices (numerical), solid line – dark solitons (analytical). The segment in blue was calculated from solutions found by the solver, and the segment in cyan is a reflection of the first data set (assuming symmetry). This parameter set is the same as was used in Fig. 3.3 (a).

### 3.8 Parameter Regimes, Types of Excitations and Their Stability

Dark soliton solutions are analytically known for all parameter values. We have numerically obtained all translating Josephson vortex solutions in two parameter regimes:  $\Gamma = 1, 0.005 \leq \nu \leq 0.33$  and  $\nu = 0.005, 0 \leq \Gamma \leq 1$ . Staggered solitons were found in the second regime; this branch always has zero angular momentum and energy higher than Josephson vortices but lower than dark solitons. It is understood to be a transitory state through which Josephson vortices are able to reverse their circulation. Wherever the staggered soliton branch does not exist, dark solitons perform the role of the transitory state.

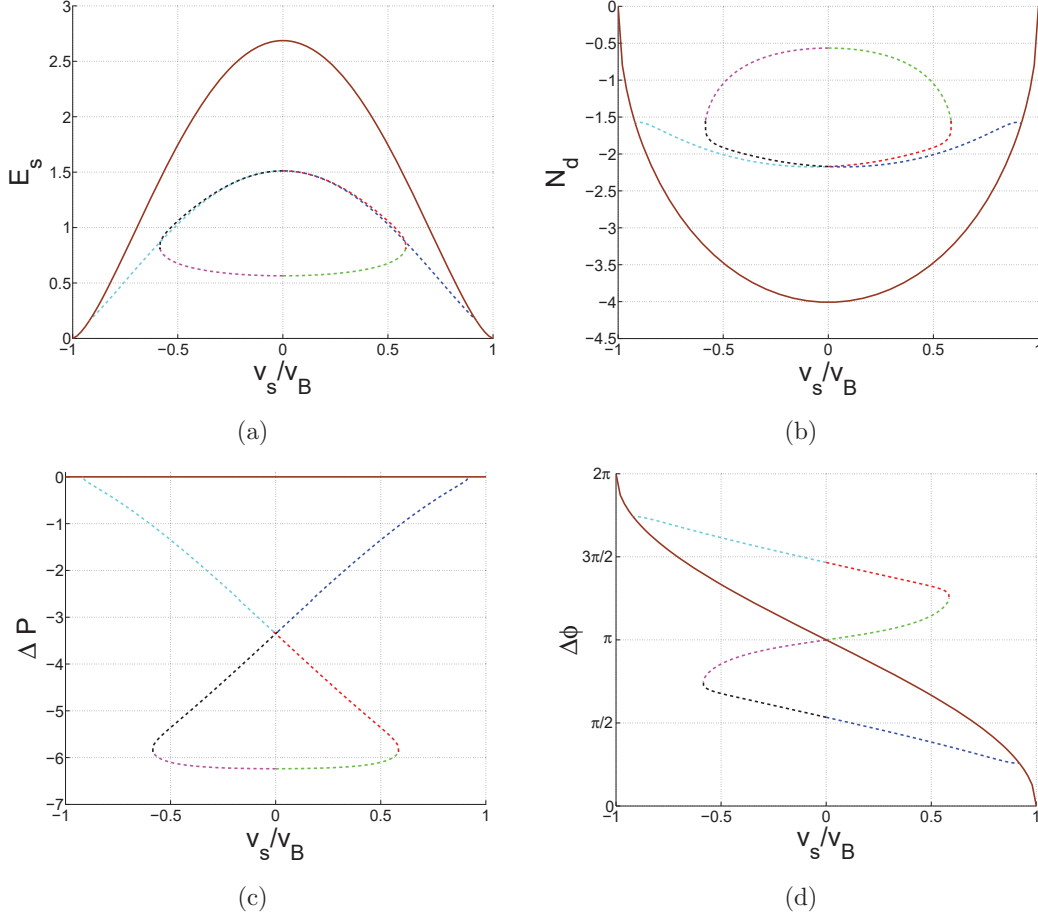


Figure 3.6: Energy (a), missing particle number (b), angular momentum (c) and phase step (d) as a function of velocity for  $\Gamma = 1$ ,  $\nu = 0.005$ . Dashed line – Josephson vortices (numerical), solid line – dark solitons (analytical). Segments in blue, black and green were calculated from solutions found by the solver, and segments in cyan, red and magenta are reflections of the first three data sets (assuming symmetry). This parameter set is the same as was used in Fig. 3.3 (b) and (c).

When  $\Gamma = 1$ , Kaurov and Kuklov [127] found that zero-velocity Josephson vortex solutions only exist for  $\nu < 1/3$ , at which point Josephson vortices merge into dark solitons. In fact, this happens at all velocities, but the merging point depends on  $v_s$ . A more natural point of view for us will be to say that at any given tunnelling value, the Josephson vortex and dark soliton dispersion relations merge smoothly at some critical momentum (associated with some critical velocity), and for larger momenta, the Josephson vortex branch does not exist. This is illustrated in Fig. 3.8 (a) where we plot the maximal velocity reached by the Josephson vortex branch (the critical velocity) as a function of  $\nu$ . We found that, with  $\Gamma = 1$ , whenever Josephson vortices and dark solitons coexist, Josephson vortices are stable and dark solitons are unstable and when Josephson vortices cease to exist, dark solitons become stable. This fact was exploited in Ref. [129] where the authors present a similar plot to

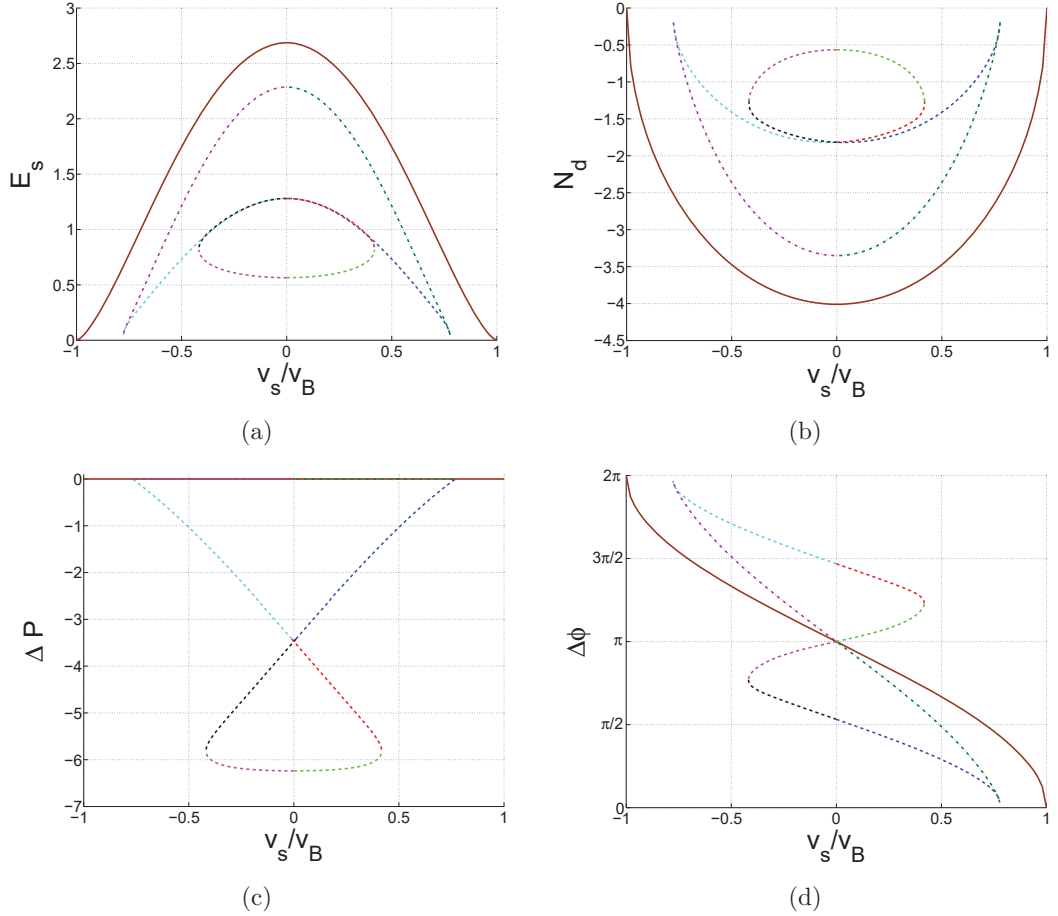
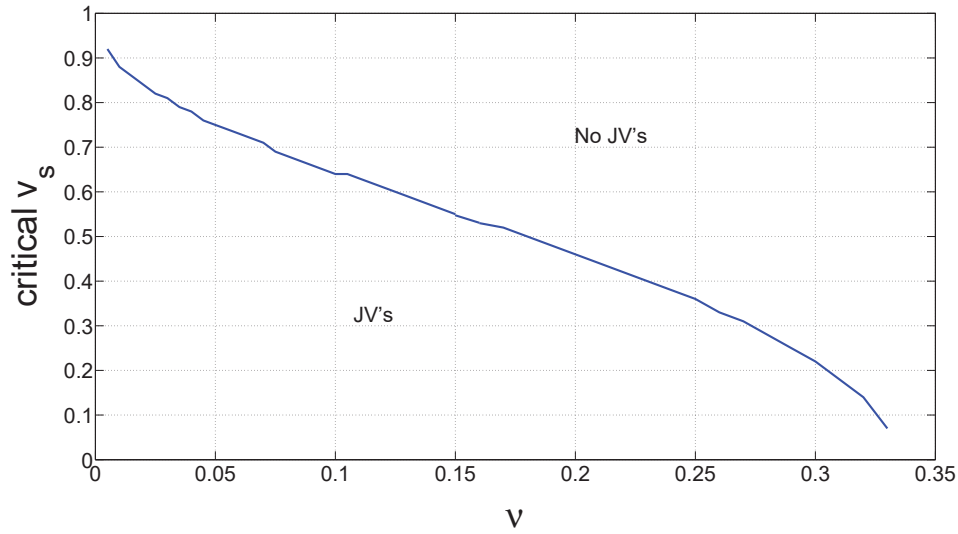


Figure 3.7: Energy (a), missing particle number (b), angular momentum (c) and phase step (d) as a function of velocity for  $\Gamma = 0.5, \nu = 0.005$ . Dashed line – Josephson vortices (numerical), dash-dotted line – staggered solitons (numerical), solid line: dark solitons (analytical). Segments in blue, black, light-green and dark-green were calculated from solutions found by the solver, and segments in cyan, red, magenta and purple are reflections of the first four data sets (assuming symmetry). This parameter set is the same as was used in Figs. 3.3 (d)-(f).

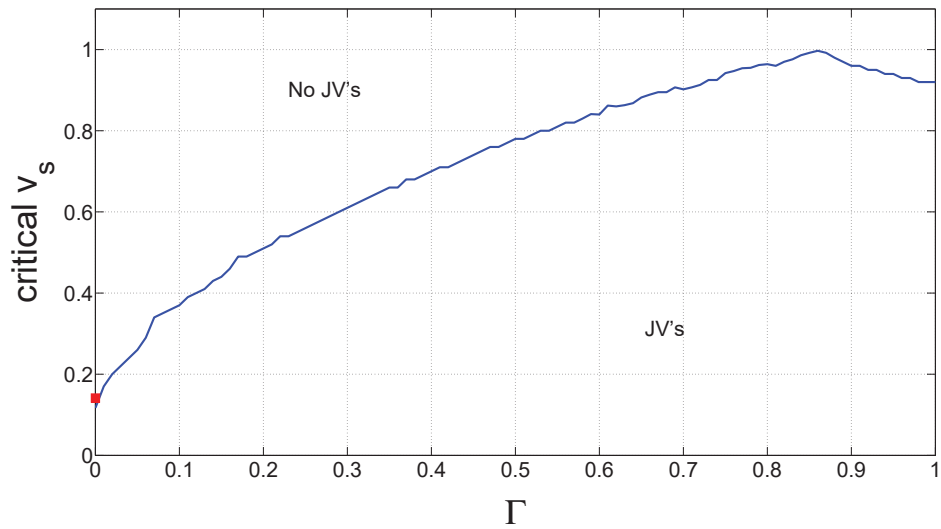
Fig. 3.8 (a) based on a stability calculation for dark solitons. An outline of the stability calculation is presented in appendix 3.A.

When  $\Gamma < 1$  we see that once again there exists a critical momentum beyond which the Josephson vortex solutions do not exist, but the Josephson vortex dispersion relation now terminates by touching the dark soliton dispersion relation non-tangentially (i.e. the slopes of the curves are different). The critical velocity is plotted as a function of  $\Gamma$  in Fig. 3.8 (b). The staggered soliton branch terminates at the exact same critical momentum and velocity as the Josephson vortex branch.

In the  $\Gamma < 1$  regime, Josephson vortices are again always stable, but the situation for dark solitons is quite different. Figure 3.9 shows a numerically-determined boundary line (plotted in blue circles) in the  $P_c$ - $\Gamma$  plane such that above this curve,



(a)



(b)

Figure 3.8: The numerical critical velocity for Josephson vortices (labelled “JV’s”) plotted as a function of  $\nu$  with  $\Gamma = 1$  (a) and as a function of  $\Gamma$  with  $\nu = 0.005$  (b). These curves separate regions of parameter space where Josephson vortex solutions exist from those where they do not. The red square is the analytical Manakov result.

dark solitons are unstable and below it they are stable. As soon as dark solitons become stable, staggered solitons appear. These are always unstable except for exactly at  $\Gamma = 0$  (the entire Manakov family of solutions is always stable). There exist small regions of stability in Fig. 3.9, bounded by the almost vertical sections of the stability-flip curve and  $0$  &  $4\pi(1 + \nu)$ , the limits of  $P_c$ . These are regions where staggered solitons and Josephson vortices do not exist and dark solitons are stable (as in the regime  $\Gamma = 1$ ). The development of these slivers of stability is seen in Fig. 3.8 (b) as a dip of the critical velocity, starting at about  $\Gamma = 0.86$ .

For zero-velocity dark solitons, we can analytically compute the points in parameter space where the stability changes – this is done in appendix 3.A.1. For  $\nu = 0.005$  as in Fig. 3.9, the result is  $\Gamma = 0.975$ , in agreement with numerical calculations (this point has been added to Fig. 3.9 as a red square). In fact, the analytical calculation also allows one to see that this stability-flip point starts at  $\Gamma = 1$  when  $\nu = 0$ , smoothly decreases and reaches  $\Gamma = 0$  at  $\nu = 1/3$ , so that outside of  $0 < \nu < 1/3$ , neither Josephson vortices nor staggered solitons exist.

Thus, there is a region of bistability for  $\Gamma < 1$  where Josephson vortices (lowest energy) and dark solitons (highest energy) are both stable, with the unstable staggered soliton branch (intermediate energy) between them. An illustration is given in Fig. 3.10 where we fix  $\nu = 0.005$ ,  $v_s = 0$ ,  $P_c = 2\pi(1 + \nu)$  and plot the energy as a function of  $\Gamma$ . The energies of dark solitons and Josephson vortices are constant since the solutions (3.4) and (3.5) are independent of  $\Gamma$ , as is the energy functional (3.10) when  $|\psi_1|^2 = |\psi_2|^2$ . Overall, this has the familiar shape of a bistability diagram with an S-shaped fold, in the sense that the two extreme solutions are stable and the intermediate solution is not. The unusual features are that the upper branch continues to the right past the fold and that the three lines do not make a single, smooth S-shaped curve.

### 3.9 Inertial Mass and Missing Particle Number

In this section we focus on the first parameter range ( $\Gamma = 1$ ) and examine some key properties of the Josephson vortex quasi-particles. To start with, we can calculate the inertial mass of Josephson vortices and Josephson vortex maxima (evaluating the derivatives in (2.23) at the minimum and maximum of the dispersion relation, respectively) as a function of  $\nu$ , which yields Fig. 3.11. The blue and red solid curves were obtained from the numerical Josephson vortex solutions. We define the bifurcation point at which the central part of the Josephson vortex dispersion relation changes concavity by the  $\nu$  value at which the  $1/m_I$  curve (red solid line in Fig. 3.11) crosses zero. This happens at  $\nu = 0.1413$ . The magenta dash-dotted line shows the variational approximation for Josephson vortices.

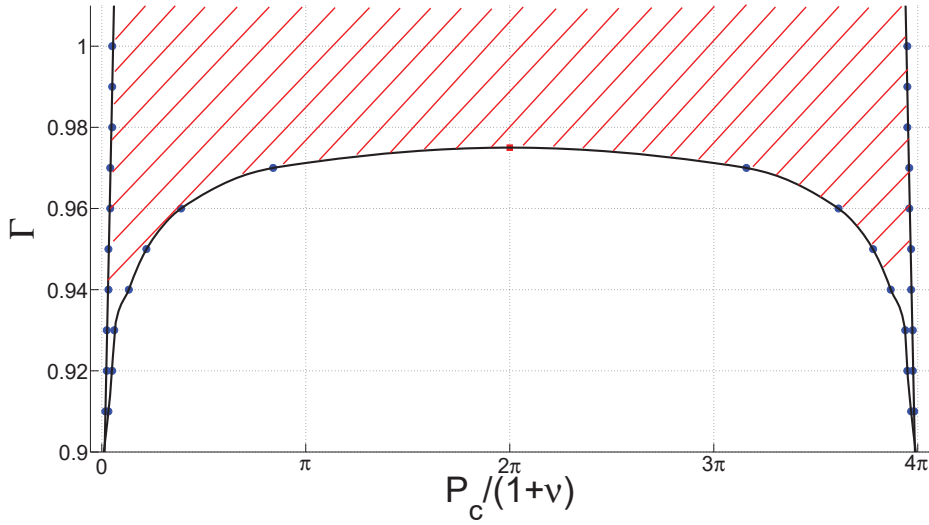


Figure 3.9: Numerically-determined blue circles are spline-fitted with the black curve to guide the eye. Above this curve (area shaded in red), dark solitons are unstable and below it they are stable. The red square is calculated analytically in appendix 3.A.1. For this plot,  $\nu = 0.005$ .

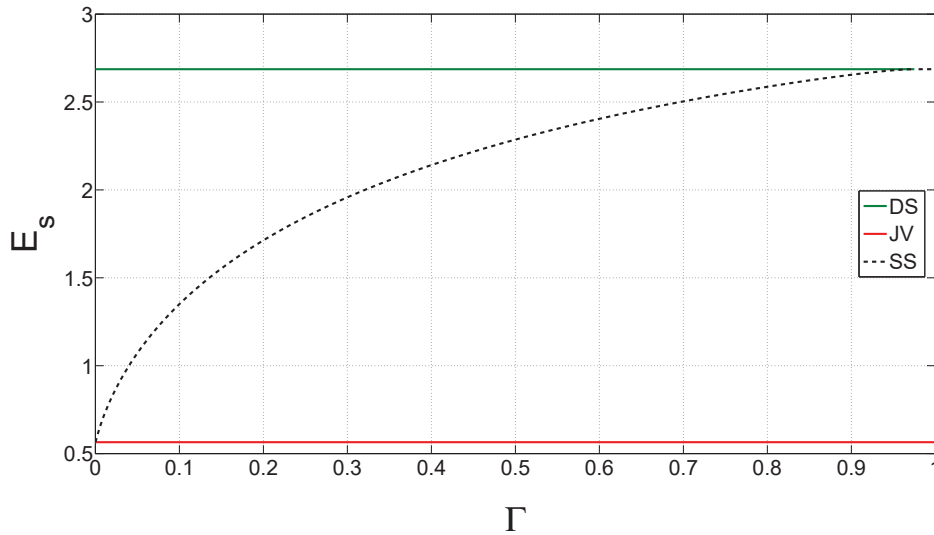


Figure 3.10: Excitation energy as a function of  $\Gamma$  for dark solitons (labelled “DS”, green), Josephson vortices (labelled “JV”, red) and staggered solitons (labelled “SS”, black). A solid line indicates stable solutions, while a dashed line – unstable. For all three curves,  $\nu = 0.005, v_s = 0, P_c = 2\pi(1 + \nu)$ .

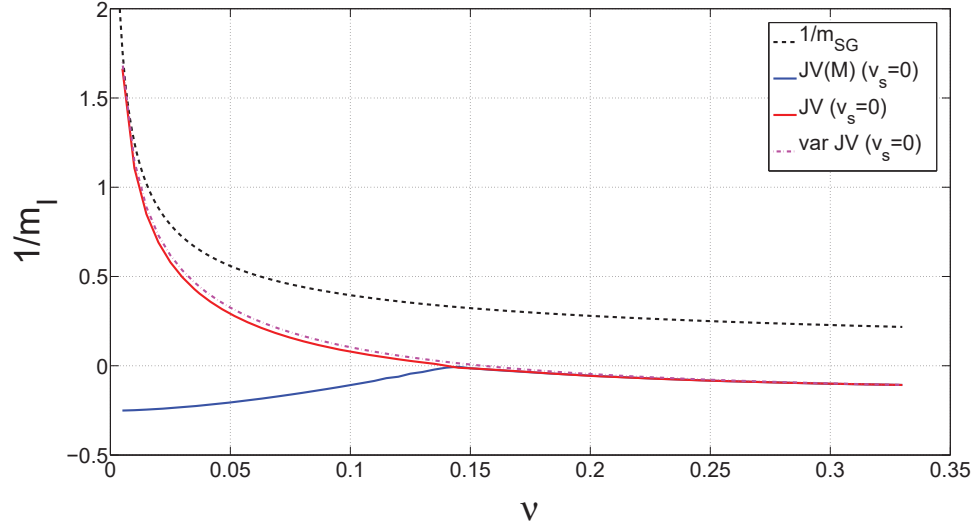


Figure 3.11: One over the inertial mass for Josephson vortices (labelled “JV”) and Josephson vortex maxima (labelled “JV(M)”) as a function of tunnelling strength with  $\Gamma = 1$ . The blue (lower) and red (upper) solid curves were obtained from the numerical Josephson vortex solutions. The magenta dash-dotted line is an approximate result obtained from a variational calculation for Josephson vortices (labelled “var JV”), equation (3.20). The black dashed line is a plot of  $1/m_{SG}$  from (3.34), discussed in section 3.11.

The inertial mass is a useful characteristic of an excitation, but experimentally, it is more common to measure  $m_I/N_d$ , the ratio of the inertial mass to the number of particles in the excitation. With this in mind, Fig. 3.12 shows  $N_d$  at the extrema of the Josephson vortex dispersion relation as a function of  $\nu$ , and Fig. 3.13 shows the ratio  $N_d/m_I$  obtained by combining the data from Figs. 3.11 and 3.12. In chapter 5, we will show that  $N_d = N_s$  at zero velocity, so  $N_d(v_s = 0)$  is proportional to  $m_p$  and thus the ratio  $N_d/m_I$  relates to the oscillation frequency in a trap. It is clear that the red curve certainly crosses zero, which means that  $m_I/N_d \rightarrow \pm\infty$  on either side of the critical point. This implies that essentially, the Josephson vortices become infinitely heavy.

### 3.10 The Sine-Gordon Equation

The second parameter regime that we have investigated ( $\nu = 0.005$ ) is particularly interesting in terms of how it compares to the analytically solvable sine-Gordon model. In order to carry out such a comparison, we first give a brief review of the sine-Gordon equation.

In appendix 3.B we derive the sine-Gordon equation from the model of section 3.2 by assuming that the densities of the two fields are practically equal to each other

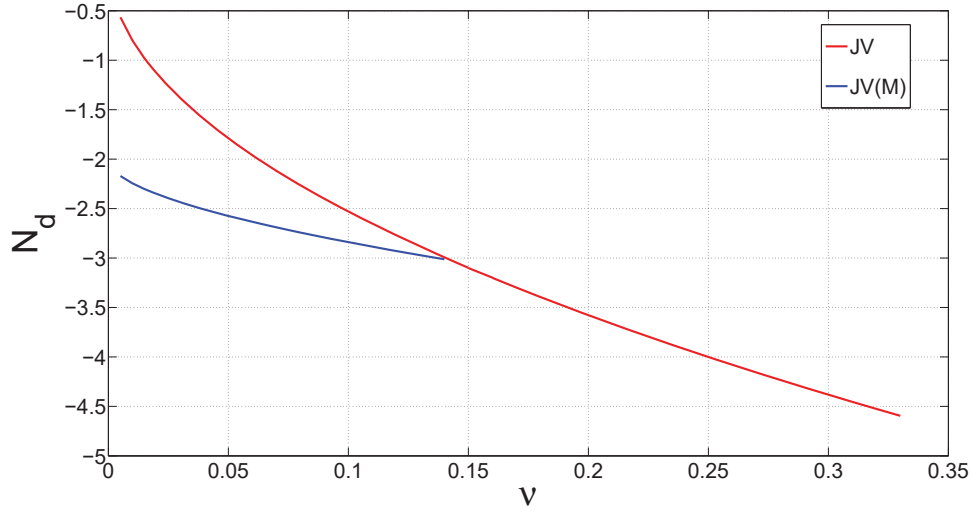


Figure 3.12: Missing particle number for Josephson vortices (labelled “JV”, red, upper curve) and Josephson vortex maxima (labelled “JV(M)”, blue, lower curve) as a function of tunnelling strength with  $\Gamma = 1$ , evaluated at the extrema of the dispersion relation.

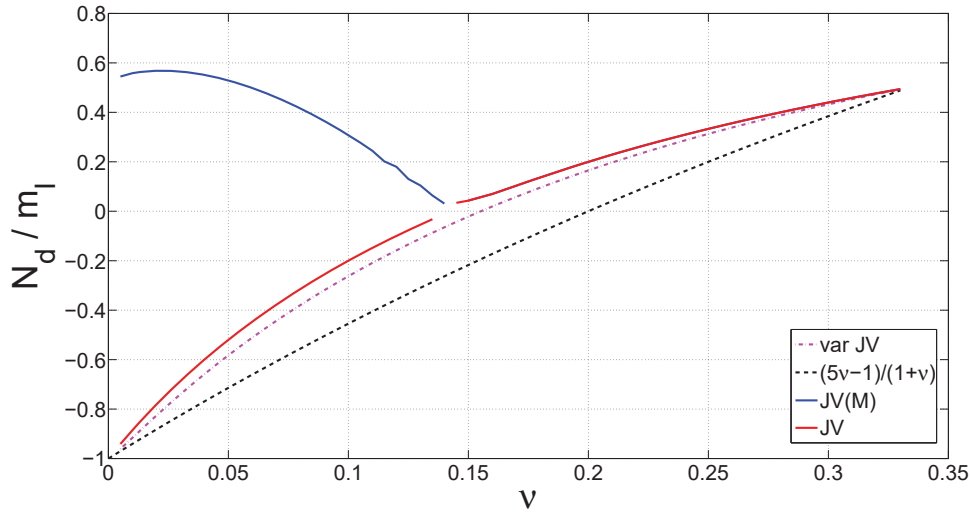


Figure 3.13: Missing particle number over inertial mass for Josephson vortices (labelled “JV”, red, lower solid line) and Josephson vortex maxima (labelled “JV(M)”, blue, upper solid line) as a function of tunnelling strength with  $\Gamma = 1$ , evaluated at the extrema of the dispersion relation. The magenta dash-dotted line is an approximate result obtained from a variational calculation for Josephson vortices (labelled “var JV”), and the black dashed line is a prediction from Ref. [129].

and are almost constant. In addition, many terms are dropped from the Lagrangian density based on the fact that the remaining terms yield the sine-Gordon equation (this selection is partly justified *a posteriori* by the success of the analysis we perform in section 3.11). This derivation allows one to express the sine-Gordon parameters through the Gross-Pitaevskii model parameters, thus enabling a direct comparison of the two models. In this section we will present some analytical results for the sine-Gordon equation [132], written with parameters determined by the procedure in appendix 3.B.

The Lagrangian density of the sine-Gordon model is

$$\mathcal{L} = \frac{\hbar^2}{4(g - g_c)} (\partial_t \phi_a)^2 - \frac{\hbar^2}{4m} \frac{\mu + J}{g + g_c} (\partial_x \phi_a)^2 + 2J \frac{\mu + J}{g + g_c} \cos(\phi_a), \quad (3.21)$$

where

$$\phi_a = \phi_1 - \phi_2. \quad (3.22)$$

The Hamiltonian density can be obtained in the usual way:

$$\begin{aligned} P_\phi &= \frac{\partial \mathcal{L}}{\partial(\partial_t \phi_a)}, \\ \mathcal{H} &= P_\phi (\partial_t \phi_a) - \mathcal{L}, \end{aligned} \quad (3.23)$$

where  $P_\phi$  is the canonical conjugate coordinate to  $\phi_a$ . The Euler-Lagrange equation

$$\frac{\partial \mathcal{L}}{\partial \phi_a} - \partial_x \frac{\partial \mathcal{L}}{\partial(\partial_x \phi_a)} - \partial_t \frac{\partial \mathcal{L}}{\partial(\partial_t \phi_a)} = 0 \quad (3.24)$$

yields the sine-Gordon equation:

$$\partial_{tt} \phi_a - \frac{\Gamma}{m} (\mu + J) \partial_{xx} \phi_a = -\frac{4J\Gamma(\mu + J)}{\hbar^2} \sin(\phi_a). \quad (3.25)$$

Rewriting in dimensionless form (see (3.2)) and in a frame moving at  $v_s$ , the sine-Gordon equation becomes

$$[v_s^2 - \Gamma(1 + \nu)] \partial_{zz} \phi_a + 4\nu\Gamma(1 + \nu) \sin(\phi_a) = 0. \quad (3.26)$$

The solution is given by

$$\begin{aligned} \zeta &= \sqrt{\frac{4\nu\Gamma(1 + \nu)}{\Gamma(1 + \nu) - v_s^2}}, \\ \phi_a &= 4 \tan^{-1} (e^{\zeta z}). \end{aligned} \quad (3.27)$$

The Hamiltonian density is

$$\mathcal{H} = \frac{1}{4} \left[ \frac{v_s^2}{\Gamma} + 1 + \nu \right] (\partial_z \phi_a)^2 - 2\nu(1 + \nu) \cos(\phi_a), \quad (3.28)$$

and the excitation energy is

$$E_s = \frac{8\nu(1 + \nu)}{\zeta} + 2\zeta \left( 1 + \nu + \frac{v_s^2}{\Gamma} \right). \quad (3.29)$$

Next, using

$$P_c(v_s) = \int_0^{v_s} d\bar{v}_s \frac{1}{\bar{v}_s} \frac{dE_s}{d\bar{v}_s}, \quad (3.30)$$

we get the canonical momentum as

$$P_c = \frac{4v_s}{\Gamma} \zeta. \quad (3.31)$$

We can eliminate  $v_s$  to get the dispersion relation:

$$E_s^2 = (1 + \nu) [\Gamma P_c^2 + 64\nu(1 + \nu)], \quad (3.32)$$

or if we choose to write (in analogy to a relativistic particle)

$$E_s^2 = m_{SG}^2 c_{SG}^4 + c_{SG}^2 P_c^2, \quad (3.33)$$

then we identify

$$m_{SG} = \frac{8\sqrt{\nu}}{\Gamma}, \quad c_{SG} = \sqrt{\Gamma(1 + \nu)}. \quad (3.34)$$

### 3.11 Relativistic Behaviour

We have seen that at  $\Gamma = 1$  and small  $\nu$ , the Gross-Pitaevskii Josephson vortex dispersion relation develops a dip about  $P_c = 2\pi(1 + \nu)$  (see Fig. 3.4), similar in shape to the central part of the dispersion relation of the sine-Gordon equation. The equivalence of the two models in this regime has been suggested before [128], and now that we have the sine-Gordon dispersion relation expressed through the Gross-Pitaevskii model parameters, we are in a position to check this statement.

First, we can compare the dispersion relations visually. This is shown in Fig. 3.14, and the Josephson vortex dispersion relation indeed seems to be very close to the sine-Gordon curve. Next, we would like to compare the sine-Gordon parameters  $m_{SG}$  and  $c_{SG}$  to their equivalents in the Gross-Pitaevskii model as a function of  $\nu$ . A sensible way of extracting these parameters from the Josephson vortex dispersion

relation is to first obtain  $c_{JV}$  from

$$c_{JV} = \sqrt{\max\left(\frac{dE_s^2}{dP_c^2}\right)}, \quad (3.35)$$

using data about  $P_c = 2\pi(1 + \nu)$ , and then obtain  $m_{JV}$  as

$$m_{JV} = \sqrt{\frac{E_s^2(P_c = 2\pi(1 + \nu))}{c_{JV}^4}}. \quad (3.36)$$

$m_{JV}$  calculated this way (for  $\nu \leq 0.14$ ) is indistinguishable from  $m_I$  plotted in Fig. 3.11 as a red solid line. Comparing the red line to the black dashed line ( $m_{SG}$ ) in Fig. 3.11, it appears that the Josephson vortex bare mass  $m_{JV}$  indeed approaches the sine-Gordon result smoothly. Note that we are unable to compute numerical Josephson vortex solutions at smaller  $\nu$  because the length-scale of the excitation diverges in the limit  $\nu \rightarrow 0$ .

As for the speed of light,  $c_{JV}$ , Fig. 3.15 shows that the functional dependence on  $\nu$  is completely different for the Gross-Pitaevskii and sine-Gordon models, and it is clear that the two only become equal at  $\nu = 0$  but the slopes remain different. We therefore conclude that the Gross-Pitaevskii model approaches the sine-Gordon model, but exhibits considerable differences at finite  $\nu$ .

There are two fundamental speeds in the Gross-Pitaevskii model, which can be found by computing linearised excitations about the vacuum state, as was done in [124]. The authors find two elementary excitation branches: gapless Bogoliubov phonons (subscript ‘‘B’’) and gapped relative-phase excitations (subscript ‘‘RP’’). A standard Bogoliubov calculation (such as the one in appendix 3.A) leads to the dimensionless oscillation frequencies

$$\omega_B = \sqrt{1 + \nu} \sqrt{\frac{1}{2}k^2 \left( \frac{1}{2(1 + \nu)}k^2 + 2 \right)}, \quad (3.37)$$

$$\omega_{RP} = \sqrt{\left(\frac{1}{2}k^2 + 2\nu\right) \left(\frac{1}{2}k^2 + 2\Gamma(1 + \nu) + 2\nu\right)}, \quad (3.38)$$

where  $k$  is a dimensionless wavenumber. If for some sufficiently small  $k$   $\omega$  becomes imaginary, the vacuum state is unstable. Thus, the vacuum can become unstable if  $\Gamma < 0$ . Incidentally,  $\Gamma = 0$  (the Manakov case) separates the miscible ( $\Gamma > 0$ ) and immiscible ( $\Gamma < 0$ ) phases of the system. The speeds associated with each branch are the speed of sound,  $c_B = \sqrt{1 + \nu}$ , and  $c_{RP} = \sqrt{\Gamma(1 + \nu) + 2\nu}$ , which can be interpreted as a speed of light. Both the elementary speeds are added to Figs. 3.15 and 3.16 for comparison with sine-Gordon and Josephson vortex results. Notice that

$c_{RP}$  is never equal to (the variational)  $c_{JV}$  for  $\Gamma > 0$ .

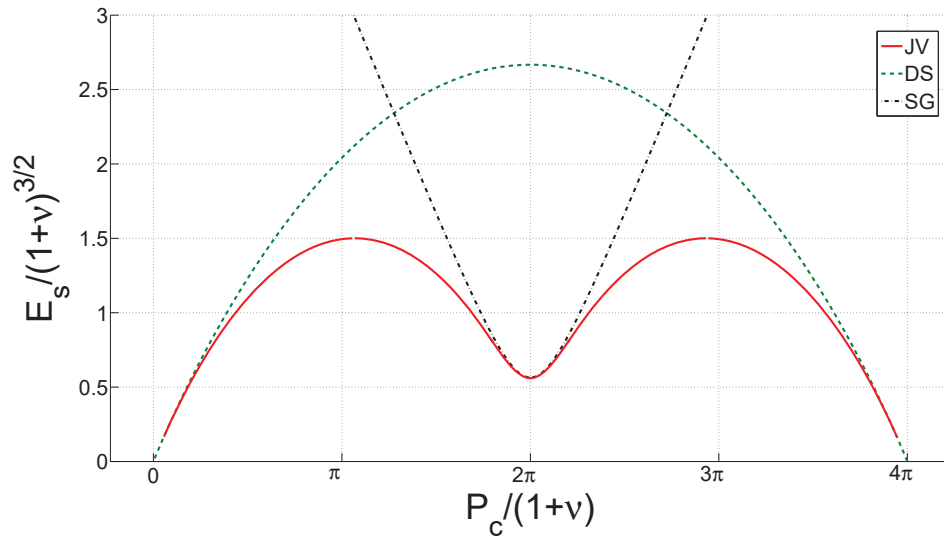


Figure 3.14: Dispersion relation of the Gross-Pitaevskii model and the sine-Gordon equation with  $\Gamma = 1, \nu = 0.005$ . Green dashed line – dark solitons (labelled “DS”), red solid line – Josephson vortices (labelled “JV”), black dash-dotted line – sine-Gordon solutions (labelled “SG”). Note that the sine-Gordon dispersion relation is artificially shifted to  $P_c = 2\pi(1 + \nu)$ . The Josephson vortex dispersion relation is very close to the sine-Gordon dispersion relation about  $P_c = 2\pi(1 + \nu)$ .

Figure 3.16 finally ventures in to the  $\Gamma < 1$  regime. Here we compare the sine-Gordon speed of light  $c_{SG}$  to its equivalent from the Gross-Pitaevskii model  $c_{JV}$  (showing both a numerical calculation and a variational approximation), and to the elementary speeds  $c_B$  and  $c_{RP}$ . We can see that the difference between  $c_{SG}$  and  $c_{JV}$  remains constant as a function of  $\Gamma$  (it only depends on  $\nu$ ) and that both the Josephson vortex and sine-Gordon speeds of light exhibit a square-root dependence on  $\Gamma$  (recall that  $c_{SG} = \sqrt{\Gamma(1 + \nu)}$ ) while  $c_B$  is independent of  $\Gamma$ . Thus, by decreasing  $\Gamma$  at a small  $\nu$  we can decouple two fundamental speeds in the Gross-Pitaevskii model dispersion relation.

### 3.12 Discussion and Conclusions

We have carried out a numerical investigation (complemented by some analytical results) of a model of two linear, parallel, long coupled Bose-Einstein condensates. The model has three distinct, dimensionless parameters:  $\nu$  (representing coupling between the condensates),  $\Gamma$  (which carries information about self- and cross- nonlinearities of the fields), and  $v_s$  (the uniform translation speed of localized excitations). This model has three types of solutions: dark solitons, Josephson vortices and a new set of solutions which we have labelled staggered solitons. Analytical

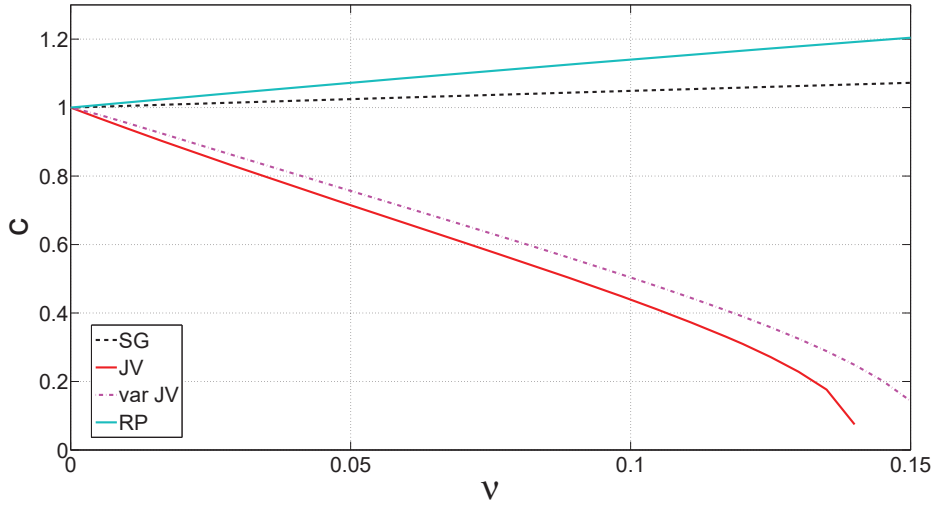


Figure 3.15: “Speed of light” from a relativistic dispersion relation for the sine-Gordon (black, dashed line, labelled “SG”) and Gross-Pitaevskii problems (red, solid line, labelled “JV”) at  $\Gamma = 1$ . The magenta dash-dotted line is an approximate result obtained from a variational calculation for Josephson vortices (labelled “var JV”). Note that for  $\Gamma = 1$ ,  $c_{SG} = c_B$ , the speed of sound, and the elementary speed of light  $c_{RP}$  is added as a solid cyan line (upper).

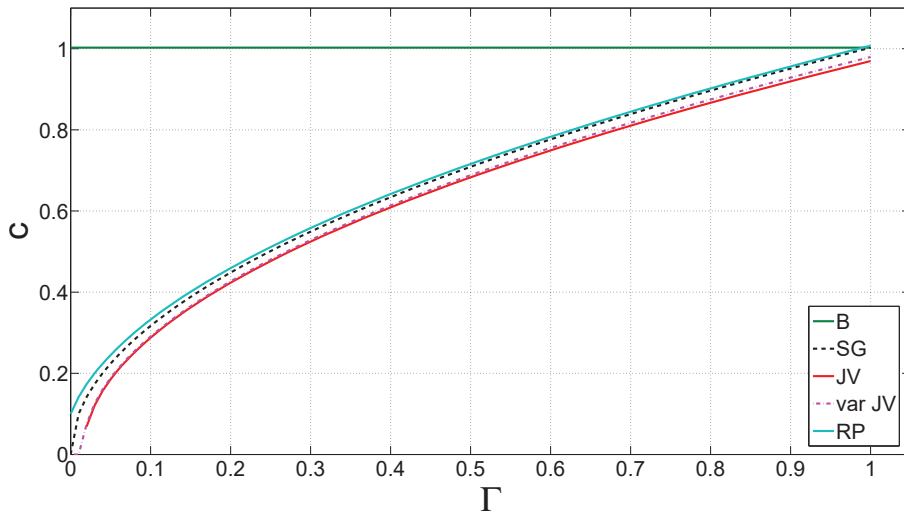


Figure 3.16: A comparison of the numerical  $c_{JV}$  from the Gross-Pitaevskii model (labelled “JV”, red lower solid line), the variational  $c_{JV}$  (labelled “var JV”, dash-dotted magenta line),  $c_{SG}$  of the sine-Gordon equation (labelled “SG”, black dashed line), the speed of sound  $c_B$  (labelled “B”, green upper solid line) and the elementary speed of light  $c_{RP}$  (labelled “RP”, cyan intermediate solid line). For all curves,  $\nu = 0.005$ .

expressions are available for dark solitons (for arbitrary parameters), zero-velocity Josephson vortices (but not Josephson vortex maxima), and the Manakov solutions for  $\Gamma = 0$ . Numerically we have found full dispersion relations for all solutions in the parameter regimes  $\Gamma = 1$ ,  $0 < \nu < 1/3$  and  $\nu = 0.005$ ,  $0 \leq \Gamma \leq 1$ .

We saw that with  $\Gamma = 1$ , there was a critical point at  $\nu \approx 0.1413$  where the central part of the Josephson vortex dispersion relation changed concavity. This corresponded to the inertial mass changing sign, going through  $\pm\infty$ . Thus, very “heavy” Josephson vortices can be created by tuning the coupling strength in this range. The heavy solitonic vortices observed experimentally in [72, 73] are closely related, but there it is not possible to change the sign of  $m_I$  by tuning a parameter.

We compared the Gross-Pitaevskii Josephson vortex dispersion relation at small  $\nu$  and  $\Gamma = 1$  to the integrable sine-Gordon dispersion relation. We expressed the sine-Gordon parameters through the Gross-Pitaevskii model parameters by deriving the sine-Gordon model from the Gross-Pitaevskii model in the small  $\nu$  limit. We found that the Josephson vortex dispersion relation about  $P_c = 2\pi(1 + \nu)$  became equivalent to the sine-Gordon one exactly at  $\nu = 0$  but that the approach was slow. This challenges the widely-used approximation, or at least suggests some caution in its application. However, by working in the small  $\nu$  regime, Josephson vortices may open the possibility for experimental study of “relativistic particles” (to a good approximation) using collective excitations of ultra-cold atoms.

When  $\Gamma < 1$ , we found that there exists a  $\Gamma$ - and  $\nu$ - dependent region where dark solitons and Josephson vortices are both stable, separated (in energy) by the unstable staggered solitons. For  $\Gamma = 1$ , dark solitons are always unstable and Josephson vortices are stable. Therefore, observing dark solitons in such a coupled Bose-Einstein condensates system could be difficult because they would quickly decay into two opposite-circulation Josephson vortices. If one worked in the bistable region, however, since dark solitons are stable they would not decay. This could potentially enable one to observe dynamics and interaction of Josephson vortices with dark solitons experimentally.

After this work was completed, I became aware of a closely-related article [133] that has considerable overlap with the results presented in this chapter.

# Appendix

## 3.A Stability Calculation

This appendix gives details of how the stability of a solution to equations (3.3) is determined. We start from the Gross-Pitaevskii equations in dimensionless form, allowing for additional time dependence, other than mere translation at  $v_s$ :

$$i\partial_\tau\psi_k = -\frac{1}{2}\partial_{zz}\psi_k + iv_s\partial_z\psi_k - \psi_k + \frac{1}{2}(1+\Gamma)|\psi_k|^2\psi_k + \frac{1}{2}(1-\Gamma)|\psi_{3-k}|^2\psi_k - \nu\psi_{3-k}. \quad (3.39)$$

To find out whether a solution is stable we must add a variation to the wavefunction:

$$\psi_k(z) \rightarrow \psi_k(z) + \delta\psi_k(z, \tau). \quad (3.40)$$

The right-hand side of (3.40) is substituted into (3.39); zeroth-order terms in  $\delta\psi_k$  give the unperturbed equations (3.39), terms of second order in  $\delta\psi_k$  and higher are discarded, and the first order terms give two linear equations for  $\delta\psi_k$ :

$$\begin{aligned} i\partial_\tau\delta\psi_k &= -\frac{1}{2}\partial_{zz}\delta\psi_k + iv_s\partial_z\delta\psi_k - \delta\psi_k - \nu\delta\psi_{3-k} + \frac{1}{2}(1+\Gamma) [2|\psi_k|^2\delta\psi_k + \psi_k^2\delta\psi_k^*] \\ &+ \frac{1}{2}(1-\Gamma) \times [|\psi_{3-k}|^2\delta\psi_k + \psi_{3-k}\psi_k\delta\psi_{3-k}^* + \psi_{3-k}^*\psi_k\delta\psi_{3-k}]. \end{aligned} \quad (3.41)$$

We then make the ansatz

$$\delta\psi_k(z, \tau) = a_k(z)e^{-i\lambda\tau} + b_k^*(z)e^{i\lambda^*\tau}. \quad (3.42)$$

Substituting (3.42) into (3.41) and separating out terms proportional to  $e^{-i\lambda\tau}$  from those proportional to  $e^{i\lambda^*\tau}$  (in light of orthogonality), we obtain four equations:

$$\begin{aligned} 0 &= (D_k - \lambda)a_k + \left[ \frac{1}{2}(1-\Gamma)\psi_{3-k}^*\psi_k - \nu \right] a_{3-k} \\ &+ \frac{1}{2}(1+\Gamma)\psi_k^2 b_k + \frac{1}{2}(1-\Gamma)\psi_{3-k}\psi_k b_{3-k}, \\ 0 &= (-D_k^* - \lambda)b_k + \left[ \nu - \frac{1}{2}(1-\Gamma)\psi_{3-k}\psi_k^* \right] b_{3-k} \\ &- \frac{1}{2}(1+\Gamma)\psi_k^{*2} a_k - \frac{1}{2}(1-\Gamma)\psi_{3-k}^*\psi_k^* a_{3-k}, \end{aligned} \quad (3.43)$$

where

$$D_k = -\frac{1}{2}\partial_{zz} + (1 + \Gamma)|\psi_k|^2 - 1 + iv_s\partial_z + \frac{1}{2}(1 - \Gamma)|\psi_{3-k}|^2. \quad (3.44)$$

When these equations are written in matrix form (in the basis  $a_1, b_1, a_2, b_2$ ), it becomes clear that solving for the  $\lambda$ 's reduces to diagonalizing the following matrix:

$$M = \begin{pmatrix} D_1 & \frac{1}{2}(1 + \Gamma)\psi_1^2 & \frac{1}{2}(1 - \Gamma)\psi_2^*\psi_1 - \nu & \frac{1}{2}(1 - \Gamma)\psi_2\psi_1 \\ -\frac{1}{2}(1 + \Gamma)\psi_1^{*2} & -D_1^* & -\frac{1}{2}(1 - \Gamma)\psi_2^*\psi_1^* & \nu - \frac{1}{2}(1 - \Gamma)\psi_2\psi_1^* \\ \frac{1}{2}(1 - \Gamma)\psi_2\psi_1^* - \nu & \frac{1}{2}(1 - \Gamma)\psi_2\psi_1 & D_2 & \frac{1}{2}(1 + \Gamma)\psi_2^2 \\ -\frac{1}{2}(1 - \Gamma)\psi_2^*\psi_1^* & \nu - \frac{1}{2}(1 - \Gamma)\psi_1\psi_2^* & -\frac{1}{2}(1 + \Gamma)\psi_2^{*2} & -D_2^* \end{pmatrix}. \quad (3.45)$$

$M$  is a matrix of operators, each of which must also be represented by a matrix. Let us consider these constituent operators first. These operate on the spatial dimension, discretized in steps of  $h$ . If the interval  $[-L, L]$  is discretized into  $N$  grid points, then  $\nu$  appearing in  $M$  is in fact  $\nu$  multiplied by the  $N \times N$  identity matrix. The wavefunctions, in turn, are represented by  $N \times N$  matrices with  $\psi$  on the main diagonal. Products of  $\psi$ 's are achieved by multiplying the appropriate  $\psi$  matrices together.

To construct  $\partial_z$  and  $\partial_{zz}$  we use a five-point stencil. In particular, if  $f(x)$  is some function and  $x$  is discretized in steps of  $h$ , then the first and second derivatives are approximated as

$$\begin{aligned} f'(x) &= \frac{-f(x + 2h) + 8f(x + h) - 8f(x - h) + f(x - 2h)}{12h}, \\ f''(x) &= \frac{-f(x + 2h) + 16f(x + h) - 30f(x) + 16f(x - h) - f(x - 2h)}{12h^2}. \end{aligned} \quad (3.46)$$

Thus, the matrices representing the first and second derivative operators only have 5 non-zero diagonals (symmetrically about the main diagonal) which contain the numbers (going from upper-most to lowest diagonal)  $\{-1, 8, 0, -8, 1\}/(12h)$  for the first- and  $\{-1, 16, -30, 16, -1\}/(12h^2)$  for the second- derivatives. In order to avoid boundary effects, on the second and pre-last rows we use a three point stencil:

$$\begin{aligned} f'(x) &= \frac{f(x + h) - f(x - h)}{2h}, \\ f''(x) &= \frac{f(x + h) - 2f(x) + f(x - h)}{h^2}. \end{aligned} \quad (3.47)$$

On the first and last rows, we also use the three point stencil but with additional assumptions. For the first derivative, we are forced to take a one-sided derivative, and for the second derivative, assume that  $f(x + h) = f(x - h)$ . This is because only one of  $x \pm h$  is part of the discrete grid when  $x$  is the first or the last point.

To find out whether a solution is stable or not, we need to know if there are any

complex eigenvalues. The accuracy of the calculation is limited by  $h$ , and in our case,  $h = L/100$  where  $2L$  is the size of the system.  $h$  is usually 0.01, but for the largest systems can get up to 0.05 or 0.06. Note that the coupled Gross-Pitaevskii equations in this discrete representation are satisfied to order  $h^2$ : the norm of the residuals is of order  $10^{-4}$ . In light of this, the cut-off for deciding whether the complex part of an eigenvalue is spurious or real is set to 0.01. Then, for each complex eigenvalue, the mod-squared eigenvector is inspected. If it is peaked in  $[-L/2, L/2]$ , it is assumed to be an actual unstable mode. If it peaks outside this range, the complex eigenvalue is assumed to be spurious.

In the  $\Gamma < 1$  parameter regime, some extra care has to be taken when computing stability. For dark solitons, spurious unstable modes sometimes satisfy our conditions for true instability defined in the paragraph above. To distinguish them from real unstable modes, we required the eigenvector mod-squared at  $\pm L$  to have decayed to one hundredth of the maximum value or more. The spurious modes have undamped oscillations beyond the region where the dark soliton is localized and are therefore ruled out by this extra condition. The next issue occurs for both dark solitons and staggered solitons: when the eigenvalue of a true unstable mode goes to zero as a function of some parameter, at some point it inevitably crosses our threshold of 0.01 (set in the paragraph above). This was suspected to occur in the high velocity limits. Therefore we checked that the pure imaginary eigenvalue belonging to the only potentially unstable eigenvector decayed smoothly as a function of velocity to zero. This confirmed that the mode in question was indeed unstable, even though its imaginary eigenvalue was less than 0.01.

### 3.A.1 Analytical Stability Calculation for Dark Solitons

We are able to analytically determine the boundary between the stable and unstable regions in parameter space for the known dark soliton solutions. This calculation is not completely general, as in order for it to work, we are forced to assume that the dark solitons are stationary, thus fixing one of the parameters;  $\nu$  and  $\Gamma$  remain arbitrary, though.

We recall that for dark solitons,  $\psi = \psi_1 = \psi_2$  given by (3.4). Numerically, one finds that the variations of the wavefunctions from (3.40) always satisfy  $\delta\psi = \delta\psi_1 = -\delta\psi_2$ , or equivalently,  $a = a_1 = -a_2$  and  $b = b_1 = -b_2$  (see (3.42)). Using this knowledge, we can reduce the  $4 \times 4$  matrix (3.45) to a  $2 \times 2$  matrix operating on  $\vec{\ell} = [a, b]^T$ :

$$M = \begin{pmatrix} \bar{D} & \Gamma\psi^2 \\ -\Gamma\psi^{*2} & -\bar{D}^* \end{pmatrix}, \quad (3.48)$$

where

$$\bar{D} = -\frac{1}{2}\partial_{zz} + iv_s\partial_z + (1 + \Gamma)|\psi|^2 - 1 + \nu. \quad (3.49)$$

Numerically we observe that the unstable eigenvector for dark solitons always has zero real part, and therefore, when dark solitons change stability (i.e. when the imaginary part of the eigenvalue goes through zero), the entire eigenvalue is zero. We are thus interested in solving  $M\vec{\ell} = \vec{0}$ . Defining the change of basis matrix

$$U = \begin{pmatrix} 1 & 1 \\ 1 & -1 \end{pmatrix}, \quad (3.50)$$

we transform our matrix equation into the new basis:  $UMU^{-1}U\vec{\ell} = U\vec{0}$ , where

$$UMU^{-1} = \frac{1}{2} \begin{pmatrix} \bar{D} - \bar{D}^* + \Gamma\psi^2 - \Gamma\psi^{*2} & \bar{D} + \bar{D}^* - \Gamma\psi^2 - \Gamma\psi^{*2} \\ \bar{D} + \bar{D}^* + \Gamma\psi^2 + \Gamma\psi^{*2} & \bar{D} - \bar{D}^* - \Gamma\psi^2 + \Gamma\psi^{*2} \end{pmatrix}, \quad (3.51)$$

and we will denote  $U\vec{\ell} = [\tilde{a}, \tilde{b}]^T$ . The choice  $v_s = 0$  guarantees that  $\psi^2 = \psi^{*2}$  and  $\bar{D} = \bar{D}^*$ , and hence the diagonal elements of (3.51) vanish. The resulting equations read

$$\begin{aligned} 0 &= \left[ -\frac{1}{2}\partial_{zz} + (1 + 2\Gamma)\psi^2 - 1 + \nu \right] \tilde{a}, \\ 0 &= \left[ -\frac{1}{2}\partial_{zz} + \psi^2 - 1 + \nu \right] \tilde{b}, \\ \psi &= \sqrt{1 + \nu} \tanh\left(\sqrt{1 + \nu}z\right). \end{aligned} \quad (3.52)$$

These equations have the same form as the (time-independent) Schrödinger equation, i.e. the eigen-problem for the Hamiltonian. In addition to the usual kinetic term we have a  $\text{sech}^2$  potential – known as the Rosen-Morse potential after the authors who first solved this problem analytically [134], and a constant term which can be interpreted as the eigenvalue. The energy spectrum consists of a few discrete bound states (localized and square-integrable), followed by a continuum of higher-energy, unbound states (delocalized). When the parameters are just right for the bound energy eigenvalues of the Hamiltonians to match the eigenvalue terms in the equations, the two equations (3.52) are satisfied with localized solutions. In other words, for such parameter values a zero eigenvalue of (3.48) exists and dark solitons switch stability.

Reference [134] derives the following results: the equation

$$[\partial_{zz} + \kappa \text{sech}^2(z)] \psi = \epsilon\psi \quad (3.53)$$

has discrete, bound eigenvalues

$$\epsilon_n = \left( \sqrt{\kappa + \frac{1}{4}} - n - \frac{1}{2} \right)^2, \quad (3.54)$$

where  $n = 0$  or  $n \in \mathbb{N}$ ,  $n \leq \sqrt{\kappa + \frac{1}{4}} - \frac{1}{2}$ .

For direct comparison of (3.52) with this result, we must rewrite the potential terms through  $\text{sech}^2$  and change to the scaled position coordinate  $\tilde{z} = \sqrt{1 + \nu}z$ . This procedure yields

$$\begin{aligned} \frac{4[\nu + \Gamma(1 + \nu)]}{1 + \nu} \tilde{a} &= [\partial_{\tilde{z}\tilde{z}} + 2(1 + 2\Gamma) \text{sech}^2(\tilde{z})] \tilde{a}, \\ \frac{4\nu}{1 + \nu} \tilde{b} &= [\partial_{\tilde{z}\tilde{z}} + 2 \text{sech}^2(\tilde{z})] \tilde{b}. \end{aligned} \quad (3.55)$$

Examining the equation for  $\tilde{b}$  and comparing to the Rosen-Morse results,  $n$  can only be 0 or 1. Moreover, we easily compute  $\epsilon_0 = 1$  and  $\epsilon_1 = 0$ . Next we set each  $\epsilon_n$  equal to the eigenvalue  $\frac{4\nu}{1+\nu}$  and see what conditions this imposes on our parameters. Doing this for  $\epsilon_1$  leads to  $\nu = 0$  and for  $\epsilon_0$  leads to  $\nu = 1/3$ . These are well-known points at which dark solitons do change stability: at  $\nu = 0$  Josephson vortices appear and dark solitons change from stable to unstable while the reverse process occurs at  $\nu = 1/3$ .

Now let us compare the equation for  $\tilde{a}$  to the Rosen-Morse results:  $n$  can be 0, 1 or 2, the latter only if  $\Gamma \geq 5/8$ . Setting  $\epsilon_n$  equal to the eigenvalue of the  $\tilde{a}$  equation gives

$$\epsilon_n = \left( \sqrt{2(1 + 2\Gamma) + \frac{1}{4}} - n - \frac{1}{2} \right)^2 = \frac{4[\nu + \Gamma(1 + \nu)]}{1 + \nu}. \quad (3.56)$$

We can use this condition to check our numerical results. Setting  $\nu = 0.005$ , and taking  $n = 0, 1, 2$  in turn, we plot the left- and right-hand sides of (3.56) as a function of  $\Gamma$ , looking for the intersection point. For  $n = 0$  (3.56) is satisfied at  $\Gamma \approx 0.975$ , for  $n = 1$  the lines do not cross and for  $n = 2$  they cross at  $\Gamma \approx 0.1565 < 5/8$ , so  $n = 2$  is not actually possible at this point in parameter space. Thus, this calculation predicts that stationary dark solitons at  $\nu = 0.005$  will change stability once, at  $\Gamma \approx 0.975$ . This point is added to Fig. 3.9 (red square) and fits perfectly on the numerical curve (blue circles).

### 3.B Derivation of the Sine-Gordon Equation

In this appendix we show how one can obtain the sine-Gordon equation from the Gross-Pitaevskii model of section 3.2. The Lagrangian density of the coupled Bose-

Einstein condensates system is given by

$$\mathcal{L} = \mathcal{L}_B - w, \quad (3.57)$$

where the energy density (also see (3.10)) is

$$w = \sum_k \left\{ \frac{\hbar^2}{2m} |\partial_x \Psi_k|^2 - \mu |\Psi_k|^2 - J \Psi_k^* \Psi_{3-k} + \frac{1}{2} g |\Psi_k|^4 \right\} + g_c |\Psi_1|^2 |\Psi_2|^2, \quad (3.58)$$

and

$$\mathcal{L}_B = \frac{i\hbar}{2} \sum_k (\Psi_k^* \partial_t \Psi_k - \Psi_k \partial_t \Psi_k^*). \quad (3.59)$$

The Gross-Pitaevskii equations (3.1) can be recovered from the Euler-Lagrange equations for the fields  $\Psi_k$  and  $\Psi_k^*$ . To proceed, we take the following ansatz for the wavefunctions:

$$\begin{aligned} \Psi_1(x, t) &= u(x, t) \cos[\Theta(x, t)] e^{\frac{i}{2}[\phi_s(x, t) + \phi_a(x, t)]}, \\ \Psi_2(x, t) &= u(x, t) \sin[\Theta(x, t)] e^{\frac{i}{2}[\phi_s(x, t) - \phi_a(x, t)]}. \end{aligned} \quad (3.60)$$

In terms of the new fields, (3.57) becomes

$$\begin{aligned} \mathcal{L} &= -\frac{\hbar}{2} u^2 [\partial_t \phi_s + \cos(2\Theta) \partial_t \phi_a] - \frac{\hbar^2}{2m} \{ (\partial_x u)^2 + u^2 (\partial_x \Theta)^2 \\ &\quad + \frac{u^2}{4} [(\partial_x \phi_s)^2 + (\partial_x \phi_a)^2] + \frac{u^2}{2} \cos(2\Theta) \partial_x \phi_s \partial_x \phi_a \} \\ &\quad + \mu u^2 + J u^2 \sin(2\Theta) \cos(\phi_a) - \frac{g}{2} u^4 [\cos^4(\Theta) + \sin^4(\Theta)] \\ &\quad - g_c u^4 \cos^2(\Theta) \sin^2(\Theta). \end{aligned} \quad (3.61)$$

We now assume that the densities of the two wavefunctions are almost the same, i.e., we take

$$\Theta(x, t) = \frac{\pi}{4} + y(x, t), \quad (3.62)$$

where  $y$  is a field of small magnitude. We expand  $\mathcal{L}$  to second order in  $y$ :

$$\begin{aligned} \mathcal{L} &= -\frac{\hbar}{2} u^2 [\partial_t \phi_s - 2y \partial_t \phi_a] - \frac{\hbar^2}{2m} \{ (\partial_x u)^2 + u^2 (\partial_x y)^2 \\ &\quad + \frac{u^2}{4} [(\partial_x \phi_s)^2 + (\partial_x \phi_a)^2] - y u^2 \partial_x \phi_s \partial_x \phi_a \} \\ &\quad + \mu u^2 + J u^2 (1 - 2y^2) \cos(\phi_a) - \frac{g}{4} u^4 (1 + 4y^2) \\ &\quad - \frac{g_c}{4} u^4 (1 - 4y^2). \end{aligned} \quad (3.63)$$

Expanding out all the brackets in (3.63), we keep only the 2<sup>nd</sup>, 6<sup>th</sup>, 9<sup>th</sup>, 12<sup>th</sup>, and 14<sup>th</sup> terms. This selection is based upon whether or not the term is needed in the reduced Lagrange density in order for it to yield the sine-Gordon equation. The reduced Lagrangian reads

$$\mathcal{L} = \hbar y u^2 \partial_t \phi_a - \frac{\hbar^2}{2m} \frac{u^2}{4} (\partial_x \phi_a)^2 + J u^2 \cos(\phi_a) - u^4 (g - g_c) y^2. \quad (3.64)$$

We write down the Euler-Lagrange equations for  $y$  and  $\phi_a$ , make the approximation that  $u$  is a constant, eliminate  $y$  between the two equations and get

$$\partial_{tt} \phi_a - \frac{\Gamma}{m} (\mu + J) \partial_{xx} \phi_a = -\frac{4\Gamma(\mu + J)}{\hbar^2} \sin(\phi_a), \quad (3.65)$$

where  $u$  was set to the background value,

$$u = \sqrt{2 \frac{\mu + J}{g + g_c}}. \quad (3.66)$$

Equation (3.25) is identical to (3.65).

# Chapter 4

## Detecting Josephson Vortices

Let us continue our study of the model of the previous chapter, adding an external trapping potential, which necessarily implies that time-dependence in the Gross-Pitaevskii equations can no longer be trivially eliminated. Similarly to chapter 3, this chapter does not directly contribute to the resolution of the central question of the thesis, but it serves to introduce and illustrate some concepts that are prevalent throughout, and in particular, logically leads to the question addressed in chapter 5.

### 4.1 Introduction

Recall that in superconductivity, a Josephson vortex is a dissipationless flow across a (long) Josephson junction [33, 135, 136]. As we have seen in the previous chapter, it has a direct analogue in cold atom physics in the form of a superflow between two linearly-coupled one-dimensional Bose-Einstein condensate strands [127, 128]. Many theoretical studies have explored this model and its excitations [119–126, 129, 130], culminating in a direct calculation of the properties of Josephson vortices across a large range of parameter regimes (chapter 3). The physical system in question has already been realised, first with three-dimensional condensates [117, 118, 137] and later with one-dimensional strands by the Vienna Atomchip group [115, 116, 138]. Thus, experimental observation of bosonic Josephson vortices is imminent. However, it is not immediately obvious how the theoretical calculations of chapter 3 are to be linked to potential experiments – providing that connection is the purpose of the current chapter. In particular, we focus on two types of experiments: observation of the interference fringes resulting from recombination of the two strands [139], and oscillatory dynamics of quasi-particle excitations in a harmonic trap [72, 73, 111].

First, we simulate the following experiment: two coherently-coupled quasi-one-dimensional Bose-Einstein condensates are initially prepared in harmonic traps (with tight transverse confinement), where the system is either in the ground or some excited state. The traps are suddenly removed, allowing the condensates to expand and spatially overlap, falling under gravity, until eventually the intensity pattern is detected on a screen. Note that this procedure is routinely carried out in the

Vienna Atomchip laboratory [139]. We show that the resulting fringe pattern carries clear signatures of the initial state, allowing one to easily differentiate between the ground state, a dark soliton, a Josephson vortex and a single-strand dark soliton or a Josephson vortex maximum – a quasi-particle which combines dark soliton and Josephson vortex properties.

Second, we solve the time-dependent Gross-Pitaevskii equations to simulate the evolution and motion of a Josephson vortex seeded in the center of a harmonic trap. This type of experiment has become ubiquitous (e.g. [72, 73, 111]), and has stimulated much progress in recent years. We find a non-trivial trajectory, where the vortex oscillates from trap center to each end of the trap *twice* before crossing zero and going over to the other side. This curious trajectory can be intuitively explained in the context of the local density approximation, which only requires knowledge of the time-independent, untrapped solutions – precisely the case considered in chapter 3. In passing, we also take the opportunity to test the validity of one of the terms in the quasi-particle equation of motion [109], and confirm that the physical mass is indeed proportional to the effective missing particle number  $N_s$  and not the actual,  $N_d$ , where the two are generally not equal (see chapter 5).

## 4.2 The Model

The physical system under consideration can be described by the following coupled Gross-Pitaevskii equations:

$$i\hbar\partial_t\Psi_{1,2} = -\frac{\hbar^2}{2m}\partial_{xx}\Psi_{1,2} - \mu\Psi_{1,2} + \frac{1}{2}m\omega^2x^2\Psi_{1,2} + g|\Psi_{1,2}|^2\Psi_{1,2} + g_c|\Psi_{2,1}|^2\Psi_{1,2} - J\Psi_{2,1}. \quad (4.1)$$

The case of  $\omega = 0$ , i.e. an infinite system with open boundary conditions, was considered in chapter 3, where we further assumed that the only time-dependence is translation at constant velocity. Recall the key features of some of the solutions studied therein: the ground state has a homogeneous density profile (with an arbitrary constant phase) in both strands. As for dark solitons, the order parameter of the two condensates is equal and is characterised by a localized density dip with a phase-step across it (note that there is no flow between the two strands).

The stationary Josephson vortex wavefunctions for the two components are complex-conjugate scalar fields. While we still have a density dip and a phase step (as for the dark soliton), the distinctive feature is a superflow circulating around the vortex core, situated half-way between the two strands. Finally, the single-strand dark soliton, as the name suggests, essentially consists of a dark soliton in one strand while the second condensate is in its ground state. This stationary excitation lies at the maximum of the Josephson vortex dispersion relation with non-zero total

momentum, motivating the nomenclature Josephson vortex maximum.

As a reminder, the dark soliton and Josephson vortex dispersion relations are illustrated in Fig. 4.1. Dark solitons always have higher energy and a single-maximum dispersion relation. Josephson vortices, on the other hand, exhibit a rich structure where at the center of the dispersion relation we have a local minimum (corresponding to a stationary Josephson vortex) and two local maxima on either side of the origin (corresponding to stationary single-strand dark solitons). For future reference, we also highlight the inflection points of the dispersion relation, where the inertial and physical masses diverge (see chapter 3). We emphasize that as long as  $g_c = 0$ , if Josephson vortex solutions exist, then dark solitons are dynamically unstable and will decay to vortices (see chapter 3). This implies that in an experiment, one can obtain Josephson vortices by creating dark solitons via phase imprinting [16, 21] and simply waiting for them to decay.

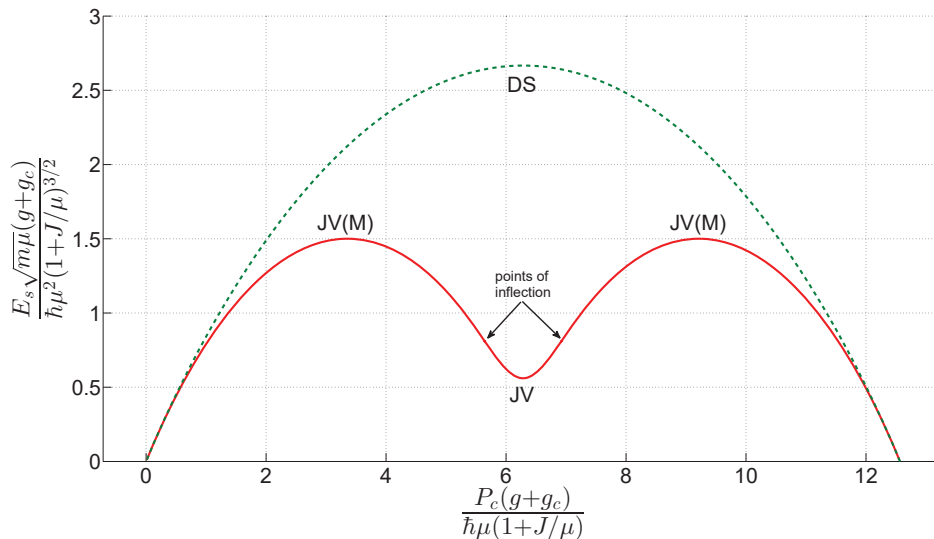


Figure 4.1: The dispersion relation (excitation energy  $E_s$  as a function of total momentum  $P_c$ ) of dark solitons (green dashed line) and Josephson vortices (red solid line) with  $g_c = 0$  and  $J/\mu = 0.005$ . The labels highlight the stationary excitations of interest: dark soliton (labelled “DS”), Josephson vortex (labelled “JV”) & Josephson vortex maximum (labelled “JV(M)”). The inflection points are also explicitly labelled.

### 4.3 The Fringe Pattern

One of the most curious observations made in the early days of cold atom physics was that if a Bose-Einstein condensate is split into two clouds by the creation of a potential barrier in a previously harmonic trap, and the clouds are released and allowed to interfere, a fringe pattern results [139, 140]. Moreover, if the condensates

were well separated in the double-well potential, individual experimental runs produced fringes with a random relative phase, so that the fringes washed-out in the ensemble average. Following these experiments, several insightful theoretical papers explained this non-trivial observation from fundamental quantum-mechanical principles [141–145], starting from number-states, with no assumptions made about the phase of the wavefunction. On the other hand, if the potential barrier is not too high and there is significant overlap between the clouds with non-negligible tunnelling, the system may still be described coherently by the Gross-Pitaevskii equations, so that the relative phase is unique [145].

Given solutions of the one-dimensional equations (4.1), one can approximate the three-dimensional wavefunctions for a gas confined very tightly in the  $y$  and  $z$  directions (trap frequency  $\omega_r$ ), and very weakly in  $x$  (trap frequency  $\omega$ ). Due to the fact that  $\omega \ll \omega_r$ , we may safely assume that we remain in the ground state of the transverse motional degrees of freedom. Moreover, we will choose to separate the condensates in  $y$  so that they are centred at  $\pm y_0$  and project the intensity pattern onto the  $x - y$  plane, so that the  $z$  coordinate may be left out of our considerations. In addition, when the trap is released, the gas will expand, but since  $\omega \ll \omega_r$ , the expansion in  $x$  will be much slower than in  $y$ , suggesting one may neglect the trapping potential along  $x$ . Under this approximation, the time-evolution of the  $x$ -component of the wavefunction is not influenced by the release of the trap.

Thus, we take the wavefunction in the  $y$ -direction to be the Gaussian ground state of the trap, evolved with the linear Schrödinger equation to time  $t$ :

$$\phi_{1,2}(y, t) = \sqrt{\frac{\sigma}{\sqrt{\pi}(\sigma^2 + i\hbar t/m)}} \exp\left[-\frac{1}{2} \frac{(y \pm y_0)^2}{\sigma^2 + i\hbar t/m}\right], \quad (4.2)$$

with  $\sigma = \sqrt{\hbar/m\omega_r}$ . The intensity pattern detected at time  $t$  is simply  $I = |\Psi_1(x, t)\phi_1(y, t) + \Psi_2(x, t)\phi_2(y, t)|^2$ . Example fringe patterns are shown in Fig. 4.2. The ground state features fringes with a Gaussian envelope along the  $y$ -direction, with no structure along  $x$  as  $\Psi_{1,2}(x)$  are constant. The  $y$ -fringes arise from  $\phi_{1,2}(y, t)$  and are thus present in all patterns, but can show additional structure for various solutions of (4.1). For instance, in Fig. 4.2 we depict three stationary excitations: a dark soliton possesses an additional dark fringe at  $x = 0$ , a Josephson vortex is characterised by a distortion of the fringes so that the  $n^{\text{th}}$  fringe at negative  $x$  connects to the  $(n + 1)^{\text{st}}$  fringe at positive  $x$  in a tanh-like curve, while a single-strand dark soliton combines a dark central fringe with distortion of the horizontal pattern, as might be expected. Our predictions thus enable direct identification of excitations created in the coupled-Bose-Einstein condensates system, and are consistent with an earlier simulation [128].

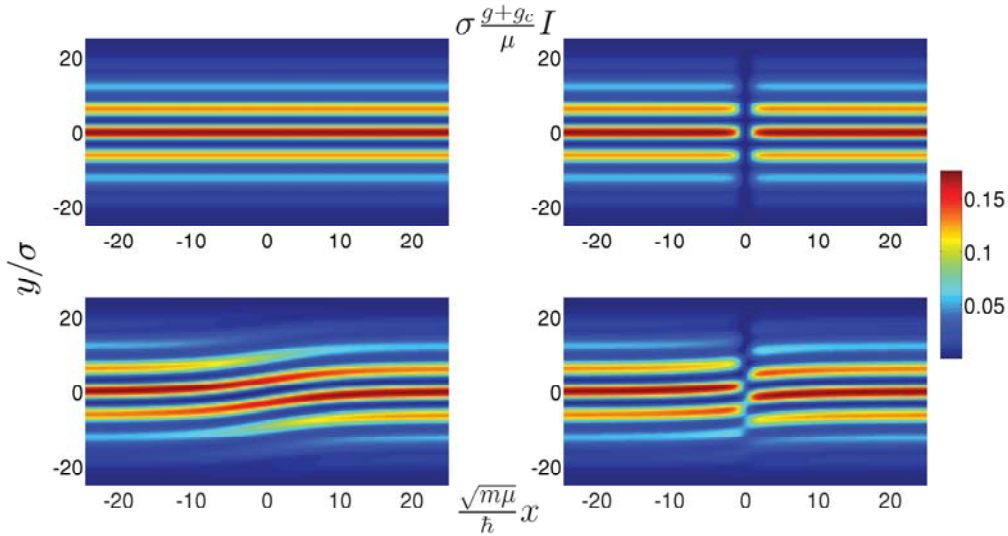


Figure 4.2: Interference fringe patterns for the ground state (top left), a dark soliton (top right), Josephson vortex (bottom left) and a single-strand dark soliton (bottom right). All excitations are stationary and are centred at  $x = 0$ . The parameters used are  $y_0 = 5\sigma$ ,  $t = 10/\omega_r$ ,  $g_c = 0$ ,  $J/\mu = 0.005$ . The colour map provides values of  $\sigma \frac{g+g_c}{\mu} I$  as a function of the scaled  $x$  and  $y$  position coordinates.

## 4.4 Trajectory in a Trap

Since the first experimental observation of dark solitons oscillating in a harmonic trap [111, 112], this technique of probing non-linear collective excitations has become routine in several state-of-the-art laboratories (e.g. [72, 73]). It has gained popularity due to the fact that observable quantities – usually the period – can be directly linked to intrinsic properties of the excitation [109, 146]. Theoretical studies often endeavour to predict this oscillation period to facilitate experimental testing of their results [67, 147–151], but the trajectory is usually assumed to be roughly sinusoidal.

We will now demonstrate that the trajectory of a Josephson vortex is much more complex, due to the rich structure of the dispersion relation (see Fig.4.1). We make use of the Matlab function `pdepe.m` (a finite difference method in space, with variable-method & variable-step time integration), with the absolute and relative tolerances set to  $10^{-8}$ . We solve the time-dependent Gross-Pitaevskii equations (4.1) with  $g_c = 0$ ,  $\mu = 200J$  and  $\hbar\omega = 2J$ . The total system size is  $2L = 21.2132\hbar/\sqrt{mJ}$ , discretized with 601 points, and the time step is  $\Delta t = 0.01\hbar/J$ . The boundary conditions require the wavefunctions to vanish at  $\pm L$ . The Thomas-Fermi profile, obtained by ignoring the derivative terms in (4.1), is used as a guess to converge to the exact background solution. As for the initial conditions, we use various moving numerically-found Josephson vortices centred at the origin times the Thomas-Fermi

profile of the trap. This generates far less noise (phonons) than initializing shifted stationary excitations. This is sufficient as an initial condition for time propagation.

Thus, we start the trajectory from a nearly stationary Josephson vortex (very close to the dispersion relation minimum) initially placed at the trap center. Following an exponential transient, the vortex begins oscillating in a pattern where each side of the trap is traversed twice before crossing zero, as shown in Fig. 4.3.

This exciting behaviour can be intuitively explained based on properties of the untrapped Josephson vortex dispersion relation. If the size of the vortex is fairly small compared to the size of the cloud, then the local density approximation may be applied (see chapter 2). Thus, as the vortex oscillates in the trap, accelerating and decelerating, it must continuously move along the dispersion relation. In fact, the dispersion relation changes with  $\mu$ , and so depends on the position of the excitation in the trap, but we have confirmed that for the entire range of motion shown in Fig. 4.3, qualitatively the dispersion relation retains the shape shown in Fig. 4.1.

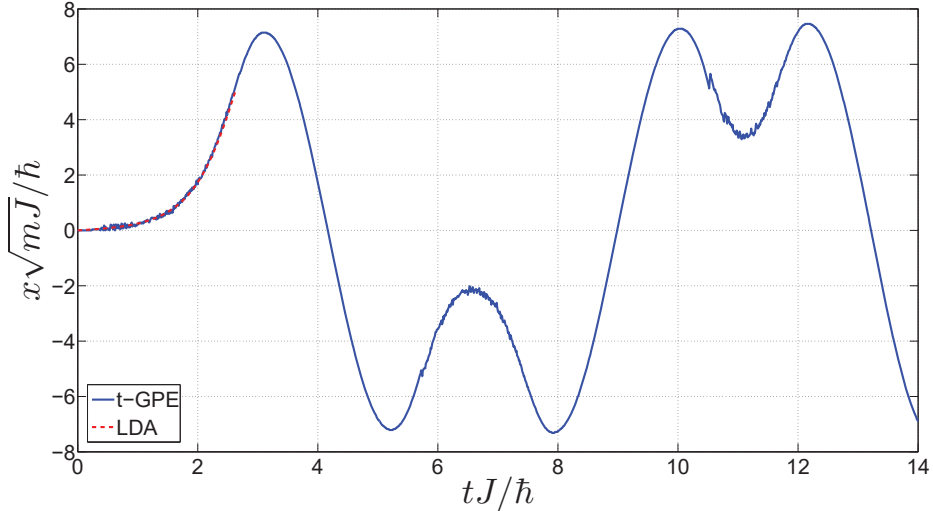


Figure 4.3: The trajectory of a Josephson vortex in a harmonic trap with  $g_c = 0$ ,  $\mu = 200J$  and  $\hbar\omega = 2J$ . The blue solid line is extracted from the solution of the time-dependent Gross-Pitaevskii equations (labelled “t-GPE”), tracking the maximal slope of the relative phase. We initialize the simulation by placing a vortex solution with velocity  $V_s = \frac{\sqrt{2}}{10} \sqrt{\frac{J}{m}}$  (very near the minimum of the dispersion relation) at the trap center. The spatial grid consists of 601 points and ranges between  $\pm 10.6066 \frac{\hbar}{\sqrt{mJ}}$ . Time is discretized in steps of  $0.01\hbar/J$ . The red dashed line (labelled “LDA”) is an approximate trajectory for the same initial condition, computed as described in section 4.5.

Recall that  $V_s = dE_s/dP_c$ , where  $E_s$  is the excitation energy and  $P_c$  the total

momentum<sup>1</sup>. This allows us to easily determine the sign of  $V_s$  along the dispersion relation by inspection. The trajectory begins with a near-stationary Josephson vortex at the dispersion relation minimum, with the vortex in the trap center. The velocity is nevertheless positive, and so it moves to the right along the trap as we climb up from the dispersion relation minimum to the right-hand maximum. Here the velocity is zero, and the vortex stops, reaching the amplitude of its oscillation at the right-hand edge of the trap. We then keep moving along the dispersion relation to the right, past the right maximum, where the velocity is negative. Consequently, the vortex begins moving to the left along the trap.

Eventually we stop descending the dispersion relation, having reached some maximal negative velocity as the vortex crosses the trap center, and begin climbing back up toward the right maximum. Here the velocity is still negative, so the vortex keeps moving left along the trap. As we reach the right dispersion relation maximum,  $V_s = 0$  and the vortex stops, having attained maximal negative displacement – i.e. at the amplitude of the oscillation at the left edge of the trap. Now we descend the dispersion relation from the right maximum towards the central minimum, where  $V_s > 0$ , so the vortex moves to the right, towards the trap center. When we arrive at the minimum,  $V_s = 0$  and the vortex stops, not having quite reached trap center. Crossing the minimum to the left,  $V_s < 0$ , and the vortex moves left once more.

We have now explained the first half of the unusual trajectory predicted for a Josephson vortex, Fig. 4.3. The same arguments can be applied to deduce the motion of the vortex as we continue across to the left “wing” of the dispersion relation and back to the central minimum, then over to the right wing of the dispersion relation etc.

## 4.5 Local Density Approximation

Our qualitative explanation of the trajectory shown in Fig. 4.3 can be made quantitative with the help of a simple equation of motion for the quasi-particle, derived in [109] (also see [67, 110] and chapter 2),  $m_I \ddot{X} = -m_P \omega^2 X$ , where  $X$  is the position coordinate of the excitation, and

$$m_P = mN_s = -m \left. \frac{dE_s}{d\mu} \right|_{v_s}, \quad (4.3)$$

$$m_I = \left( \frac{d^2 E_s}{dP_c^2} \right)^{-1}. \quad (4.4)$$

---

<sup>1</sup>Here  $E_s$  and  $P_c$  are dimensionful quantities (in contrast to chapter 3).

For small amplitude oscillations about an extremum of the dispersion relation, one may approximately take the inertial and physical masses ( $m_I$  and  $m_P$ , respectively) as constant throughout the motion, and compute them at the extremum. Furthermore, if  $m_I$  and  $m_P$  have the same sign, the quasi-particle will oscillate in simple harmonic motion about the trap center, and if the masses have different signs, it will get exponentially expelled from the trap.

It is also possible to let  $m_I$  and  $m_P$  change along the trajectory, which allows one to lift the restriction of “small-amplitude” oscillations. The approximate trajectory may be calculated in the following way. In (4.1), we replace  $\frac{1}{2}m\omega^2x^2$  by  $\frac{1}{2}m\omega^2X^2$ , thereby removing the inhomogeneous term at the expense of modifying the effective chemical potential to that seen by the excitation at position  $X$ . Next, explicit time-dependence is removed by transforming to a frame moving with the excitation at velocity  $V_s$ , so that the term  $i\hbar\partial_t\Psi_{1,2}$  is replaced by  $-i\hbar V_s\partial_z\Psi_{1,2}$ , where  $z = x - V_s t$ . To complete the transformation we must also replace  $\partial_{xx}$  by  $\partial_{zz}$ , which yields two coupled differential equations where  $\Psi_{1,2}$  now depend only on one variable,  $z$ .

The trajectory is started from some initial condition,  $\Psi_{1,2}(z)$  – for example, the same Josephson vortex used to generate Fig. 4.3, at some  $X(t = 0)$ . We calculate  $m_I$  and  $m_P$ , which requires varying  $P_c$  and  $\mu$ , re-solving the boundary value problem, and taking numerical derivatives. We then solve for  $X(\Delta t)$ , taking one step forward in time (using 4<sup>th</sup> order Runge-Kutta with time-step  $\Delta t = 0.01\hbar/J$ ), which also yields the new value of  $V_s = \dot{X}$ .  $X$  and  $V_s$  are inserted into the Gross-Pitaevskii equations for  $\Psi_{1,2}(z)$ , which are subsequently solved (as described in chapter 3). The process continues in this manner, boot-strapping the two sets of equations, obtaining new parameter values from one for the other at each iteration.

The advantage of this approximate method is that space and time are essentially decoupled. It performs very well as long as all the parameters remain finite, as is shown in Fig. 4.3. Unfortunately, it is not able to reproduce the full trajectory of Fig. 4.3 because when we cross the inflection points of the dispersion relation (see Fig. 4.1), both  $m_I$  and  $m_P$  diverge and the numerics break down.

Nonetheless, the machinery described in this section can be used to answer an interesting fundamental question regarding the physical mass appearing in the equation of motion. The derivation of this equation is based on the assumption that the energy of the quasi-particle is a constant of the motion, and leads to (4.3) where  $N_s$  is the effective missing particle number. However, intuitively, one would expect the physical mass to be given by  $mN_d$ , where  $N_d$  is the actual missing particle number, in analogy to the buoyancy force on an air bubble in liquid.

We are therefore in a position to explicitly test which missing particle number,  $N_s$  or  $N_d$ , should appear in the physical mass. As shown later in chapter 5,  $N_s$  and  $N_d$  are unequal for Josephson vortices (except for the stationary cases, when  $N_s = N_d$

in general). We can compute the trajectory using the local density approximation recipe, first using  $m_P = mN_s$ , then with  $m_P = mN_d$ , and compare the results to the exact, time-dependent Gross-Pitaevskii problem. Initiating simulations close to the inflection point (where the difference between  $N_s$  and  $N_d$  is maximal), we obtain Fig. 4.4, indicating that the correct physical mass is given by  $m_P = mN_s$ , in agreement with energy-conservation principles. Note that we have repeated the comparison using several different points along the dispersion relation to initiate simulations, and in all other cases the differences between the two approximate trajectories were far smaller, with the exact Gross-Pitaevskii result usually lying between them. Whenever the exact Gross-Pitaevskii result was visibly closer to one or the other, however, it always favoured  $m_P = mN_s$ .

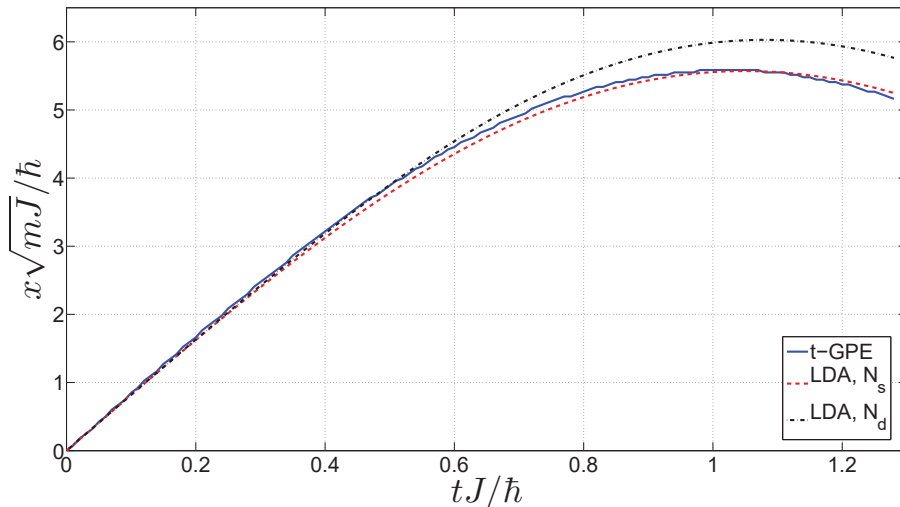


Figure 4.4: Comparison of the trajectories obtained from the full time-dependent simulations (labelled “t-GPE”, blue solid line), the local density approximation with  $m_P = mN_s$  (labelled “LDA,  $N_s$ ”, red dashed line) and with  $m_P = mN_d$  (labelled “LDA,  $N_d$ ”, black dash-dotted line). All parameter values are as for Fig. 4.3, except the initial vortex is taken very close to the inflection point of the dispersion relation, with  $V_s = 8.20244\sqrt{\frac{J}{m}}$ .

In conclusion, we have computed fringe patterns for interference experiments which allow for unambiguous identification of Josephson vortices, predicted a complex oscillatory trajectory for these excitations in a harmonic trap, and numerically confirmed a previously-derived but unintuitive term in the local density approximation equation of motion.

After this work was completed, I became aware of a closely-related article [133], significantly overlapping with the results of the current chapter.

# Chapter 5

## Missing Particle Number

In chapter 2, we have met the concept of the effective missing particle number which was defined through the derivative of the excitation energy with respect to chemical potential. In this chapter we will be concerned with deriving a similar formula for the actual missing particle number: an equation that allows one to extract the missing particle number (and then the phase step) of a solitonic excitation from the dispersion relation. This equation will later be applied to obtain the missing particle number and phase step of excitations in the Lieb-Liniger and Yang-Gaudin models (chapter 10).

### 5.1 Introduction

In addition to exploring ground state properties of atomic condensates [12–14], non-linear collective excited states are accessible and have been extensively studied [80]. The common feature of such solitonic excitations is a localized, moving depletion cloud in the superfluid, with or without an impurity particle at its core [152] (a common illustrative example is the dark soliton, reviewed in chapter 2.) Recall the definition of the missing particle number associated with the excitation: it is the number of particles removed in the creation of the density dip in the otherwise uniform background. On the other hand, as we have seen in the previous chapter, the physical mass is a constant in the equation of motion of such an excitation when it is treated as a Landau quasi-particle and dynamics in a harmonic trap are considered [109]. One can then define the *effective* missing particle number as simply the ratio of the physical mass and the mass of a single superfluid particle. Intuitively, one would expect the actual and effective missing particle numbers to be equal, however, as we will show, that is not generally the case (it is only so at zero velocity).

The simplest way of obtaining the missing particle number is by direct integration of the density profile. When a mean-field description of the system is easily accessible, this is a simple and fast approach. However, it is not always the case: for example, mean-field theory is inapplicable in the strong-interaction regime, or there may be no density dip in the state of interest and a solitonic interpretation of the excitation is only hypothesized (e.g. chapter 12). In such cases, one needs

a different approach to extracting the missing particle number. Fortunately, it is possible to do so if we know the dispersion relation of the excitation [109, 152], that is, the excitation energy as a function of the canonical momentum.

The idea was first introduced by Scott *et al.* [109] where a very simple formula was obtained for the effective missing particle number:

$$N_s = - \left. \frac{dE_s}{d\mu} \right|_{v_s} \quad (5.1)$$

where  $E_s$  is the excitation energy in the grand canonical ensemble,  $\mu$  the chemical potential and  $v_s$  the propagation speed of the excitation. This expression can be derived by considering a solitonic excitation in a trapped superfluid in the local density approximation, and requiring its energy to be a constant of the motion (see chapter 2). In particular, this definition of  $N_s$  is simply the physical mass divided by the mass of a single superfluid particle. We will refer to this formula as the ‘‘SDPS’’ equation, after the authors. This definition was then successfully applied by others (e.g. [147]), leading to reasonable and self-consistent results. More recently, Schechter *et al.* [152] have derived a far more involved equation for the actual missing particle number, in particular:

$$N_d = - \left. \frac{d\Omega'_d}{d\mu'} \right|_{j'} = - \left. \frac{d(E'_d - \mu' N_d)}{d\mu'} \right|_{j'} = - \left. \frac{d(E_s - v_s P_c)}{d\mu'} \right|_{j'} \quad (5.2)$$

where

$$j' = -n_0 v_s, \quad (5.3)$$

$$\mu' = \mu + \frac{1}{2} m v_s^2 \quad (5.4)$$

are the super-current and chemical potential of the uniform background state with one-dimensional density  $n_0$  and chemical potential  $\mu$ , in a moving frame of reference at velocity  $v_s$ . Further, in the above,  $E'_d$  is the canonical excitation energy (in the notation of [152]),  $P_c$  is the canonical momentum,  $n_0$  is the constant background density in the excited state far away from the localized density dip, and  $m$  is the mass of the particles making up the superfluid. Thus,  $\Omega'_d$  is essentially the excitation energy of the soliton in the grand canonical ensemble in a moving reference frame at velocity  $v_s$ . In turn, this equation will be coined the ‘‘SGR’’ formula, also after the authors. These two definitions are certainly not equivalent.

Whereas the derivation of equation (5.1) is quite straight-forward [67, 109], (5.2) is obtained in [152] based on general principles laid out in the textbook by Popov [153]. Popov’s formalism, however, is perhaps not sufficiently well-known to the ultra-cold-atom community for the average reader to confidently follow all the steps

in the derivation. Thus, there is some ambiguity about the two formulae and whether the actual and effective missing particle number are truly distinct quantities. This uncertainty is further compounded by the fact that in many cases the two definitions give the same result (which is known to be correct from the density-integral calculation).

It is our purpose to give an alternative derivation of the formula for extracting the actual missing particle number from the dispersion relation. We begin in section 5.2 by rewriting the SGR formula directly through the physical quantities appearing in the model, so that it can be more easily applied. Then in section 5.3 we develop a simple argument based on the Hellmann-Feynman theorem for functionals (appendix 5.A) that leads us to the SGR formula as the correct equation for the actual missing particle number. Next, we consider the necessary conditions for the SDPS and SGR definitions to become equivalent (section 5.4), presenting several analytical and numerical examples where the effective and actual missing particle number are the same (sections 5.4.1 & 5.4.2), followed by numerical examples where the effective missing particle number is distinctly different to the actual (section 5.4.2). We conclude in section 5.5.

## 5.2 The SGR Formula

Let us begin by rewriting the SGR  $N_d$ : we must express everything in terms of the physical quantities in the laboratory frame, that is, eliminate  $\mu'$  and  $j'$  from equation (5.2). Thus, we would like to change from the SGR variables  $\mu', j'$  to the two natural free parameters (apart from the coupling strength) on which the dispersion relation depends:  $n_0$  and  $v_s$ . The chemical potential  $\mu$ , which is a property of the ground state, depends on  $n_0$  and the coupling strength. The total differentials of the SGR free variables written through our free variables are

$$dj' = -n_0 dv_s - v_s dn_0, \quad (5.5)$$

$$d\mu' = \left. \frac{d\mu}{dn_0} \right|_{v_s} dn_0 + mv_s dv_s. \quad (5.6)$$

We will also need the total differential of  $\Omega'_d$  written through  $dn_0$  and  $dv_s$ . It is

$$\begin{aligned} d\Omega'_d &= d(E_s - v_s P_c) = \left. \frac{dE_s}{dn_0} \right|_{v_s} dn_0 + \left. \frac{dE_s}{dv_s} \right|_{n_0} dv_s \\ &\quad - v_s \left. \frac{dP_c}{dn_0} \right|_{v_s} dn_0 - P_c dv_s - v_s \left. \frac{dP_c}{dv_s} \right|_{n_0} dv_s. \end{aligned} \quad (5.7)$$

Since  $j'$  must be kept constant for the derivative with respect to  $\mu'$  we set  $dj' = 0$ , which immediately yields

$$dv_s = -\frac{v_s}{n_0} dn_0. \quad (5.8)$$

This means  $dv_s$  is no longer free, it is directly linked to  $dn_0$ . To calculate  $N_d$  we need to take  $-d\Omega'_d$  from (5.7), divide by  $d\mu'$  from (5.6) and substitute  $dv_s$  from (5.8) into the resulting expression. This will impose the constraint that  $j'$  is to be kept constant. This gives

$$N_d = \frac{-\frac{dE_s}{dn_0}\Big|_{v_s} - \frac{v_s P_c}{n_0} + \frac{v_s}{n_0} \frac{dE_s}{dv_s}\Big|_{n_0} + v_s \frac{dP_c}{dn_0}\Big|_{v_s} - \frac{v_s^2}{n_0} \frac{dP_c}{dv_s}\Big|_{n_0}}{\frac{d\mu}{dn_0}\Big|_{v_s} - \frac{mv_s^2}{n_0}}. \quad (5.9)$$

Considering that

$$\frac{dE_s}{dP_c}\Big|_{\mu} = v_s, \quad (5.10)$$

it is clear that

$$\frac{dE_s}{dv_s}\Big|_{\mu} = v_s \frac{dP_c}{dv_s}\Big|_{\mu}, \quad (5.11)$$

which makes two out of the three final terms in the numerator cancel:

$$\frac{v_s}{n_0} \frac{dE_s}{dv_s}\Big|_{n_0} + v_s \frac{dP_c}{dn_0}\Big|_{v_s} - \frac{v_s^2}{n_0} \frac{dP_c}{dv_s}\Big|_{n_0} = v_s \frac{dP_c}{dn_0}\Big|_{v_s}. \quad (5.12)$$

Thus, we can simplify  $N_d$  to

$$N_d = \frac{-\frac{dE_s}{dn_0}\Big|_{v_s} - \frac{v_s P_c}{n_0} + v_s \frac{dP_c}{dn_0}\Big|_{v_s}}{\frac{d\mu}{dn_0}\Big|_{v_s} - \frac{mv_s^2}{n_0}}, \quad (5.13)$$

and multiplying both top and bottom by  $dn_0/d\mu$ , we arrive at the final form of the SGR formula:

$$N_d = \frac{-\frac{dE_s}{d\mu}\Big|_{v_s} + v_s \frac{dP_c}{d\mu}\Big|_{v_s} - \frac{v_s}{n_0} \frac{dn_0}{d\mu} P_c}{1 - \frac{mv_s^2}{n_0} \frac{dn_0}{d\mu}}. \quad (5.14)$$

### 5.3 Main Derivation

Consider some general one-dimensional superfluid system described in mean-field theory, obeying some non-linear Schrödinger equation. Assume we are interested in solutions whose only time dependence is translation at constant velocity and introduce  $z = x - v_s t$ , the position coordinate in the moving frame. We can construct a functional such that setting its functional derivative to zero yields the non-linear

Schrödinger equation. This functional will be of the form  $\mathcal{L} = L_B - W$  where

$$W[\psi] = \int dz \frac{\hbar^2}{2m} |\partial_z \psi|^2 - \mu |\psi|^2 + u[\psi], \quad (5.15)$$

$$L_B[\psi] = \int dz -\frac{i\hbar v_s}{2} (\psi^* \partial_z \psi - \psi \partial_z \psi^*). \quad (5.16)$$

Note that  $\mathcal{L}$  is essentially the Lagrangian in the special case when time-dependence is pure translation and  $x, t$  can be replaced by a single coordinate,  $z$ . The equation arising from setting the functional derivative of  $\mathcal{L}$  to zero is

$$0 = -i\hbar v_s \partial_z \psi + \frac{\hbar^2}{2m} \partial_{zz} \psi + \mu \psi - g(|\psi|^2) \psi, \quad (5.17)$$

with the last term coming from the functional derivative of  $U[\psi]$  in  $\mathcal{L}[\psi]$ . Thus the only difference between the case considered here and the Gross-Pitaevskii equation is that we do not specify the interaction term. The functional derivative is taken according to

$$\frac{\delta \mathcal{L}}{\delta \psi^*} = \frac{\partial \mathcal{L}}{\partial \psi^*} - \frac{d}{dz} \frac{\partial \mathcal{L}}{\partial (\partial_z \psi^*)}. \quad (5.18)$$

Let us say we have some solution  $\psi_s$  to equation (5.17), featuring a localized excitation in the form of a density kink and a phase drop across it. Furthermore,  $\psi_s$  obeys open boundary conditions, not periodic boundary conditions, as we assume the phase at  $\pm\infty$  is generally not the same. There is also a constant, uniform solution  $\psi_0$  which is assumed to solve the exact same equation as  $\psi_s$  (i.e. at the same chemical potential).

It is our intention to eventually use the Hellmann-Feynman theorem of appendix 5.A. The conditions of applicability require that the wavefunctions involved obey periodic boundary conditions and extremize the functional of interest. With this in mind, introduce the periodic wavefunction corresponding to  $\psi_s$  with a phase factor to make the phase continuous and smooth at the boundaries:

$$\psi_{pbc} = \exp(i\Delta\phi z/L) \psi_s, \quad (5.19)$$

where  $\Delta\phi = -\arg[\psi_s(+\infty)] + \arg[\psi_s(-\infty)]$  and  $L$  is the size of the system – at the moment finite, but we will be taking the limit as  $L \rightarrow \infty$  at the end of the derivation, and so we shall work to order  $\mathcal{O}(\frac{1}{L})$ .

In addition, introduce  $\tilde{\mathcal{L}}[\psi]$ , a functional just like  $\mathcal{L}[\psi]$  except that the param-

eters  $\mu$  and  $v_s$  are replaced by  $\tilde{\mu}$  and  $\tilde{v}_s$ , where

$$\tilde{\mu} = \mu - mv_s v_{cf}, \quad (5.20)$$

$$\tilde{v}_s = v_s + v_{cf}, \quad (5.21)$$

$$v_{cf} = \frac{\hbar \Delta \phi}{mL}, \quad (5.22)$$

and  $v_{cf}$  is the counter-flow velocity of the superfluid, induced by the periodic boundary conditions. These parameters are chosen by requiring  $\tilde{\mathcal{L}}[\psi_{pbc}]$  to be extremized by  $\psi_{pbc}$ , neglecting terms  $\mathcal{O}(\frac{1}{L^2})$ . We also need to define a uniform, constant solution  $\tilde{\psi}_0$ , which solves (5.17) with  $\mu \rightarrow \tilde{\mu}$ .

In order to proceed, we need the result of the Hellmann-Feynman theorem for functionals presented in appendix 5.A. Applying the Hellmann-Feynman theorem, we can write

$$\left. \frac{d}{d\tilde{\mu}} \right|_{\tilde{v}_s} \left( \tilde{\mathcal{L}}[\psi_{pbc}] - \tilde{\mathcal{L}}[\tilde{\psi}_0] \right) = \int dz |\psi_{pbc}|^2 - |\tilde{\psi}_0|^2. \quad (5.23)$$

Note that both  $\psi_{pbc}$  and  $\tilde{\psi}_0$  obey periodic boundary conditions and so the boundary term is zero in both cases, and also that both wavefunctions extremize  $\tilde{\mathcal{L}}$  (up to terms  $\mathcal{O}(\frac{1}{L^2})$ ) so the functional derivative terms will not contribute (see appendix 5.A for details).

We would now like to write the number of particles in the  $\tilde{\psi}_0$  state,  $\langle N \rangle_{\tilde{\mu}}$ , through the number of particles in the  $\psi_0$  state,  $\langle N \rangle_{\mu}$ , plus some correction. Thus we do a first order Taylor expansion:

$$\langle N \rangle_{\tilde{\mu}} \approx \langle N \rangle_{\mu} + \left. \frac{\partial \langle N \rangle}{\partial \mu} \right|_{\langle N \rangle_{\mu}} (\tilde{\mu} - \mu). \quad (5.24)$$

Now, using the notation  $n_0 = |\psi_0|^2$  for the density of the uniform background state, the derivative featuring in the Taylor expansion is just  $L \times dn_0/d\mu$ . Substituting it in and writing out  $v_{cf}$ , the correction to the particle number (i.e. the second term on the right-hand side of (5.24)) is

$$-\hbar \Delta \phi v_s \frac{dn_0}{d\mu}. \quad (5.25)$$

Therefore, the right-hand side of (5.23) is none other than

$$N_d + \hbar \Delta \phi v_s \frac{dn_0}{d\mu}, \quad (5.26)$$

where

$$N_d = \int dz |\psi_s|^2 - |\psi_0|^2, \quad (5.27)$$

is the usual integral of the density difference calculation of the actual missing particle number.

We now turn to the left-hand side of (5.23). As can be readily shown,  $\tilde{\mathcal{L}}[\psi_{pbc}] = \mathcal{L}[\psi_s]$ , up to terms  $\mathcal{O}(\frac{1}{L^2})$ . On the other hand,  $-\tilde{\mathcal{L}}[\tilde{\psi}_0]$  can be expanded as a first order Taylor series, similar to what we have done for the particle number in (5.24). We should note that  $-\mathcal{L}[\psi_0]$  is actually  $W[\psi_0]$  and is *not* the same as the ground state energy ( $E_{GS}$ ), because  $W$  includes the chemical potential term and is thus the grand canonical ensemble energy. By definition,  $\frac{dE_{GS}}{dN} = \mu$  but the derivative of  $W$  needs to be calculated:

$$\frac{dW}{dN} = \frac{d}{dN} (E_{GS} - \mu N) = -\frac{d\mu}{dN} N = -\frac{d\mu}{dn_0} \frac{dn_0}{dN} N = -n_0 \frac{d\mu}{dn_0}. \quad (5.28)$$

Therefore, doing the Taylor expansion:

$$-\tilde{\mathcal{L}}[\tilde{\psi}_0] \approx -\mathcal{L}[\psi_0] + v_s n_0 \hbar \Delta \phi. \quad (5.29)$$

If  $E_s$  retains its definition as  $W[\psi_s] - W[\psi_0]$  and  $P_s$  is such that  $v_s P_s = L_B[\psi_s]$ , then equation (5.23) becomes

$$\left. \frac{d}{d\mu} \right|_{v_s} (v_s P_s - E_s + v_s n_0 \hbar \Delta \phi) = N_d + v_s \frac{dn_0}{d\mu} \hbar \Delta \phi, \quad (5.30)$$

where we have finally taken the limit as  $L \rightarrow \infty$  and so  $\tilde{\mu}, \tilde{v}_s \rightarrow \mu, v_s$ .

Now, for a system of bosons we use the relations

$$P_s = m v_s N_d, \quad (5.31)$$

$$P_c = P_s + \hbar n_0 \Delta \phi, \quad (5.32)$$

express  $\Delta \phi$  through  $N_d$  and  $P_c$ , substitute into (5.30), and rearranging for  $N_d$  we arrive at the SGR formula:

$$N_d = \frac{-\frac{dE_s}{d\mu} + v_s \frac{dP_c}{d\mu} - \frac{v_s}{n_0} \frac{dn_0}{d\mu} P_c}{1 - \frac{m v_s^2}{n_0} \frac{dn_0}{d\mu}}. \quad (5.33)$$

For fermions, we assume that the boson equation (5.30) holds, but all the quantities describe bosonic pairs. We need to rewrite it through fermionic quantities. The relations are as follows:

$$N_d^B = \frac{1}{2} N_d^F, \quad n_0^B = \frac{1}{2} n_0^F, \quad \mu_B = 2\mu_F, \quad \frac{d}{d\mu_B} = \frac{1}{2} \frac{d}{d\mu_F}, \quad m_B = 2m_F. \quad (5.34)$$

Note that  $P_s = m_B v_s N_d^B = m_F v_s N_d^F$  and  $E_s$  are the same regardless of whether we look at the excitation as being made up of bosonic or fermionic particles. Thus, equation (5.30) for bosons

$$N_d^B + \hbar \Delta \phi v_s \frac{dn_0^B}{d\mu_B} = \frac{d}{d\mu_B} \Big|_{v_s} (v_s P_s - E_s + n_0^B \hbar \Delta \phi v_s), \quad (5.35)$$

becomes

$$N_d^F + \frac{1}{2} \hbar \Delta \phi v_s \frac{dn_0^F}{d\mu_F} = \frac{d}{d\mu_F} \Big|_{v_s} \left( v_s P_s - E_s + \frac{1}{2} n_0^F \hbar \Delta \phi v_s \right). \quad (5.36)$$

Now then, for Fermions we have

$$P_s = m_F v_s N_d^F, \quad (5.37)$$

$$P_c = P_s + \frac{1}{2} \hbar n_0^F \Delta \phi, \quad (5.38)$$

and expressing  $\Delta \phi$  through  $N_d$  and  $P_c$  as before, we once again arrive at the SGR formula where all quantities are fermionic:

$$N_d^F = \frac{-\frac{dE_s}{d\mu_F} + v_s \frac{dP_c}{d\mu_F} - \frac{v_s}{n_0^F} \frac{dn_0^F}{d\mu_F} P_c}{1 - \frac{m_F v_s^2}{n_0^F} \frac{dn_0^F}{d\mu_F}}. \quad (5.39)$$

### 5.3.1 Canonical Ensemble

We will now show that equation (5.30), and therefore the final SGR formula, still holds if  $E_s$  – the grand canonical energy difference between the excited and homogeneous states at the same chemical potential – is replaced by  $E_{c,N}$ , the difference of the canonical energy between the excited and homogeneous states at the same particle number. This is highlighted with the foresight that one may wish to apply the equation we derive to systems more naturally described in the canonical ensemble, as in chapter 10.

We must account for the fact that in the grand canonical ensemble we are comparing the excited state to a background state with the same  $\mu$  (denoted below by the subscript  $BG, \mu$ ), and in the canonical ensemble, to a ground state with the same  $N$  (denoted by the subscript  $BG, N$ ). The soliton state will be marked by subscript  $s$ . We will use  $W$  as the energy operator in the grand canonical ensemble; its connection to the canonical ensemble energy is  $W = H - \mu N$ .

Thus we want to construct  $E_{c,N} = \langle H \rangle_s - \langle H \rangle_{BG,N}$  starting from  $E_s = \langle W \rangle_s - \langle W \rangle_{BG,\mu} = \langle H \rangle_s - \mu \langle N \rangle_s - \langle H \rangle_{BG,\mu} + \mu \langle N \rangle_{BG,\mu} = \langle H \rangle_s - \langle H \rangle_{BG,\mu} - \mu N_d$ . Recall that  $N_d$  is defined as  $N_d = \langle N \rangle_s - \langle N \rangle_{BG,\mu}$ . Hence we simply have

$$E_{c,N} = E_s + \langle H \rangle_{BG,\mu} - \langle H \rangle_{BG,N} + \mu N_d. \quad (5.40)$$

Let us see what the last three terms on the right-hand side above evaluate to.  $\langle H \rangle_{BG,N}$  has  $N$  particles and a uniform density of  $\frac{N}{L}$  while  $\langle H \rangle_{BG,\mu}$  has  $N - N_d$  particles and a uniform density of  $\frac{N-N_d}{L}$ . Since  $N_d/L$  goes to zero in the thermodynamic limit, we can evaluate the energy difference using a first order Taylor expansion in the density:

$$\begin{aligned}
\langle H \rangle_{BG,\mu} - \langle H \rangle_{BG,N} &= E_{GS} \left( \frac{N - N_d}{L} \right) - E_{GS} \left( \frac{N}{L} \right) \\
&\approx E_{GS} \left( \frac{N}{L} \right) + \frac{dE_{GS}}{dn_0} \times \left( \frac{-N_d}{L} \right) - E_{GS} \left( \frac{N}{L} \right) \\
&= \frac{dE_{GS}}{dN} L \left( \frac{-N_d}{L} \right) = -\mu N_d.
\end{aligned} \tag{5.41}$$

Therefore the last three terms on the right-hand side of (5.40) cancel to first order, which is sufficient since we are taking  $L \rightarrow \infty$  at the end. This implies that as long as we are in the thermodynamic limit, it does not matter whether we use the grand canonical ensemble and keep  $\mu$  constant, or use the canonical ensemble and keep  $N$  constant when calculating the excitation energy.

## 5.4 SDPS-SGR Equivalence

Our derivation has thus led us to the SGR formula as the correct method of extracting the actual missing particle number from the dispersion relation. We notice that if the soliton is stationary ( $v_s = 0$ ), the SGR formula trivially simplifies to the SDPS one. Remarkably, in some cases, the two formulae give the same result at *all* velocities. By setting the two expressions equal ( $N_s = N_d$ ), we easily arrive at the necessary condition to ensure the two formulae are equivalent for all velocities. Below we list all three forms of this condition:

$$mv_s \frac{dN_d}{d\mu} + \hbar n_0 \frac{d\Delta\phi}{d\mu} = 0, \tag{5.42}$$

$$\frac{dP_c}{dn_0} = \hbar \Delta\phi, \tag{5.43}$$

$$mv_s \left. \frac{dE_s}{d\mu} \right|_{v_s} = \left[ n_0 \left. \frac{d\mu}{dn_0} \frac{d}{d\mu} \right|_{v_s} - 1 \right] \int_{-c}^{v_s} \frac{1}{v'_s} \left. \frac{dE_s}{dv'_s} \right|_{\mu} dv'_s. \tag{5.44}$$

The last version, equation (5.44), is arguably the most general because it does not assume the existence of a phase step (or, indeed, a coherent phase at all). On the other hand, as an integro-differential equation, it is fairly difficult to use in practice. We can differentiate both sides with respect to  $v_s$ , turning (5.44) into a partial

differential equation for  $E_s(\mu, v_s)$ :

$$mv_s \frac{dE_s}{d\mu} + \frac{dE_s}{dv_s} - m(v_c^2 - v_s^2) \frac{d^2 E_s}{d\mu dv_s} = 0, \quad (5.45)$$

where  $v_c = \sqrt{\frac{n_0}{m} \frac{d\mu}{dn_0}}$  is the speed of sound, with the boundary conditions  $E_s(\mu, v_s = \pm v_c) = 0$  and initial condition  $E_s(\mu = 0, v_s) = 0$ . Thus the SDPS (effective) and SGR (actual) formulae for the missing particle number will coincide for any solitonic excitation whose excitation energy satisfies the above differential equation.

Next, we test the equivalence on several examples. The derivation of section 5.3 can be generalised as described in section 5.5, which justifies the application of the SGR formula to all but the last two analytical examples presented.

### 5.4.1 Analytical Examples

We are aware of several analytical solutions in a number of systems that possess the property of SDPS-SGR equivalence. Here we list the relevant physical quantities for each example, so that both formulae can be explicitly evaluated and compared. The first three of the examples are treated in mean-field theory, and so a direct calculation of the missing particle number is also possible.

(1) Dark solitons in the one-dimensional Gross-Pitaevskii equation on the infinite line (chapter 2):

$$E_s = \frac{4\hbar\mu^{3/2}}{3g\sqrt{m}}(1-s^2)^{3/2}, \quad (5.46)$$

$$\frac{dE_s}{d\mu} = \frac{2\hbar}{g} \sqrt{\frac{\mu}{m}} \sqrt{1-s^2}, \quad (5.47)$$

$$P_c = \frac{2\mu\hbar}{g} \left[ \cos^{-1}(s) - s\sqrt{1-s^2} \right], \quad (5.48)$$

$$\frac{dP_c}{d\mu} = \frac{2\hbar}{g} \cos^{-1}(s), \quad (5.49)$$

$$n_0 = \mu/g, \quad (5.50)$$

$$\frac{dn_0}{d\mu} = 1/g, \quad (5.51)$$

where

$$s = \sqrt{\frac{m}{\mu}} v_s. \quad (5.52)$$

Both equations (5.1) and (5.14), as well as the direct density integral calculation give

$$N_s = N_d = -\frac{2\hbar}{g} \sqrt{\frac{\mu}{m}} \sqrt{1-s^2}. \quad (5.53)$$

(2) Dark solitons in the two coupled one-dimensional Bose-Einstein condensates model (chapter 3):

$$E_s = \frac{\hbar\mu^{3/2}}{\sqrt{m}(g+g_c)} \frac{8}{3} (1+\nu-s^2)^{3/2}, \quad (5.54)$$

$$\frac{dE_s}{d\mu} = \frac{4\hbar}{g+g_c} \sqrt{\frac{\mu}{m}} \sqrt{1+\nu-s^2}, \quad (5.55)$$

$$P_c = -\frac{4\hbar\mu}{g+g_c} \left\{ s\sqrt{1+\nu-s^2} - \pi(1+\nu) + (1+\nu) \tan^{-1} \left( \frac{s}{\sqrt{1+\nu-s^2}} \right) \right\}, \quad (5.56)$$

$$\frac{dP_c}{d\mu} = \frac{4\hbar}{g+g_c} \left[ \pi - \tan^{-1} \left( \frac{s}{\sqrt{1+\nu-s^2}} \right) \right], \quad (5.57)$$

$$n_0 = 2 \frac{\mu+J}{g+g_c}, \quad (5.58)$$

$$\frac{dn_0}{d\mu} = \frac{2}{g+g_c}. \quad (5.59)$$

where

$$s = \sqrt{\frac{m}{\mu}} v_s, \quad \nu = \frac{J}{\mu}. \quad (5.60)$$

Both equations (5.1) and (5.14), as well as the direct density integral calculation give

$$N_s = N_d = -\frac{4\hbar}{g+g_c} \sqrt{\frac{\mu}{m}} \sqrt{1+\nu-s^2}. \quad (5.61)$$

(3) Manakov solutions in the two coupled one-dimensional Bose-Einstein condensates model (chapter 3):

$$E_s = \frac{4\hbar\mu^{3/2}\sqrt{4\nu-s^2}}{\sqrt{m}(g+g_c)} \left[ \frac{2}{3}(4\nu-s^2) - (3\nu-1) \right], \quad (5.62)$$

$$\frac{dE_s}{d\mu} = \frac{4\hbar}{g+g_c} \sqrt{\frac{\mu}{m}} \sqrt{4\nu-s^2}, \quad (5.63)$$

$$P_c = -\frac{4\hbar\mu}{g+g_c} \left\{ s\sqrt{4\nu-s^2} - \pi(1+\nu) + (1+\nu) \tan^{-1} \left( \frac{s}{\sqrt{4\nu-s^2}} \right) \right\}, \quad (5.64)$$

$$\frac{dP_c}{d\mu} = \frac{4\hbar}{g+g_c} \left[ \pi - \tan^{-1} \left( \frac{s}{\sqrt{4\nu-s^2}} \right) \right], \quad (5.65)$$

$$n_0 = 2 \frac{\mu+J}{g+g_c}, \quad (5.66)$$

$$\frac{dn_0}{d\mu} = \frac{2}{g+g_c}. \quad (5.67)$$

where

$$s = \sqrt{\frac{m}{\mu}} v_s, \quad \nu = \frac{J}{\mu}. \quad (5.68)$$

Both equations (5.1) and (5.14), as well as the direct density integral calculation give

$$N_s = N_d = -\frac{4\hbar}{g + g_c} \sqrt{\frac{\mu}{m}} \sqrt{4\nu - s^2}. \quad (5.69)$$

(4) Hole excitations in the Tonks-Girardeau gas of hard-core bosons [47]:

$$E_s = \mu - \frac{mv_s^2}{2}, \quad (5.70)$$

$$\frac{dE_s}{d\mu} = 1, \quad (5.71)$$

$$P_c = \sqrt{2m\mu} - mv_s, \quad (5.72)$$

$$\frac{dP_c}{d\mu} = \sqrt{\frac{m}{2\mu}}, \quad (5.73)$$

$$n_0 = \frac{\sqrt{2m\mu}}{\pi\hbar}, \quad (5.74)$$

$$\frac{dn_0}{d\mu} = \sqrt{\frac{m}{2\mu}} \frac{1}{\pi\hbar}. \quad (5.75)$$

Both equations (5.1) and (5.14) give

$$N_s = N_d = -1. \quad (5.76)$$

(5) Dark solitons in the unitary Fermi gas [147] (this is an analytical approximation that showed spectacular agreement with Bogoliubov-de Gennes theory):

$$E_s = \frac{Am\mu^2}{(1+\beta)^{3/2}\hbar^2} \frac{3^{3/2}}{4\pi} \left( \frac{1}{3} - \frac{mv_s^2}{2\mu} \right)^2, \quad (5.77)$$

$$\frac{dE_s}{d\mu} = \frac{\sqrt{3}Am\mu}{2\pi(1+\beta)^{3/2}\hbar^2} \left( \frac{1}{3} - \frac{mv_s^2}{2\mu} \right), \quad (5.78)$$

$$P_c = -\frac{\sqrt{3}A\mu m^2 v_s}{2\pi\hbar^2(1+\beta)^{3/2}} \left( 1 - \frac{mv_s^2}{2\mu} \right), \quad (5.79)$$

$$\frac{dP_c}{d\mu} = -\frac{\sqrt{3}Am^2 v_s}{2\pi\hbar^2(1+\beta)^{3/2}}, \quad (5.80)$$

$$n_0 = \frac{A}{3\pi^2} \left( \frac{2m\mu}{\hbar^2(1+\beta)} \right)^{3/2}, \quad (5.81)$$

$$\frac{dn_0}{d\mu} = \frac{Am}{\pi^2} \frac{(2m\mu)^{1/2}}{(\hbar^2(1+\beta))^{3/2}}. \quad (5.82)$$

Both equations (5.1) and (5.14) give

$$N_s = N_d = -\frac{\sqrt{3}Am\mu}{2\pi(1+\beta)^{3/2}\hbar^2} \left( \frac{1}{3} - \frac{mv_s^2}{2\mu} \right). \quad (5.83)$$

### 5.4.2 Numerical Examples

In addition to the examples above, we have tested SDPS-SGR equivalence numerically for solutions that are not known analytically. Firstly, recall that the system of two coupled one-dimensional Bose-Einstein condensates studied in chapter 3 has Josephson vortex and staggered-soliton solutions. We work with dimensionless quantities similar to those specified by equation (3.2) but use  $J$  instead of  $\mu$  in all of the scaling factors. For the staggered solitons, we take  $\theta = 0$ ,  $v_s = 1$ ,  $\Gamma = 1/2$  and continue the solution by varying  $\mu/J$ , keeping all other parameters fixed. Then we compute  $N_d$  according to the direct integral-of-the-density definition and the SGR formula, and  $N_s$  from the SDPS formula. The results are shown in Fig. 5.1 (a) where it is evident that all three calculation agree very closely.

For the Josephson vortices, we take  $v_s = 1$  and  $\Gamma = 1$  in our simulations. With reference to Fig. 3.6 (a), since there is a loop in the plot of excitation energy as a function of velocity, there are three distinct Josephson vortex solutions at the point in parameter space we have specified – we test all three. Panel (b) of Fig. 5.1 corresponds to a continuation of a point on the blue dashed-line segment in Fig. 3.6 (a) (not part of the loop), (c) to the green dashed-line segment in Fig. 3.6 (a) (lower section of the loop), and (d) to the red dashed-line segment in Fig. 3.6 (a) (upper section of the loop). In all three cases, it is clear that only the SGR  $N_d$  coincides with the true missing particle number.

Next, we test the equivalence in a three-dimensional Bose-Einstein condensate with cylindrical geometry, explored in the last section of [154] and in [110]<sup>1</sup>. There, one solves the three-dimensional Gross-Pitaevskii equation, looking for solutions translating at  $\tilde{v}_s$  (the velocity of the excitation on a ring with periodic boundary conditions),  $z$  being the co-moving axial coordinate in a cylindrical set of coordinates  $(r, \theta, z)$ :

$$-i\hbar\tilde{v}_s\partial_z\psi = \left[ -\frac{\hbar^2}{2m}\nabla^2 + \frac{1}{2}m\omega_r^2r^2 + g_{3D}N|\psi|^2 - \tilde{\mu} \right] \psi. \quad (5.84)$$

Note the transverse trapping potential, which confines the three-dimensional gas to a cylindrical geometry. Moreover, for numerical purposes,  $\psi$  is normalized to one, so the number of particles in the system only scales the non-linearity. We numerically impose periodic boundary conditions in  $z$  and solve the finite (but large) system case,

---

<sup>1</sup>Please note that all the simulations for this example were performed by our collaborator, Dr. Antonio Muñoz Mateo, who then kindly sent me the data and a detailed description of the calculations.

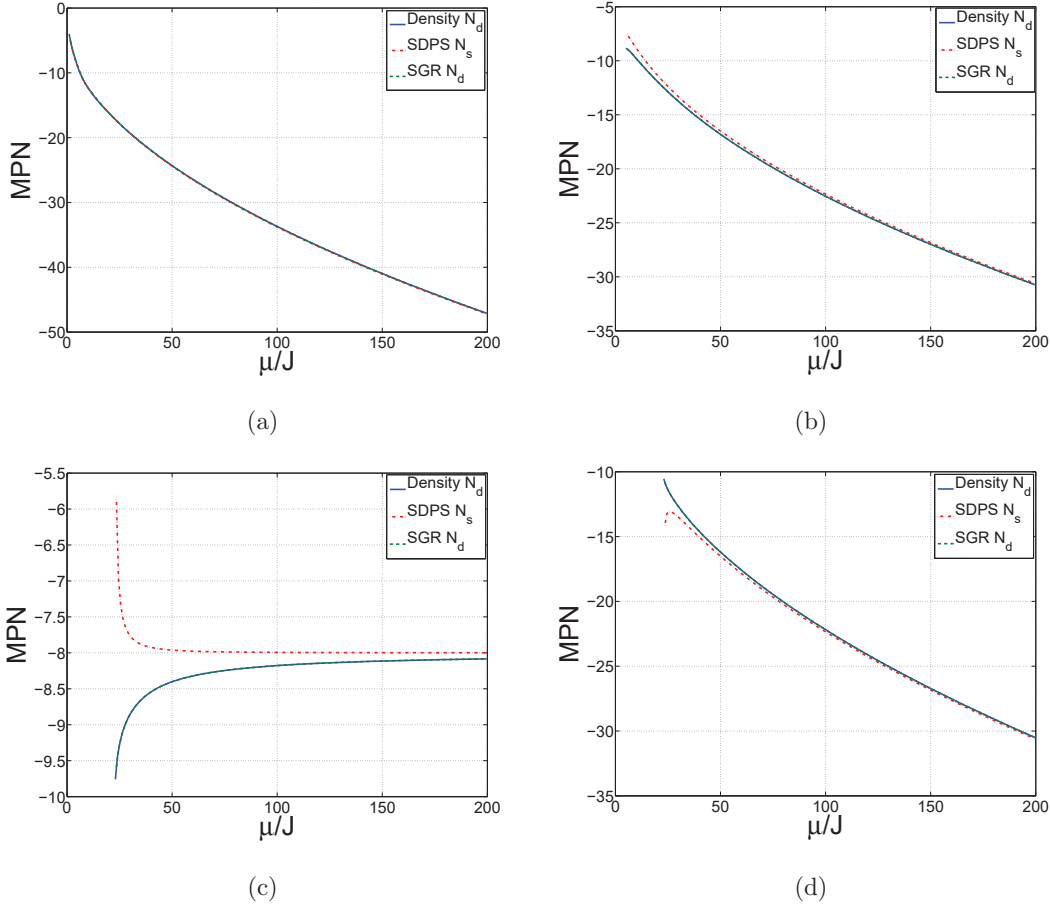


Figure 5.1: Missing particle number (labelled “MPN”, in units of  $\frac{\hbar J}{\sqrt{mJ(g+g_c)}}$ ) for staggered solitons (a) and Josephson vortices (b)-(d) found numerically in chapter 3. The equations are numerically integrated with  $v_s = 1$  for all panels. For (a),  $\theta = 0, \Gamma = 1/2$  and for (b)-(d),  $\Gamma = 1$ . The last three panels correspond to three distinct Josephson vortex solutions at the given parameter values. In each case, the initial point was taken from computations performed in chapter 3 and then continued in chemical potential, while keeping all other parameters fixed (notably, the velocity). Then, the missing particle number is calculated according to three methods: density integral (blue solid lines), the SDPS (red dash-dotted lines) and SGR (green dashed lines) formulae. In (a), for the staggered solitons, all three calculations are equivalent, but in (b)-(d), the SDPS formula clearly gives results inconsistent with the other two methods, which agree spectacularly among themselves.

then extracting the relevant quantities in the infinite system with open boundary conditions by transforming away the counter-flow, so that  $v_s = \tilde{v}_s - v_{cf}$ . The Gross-Pitaevskii equation is solved numerically by the Newton-Raphson method, with  $\psi$  expanded as a product of harmonic modes of the trapping potential in the transverse plane, and plane-waves in  $z$ .

To obtain dark solitons, the initial guess for the solver is the Gross-Pitaevskii dark soliton in the thermodynamic limit (see first example in section 5.4.1). As discussed in [110, 154], a whole family of solutions exists in this system, referred to as *Chladni solitons*, which bifurcate from the dark solitons. To find other Chladni excitations, we add a small weight of the unstable dark solitons of the Bogoliubov de-Gennes equation [155] to the numerical dark soliton already found, which seeds a dark soliton that decays into various Chladni excitations.

During this procedure,  $\tilde{\mu}$  is specified and  $N$  is adjusted until the Gross-Pitaevskii equation is satisfied. Now, in order to find the corresponding background state, we must first compute the chemical potential associated with the open boundary conditions solitonic solution,  $\mu$ . The  $\tilde{\mu}$  entering the Gross-Pitaevskii equation (5.84) is essentially that of equation (5.20),

$$\tilde{\mu} = \mu - mv_s v_{cf} - \frac{1}{2}mv_{cf}^2, \quad (5.85)$$

where we have now kept the last term which was dropped previously since we were working to first order in  $1/L$ . Thus the relevant chemical potential  $\mu$  is extracted from the value set in the Gross-Pitaevskii equation  $\tilde{\mu}$  by adding  $mv_s v_{cf} + \frac{1}{2}mv_{cf}^2$ . Once the correct chemical potential is determined, we search for a constant solution (constant in  $z$  – clearly the solution is not homogeneous in the radial direction due to the trap) using the same system size,  $L$ .

The parameters used are as follows. The transverse potential frequency is  $\omega_r = 2\pi \times 71.3$  Hz, the (bosonic) interaction strength is  $g_{3D} = \frac{4\pi\hbar^2 a_{3D}}{m}$  with  $a_{3D} = 0.06$   $\mu\text{m}$ , and the mass is that of two Lithium-6 atoms (Ref. [154] considered a fermionic condensate). The system length is taken as  $L = 2\pi \times 8.547467$   $\mu\text{m}$ .

The energy of a given state is evaluated using a three-dimensional analogue of the functional  $W$  of equation (5.15). Since the wavefunction has periodic boundary conditions, we need to subtract the counterflow energy, which amounts to adding the following correction to the excitation energy  $\frac{1}{2}mN_x v_{cf}^2 - v_{cf} P_c$  (see chapter 11), where  $N_x$  is the number of particles in the excited state, and  $P_c$  is the total momentum in the excited state with periodic boundary conditions, computed from a three-dimensional analogue of (5.16) without the factor of  $v_s$ . Finally, the SGR formula requires  $P_c$  of the infinite system, which must be obtained from  $P_c = P_s + P_{cf}$ , where  $P_s = mN_d v_s$  (with  $N_d$  given by the density definition) and  $P_{cf} = \hbar n_0 \Delta\phi = mN_x v_{cf}$ .

We have evaluated all three formulae for the missing particle number for four Chladni solitons: a dark soliton, a vortex ring, a solitonic vortex and a double solitonic vortex, plotted respectively in Fig. 5.2 (a)-(d). Once again, we see that the SGR formula always agrees with the density definition, while the SDPS equation only agrees with the other two for dark solitons.

## 5.5 Discussion and Conclusions

We have presented a clear derivation of the SGR formula for extracting the actual missing particle number of solitonic excitations from the dispersion relation for a superfluid one-dimensional system in the thermodynamic limit. The argument is largely based on the Hellmann-Feynman theorem for functionals. Moreover, we have investigated when the SGR formula for the actual missing particle number becomes equivalent to the SDPS effective one for all velocities, giving general conditions and both analytical and numerical mean-field examples.

We remark that it is easy to generalize our derivation from one dimension to a three-dimensional system in a quasi-one-dimensional geometry, with the constraining potential depending on the radial ( $r$ ) and azimuthal-angle ( $\theta$ ) coordinates. One can even include several components (say  $N_c$ ) of condensate atoms, interacting via nearest-neighbour tunnelling, as long as the non-linearity depends purely on the modulus-squares of the wavefunction components. Each component wavefunction must vanish as  $r \rightarrow \infty$  and be continuous in  $\theta$  across  $0, 2\pi$ . As  $z \rightarrow \pm\infty$ , each component may tend to a different background density  $n_k(r, \theta)$ . Given the non-zero tunnelling between the different components, all components of the condensate must have the same phase-step,  $\Delta\phi$ . Under these conditions, the derivation of the SGR formula proceeds in an exactly analogous way and the final result is identical, with the understanding that the one-dimensional density  $n_0$  is replaced by a (total) linear density

$$n_0 = \sum_{k=1}^{N_c} \int_0^{2\pi} \int_0^{\infty} r n_k(r, \theta) dr d\theta. \quad (5.86)$$

This more general version of the derivation [156] is somewhat more cumbersome (mostly in terms of notation and the need for vector calculus when presenting the Hellmann-Feynman theorem of appendix 5.A), so here we have chosen to present the pure one-dimensional case for clarity of argument and readability.

Furthermore, one may question whether the derivation of section 5.3 is truly limited to systems obeying a non-linear Schrödinger equation, as in (5.17). In fact, it is possible to proceed with the same arguments assuming the following general points.

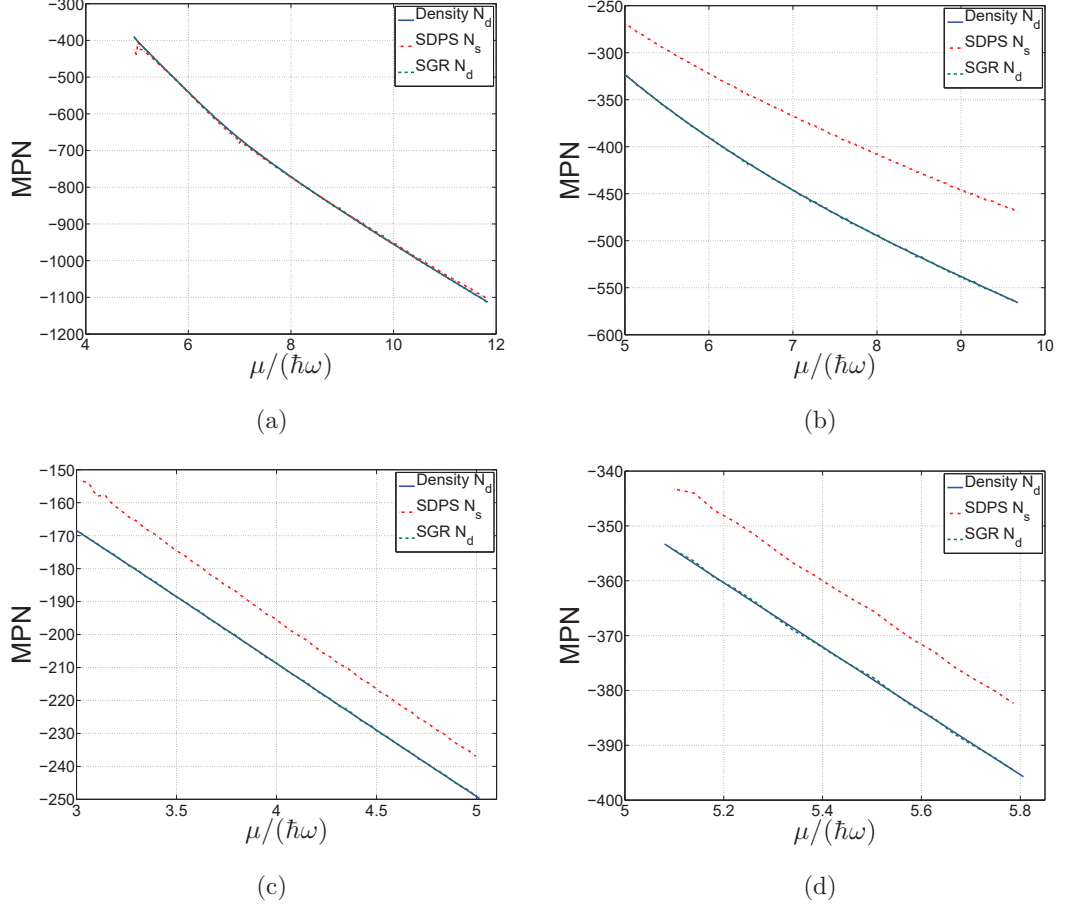


Figure 5.2: Missing particle number (labelled “MPN”) for a dark soliton with  $v_s = -0.28\sqrt{\frac{\hbar\omega_r}{m}}$  (a), vortex ring with  $v_s = 0.8\sqrt{\frac{\hbar\omega_r}{m}}$  (b), solitonic vortex with  $v_s = -0.32\sqrt{\frac{\hbar\omega_r}{m}}$  (c) and double solitonic vortex with  $v_s = -0.36\sqrt{\frac{\hbar\omega_r}{m}}$  (d) found numerically in [154]. The Gross-Pitaevskii equation is numerically integrated, as described in the text. The parameters are  $\omega_r = 2\pi \times 71.3$  Hz,  $g_{3D} = \frac{4\pi\hbar^2 a_{3D}}{m}$  with  $a_{3D} = 0.06\mu\text{m}$ ,  $m = 2.3052 \times 10^{-26}$  kg [154],  $L = 2\pi \times 8.547467\mu\text{m}$ . In each case, the missing particle number is calculated according to three methods: density integral (blue solid line), the SDPS (red dash-dotted line) and SGR (green dashed line) formulae. In (a), for the dark solitons, all three calculations are equivalent, but in (b)-(d), the SDPS formula clearly gives results inconsistent with the other two methods, which agree well among themselves. The visible scatter in the data is numerical noise.

The system must be Lagrangian and superfluid<sup>2</sup>, so that the order parameter has a coherent phase, the spatial derivative of which gives rise to super-currents. The geometry is elongated, with translational invariance along the longitudinal direction, ensuring Galilean invariance. The number of particles must be sufficiently large so that a continuous description of the problem is appropriate. As always, we are concerned with solitonic excitations maintaining their shape as they translate at constant velocity. These solitary waves must have both a density depletion and a phase step. Conversely, the state of the system must be fully describable by the density and phase profiles – there must be no other quantity (such as charge or spin) which may change upon introduction of the impurity to a uniform background.

With these assumptions, using a Galilean transformation to a moving frame at  $v_s$ , we can show that the lab-frame Lagrangian with open boundary conditions  $\mathcal{L}$  is the negative of the grand canonical ensemble energy in the moving frame at  $v_s$ ,  $W_M$ , i.e.

$$W_M = H_M - \mu_M N = H - v_s P - \mu N = -\mathcal{L}, \quad (5.87)$$

where the subscript  $M$  indicates a moving-frame quantity and no subscript a lab-frame one. Moreover, in the above,  $H$  is the canonical energy,  $\mu$  the chemical potential,  $N$  the number of particles,  $v_s$  the speed of the soliton and  $P$  the total momentum (in this case equal to  $P_s$ , the momentum of the soliton).

Likewise, the lab-frame Lagrangian with periodic boundary conditions is the negative of the grand canonical ensemble energy in the moving frame at  $\tilde{v}_s$ :

$$\begin{aligned} W_M &= H_M - \mu_M N = H - \tilde{v}_s P - (\mu - mv_s v_{cf} - mv_{cf}^2) N \\ &= H - \tilde{v}_s P - \tilde{\mu} N = -\tilde{\mathcal{L}}, \end{aligned} \quad (5.88)$$

to  $\mathcal{O}(1/L)$ , where  $\tilde{\mu}, \tilde{v}_s, v_{cf}$  are defined by (5.20)-(5.22). This time, the total momentum  $P$  is  $P_c$ , which includes both the solitonic and backflow contributions.

Thus, it is possible to deduce the functional to be extremized without reference to a specific equation of motion, or the assumption of particular expressions for the energy and momentum.

Finally, we introduce abstract state vectors  $\vec{X}$ , which carry all the essential information necessary to uniquely specify the states. This includes, but is not limited to the order parameter. In particular,  $\vec{X}$  is such that extremizing the Lagrangian with respect to all the elements of  $\vec{X}$  yields the equations of motion for the system. Finally, invoking the principle of least action, the derivation proceeds as before.

After this work was completed, I became aware of a very similar article [158] that closely parallels the arguments presented here.

---

<sup>2</sup>Although if the system approximately obeys equations usually applicable to superfluids for finite time intervals, the derivation is approximately applicable during those time intervals, e.g. [157].

# Appendix

## 5.A Hellmann-Feynman Theorem

In this appendix we derive the Hellmann-Feynman theorem for functionals. Consider a simplified case when the Lagrangian  $\mathcal{L}$  only depends on one real function  $\psi(z)$  and on one parameter  $\mu$ :

$$\mathcal{L}[\psi] = \int dz \mathcal{L}[\psi, \partial_z \psi, \mu]. \quad (5.89)$$

We can take the derivative of  $\mathcal{L}$  with respect to  $\mu$  using the chain rule:

$$\frac{d\mathcal{L}}{d\mu} = \int dz \frac{\partial \mathcal{L}}{\partial \psi} \frac{d\psi}{d\mu} + \frac{\partial \mathcal{L}}{\partial (\partial_z \psi)} \frac{d(\partial_z \psi)}{d\mu} + \frac{\partial \mathcal{L}}{\partial \mu}. \quad (5.90)$$

Recall the definition of the functional derivative

$$\frac{\delta \mathcal{L}}{\delta \psi} = \frac{\partial \mathcal{L}}{\partial \psi} - \frac{d}{dz} \frac{\partial \mathcal{L}}{\partial (\partial_z \psi)}, \quad (5.91)$$

and use it to express  $\frac{\partial \mathcal{L}}{\partial \psi}$  through  $\frac{\delta \mathcal{L}}{\delta \psi}$ , then substituting back into (5.90):

$$\begin{aligned} \frac{d\mathcal{L}}{d\mu} &= \int dz \frac{\delta \mathcal{L}}{\delta \psi} \frac{d\psi}{d\mu} + \partial_z \left[ \frac{\partial \mathcal{L}}{\partial (\partial_z \psi)} \right] \frac{d\psi}{d\mu} \\ &+ \frac{\partial \mathcal{L}}{\partial (\partial_z \psi)} \frac{d(\partial_z \psi)}{d\mu} + \frac{\partial \mathcal{L}}{\partial \mu}. \end{aligned} \quad (5.92)$$

The two middle terms on the right-hand side of the above equation can be combined via the product rule to one term:

$$\int dz \partial_z \left[ \frac{\partial \mathcal{L}}{\partial (\partial_z \psi)} \frac{d\psi}{d\mu} \right]$$

and by the fundamental theorem of calculus, we get

$$\frac{d\mathcal{L}}{d\mu} = \int \frac{\delta \mathcal{L}}{\delta \psi} \frac{d\psi}{d\mu} + \frac{\partial \mathcal{L}}{\partial \mu} dz + \left[ \frac{\partial \mathcal{L}}{\partial (\partial_z \psi)} \frac{d\psi}{d\mu} \right]_{-\infty}^{\infty}. \quad (5.93)$$

The first term on the right-hand side is the “functional derivative” term and the last the “boundary” term. The Hellmann-Feynman theorem is satisfied if both vanish. This is guaranteed if  $\psi$  extremizes  $\mathcal{L}$  and has periodic boundary conditions.

# Chapter 6

## The Bethe Ansatz

The preceding chapters were all concerned with mean-field one-dimensional bosonic systems, applicable in the weakly-interacting regime. When the interactions are stronger, however, the mean-field description breaks down. Fortunately, in one dimension, particles with contact interactions (of any symmetry and with an arbitrary number of spin states) can be solved via the Bethe ansatz [51]. In this chapter we will present the derivation of the (finite) Bethe ansatz equations for the Lieb-Liniger model (spinless bosons) and the Yang-Gaudin model (spin-1/2 fermions) with periodic boundary conditions. These are then solved in chapters 7 & 8.

### 6.1 The Bethe Ansatz Wavefunction

The Lieb-Liniger model is the simplest of all of the  $\delta$ -function interacting models in one dimension as it describes one species of identical bosons. It was the first to be solved in the seminal papers [46, 47], followed by the Yang-Gaudin model, describing two spin-components of fermions [48, 49], which is the next sensible level of complexity. The derivations for both models can be done in parallel up to the stage of the spin wavefunction – thus, for the spatial part of the solution we follow appendix A1 of [159] which repeats the arguments of Yang [48], but providing sufficient details to be comprehensible. For the spin wavefunction of the Yang-Gaudin model we follow [160], which once again comprehensibly elaborates on the original approach of [48].

The Hamiltonian for both models reads

$$H = -\frac{\hbar^2}{2m} \sum_{j=1}^N \frac{d^2}{dx_j^2} + \frac{\hbar^2}{m} c \sum_{\langle i,j \rangle} \delta(x_i - x_j), \quad (6.1)$$

where in the second term the sum is over all distinct pairs. The particles are confined to a ring with circumference  $L$  and have mass  $m$ . It is customary to set  $\hbar = 1$  and  $2m = 1$  in the course of the derivation for simplicity, but we will restore full units

once it is complete. Thus the Hamiltonian becomes

$$H = - \sum_{j=1}^N \frac{d^2}{dx_j^2} + 2c \sum_{\langle i,j \rangle} \delta(x_i - x_j). \quad (6.2)$$

For the Lieb-Liniger model, all  $N$  particles are spinless bosons, while for the Yang-Gaudin model,  $M \leq N/2$  are spin-down fermions and the other  $N - M$  are spin-up. Since the Hamiltonian is spin-independent, it commutes with  $\mathbf{S}^2$  and  $S_z$ , the magnitude and  $z$ -component of the total spin angular momentum operator. This implies that the total wavefunction factorizes into a spatial component times a spin component. Next, recall that the total wavefunction for identical<sup>1</sup> bosons (fermions) is totally (anti-) symmetric under particle exchange. This total (anti-) symmetry holds if we swap the position coordinates *and* spin labels of any two particles.

Of course, for bosons (fermions) this means that the spatial and spin wavefunctions must have the same (opposite) symmetry under the exchange of particles  $i$  and  $j$ . This statement is equivalent to saying that the Young tableaux for the two components of the wavefunction must be the same shape for bosons and conjugates for fermions<sup>2</sup> (see Fig. 6.1 (a) for an illustration of Young tableaux conjugation). For the spin wavefunction we will choose a single-row tableau for bosons and a two-row tableau for fermions. In the latter case, the rows are  $N - M$  and  $M$  long, each row full of one type of spin label. An example of these tableaux is shown in Fig. 6.1 (b).

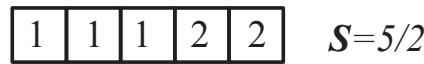
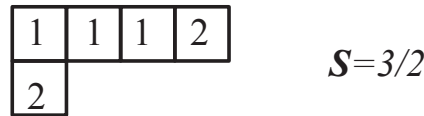
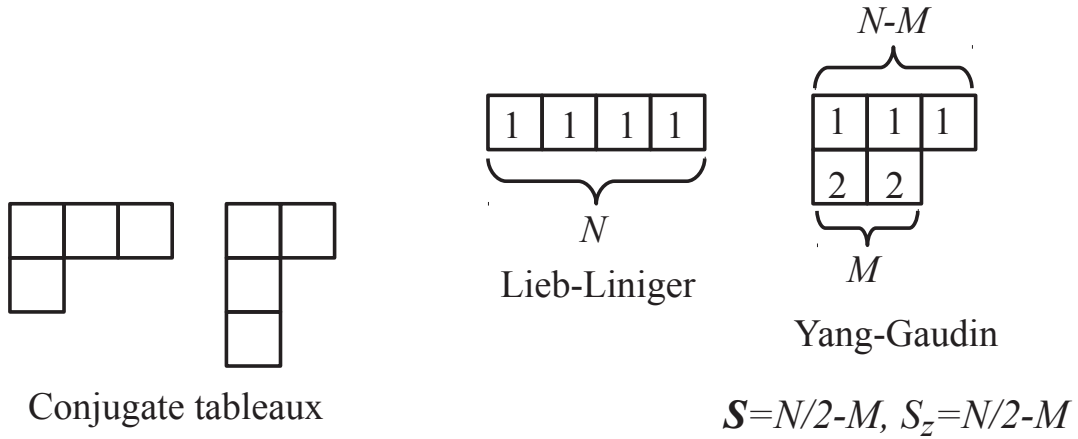
Note that for the Yang-Gaudin model this is not the only possible choice. For  $SU(2)$  objects, the spin wavefunction can only have a Young tableau of two rows or less. This is because we cannot have a column that is 3 boxes long (or longer), as numbers must strictly increase down each column (in our case the available numbers are 1 & 2) and either stay constant or grow along rows. Starting from the two-row tableau ( $N - M$  and  $M$  long), we can then move a box with label “2” from the end of the second row and attach it to the end of the top row, which gives another valid Young tableau. This can be repeated for all the boxes in the second row, as demonstrated in Fig. 6.1 (c) for a particular example. The resulting states all have  $S_z = 0$ , but different  $S$  values.

In fact, for  $SU(2)$  objects only, the total spin of the many-particle state can be inferred from the structure of the Young tableau. All columns that are 2 boxes long have  $S = 0$ , so we need only consider the excess, unpaired boxes. If there is one unpaired box, then that is an  $S = 1/2$  (doublet) state. Two unpaired boxes have  $S = 1/2 + 1/2 = 1$ , a spin-triplet. The  $S$  value is labelled on Fig. 6.1 (c)

---

<sup>1</sup>Identical means that all the properties of the atoms are the same, up to the spin state, which can be arbitrary.

<sup>2</sup>For an exposition on Young tableaux, see [161], section 6.5.



$S_z=1/2$  for all

(c)

Figure 6.1: (a) An example of conjugate Young tableaux (rows become columns and *vice versa*). (b) The Young tableaux chosen for the spin wavefunction for the Lieb-Liniger model (left, illustration uses  $N = 4$ ) and the Yang-Gaudin model (right, schematic shown for  $N = 5$ ,  $M = 2$ ). The spin state associated with the Yang-Gaudin tableau has  $S = S_z = N/2 - M$ . (c) All valid Young tableaux for the case  $N = 5$ ,  $M = 2$  in the Yang-Gaudin model. All three tableaux have the same  $S_z = N/2 - M$ , but different  $S$  values, determined from 1/2 times the number of unpaired boxes.

for each possible tableau as an illustration of the process. Thus the shape of the tableau determines the total spin  $S$ . Since we choose one particular tableau for the Yang-Gaudin model, the states described by the Bethe ansatz equations which we shall derive all have  $S = N/2 - M$  and  $S_z = N/2 - M$ .

The ansatz for the total wavefunction reads

$$\psi(\vec{x}, \vec{\sigma}) = \sum_P A_{\vec{\sigma}}(P|Q) \exp(i\vec{k}_P \cdot \vec{x}_Q). \quad (6.3)$$

There are  $N$  particles, so  $\vec{x}$  and  $\vec{k}$  are  $N$ -component vectors. All the entries of  $\vec{k}$  are assumed to be distinct.  $P$  and  $Q$  are permutations of the ordered set of integers  $\{1, \dots, N\}$  which specify the labels on the  $x$ 's and  $k$ 's, and in particular which  $x$  is paired with which  $k$ . The sum is over all  $N!$  possible permutations  $P$ .  $Q$  is such that the elements of  $\vec{x}_Q$  are strictly increasingly ordered.

$\vec{\sigma}$  is a vector of spin labels (or *coordinates*), one for each particle. For a single component (either one type of bosons or fermions), all particles have the same spin so  $\vec{\sigma}$  can be dropped. For two spin components (as an example), each  $\sigma_j$  is a variable that can take on labels “1” or “2”. If  $M$  is unspecified, there are (number of spin components) <sup>$N$</sup>  possible  $\vec{\sigma}$  vectors.

## 6.2 Spatial Part of the Bethe Ansatz

Let  $P_{ij}$  be the total permutation operator (spin labels and spatial coordinates) which acts on the expansion coefficients in the following way:

$$[P_{ij}]_{\vec{\sigma}}^{\vec{\sigma}'} A_{\vec{\sigma}'}(P|Q) = A_{\vec{\sigma}}(P|Q'), \quad (6.4)$$

where

- $\sigma_i = \sigma'_j$  and  $\sigma_j = \sigma'_i$ , and all the other entries of  $\vec{\sigma}$  &  $\vec{\sigma}'$  are identical,
- $Q'$  only differs from  $Q$  in two entries:  $Q_a = i$  and  $Q_b = j$  while  $Q'_a = j$  and  $Q'_b = i$ .

Moreover, we use the index contraction notation for inner products of tensors to account for spin-label changes.

Now let us consider continuity when any two particles pass through each other. Assume we have a permutation  $Q$  with  $Q_a = i$  and  $Q_b = j$  such that  $x_i < x_j$ . What is the condition on the wavefunction so that it is continuous as the particles pass through to give  $x_j < x_i$ ? Recall the  $\vec{k}_P \cdot \vec{x}_Q$  inner product in the exponent:  $Q_a$  and  $Q_b$  are paired with  $P_a$  and  $P_b$  (for any given permutation  $P$ ). However, when  $x_i < x_j$   $Q$  reads  $\dots, a, b, \dots$  and when  $x_j < x_i$ ,  $Q'$  reads  $\dots, b, a, \dots$ . Moreover,

there is a sum over  $P$  in the ansatz, so there will be a different permutation of the  $k$ 's,  $P'$ , where  $P_a$  and  $P_b$  are swapped, and this is true on both sides of  $x_i = x_j$ . The relevant terms on the left- and right-hand sides respectively are then

$$A_{\bar{\sigma}}(P|Q) \exp(i\vec{k}_P \cdot \vec{x}_Q) + A_{\bar{\sigma}}(P'|Q) \exp(i\vec{k}_{P'} \cdot \vec{x}_Q), \quad (6.5)$$

$$A_{\bar{\sigma}}(P|Q') \exp(i\vec{k}_P \cdot \vec{x}_{Q'}) + A_{\bar{\sigma}}(P'|Q') \exp(i\vec{k}_{P'} \cdot \vec{x}_{Q'}). \quad (6.6)$$

Seeing as the  $N$ -particle plane waves are orthogonal unless all the  $x$ 's are paired up with exactly the same  $k$ 's, and realizing that as the particles pass through each other,  $x_i = x_j$  (which allows us to cancel the exponentials), we see that we must have the relation

$$A_{\bar{\sigma}}(P|Q) + A_{\bar{\sigma}}(P'|Q) = A_{\bar{\sigma}}(P|Q') + A_{\bar{\sigma}}(P'|Q'). \quad (6.7)$$

We can go further: we can obtain an additional relation between these coefficients based on the  $\delta$ -function interaction of the Hamiltonian (which they experience as they pass through each other). It is possible to replace the  $\delta$ -function interaction term in the Hamiltonian by additional boundary conditions: a jump in the derivatives as two particles exchange positions, given by [46]

$$\left( \frac{\partial}{\partial x_j} - \frac{\partial}{\partial x_i} \right) \psi \Big|_{x_j=x_i^+} - \left( \frac{\partial}{\partial x_j} - \frac{\partial}{\partial x_i} \right) \psi \Big|_{x_j=x_i^-} = 2c \psi|_{x_j=x_i}. \quad (6.8)$$

We can see this by integrating the time-independent Schrödinger equation with respect to  $x_i$  and  $x_j$ , assumed to be infinitesimally close to each other, with  $x_i < x_j$ . The integral over  $x_i$  is to be done over  $[x_i - \epsilon_i, x_i + \epsilon_i]$  and that over  $x_j$  in the range  $[x_j - \epsilon_j, x_j + \epsilon_j]$ . Taking the limit as  $\epsilon_{i,j} \rightarrow 0$ , one arrives at (6.8).

Now, the only terms in the wavefunction that matter when evaluating (6.8) are the ones we have singled out for the continuity equation, (6.5) & (6.6). When applying the derivative step condition, we use the terms in (6.5), applicable when  $x_j > x_i$ , and the terms in (6.6) when  $x_i > x_j$ . Differentiation of the exponentials brings down factors of  $ik_{P_a}$  and  $ik_{P_b}$ . After cancelling the exponentials, the left-hand side of the  $\delta$ -function interaction equation (6.8) then becomes

$$i(k_{P_b} - k_{P_a}) [A_{\bar{\sigma}}(P|Q) + A_{\bar{\sigma}}(P|Q') - A_{\bar{\sigma}}(P'|Q) - A_{\bar{\sigma}}(P'|Q')]. \quad (6.9)$$

The middle two terms in the square brackets can be rewritten through the first and last terms by making use of (6.7), which makes the left-hand side of (6.8)

$$2i(k_{P_b} - k_{P_a}) [A_{\bar{\sigma}}(P|Q) - A_{\bar{\sigma}}(P'|Q')], \quad (6.10)$$

while the right-hand side can be taken directly from (6.7). All together, we have

$$i(k_{P_b} - k_{P_a}) [A_{\vec{\sigma}}(P|Q) - A_{\vec{\sigma}}(P'|Q')] = c [A_{\vec{\sigma}}(P|Q) + A_{\vec{\sigma}}(P'|Q)]. \quad (6.11)$$

Rearranging this equation yields

$$\begin{aligned} [i(k_{P_b} - k_{P_a}) - c]A_{\vec{\sigma}}(P|Q) &= cA_{\vec{\sigma}}(P'|Q) + i(k_{P_b} - k_{P_a})A_{\vec{\sigma}}(P'|Q') = \\ cA_{\vec{\sigma}}(P'|Q) + i(k_{P_b} - k_{P_a})[P_{ij}]_{\vec{\sigma}}^{\vec{\sigma}'} A_{\vec{\sigma}'}(P'|Q), \end{aligned} \quad (6.12)$$

where in the last line we have used (6.4) to ensure that on the right-hand side we have terms with the same  $Q$  and  $\vec{\sigma}$  as on the left-hand side but a different  $P$ -permutation ( $P'$  instead of  $P$ ). We can therefore define the operator that permutes two entries of  $P$  (and the corresponding ones in  $\vec{\sigma}$ ) as

$$A_{\vec{\sigma}}(P|Q) = \left( \frac{i(k_{P_b} - k_{P_a})P_{ij} + c}{i(k_{P_b} - k_{P_a}) - c} \right)_{\vec{\sigma}}^{\vec{\sigma}'} A_{\vec{\sigma}'}(P'|Q) = [Y_{ij}(k_{P_b} - k_{P_a})]_{\vec{\sigma}}^{\vec{\sigma}'} A_{\vec{\sigma}'}(P'|Q). \quad (6.13)$$

Note that in the middle expression above  $P_{ij}$  lacks spin indices, and is implied to only operate on  $Q$ , while the spin permutation operation is instead carried by the entire fraction. Furthermore, we can also define an operator which permutes two entries in  $P$ , the corresponding ones in  $Q$ , and leaves the spin labels unaltered:

$$X_{ij}(u) := [Y_{ij}(u)]_{\vec{\sigma}}^{\vec{\sigma}'} [P_{ij}]_{\vec{\sigma}}^{\vec{\sigma}'}, \quad (6.14)$$

which acts on the expansion coefficients as

$$A_{\vec{\sigma}}(P|Q) = X_{ij}(k_{P_b} - k_{P_a})A_{\vec{\sigma}}(P'|Q'). \quad (6.15)$$

It is now time to impose periodic boundary conditions. Due to our choice to have  $Q$  such that the  $x$ 's are increasingly ordered, periodic boundary conditions can be imposed with reference only to the first entry of  $P$  and  $Q$ . In particular, periodic boundary conditions require that  $\psi|_{x_{Q_1}=0} = \psi|_{x_{Q_1}=L}$ . Recalling our ansatz (6.3), the plane waves took the form  $\exp(i\vec{k}_P \cdot \vec{x}_Q)$ . So when  $x_{Q_1} = 0$  the inner product in the exponential reads  $0 + k_{P_2}x_{Q_2} + \dots + k_{P_N}x_{Q_N}$ . When  $x_{Q_1} = L$  this  $x$  coordinate is the largest out of the  $N$  and needs to be permuted to the end of  $Q$ . In order for all the other  $x$ 's to have the same  $k$  coefficients (linear independence of the different plane waves in the expansion implies that only this term matters), we need to consider the  $P$  permutation where  $P_1$  is also permuted to the end of  $P$ . The inner product then reads  $k_{P_2}x_{Q_2} + \dots + k_{P_N}x_{Q_N} + k_{P_1}L$ . Now,  $\exp(ik_{P_1}L)$  is a number, independent of the  $x$ -coordinates, so it needs to be absorbed into the expansion coefficient. In other words, we have permuted the first entry of both  $P$  and  $Q$  to the end which brought

out an additional exponential factor:

$$A_{\vec{\sigma}}(P|Q) = A_{\vec{\sigma}}(P_2, \dots, P_N, P_1|Q_2, \dots, Q_N, Q_1) \exp(ik_{P_1}L). \quad (6.16)$$

Of course, this equation can be generalized: permuting any  $j^{\text{th}}$  element of  $P$  and  $Q$  from the beginning to the end of the chain will yield an additional factor of  $\exp(ik_{P_j}L)$  to the  $A$  coefficient. This can be written in a concise manner using a chain of the  $X$  operators. Assume that  $P$  and  $Q$  are originally the identity permutation of the ordered set  $\{1, \dots, N\}$ . Therefore, in the equation that follows, when we need to write  $X_{ij}(k_{P_b} - k_{P_a})$  we can suppress the  $(k_{P_b} - k_{P_a})$  argument of  $X$  since it will always be simply  $k_i - k_j$ . This way, the periodic boundary conditions can be written as a set of  $N$  equations:

$$\begin{aligned} A_{\vec{\sigma}}(1, \dots, j-1, j+1, \dots, N, j|1, \dots, j-1, j+1, \dots, N, j) \exp(ik_jL) = \\ X_{1,j} \dots X_{j-1,j} X_{j+1,j} \dots X_{N,j} \\ A_{\vec{\sigma}}(1, \dots, j-1, j+1, \dots, N, j|1, \dots, j-1, j+1, \dots, N, j). \end{aligned} \quad (6.17)$$

Let us think about what happens on the right-hand side: we begin from  $P, Q$  which are identities except that the  $j^{\text{th}}$  particle is moved to the end. Then we permute the  $j^{\text{th}}$  particle through each and every one of the particles on the left of it in turn, and we do this both in  $P$  and in  $Q$ . Finally, we get to the first particle in the chain and permute through it too, which puts the  $j^{\text{th}}$  particle at the start of the chain. The periodic boundary conditions equation states that this chain of permutations is equivalent to multiplying the expansion coefficient by  $\exp(ik_jL)$ .

Now, for a single component of either bosons or fermions, the  $\vec{\sigma}$  label can be dropped and the eigenvalue of  $P_{ij}$  is  $\pm 1$ , respectively. Then the product of the  $X_{mn}$  operators (upper sign for bosons, lower for fermions),

$$X_{mn}(k_m - k_n) = \frac{i(k_m - k_n) + cP_{mn}}{i(k_m - k_n) - c} = \frac{i(k_m - k_n) \pm c}{i(k_m - k_n) - c} \quad (6.18)$$

immediately gives the Bethe ansatz equations. For the Lieb-Liniger model, these read

$$\exp(ik_jL) = \prod_{m \neq j} \frac{i(k_m - k_j) + c}{i(k_m - k_j) - c} = - \prod_{m=1}^N \frac{k_j - k_m + ic}{k_j - k_m - ic}, \quad (6.19)$$

and for one spin component of fermions, they reduce to

$$\exp(ik_jL) = 1, \quad (6.20)$$

as expected.

For two-component fermions, more work is needed. Let us first rewrite (6.17) such that the  $P, Q$  permutations appearing in  $A$  are the identity, using

$$\begin{aligned} A_{\bar{\sigma}}(1, \dots, j-1, j+1, \dots, N, j | 1, \dots, j-1, j+1, \dots, N, j) = \\ X_{j,N} \dots X_{j,j+1} A_{\bar{\sigma}}(1, 2, \dots, N | 1, 2, \dots, N). \end{aligned} \quad (6.21)$$

Upon substitution into (6.17), we need to use the first of the identities involving the  $X$ -operators (these can be verified by simple permutation of indices):

$$\begin{aligned} X_{ij} X_{ji} &= 1, \\ X_{ij} X_{kl} &= X_{kl} X_{ij}, \\ X_{jk} X_{ik} X_{ij} X_{kj} X_{ki} X_{ji} &= 1. \end{aligned} \quad (6.22)$$

From the first identity, it is clear that the inverse of  $X_{j,N} \dots X_{j,j+1}$  is  $X_{j+1,j} \dots X_{N,j}$ . Applying this inverse operator from the left on both side of (6.17), on the left-hand side we are left with  $A_{\bar{\sigma}}(1, 2, \dots, N | 1, 2, \dots, N) \exp(ik_j L)$ , while on the right, we have the following chain of  $X$  operators:

$$X_{j+1,j} \dots X_{N,j} X_{1,j} \dots X_{j-1,j} [X_{j+1,j} \dots X_{N,j} X_{j,N} \dots X_{j,j+1}], \quad (6.23)$$

acting on the same  $A$ . Now, the term in the brackets is one, by the first  $X$  identity. We arrive at the  $N$  equations

$$\begin{aligned} A_{\bar{\sigma}}(1, 2, \dots, N | 1, 2, \dots, N) \exp(ik_j L) = \\ X_{j+1,j} \dots X_{N,j} X_{1,j} \dots X_{j-1,j} A_{\bar{\sigma}}(1, 2, \dots, N | 1, 2, \dots, N). \end{aligned} \quad (6.24)$$

The beauty of writing the equations this way is that now the  $A$  coefficient does not carry a  $j$  label, and it becomes clear that there exists a common eigenvector  $A$  of  $N$  operators (the products of the  $X$ 's, which *do* carry a  $j$  label), with different eigenvalues (also  $j$ -dependent). This completes the work on the spatial component of the wavefunction. We may now drop the  $(Q|P)$  arguments of  $A$  as they are always the identity permutations.

### 6.3 Spin Part of the Bethe Ansatz

The next step is the diagonalization of these  $N$  operators in spin-space. If we constrain the problem to have  $M \leq N/2$  spin-down particles, then there are  $\binom{N}{M}$  product basis states spanning the spin Hilbert space. The common eigenvector we are after can then be thought of as a linear combination of these basis states. Call this common eigenvector  $A$  (i.e. drop the spin label, as we are now working fully in

spin-space).

In order to proceed, we write the overall permutation operator  $[P_{ij}]_{\vec{\sigma}}^{\vec{\sigma}'}$  as a product of a permutation operator on  $Q$ ,  $P_{ij}(Q)$ , and a permutation operator on  $\vec{\sigma}$ ,  $P_{ij}(\vec{\sigma})$ . Note that each of these permutation operators is its own inverse. Thus,

$$\begin{aligned} X_{ij}(k_i - k_j) &= [Y_{ij}(k_i - k_j)]_{\vec{\sigma}'}^{\vec{\sigma}} [P_{ij}]_{\vec{\sigma}}^{\vec{\sigma}'} = \left( \frac{i(k_i - k_j)[P_{ij}]_{\vec{\sigma}'}^{\vec{\sigma}} + cP_{ij}(\vec{\sigma})}{i(k_i - k_j) - c} \right) [P_{ij}]_{\vec{\sigma}}^{\vec{\sigma}'} \\ &= \frac{i(k_i - k_j) + cP_{ij}(Q)}{i(k_i - k_j) - c}. \end{aligned} \quad (6.25)$$

Now, the eigenvalue of  $[P_{ij}]_{\vec{\sigma}}^{\vec{\sigma}'}$  is -1 (for fermions), so  $P_{ij}(Q)P_{ij}(\vec{\sigma}) = -1$  and multiplying both sides by  $P_{ij}(Q)$  we find  $P_{ij}(Q) = -P_{ij}(\vec{\sigma})$ . Therefore,

$$X_{mn}(k_m - k_n) = \frac{i(k_m - k_n) - cP_{mn}(\vec{\sigma})}{i(k_m - k_n) - c}. \quad (6.26)$$

We may now drop the explicit  $\vec{\sigma}$  argument of  $P_{ij}$ , with the understanding that the remaining permutation operators appearing in the chain of  $X$ 's act only on the spin part of the wavefunction.

Next we specify an ansatz for  $A$  (hence this approach is known as the *nested* Bethe ansatz): let  $\{y_1, y_2, \dots, y_M\}$  be  $M$  distinct integers drawn from the set  $\{1, 2, \dots, N\}$  – these will be the particles we will give spin-down labels to. Moreover, let there be some  $M$  distinct numbers  $\alpha_m$ , and  $P, Q$  denote permutations of the ordered set  $\{1, 2, \dots, M\}$ . Then we take

$$\Phi = \sum_P a(P) F(\alpha_{P_1}, y_{Q_1}) \dots F(\alpha_{P_M}, y_{Q_M}), \quad (6.27)$$

where

$$F(\alpha, y) = \prod_{j=1}^{y-1} \frac{ik_j - i\alpha - c/2}{ik_{j+1} - i\alpha + c/2}, \quad (6.28)$$

and  $Q$  is such that the  $y$ 's are increasingly ordered.  $\Phi$  satisfies cyclic boundary conditions (details are given later).  $A$ , the common eigenvector we are after, is given by

$$|A\rangle = \sum_{\vec{\sigma}} \Phi(\vec{\sigma}) |\vec{\sigma}\rangle, \quad (6.29)$$

a linear combination of all the possible spin product basis states, with  $\Phi$  as the expansion coefficients.

### 6.3.1 Statement of Results

First let us give an overview of the final results without proof. The Bethe ansatz equations for the Yang-Gaudin model are in the form of two sets of inter-coupled

equations, referred to as first- and second-level equations. If we denote the chain of  $X$  operators in (6.24)  $\Omega_j$ , i.e.

$$\Omega_j = X_{j+1,j} \dots X_{N,j} X_{1,j} \dots X_{j-1,j}, \quad (6.30)$$

then (6.29) is an eigenvector of the operators  $\Omega_j$  with eigenvalue

$$\mu_j = \prod_{m=1}^M \frac{ik_j - i\alpha_m - c/2}{ik_j - i\alpha_m + c/2}. \quad (6.31)$$

The first level Bethe ansatz equations come from equation (6.24), with the eigenvalue given by  $\mu_j$  of (6.31):

$$\exp(ik_j L) |A\rangle = \Omega_j |A\rangle = \mu_j |A\rangle, \quad (6.32)$$

$$\exp(ik_j L) = \prod_{m=1}^M \frac{ik_j - i\alpha_m - c/2}{ik_j - i\alpha_m + c/2}. \quad (6.33)$$

One side of the second level equations comes from the application of the cyclic boundary condition to  $\Phi$  (as described in the next subsection), the expansion coefficients of the spin basis states in  $A$ . The other side of the second level equations comes about as a requirement for the eigenvalue problem above to be satisfied with eigenvalue  $\mu_j$ . The links between the two sides of the second level equations are the ratios of the expansion coefficients  $a(P)$  in the expansion of  $\Phi$  in terms of products of  $F$ -functions of equation (6.28).

The second level equations take the form

$$-\prod_{j=1}^N \frac{ik_j - i\alpha_m - c/2}{ik_j - i\alpha_m + c/2} = \prod_{n=1}^M \frac{i\alpha_m - i\alpha_n + c}{i\alpha_m - i\alpha_n - c}. \quad (6.34)$$

Now in equation (6.33), multiply the top and bottom of the fraction by  $-i$ . Meanwhile, consider the one-over version of equation (6.34), and multiply the top and bottom of the left-hand side fraction by  $i$  and of the right-hand side fraction by  $-i$ . This leads to the standard form of the Yang-Gaudin Bethe ansatz equations:

$$\exp(ik_j L) = \prod_{n=1}^M \frac{k_j - \alpha_n + ic/2}{k_j - \alpha_n - ic/2}, \quad (6.35)$$

$$\prod_{j=1}^N \frac{\alpha_m - k_j + ic/2}{\alpha_m - k_j - ic/2} = -\prod_{n=1}^M \frac{\alpha_m - \alpha_n + ic}{\alpha_m - \alpha_n - ic}. \quad (6.36)$$

### 6.3.2 Outline of Proof

We will now give a sketch of the steps necessary to prove the statements made in the previous subsection. First, a few observations: note that in the  $F$ -functions, if the product runs from 1 to 0, the result is by definition unity. Furthermore, defining  $k_{N+1} = k_1$ , when the product runs from 1 to  $N$  we can just replace the  $j + 1$  index in the denominator by  $j$  and denote the resultant by  $F(\alpha) := F(\alpha, N + 1)$ .

Now, we mentioned that  $\Phi$  has cyclic boundary conditions. What this actually means is that  $\Phi$  with  $y_{Q_1} = 1$  is equal to  $\Phi$  with  $y_{Q_M} = N + 1$  (with the definition  $k_{N+1} = k_1$ ). In more detail, we write out  $\Phi$  as in (6.27) twice, on both sides of an equality. On the left-hand side set  $y_{Q_1} = 1$ . On the right-hand side permute the  $y$ 's cyclically so that  $y_{Q_1}$  goes to the back of the chain and becomes  $y_{Q_M} = N + 1$ , while all the other  $y$ 's simply move one step to the left. In other words, on the right-hand side set  $y_{Q_M} = N + 1$ , and replace  $Q_{1\dots M-1}$  by  $Q_{1\dots M-1} + 1$ . The resulting equation is the cyclic boundary condition.

From the cyclic boundary condition, we can obtain one side of the second-level equations: we match up terms on the left-hand side that have  $F(\alpha_m, 1)$  to those on right-hand side that have  $F(\alpha_m, N + 1)$  with all the other  $M - 1$   $F$ -functions in the product identical (that is with the same  $\alpha$  and  $y$  arguments). Each of the  $M!$  matched-up pairs constitutes an equation. We cancel all the identical  $F(\alpha, y)$  terms, which gives us  $M!$  equations of the form  $F(\alpha_m) = a(m, \dots)/a(\dots, m)$  where the dots denote the same sequence of all the other integers (except for  $m$ ) in the interval  $[1, M]$ .

There are redundancies in these  $M!$  equations: in fact, the essential information can be distilled to  $M$  equations where the dots denote the same sequence of all the other integers (except for  $m$ ) in the interval  $[1, M]$  *in increasing order*<sup>3</sup>. Separately, we will be able to express the right-hand side of these equations only through the  $\alpha$ 's as part of the eigenvalue problem.

As for the eigenvalue problem, we must demonstrate that  $A$  from (6.29) is an eigenvector of the operators  $\Omega_j$  with eigenvalue  $\mu_j$  for all  $j$ . However, it is sufficient to verify it for any one  $j$  value, since all the particles are equivalent in the sense that we are on a ring and by cyclic permutations can shift the particles around until they become the  $j^{\text{th}}$  one.

In principle, our task is to apply  $\Omega_j$  to each of the  $|\vec{\sigma}\rangle$  basis states and compute the result (in general, it is a combination of all the basis states). Then we use that information to construct the result of applying  $\Omega_j$  to  $A$ . Finally, we inspect each

---

<sup>3</sup>This is in direct analogy to the step where we apply periodic boundary conditions to the spatial wavefunction, first assuming that  $P$  &  $Q$  are the identity permutations, and then writing down the effect on the expansion coefficient of moving the  $j^{\text{th}}$  particle from the start of the chain to the end, with all other particles increasingly ordered by their label, as in equation (6.17).

basis state individually: we compare its coefficient in  $\Omega_j A$  to that in  $\mu_j A$ . If the coefficients match, the eigenvalue problem is satisfied as stated. If the coefficients are not trivially equal, we must *set* them equal, thereby demanding that the eigenvalue problem holds. This gives us the necessary relations between the coefficients  $a(P)$  to complete the second level Bethe ansatz equations.

Now, the general problem for an arbitrary  $M, N$  is incredibly difficult and cumbersome. With the nested Bethe ansatz, one usually proves the  $M = 1, 2$  cases only, which is of course not a rigorous, complete proof, but it serves to provide the reader with intuition for how this calculation unfolds. This is done in appendices 6.A & 6.B. A general proof is in principle possible through the algebraic Bethe ansatz [54] or using Gaudin's technique [50], although conceptually these approaches are more complicated.

## 6.4 Exponential to Logarithmic Form

Finally, it is possible to transform the exponential Bethe ansatz equations to a logarithmic form which is often easier to solve numerically. We will need the identity

$$\tan^{-1}(x) = \frac{i}{2} \ln \left( \frac{1 - ix}{1 + ix} \right), \quad (6.37)$$

where  $x$  can be complex. Inverting this formula for the argument of the logarithm, we cast the fractions in the exponential equations in to the same form. This produces a minus sign to a power that in general depends on  $N$  and/or  $M$ . In particular, for the Lieb-Liniger model, we obtain

$$\exp(ik_j L) = (-1)^{N+1} \prod_n \exp[i\theta(k_j - k_n)], \quad (6.38)$$

where

$$\theta(k) = -2 \tan^{-1} \left( \frac{k}{c} \right). \quad (6.39)$$

Taking the logarithm, we find

$$k_j L = 2\pi n_j + \sum_{\ell=1}^N \theta(k_j - k_\ell), \quad (6.40)$$

where the  $n_j$ 's are quantum numbers that specify the state. The power on the  $(-1)$  then gives constraints for the quantum numbers: for odd (even)  $N$ , the  $n_j$ 's are (1/2-)integers.

For the Yang-Gaudin model, the first level equation becomes

$$\exp(ik_j L) = (-1)^M \prod_{n=1}^M \exp \{i\theta[2(k_j - \alpha_n)]\}, \quad (6.41)$$

and taking the logarithm,

$$k_j L = 2\pi n_j + \sum_{m=1}^M \theta[2(k_j - \alpha_m)], \quad (6.42)$$

where the  $n_j$ 's are (1/2-)integers for even (odd)  $M$ . The second level equation reads

$$(-1)^N \prod_{j=1}^N \exp \{i\theta[2(\alpha_m - k_j)]\} = (-1)^{M+1} \prod_{n=1}^M \exp \{i\theta[\alpha_m - \alpha_n]\}, \quad (6.43)$$

and taking the logarithm, it becomes

$$0 = 2\pi \ell_m - \sum_{n=1}^M \theta(\alpha_m - \alpha_n) + \sum_{j=1}^N \theta[2(\alpha_m - k_j)], \quad (6.44)$$

where the  $\ell_m$ 's are (1/2-)integers for even (odd)  $N - M - 1$ .

### 6.4.1 Final Remarks

It is a requirement of the Bethe ansatz that the  $k_j$ 's must be distinct within a given solution, as must be the  $\alpha_m$ 's [46, 48]. Moreover, for the Lieb-Liniger model it has been proven that for a given set of quantum numbers, the solution is unique [54, 58].

Note that since we have replaced the  $\delta$ -interaction term in the Hamiltonian by additional boundary conditions (6.8), the remaining Hamiltonian is that of  $N$  free particles. Since our ansatz is a superposition of plane waves, it is clear that the energy and momentum of the wavefunction are given by

$$P = \hbar \sum_{j=1}^N k_j, \quad (6.45)$$

$$E = \frac{\hbar^2}{2m} \sum_{j=1}^N k_j^2. \quad (6.46)$$

Furthermore, we emphasize that for a given  $M$ , the Yang-Gaudin Bethe ansatz equations listed above are limited to one (spin) Young tableau. Thus there are physical spin-states that are excluded from the mathematical description of these equations. However, because the Hamiltonian is spin-independent, states with the same  $S$  but different  $S_z$  are degenerate in energy. Furthermore, note that for the

Lieb-Liniger model there exists a valid solution for an arbitrary choice of the quantum numbers. In contrast, in the Yang-Gaudin model, given an arbitrary set of  $n_j$ 's, there is only one set of  $\ell_m$ 's that produces valid solutions.

Now, we have essentially claimed that the guessed spin wavefunction (6.27) has the symmetry of a two-row Young tableau ( $N - M$  &  $M$  long), however we did not demonstrate this explicitly. It is trivial to confirm that  $\Phi$  is symmetric under exchange of any two like-spin particles, but the antisymmetry with respect to the two different spins is more challenging. We may be certain, however, that  $\Phi$  corresponds to the claimed tableau because in his thesis [50], Gaudin bypasses making an ansatz for  $\Phi$  altogether. Instead, he arrives at the same Yang-Gaudin Bethe ansatz equations simply by imposing the symmetry conditions associated with our chosen tableau.

Finally, we may wonder whether it is at all possible to obtain Bethe ansatz equations for the other Young tableaux – that is, the other spin states. To my knowledge, these have never been presented or even mentioned in the literature. Perhaps the symmetry associated with the more complicated tableaux makes an ansatz too difficult to write down, or alternatively, from Gaudin's point of view, the “mixed” symmetry conditions may be too difficult to impose. We remark that in his thesis [50] (chapter one), Gaudin mentions that the results for the other Young tableaux can be obtained by permutation once you solve the problem for one spin state. On the other hand, this statement is not repeated in his book [162], written many years later, so perhaps the initial claim was not well-founded.

# Appendix

In the appendices that follow, we prove the claims made in section 6.3.1 for  $M = 1$  & 2 with arbitrary  $N$ .

## 6.A M=1

Since we only need to prove that the eigenvalue problem holds for one particular value of  $j$ , we will always choose  $j = 1$ , as it is the simplest. In this case, the operator of interest is

$$\Omega_1 = X_{2,1} X_{3,1} \dots X_{N,1}. \quad (6.47)$$

We need to introduce the spin basis states  $|\{y_m\}\rangle$ , which specify the locations of the spin-down fermions along the chain. For only one spin-down particle, there are  $N$  basis states, written as  $|y\rangle$ , where  $y \in \{1, 2, \dots, N\}$ . We also define the short-hand notation

$$X_{mn} = \frac{i(k_m - k_n) - cP_{mn}}{i(k_m - k_n) - c} \equiv a_{mn} + b_{mn}P_{mn}. \quad (6.48)$$

Recall that we have specialized  $X_{mn}$  to fermions and that the permutation operators  $P_{ij}$  only act on the spin labels. Also note that  $a_{n,n} = 0$  while  $b_{n,n} = 1$ . Our first goal is to calculate  $\Omega_1 |y\rangle$ . A separate computation is always required for  $y_1 = 1$  (of course in this case we only have one  $y$ ). It is possible to carefully track what happens upon applying  $\Omega_1$  to various spin kets. The key useful facts are:  $P_{n,1} |n\rangle = |1\rangle$  and  $P_{n,1} |m \neq n\rangle = |m\rangle$ , so that  $X_{n,1} |m \neq n\rangle = |m\rangle$ . Using this, we obtain

$$\Omega_1 |y \neq 1\rangle = a_{y,1} |y\rangle + \sum_{n=2}^{y-1} b_{y,1} \left( \prod_{m=n+1}^{y-1} a_{m,1} \right) b_{n,1} |n\rangle + b_{y,1} \left( \prod_{m=2}^{y-1} a_{m,1} \right) |1\rangle, \quad (6.49)$$

$$\Omega_1 |1\rangle = b_{N,1} |N\rangle + \sum_{n=2}^{N-1} \left( \prod_{m=n+1}^N a_{m,1} \right) b_{n,1} |n\rangle + \left( \prod_{m=2}^N a_{m,1} \right) |1\rangle. \quad (6.50)$$

Notice that  $\Omega_1 |y \neq 1\rangle$  produces all basis states  $|n \leq y\rangle$ , while  $\Omega_1 |1\rangle$  gives all basis states  $|n \leq N\rangle$ . We now need to demonstrate that for all spin basis states,

$$\mu_1 \langle y|A\rangle = \langle y|\Omega_1|A\rangle. \quad (6.51)$$

Usually, the cases when  $y_1 = 1$  and  $y_M = N$  are done separately, and the rest are treated all together.

We will need the cyclicity condition, which for  $M = 1$  reads

$$F(\alpha_1, 1) = F(\alpha_1, N + 1), \quad (6.52)$$

which means  $F(\alpha_1, N + 1) = 1$  as  $F(\alpha_1, 1) \equiv 1$ , which is consistent with the second level equations for  $M = 1$ . Recall also that for  $M = 1$ ,  $\mu_1 = \frac{ik_1 - i\alpha_1 - c/2}{ik_1 - i\alpha_1 + c/2}$ .

We begin from  $y = N$ , as that is the simplest case. Collecting terms proportional to  $|N\rangle$  on both sides of (6.51), we need to show that

$$b_{N,1}F(\alpha_1, 1) + a_{N,1}F(\alpha_1, N) = \frac{ik_1 - i\alpha_1 - c/2}{ik_1 - i\alpha_1 + c/2}F(\alpha_1, N). \quad (6.53)$$

On the left-hand side we can use cyclicity for the first term, and get

$$b_{N,1}F(\alpha_1, N + 1) + a_{N,1}F(\alpha_1, N). \quad (6.54)$$

This step will always be required – whenever we get a term involving  $F(\alpha_1, 1)$ , we will replace it with one involving  $F(\alpha_1, N + 1)$  using the cyclic boundary condition. Moreover,

$$F(\alpha_1, N + 1) = F(\alpha_1, N) \frac{ik_N - i\alpha_1 - c/2}{ik_1 - i\alpha_1 + c/2}, \quad (6.55)$$

so we just need to show that

$$b_{N,1} \frac{ik_N - i\alpha_1 - c/2}{ik_1 - i\alpha_1 + c/2} + a_{N+1} = \frac{ik_1 - i\alpha_1 - c/2}{ik_1 - i\alpha_1 + c/2}. \quad (6.56)$$

This can be done with a few lines of elementary algebra. Now let us move on to  $|N - 1\rangle$ . Collecting terms proportional to this basis state

$$\begin{aligned} & F(\alpha_1, N)b_{N,1}b_{N-1} + F(\alpha_1, N - 1)a_{N-1,1} + F(\alpha_1, 1)a_{N,1}b_{N-1,1} \\ &= \frac{ik_1 - i\alpha_1 - c/2}{ik_1 - i\alpha_1 + c/2}F(\alpha_1, N - 1), \end{aligned} \quad (6.57)$$

we then use cyclicity. Let us add the first and third terms on the left-hand side together:

$$\begin{aligned} & F(\alpha_1, N)b_{N,1}b_{N-1} + F(\alpha_1, N + 1)a_{N,1}b_{N-1,1} \\ &= F(\alpha_1, N)b_{N-1,1} \left( b_{N,1} + a_{N,1} \frac{ik_N - i\alpha_1 - c/2}{ik_1 - i\alpha_1 + c/2} \right) \\ &= F(\alpha_1, N - 1)b_{N-1,1} \left[ \frac{ik_{N-1} - i\alpha_1 - c/2}{ik_N - i\alpha_1 + c/2} \left( b_{N,1} + a_{N,1} \frac{ik_N - i\alpha_1 - c/2}{ik_1 - i\alpha_1 + c/2} \right) \right]. \end{aligned} \quad (6.58)$$

Now, the term in the round brackets is equal to  $\frac{ik_N - i\alpha_1 + c/2}{ik_1 - i\alpha_1 + c/2}$ , which can be easily

shown. This means that the left-hand side of the eigenvalue problem now reads

$$\begin{aligned} & F(\alpha_1, N-1)b_{N-1,1} \frac{ik_{N-1} - i\alpha_1 - c/2}{ik_1 - i\alpha_1 + c/2} + F(\alpha_1, N-1)a_{N-1,1} \\ &= \frac{ik_1 - i\alpha_1 - c/2}{ik_1 - i\alpha_1 + c/2} F(\alpha_1, N-1), \end{aligned} \quad (6.59)$$

where the sum to obtain the right-hand side requires only elementary algebra.

We now consider a general  $|y \neq 1, N\rangle$ . Collecting terms, we need to show that

$$\begin{aligned} & F(\alpha_1, y)a_{y,1} + \sum_{n=y+1}^N F(\alpha_1, n)b_{n,1} \left( \prod_{m=y+1}^{n-1} a_{m,1} \right) b_{y,1} + F(\alpha_1, 1) \left( \prod_{m=y+1}^N a_{m,1} \right) b_{y,1} \\ &= \frac{ik_1 - i\alpha_1 - c/2}{ik_1 - i\alpha_1 + c/2} F(\alpha_1, y). \end{aligned} \quad (6.60)$$

In order to proceed, we will prove a general identity:

$$\begin{aligned} & \left( \prod_{m=y+1}^N a_{m,1} \right) F(\alpha_1, N+1) + \sum_{z=y+1}^N F(\alpha_1, z)b_{z,1} \left( \prod_{m=y+1}^{z-1} a_{m,1} \right) \\ &= \frac{ik_y - i\alpha_1 - c/2}{ik_1 - i\alpha_1 + c/2} F(\alpha_1, y). \end{aligned} \quad (6.61)$$

We try a proof by induction, but the base case is  $y = N-1$  (which we have already proved) and the induction assumes the statement is true for  $y$  and deduces it is also true for  $y-1$ . That is, in contrast to the conventional procedure, the induction variable decreases from step to step. Writing out the equation for  $y-1$ , we separate out all the new terms, trying to explicitly bring out the terms we had for the  $y$  case, on both sides of the equation:

$$\begin{aligned} & a_{y,1} \left( \prod_{m=y+1}^N a_{m,1} \right) F(\alpha_1, N+1) + F(\alpha_1, y)b_{y,1} \left( \prod_{m=y}^{y-1} a_{m,1} \right) \\ &+ \sum_{z=y+1}^N F(\alpha_1, z)b_{z,1} \left( \prod_{m=y+1}^{z-1} a_{m,1} \right) a_{y,1} \\ &= F(\alpha_1, y-1) \frac{ik_{y-1} - i\alpha_1 - c/2}{ik_1 - i\alpha_1 + c/2} \frac{ik_y - i\alpha_1 + c/2}{ik_y - i\alpha_1 + c/2} \\ &= F(\alpha_1, y-1) \frac{ik_{y-1} - i\alpha_1 - c/2}{ik_y - i\alpha_1 + c/2} \frac{ik_y - i\alpha_1 + c/2}{ik_1 - i\alpha_1 + c/2} \\ &= F(\alpha_1, y) \frac{ik_y - i\alpha_1 + c/2}{ik_1 - i\alpha_1 + c/2} \frac{ik_y - i\alpha_1 - c/2}{ik_1 - i\alpha_1 - c/2} \\ &= F(\alpha_1, y) \frac{ik_y - i\alpha_1 - c/2}{ik_1 - i\alpha_1 + c/2} \frac{ik_y - i\alpha_1 + c/2}{ik_y - i\alpha_1 - c/2}. \end{aligned} \quad (6.62)$$

Notice that several times during the manipulation of the right-hand side we multiplied by convenient factors of one. If we briefly write down (6.61) using short-hand notation as  $X + Y = Z$ , then the  $y - 1$  case that we need to prove reads

$$a_{y,1}X + b_{y,1}F(\alpha_1, y) + a_{y,1}Y = Z \frac{ik_y - i\alpha_1 + c/2}{ik_y - i\alpha_1 - c/2}. \quad (6.63)$$

The second and third terms can be combined through the inductive hypothesis to give  $a_{y,1}Z$ . Also, we notice that the second term features  $F(\alpha_1, y) = Z \frac{ik_1 - i\alpha_1 + c/2}{ik_y - i\alpha_1 - c/2}$ . This allows us to cancel  $Z$  through, and it remains to prove that

$$a_{y,1} + b_{y,1} \frac{ik_1 - i\alpha_1 + c/2}{ik_y - i\alpha_1 - c/2} = \frac{ik_y - i\alpha_1 + c/2}{ik_y - i\alpha_1 - c/2}. \quad (6.64)$$

This is a matter of trivial rearrangement, so (6.61) stands proved. It remains to prove the general relation

$$\frac{ik_y - i\alpha_1 - c/2}{ik_1 - i\alpha_1 + c/2} b_{y,1} + a_{y,1} = \frac{ik_1 - i\alpha_1 - c/2}{ik_1 - i\alpha_1 + c/2}, \quad (6.65)$$

but we have already done that for  $y = N - 1$  in equation (6.59), and the label on the  $k$  that fully cancels out is certainly irrelevant. Combining this result with (6.61), we can write down the general identity

$$\begin{aligned} & b_{y,1} \left( \prod_{m=y+1}^N a_{m,1} \right) F(\alpha_1, N+1) + b_{y,1} \sum_{z=y+1}^N F(\alpha_1, z) b_{z,1} \left( \prod_{m=y+1}^{z-1} a_{m,1} \right) + a_{y,1} F(\alpha_1, y) \\ &= \frac{ik_1 - i\alpha_1 - c/2}{ik_1 - i\alpha_1 + c/2} F(\alpha_1, y). \end{aligned} \quad (6.66)$$

Examining the left-hand side of (6.60), we see that by (6.66) we immediately get the right-hand side (of course, taking into account cyclic boundary conditions which in this case are trivial).

In the special case of  $|1\rangle$ , collecting terms, we need to show that

$$\sum_{y=2}^N F(\alpha_1, y) b_{y,1} \left( \prod_{m=2}^{y-1} a_{m,1} \right) + F(\alpha_1, 1) \left( \prod_{m=2}^N a_{m,1} \right) = \frac{ik_1 - i\alpha_1 - c/2}{ik_1 - i\alpha_1 + c/2} F(\alpha_1, 1). \quad (6.67)$$

Identity (6.66) with  $y = 1$  reduces to (6.61) with  $y = 1$  and reads

$$\left( \prod_{m=2}^N a_{m,1} \right) F(\alpha_1, N+1) + \sum_{z=2}^N F(\alpha_1, z) b_{z,1} \left( \prod_{m=2}^{z-1} a_{m,1} \right) = \frac{ik_1 - i\alpha_1 - c/2}{ik_1 - i\alpha_1 + c/2} F(\alpha_1, 1). \quad (6.68)$$

Again (6.68) immediately proves the eigenvalue problem for  $y = 1$  (taking into

account the cyclic boundary conditions, naturally). This completes the proof for  $M = 1$ .

## 6.B M=2

In this case the cyclic boundary condition reads

$$\begin{aligned} & a(1, 2)F(\alpha_1, 1)F(\alpha_2, y) + a(2, 1)F(\alpha_2, 1)F(\alpha_1, y) \\ & = a(1, 2)F(\alpha_1, y)F(\alpha_2, N + 1) + a(2, 1)F(\alpha_2, y)F(\alpha_1, N + 1), \end{aligned} \quad (6.69)$$

and the general explanation given earlier means that  $a(1, 2)/a(2, 1) = F(\alpha_1)$  and  $a(2, 1)/a(1, 2) = F(\alpha_2)$  – this gives us half of the second level Bethe ansatz equations. The other half will come into play later. Also, recall that for  $M = 2$ ,  $\mu_1 = \frac{ik_1 - i\alpha_1 - c/2}{ik_1 - i\alpha_1 + c/2} \times \frac{ik_1 - i\alpha_2 - c/2}{ik_1 - i\alpha_2 + c/2}$ .

The spin basis states are now of the form  $|x, y\rangle$  as there are two spin down coordinates. We need to determine the action of  $\Omega_1$  on these, which is much more involved this time. We carefully track the states resulting from successive permutations, and find the following formulae:

$$\begin{aligned}
\Omega_1 |x \neq 1, y\rangle &= a_{y,1} \left[ a_{x,1} |x, y\rangle + \sum_{n=2}^{x-1} b_{x,1} \left( \prod_{m=n+1}^{x-1} a_{m,1} \right) b_{n,1} |n, y\rangle + b_{x,1} \left( \prod_{m=2}^{x-1} a_{m,1} \right) |1, y\rangle \right] \\
&+ \sum_{k=x+1}^{y-1} b_{y,1} \left( \prod_{j=k+1}^{y-1} a_{j,1} \right) b_{k,1} \left[ a_{x,1} |x, k\rangle + \sum_{n=2}^{x-1} b_{x,1} \left( \prod_{m=n+1}^{x-1} a_{m,1} \right) b_{n,1} |n, k\rangle + b_{x,1} \left( \prod_{m=2}^{x-1} a_{m,1} \right) |1, k\rangle \right] \\
&+ b_{y,1} \left( \prod_{j=x+1}^{y-1} a_{j,1} \right) \left[ b_{x-1,1} |x-1, x\rangle + \sum_{n=2}^{x-2} \left( \prod_{m=n+1}^{x-1} a_{m,1} \right) b_{n,1} |n, x\rangle + \left( \prod_{m=2}^{x-1} a_{m,1} \right) |1, x\rangle \right], \tag{6.70}
\end{aligned}$$

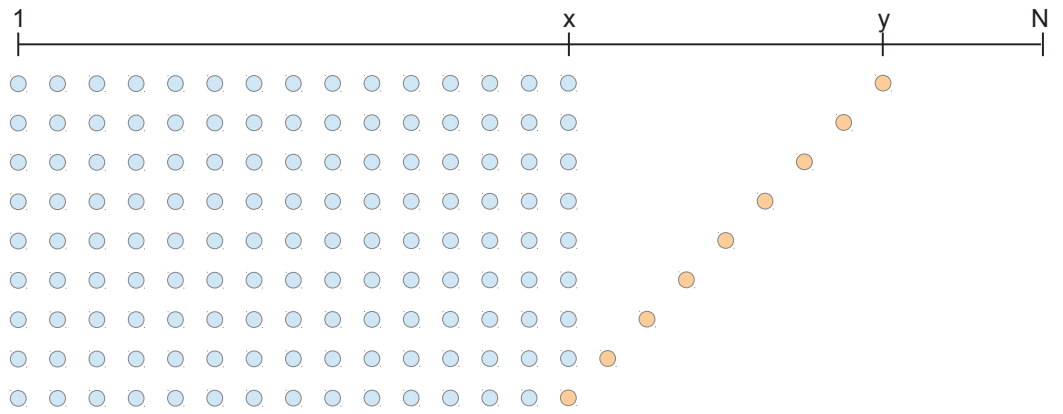
$$\begin{aligned}
\Omega_1 |1, y\rangle &= b_{N,1} \left[ a_{y,1} |y, N\rangle + \sum_{n=2}^{y-1} b_{y,1} \left( \prod_{m=n+1}^{y-1} a_{m,1} \right) b_{n,1} |n, N\rangle + b_{y,1} \left( \prod_{m=2}^{y-1} a_{m,1} \right) |1, N\rangle \right] \\
&+ \sum_{k=y+1}^{N-1} b_{k,1} \left( \prod_{j=k+1}^N a_{j,1} \right) \left[ a_{y,1} |y, k\rangle + \sum_{n=2}^{y-1} b_{y,1} \left( \prod_{m=n+1}^{y-1} a_{m,1} \right) b_{n,1} |n, k\rangle + b_{y,1} \left( \prod_{m=2}^{y-1} a_{m,1} \right) |1, k\rangle \right] \\
&+ \left( \prod_{m=y+1}^N a_{m,1} \right) \left[ b_{y-1,1} |y-1, y\rangle + \sum_{n=2}^{y-2} \left( \prod_{m=n+1}^{y-1} a_{m,1} \right) b_{n,1} |n, y\rangle + \left( \prod_{m=2}^{y-1} a_{m,1} \right) |1, y\rangle \right]. \tag{6.71}
\end{aligned}$$

At first sight, these equations may look intimidating, but the sketches of Fig. 6.2 help us visualize them. The terms produced from  $\Omega_1 |x \neq 1, y\rangle$  have basis states  $|1 \leq n \leq x, x \leq m \leq y\rangle$  and those produced from  $\Omega_1 |1, y\rangle$  have basis states  $|1 \leq n \leq y, y \leq m \leq N\rangle$ . In these formulae, each row keeps the position of the second spin-down particle fixed, and runs through all possible positions for the first particle in decreasing order. The different rows then correspond to different positions of the second particle, also listed in decreasing order.

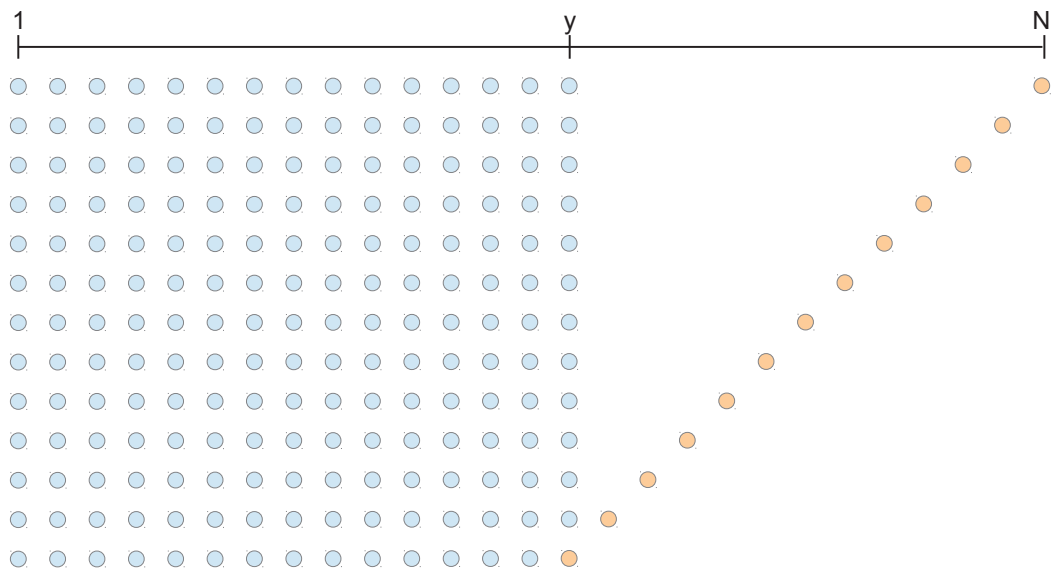
Of course one notices immediately that the coefficients follow a pattern. Let us refer to the  $y_1 \neq 1$  case as “general” and  $y_1 = 1$  as “special”, and define the general & special coefficients by those of the basis states from the  $M = 1$  case formulae. Then we observe that the external (outside the square brackets) coefficients of the general formula for  $M = 2$  follow the general pattern. The internal coefficients (inside the square brackets) of all but the last row are general, while those of the last row are special. For the special formula, external coefficients have special form, while the internal coefficients are again general for all but the last row, and special for the last.

We will prove the eigenvalue problem for all  $|\alpha, \beta\rangle$  by separating them into three cases:  $|\alpha \neq 1, \beta \neq N\rangle$ ,  $|\alpha, N\rangle$  and  $|1, \beta\rangle$ . Notice that we are using  $\alpha, \beta$  to specify the basis state onto which we are projecting, and we shall be collecting terms from all the possible  $x, y$  states that contribute. The first two cases will turn out to work in an analogous way, but the last one will be quite unique and will not fit into the general scheme that we will develop.

So, collecting terms very carefully, we get the following formulae to prove:



(a)  $x \neq 1, y$



(b)  $1, y$

Figure 6.2: Sketches of the spin basis states resulting from applying  $\Omega_1$  to  $|x \neq 1, y\rangle$  (a) and  $|1, y\rangle$  (b). Each row in the picture corresponds to a row in the formula, and they are listed in the same order. The blue/pink dots represent the position of the first/second spin-down particle (hence the pink circles are on the far right of each row). Within a row, each of the blue circles pairs up with the pink circle of that row to give a produced basis state. This corresponds to the many terms inside each of the square brackets in the formulae. Information about the coefficients is not encoded in this picture.

$$\begin{aligned}
\langle \alpha \neq 1, \beta \neq N | \Omega_1 | A \rangle &= \Phi(\alpha, \beta) a_{\beta,1} a_{\alpha,1} + \sum_{x=\alpha+1}^{\beta-1} \Phi(x, \beta) a_{\beta,1} b_{x,1} \left( \prod_{m=\alpha+1}^{x-1} a_{m,1} \right) b_{\alpha,1} \\
&+ \sum_{y=\beta+1}^N \Phi(\beta, y) b_{y,1} \left( \prod_{j=\beta+1}^{y-1} a_{j,1} \right) \left( \prod_{m=\alpha+1}^{\beta-1} a_{m,1} \right) b_{\alpha,1} + \sum_{y=\beta+1}^N \Phi(\alpha, y) b_{y,1} \left( \prod_{j=\beta+1}^{y-1} a_{j,1} \right) b_{\beta,1} a_{\alpha,1} \\
&+ \sum_{x=\alpha+1}^{\beta-1} \sum_{y=\beta+1}^N \Phi(x, y) b_{y,1} \left( \prod_{j=\beta+1}^{y-1} a_{j,1} \right) b_{\beta,1} b_{x,1} \left( \prod_{m=\alpha+1}^{x-1} a_{m,1} \right) b_{\alpha,1} \\
&+ \Phi(1, \alpha) b_{\beta,1} \left( \prod_{j=\beta+1}^N a_{j,1} \right) a_{\alpha,1} + \Phi(1, \beta) \left( \prod_{j=\beta+1}^N a_{j,1} \right) \left( \prod_{m=\alpha+1}^{\beta-1} a_{m,1} \right) b_{\alpha,1} \\
&+ \sum_{y=\alpha+1}^{\beta-1} \Phi(1, y) b_{\beta,1} \left( \prod_{j=\beta+1}^N a_{j,1} \right) b_{y,1} \left( \prod_{m=\alpha+1}^{y-1} a_{m,1} \right) b_{\alpha,1} = \mu_1 \Phi(\alpha, \beta),
\end{aligned} \tag{6.72}$$

$$\begin{aligned}
\langle \alpha, N | \Omega_1 | A \rangle &= \Phi(\alpha, N) a_{N,1} a_{\alpha,1} + \sum_{x=\alpha+1}^{N-1} \Phi(x, N) a_{N,1} b_{x,1} \left( \prod_{m=\alpha+1}^{x-1} a_{m,1} \right) b_{\alpha,1} + \Phi(1, \alpha) b_{N,1} a_{\alpha,1} \\
&+ \sum_{y=\alpha+1}^{N-1} \Phi(1, y) b_{N,1} b_{y,1} \left( \prod_{m=\alpha+1}^{y-1} a_{m,1} \right) b_{\alpha,1} + \Phi(1, N) \left( \prod_{m=\alpha+1}^{N-1} a_{m,1} \right) b_{\alpha,1} = \mu_1 \Phi(\alpha, N),
\end{aligned} \tag{6.73}$$

$$\begin{aligned}
\langle 1, \beta | \Omega_1 | A \rangle &= \sum_{y=\beta+1}^N \Phi(\beta, y) b_{y,1} \left( \prod_{j=\beta+1}^{y-1} a_{j,1} \right) \left( \prod_{m=2}^{\beta-1} a_{m,1} \right) + \sum_{x=2}^{\beta-1} \Phi(x, \beta) a_{\beta,1} b_{x,1} \left( \prod_{m=2}^{x-1} a_{m,1} \right) \\
&+ \sum_{x=2}^{\beta-1} \sum_{y=\beta+1}^N \Phi(x, y) b_{y,1} \left( \prod_{j=\beta+1}^{y-1} a_{j,1} \right) b_{\beta,1} b_{x,1} \left( \prod_{m=2}^{x-1} a_{m,1} \right) + \Phi(1, \beta) \left( \prod_{j=\beta+1}^N a_{j,1} \right) \left( \prod_{m=2}^{\beta-1} a_{m,1} \right) \\
&+ \sum_{y=2}^{\beta-1} \Phi(1, y) b_{\beta,1} \left( \prod_{j=\beta+1}^N a_{j,1} \right) b_{y,1} \left( \prod_{m=2}^{y-1} a_{m,1} \right) = \mu_1 \Phi(1, \beta).
\end{aligned} \tag{6.74}$$

First of all, we use the cyclic boundary condition to replace all  $\Phi(1, y)$  by  $\Phi(y, N+1)$ . Now, each  $\Phi$  is a sum over permutations of products of  $F$ -functions. For the first few steps of what we need to do, it is possible to only explicitly keep track of the terms with  $a(P = I)$  where  $I$  is the identity permutation, as the other terms can be obtained at any stage by relabelling the  $\alpha_m$ 's according to the desired permutation. Thus we go through and replace all  $\Phi(x, y)$  by  $a(1, 2)F(\alpha_1, x)F(\alpha_2, y)$ , and then append  $+a(2, 1)\{\alpha_1 \leftrightarrow \alpha_2\}$  which means add the same terms with a different expansion prefactor and the  $\alpha_m$ 's swapped.

We will now use various identities to rewrite some of the terms appearing in the above three equations. We begin from (6.72), where we use the general identity (6.66). The 6<sup>th</sup>, 4<sup>th</sup> and 1<sup>st</sup> terms can be combined into

$$\begin{aligned}
& a(1, 2)a_{\alpha,1}F(\alpha_1, \alpha) \left[ b_{\beta,1} \left( \prod_{j=\beta+1}^N a_{j,1} \right) F(\alpha_2, N+1) \right. \\
& \left. + b_{\beta,1} \sum_{z=\beta+2}^N b_{z,1} \left( \prod_{j=\beta+1}^{z-1} a_{j,1} \right) F(\alpha_2, z) + a_{\beta,1}F(\alpha_2, \beta) \right] \\
& = a(1, 2)a_{\alpha,1}F(\alpha_1, \alpha) \frac{ik_1 - i\alpha_2 - c/2}{ik_1 - i\alpha_2 + c/2} F(\alpha_2, \beta). \tag{6.75}
\end{aligned}$$

The 8<sup>th</sup>, 5<sup>th</sup> and 2<sup>nd</sup> terms can be combined into

$$\begin{aligned}
& a(1, 2) \sum_{x=\alpha+1}^{\beta-1} F(\alpha_1, x)b_{x,1} \left( \prod_{m=\alpha+1}^{x-1} a_{m,1} \right) b_{\alpha,1} \left[ F(\alpha_2, N+1)b_{\beta,1} \left( \prod_{j=\beta+1}^N a_{j,1} \right) \right. \\
& \left. + \sum_{y=\beta+1}^N F(\alpha_2, y)b_{y,1} \left( \prod_{j=\beta+1}^{y-1} a_{j,1} \right) b_{\beta,1} + a_{\beta,1}F(\alpha_2, \beta) \right] \\
& = a(1, 2) \sum_{x=\alpha+1}^{\beta-1} F(\alpha_1, x)b_{x,1} \left( \prod_{m=\alpha+1}^{x-1} a_{m,1} \right) b_{\alpha,1} \frac{ik_1 - i\alpha_2 - c/2}{ik_1 - i\alpha_2 + c/2} F(\alpha_2, \beta). \tag{6.76}
\end{aligned}$$

The 3<sup>rd</sup> and 7<sup>th</sup> terms are for the minute left unchanged. All together, at this stage we have

$$\begin{aligned}
\langle \alpha \neq 1, \beta \neq N | \Omega_1 | A \rangle & = a(1, 2) \frac{ik_1 - i\alpha_2 - c/2}{ik_1 - i\alpha_2 + c/2} F(\alpha_2, \beta) \\
& \left[ a_{\alpha,1}F(\alpha_1, \alpha) + \sum_{x=\alpha+1}^{\beta-1} F(\alpha_1, x)b_{x,1} \left( \prod_{m=\alpha+1}^{x-1} a_{m,1} \right) b_{\alpha,1} \right] \\
& + \sum_{y=\beta+1}^N a(1, 2)F(\alpha_1, \beta)F(\alpha_2, y)b_{y,1} \left( \prod_{j=\beta+1}^{y-1} a_{j,1} \right) \left( \prod_{m=\alpha+1}^{\beta-1} a_{m,1} \right) b_{\alpha,1}
\end{aligned}$$

$$\begin{aligned}
& +a(1,2)F(\alpha_1, \beta)F(\alpha_2, N+1) \left( \prod_{j=\beta+1}^N a_{j,1} \right) \left( \prod_{m=\alpha+1}^{\beta-1} a_{m,1} \right) b_{\alpha,1} \\
& +a(2,1)\{\alpha_1 \leftrightarrow \alpha_2\}
\end{aligned} \tag{6.77}$$

Now let us do the same for (6.73). Here we use the special identity that holds for  $y = N$  (we proved it earlier – see (6.53))

$$b_{N,1}F(\alpha, N+1) + a_{N,1}F(\alpha, N) = \frac{ik_1 - i\alpha - c/2}{ik_1 - i\alpha + c/2}F(\alpha, N). \tag{6.78}$$

The first four terms can be written as

$$\begin{aligned}
& a(1,2) [b_{N,1}F(\alpha_2, N+1) + a_{N,1}F(\alpha_2, N)] \\
& \left[ F(\alpha_1, \alpha)a_{\alpha,1} + \sum_{x=\alpha+1}^{N-1} F(\alpha_1, x)b_{x,1} \left( \prod_{m=\alpha+1}^{x-1} a_{m,1} \right) b_{\alpha,1} \right] \\
& = a(1,2) \frac{ik_1 - i\alpha_2 - c/2}{ik_1 - i\alpha_2 + c/2} F(\alpha_2, N) \\
& \left[ F(\alpha_1, \alpha)a_{\alpha,1} + \sum_{x=\alpha+1}^{N-1} F(\alpha_1, x)b_{x,1} \left( \prod_{m=\alpha+1}^{x-1} a_{m,1} \right) b_{\alpha,1} \right].
\end{aligned} \tag{6.79}$$

The 5<sup>th</sup> term is for now unmodified. All together, at this stage we have

$$\begin{aligned}
\langle \alpha, N | \Omega_1 | A \rangle & = a(1,2) \frac{ik_1 - i\alpha_2 - c/2}{ik_1 - i\alpha_2 + c/2} F(\alpha_2, N) \\
& \left[ F(\alpha_1, \alpha)a_{\alpha,1} + \sum_{x=\alpha+1}^{N-1} F(\alpha_1, x)b_{x,1} \left( \prod_{m=\alpha+1}^{x-1} a_{m,1} \right) b_{\alpha,1} \right] \\
& +a(1,2)F(\alpha_1, N)F(\alpha_2, N+1) \left( \prod_{m=\alpha+1}^{N-1} a_{m,1} \right) b_{\alpha,1} + a(2,1)\{\alpha_1 \leftrightarrow \alpha_2\}.
\end{aligned} \tag{6.80}$$

We will deal with (6.74) last, as none of these summation manipulations are of any use there. For now we will go back to manipulating the other two matrix elements. Once again, begin with (6.77). We can use (6.59) (with  $N - 1$  replaced by a general variable  $y$ ) to rewrite the first term in the square brackets, which now reads

$$\begin{aligned}
& \frac{ik_1 - i\alpha_1 - c/2}{ik_1 - i\alpha_1 + c/2} F(\alpha_1, \alpha) - b_{\alpha,1} \frac{ik_\alpha - i\alpha_1 - c/2}{ik_1 - i\alpha_1 + c/2} F(\alpha_1, \alpha) \\
& + \sum_{x=\alpha+1}^{\beta-1} F(\alpha_1, x)b_{x,1} \left( \prod_{m=\alpha+1}^{x-1} a_{m,1} \right) b_{\alpha,1}.
\end{aligned} \tag{6.81}$$

The second and third terms in the brackets can be combined to give

$$\begin{aligned}
& -b_{\alpha,1} \frac{ik_{\alpha} - i\alpha_1 - c/2}{ik_1 - i\alpha_1 + c/2} F(\alpha_1, \alpha) + \sum_{x=\alpha+1}^{\beta-1} F(\alpha_1, x) b_{x,1} \left( \prod_{m=\alpha+1}^{x-1} a_{m,1} \right) b_{\alpha,1} \\
& = -\frac{ik_{\beta-1} - i\alpha_1 - c/2}{ik_1 - i\alpha_1 + c/2} \left( \prod_{m=\alpha+1}^{\beta-1} a_{m,1} \right) b_{\alpha,1} F(\alpha_1, \beta - 1). \tag{6.82}
\end{aligned}$$

This can be shown by the following manipulations: cancel  $b_{\alpha,1}$  through, the second term on the left-hand side can be expanded using (6.61), combine the two summation terms which have the same structure, leaving a sum from  $\beta$  to  $N$ , cancel  $\left( \prod_{m=\alpha+1}^{\beta-1} a_{m,1} \right)$  through, and the resulting equation is just (6.61), which is a true identity.

Next, lines 3 and 4 of (6.77) can be combined by factoring out common factors

$$\begin{aligned}
& a(1,2) b_{\alpha,1} F(\alpha_1, \beta) \left( \prod_{m=\alpha+1}^{\beta-1} a_{m,1} \right) \\
& \left[ \sum_{y=\beta+1}^N F(\alpha_2, y) b_{y,1} \left( \prod_{j=\beta+1}^{y-1} a_{j,1} \right) + F(\alpha_2, N+1) \left( \prod_{j=\beta+1}^N a_{j,1} \right) \right]. \tag{6.83}
\end{aligned}$$

By (6.61), the terms in the brackets are equal to  $\frac{ik_{\beta} - i\alpha_2 - c/2}{ik_1 - i\alpha_2 + c/2} F(\alpha_2, \beta)$ . All together, then, (6.77) becomes

$$\begin{aligned}
\langle \alpha \neq 1, \beta \neq N | \Omega_1 | A \rangle & = a(1,2) \frac{ik_1 - i\alpha_2 - c/2}{ik_1 - i\alpha_2 + c/2} F(\alpha_2, \beta) \tag{6.84} \\
& \left[ \frac{ik_1 - i\alpha_1 - c/2}{ik_1 - i\alpha_1 + c/2} F(\alpha_1, \alpha) - \frac{ik_{\beta-1} - i\alpha_1 - c/2}{ik_1 - i\alpha_1 + c/2} \left( \prod_{m=\alpha+1}^{\beta-1} a_{m,1} \right) b_{\alpha,1} F(\alpha_1, \beta - 1) \right] \\
& + a(1,2) b_{\alpha,1} F(\alpha_1, \beta) \left( \prod_{m=\alpha+1}^{\beta-1} a_{m,1} \right) \frac{ik_{\beta} - i\alpha_2 - c/2}{ik_1 - i\alpha_2 + c/2} F(\alpha_2, \beta) + a(2,1) \{ \alpha_1 \leftrightarrow \alpha_2 \}.
\end{aligned}$$

We now turn to (6.80). Again use (6.59) on the first term in the brackets. Then combine the second and third terms in the brackets using (6.82) with  $\beta$  replaced by  $N$ . Thus (6.80) becomes

$$\begin{aligned}
\langle \alpha, N | \Omega_1 | A \rangle & = a(1,2) \frac{ik_1 - i\alpha_2 - c/2}{ik_1 - i\alpha_2 + c/2} F(\alpha_2, N) \\
& \left[ \frac{ik_1 - i\alpha_1 - c/2}{ik_1 - i\alpha_1 + c/2} F(\alpha_1, \alpha) - \frac{ik_{N-1} - i\alpha_1 - c/2}{ik_1 - i\alpha_1 + c/2} \left( \prod_{m=\alpha+1}^{N-1} a_{m,1} \right) b_{\alpha,1} F(\alpha_1, N - 1) \right] \\
& + a(1,2) F(\alpha_1, N) F(\alpha_2, N + 1) \left( \prod_{m=\alpha+1}^{N-1} a_{m,1} \right) b_{\alpha,1} + a(2,1) \{ \alpha_1 \leftrightarrow \alpha_2 \}. \tag{6.85}
\end{aligned}$$

As for (6.74), we can factor out some of the terms and write it as

$$\begin{aligned}
\langle 1, \beta | \Omega_1 | A \rangle &= a(1, 2) \left[ F(\alpha_1, \beta) \left( \prod_{m=2}^{\beta-1} a_{m,1} \right) + \sum_{x=2}^{\beta-1} F(\alpha_1, x) b_{\beta,1} \left( \prod_{m=2}^{x-1} a_{m,1} \right) b_{x,1} \right] \\
&\left[ \left( \prod_{m=\beta+1}^N a_{m,1} \right) F(\alpha_2, N+1) + \sum_{y=\beta+1}^N F(\alpha_2, y) \left( \prod_{m=\beta+1}^{y-1} a_{m,1} \right) b_{y,1} \right] \\
&+ a(1, 2) F(\alpha_2, \beta) a_{\beta,1} \sum_{x=2}^{\beta-1} F(\alpha_1, x) b_{x,1} \left( \prod_{m=2}^{x-1} a_{m,1} \right) \\
&+ a(2, 1) \{ \alpha_1 \leftrightarrow \alpha_2 \} = \mu_1 \Phi(1, \beta). \tag{6.86}
\end{aligned}$$

The proof of (6.86) is left as an exercise for the enthusiastic reader.

Next, we need to prove that (6.84) is equal to the right-hand side of (6.72), and (6.85) is equal to the right-hand side of (6.73). Begin with the former. It is clear that upon expanding the bracket, the first term and its  $a(2, 1) \{ \alpha_1 \leftrightarrow \alpha_2 \}$  partner give the right-hand side of (6.72). Therefore, we must prove that the second and third terms together with their  $a(2, 1) \{ \alpha_1 \leftrightarrow \alpha_2 \}$  partners cancel. This can be proved by following these steps. First, cancel the product over  $a_{m,1}$  and  $b_{\beta,1}$  through. Then we replace  $F(\alpha_{1,2}, \beta - 1)$  by  $F(\alpha_{1,2}, \beta) \frac{ik_\beta - i\alpha_{1,2} + c/2}{ik_{\beta-1} - i\alpha_{1,2} - c/2}$ . Next we cancel  $F(\alpha_1, \beta) F(\alpha_2, \beta)$  through, and obtain the following equation to prove:

$$\begin{aligned}
&-a(1, 2) \frac{ik_1 - i\alpha_2 - c/2}{ik_1 - i\alpha_2 + c/2} \frac{ik_\beta - i\alpha_1 + c/2}{ik_1 - i\alpha_1 + c/2} + a(1, 2) \frac{ik_\beta - i\alpha_2 - c/2}{ik_1 - i\alpha_2 + c/2} \\
&-a(2, 1) \frac{ik_1 - i\alpha_1 - c/2}{ik_1 - i\alpha_1 + c/2} \frac{ik_\beta - i\alpha_2 + c/2}{ik_1 - i\alpha_2 + c/2} + a(2, 1) \frac{ik_\beta - i\alpha_1 - c/2}{ik_1 - i\alpha_1 + c/2} = 0. \tag{6.87}
\end{aligned}$$

Solving this equation for  $a(1, 2)/a(2, 1)$ , after some simple algebra, we find that  $\frac{a(1,2)}{a(2,1)} = \frac{\alpha_1 - \alpha_2 - ic}{\alpha_1 - \alpha_2 + ic}$ , which trivially implies that  $\frac{a(2,1)}{a(1,2)} = \frac{\alpha_2 - \alpha_1 - ic}{\alpha_2 - \alpha_1 + ic}$ . These are the right-hand sides of the second level Bethe ansatz equations.

Now we move on to show that the second and third terms of (6.85) cancel with their  $a(2, 1) \{ \alpha_1 \leftrightarrow \alpha_2 \}$  partners. Noting that  $F(\alpha_2, N+1) = F(\alpha_2, N) \frac{ik_N - i\alpha_2 - c/2}{ik_1 - i\alpha_2 + c/2}$ , we immediately observe that we get the same exact equation to prove all over again, except that  $\beta$  is replaced by  $N$ . Since  $k_\beta$  cancels, it certainly does not matter if we rename it. Therefore, we again get the same ratios of the expansion coefficients.

In other words, for  $M = 2$  we have proved that the original eigenvalue problem for  $A$  ( $\Omega_1 | A \rangle = \mu_1 | A \rangle$ ) is satisfied with the eigenvalue given by  $\mu_1$  if the second level equations hold.

# Chapter 7

## Lieb-Liniger Model

In this chapter we will review the basic properties of the finite Lieb-Liniger model, focusing on the ground state and elementary excitations. Apart from the overwhelming importance of the material covered here to our work in the rest of the thesis, this chapter also introduces many key concepts in the framework of the simpler Lieb-Liniger model, which we will encounter again when exploring the more complex Yang-Gaudin model. The thermodynamic limit of the Lieb-Liniger model is reviewed in chapter 9.

### 7.1 Introduction

The Lieb-Liniger model represents spin-0 bosons on a one-dimensional ring with contact interactions. As such, it is the simplest of the family of Bethe ansatz-solvable models described by the same Hamiltonian but with (in general) particles of several spin components. It was first solved in [46, 47], then reviewed in the literature by many authors, e.g. [163], who also provide a comprehensive list of experimental realizations of the system (see table 1). Another notable experiment is [56] where the elementary excitations were directly probed.

Due to its simplicity and the fact that the Bethe ansatz provides an exact solution, the Lieb-Liniger model is quite heavily used to understand one-dimensional gases and as a prototypical model for developing new theoretical machinery. For example, [164, 165] use the Lieb-Liniger model to study superfluidity and drag forces in one dimension, while [96, 97] apply the algebraic Bethe ansatz to the Lieb-Liniger model, and in so doing, illustrate and explain the theory very clearly. New physics of the Lieb-Liniger model continues to be discovered, exemplified by the relatively-recent concept of the super Tonks-Girardeau gas [166, 167] (see section 7.5). A common theme in contemporary theoretical work is the addition of a trap, harmonic or otherwise: e.g., [168] studies the expansion of the one-dimensional gas after release from a generalised trapping potential.

Fundamental research on the Bethe ansatz equations is also ongoing: [169] solve the ground state Bethe ansatz equations for attractive and repulsive interactions, while [170] also considers excited states. These articles solve the attractive Bethe

ansatz equations exactly, without assuming so-called string-states (see section 7.5), which is technically rather more involved. Finally, since the equations describing the thermodynamics of the Lieb-Liniger model are well-known [91], finite-temperature calculations for the Lieb-Liniger model can be used as a tool to understand the finite-temperature one-dimensional Bose gas.

## 7.2 The Model

Recall that the Hamiltonian of the Lieb-Liniger model is given by (6.1) with all  $N$  particles being spin-0 bosons confined to a one-dimensional ring. The dimensionless interaction strength is  $\gamma = c/n_0$  with  $n_0 = N/L$ . In this thesis we will predominantly focus on the repulsive regime where  $\gamma > 0$ . The Bethe ansatz equations in exponential form are

$$\exp(ik_j L) = - \prod_{m=1}^N \frac{k_j - k_m + ic}{k_j - k_m - ic}, \quad (7.1)$$

or, recast into logarithmic form,

$$k_j L = 2\pi n_j + \sum_{\ell=1}^N \theta(k_j - k_\ell), \quad (7.2)$$

with the two-body phase shift function

$$\theta(k) = -2 \tan^{-1} \left( \frac{k}{c} \right), \quad (7.3)$$

and the  $n_j$ 's being quantum numbers that specify the state: for odd (even)  $N$ , the  $n_j$ 's are (1/2-) integers. The Bethe ansatz equations are solved for the  $N$  variables,  $\{k_j\}$ , known as “quasi-momenta” or “rapidities”.

Since the Bethe ansatz wavefunction (6.3) diagonalizes both the Hamiltonian and the total momentum, the eigenvalues of these operators are easily extracted from the Bethe ansatz: the momentum and energy of any given state are found from

$$P = \hbar \sum_{j=1}^N k_j, \quad (7.4)$$

$$E = \frac{\hbar^2}{2m} \sum_{j=1}^N k_j^2. \quad (7.5)$$

We note that the simplest limit is the case when  $c \rightarrow \infty$  (the Tonks-Girardeau limit), as then  $\theta(k) = 0$  and the Bethe ansatz equations reduce to  $k_j L = 2\pi n_j$ , the quasi-momenta associated with a single free spin component of fermions. In fact, the Tonks-Girardeau limit of the Lieb-Liniger model is analytically mappable on to

free fermions [43, 171], so it is often convenient to understand the physics in this limit before considering the case of general interactions.

In order to numerically solve the Bethe ansatz equations, we make use of the Matlab function `fsolve.m` (implementing the trust-region dogleg algorithm), with absolute and relative tolerances set to  $10^{-8}$ . First, we obtain the roots in the Tonks-Girardeau limit (where the guess  $k_j = 2\pi n_j/L$  is perfectly sufficient to converge to the solution), and then follow the solutions down in  $\gamma$  to the desired value of the interaction. In particular, we always initially solve at  $\gamma = 100$  and follow with an adaptive step of  $\gamma/10$ , always using the solutions found at the previous step as the guess for the next.

### 7.3 Ground State

In the ground state, the quantum numbers are

$$n_j = -\frac{N+1}{2} + j, \quad j = 1, 2, \dots, N, \quad (7.6)$$

as illustrated in Fig. 7.1 (a). This implies that in the Tonks-Girardeau limit we have a tightly-packed Fermi-sphere (in  $k$ -space), with the  $k_j$ 's spaced by  $2\pi/L$ , but in contrast to free fermions, if  $N$  is even, the rapidities take on odd multiples of  $\pi/L$  and are symmetrically arranged about zero. In fact, the ground state rapidities are compactly and symmetrically arranged about zero at any  $\gamma$ . Thus, the momentum of the ground state is always zero. As  $\gamma$  decreases, the range of the ground state rapidities in  $k$ -space decreases, with the  $k_j$ 's becoming very closely spaced.

The ground state energy as a function of  $\gamma$  is plotted in Fig. 7.2 for a system with  $N = 10$ , while in the Tonks-Girardeau limit, it can be obtained analytically as:

$$E_g = \frac{\hbar^2 n_0^2 \pi^2}{2m \ 3N} (N^2 - 1). \quad (7.7)$$

### 7.4 Elementary Excitations

The simplest type of excitations one can make from the ground state are known as type-I or particle excitations. Here, we take the highest  $n_j$  of the ground state quantum numbers,  $n_N$ , and progressively add one to it, with each cycle yielding a valid set of quantum numbers, representing a type-I excitation. This is illustrated in Fig. 7.1 (b), and mathematically can be stated as

$$n_N \rightarrow n_N + \ell, \quad \ell \in \mathbb{N}. \quad (7.8)$$

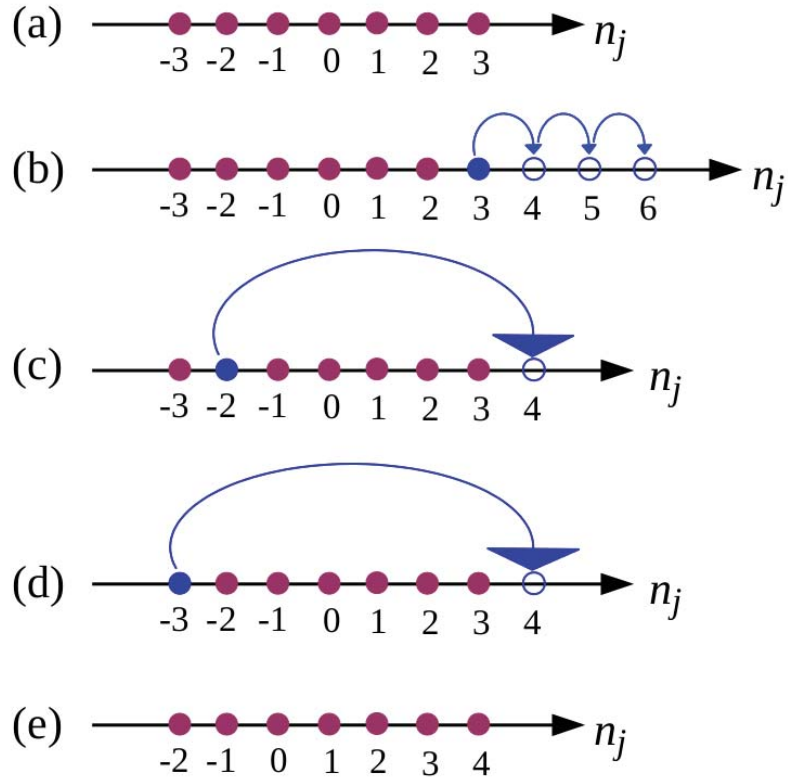


Figure 7.1: An illustration of the quantum numbers in a system with seven bosons, depicting various states and excitations. (a) Ground state quantum numbers. (b) Type-I/particle excitations: the highest  $n_j$  of the ground state is progressively increased by one, with each resulting set of quantum numbers giving a type-I excitation. (c) Type-II/hole excitations: each of the ground state  $n_j$ 's in turn is set to  $n_N + 1$ , with each resulting set of quantum numbers giving a type-II excitation. (d) A particular type-II excitation (when the smallest  $n_j$  is moved) called an “umklapp” excitation, which is special because the resulting quantum-number distribution [shown in (e)] is simply the ground state quantum numbers, all shifted up by one.

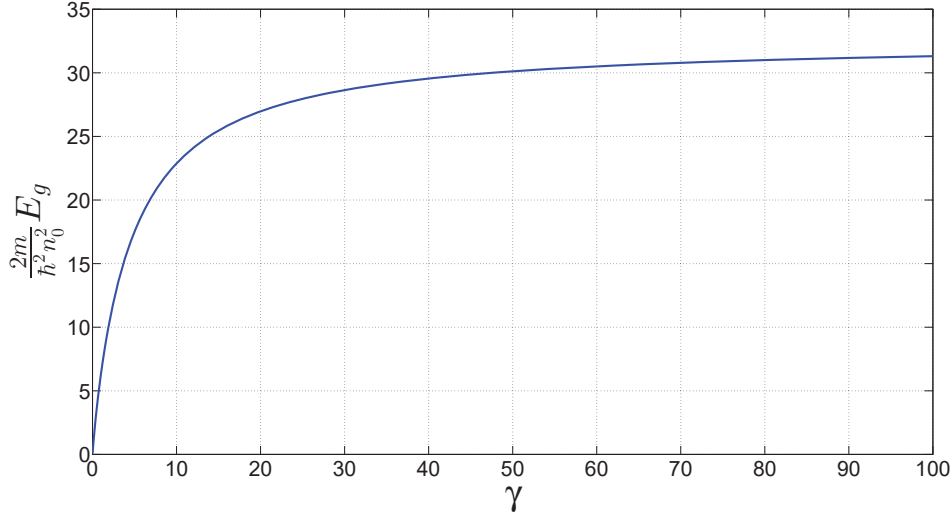


Figure 7.2: The ground state energy of the Lieb-Liniger model as a function of interaction strength in a system with ten particles.

The type-I dispersion relation (excitation energy versus momentum) for  $N = 10, \gamma = 1$  is shown in Fig. 7.3 as blue diamonds. It is always concave up and the shape of the curve is reminiscent of a free, classical particle – an approximately parabolic dependence.

The other kind of elementary excitations are known as type-II or holes [see Fig. 7.1 (c)], whereby we set each of the ground state quantum numbers in turn to the highest  $n_j$  plus one, that is

$$n_j \rightarrow n_N + 1, \quad 1 \leq j \leq N. \quad (7.9)$$

Note that for any given  $j$ , the other ground state quantum numbers are unmodified in the excited state. For each  $j$  we have a valid set of quantum numbers which corresponds to a type-II excitation. The type-II dispersion relation for  $N = 10, \gamma = 1$  is shown in Fig. 7.3 as red circles; it is always concave down.

Note that in the Tonks-Girardeau limit the Lieb-Liniger model reduces to essentially free fermions, and type-I & II excitations become literally particles and holes (respectively) – single-particle excitations in the usual sense.

A special case of type-II excitations occurs when  $j = 1$  [see Fig. 7.1 (d)], referred to as an “umklapp” excitation. Notice that the resulting excited-state quantum numbers [Fig. 7.1 (d)] are gapless – they have the same compact structure as the ground state  $n_j$ ’s, with the only difference being that they are all larger by one. Such a translation of the ground state quantum numbers corresponds to a boost of the whole system: it is the ground state translated so that the moving state has momentum  $2\pi\hbar n_0$ . This explains the fact that the final point on the type-

II dispersion relation, the umklapp point, falls on the system translation parabola (shown as a black dashed line in Fig. 7.3),  $E = P^2/(2mN)$ .

With reference to Fig. 7.3, we notice that type-I excitations are considerably higher energy than type-II (this is true for all  $\gamma$  &  $N$ ), and since we are interested in low-energy excitations, we will not study type-I excitations in detail. Furthermore, the nature of type-I excitations is understood as phonons (Bogoliubov excitations) [47], so their quantum-mechanical interpretation is clear, allowing us to concentrate on type-II excitations.

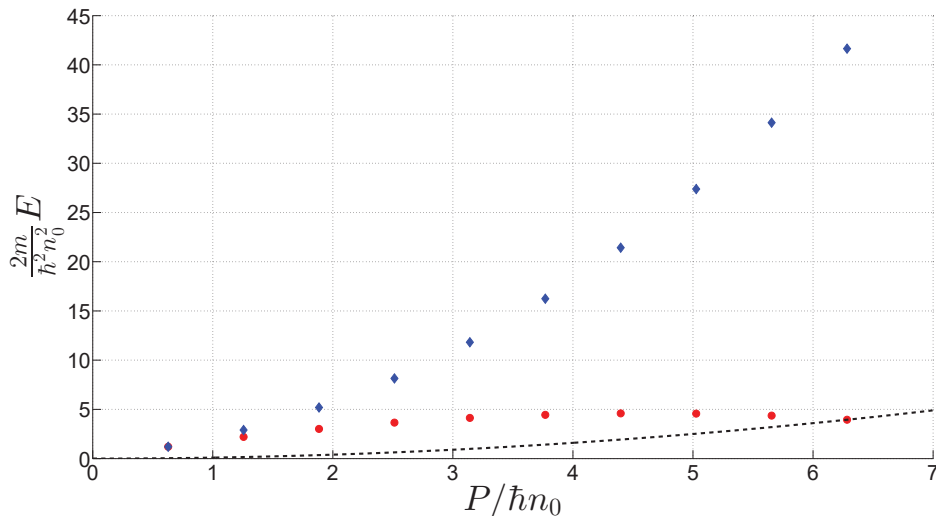


Figure 7.3: Dispersion relations of elementary excitations in the Lieb-Liniger model with  $\gamma = 1$ ,  $N = 10$ . Blue diamonds – type-I, red circles – type-II, black dashed line – system translation parabola,  $E = P^2/(2mN)$ .

Now, after creating an umklapp excitation, it is perfectly possible to create type-II excitations, this time starting from these shifted  $n_j$ 's instead of the true ground state quantum numbers. Thus, while the particle branch can be continued indefinitely as  $\ell$  is unbounded, the type-II branch can be extended to arbitrary momenta by “cycling through” the umklapp excitations. The dispersion relation for six such cycles (or “wings”) is shown in Fig. 7.4. Each cusp in the dispersion relation is an umklapp point, which inevitably falls on the system translation parabola.

Since each wing of the type-II dispersion relation contains all the information about hole excitations (and the difference between the wings is simply how fast the entire system is translating), we can limit our investigations to the first wing only. Also, note that in the thermodynamic limit the mass of the system diverges as  $\mathcal{O}(N)$ , and the energy of the system translation parabola vanishes. In this limit, all the umklapp points touch the  $P$ -axis and the wings become fully periodic and symmetric.

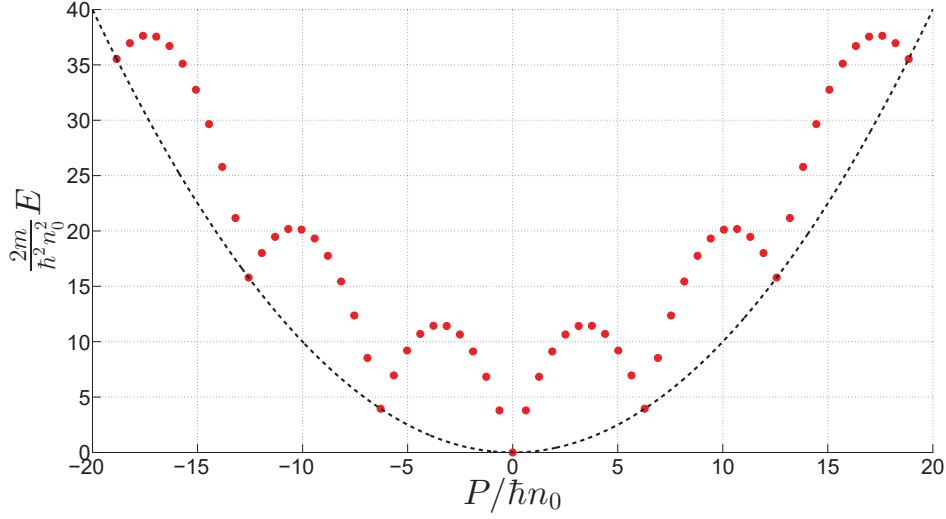


Figure 7.4: The dispersion relation of type-II excitations (red circles), extended to six cycles, or “wings”. The cusps are umklapp points that fall on the system translation parabola (black dashed line). The parameters used are  $N = 10$  and  $\gamma = 100$ .

Finally, in Fig. 7.5 we demonstrate the dependence of the type-II dispersion relation on  $\gamma$ . The excitation energy decreases as a function of  $\gamma$  and as interactions vanish, the dispersion relation tends to a straight line connecting the origin and the umklapp point. Note that for obvious reasons, the umklapp point is independent of interactions.

In the strongly-interacting limit, since the rapidities associated with the ground and type-II states are known, we can obtain an analytical expression for the type-II dispersion relation:

$$E = \frac{\hbar^2 n_0^2}{2m} \left[ -\frac{P^2}{n_0^2 \hbar^2} + \frac{2P\pi(N+1)}{n_0 \hbar N} \right]. \quad (7.10)$$

### 7.4.1 Comparison to Dark Solitons

In chapter 2 we have examined the dispersion relation of Gross-Pitaevskii dark solitons and the qualitative similarity to the type-II dispersion relation is immediately apparent. We are now in a position to make a quantitative comparison: Fig. 7.6 shows the dispersion relations of both types of excitation for three parameter sets. The top panel corresponds to  $\gamma = 0.01$ ,  $N = 100$ , i.e. weak interactions and a large particle number, where the Gross-Pitaevskii mean-field picture is expected to be applicable. In the middle panel, we decrease the particle number to 10 (leaving  $\gamma$  small), and in the bottom panel we also increase  $\gamma$  to 1 (intermediate interactions).

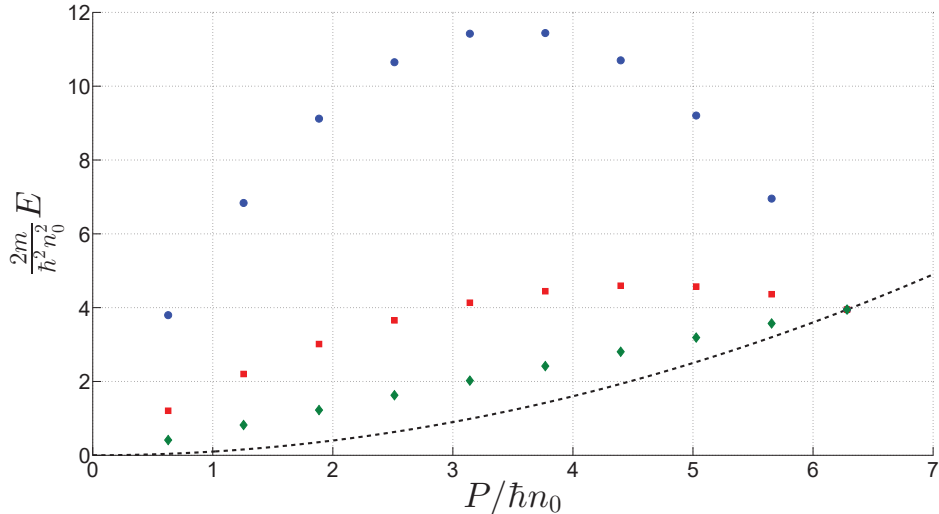


Figure 7.5: The dispersion relation of type-II excitations in a system with  $N = 10$  at three values of the repulsion:  $\gamma = 100$  (blue circles),  $\gamma = 1$  (red squares) and  $\gamma = 0.01$  (green diamonds).

In all three cases – in the mean-field regime and out of it – the dispersion relations match very well, indicating a close connection between Gross-Pitaevskii dark solitons and type-II Lieb-Liniger states.

## 7.5 Attractive Regime

Even though the attractive regime is not directly relevant to our work, we discuss it briefly in this section for completeness. As  $\gamma$  smoothly passes from  $0^+$  through 0 to  $0^-$ , the ground state fundamentally changes its nature. Since the particles obey Bose statistics, attractive interactions favour bound states [172]. In the context of the Bethe ansatz, a bound state is associated with complex rapidities: several  $k_j$ 's have the same real part, and different imaginary parts, such that the sum of the imaginary parts vanishes (as the momentum eigenvalue must be real). Such states are called *string* states. The ground state of the attractive system is a string state of all  $N$  particles at zero momentum [169, 173]. Excitations can take the form of boosting the  $N$ -body string, or breaking it up into smaller strings at different momenta [170]. The physical interpretation of such bound states is bright solitons [173–175].

Another way to access the attractive regime is by letting  $\gamma \rightarrow \infty$ , so that  $1/\gamma$  passes through zero, and  $\gamma$  becomes large and negative. This regime is known as the (bosonic) super Tonks-Girardeau gas, predicted theoretically in [166, 167] and observed experimentally in [176]. In this scenario, first one creates the repulsive

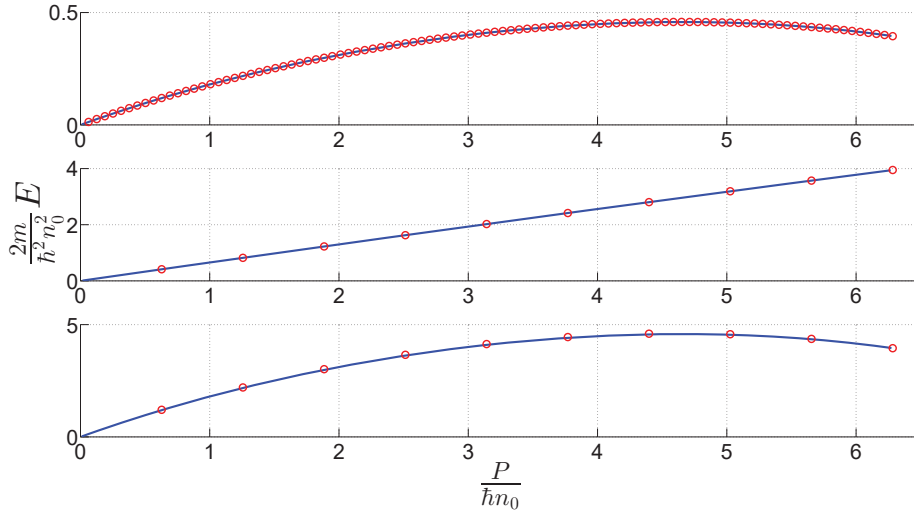


Figure 7.6: The dispersion relations of dark solitons (blue lines) and type-II excitations (red circles). Top panel:  $\gamma = 0.01$ ,  $N = 100$ , middle panel:  $\gamma = 0.01$ ,  $N = 10$ , bottom panel:  $\gamma = 1$ ,  $N = 10$ .

Lieb-Liniger model and increases  $\gamma$  into the Tonks-Girardeau regime (as was done in [74, 75]), so that the system is in the Tonks-Girardeau ground state with all the rapidities spaced by  $2\pi/L$ . Then the ground state is followed in  $1/\gamma$  through zero into the super Tonks-Girardeau regime. The Tonks-Girardeau ground state remains a valid solution of the Bethe ansatz equations even in the super Tonks-Girardeau regime because the  $\theta$  functions vanish if  $c \rightarrow \pm\infty$ . Of course it is no longer the ground state (which, in this regime, is an unbreakable bound state of all the particles), but rather a highly excited state. Interestingly, the super Tonks-Girardeau “ground state” is quite stable, as it has kinetic energy which the system cannot lose easily in order to decay into the real ground state.

# Chapter 8

## Yang-Gaudin Model

In this chapter we analyse the ground state and low-energy type-II excitations of the finite Yang-Gaudin model for both attractive and repulsive interactions. Due to the presence of spin, the spectrum and structure of the excitations is richer than in the Lieb-Liniger model. With the objective of searching for dark solitons in the one-dimensional Fermi gas, we carefully study all three elementary type-II excitations across the range of interactions (the thermodynamic limit is explored in chapter 9). Here we report on the solutions of the Bethe ansatz equations (so this chapter is quite technical), whereas the physical interpretation and observable implications are discussed in chapter 13. There, we will identify dark soliton-like excitations for both repulsive and attractive interactions, and explore low-energy spin excitations in the repulsive regime. The understanding and any further analysis of these excitations must begin with the solution of the finite Bethe ansatz equations.

A secondary motivating reason to perform such an exhaustive survey of all low-energy type-II excitations of the Yang-Gaudin model is that a similar complete record is unavailable in the literature (to the best of my knowledge).

### 8.1 Introduction

The Yang-Gaudin model was originally solved by Yang [48] for the repulsive regime and Gaudin [49, 50] for the attractive, the first of the multicomponent models to be solved by the Bethe ansatz [52], later generalized to an arbitrary number of components [51] and extended to bosonic systems [177]. It describes the physics of two spin components of fermions confined to one dimension with periodic boundary conditions. The fermions interact with each other through a two-body contact potential (a  $\delta$ -function), which can be attractive or repulsive. Currently, the Yang-Gaudin model can be directly realized in the laboratory with cold-atom systems [57, 76–78] (also see [79]).

Despite the fact that the exact solution of the finite Yang-Gaudin model has been known for almost half a century, theoretical studies are continuing to the present day. In particular, analytical asymptotic results are being sought [178, 179], the Yang-Gaudin model is used to describe (part-of) the Bose-Einstein condensate-

Bardeen-Cooper-Schrieffer crossover [180, 181], and to investigate impurity effects in one dimension related to Fulde-Ferrell-Larkin-Ovchinnikov states [182, 183].

Motivated by the possible interpretation of type-II (hole) excitations in the Lieb-Liniger model [46, 47] as dark solitons (chapter 12), we perform a study of all fundamental type-II excitations in the Yang-Gaudin model. Elementary excitations of the Yang-Gaudin model have been studied previously, both in finite systems (e.g. [178]) and in the thermodynamic limit (e.g. [184]), however to our knowledge no complete and methodical study such as the one presented here is available in the literature. Therefore, in the present chapter we address the finite-system case, while the thermodynamic limit of all branches is studied in chapter 9.

The main result of the chapter consists of tracking the ground state and three fundamental type-II branches of the free system to the infinitely-attractive and infinitely-repulsive limits. With no interactions, these three branches are the single fermion hole, the double fermion hole and the spin-flip. In the two limits listed above (respectively), the physical nature of the excitations changes: the single fermion hole becomes a dimer hole and a system translation, the double fermion hole becomes a double dimer hole and a single fermion hole, and the spin-flip remains a spin-flip for attractive interactions while becoming a system translation for strongly repulsive interactions.

For all states of interest with attractive interactions, and for single fermion holes with repulsive interactions, the exact Bethe ansatz equations can only be solved in a limited range around zero interactions due to the particular structure of the solutions. In these cases, in order to examine the limiting regimes, we derive approximate equations that essentially assume for finite coupling strengths a result that is only true for infinite interactions. We follow all excitation branches as far as possible using the exact equations, then demonstrate continuity with the approximate equations (when applicable), and use the latter to track the solutions further. For the single fermion holes, the use of the exact equations in the vicinity of vanishing interactions is absolutely essential, as the structure of the solutions is different to that assumed under the approximate equations. Solving the exact exponential equations is somewhat more difficult, so our results and the technical details presented here can be used as guidelines or a starting point for future research concerned with the lowest-energy excitations of the Yang-Gaudin model. For example, [170] performs a similar computation for the Lieb-Liniger model which was quite helpful to us during our investigation.

Another interesting result that emerges from our work is that in the infinitely-repulsive system, one can access the classical translation parabola of the entire system at all values of the total quantized momentum. In this regard, the Yang-Gaudin model does not become a true Tonks-Girardeau gas in this limit. This was

realized to some degree in [185], but the implications for the excitation spectrum were not considered. These excitations are made accessible purely due to the spin degree of freedom, and would also be present in the two-component Bose gas. This is explored further in chapter 13.

The chapter is structured in the following way: in section 8.2 we introduce the model and give the Bethe ansatz equations to be solved. Then in sections 8.3, 8.4, 8.5, and 8.6 we track the ground state, single fermion holes, double fermion holes and spin-flip excitations from the free system case to both limits of infinite interaction. This is done by using the exact equations, followed by the approximate (when applicable) in the strong-coupling limits. All the technical details related to the numerical solution of the Bethe ansatz equations are found in appendix 8.A. Finally, we conclude in section 8.7.

## 8.2 The Model

Recall that the Yang-Gaudin model describes spin-1/2 fermions, confined to a one-dimensional ring and interacting via a two-body  $\delta$ -function potential, with the Hamiltonian given by (6.1). There are  $N$  fermions in total,  $M \leq N/2$  of which are spin-down and the rest are spin-up. As always, the one-dimensional density is  $n_0 = N/L$ , and the dimensionless coupling parameter is  $\gamma = c/n_0$ .

### 8.2.1 Free Case

Consider first the non-interacting case where  $\gamma = 0$  and we have two spin components of free fermions. If we choose  $N = 2M$  (i.e. a balanced system), then the ground state has a very simple structure: it consists of two overlapping Fermi spheres with the fermion wavenumbers being integer multiples of  $2\pi/L$ . If  $M$  is odd, then the ground state is non-degenerate, and if  $M$  is even, there are three possible configurations that all have the same energy: one with zero total momentum, and two with  $P = \pm M(2\pi/L)\hbar n_0$ .

It so happens that for even  $M$ , the zero-momentum configuration is the true ground state for attractive interactions. This state has the structure of a “single fermion hole” (see below), and can be solved for as described in section 8.4. Curiously, for repulsive interactions, the non-zero momentum state has the lowest energy. It can then be solved for in a similar way to the odd- $M$  ground state, discussed in section 8.3.

This complication with even  $M$  vanishes in the thermodynamic limit – it is a finite size effect – and only the odd  $M$  case directly generalizes to the infinite system. In particular, in the thermodynamic limit, the ground state always has zero momentum, and for weak interactions, smoothly connects to the fully-paired configuration.

Therefore, in the rest of the chapter, we focus on the simpler and more relevant odd  $M$  scenario.

Thus, starting from the free ground state, one can create three types of elementary hole excitations:

- (1) a single fermion hole: take one fermion of either spin component and place it in the first available “slot” immediately outside of the occupied Fermi sphere,
- (2) a double fermion hole: take two fermions (one of either spin component) with the same wavenumber and place both in the first available “slot” immediately outside of the occupied Fermi sphere,
- (3) a spin-flip: flip the spin of one fermion of either spin component.

In the following sections, we track the ground state and these three fundamental type-II branches across the entire coupling-strength range,  $-\infty < \gamma < \infty$ .

## 8.2.2 Interacting Case

As mentioned previously, for any  $\gamma \neq 0$ , the Yang-Gaudin model can be solved exactly by the Bethe ansatz. The exact Bethe ansatz equations in exponential form are [48, 49]:

$$\exp(ik_j L) = \prod_{n=1}^M \frac{k_j - \alpha_n + ic/2}{k_j - \alpha_n - ic/2}, \quad (8.1)$$

$$\prod_{j=1}^N \frac{\alpha_m - k_j + ic/2}{\alpha_m - k_j - ic/2} = - \prod_{n=1}^M \frac{\alpha_m - \alpha_n + ic}{\alpha_m - \alpha_n - ic}. \quad (8.2)$$

In these equations, the  $k_j$ 's are so-called charge rapidities – the quasi-momenta of the fermions, so that the total momentum and energy of the system are

$$P = \hbar \sum_{j=1}^N k_j, \quad (8.3)$$

$$E = \frac{\hbar^2}{2m} \sum_{j=1}^N k_j^2. \quad (8.4)$$

The  $\alpha_m$ 's are spin rapidities – auxiliary variables, present due to the spin degree of freedom. The  $\alpha_m$ 's do not contribute to the energy or momentum but must be solved for as they are coupled to the  $k_j$ 's.

The exponential equations may be rewritten in a much more convenient logarithmic-

mic form:

$$k_j L = 2\pi n_j + \sum_{m=1}^M \theta[2(k_j - \alpha_m)], \quad (8.5)$$

$$0 = 2\pi \ell_m - \sum_{n=1}^M \theta(\alpha_m - \alpha_n) + \sum_{j=1}^N \theta[2(\alpha_m - k_j)], \quad (8.6)$$

where

$$\theta(k) = -2 \tan^{-1} \left( \frac{k}{c} \right) \quad (8.7)$$

is the two-body phase-shift function of the  $\delta$ -function potential. The  $n_j$ 's and  $\ell_m$ 's are distinct quantum numbers (within each set) that specify the state. In particular, the  $n_j$ 's ( $\ell_m$ 's) are integers if  $M$  ( $N-M-1$ ) is even, and half-integers if  $M$  ( $N-M-1$ ) is odd.

The Bethe ansatz equations can be solved numerically on a standard desktop machine. All the technical details regarding the numerical solutions can be found in appendix 8.A.

## 8.3 Ground State

### 8.3.1 Exact

Let us begin by exploring the ground state of the interacting system. In the range where  $|\gamma| \ll 1$ , an analytical approximate result is available [50]: define the set of integers  $q_m$  as

$$q_m = -\frac{M+1}{2} + m, \quad m = 1, 2, \dots, M, \quad (8.8)$$

Then  $\alpha_m = \frac{2\pi}{L} q_m$  and  $k_{2m,2m-1} = \frac{2\pi}{L} q_m \pm \sqrt{\frac{c}{L}}$ . An example is shown in Fig. 8.1, illustrating the rapidities. When  $\gamma > 0$ , the  $k_j$ 's are split along the real axis, so one can use either the exponential or logarithmic equations to solve for the quasi-momenta. For the exponential equations one simply begins from the approximate expressions for the rapidities given above at some small  $\gamma$  value and then follows the solution in  $\gamma$ . For the logarithmic equations we need to specify the quantum numbers that determine the ground state. For the balanced ground state, these are

$$\ell_m = -\frac{M+1}{2} + m, \quad m = 1, 2, \dots, M, \quad (8.9)$$

$$n_j = -\frac{N+1}{2} + j, \quad j = 1, 2, \dots, N. \quad (8.10)$$

For the logarithmic equations it is easier to start from the  $\gamma \rightarrow \infty$  limit (where it suffices to guess  $k_j = \frac{2\pi n_j}{L}$  and  $\alpha_m = \frac{2\pi \ell_m}{L}$  in order to converge to the solution) and

follow down in  $\gamma$ .

When  $\gamma < 0$  pairs of  $k_j$ 's become complex conjugates and only the exponential equations apply. In contrast to the repulsive case where either form of the Bethe ansatz equations can be solved easily with any  $\gamma$  value, for  $\gamma < 0$  there is a limited range where the exponential equations can be solved in practice.

### 8.3.2 String Hypothesis for $\gamma < 0$

It is known that as  $\gamma \rightarrow -\infty$  the real part of the  $k_j$  pairs remains equal to  $\alpha_m$  while the imaginary part becomes  $\pm i\frac{c}{2}$ , which causes divergent singularities in the exact Bethe ansatz equations [50]. In order to deal with this problem, one can make the so-called string hypothesis. Here one assumes that the imaginary parts of the paired  $k_j$ 's have already reached their  $\gamma \rightarrow -\infty$  limits. In particular, in the general case of  $M < N/2$ , we take  $2M$  of the  $k_j$ 's to be  $\alpha_m \pm i\frac{c}{2}$ , and the remaining  $N - 2M$  real  $k_j$ 's are left as unknown variables.

Substituting these expressions for the  $k_j$ 's into the exponential Bethe ansatz equations, we arrive at simpler exponential equations where now all remaining variables (the  $\alpha_m$ 's and the unpaired  $k_j$ 's) are real and distinct. It is then possible to take the logarithm, which leads to [52]:

$$k_j L = 2\pi n_j + \sum_{m=1}^M \theta[2(k_j - \alpha_m)], \quad (8.11)$$

$$2\alpha_m L = 2\pi \ell_m + \sum_{n=1}^M \theta(\alpha_m - \alpha_n) + \sum_{j=1}^{N-2M} \theta[2(\alpha_m - k_j)], \quad (8.12)$$

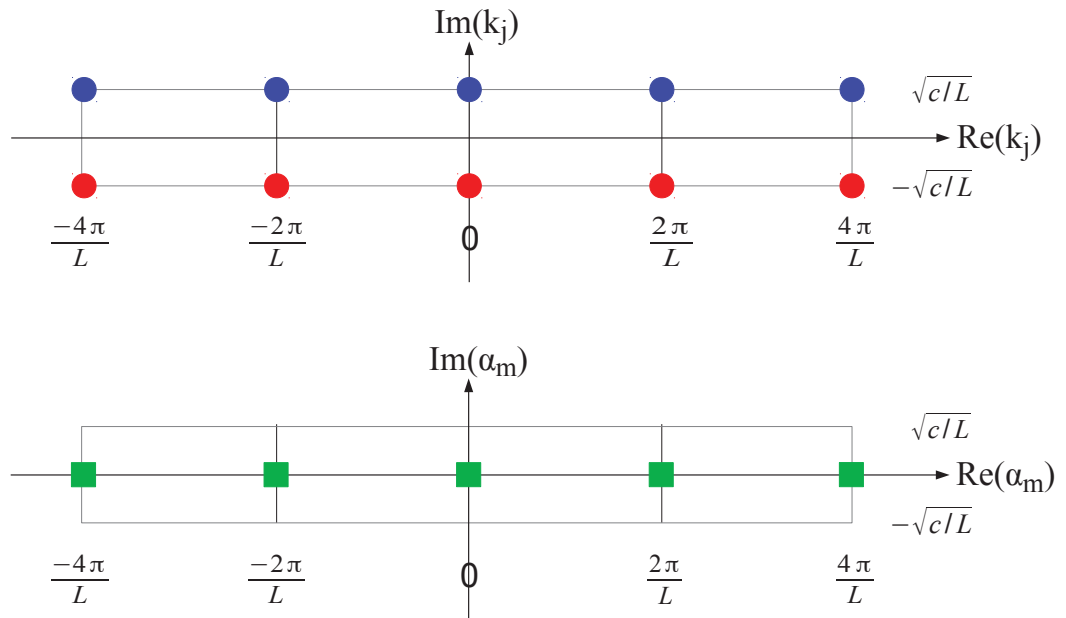
where the  $n_j$ 's and  $\ell_m$ 's are again quantum numbers, as before. If  $M$  is even (odd), the  $n_j$ 's are (half-)integers, and if  $N - M + 1$  is even (odd), the  $\ell_m$ 's are (half-)integers. Since we know the relation between the  $\alpha_m$ 's and the  $k_j$ 's associated with them, it is easy to write the momentum and energy as

$$P = \hbar \left[ \sum_{j=1}^{N-2M} k_j + \sum_{m=1}^M 2\alpha_m \right], \quad (8.13)$$

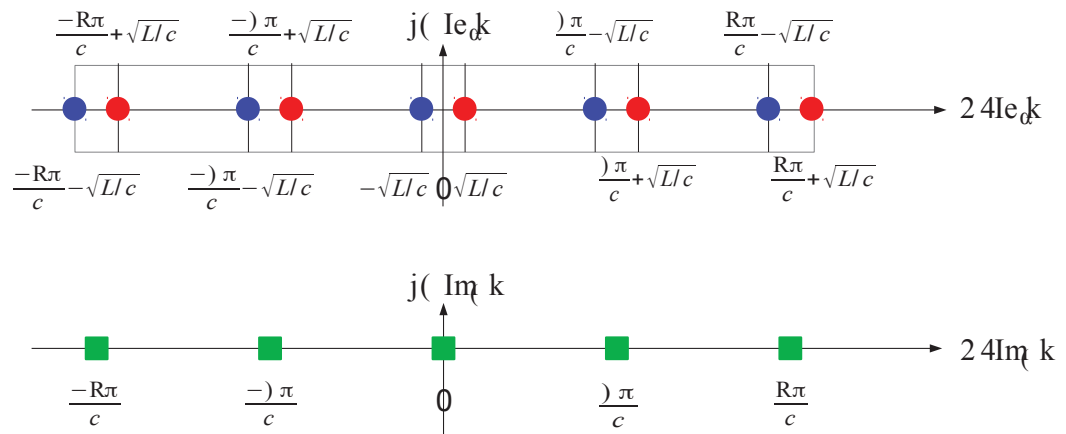
$$E = \frac{\hbar^2}{2m} \left[ \sum_{j=1}^{N-2M} k_j^2 + \sum_{m=1}^M \left( 2\alpha_m^2 - \frac{c^2}{2} \right) \right]. \quad (8.14)$$

Note the total binding energy of  $-\frac{\hbar^2}{2m} M \frac{c^2}{2}$ . When there are no unpaired fermions, the two string hypothesis Bethe ansatz equations reduce to (8.12) only, without the last term on the right-hand side. The quantum numbers for the balanced ground state are

$$\ell_m = -\frac{M+1}{2} + m, \quad m = 1, 2, \dots, M, \quad (8.15)$$



(a)



(b)

Figure 8.1: An example of the ground state rapidities for  $|\gamma| \ll 1$ . In (a),  $\gamma < 0$  and in (b),  $\gamma > 0$ . Here we used  $N = 10$ ,  $M = 5$ . Red and blue circles show the  $k_j$ 's in the complex plane, with the colour differentiating spin types, while green squares show the  $\alpha_m$ 's.

In order to solve the logarithmic string hypothesis equations it is easier to start from the  $\gamma \rightarrow -\infty$  limit where it suffices to guess  $\alpha_m = \frac{\pi \ell_m}{L}$  in order to converge to the solution.

### 8.3.3 Overview

Figure 8.2 shows the ground state energy as a function of coupling strength across the entire range of interactions for a system with  $N = 14, M = 7$ . In particular, the inset allows us to compare the performance of the string hypothesis equations to the exact exponential equations in the region where  $\gamma < 0$  and  $|\gamma| \approx 1$  or less. We see that the energy of the ground state is captured very well indeed, which validates the use of the string hypothesis in cases when all particles of opposite spins are paired up into dimers.

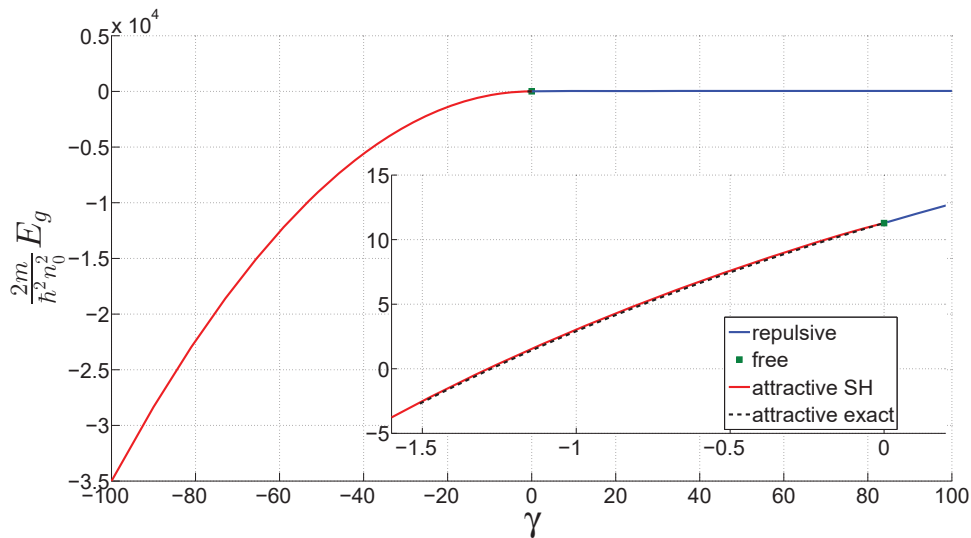
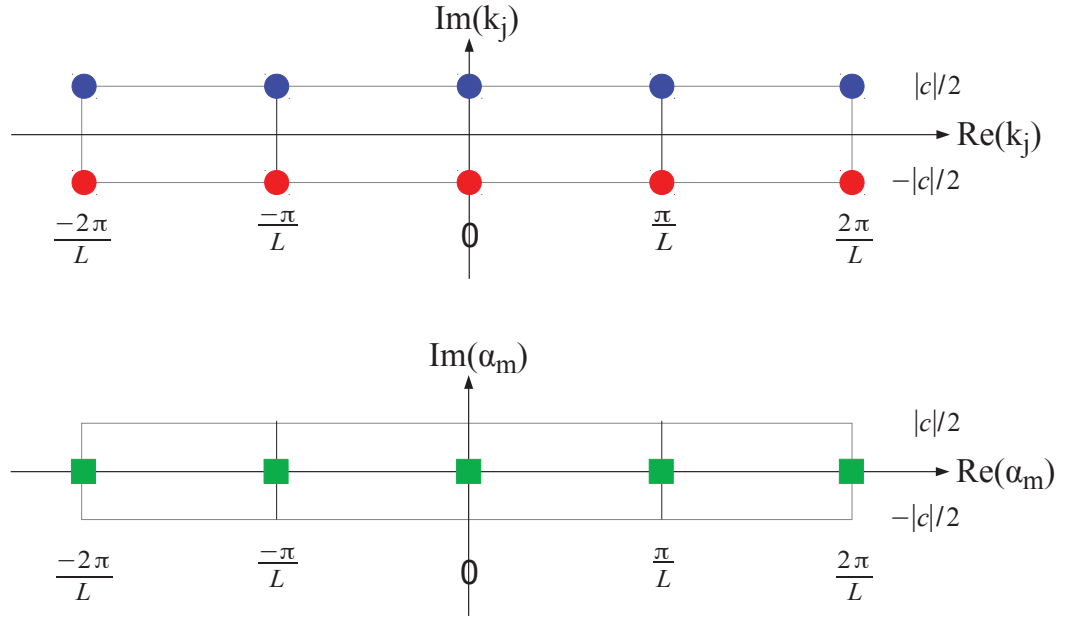


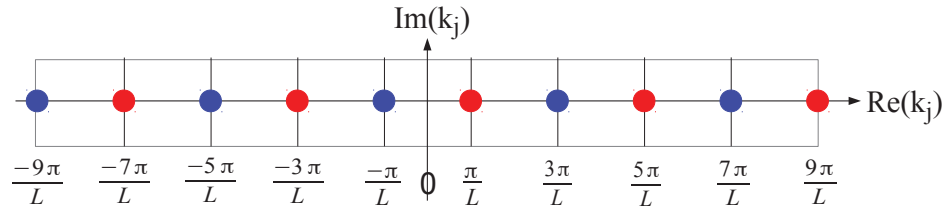
Figure 8.2: Ground state energy as a function of coupling strength  $\gamma$  for a system with  $N = 14, M = 7$ . The inset zooms in around the region where exact results from the exponential equations are available in the attractive regime, and demonstrates that the string hypothesis (labelled “SH”) results compare well to the exact energy.

The structure of the ground state in the limiting cases  $\gamma \rightarrow \pm\infty$  is easily obtained by taking the limit of the Bethe ansatz equations in logarithmic form. When  $\gamma \rightarrow -\infty$ , the  $\alpha_m$ 's approach  $\frac{\pi}{L}\ell_m$  where the  $\ell_m$ 's are given by (8.15) (so the corresponding charge rapidities approach  $\frac{\pi}{L}\ell_m \pm i\frac{\xi}{2}$ ), and when  $\gamma \rightarrow \infty$ , the  $k_j$ 's (of the ground state) approach  $\frac{2\pi}{L}n_j$  with the  $n_j$ 's specified by (8.10). However, the latter is only true as long as  $\sum \ell_m$  of (8.9) vanishes – see section 8.6.4. An example of both limits is shown in Fig. 8.3, illustrating the rapidities.

Analytical expressions can be derived for the ground state energy (with  $M$  odd)



(a)



(b)

Figure 8.3: An example of the ground state rapidities in the limits  $\gamma \rightarrow -\infty$  (a) and  $\gamma \rightarrow \infty$  (b). For the case of divergent repulsive interactions, we do not have an analytical approximation for the  $\alpha_m$ 's. However, we can certainly state that they are real and symmetrically arranged about zero. Here we used  $N = 10$ ,  $M = 5$ . Red and blue circles show the  $k_j$ 's in the complex plane, with the colour differentiating spin types, while green squares show the  $\alpha_m$ 's.

in the limits  $|\gamma| \ll 1$  and  $\gamma \rightarrow \pm\infty$ :

$$E_g(|\gamma| \ll 1) = \frac{\hbar^2 n_0^2}{2m} \left[ M\gamma + \frac{\pi^2}{3N}(M^2 - 1) \right], \quad (8.16)$$

$$E_g(\gamma \rightarrow +\infty) = \frac{\hbar^2 n_0^2}{2m} \frac{\pi^2}{3N}(N^2 - 1), \quad (8.17)$$

$$E_g(\gamma \rightarrow -\infty) = \frac{\hbar^2 n_0^2}{2m} \left[ -\frac{\gamma^2 N}{4} + \frac{\pi^2}{12N}(M^2 - 1) \right]. \quad (8.18)$$

## 8.4 Single Fermion Holes

We now move on to tracking the single fermion hole excitations of the free system as a function of interaction strength. This branch is the most complicated out of all three that are of interest to us, and requires the use of the exact exponential equations in the vicinity of  $\gamma \approx 0$  for both signs of the interaction strength.

### 8.4.1 Exact

Recalling the known structure of the balanced ground state at  $|\gamma| \ll 1$ , when a single  $k_j$  is moved from  $\frac{2\pi}{L}q_m \pm \sqrt{c/L}$  out of the Fermi spheres to  $\frac{2\pi}{L}(q_M + 1)$ , its partner moves from  $\frac{2\pi}{L}q_m \mp \sqrt{c/L}$  to  $\frac{2\pi}{L}q_m$  and  $\alpha_m$  shifts to half-way between its associated  $k_j$ 's. For half of the excitations, this means  $\alpha_m$  becomes a half-integer multiple of  $2\pi/L$  and for the other half,  $\alpha_m$  is expelled to a position already occupied by another  $\alpha$ . In the latter case, these two  $\alpha$ 's split away from each other by  $\pm i\sqrt{c/L}$ . This description of the single fermion holes in the regime  $|\gamma| \ll 1$  applies for both attractive and repulsive interactions, so that splitting on the imaginary axis for  $\gamma > 0$  (by  $\pm i\sqrt{c/L}$ ) becomes splitting on the real line when  $\gamma < 0$ . An example of all four scenarios is shown in Figs. 8.4 & 8.5, illustrating the rapidities.

Knowing the approximate rapidities outlined in the paragraph above, we can pick up and follow the solutions using the exact exponential equations. Figure 8.6 shows an example of the rapidities as a function of coupling strength for the specific case of  $N = 6, M = 3$  (we use a small system to ensure the diagrams are easily readable). Since we have two spin components of fermions, at  $\gamma = 0$  the one fermion hole can be created by taking out either of the two fermions at  $k_j = \frac{2\pi}{L}q_m \pm \sqrt{c/L}$  – either option results in the exact same excited state (uniquely characterized by the set of rapidities). We can make the following general observations regarding the behaviour of the rapidities: in the attractive regime, the two  $k_j$ 's that are separated to form the single fermion hole at  $\gamma \approx 0$  always merge to once again form a dimer at some smaller  $\gamma$  value.

For repulsive interactions, the single fermion hole state that is formed by separating the two  $k_j$ 's associated with  $\alpha_M$  (i.e. the highest  $\alpha$  value in the ground state

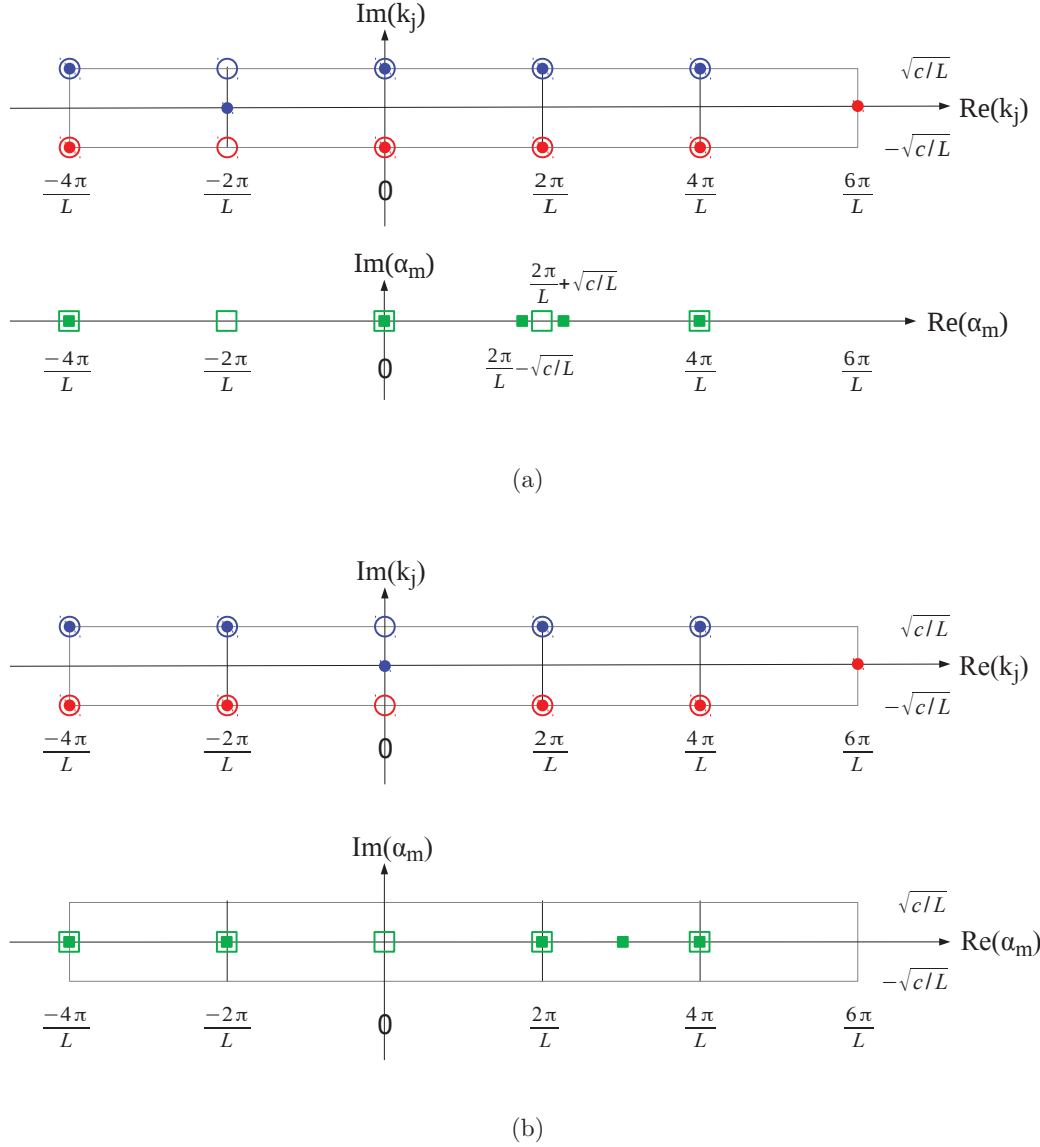


Figure 8.4: An example of the rapidities in two particular single-fermion hole excitations for  $|\gamma| \ll 1$ ,  $\gamma < 0$ . Here we used  $N = 10$ ,  $M = 5$ . For (a),  $m = 2$  (see the mathematical description of the excitations in the text) and for (b),  $m = 3$ . Red and blue circles show the  $k_j$ 's in the complex plane, with the colour differentiating spin types, while green squares show the  $\alpha_m$ 's. Empty symbols show the ground state rapidities, and filled symbols, those of the excited state.

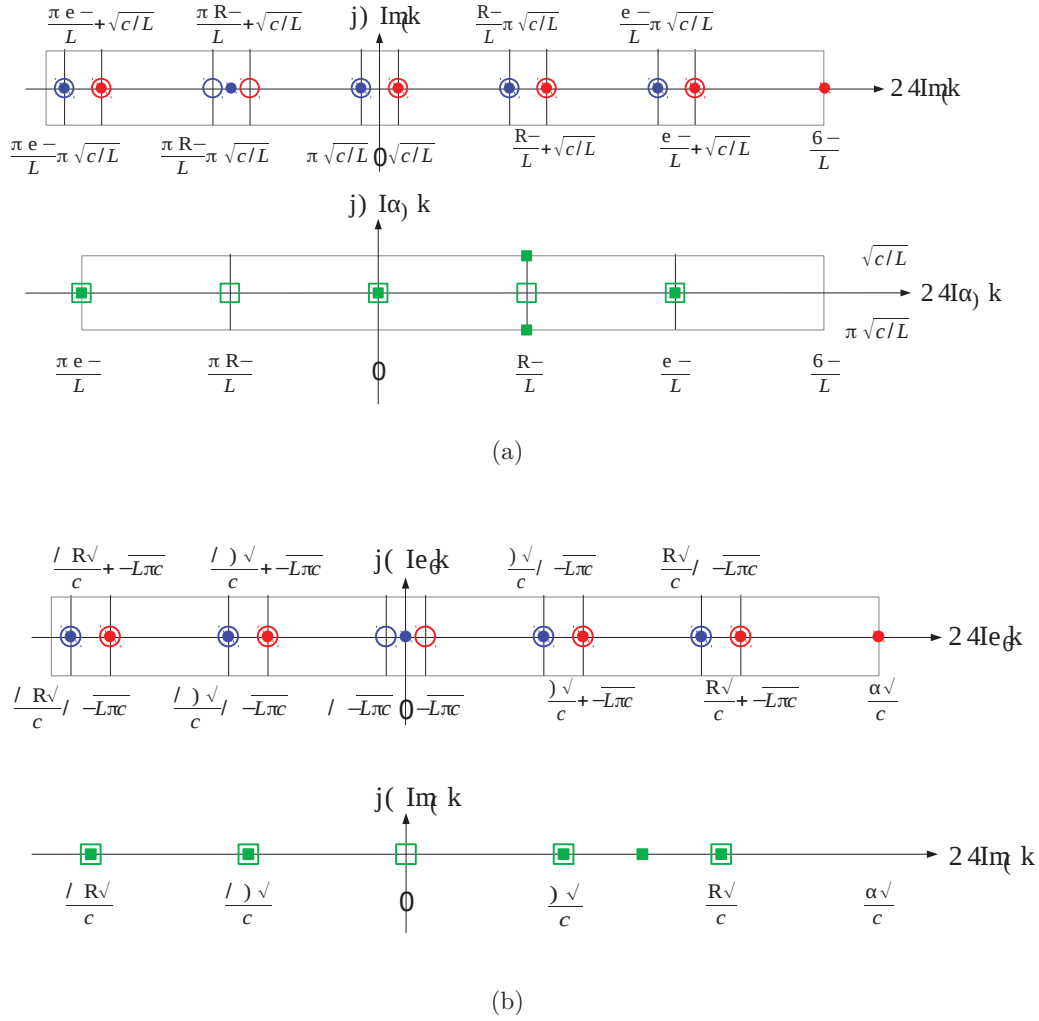


Figure 8.5: An example of the rapidities in two particular single-fermion hole excitations for  $|\gamma| \ll 1$ ,  $\gamma > 0$ . Here we used  $N = 10$ ,  $M = 5$ . For (c),  $m = 2$  (see the mathematical description of the excitations in the text) and for (d),  $m = 3$ . Red and blue circles show the  $k_j$ 's in the complex plane, with the colour differentiating spin types, while green squares show the  $\alpha_m$ 's. Empty symbols show the ground state rapidities, and filled symbols, those of the excited state.

distribution) always has real rapidities for all  $\gamma > 0$ . In fact, this state coincides with the first excited state of the double fermion hole branch (see later). All other states on the single fermion hole dispersion relation alternate in behaviour: half begin at  $|\gamma| \ll 1$  with all  $\alpha_m$ 's being real and at some higher  $\gamma$  value witness the merging of two  $\alpha$ 's into a complex-conjugate pair. For the other half of the one fermion holes, two of the  $\alpha_m$ 's are complex-conjugates directly from the onset of repulsion. In either case, for all but the lowest-momentum excitation on this branch, at sufficiently large  $\gamma$ , we always have one pair of complex-conjugate  $\alpha_m$ 's.

Once again, the exact exponential Bethe ansatz equations can only be solved directly in a limited range about  $\gamma \approx 0$ . Once the imaginary part of the complex rapidities approaches its infinite-coupling limit sufficiently, we have divergent terms and the numerical solution breaks down. In order to continue tracking the solutions in  $\gamma$ , we need to use the string hypothesis.

### 8.4.2 String Hypothesis for $\gamma < 0$

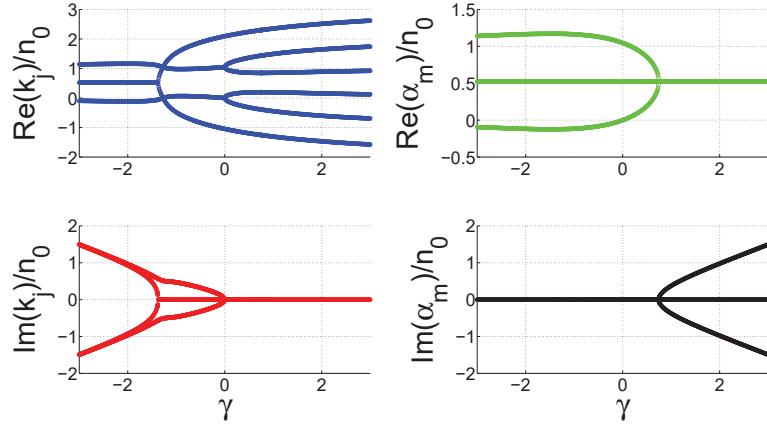
In the attractive case, since at sufficiently small  $\gamma$ 's the single fermion hole states regain the fully dimerized structure, we may use equation (8.12) without the last term on the right-hand side to describe them. Using the logarithmic equations, it is easier to pick up the solutions from the  $\gamma \rightarrow -\infty$  limit where we can use  $\alpha_m = \frac{\pi \ell_m}{L}$  as an initial guess. The quantum numbers necessary to create these excitations are obtained by starting from the ground state quantum numbers and for each  $m$ , taking

$$\ell_m \rightarrow \ell_M + 1, \quad 1 \leq m \leq M. \quad (8.19)$$

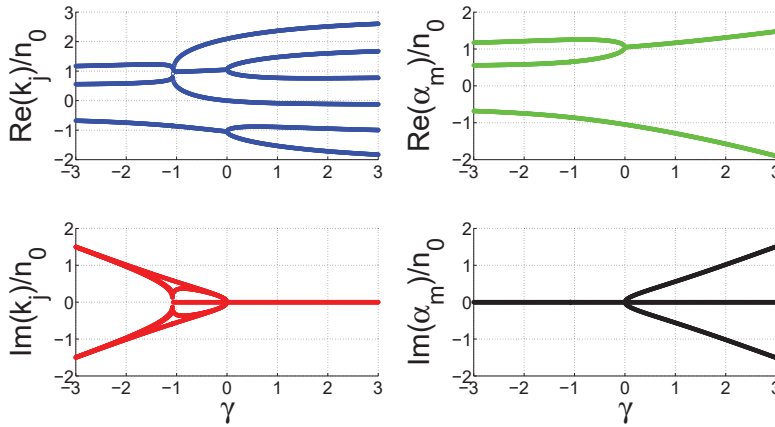
In the strongly-attractive limit these excitations are single *dimer* holes, which is directly reflected in the quantum number choice. As  $\gamma$  increases to zero, the nature of the excitations changes and they smoothly connect to the single fermion holes found using the exact equations.

### 8.4.3 String Hypothesis for $\gamma > 0$

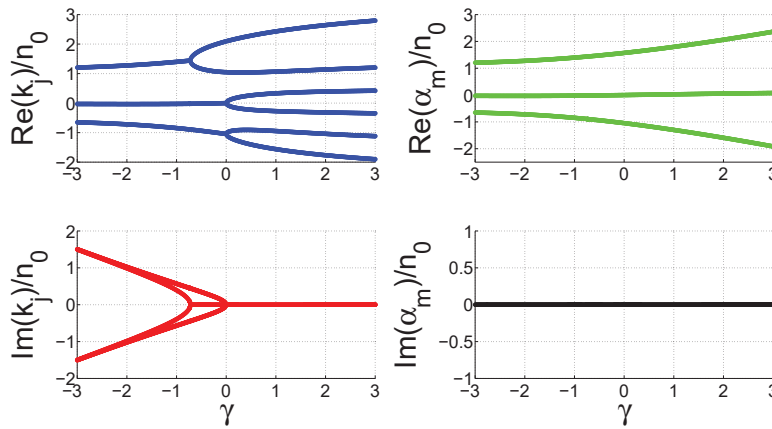
For repulsive interactions, we need to derive a new set of string hypothesis equations appropriate for the case when one has a single pair of complex conjugate  $\alpha_m$ 's. By solving the exact exponential equations, we observe that the imaginary part of the complex  $\alpha_m$ 's becomes  $\pm c/2$  as  $\gamma \rightarrow \infty$ , just as in the attractive regime. Thus we take  $\alpha_{M-1} = A + ic/2$  and  $\alpha_M = A - ic/2$ . Substituting these into the full exponential Bethe ansatz equations, we get  $N$  equations for the  $k_j$ 's,  $M - 2$  for the remaining  $\alpha_m$ 's, and one (obtained from the product of the equations for  $\alpha_{M-1}$  and



(a)



(b)



(c)

Figure 8.6: The real and imaginary parts of charge and spin rapidities for the single fermion hole excitations in a system with  $N = 6$ ,  $M = 3$ . In order to obtain these solutions, we begin from the known approximate rapidities at  $|\gamma| \ll 1$  (see text) and follow these in coupling strength, solving the exact exponential Bethe ansatz equations.

$\alpha_M$ ) for  $A$ . These are

$$\exp(ik_j L) = \frac{k_j - A + ic}{k_j - A - ic} \prod_{n=1}^{M-2} \frac{k_j - \alpha_n + \frac{ic}{2}}{k_j - \alpha_n - \frac{ic}{2}}, \quad (8.20)$$

$$\prod_{j=1}^N \frac{\alpha_m - k_j + \frac{ic}{2}}{\alpha_m - k_j - \frac{ic}{2}} = -\frac{\alpha_m - A + \frac{i3c}{2}}{\alpha_m - A - \frac{i3c}{2}} \times \frac{\alpha_m - A + \frac{ic}{2}}{\alpha_m - A - \frac{ic}{2}} \prod_{n=1}^{M-2} \frac{\alpha_m - \alpha_n + ic}{\alpha_m - \alpha_n - ic}, \quad (8.21)$$

$$\prod_{j=1}^N \frac{A - k_j + ic}{A - k_j - ic} = \prod_{n=1}^{M-2} \frac{A - \alpha_n + \frac{i3c}{2}}{A - \alpha_n - \frac{i3c}{2}} \times \frac{A - \alpha_n + \frac{ic}{2}}{A - \alpha_n - \frac{ic}{2}}. \quad (8.22)$$

Since all variables are now real, the string hypothesis exponential equations are easily solved numerically for any  $\gamma$ . Thus, we follow the one fermion hole excitations from  $\gamma = 0$  to a reasonably high  $\gamma$  where the string hypothesis is almost exact, and pick up the solutions using the string hypothesis equations. We can then follow the solutions to arbitrarily large  $\gamma$  values.

For completeness, we present the string hypothesis equations in logarithmic form as well, since it is precisely this form that is necessary to go to the thermodynamic limit, as is done in chapter 9:

$$k_j L = 2\pi n_j + \sum_{n=1}^{M-2} \theta[2(k_j - \alpha_n)] + \theta(k_j - A), \quad (8.23)$$

$$0 = 2\pi \ell_m - \sum_{n=1}^{M-2} \theta(\alpha_m - \alpha_n) + \sum_{j=1}^N \theta[2(\alpha_m - k_j)] - \theta[2(\alpha_m - A)] - \theta\left[\frac{2}{3}(\alpha_m - A)\right], \quad (8.24)$$

$$0 = 2\pi \ell_{M-1} + \sum_{n=1}^{M-2} \theta\left[\frac{2}{3}(A - \alpha_n)\right] - \sum_{j=1}^N \theta(A - k_j) + \sum_{n=1}^{M-2} \theta[2(A - \alpha_n)]. \quad (8.25)$$

The quantum numbers corresponding to single fermion holes are: assuming  $N/2$  is odd, the  $n_j$ 's are integers, not symmetrically distributed about zero because  $N$  is always even. We choose to put the extra  $n_j$  at positive momentum. Thus, for example, for  $N = 6$  the  $n_j$ 's would be  $-2, \dots, 3$ . The  $n_j$ 's are the same for all the excited states.

Next, the quantum number  $\ell_{M-1}$  is always zero, for all of these states. The others,  $\ell_m$  for  $m = 1, \dots, M - 2$ , are to be constructed as follows: given that  $M - 2$  is odd, we start with integers symmetrically distributed about zero. This is one of our excited states. The other excited states are obtained by subtracting one from each of the  $\ell_m$  quantum numbers in turn, leaving the previous  $\ell_m$ 's in the subtracted form for each consecutive state. For example, for  $M = 5$ , we would have the  $\ell_m$ 's given by  $\{-1, 0, 1\}$  as the starting point – this is already one of the excited states.

The others would have  $\{\ell_m\} = \{-2, 0, 1\}, \{-2, -1, 1\}, \{-2, -1, 0\}$ .

#### 8.4.4 Overview

The single fermion hole at  $\gamma = 0$  changes its nature drastically as  $\gamma \rightarrow \pm\infty$ . As already mentioned, in the infinitely-attractive regime the excitation becomes a single dimer hole: for each  $m$  in turn,  $\alpha_m$  (and therefore, by the structure of the string hypothesis for  $\gamma < 0$ , its two associated  $k_j$ 's) move out from  $\frac{\pi}{L}\ell_m$  to  $\frac{\pi}{L}(\ell_M + 1)$ , where the  $\ell_m$ 's refer to the ground state quantum numbers (8.15). In the opposite limit (infinitely-repulsive), these excitations become a system translation with  $k_j = \frac{2\pi}{L}(n_j + \frac{m}{N})$  where  $m = 1, \dots, M$  and the  $n_j$ 's are the ground state quantum numbers (8.9). An example of both limits is shown in Fig. 8.7, illustrating the rapidities.

The changing nature of the excitation can be clearly seen in Fig. 8.8 (top panel) where we show the dispersion relation for the case of  $N = 14, M = 7$ . As  $\gamma$  decreases to  $-\infty$  the dispersion relation drops from the free-system position so that the unklapp point (the highest-momentum point shown) falls from the half-system translation parabola to the full-system translation parabola, given by  $E = P^2/(2mM)$  and  $E = P^2/(2mN)$ , respectively. As  $\gamma$  increases to  $\infty$ , the entire excitation branch drops, changes curvature, and eventually merges with the full-system translation parabola. The fact that the  $\gamma \rightarrow \infty$  limit of the Yang-Gaudin model supports translation excitations and how this can be seen from the Bethe ansatz equations is further discussed in section 8.6.4.

The bottom panel of Fig. 8.8 compares the exact and string hypothesis dispersion relations at  $\gamma = 1$  and  $\gamma = -2$ , roughly the highest and lowest  $\gamma$  values that can be tackled by the exact exponential equations at the given number of particles. We see that the repulsive string hypothesis is absolutely excellent by this time while the attractive string hypothesis energy is still visibly lower than the true energy. This difference is due to two factors: firstly, in the attractive regime we have  $M$  complex pairs, while in the repulsive only one, and second, in the attractive regime the complex pairs are the  $k_j$ 's which directly contribute to the energy, while in the repulsive, the single  $\alpha$  complex pair clearly does not.

Analytical expressions can be derived for the dispersion relation (with  $M$  odd) in the limits  $|\gamma| \ll 1$  and  $\gamma \rightarrow \pm\infty$ :

$$E(|\gamma| \ll 1) = \frac{\hbar^2 n_0^2}{2m} \left[ \frac{2\pi(M+1)}{N} \frac{P}{n_0 \hbar} - \frac{P^2}{\hbar^2 n_0^2} - \frac{2\gamma}{N} \right], \quad (8.26)$$

$$E(\gamma \rightarrow +\infty) = \frac{P^2}{2mN}, \quad (8.27)$$

$$E(\gamma \rightarrow -\infty) = \frac{\hbar^2 n_0^2}{2m} \left[ -\frac{P^2}{2n_0^2 \hbar^2} + \frac{P\pi(M+1)}{n_0 \hbar N} \right]. \quad (8.28)$$

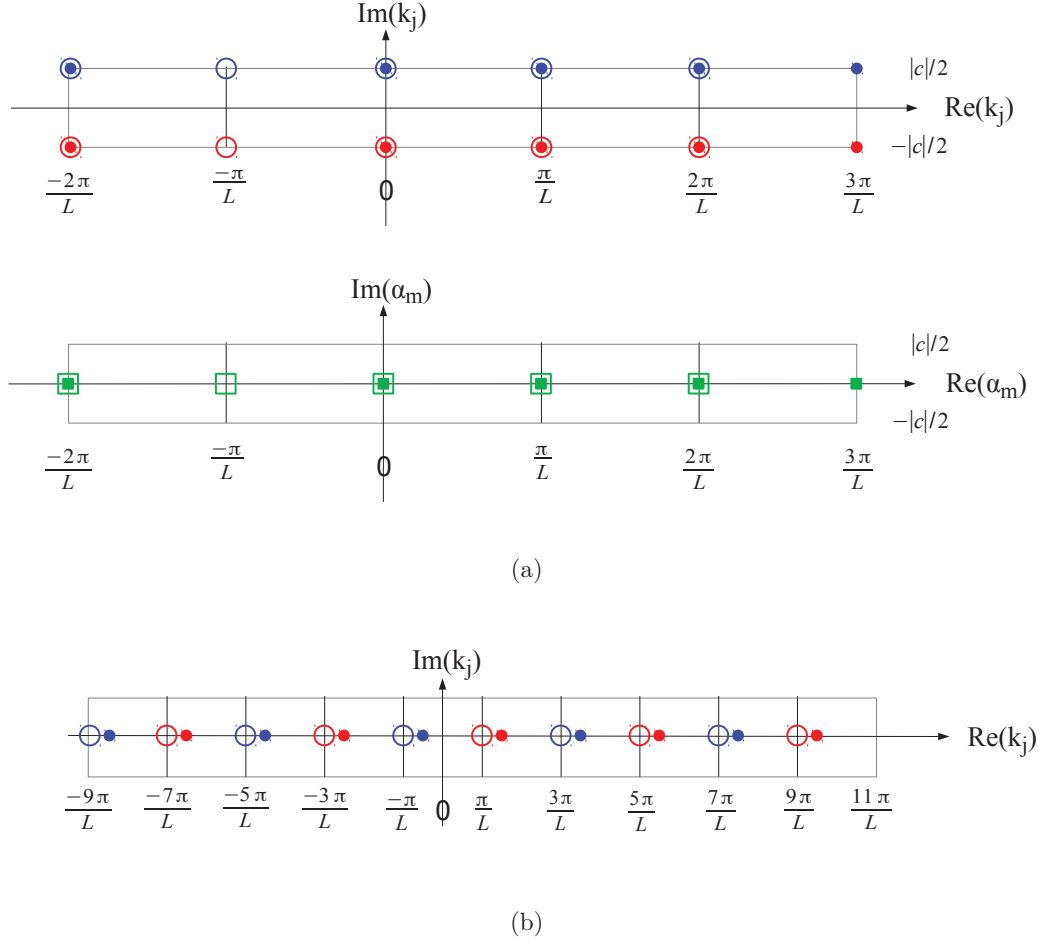


Figure 8.7: An example of the rapidities in a particular single-fermion hole excitation for  $\gamma \rightarrow -\infty$  (a) where it becomes a dimer hole and  $\gamma \rightarrow \infty$  (b) where the excitation is a system translation. Here we used  $N = 10$ ,  $M = 5$  and  $m = 2$  (see the mathematical description of the excitations in the text). For the case of divergent repulsive interactions, we do not have an analytical approximation for the  $\alpha_m$ 's. However, we can certainly state that  $\alpha_m$  and  $\alpha_M$  of the ground state merge into a complex conjugate pair, the real part of which is approximately the average of the ground state  $\alpha_m$  and  $\alpha_M$ , and the imaginary part is  $\pm c/2$ . In (b), the  $k_j$ 's of the excited state are shifted by  $2\pi/L \times m/N$  compared to their ground state values. Red and blue circles show the  $k_j$ 's in the complex plane, with the colour differentiating spin types, while green squares show the  $\alpha_m$ 's. Empty symbols show the ground state rapidities, and filled symbols, those of the excited state.

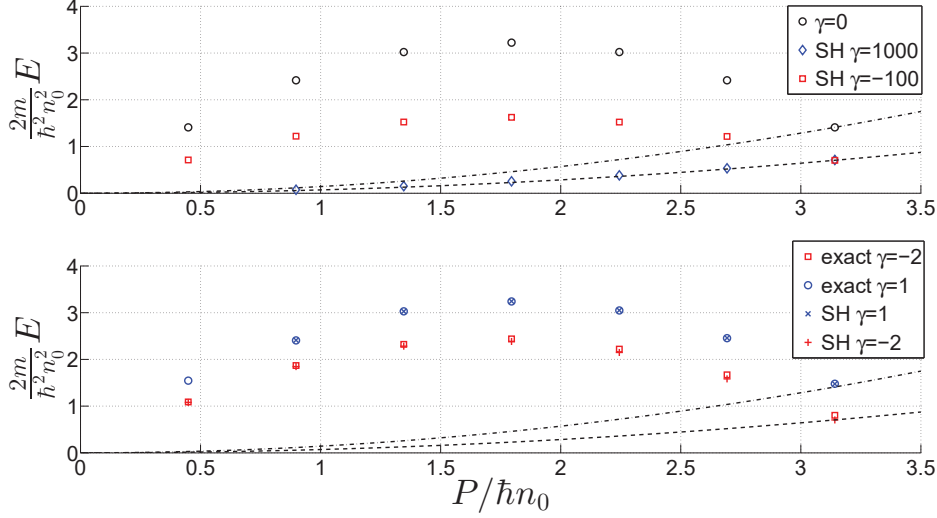


Figure 8.8: Dispersion relations for the single fermion hole branch at various coupling-strengths in a system with  $N = 14$ ,  $M = 7$ . On both panels, the dashed line shows the full-system translation parabola ( $E = P^2/(2mN)$ ) and the dash-dotted line shows the half-system translation parabola ( $E = P^2/(2mM)$ ). Top panel: black circles:  $\gamma = 0$  (free system), red squares:  $\gamma = -100$  (using the string hypothesis, labelled “SH”), blue diamonds:  $\gamma = 1000$  (also using string hypothesis equations). Thus in the strongly-attractive limit this branch becomes single dimer holes, and in the strongly repulsive, a translation of the entire system. The bottom panel shows continuity between the exact and string hypothesis equations at sufficiently large  $|\gamma|$ . The cases shown are: blue circles:  $\gamma = 1$ , exact exponential equations, blue crosses:  $\gamma = 1$ , string hypothesis equations, red squares:  $\gamma = -2$ , exact exponential equations, red pluses:  $\gamma = -2$ , string hypothesis equations.

In the  $\gamma \rightarrow +\infty$  limit the single fermion hole dispersion relation becomes identical to that of the spin-flip branch, and the relevant calculation is found in section 8.6.4.

## 8.5 Double Fermion Holes

Although not the lowest energy branch, the double fermion hole of the free system is particularly interesting because it can be interpreted as a simple hole excitation in all limits ( $\gamma = 0$  and  $\gamma \rightarrow \pm\infty$ ). It is also the only out of the three branches studied here that has a fixed umklapp as a function of  $\gamma$ , and as such most-closely resembles type-II excitations in the Lieb-Liniger model for bosons [47].

### 8.5.1 Exact

On the repulsive side ( $\gamma > 0$ ), we may use the Bethe ansatz equations in logarithmic form (8.5)-(8.6) as all rapidities are real and the quantum numbers are distinct. Double fermion holes are obtained by starting from the balanced ground state, and

setting each of the  $n_j$  quantum numbers in turn to the highest  $n_j$  plus one:

$$n_j \rightarrow n_N + 1, \quad 1 \leq j \leq N. \quad (8.29)$$

In the strongly-repulsive regime, these excitations are single fermion holes from the collective Fermi sphere of both spin components combined, which is reflected in the quantum numbers. An example is shown in Fig. 8.9, illustrating the rapidities. As  $\gamma$  is reduced to zero, the nature of the excitations changes and they smoothly become double fermion holes in the free system.

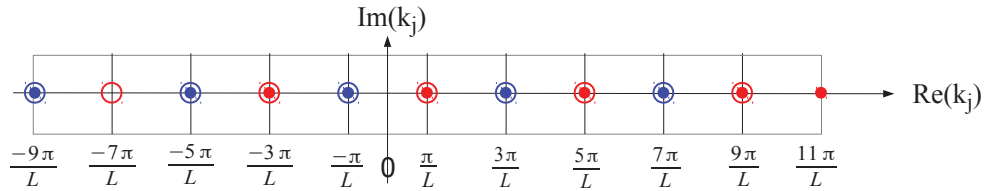
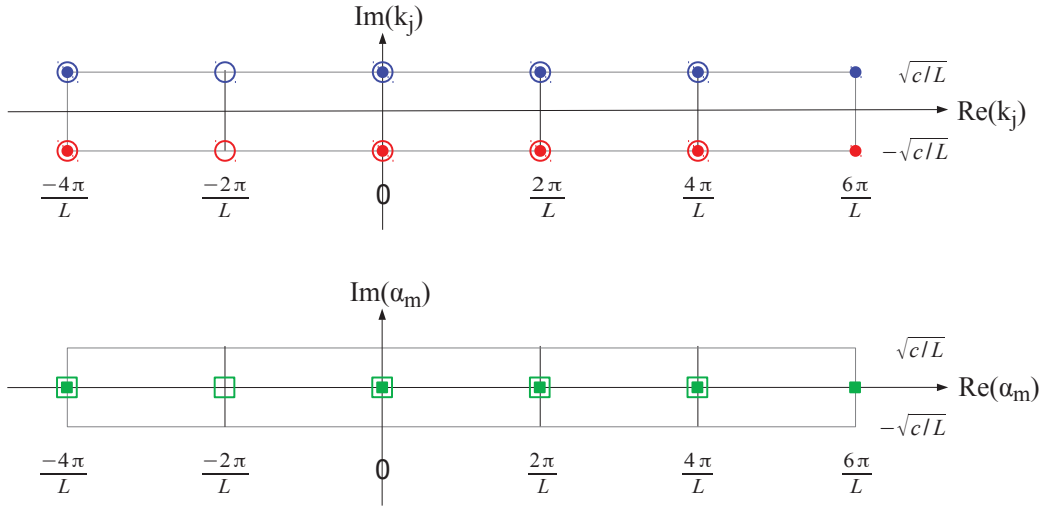


Figure 8.9: An example of the rapidities in a particular double-fermion hole excitation for  $\gamma \rightarrow \infty$  where it becomes a single fermion hole. Here we used  $N = 10$ ,  $M = 5$  and  $j = 2$  (see the mathematical description of the excitations in the text). For divergent repulsive interactions, we do not have an analytical approximation for the  $\alpha_m$ 's. However, we can certainly state that the spin rapidities are unshifted from their ground state values. Red and blue circles show the  $k_j$ 's in the complex plane, with the colour differentiating spin types, while green squares show the  $\alpha_m$ 's. Empty symbols show the ground state rapidities, and filled symbols, those of the excited state.

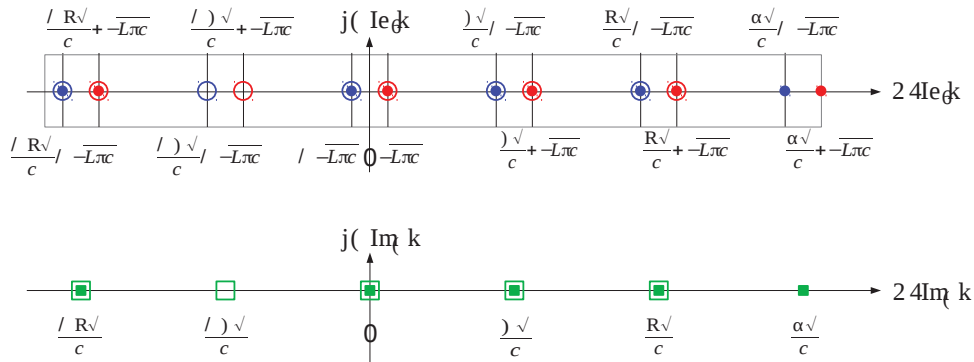
In practice, using the logarithmic equations, it is easiest to pick up these solutions in the  $\gamma \rightarrow \infty$  limit (where we can use an initial guess of  $k_j = \frac{2\pi}{L}n_j$  and  $\alpha_m = \frac{2\pi}{L}\ell_m$ ) and follow in  $\gamma$  down to vanishing interactions.

When  $|\gamma| \ll 1$ , the double fermion holes have the following rapidities (approximately): starting from the almost-free balanced ground state configuration, for each  $m$  in turn,  $\alpha_m = \frac{2\pi}{L}(q_M + 1)$  and  $k_{2m,2m-1} = \frac{2\pi}{L}(q_M + 1) \pm \sqrt{c/L}$ . An example is shown in Fig. 8.10, illustrating the rapidities.

It is easy to see that the  $\gamma \rightarrow 0$  limit described in the previous paragraph only captures  $M$  possible excitations. On the other hand, in the repulsive regime there are certainly  $N$  points on this branch (one for each  $n_j$ ). The remaining points are slightly different and will be henceforth referred to as the complimentary branch to double fermion holes.



(a)



(b)

Figure 8.10: An example of the rapidities in a particular double-fermion hole excitation for  $|\gamma| \ll 1$ ,  $\gamma < 0$  (a) and  $\gamma > 0$  (b). Here we used  $N = 10$ ,  $M = 5$  and  $m = 2$  (see the mathematical description of the excitations in the text). Red and blue circles show the  $k_j$ 's in the complex plane, with the colour differentiating spin types, while green squares show the  $\alpha_m$ 's. Empty symbols show the ground state rapidities, and filled symbols, those of the excited state.

### 8.5.1.1 Compliment

The other  $M$  excited states on the double fermion hole dispersion relation resulting from (8.29) in the repulsive regime have the following structure near  $\gamma = 0$ : the lowest-momentum excitation is essentially a single fermion hole with  $k_{2M} = \frac{2\pi}{L}(q_M + 1)$ ,  $k_{2M-1} = \frac{2\pi}{L}q_M$  and  $\alpha_m$  set to the average of these two newly unpaired fermions.

The other  $M - 1$  excitations involve setting  $k_{2m} = \frac{2\pi}{L}q_m$ ,  $k_{2(m+1)} = \frac{2\pi}{L}q_{m+1}$ ,  $\alpha_m$  to the average of  $k_{2m}$  and  $k_{2(m+1)}$ ,  $\alpha_{m+1} = \frac{2\pi}{L}(q_M + 1)$  and  $k_{2m-1, 2(m+1)-1} = \frac{2\pi}{L}(q_M + 1) \pm \sqrt{c/L}$ . An example is shown in Fig. 8.11, illustrating the rapidities.

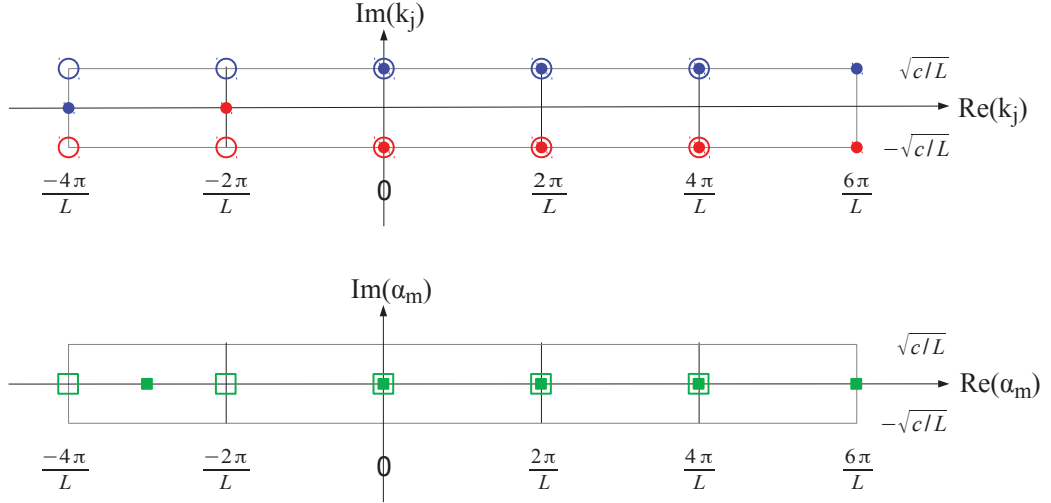


Figure 8.11: An example of the rapidities in a particular complimentary double-fermion hole excitation for  $|\gamma| \ll 1$ ,  $\gamma < 0$ . Here we used  $N = 10$ ,  $M = 5$  and  $m = 2$  (see the mathematical description of the excitations in the text). Red and blue circles show the  $k_j$ 's in the complex plane, with the colour differentiating spin types, while green squares show the  $\alpha_m$ 's. Empty symbols show the ground state rapidities, and filled symbols, those of the excited state.

Knowing the form of the solutions in the vicinity of  $\gamma = 0$ , we can pick them up and follow down in  $\gamma$  using the exact exponential equations. Thus, the exact equations can be solved for some limited region of attractive interactions.

### 8.5.2 String Hypothesis for $\gamma < 0$

As  $\gamma$  decreases below 0 significantly, the exact exponential equations begin to fail and we then resort to the string hypothesis for a description of the strongly-attractive regime. Since the structure of the excited states is fully dimerized, we can use (8.12) without the last term. The double fermion hole branch is obtained by starting from the balanced ground state and setting two of the  $\ell_m$  quantum numbers in turn to

the highest  $\ell_m$  plus one and two, respectively:

$$\ell_m \rightarrow \ell_M + 1, \quad \ell_{m+1} \rightarrow \ell_M + 2, \quad 1 \leq m \leq M - 1. \quad (8.30)$$

This dispersion relation is completed by one last point:  $\ell_M \rightarrow \ell_M + 2$ . The solutions can be picked up from the  $\gamma \rightarrow -\infty$  limit with the usual guess of  $\frac{\pi}{L}\ell_m$ . From the quantum numbers, we can predict *a priori* that in the  $\gamma \rightarrow -\infty$  limit this excitation is a double *dimer* hole, which is indeed the case. As  $\gamma$  increases, the excitations smoothly become double fermion holes at  $\gamma = 0$  and single fermion holes at  $\gamma \rightarrow \infty$ .

### 8.5.2.1 Compliment

The complementary branch certainly requires breaking dimers, so we must use the general string hypothesis equations for attractive interactions, (8.11)-(8.12). We start from the balanced ground state quantum numbers (a list of  $\ell_m$ 's), and for each  $m$ , set  $\ell_m \rightarrow \ell_M + 1$ , shift all  $\ell_m$ 's by  $+0.5$ , arrange the new list of  $\ell_m$ 's in increasing order and delete the  $m^{\text{th}}$   $\ell$  in the new list. Also, take  $n_j = [0 \ 1]$  for odd  $M$ .

As always, it is best to pick up the solutions in the  $\gamma \rightarrow -\infty$  limit, guessing the roots as  $k_j = \frac{2\pi}{L}n_j$  and  $\alpha_m = \frac{\pi}{L}\ell_m$ . Since the excited state has one dimer less than the ground state, this branch will certainly have an energy gap, much like the spin-flip excitations (see below).

### 8.5.3 Overview

The nature of the double fermion hole at  $\gamma = 0$  also changes completely in the limits  $\gamma \rightarrow \pm\infty$ . In the infinitely-repulsive regime, both the double fermion holes and the complimentary excitations identified at  $\gamma = 0$  become single fermion holes out of the joint Fermi sphere. In terms of the rapidities, for each  $j$  in turn,  $k_j$  moves from the ground state position of  $k_j = \frac{2\pi}{L}n_j$  [the  $n_j$ 's are given by (8.9)] to  $k_j = \frac{2\pi}{L}(n_N + 1)$ .

In the infinitely-attractive regime, the double fermion holes become double dimer holes, such that for each  $m = 1, \dots, M - 1$ ,  $\alpha_{m,m+1}$  (and by implication the  $k_j$ 's they represent) move out from  $\frac{\pi}{L}\ell_{m,m+1}$  to  $\frac{\pi}{L}(\ell_M + 1)$  and  $\frac{\pi}{L}(\ell_M + 2)$ , completed by the final state where  $\alpha_M$  moves from  $\frac{\pi}{L}\ell_M$  to  $\frac{\pi}{L}(\ell_M + 2)$ . Here the  $\ell_m$ 's refer to the ground state quantum numbers (8.15). An example is shown in Fig. 8.12 (a), illustrating the rapidities.

The complimentary branch develops an energy gap as  $\gamma$  drops below zero, and becomes a highly excited state. It is of no particular interest, so we will not explicitly describe the limiting case solutions. However, these can be easily obtained from the quantum numbers used in the string hypothesis Bethe ansatz equations (8.11)-(8.12). An example is shown in Fig. 8.12 (b), illustrating the rapidities.

The evolution of the dispersion relation with coupling strength is shown in Fig. 8.13 (top panel) where we specifically choose  $N = 14, M = 7$ . At  $\gamma = 0$  we see that the

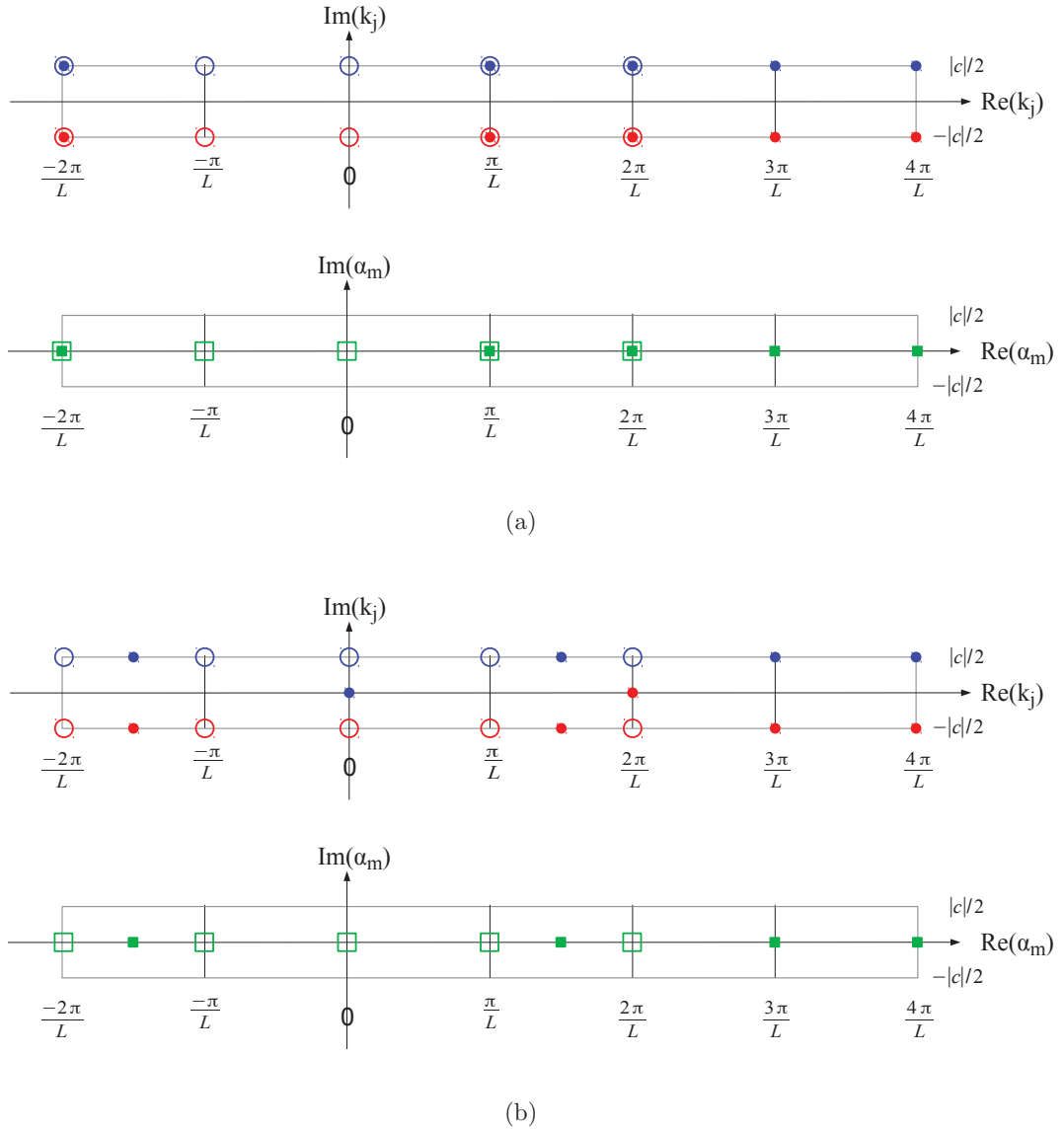


Figure 8.12: An example of the rapidities in a particular double-fermion hole excitation (a) and its complement (b) for  $\gamma \rightarrow -\infty$  where the former becomes a dimer hole and the latter a highly-excited gapped state. Here we used  $N = 10$ ,  $M = 5$  and  $m = 2$  (see the mathematical description of the excitations in the text). Red and blue circles show the  $k_j$ 's in the complex plane, with the colour differentiating spin types, while green squares show the  $\alpha_m$ 's. Empty symbols show the ground state rapidities, and filled symbols, those of the excited state.

double fermion holes and complimentary excitations alternate, falling on the same curve. As  $\gamma$  decreases to  $-\infty$  the vertical range of the double fermion hole dispersion relation diminishes, but the umklapp point is fixed. The points that belong to the complimentary branch develop a gap and rise far above the low energy excitations. As  $\gamma$  increases from 0 to  $\infty$ , the height of the dispersion relation increases, but the umklapp point remains fixed.

The bottom panel of Fig. 8.13 compares the exact and string hypothesis dispersion relations at  $\gamma = -1$  for both double fermion holes and the complimentary excitations. Both are in very good agreement, as one would expect because the structure of these excitations fits the string hypothesis directly from the onset of attraction between the particles.

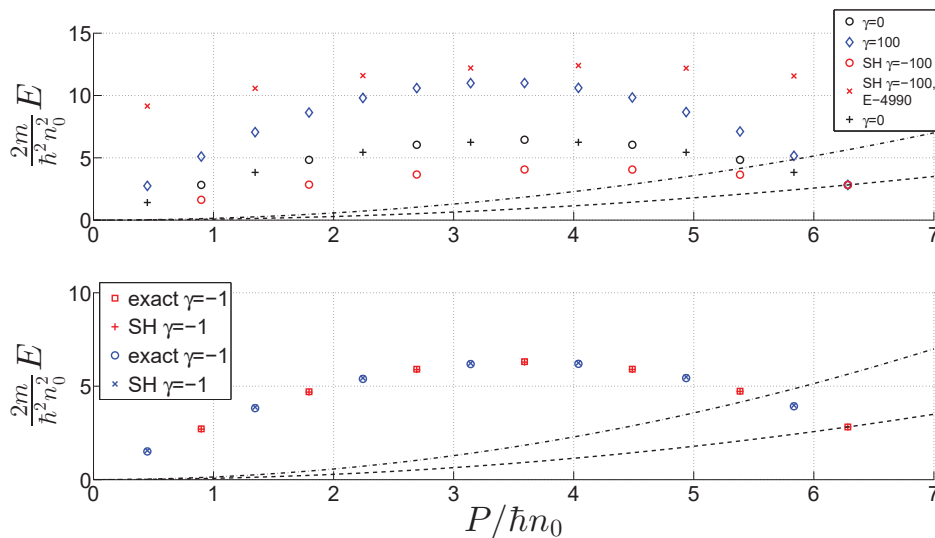


Figure 8.13: Dispersion relations for the double fermion hole branch at various coupling-strengths in a system with  $N = 14, M = 7$ . On both panels, the dashed line shows the full-system translation parabola ( $E = P^2/(2mN)$ ) and the dash-dotted line shows the half-system translation parabola ( $E = P^2/(2mM)$ ). Top panel: black circles:  $\gamma = 0$ , true double fermion holes, black pluses:  $\gamma = 0$ , complimentary excitations, blue diamonds:  $\gamma = 100$ , red circles:  $\gamma = -100$ , true double fermion holes (using the string hypothesis, labelled “SH”), red crosses:  $\gamma = -100$ , complimentary excitations using the string hypothesis (shifted down in energy by 4990). Thus in the strongly-attractive limit this branch becomes double dimer holes, and in the strongly repulsive, a single fermion hole. The bottom panel shows continuity between the exact and string hypothesis equations at  $\gamma = -1$ . The cases shown are: blue circles: complimentary excitations, exact exponential equations, blue crosses: complimentary excitations, string hypothesis equations, red squares: double fermion holes, exact exponential equations, red pluses: double fermion holes, string hypothesis equations.

Analytical expressions can be derived for the dispersion relation (with  $M$  odd)

in the limits  $|\gamma| \ll 1$  and  $\gamma \rightarrow \pm\infty$ :

$$E(|\gamma| \ll 1) = \frac{\hbar^2 n_0^2}{2m} \left[ -\frac{P^2}{2n_0^2 \hbar^2} + \frac{2P\pi(M+1)}{n_0 \hbar N} \right], \quad (8.31)$$

$$E(\gamma \rightarrow +\infty) = \frac{\hbar^2 n_0^2}{2m} \left[ -\frac{P^2}{n_0^2 \hbar^2} + \frac{2P\pi(N+1)}{n_0 \hbar N} \right], \quad (8.32)$$

$$E(\gamma \rightarrow -\infty) = \frac{\hbar^2 n_0^2}{2m} \left[ -\frac{P^2}{4n_0^2 \hbar^2} + \frac{P\pi(M+2)}{n_0 \hbar N} \right]. \quad (8.33)$$

## 8.6 Spin-Flip Excitations

The spin-flip branch is interesting in that it develops an energy gap for attractive interactions as a dimer must be broken to create it. In addition, in the  $\gamma \rightarrow -\infty$  limit, a spin-flip can be considered as an introduction of two impurity particles (single fermions) to a large system of strongly-bound dimers. In the opposite limit of  $\gamma \rightarrow \infty$ , we shall see that this branch provides the simplest way to access the classical translation parabola.

### 8.6.1 Exact

For  $\gamma > 0$ , once again we can solve the logarithmic Bethe ansatz equations (8.5)-(8.6). The spin-flip excitations are obtained by starting from the balanced ground state, adding  $1/2$  to all the  $n_j$ 's, subtracting  $1/2$  from all the  $\ell_m$ 's, and then simply deleting each of the  $\ell_m$ 's on the list in turn, leaving  $M-1$   $\alpha_m$ 's. It is best to pick up these excitations in the strongly repulsive limit (where we can use an initial guess of  $k_j = \frac{2\pi}{L}n_j$  and  $\alpha_m = \frac{2\pi}{L}\ell_m$ ) and then follow down in  $\gamma$  to  $\gamma = 0$ .

The operations performed on the quantum numbers directly reflect the fact that the excitation is a spin-flip. However, as we approach the strongly-interacting limit, the nature of the excitation changes continuously to a translation of the entire system. This is shown analytically in section 8.6.4 below where we take the  $\gamma \rightarrow \infty$  limit of the logarithmic equations. An example is shown in Fig. 8.14, illustrating the rapidities.

As  $\gamma \rightarrow 0$ , the spin-flip solutions can be described as follows: starting from the  $|\gamma| \ll 1$  balanced ground state rapidities, delete each  $\alpha_m$  from the list of variables in turn, set  $k_{2m} = \frac{2\pi}{L}q_m$  and  $k_{2m-1} = \frac{2\pi}{L}(q_M+1)$ . An example is shown in Fig. 8.15, illustrating the rapidities.

Knowing the form of the solutions in the vicinity of  $\gamma = 0$ , we can pick them up and follow down in  $\gamma$  using the exact exponential equations. Thus, for some limited region of attractive interactions the exact equations can be solved.

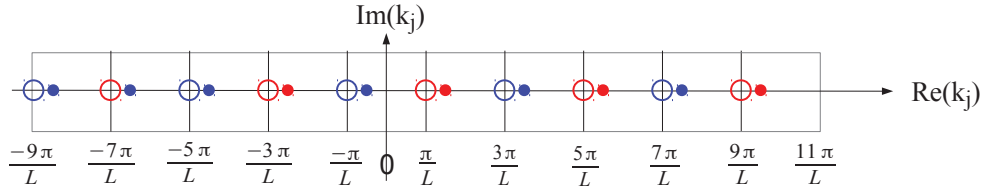


Figure 8.14: An example of the rapidities in a particular spin-flip excitation for  $\gamma \rightarrow \infty$ , where the excitation is a system translation. Here we used  $N = 10$ ,  $M = 5$  and  $m = 2$  (see the mathematical description of the excitations in the text). For the case of divergent repulsive interactions, we do not have an analytical approximation for the  $\alpha_m$ 's. However, we can certainly state that the remaining  $M - 1$   $\alpha_m$ 's are significantly shifted away from their ground state values (but remain real). The  $k_j$ 's of the excited state are shifted by  $2\pi/L \times m/N$  compared to their ground state values. Red and blue circles show the  $k_j$ 's in the complex plane, with the colour differentiating spin types. Empty symbols show the ground state rapidities, and filled symbols, those of the excited state.

### 8.6.2 String Hypothesis for $\gamma < 0$

As  $\gamma$  decreases below 0 significantly, the exact exponential equations begin to fail and we then resort to the string hypothesis for a description of the strongly-attractive regime. Since the spin-flip excitation requires breaking a dimer, we must use the general string hypothesis equations for attractive interactions, (8.11)-(8.12). The spin-flip dispersion relation is obtained by starting from the balanced ground state, adding 0.5 to all the  $\ell_m$ 's and for each  $m$  in turn deleting  $\ell_m$  from the quantum number list. Furthermore, assuming  $M$  is odd we take  $n_{1,2} = \{0, 1\}$ . An example is shown in Fig. 8.16, illustrating the rapidities.

Once again we pick up the solutions in the  $\gamma \rightarrow -\infty$  limit, guessing the rapidities as  $k_j = \frac{2\pi}{L}n_j$  and  $\alpha_m = \frac{\pi}{L}\ell_m$ . Since the creation of the excited state requires breaking a dimer over the balanced ground state, this branch will have an energy gap that roughly scales as the binding energy of each dimer.

### 8.6.3 Overview

The nature of the spin-flip excitations at  $\gamma = 0$  is unaltered in the limit  $\gamma \rightarrow -\infty$  but changes significantly as  $\gamma \rightarrow \infty$ . In the infinitely-repulsive limit, these excitations become a system translation with  $k_j$ 's exactly as for the single fermion branch.

The dispersion relation is shown in Fig. 8.17 (top panel) for several  $\gamma$  values for the case of  $N = 14, M = 7$ . At  $\gamma = 0$  the spin-flip dispersion relation is identical to the single fermion holes, and the umklapp point lies on the half-system

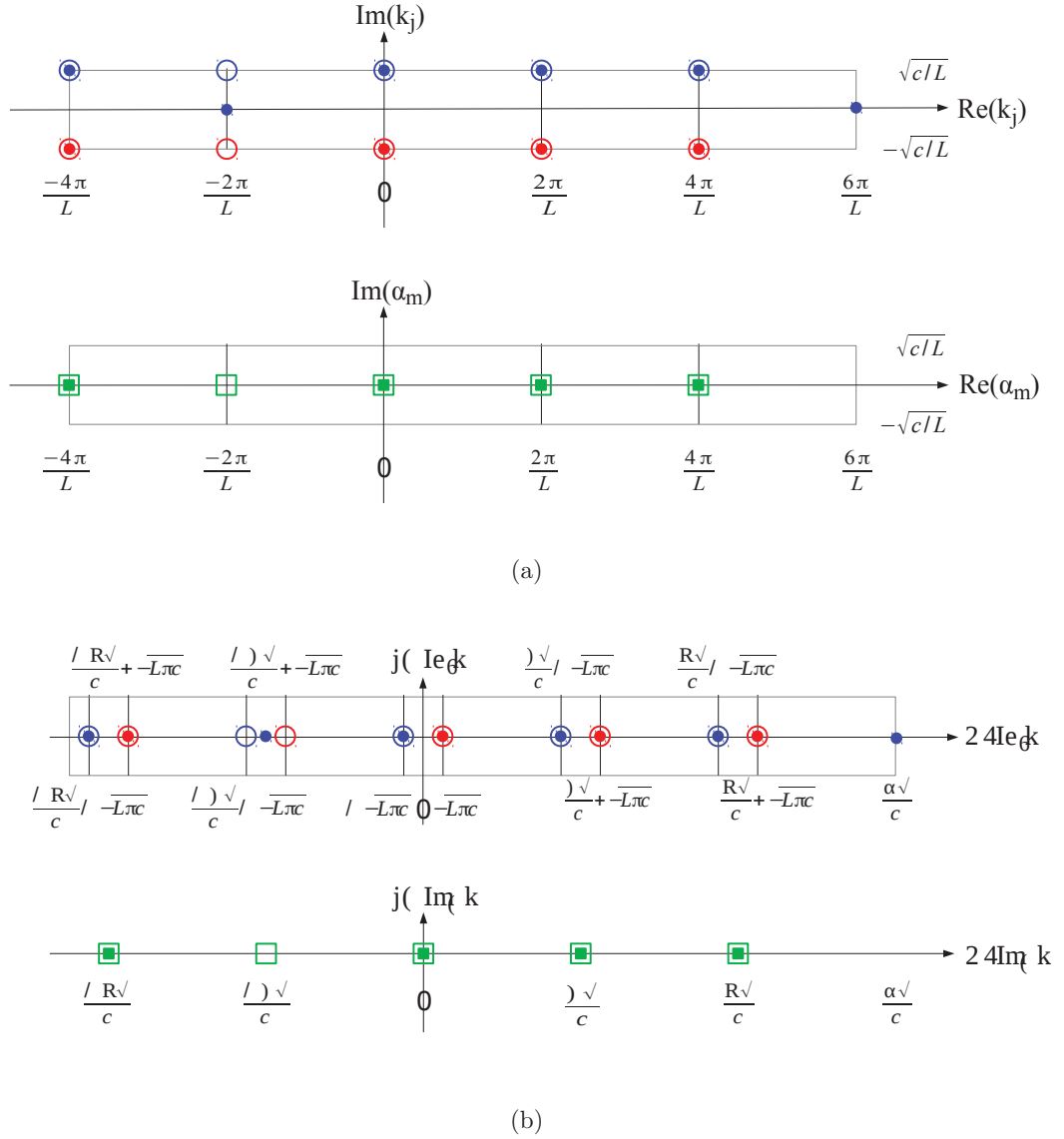


Figure 8.15: An example of the rapidities in a particular spin-flip excitation for  $|\gamma| \ll 1$ ,  $\gamma < 0$  (a) and  $\gamma > 0$  (b). Here we used  $N = 10$ ,  $M = 5$  and  $m = 2$  (see the mathematical description of the excitations in the text). Red and blue circles show the  $k_j$ 's in the complex plane, with the colour differentiating spin types, while green squares show the  $\alpha_m$ 's. Empty symbols show the ground state rapidities, and filled symbols, those of the excited state.

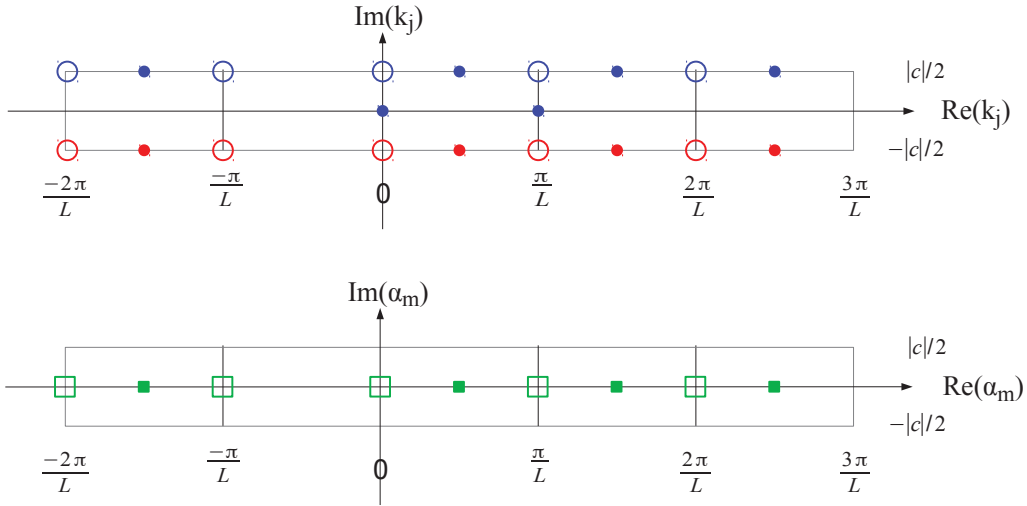


Figure 8.16: An example of the rapidities in a particular spin-flip excitation for  $\gamma \rightarrow -\infty$  where it becomes a highly-excited gapped state. Here we used  $N = 10$ ,  $M = 5$  and  $m = 2$  (see the mathematical description of the excitations in the text). Red and blue circles show the  $k_j$ 's in the complex plane, with the colour differentiating spin types, while green squares show the  $\alpha_m$ 's. Empty symbols show the ground state rapidities, and filled symbols, those of the excited state.

translation curve. As  $\gamma$  decreases to  $-\infty$  the dispersion relation develops a gap and rises far above the low-lying excitations. As  $\gamma$  increases to  $\infty$ , the dispersion relation falls and curves inwards, so that it eventually overlaps the full-system translation parabola, the umklapp point having descended with the rest of the points. Again, in the infinitely-repulsive limit the spin-flip excitations have an identical dispersion relation to single fermion holes.

The bottom panel of Fig. 8.17 compares the exact and string hypothesis dispersion relations at  $\gamma = -1$ . There is a constant small off-shift between the data sets, arising from the fact that the binding energy added to this branch has not yet reached the  $\gamma \rightarrow \infty$  limit, as assumed in the string hypothesis equations.

### 8.6.4 $c \rightarrow \infty$ limit

We have seen that in the  $\gamma \rightarrow \infty$  limit the Yang-Gaudin model supports translation excitations where the  $k_j$ 's do not take on integer multiples of  $2\pi/L$  but can be shifted away from these by a multiple of  $2\pi/(LN)$ . At first glance this is surprising because the equivalent limit of the Lieb-Liniger model truly yields a Tonks-Girardeau gas, equivalent to free fermions up to the fact that the bosons can occupy half-integer multiples of  $2\pi/L$ . In this section we will carefully take the strong-repulsion limit of

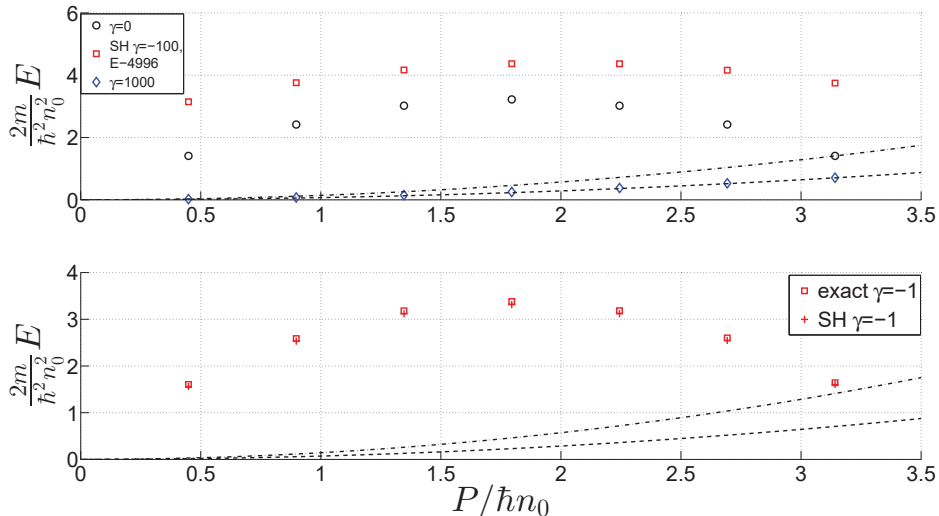


Figure 8.17: Dispersion relations for the spin-flip branch at various coupling-strengths in a system with  $N = 14, M = 7$ . On both panels, the dashed line shows the full-system translation parabola ( $E = P^2/(2mN)$ ) and the dash-dotted line shows the half-system translation parabola ( $E = P^2/(2mM)$ ). Top panel: black circles:  $\gamma = 0$ , blue diamonds:  $\gamma = 1000$ , red squares:  $\gamma = -100$  (using the string hypothesis, labelled “SH”), shifted down in energy by 4996. Thus in the strongly-attractive limit this branch remain a spin-flip, and in the strongly repulsive, becomes a system translation. The bottom panel shows continuity between the exact and string hypothesis equations at  $\gamma = -1$ . The cases shown are: red squares: exact exponential equations, red pluses: string hypothesis equations.

the logarithmic Bethe ansatz equations and show that this result is indeed correct and the translation parabola is truly accessible.

Thus, we take equations (8.5)-(8.6), and consider  $\gamma \rightarrow \infty$ . If we work to zeroth order in  $1/c$ , we have to set all the  $\theta$  functions to zero, but of course this makes it impossible to satisfy (8.6). Therefore we work to first order in  $1/c$  and expand all the  $\theta$  functions as a first order Taylor expansion about zero. We arrive at two sets of equations that involve the quantum numbers  $n_j$  and  $\ell_m$ ,  $N, M, L, c$  and two sums  $\sum_j k_j$  and  $\sum_m \ell_m$ . Next, we rearrange for  $k_j$  and  $\alpha_m$ :

$$k_j = \frac{2\pi n_j c + 4 \sum \alpha_m}{cL + 4M}, \quad (8.34)$$

$$\alpha_m = \frac{-2\pi \ell_m c + 2 \sum \alpha_m - 4 \sum k_j}{2M - 4N}. \quad (8.35)$$

Taking the sum on both sides (in the first case over  $j$ , in the second over  $m$ ), we solve the resulting equations for the sums (at this point, these are two algebraic

equations in two variables). This leads to

$$\sum k_j = \frac{2\pi(\sum \ell_m + \sum n_j)}{L}, \quad (8.36)$$

$$\sum \alpha_m = \frac{\pi [cL \sum \ell_m + 4M (\sum \ell_m + \sum n_j)]}{2LN}. \quad (8.37)$$

These equations, when used with the quantum numbers of the spin-flip branch, give the correct  $k_j$ 's as returned by numerically solving the full Bethe ansatz equations. On the other hand, they are completely insufficient to correctly predict the  $\alpha_m$ 's, where higher orders need to be retained for even a rough level of approximation.

Now, these expressions are still not transparent enough to be able to easily see the origin of the translational excitations. Since we know that  $4M \ll cL$  for the large- $c$  regime considered here, we neglect terms of order  $4M$  compared to terms of order  $cL$ . This leads to

$$k_j = \frac{2\pi}{L} \left( n_j + \frac{\sum \ell_m}{N} \right), \quad (8.38)$$

which exactly reproduces the limiting behaviour of the spin-flip branch when the appropriate  $\ell_m$ 's are used. The above expression, (8.38), has been found in [185] as well, but the additional excitations possible in such a system were not studied.

Interestingly, if we express the excitation energy as a function of the excitation momentum using the approximate rapidities (8.34)-(8.35), with the sums given by (8.36)-(8.37), all first order corrections in  $1/c$  cancel and we find the dispersion relation  $E = P^2/(2mN)$ , the full-system translation parabola.

We have performed the same calculation for the string hypothesis equations of the single fermion holes branch, equations (8.23)-(8.25), and found the same classical dispersion relation but with an additional energy gap that scales with  $N$  as  $\mathcal{O}(1)$  and with  $\gamma$  as  $\mathcal{O}(1/\gamma)$ . By comparing the approximate dispersion relation to exact numerical solutions of the Bethe ansatz equations, we were able to show that this gap is not physically significant – it is an artefact arising from the fact that we only considered a first order expansion of the Bethe ansatz equations, and is most likely cancelled by contributions from higher orders. Further supporting evidence for this claim is the fact that we do not find a gap in the thermodynamic limit at any  $\gamma$  (see chapter 9), whereas the energy gap obtained from this calculation does not vanish as  $N \rightarrow \infty$  and would thus be expected to survive. Thus the single fermion hole dispersion relation also approaches  $E = P^2/(2mN)$  as  $\gamma \rightarrow \infty$ .

Finally, analytical expressions can be derived for the dispersion relation (with  $M$

odd) in the limits  $|\gamma| \ll 1$  and  $\gamma \rightarrow \pm\infty$ :

$$E(|\gamma| \ll 1) = \frac{\hbar^2 n_0^2}{2m} \left[ -\frac{2\gamma}{N} - \frac{P^2}{n_0^2 \hbar^2} + \frac{2P\pi(M+1)}{n_0 \hbar N} \right], \quad (8.39)$$

$$E(\gamma \rightarrow +\infty) = \frac{P^2}{2mN}, \quad (8.40)$$

$$E(\gamma \rightarrow -\infty) = \frac{\hbar^2 n_0^2 \pi^2}{2m} \left[ -\frac{P^2}{2\pi^2 n_0^2 \hbar^2} + \frac{\gamma^2}{2\pi^2} + \frac{-3M+4-M^2}{2N^2} + \frac{P(M+2)}{n_0 \pi \hbar N} \right]. \quad (8.41)$$

## 8.7 Discussion and Conclusions

In this chapter we have followed the ground state and the three elementary type-II excitations of the free system from zero interaction to  $\gamma \rightarrow \pm\infty$ . In the process, we derived string hypothesis equations that were used when the imaginary parts of complex-conjugate rapidities became very close to  $c/2$ . We demonstrated continuity between the exact and approximate equations for the ground state and all excited states. Moreover, for the single fermion holes, we explicitly showed the evolution of the rapidities as a function of  $\gamma$  in the region about  $\gamma = 0$  where it is essential that the direct exponential Bethe ansatz equations are used because the structure of the state is different from that assumed under the string hypothesis.

We were able to identify the nature of the excitations in the extreme limits of  $\gamma \rightarrow \pm\infty$ : the single fermion holes become single dimer holes as  $\gamma \rightarrow -\infty$  and a system translation as  $\gamma \rightarrow \infty$ , the double fermion holes turn into double dimer holes as  $\gamma \rightarrow -\infty$  and single fermion holes as  $\gamma \rightarrow \infty$ , and finally, the spin-flip branch retains its nature for  $\gamma < 0$  and becomes a system translation as  $\gamma \rightarrow \infty$ .

In the course of our study, we have shown that the strong-repulsion limit of the Yang-Gaudin model is very different from the Tonks-Girardeau gas (the correct limit for the Lieb-Liniger model). In his thesis [185], Zvonarev has already pointed out the correct limiting solutions, showing a clear contribution from the spin degree of freedom, but has not investigated the consequences. Here we showed that the two-component Fermi gas with periodic boundary conditions allows the system translation excitations to be accessed at any momentum value (not just at the umklapp points) in the infinitely-repulsive regime.

Finally, the elementary type-II excitations of the Yang-Gaudin model are of particular interest in light of the possible connection of these states to dark solitons. In chapter 12, we will use the algebraic Bethe ansatz to show that dark solitons can be interpreted as localized superpositions of type-II states of the Lieb-Liniger model [46, 47]. Perhaps a similar calculation will be possible for the Yang-Gaudin model in the near future, but for the present, one can transfer some of the finding to the Yang-Gaudin model by analogy – this is expanded on in chapter 13.

# Appendix

## 8.A Technical Details

In this appendix we provide all the details on how the Bethe ansatz equations were solved numerically. We used the Matlab environment, and in particular the `fsolve.m` function (implementing the trust-region dogleg algorithm), included in the optimization toolbox. Absolute and relative tolerances are set to  $10^{-8}$ .

In order to solve any of the logarithmic equations (where all variables are necessarily real and distinct), we always begin from the strong-coupling limit, taken as  $|\gamma| = 100$ . In this regime, one can use  $2\pi/L$ -multiples of the quantum numbers as an initial guess, and the solver easily picks up the correct solution. Now, usually this guess is sufficient at any  $\gamma$  (with the logarithmic equations), but we find it is better to follow the solutions from  $|\gamma| = 100$  down to whatever value one needs. This is done with an adapting step of  $\gamma/10$ , since in the strong-coupling regime the solutions change very little and large steps can be taken, while in the weak-coupling regime the converse is true. At each consecutive  $\gamma$ -step, the guess is taken as the solution at the previous step. This following-in- $\gamma$  procedure greatly improves efficiency and accuracy for large systems ( $N \sim 100 - 1000$ ) but is optional for small systems ( $N \sim 10$ ).

If one wishes to solve the exact exponential equations for the ground state of the repulsive system where all rapidities are real and distinct, then one must start from the known approximate solutions in the small  $|\gamma|$  limit as the guess (we always use  $\gamma = \pm 0.01$  in practice), and then follow in  $\gamma$  up to whatever value is needed, exactly as above.

In order to solve the exponential string hypothesis equations (8.20)-(8.22), we first solve the exact exponential Bethe ansatz equations for the single fermion hole from  $|\gamma| \ll 1$  to as high a value as we can (see below), and then use that solution as a guess for the string hypothesis equations at the same  $\gamma$ . Having picked up the solution, we then follow in  $\gamma$  with an adaptive step as before ( $\gamma/10$ ), except that the guess at each step is taken as a linear interpolation using the previous two  $\gamma$ -values.

Now, solving the exact exponential Bethe ansatz equations with complex rapidities is a somewhat more involved task. Here there are two possibilities: either the structure of the solution changes with  $\gamma$  (for example, distinct real rapidities may merge into a complex-conjugate pair), or it does not. In the latter case, the situation is simpler, so we start there. The simplest of all cases is the ground state for  $\gamma < 0$ ,

due to the symmetry of the solution. As such, we can track the solution somewhat further than for excited states.

For the ground state with  $\gamma < 0$  we begin from the known approximate solutions at  $\gamma \approx 0$  and track in  $\gamma$  using a fixed step of 0.01. Once again, we use a linear interpolation based on the previous two points as a guess for the next. Whenever the solver fails to converge to a valid solution, we call the solver a maximum of five times more, at each attempt adding a vector of (real) random numbers to the initially-used guess of order  $10^{-4}n_0$ . If all five attempts are exhausted unsuccessfully, the program aborts.

As for excited states where the structure of the solution does not change, the list includes double fermion holes, the complimentary excitations of section 8.5.1.1 and spin-flips, all with attractive interactions. As always, we begin from the  $|\gamma| \ll 1$  limit to pick up the solutions. Then we follow in  $\gamma$  using an adaptive step and linear interpolation for predictive guessing. For each individual point on the dispersion relation we begin with a step of  $\gamma/10$ , and whenever the solver fails, the step is reduced by a factor of two. If the smaller step does not help converge to a valid solution, the program is aborted.

Finally, consider the single fermion branch with  $\gamma > 0$  and  $\gamma < 0$ , where the structure of the solution changes as a function of  $\gamma$ . As always, we begin from  $\gamma = \pm 0.01$  where solutions are approximately known, use a fixed step of 0.01 (unless we are in the vicinity of a merging – see below) and linear interpolation for predictive guessing. At each step, the solver is called once and the solutions are inspected. The Bethe ansatz equations must have distinct roots, so that no two  $k_j$ 's and no two  $\alpha_m$ 's are equal. At points where two real rapidities merge into a complex-conjugate pair, the solver often fails to automatically split up these roots along the imaginary axis, so this must be tested for and corrected.

Thus, having made an initial attempt to solve at a given  $\gamma$  value, we test whether any of the  $k_j$ 's (for  $\gamma < 0$ ) or any of the  $\alpha_m$ 's (for  $\gamma > 0$ ) have been returned equal (in this case they will also necessarily be real). If so, we modify the guess by splitting up these rapidities by  $\pm 0.1in_0$  ( $\gamma < 0$ ) and by  $\pm 0.05in_0$  ( $\gamma > 0$ ). Occasionally for the repulsive system three  $\alpha_m$ 's may be initially returned as equal and real (not two) – in this case, the guesses for two of these are split up into the complex plane, while the third is left as real. Having modified the guess to help the solver pick up the correct solution, we call it again and reduce step size to 0.001 in a  $\gamma$ -interval of 0.01 immediately following the merging point. The step is reduced because usually variables change very rapidly in the vicinity of a merging and in order for our linear guess to be effective, the  $\gamma$ -step must be smaller. Once we perform 10 of these reduced steps, the step size is returned to normal.

Regardless of whether a merging takes place at any given  $\gamma$  value, if the solver

fails to converge, we make a maximum of ten further attempts to solve by adding small (real) random numbers of order  $10^{-4}n_0$  to the initial guess (which may have already been “manually” modified due to a merging). If all ten attempts fail, the program is aborted.

# Chapter 9

## Thermodynamic Limit

In this chapter we will present the solutions of the Bethe ansatz equations for both the Lieb-Liniger & Yang-Gaudin models in the thermodynamic limit, that is, when  $N, L \rightarrow \infty$  with  $n_0 = N/L$  held fixed. The finite-system Bethe ansatz algebraic equations become integral equations for the densities of the rapidities in quasi-momentum space. We solve these for the ground state and all type-II excitations considered in the previous two chapters (so once again, this chapter provides technical details with physical discussions delegated to later chapters). The thermodynamic limit solutions are required to compute the missing particle number and phase step of the type-II states, as is done in the next chapter, as well as the physical and inertial masses. These quantities will be invaluable in the study of quantum dark solitons of the Lieb-Liniger model (chapter 12) and for the characterization of the different Yang-Gaudin type-II excitations. In fact, we will identify type-II branches which may be understood as dark solitons for both repulsive and attractive interactions (chapter 13). Moreover, from our work in chapter 12, it will become apparent that the dispersion relation of the quantum dark solitons is that of the corresponding type-II states, so the dispersion relations computed in this chapter give a direct prediction regarding solitonic excitations in the one-dimensional Bose and Fermi-gases.

Another reason to present the thermodynamic limit equations for all the low-energy type-II excitations of the Yang-Gaudin model is that there are some small discrepancies and inaccuracies in the literature in this regard, while our work here is fully self-consistent and follows directly from the finite system results.

### 9.1 Introduction

In addition to the introduction given in chapter 8, continuing our discussion of one-dimensional Bethe ansatz-solvable models, previous theoretical work of direct relevance to our results here can be divided into two main categories. First, the unified picture of the Bose-Einstein condensate-Bardeen-Cooper-Schrieffer crossover in one dimension [82, 186–188], which highlights the fact that both the Lieb-Liniger and Yang-Gaudin models can be realized in a single physical system. Second, previous

exploration of the elementary excitations in these models, notably [47] and chapter 8 (and related works [180, 181, 184]). An excellent, more complete review of the recent theoretical and experimental work on the Lieb-Liniger and Yang-Gaudin models can be found in [163, 183].

In this chapter we present all the thermodynamic limit Bethe ansatz equations that describe the ground and excited states in both the Lieb-Liniger and Yang-Gaudin models, restricting ourselves to repulsive interactions in the first case but not in the second. The relevant integral equations are given in section 9.2, subdivided by model, the sign of the interaction and excitation branch. Note that the Yang-Gaudin type-II excitations are referred to and classified as in chapter 8 (which deals with the finite-system case). The method followed to derive these thermodynamic limit equations is outlined in appendix 9.A. Approximate analytical solutions of the thermodynamic limit Bethe ansatz equations in limiting cases and all relevant system properties are summarized in appendix 10.A, given at the end of the next chapter which introduces some further useful thermodynamic limit quantities.

## 9.2 Thermodynamic Limit Equations

The Hamiltonian for both the Lieb-Liniger and Yang-Gaudin models is identical and is given by (6.1). The difference between the models is that the Lieb-Liniger case considers  $N$  identical bosons and the Yang-Gaudin case  $N$  fermions,  $M \leq N/2$  of which are spin-down and the rest are spin-up. Furthermore,  $m$  is the mass of each particle, and the particles are confined to a ring of circumference  $L$ . Recall that  $\gamma = \frac{c}{n_0}$ , where  $n_0 = N/L$  is the one-dimensional density. In fact,  $\gamma$  is the only dimensionless parameter characterizing the ground state in the thermodynamic limit (defined by  $N, L \rightarrow \infty$  with  $n_0$  remaining finite) of the Lieb-Liniger model. In the Yang-Gaudin case, one additionally has the parameter  $M/N$  (we shall focus on the balanced case of  $M/N = 1/2$ ).

For finite  $N, L$ , Hamiltonian (6.1) can be diagonalized by the Bethe ansatz [52], which leads to a set of coupled algebraic equations for the quasi-momenta: in the case of a single spin component of particles (as in the Lieb-Liniger model), one only has  $N$  so-called *charge rapidities* which contribute directly to the momentum and energy of the state, while if a second spin component is present (as in the Yang-Gaudin model), one also has  $M$  *spin rapidities* which do not enter the expressions for the momentum or energy but can rather be thought of as auxiliary variables. The relevant finite-system equations for the Lieb-Liniger model can be found in chapter 7, alongside the quantum numbers necessary to obtain the ground state and type-II excitations. As for the Yang-Gaudin model, in chapter 8 we performed a detailed study of the ground state and all the type-II excited branches we are interested

in here, so the finite-system Bethe ansatz equations and the quantum numbers are found therein.

In the thermodynamic limit, the coupled algebraic equations of the Bethe ansatz become Fredholm integral equations of the second kind. In appendix 9.A, we give a brief description of how one can obtain the integral equations from the algebraic ones for the ground state and type-II excitations. The ground state integral equations can be found in [46] for the Lieb-Liniger model and in [189] for the Yang-Gaudin. As for type-II excited states, [47] derives the equations for the Lieb-Liniger model, but while some earlier works examining excitations in the Yang-Gaudin model do exist [180, 181, 184], we believe our account here is the first complete and consistent summary of elementary type-II excitations in the thermodynamic limit of the Yang-Gaudin model.

In this chapter we present all the integral equations and related quantities that characterize the ground and excited states of interest. We also illustrate by showing dispersion relations for all relevant branches at several interaction-strength values. These are computed by solving the integral equations numerically on Matlab, using the “Fie” package [190], freely available online (together with a detailed description of the algorithms). For the Lieb-Liniger and attractive Yang-Gaudin models, absolute tolerance is set to  $10^{-8}$  and relative tolerance to  $10^{-4}$ . For the repulsive Yang-Gaudin model, both tolerances are taken as  $10^{-6}$ .

## 9.2.1 Repulsive Lieb-Liniger

In the case of the repulsive Lieb-Liniger model,  $\gamma > 0$  and all  $N$  particles are identical bosons. The simplest limit is the  $\gamma \rightarrow \infty$  limit where the Lieb-Liniger system becomes a Tonks-Girardeau gas, practically equivalent to a free fermion system [46, 47]. In this limit, type-II excitations are simply hole-excitations: a single particle taken out of the Fermi sphere.

In the opposite limit,  $\gamma \rightarrow 0$ , the ground state sees all the particles “condensing” into the zero-momentum mode [46] (of course no true condensation takes place). In the attractive case ( $\gamma < 0$ ), the ground state is a global “string-state” where all the particles are bound together [170] in what can be understood as a bright soliton [173]. The attractive case is not explored here.

### 9.2.1.1 Ground State

Let us start from the ground state properties, which can be found upon solving the following integral equation:

$$2c \int_{-K}^K \frac{f(p)}{c^2 + (p-k)^2} dp = 2\pi f(k) - 1. \quad (9.1)$$

Here, the rapidity density  $f(k)$  is such that

$$\int_{-K}^K f(k)dk = n_0, \quad (9.2)$$

and  $k$  is the continuous version of the charge rapidities of the bosons appearing in the finite problem. The ground state energy and momentum can be found from

$$E_g = \frac{\hbar^2}{2m} L \int_{-K}^K k^2 f(k)dk, \quad (9.3)$$

$$P_g = \hbar L \int_{-K}^K k f(k)dk = 0. \quad (9.4)$$

In order to solve the integral equation numerically we introduce the following scaled variables:

$$k = Kx, \quad c = K\lambda, \quad f(k) = f(Kx) = g(x). \quad (9.5)$$

The scaled integral equation becomes

$$1 + 2\lambda \int_{-1}^1 \frac{g(x)}{\lambda^2 + (x-y)^2} dx = 2\pi g(y), \quad (9.6)$$

and the normalization condition on  $f(k)$  reads

$$\int_{-1}^1 K g(x) dx = n_0. \quad (9.7)$$

The ‘‘Fermi momentum’’  $K$  is calculated as

$$K = \frac{n_0 \gamma}{\lambda}, \quad (9.8)$$

and  $\lambda$  in turn is found from

$$\lambda = \gamma \int_{-1}^1 g(x) dx. \quad (9.9)$$

The ground state energy is written as

$$E_g = \frac{\hbar^2}{2m} L K^3 \int_{-1}^1 x^2 g(x) dx, \quad (9.10)$$

and introducing  $e(\gamma)$  so that

$$E_g = \frac{\hbar^2}{2m} N n_0^2 e(\gamma), \quad (9.11)$$

$e$  is calculated as

$$e(\gamma) = \left(\frac{\gamma}{\lambda}\right)^3 \int_{-1}^1 x^2 g(x) dx. \quad (9.12)$$

Finally, the chemical potential, defined as  $dE_g/dN$ , is given by

$$\mu = \frac{\hbar^2}{2m} n_0^2 \left( 3e - \gamma \frac{de}{d\gamma} \right). \quad (9.13)$$

### 9.2.1.2 Single Boson Holes

First, let us recall the  $\theta$  function (the two-body phase shift of the  $\delta$  potential) that will feature in all the sections below:

$$\theta(k) = -2 \tan^{-1} \left( \frac{k}{c} \right). \quad (9.14)$$

The equation to be solved for type-II excitations is

$$2\pi J(k) = 2c \int_{-K}^K \frac{J(r)}{c^2 + (r-k)^2} dr + \theta(Q-k) + \pi, \quad (9.15)$$

where  $|Q| \leq K$  parametrizes the excitation momentum. The energy and momentum of the excitation are found from

$$P = \hbar \left[ -Q + \int_{-K}^K J(k) dk \right], \quad (9.16)$$

$$E = \frac{\hbar^2}{2m} \left[ -Q^2 + 2 \int_{-K}^K k J(k) dk \right] + \mu. \quad (9.17)$$

To solve these equations numerically we need to introduce the following additional scaled variables [also see (9.5)]:

$$r = Ky, \quad Q = Kq, \quad J(k) = J(Kx) = h(x). \quad (9.18)$$

The integral equation becomes

$$2\pi h(x) = 2\lambda \int_{-1}^1 \frac{h(y)}{\lambda^2 + (x-y)^2} dy + \pi - 2 \tan^{-1} \left( \frac{q-x}{\lambda} \right). \quad (9.19)$$

Excitation energy and momentum are computed from

$$P = \hbar K \left[ -q + \int_{-1}^1 h(x) dx \right], \quad (9.20)$$

$$E = \frac{\hbar^2}{2m} K^2 \left[ -q^2 + 2 \int_{-1}^1 x h(x) dx \right] + \mu. \quad (9.21)$$

Figure 9.1 shows three example dispersion relations, spanning the weak-, intermediate- and strong-coupling regimes.

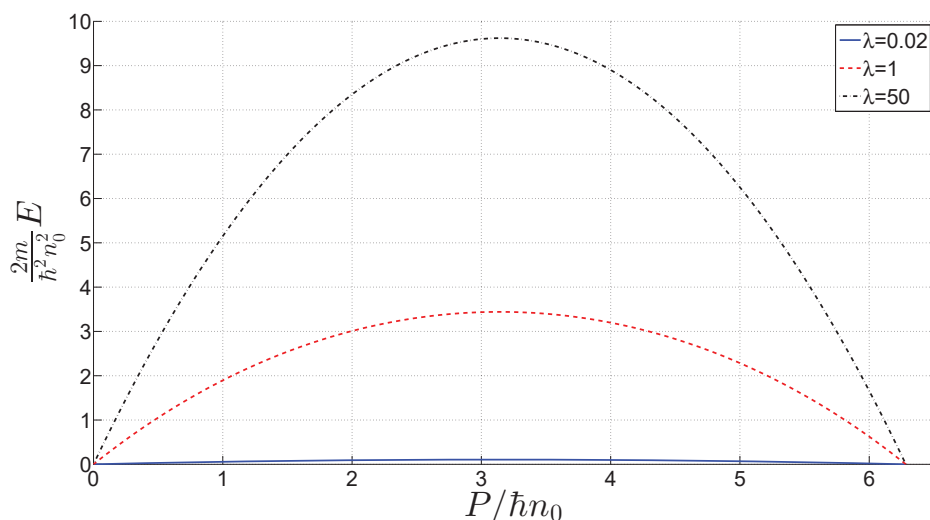


Figure 9.1: Dispersion relations for type-II excitations in the Lieb-Liniger model (single boson holes in the  $\gamma \rightarrow \infty$  limit). Blue solid line:  $\lambda = 0.02, \gamma = 0.0015325$ , red dashed line:  $\lambda = 1, \gamma = 1.7254$ , black dash-dotted line:  $\lambda = 50, \gamma = 155.08$ .

In Fig. 9.2 we compare the Lieb-Liniger type-II dispersion relation to that of the Gross-Pitaevskii dark soliton on an infinite ring, both at weak and intermediate interactions. While agreement is seen in both cases, it deteriorates visibly with increasing  $\gamma$ . Nonetheless, the agreement in the mean-field regime for infinite systems as well as finite (see chapter 7) implies a fundamental connection between these two excitations. It is interesting that in the vanishing  $\gamma$  regime (the mean-field limit), the type-II dispersion relation has been analytically shown to tend to that of the

Gross-Pitaevskii dark soliton [60]. In fact, this limit of the Lieb-Liniger model is in general captured well by mean-field Gross-Pitaevskii theory [46].

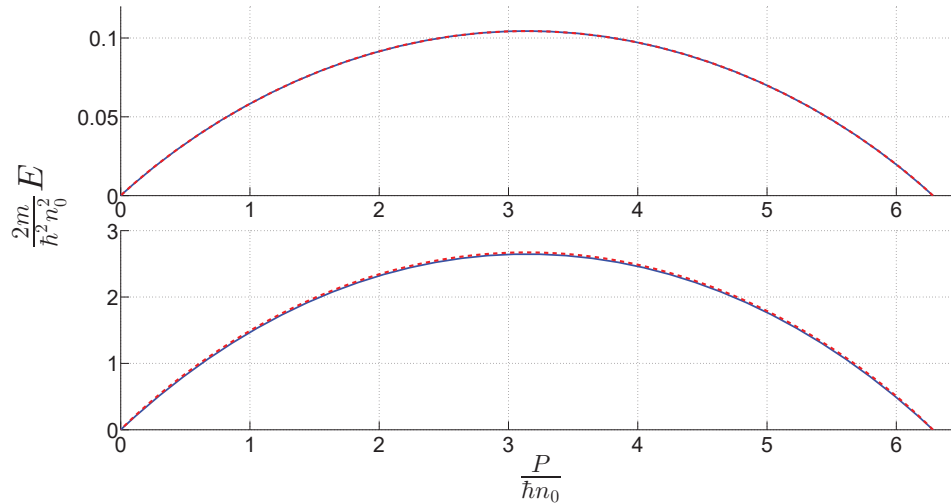


Figure 9.2: Dispersion relations for Lieb-Liniger type-II excitations (blue solid lines) and Gross-Pitaevskii dark solitons (red dashed lines). Top panel:  $\lambda = 0.02, \gamma = 0.0015325$ , bottom panel:  $\lambda = 0.7, \gamma = 1.003618$ .

### 9.2.2 Attractive Yang-Gaudin

When several spin components of fermions are present in the system with attractive interactions, the ground state always takes the form of bound states, in our case – dimers. However, the system need not be fully dimerized, even if it is balanced (as in our case): excited states may well have unpaired fermions. In chapter 8, we studied the finite-system case and showed that when  $|c|L \gg 1$  the exact Bethe ansatz equations can be replaced by the approximate, simpler ones that assume the string hypothesis (see chapter 8 for details). Since in the thermodynamic limit  $L \rightarrow \infty$ , it is perfectly valid to work under the string hypothesis for any  $c$ .

In the  $\gamma \rightarrow 0$  limit, the ground state is that of two spin components of free fermions, and the elementary type-II excitations are a single fermion hole, a double fermion hole, and a spin-flip. As  $\gamma \rightarrow -\infty$ , these branches become a single dimer hole, a double dimer hole, and a spin-flip (respectively), as shown in chapter 8, and the ground state becomes a Tonks-Girardeau gas of dimers.

### 9.2.2.1 Ground State

The general (for an arbitrary  $M/N$ ) ground state properties can be found upon solving the following integral equations [189]:

$$\frac{1}{2\pi} = \rho(k) - \frac{2c}{\pi} \int_{-b}^b \frac{r(\alpha)}{c^2 + 4(k - \alpha)^2} d\alpha, \quad (9.22)$$

$$\frac{1}{\pi} = r(\alpha) - \frac{c}{\pi} \int_{-b}^b \frac{r(\alpha')}{c^2 + (\alpha - \alpha')^2} d\alpha' - \frac{2c}{\pi} \int_{-a}^a \frac{\rho(k)}{c^2 + 4(\alpha - k)^2} dk. \quad (9.23)$$

Here,  $\rho(k)$  and  $r(\alpha)$  are such that

$$\int_{-b}^b r(\alpha) d\alpha = \frac{M}{L}, \quad (9.24)$$

$$\int_{-a}^a \rho(k) dk = \frac{N - 2M}{L}, \quad (9.25)$$

and  $\alpha$  &  $k$  can be thought of as the dimer & single-fermion charge rapidities, respectively. Now, it is common and convenient to set the reference point for energy measurements at the binding energy of the total system, namely at  $-\frac{\hbar^2}{2m} \frac{Mc^2}{2}$ . Clearly whether the binding energy is included explicitly or not does not affect the dispersion relations (or the missing particle number – see chapter 10), so we proceed with this convention. The ground state energy and momentum can be found from

$$E_g = \frac{\hbar^2}{2m} \left[ L \int_{-a}^a k^2 \rho(k) dk + L \int_{-b}^b 2\alpha^2 r(\alpha) d\alpha \right], \quad (9.26)$$

$$P_g = \hbar \left[ L \int_{-a}^a k \rho(k) dk + 2L \int_{-b}^b \alpha r(\alpha) d\alpha \right] = 0. \quad (9.27)$$

In the case when  $M = N/2$ , the first equation drops out and the second is simplified considerably, namely:

$$\frac{1}{\pi} = r(\alpha) - \frac{c}{\pi} \int_{-b}^b \frac{r(\alpha')}{c^2 + (\alpha - \alpha')^2} d\alpha'. \quad (9.28)$$

The normalization condition is

$$\int_{-b}^b r(\alpha) d\alpha = \frac{M}{L}, \quad (9.29)$$

and the ground state energy and momentum are

$$E_g = \frac{\hbar^2}{2m} L \int_{-b}^b 2\alpha^2 r(\alpha) d\alpha, \quad (9.30)$$

$$P_g = \hbar 2L \int_{-b}^b \alpha r(\alpha) d\alpha = 0. \quad (9.31)$$

We shall proceed to give details only on the balanced ground state, as it is generally the one of interest. In order to solve the integral equation numerically we introduce the following scaled variables:

$$\alpha = bx, \quad c = b\lambda, \quad r(\alpha) = r(bx) = g(x). \quad (9.32)$$

The scaled integral equation becomes

$$1 = \pi g(x) - \lambda \int_{-1}^1 \frac{g(x')}{\lambda^2 + (x - x')^2} dx', \quad (9.33)$$

and the normalization condition reads

$$\int_{-1}^1 b g(x) dx = \frac{M}{L}. \quad (9.34)$$

The ‘‘Fermi momentum’’  $b$  can be found from

$$b = \frac{n_0 \gamma}{\lambda}, \quad (9.35)$$

and  $\lambda$  in turn is found from

$$\lambda = 2\gamma \int_{-1}^1 g(x) dx. \quad (9.36)$$

The ground state energy becomes

$$E_g = \frac{\hbar^2}{2m} 2Lb^3 \int_{-1}^1 x^2 g(x) dx. \quad (9.37)$$

If  $e(\gamma)$  is once again defined by (9.11), then  $e(\gamma)$  is found according to (9.12) but with an additional factor of two, and  $\mu$  (defined the same way as for the Lieb-Liniger model) is given by (9.13). Note that in the fully dimerized problem, the chemical potential for dimers is twice that of single fermions.

### 9.2.2.2 Single and Double Fermion Holes

First, we will study the single and double fermion holes (at  $\gamma = 0$ ) which become the single and double dimer holes as  $\gamma \rightarrow -\infty$ . Under the string hypothesis in the thermodynamic limit, these branches can be described with the system fully consisting of dimers, so we only need one integral equation. In this section we will give the equations for both a single dimer and two adjacent dimer holes simultaneously. The differences in the description are so minute, that we will simply add factors of two “2×” (with an explicit multiplication sign) where-ever they are needed in the case of double-dimers.

The equation to be solved is

$$2\pi J(\alpha) = 2c \int_{-b}^b \frac{J(\alpha')}{c^2 + (\alpha - \alpha')^2} d\alpha' + 2 \times [\pi - \theta(\alpha - Q)], \quad (9.38)$$

where  $|Q| \leq b$  parametrizes the excitation momentum. The energy and momentum of the excitation are found from

$$P = \hbar \left[ -2 \times 2Q + 2 \int_{-b}^b J(\alpha) d\alpha \right], \quad (9.39)$$

$$E = \frac{\hbar^2}{2m} \left[ -2 \times 2Q^2 + 2 \times 2\mu + 4 \int_{-b}^b \alpha J(\alpha) d\alpha \right]. \quad (9.40)$$

To solve these equations numerically we need to introduce the following scaled variables [in addition to (9.32)]:

$$Q = bq, \quad J(\alpha) = J(bx) = h(x). \quad (9.41)$$

The integral equation becomes

$$\pi h(x) = \lambda \int_{-1}^1 \frac{h(x')}{\lambda^2 + (x - x')^2} dx' + 2 \times \left[ \frac{\pi}{2} - \tan^{-1} \left( \frac{q - x}{\lambda} \right) \right]. \quad (9.42)$$

Excitation energy and momentum are found from

$$P = \hbar 2b \left[ -2 \times q + \int_{-1}^1 h(x) dx \right], \quad (9.43)$$

$$E = \frac{\hbar^2}{2m} 2b^2 \left[ -2 \times q^2 + 2 \int_{-1}^1 x h(x) dx \right] + 2 \times 2\mu. \quad (9.44)$$

Figure 9.3 shows example dispersion relations for both branches. It is clear that the double fermion branch is simply the single fermion branch scaled by a factor of two, both in energy and momentum.

### 9.2.2.3 Spin-Flip Excitations

Next, we examine the spin-flip branch, where a dimer is broken and the spin of one of the fermions is flipped. Since the binding energy of a dimer in the thermodynamic limit is proportional to  $c^2/2$ , the dispersion relation has an energy gap that grows approximately as  $c^2$ .

The equation to be solved is

$$2\pi J(\alpha) = 2c \int_{-b}^b \frac{J(\alpha')}{c^2 + (\alpha - \alpha')^2} d\alpha' - \theta(\alpha - Q) + \theta[2(\alpha + b)] + \theta[2(\alpha - b)] + \pi, \quad (9.45)$$

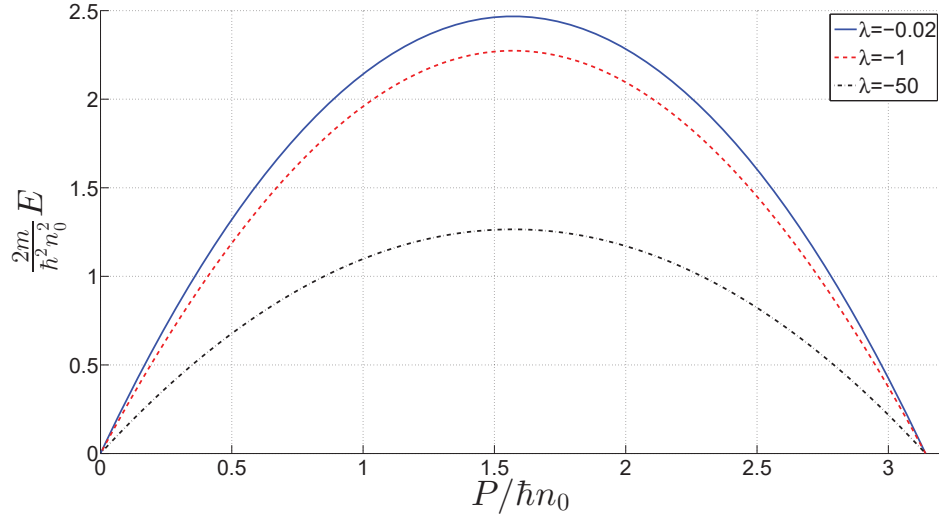
where  $|Q| \leq b$  parametrizes the excitation momentum. The energy and momentum of the excitation are found from

$$P = \hbar \left[ 2 \int_{-b}^b J(\alpha) d\alpha - 2Q \right], \quad (9.46)$$

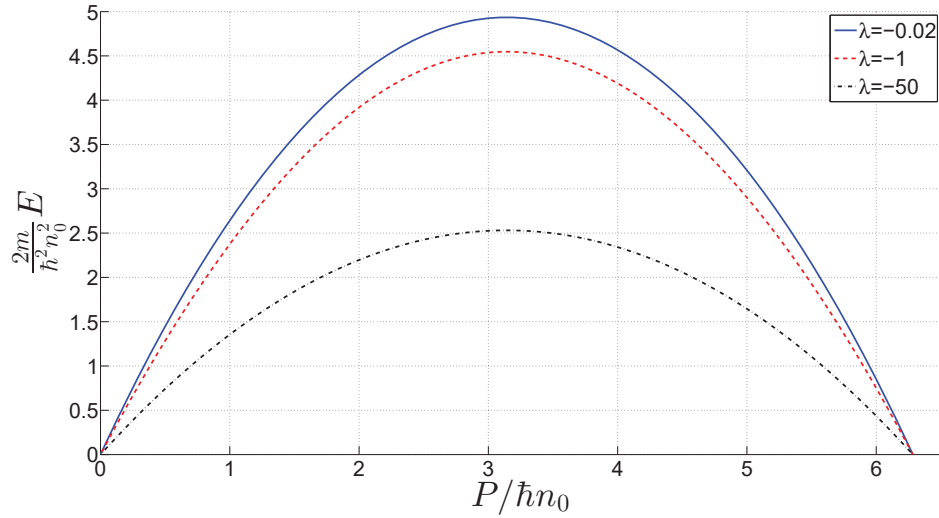
$$E = \frac{\hbar^2}{2m} \left[ 4 \int_{-b}^b \alpha J(\alpha) d\alpha - 2Q^2 + 2b^2 + \frac{c^2}{2} \right]. \quad (9.47)$$

To solve these equations numerically we use the scaled variables of (9.32) and (9.41), so that the integral equation becomes

$$\begin{aligned} \pi h(x) &= \lambda \int_{-1}^1 \frac{h(x')}{\lambda^2 + (x - x')^2} dx' + \tan^{-1} \left( \frac{x - q}{\lambda} \right) \\ &- \tan^{-1} \left[ \frac{2(x + 1)}{\lambda} \right] - \tan^{-1} \left[ \frac{2(x - 1)}{\lambda} \right] + \frac{\pi}{2}. \end{aligned} \quad (9.48)$$



(a)



(b)

Figure 9.3: Dispersion relations for single (a) and double (b) fermion holes (referring to the excitations according to their nature in the  $\gamma \rightarrow 0$  limit), which become single and double dimer holes in the  $\gamma \rightarrow -\infty$  limit (respectively). Blue solid line:  $\lambda = -0.02, \gamma = -0.030815$ , red dashed line:  $\lambda = -1, \gamma = -1.1363$ , black dash-dotted line:  $\lambda = -50, \gamma = -39.770$ .

Excitation energy and momentum are found from

$$P = \hbar 2b \left[ \int_{-1}^1 h(x) dx - q \right], \quad (9.49)$$

$$E = \frac{\hbar^2}{2m} \left\{ 2b^2 \left[ 2 \int_{-1}^1 x h(x) dx - q^2 + 1 \right] + \frac{c^2}{2} \right\}. \quad (9.50)$$

Figure 9.4 shows three example dispersion relations, with the strongest-coupling case shifted down as indicated on the figure so that it is visible on the same scale.

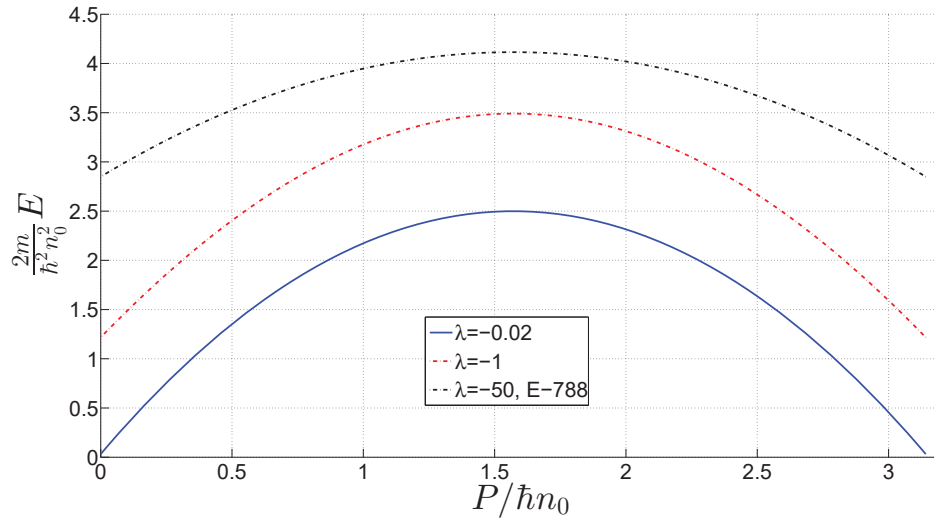


Figure 9.4: Dispersion relations for spin-flip excitations. Blue solid line:  $\lambda = -0.02, \gamma = -0.030815$ , red dashed line:  $\lambda = -1, \gamma = -1.1363$ , black dash-dotted line:  $\lambda = -50, \gamma = -39.770$ . In the last case, the dispersion relation is shifted by 788 due to the large gap.

### 9.2.3 Repulsive Yang-Gaudin

Having familiarized ourselves with the attractive regime, we now move on to the repulsive. At weak coupling, the ground state is once again that of two spin components of free fermions, while at strong interactions, the ground state has the structure (in momentum space) of a single spin component of fermions with  $N$  particles. In chapter 8, we followed the three elementary type-II excitation branches of the free system to  $\gamma \rightarrow \infty$ , and showed that the single fermion hole, double fermion hole, and the spin-flip excitations become a global translation of the system, a single fermion hole and global translation of the system, respectively. Moreover, in the finite-system case, the single fermion hole features complex spin rapidities, and string hypothesis

equations were derived which are again valid in the thermodynamic limit.

### 9.2.3.1 Ground State

The ground state properties can be found upon solving the following integral equations [189]:

$$\frac{1}{2\pi} = \rho(k) - \frac{2c}{\pi} \int_{-b}^b \frac{r(\alpha)}{c^2 + 4(k - \alpha)^2} d\alpha, \quad (9.51)$$

$$0 = r(\alpha) + \frac{c}{\pi} \int_{-b}^b \frac{r(\alpha')}{c^2 + (\alpha - \alpha')^2} d\alpha' - \frac{2c}{\pi} \int_{-a}^a \frac{\rho(k)}{c^2 + 4(\alpha - k)^2} dk. \quad (9.52)$$

Here,  $\rho(k)$  and  $r(\alpha)$  are such that

$$\int_{-a}^a \rho(k) dk = \frac{N}{L}, \quad (9.53)$$

$$\int_{-b}^b r(\alpha) d\alpha = \frac{M}{L}, \quad (9.54)$$

where  $k$  &  $\alpha$  represent charge & spin rapidities of the finite-system problem. The ground state energy and momentum can be found from

$$E_g = \frac{\hbar^2}{2m} L \int_{-a}^a k^2 \rho(k) dk, \quad (9.55)$$

$$P_g = \hbar L \int_{-a}^a k \rho(k) dk = 0. \quad (9.56)$$

In order to solve the integral equations numerically we introduce the following scaled variables:

$$\begin{aligned} k &= ay, \quad \alpha = ax, \quad c = a\lambda, \\ \rho(k) &= \rho(ay) = g(y), \quad r(\alpha) = r(ax) = f(x). \end{aligned} \quad (9.57)$$

Because absolute scaling is not possible here (with both  $a$  and  $b$  being unknown), at each coupling strength  $b/a$  must be chosen so that the normalization conditions on  $\rho(k)$  and  $r(\alpha)$  are satisfied. For a balanced ground state with  $N = 2M$  the condition reads

$$\int_{-b/a}^{b/a} f(x) \left\{ 1 - \frac{\lambda}{\pi} A(\lambda, x) \right\} dx = \frac{1}{2\pi} \quad (9.58)$$

with  $A(\lambda, x)$  defined below. The scaled integral equations become

$$g(y) = \frac{1}{2\pi} + \frac{2\lambda}{\pi} \int_{-b/a}^{b/a} \frac{f(x')}{\lambda^2 + 4(y - x')^2} dx', \quad (9.59)$$

$$\begin{aligned} 0 &= f(x) + \frac{\lambda}{\pi} \int_{-b/a}^{b/a} \frac{f(x')}{\lambda^2 + (x - x')^2} dx' - \frac{\lambda}{\pi^2} \int_{-1}^1 \frac{1}{\lambda^2 + 4(x - y)^2} dy \\ &\quad - \left(\frac{2\lambda}{\pi}\right)^2 \int_{-b/a}^{b/a} f(x') \int_{-1}^1 \frac{1}{\lambda^2 + 4(x - y)^2} \frac{1}{\lambda^2 + 4(y - x')^2} dy dx', \end{aligned} \quad (9.60)$$

where in the second equation, we have already substituted for  $g(y)$  from the first. Some of the integrals with respect to  $y$  appearing in the main integral equation (9.60) can be done analytically. Define and calculate

$$A(\lambda, x) = \int_{-1}^1 \frac{1}{\lambda^2 + 4(x - y)^2} dy = \frac{1}{2\lambda} \tan^{-1} \left( \frac{2(y - x)}{\lambda} \right) \Big|_{y=-1}^{y=1}, \quad (9.61)$$

and

$$\begin{aligned} B(\lambda, x, x') &= \int_{-1}^1 \frac{1}{\lambda^2 + 4(x - y)^2} \frac{1}{\lambda^2 + 4(x' - y)^2} dy = \\ &= \frac{1}{16\lambda(x - x') [(x - x')^2 + \lambda^2]} \left\{ \lambda \ln [4(x' - y)^2 + \lambda^2] - \lambda \ln [4(x - y)^2 + \lambda^2] \right. \\ &\quad \left. - 2(x - x') \tan^{-1} \left[ \frac{2}{\lambda}(x - y) \right] - 2(x - x') \tan^{-1} \left[ \frac{2}{\lambda}(x' - y) \right] \right\} \Big|_{y=-1}^{y=1} \quad \text{if } x \neq x', \\ &= \frac{1}{4\lambda^3} \left\{ \frac{2\lambda(y - x)}{4(x - y)^2 + \lambda^2} + \tan^{-1} \left[ \frac{2}{\lambda}(y - x) \right] \right\} \Big|_{y=-1}^{y=1} \quad \text{if } x = x'. \end{aligned} \quad (9.62)$$

With these definitions, equation (9.60) becomes

$$\pi f(x) - \lambda \int_{-b/a}^{b/a} \left[ \frac{4\lambda}{\pi} B(\lambda, x, x') - \frac{1}{\lambda^2 + (x - x')^2} \right] f(x') dx' = \frac{\lambda}{\pi} A(\lambda, x). \quad (9.63)$$

Once  $f(x)$  is solved for numerically, it must be reinserted into (9.59) and the integral with respect to  $x'$  must be computed numerically.

The normalization condition on  $\rho(k)$  becomes

$$\int_{-1}^1 ag(y)dy = \frac{N}{L} = n_0. \quad (9.64)$$

The ‘‘Fermi momentum’’  $a$  can be found from

$$a = \frac{n_0\gamma}{\lambda}, \quad (9.65)$$

and  $\lambda$  in turn is found from

$$\lambda = \gamma \int_{-1}^1 g(y)dy. \quad (9.66)$$

The ground state energy becomes

$$E_g = \frac{\hbar^2}{2m} La^3 \int_{-1}^1 y^2 g(y)dy. \quad (9.67)$$

If  $e(\gamma)$  is once again defined by (9.11), then  $e(\gamma)$  is found according to (9.12) but with  $x$  replaced by  $y$ , and  $\mu$  (defined the same way as for the Lieb-Liniger model) is given by (9.13).

### 9.2.3.2 Single Fermion Holes

We begin from single fermion holes (in the  $\gamma = 0$  limit), which in the  $\gamma \rightarrow \infty$  limit become a global system translation excitation. The equations to be solved are

$$\begin{aligned} 2\pi\Omega(k) &= 4c \int_{-b}^b \frac{R(\alpha)}{c^2 + 4(k - \alpha)^2} d\alpha + \theta(k - (b + Q)/2) \\ &\quad - \theta[2(k - b)] - \theta[2(k - Q)], \end{aligned} \quad (9.68)$$

$$\begin{aligned} 2\pi R(\alpha) &= -2c \int_{-b}^b \frac{R(\alpha')}{c^2 + (\alpha - \alpha')^2} d\alpha' + 4c \int_{-a}^a \frac{\Omega(k)}{c^2 + 4(\alpha - k)^2} dk + 2\pi + \theta(\alpha - b) \\ &\quad + \theta(\alpha - Q) - \theta[2(\alpha - (b + Q)/2)] - \theta[2/3(\alpha - (b + Q)/2)], \end{aligned} \quad (9.69)$$

where  $|Q| \leq b$  parametrizes the excitation momentum. To solve these equations numerically we need to introduce the following scaled variables [in addition to (9.57)]:

$$Q = aq, \quad \Omega(k) = \Omega(ay) = h(y), \quad R(\alpha) = R(ax) = f(x). \quad (9.70)$$

The scaled equations become

$$\begin{aligned}\pi h(y) &= 2\lambda \int_{-b/a}^{b/a} \frac{f(x')}{\lambda^2 + 4(y-x')^2} dx' - \tan^{-1} \left[ \frac{y - (b/a + q)/2}{\lambda} \right] \\ &+ \tan^{-1} \left[ \frac{2(y - b/a)}{\lambda} \right] + \tan^{-1} \left[ \frac{2(y - q)}{\lambda} \right],\end{aligned}\quad (9.71)$$

$$\begin{aligned}\pi f(x) &= \pi + \lambda \int_{-b/a}^{b/a} \left[ \frac{4\lambda}{\pi} B(\lambda, x', x) - \frac{1}{\lambda^2 + (x-x')^2} \right] f(x') dx' \\ &+ \frac{2\lambda}{\pi} D(\lambda, x, q) - \tan^{-1} \left[ \frac{x - b/a}{\lambda} \right] - \tan^{-1} \left[ \frac{x - q}{\lambda} \right] \\ &+ \tan^{-1} \left[ \frac{2[x - (q + b/a)/2]}{\lambda} \right] + \tan^{-1} \left[ \frac{2/3[x - (q + b/a)/2]}{\lambda} \right],\end{aligned}\quad (9.72)$$

$$\begin{aligned}D(\lambda, x, q) &= \int_{-1}^1 \frac{1}{\lambda^2 + 4(x-y)^2} \left\{ \tan^{-1} \left[ \frac{y - (b/a + q)/2}{\lambda} \right] \right. \\ &\left. + \tan^{-1} \left[ \frac{2(y - b/a)}{\lambda} \right] + \tan^{-1} \left[ \frac{2(y - q)}{\lambda} \right] \right\} dy.\end{aligned}\quad (9.73)$$

The energy and momentum of the excitation are found from

$$P = \hbar \int_{-a}^a \Omega(k) dk = \hbar a \int_{-1}^1 h(y) dy, \quad (9.74)$$

$$E = \frac{\hbar^2}{2m} 2 \int_{-a}^a k \Omega(k) dk = \frac{\hbar^2}{2m} 2a^2 \int_{-1}^1 y h(y) dy. \quad (9.75)$$

Figure 9.5 shows three example dispersion relations. We see that as  $\gamma \rightarrow \infty$ , this excitation branch vanishes because the system is infinitely heavy (as  $N \rightarrow \infty$  in the thermodynamic limit).

### 9.2.3.3 Double Fermion Holes

The double fermion hole in the  $\gamma \rightarrow 0$  limit becomes a single fermion hole as  $\gamma \rightarrow \infty$ . The equations to be solved are

$$\pi \Omega(k) = 2c \int_{-b}^b \frac{R(\alpha)}{c^2 + 4(k - \alpha)^2} d\alpha, \quad (9.76)$$

$$\begin{aligned}2\pi R(\alpha) &= -2c \int_{-b}^b \frac{R(\alpha')}{c^2 + (\alpha - \alpha')^2} d\alpha' + 4c \int_{-a}^a \frac{\Omega(k)}{c^2 + 4(\alpha - k)^2} dk \\ &- \theta[2(\alpha - Q)] + 2\pi,\end{aligned}\quad (9.77)$$

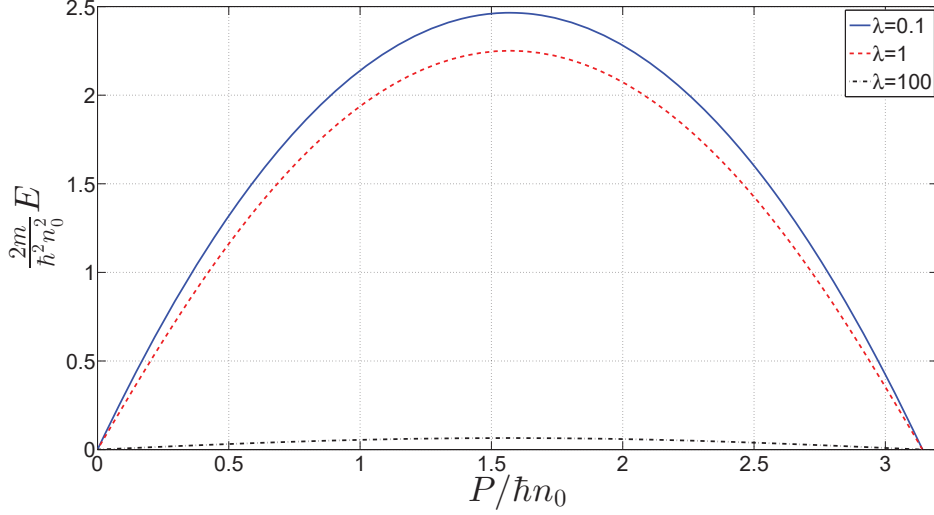


Figure 9.5: Dispersion relations for single fermion holes (referring to the excitations according to their nature in the  $\gamma \rightarrow 0$  limit), which become a global system translation excitation in the  $\gamma \rightarrow \infty$  limit. Blue solid line:  $\lambda = 0.1, \gamma = 0.16886$ , red dashed line:  $\lambda = 1, \gamma = 2.2491$ , black dash-dotted line:  $\lambda = 100, \gamma = 312.773$ . The plots shown here are identical to those that are obtained for the spin-flip branch.

where  $|Q| \leq a$  parametrizes the excitation momentum. The energy and momentum of the excitation are found from

$$P = \hbar \left[ -Q + \int_{-a}^a \Omega(k) dk \right], \quad (9.78)$$

$$E = \frac{\hbar^2}{2m} \left[ -Q^2 + 2 \int_{-a}^a k \Omega(k) dk \right] + \mu. \quad (9.79)$$

Recalling the scaled variables from (9.57) and (9.70), the scaled equations become

$$h(y) = \frac{2\lambda}{\pi} \int_{-b/a}^{b/a} \frac{f(x')}{\lambda^2 + 4(y-x')^2} dx', \quad (9.80)$$

$$\begin{aligned} \pi f(x) &= \lambda \int_{-b/a}^{b/a} \left[ \frac{4\lambda}{\pi} B(\lambda, x', x) - \frac{1}{\lambda^2 + (x-x')^2} \right] f(x') dx' \\ &+ \pi + \tan^{-1} \left( 2 \frac{x-q}{\lambda} \right). \end{aligned} \quad (9.81)$$

Excitation energy and momentum are found from

$$P = \hbar a \left[ -q + \int_{-1}^1 h(y) dy \right], \quad (9.82)$$

$$E = \frac{\hbar^2}{2m} a^2 \left[ -q^2 + 2 \int_{-1}^1 y h(y) dy \right] + \mu. \quad (9.83)$$

Figure 9.6 shows three example dispersion relations across the range of interactions.

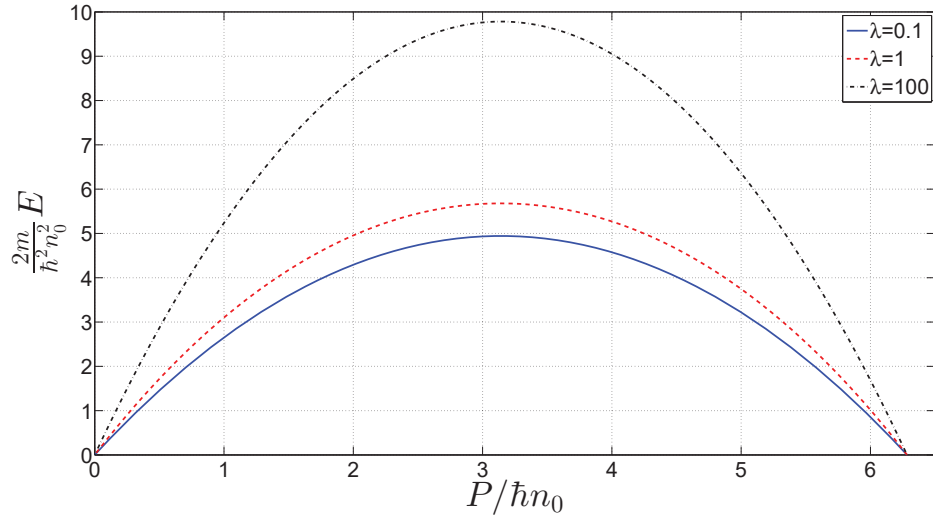


Figure 9.6: Dispersion relations for double fermion holes (referring to the excitations according to their nature in the  $\gamma \rightarrow 0$  limit) which become one fermion holes in the  $\gamma \rightarrow \infty$  limit. Blue solid line:  $\lambda = 0.1, \gamma = 0.16886$ , red dashed line:  $\lambda = 1, \gamma = 2.2491$ , black dash-dotted line:  $\lambda = 100, \gamma = 312.773$ .

#### 9.2.3.4 Spin-Flip Excitations

Once again we return to spin-flip excitations, which in the  $\gamma \rightarrow \infty$  limit become a global system translation excitation. The equations to be solved are

$$\pi\Omega(k) = 2c \int_{-b}^b \frac{R(\alpha)}{c^2 + 4(k - \alpha)^2} d\alpha - \frac{1}{2} \theta [2(k - Q)], \quad (9.84)$$

$$\begin{aligned}
2\pi R(\alpha) &= -2c \int_{-b}^b \frac{R(\alpha')}{c^2 + (\alpha - \alpha')^2} d\alpha' \\
&+ 4c \int_{-a}^a \frac{\Omega(k)}{c^2 + 4(\alpha - k)^2} dk + \theta(\alpha - Q) + \pi, \tag{9.85}
\end{aligned}$$

where  $|Q| \leq b$  parametrizes the excitation momentum. The energy and momentum of the excitation are found from

$$P = \hbar \int_{-a}^a \Omega(k) dk, \tag{9.86}$$

$$E = \frac{\hbar^2}{2m} 2 \int_{-a}^a k \Omega(k) dk. \tag{9.87}$$

Recalling the scaled variables from (9.57) and (9.70), the scaled equations become

$$h(y) = \frac{2\lambda}{\pi} \int_{-b/a}^{b/a} \frac{f(x')}{\lambda^2 + 4(y - x')^2} dx' + \frac{1}{\pi} \tan^{-1} \left[ \frac{2(y - q)}{\lambda} \right], \tag{9.88}$$

$$\begin{aligned}
\pi f(x) &= \lambda \int_{-b/a}^{b/a} \left[ \frac{4\lambda}{\pi} B(\lambda, x', x) - \frac{1}{\lambda^2 + (x - x')^2} \right] f(x') dx' \\
&+ \frac{\pi}{2} - \tan^{-1} \left( \frac{x - q}{\lambda} \right) + \frac{2\lambda}{\pi} C(\lambda, x, q), \tag{9.89}
\end{aligned}$$

$$C(\lambda, x, q) = \int_{-1}^1 \frac{1}{\lambda^2 + 4(x - y)^2} \tan^{-1} \left[ \frac{2(y - q)}{\lambda} \right] dy. \tag{9.90}$$

Excitation energy and momentum are found from

$$P = \hbar a \int_{-1}^1 h(y) dy, \tag{9.91}$$

$$E = \frac{\hbar^2}{2m} 2a^2 \int_{-1}^1 y h(y) dy. \tag{9.92}$$

We find that for all interaction strengths, the spin-flip dispersion relations are identical to those of the single fermion hole branch, Fig. 9.5.

# Appendix

## 9.A Thermodynamic Limit Equations: Outline of Derivation

The ground state thermodynamic limit equations can be obtained from the finite-system equations in the following way: we take the difference of two Bethe ansatz equations – that for  $k_{j+1}$  and that for  $k_j$  (and likewise for  $\alpha_{m+1}$  and  $\alpha_m$  when applicable), two adjacent rapidities. Since the quantum numbers in the ground state are always compactly and symmetrically distributed about zero, we know that  $n_{j+1} - n_j = 1$  (similarly,  $\ell_{m+1} - \ell_m = 1$ ). We do a first order Taylor expansion for the  $\theta$ -function featuring the higher-index rapidity, with the difference of the rapidities as the small parameter. Next, define the rapidity density  $k_{j+1} - k_j = \frac{1}{L\rho(k)}$  (and, when applicable,  $\alpha_{m+1} - \alpha_m = \frac{1}{Lr(\alpha)}$ ), and pass to the continuum limit with the following replacements

$$\sum_j \rightarrow L \int_{-a}^a \rho(k) dk, \quad (9.93)$$

$$\sum_m \rightarrow L \int_{-b}^b r(\alpha) d\alpha, \quad (9.94)$$

where we have used the repulsive Yang-Gaudin model as an example. Note that both the Lieb-Liniger and Yang-Gaudin thermodynamic limit ground state equations are available in the literature (e.g. [46, 189]).

Next, we will indicate how one can obtain the excited-state equations starting from the ground state, since we are not aware of a methodical account of all the Yang-Gaudin branches studied here elsewhere. The reader is referred to chapters 7 & 8 for the finite-system equations.

Usually one has to choose the most convenient ground state to begin from: this can either be the ground state with  $N$  particles (and  $M$  spin rapidities in the Yang-Gaudin case), or it may have one less charge or spin rapidity, indicating one less particle in the system or a spin-flip for one of the particles with respect to the balanced ground state. This chosen initial ground state is then perturbed in a way that reflects the nature of the excitation: for example, a rapidity may be explicitly removed to create a hole excitation, or one rapidity is replaced by others (for example

if a dimer is broken to create two free fermions).

This perturbation to the system shifts all other rapidities in our initial ground state, and this shifted ground state will be denoted by an asterisk. The explicit removal or addition of rapidities, together with the shift of all others, will yield the excited state of interest. This excited state must be compared to the initial ground state from which we constructed it, which may well not be the ground state of interest. If that is the case, we must then correct for the “wrong” ground state explicitly, which is usually much simpler than beginning from the correct but inconvenient state.

Let us begin by examining the well-known example of the Lieb-Liniger type-II excitations. In our notation, the equations are derived by following the recipe:

$$\{[E^*(N+1) - 1k] - E(N+1)\} + \{E(N+1) - E(N)\}. \quad (9.95)$$

This means we must take the finite-system Bethe ansatz equations<sup>1</sup> of  $N+1$  bosons, remove one charge rapidity (denoted here by  $k$ ) with the other rapidities shifted from their true ground state values (denoted by the asterisk) and compare the resulting system to the true ground state of  $N+1$  particles. Finally, we add a ground state correction that ensures that both the excited and the ground states have  $N$  particles (in practice, the ground state correction simply contributes a  $\mu$  term to the excitation energy since the energy cost of adding a particle to the ground state is precisely  $\mu$ ).

Likewise, the recipe for all other branches in the Yang-Gaudin model are as follows (as usual, we assume  $M = N/2$ ):

- Attractive regime; single fermion holes as  $\gamma \rightarrow 0$ , single dimer holes as  $\gamma \rightarrow -\infty$ :

$$\{[E^*(M+1) - 1\alpha] - E(M+1)\} + \{E(M+1) - E(M)\}. \quad (9.96)$$

Recall that  $\alpha$  denotes charge rapidities of dimers in the attractive Yang-Gaudin model (under the string hypothesis). Since the system is fully dimerized, the quantities in the parentheses immediately following  $E$  indicate the number of dimers.

- Attractive regime; double fermion holes as  $\gamma \rightarrow 0$ , double dimer holes as  $\gamma \rightarrow -\infty$ :

$$\{[E^*(M+2) - 2\alpha] - E(M+2)\} + \{E(M+2) - E(M)\}. \quad (9.97)$$

---

<sup>1</sup>Note that one must use the equations in logarithmic form and if applicable, under the string hypothesis.

- Attractive regime; spin-flip:

$$[E^*(M, 0) - 1\alpha + 2k] - E(M, 0). \quad (9.98)$$

Recall that  $k$  denotes charge rapidities of single fermions in the attractive Yang-Gaudin model (under the string hypothesis). Now that we also have free fermions in the system, the second number in the brackets indicates how many free fermions we have. The two added  $k$ 's (resulting from a broken dimer) are placed at  $\pm b$ , i.e. on the Fermi surface.

- Repulsive regime; single fermion holes as  $\gamma \rightarrow 0$ , system translation as  $\gamma \rightarrow \infty$ :

$$[E^*(N, M) - 2\alpha + 1A] - E(N, M). \quad (9.99)$$

In the repulsive Yang-Gaudin model,  $\alpha$  denotes spin rapidities and  $A$  is the real part of two complex-conjugate  $\alpha$ 's under the string hypothesis in the approximate equations derived in chapter 8 to describe this branch. The quantities in brackets show the total number of fermions and the number of spin-up particles. One of the removed  $\alpha$ 's is taken out from the Fermi edge at  $b$  and the other at  $Q \in [-b, b]$ . The  $A$  that replaces these two complex-conjugate  $\alpha$ 's is placed at momentum  $(b + Q)/2$ .

- Repulsive regime; double fermion holes as  $\gamma \rightarrow 0$ , single fermion holes as  $\gamma \rightarrow \infty$ :

$$\{[E^*(N + 1, M) - 1k] - E(N + 1, M)\} + \{E(N + 1, M) - E(N, M)\}. \quad (9.100)$$

The numbers in parentheses have the same meaning as in the above case, and  $k$  denotes charge rapidities of fermions.

- Repulsive regime; spin-flip as  $\gamma \rightarrow 0$ , system translation as  $\gamma \rightarrow \infty$ :

$$[E^*(N, M) - 1\alpha] - E(N, M). \quad (9.101)$$

Now let us outline in more detail how the equations are derived: the shift in  $k_j$  due to the perturbation is written as  $L\delta k_j$  (likewise for  $\alpha_m$  where the shift is  $L\delta\alpha_m$ ). We write down the finite-system Bethe ansatz equations for the chosen initial ground state, shifting all the rapidities. Then we explicitly subtract and/or add any interaction terms that are associated with the rapidities that must be added or removed, which are themselves not shifted. Next, we expand the interaction terms [in the case of the  $\delta$ -function potential, the two-body phase-shifts are given by the  $\theta$

function of (9.14)] as a first order Taylor expansion about the unshifted rapidities, with the first order terms proportional to the shifts.

We now subtract the Bethe ansatz equations of the unperturbed, conveniently-chosen ground state. At this point we may pass to the continuous limit by using the ground state quasi-momenta density function(s) that appear in the ground state thermodynamic limit equations. In the repulsive Yang-Gaudin case, for example, we would use equations (9.93)–(9.94). Some of the terms appearing under the integrals in the equations can be simplified by substituting for them from the ground state thermodynamic limit integral equations. Finally, we define new functions that are products of  $L$ , the ground state distributions, and the shifts: in the repulsive Yang-Gaudin model, for example, we have  $\Omega(k) = L \delta k \rho(k)$  and  $R(\alpha) = L \delta \alpha r(\alpha)$ .

It remains to compute the energy and momentum. This is done according to our recipes, by writing down the finite-system total  $P$  and  $E$  of the excited state (shifted and with explicit rapidities added or removed), subtracting those of the convenient ground state, and when necessary, adding the ground state correction. The resulting quantities can be expressed through the “shift functions” of the integrals equations (e.g.  $\Omega(k)$  and  $R(\alpha)$  for repulsive Yang-Gaudin), the explicit rapidities added or removed and the chemical potential.

# Chapter 10

## Extracting Solitonic Properties from the Bethe Ansatz

In this chapter we apply the formulae derived in chapter 5, allowing for the computation of the missing particle number and phase step from the thermodynamic limit dispersion relation, to all type-II excitations of the Lieb-Liniger and Yang-Gaudin models. Of course, type-II Bethe ansatz states do not satisfy the assumptions of the derivation (the solitonic nature of the excitation), but since we are considering the relation of dark solitons to type-II states, we perform the computation with investigative purposes: upon examining the results we will decide whether they are reasonable, which will yield information about the nature of the excitations in either scenario.

With the knowledge we have thus far, we can make an educated guess regarding which of the type-II branches in the Yang-Gaudin model are soliton-like and which are not. For example, any excitation involving the spin degree of freedom will most certainly not be a (conventional) dark soliton<sup>1</sup>. What is the rationale, then, for computing solitonic properties for these branches? As it were, in chapter 11, we develop an approximation to the finite system dispersion relation of a solitonic excitation, based on the thermodynamic limit results. This calculation is heavily based on the missing particle number and phase step, and certainly assumes the solitonic nature of the states. In chapter 13, we will apply this approximation to all type-II branches of the Yang-Gaudin model studied, and find that it works very well for the branches that are intuitively expected to be dark soliton-like, and fails spectacularly for the others. This will serve to reassure that the success of the finite-system approximation is not trivial – it carries physical implications about the excitations studied, working well when the state is soliton-like, and failing otherwise.

For the Lieb-Liniger type-II excitations, the physical meaning of the missing particle number and phase step is unveiled in chapter 12. This is then carried over by analogy for the dark soliton-like type-II excitations of the Yang-Gaudin model in chapter 13. It will become clear that the physical properties of all type-II excitations that are associated with dark solitons are shared by the corresponding quantum dark

---

<sup>1</sup>Spin – or “magnetic” – dark solitons have also been studied [191].

solitons, and as such, this chapter contains physical predictions of solitonic properties across the range of interactions in one-dimensional Bose- and Fermi-gases. Thus, while the chapter involves a significant amount of technical details, the calculations will be invaluable to us later on.

## 10.1 Introduction

With the physical systems described by the Lieb-Liniger & Yang-Gaudin models practically within reach, and the elementary excitations theoretically understood, the next natural step would be to create and observe these excitations. Here we are interested in type-II excitations [47], which have been associated with dark solitons [59] for over 25 years [60], but since the concrete connection has proven fairly difficult to establish, ongoing efforts to understand and clarify the issue are continuing (e.g. [65, 66] and chapter 12). If type-II excitations *can* be interpreted as solitons, then solitonic properties can be assigned to these excitation branches. Furthermore, if direct measurement will reveal these properties [65, 66], then there is merit in theoretically predicting these.

Two key characteristics of dark solitons are the missing particle number (the number of particles removed from a uniform background density in order to produce the soliton density dip) and the phase step across the soliton. These quantities cannot be directly computed for type-II states of the Lieb-Liniger or Yang-Gaudin models because all Bethe ansatz eigenstates simultaneously diagonalize the Hamiltonian and total-momentum operators and are thus spatially uniform. In addition, for an arbitrary coupling strength, a mean-field order parameter cannot be defined and with it, the global coherent phase. As such, it is difficult to assign meaning to the concept of a phase step. On the other hand, there exist formulae that allow one to extract both the missing particle number and the phase step out of the dispersion relation of the excitation in the thermodynamic limit (chapter 5), which is readily available in the Bethe ansatz formalism.

In fact, an earlier publication [148] has already applied this idea to the Lieb-Liniger model<sup>2</sup>, but the authors have computed the effective missing particle number, not the actual, as shown in chapter 5. In the thesis [192], the SGR formula (see chapter 5) from [152] for the actual missing particle number was applied to the Lieb-Liniger model and a much simpler expression was derived, but no numerical testing of the results was performed. Here we apply the actual missing particle number SGR formula to all elementary type-II branches in the Lieb-Liniger and Yang-Gaudin models (chapter 9), and compare to the simpler expression derived in

---

<sup>2</sup>Astrakharchik and Pitaevskii performed their calculation independently and in parallel to ourselves.

[192] (for ease of reference, we shall coin this simpler formula *Campbell's* formula, after the author). Thus, we present a complete overview of solitonic properties for all elementary type-II branches, as derived from the dispersion relations, across the Bose-Einstein condensate-Bardeen-Cooper-Schrieffer crossover, using the Lieb-Liniger and Yang-Gaudin models.

Knowledge of the missing particle number and the dispersion relation itself allows one to compute the physical and inertial masses of the soliton, and the ratio of the two determines the oscillation frequency of the soliton in a harmonic trap ([109] and chapter 4). We present the masses and the mass-ratio as a function of coupling strength for all relevant branches in both models. This information serves as a useful experimental prediction for the possible detection of these excitations in the laboratory.

In section 10.2 we introduce the equations for the missing particle number and phase step, presenting the general expressions from chapter 5 and briefly describing Campbell's formula for Lieb-Liniger type-II excitations which shall serve as a prototype for all other branches. The full details of the computation are provided for the Lieb-Liniger case, while for all other branches we simply point out the differences, with the majority of the calculation remaining unmodified.

Then, in section 10.3 we show the physical and inertial masses, as well as their ratio, as a function of coupling strength for all branches. We discuss our findings and conclude in section 10.4. Approximate analytical solutions of the thermodynamic limit Bethe ansatz equations in limiting cases and all relevant system properties are summarized in appendix 10.A.

## 10.2 Missing Particle Number and Phase Step

In the previous chapter, we saw that the Bethe ansatz provides us with means to compute the thermodynamic limit dispersion relation for all type-II excitations of interest, as well as ground state properties. In chapter 5, we rederived and conveniently rewrote the SGR formula originally obtained in [152] for the missing particle number of a solitonic excitation, assuming a Lagrangian, superfluid system. This equation reads

$$N_d = \frac{-\left.\frac{dE_s}{d\mu}\right|_{v_s} + v_s \left.\frac{dP_c}{d\mu}\right|_{v_s} - \frac{v_s}{n_0} \frac{dn_0}{d\mu} P_c}{1 - \frac{mv_s^2}{n_0} \frac{dn_0}{d\mu}}, \quad (10.1)$$

where  $N_d$  is the missing particle number,  $E_s$  the excitation energy in the grand canonical ensemble compared to a ground state at the same chemical potential ( $\mu$ ),  $P_c$  the total momentum,  $v_s$  the soliton speed and  $n_0$  is the density of the ground

state at the same chemical potential as the soliton solution. Notice that during differentiation with respect to  $\mu$ ,  $v_s$  needs to be held constant. In the derivation of chapter 5 it was also shown that, as long as we work in the thermodynamic limit, the formula still applies if  $E_s$  is replaced by the canonical excitation energy where  $N$  (not  $\mu$ ) is held fixed.

It is clear that the results of chapter 9 furnish us with all the necessary information to evaluate  $N_d$  for all the type-II branches (simply set  $P_c \rightarrow P$  and  $E_s \rightarrow E$ ), even if the concept of the missing particle number is questionable, since type-II excitations do not have a solitonic density profile. This section is dedicated to carefully applying (10.1) to all type-II branches studied in chapter 9. This calculation is motivated by the suspected connection between type-II excitations and dark solitons (chapter 12). Once  $N_d$  is computed, we will be able to examine the results and check for consistency in light of the fact that the limiting behaviour (with coupling strength) of all branches is well-understood and the physical nature of the excitations is known (chapters 7 & 8).

Note that if one has already obtained the particle number  $N_d$ , one can calculate the phase step across the excitations ( $\Delta\phi$ ) from  $P_c = P_s + \hbar n_B \Delta\phi$  (chapter 5) where  $n_B$  is the density of bosonic particles, which is simply  $n_0$  for the Lieb-Liniger model and  $n_0/2$  for the Yang-Gaudin. The total momentum  $P_c$  is made up of  $P_s = mv_s N_d$ , the soliton momentum, and  $P_{cf} = \hbar n_B \Delta\phi$ , the counter-flow momentum of the superfluid background which must be present in a ring geometry to connect the phase at  $x = \pm L/2$ .

We emphasize that [148] has previously computed the *effective* missing particle number  $N_s$  (related to the dynamics of a quasi-particle in a trap) for type-II excitations in the Lieb-Liniger model according to the SPDS formula,

$$N_s = - \left. \frac{dE_s}{d\mu} \right|_{v_s}, \quad (10.2)$$

which is only equivalent to (10.1), the actual missing particle number, at zero velocity. In addition, Campbell's formula from [192] allows one to indirectly evaluate (10.1) for type-II excitations in the Lieb-Liniger model in a very simple way: one only needs to solve the integral equations of the ground and excited states once, with no need for differentiation of any kind. However, the dissertation [192] is highly theoretical with no numerical calculations presented. We will review Campbell's formula and compare it to the full derivative formula (10.1) for all type-II branches.

Since the form of the calculation is very similar for all branches, the full details will only be provided for the Lieb-Liniger case, while for the others, we will only point out the minor differences. The thermodynamic limit quantities relevant in each case are to be found in the corresponding subsection of chapter 9. Our calculations

are illustrated by plotting  $N_d$  and  $\Delta\phi$  as a function of momentum across the range of interaction strengths.

## 10.2.1 Repulsive Lieb-Liniger

We shall see that in the weak-repulsion limit,  $N_d$  and  $\Delta\phi$  tend to those of the dark solitons in the one-dimensional Gross-Pitaevskii equation, and in the Tonks-Girardeau limit, both become independent of the excitation momentum, taking on the values  $N_d = -1$  and  $\Delta\phi = \pi$ , corresponding to a single boson hole. Both the Gross-Pitaevskii-dark soliton and Tonks-Girardeau-hole excitations are treated analytically in chapter 5, with the expressions for  $N_d$  explicitly given.

### 10.2.1.1 Single Boson Holes

We begin by evaluating (10.1) directly. Define

$$f_1(\gamma) = \left[ \int_{-1}^1 g(x) dx \right]^2, \quad (10.3)$$

$$f_2(\gamma, q) = 2 \int_{-1}^1 x h(x) dx, \quad (10.4)$$

$$f_3(\gamma, q) = \int_{-1}^1 h(x) dx, \quad (10.5)$$

and write the excitation energy and momentum through the scaled variables as

$$E = \frac{\hbar^2}{2m} \frac{n_0^2}{f_1(\gamma)} [-q^2 + f_2(\gamma, q)] + \mu, \quad (10.6)$$

$$P = \hbar \frac{n_0}{\sqrt{f_1(\gamma)}} [-q + f_3(\gamma, q)]. \quad (10.7)$$

The velocity is defined as

$$v_s \equiv \frac{dE}{dP} = \frac{dE}{dq} \frac{dq}{dP} = \frac{\hbar}{2m} \frac{n_0}{\sqrt{f_1}} \left\{ \begin{array}{l} -2q + \frac{df_2}{dq} \\ -1 + \frac{df_3}{dq} \end{array} \right\}. \quad (10.8)$$

To begin with, we need to take the derivative of  $E$  with respect to  $\mu$ :

$$\frac{dE}{dn_0} = \frac{\hbar^2}{2m} \frac{2n_0 f_1 - n_0^2 \frac{df_1}{dn_0}}{f_1^2} [-q^2 + f_2] + \frac{\hbar^2}{2m} \frac{n_0^2}{f_1} \left( -2q \frac{dq}{dn_0} + \frac{df_2}{dn_0} \right) + \frac{d\mu}{dn_0}, \quad (10.9)$$

$$\frac{dE}{d\mu} = \frac{dE}{dn_0} \frac{dn_0}{d\mu}. \quad (10.10)$$

Differentiating the chemical potential, we get

$$\frac{d\mu}{dn_0} = \frac{\hbar^2}{2m} [2n_0\alpha(\gamma) - c\beta(\gamma)], \quad (10.11)$$

$$\alpha(\gamma) = 3e(\gamma) - \gamma \frac{de(\gamma)}{d\gamma}, \quad (10.12)$$

$$\beta(\gamma) = 2 \frac{de(\gamma)}{d\gamma} - \gamma \frac{d^2e(\gamma)}{d\gamma^2}. \quad (10.13)$$

The derivatives we need are

$$\frac{df_1}{dn_0} = \frac{df_1}{d\gamma} \frac{d\gamma}{dn_0}, \quad (10.14)$$

$$\frac{df_2}{dn_0} = \frac{df_2}{d\gamma} \frac{d\gamma}{dn_0} + \frac{df_2}{dq} \frac{dq}{dn_0}. \quad (10.15)$$

Next, we need  $dq/dn_0$  keeping  $v_s$  constant and we have no closed analytical expression for  $q$ . Still, this derivative can be done. Defining  $\tilde{v}_s = v_s/n_0$  and going back to (10.8):

$$\tilde{v}_s = \frac{v_s}{n_0} = \frac{\hbar}{2m} \frac{1}{\sqrt{f_1}} \left\{ \frac{-2q + \frac{df_2}{dq}}{-1 + \frac{df_3}{dq}} \right\}. \quad (10.16)$$

The right-hand side only explicitly depends on  $q$  and  $\gamma$ . Therefore, there exists some relation linking  $\tilde{v}_s, q, \gamma$  which can in principle be solved to give  $q(\tilde{v}_s, \gamma)$ . In this case, we have

$$\frac{dq}{dn_0} = \frac{dq}{d\gamma} \frac{d\gamma}{dn_0} + \frac{dq}{d\tilde{v}_s} \frac{d\tilde{v}_s}{dn_0}. \quad (10.17)$$

The difficult derivative appearing here is  $\frac{dq}{d\gamma}$  keeping  $v_s$  constant. Since  $\tilde{v}_s$  is only a function of  $\gamma$  and  $q$ , we can write

$$d\tilde{v}_s = \frac{\partial \tilde{v}_s}{\partial \gamma} d\gamma + \frac{\partial \tilde{v}_s}{\partial q} dq. \quad (10.18)$$

We want to keep  $\tilde{v}_s$  constant, so  $d\tilde{v}_s$  must be zero, from which we get

$$\frac{dq}{d\gamma} = - \frac{\partial \tilde{v}_s}{\partial \gamma} \frac{\partial q}{\partial \tilde{v}_s}. \quad (10.19)$$

All together, we have

$$\frac{dq}{dn_0} = \frac{1}{n_0^2} \left( c \frac{\partial \tilde{v}_s}{\partial \gamma} - v_s \right) \frac{\partial q}{\partial \tilde{v}_s}. \quad (10.20)$$

$\frac{\partial \tilde{v}_s}{\partial q}$  and  $\frac{\partial \tilde{v}_s}{\partial \gamma}$  are to be found numerically, but since  $\tilde{v}_s$  is defined by the right-hand side of (10.16), this can be done. We now have all the necessary equations to compute  $\left. \frac{dE}{d\mu} \right|_{v_s}$ .

Next, we need to compute  $\left. \frac{dP}{d\mu} \right|_{v_s}$ . Taking the derivative of (10.7):

$$\frac{dP}{dn_0} = \frac{\hbar}{\sqrt{f_1}} (f_3 - q) - \hbar \frac{n_0}{2} f_1^{-3/2} \frac{df_1}{dn_0} (f_3 - q) + \hbar \frac{n_0}{\sqrt{f_1}} \left( \frac{df_3}{dn_0} - \frac{dq}{dn_0} \right), \quad (10.21)$$

$$\frac{dP}{d\mu} = \frac{dP}{dn_0} \frac{dn_0}{d\mu}. \quad (10.22)$$

The only new derivative appearing here is

$$\frac{df_3(\gamma, q)}{dn_0} = \frac{df_3}{d\gamma} \frac{d\gamma}{dn_0} + \frac{df_3}{dq} \frac{dq}{dn_0}. \quad (10.23)$$

We now have everything we need to calculate  $N_d$  from (10.1) directly.

In contrast, Campbell's equations derived in [192] allow us to compute  $N_d$  and  $\Delta\phi$  in a much more efficient manner<sup>3</sup>:

$$N_d = -2\pi g(1) [h(1) - h(-1)] - 1, \quad (10.24)$$

$$\Delta\phi = \frac{1}{2g(1)} [h(1) + h(-1)]. \quad (10.25)$$

Figure 10.1 shows  $N_d$  and  $\Delta\phi$  calculated from (10.1) and from (10.24)-(10.25) for several  $\gamma$  values across the range of interactions. In all cases the two formulae agree very well, which validates the use of Campbell's formulae. Any deviations are caused by differences in numerical accuracy, since the direct evaluation of (10.1) inevitably introduces additional inaccuracy through the many derivatives which are done numerically.

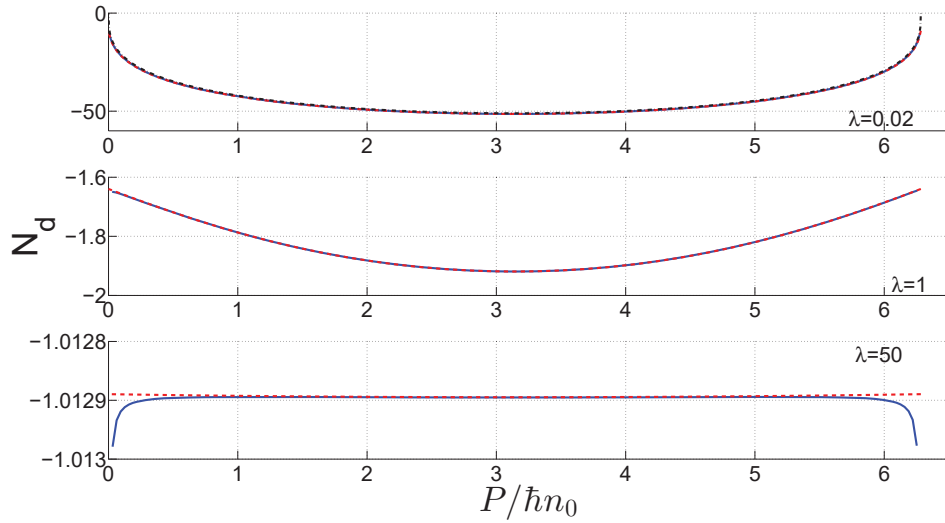
In the limit  $\gamma \rightarrow \infty$  (bottom panels of Fig. 10.1), we may compare to the Tonks-Girardeau gas, where  $N_d = -1$ ,  $\Delta\phi = \pi$ , independent of  $P$  (chapter 5). Clearly the Lieb-Liniger calculation is approaching the Tonks-Girardeau limit. In the opposite limit of  $\gamma \rightarrow 0$  (top panels of Fig. 10.1), we may compare to Gross-Pitaevskii dark soliton results (chapter 5). There is practically no visible difference between the dark soliton  $N_d$  and  $\Delta\phi$  and the Lieb-Liniger results, except that at the end-points (at  $P = 0$ ,  $2\pi\hbar n_0$ ) the dark soliton missing particle number actually vanishes, while it does not do so for Lieb-Liniger type-II excitations. The similarity of solitonic properties between dark solitons and type-II excitations in the Gross-Pitaevskii regime reinforces the idea that the two are closely linked.

## 10.2.2 Yang-Gaudin Model

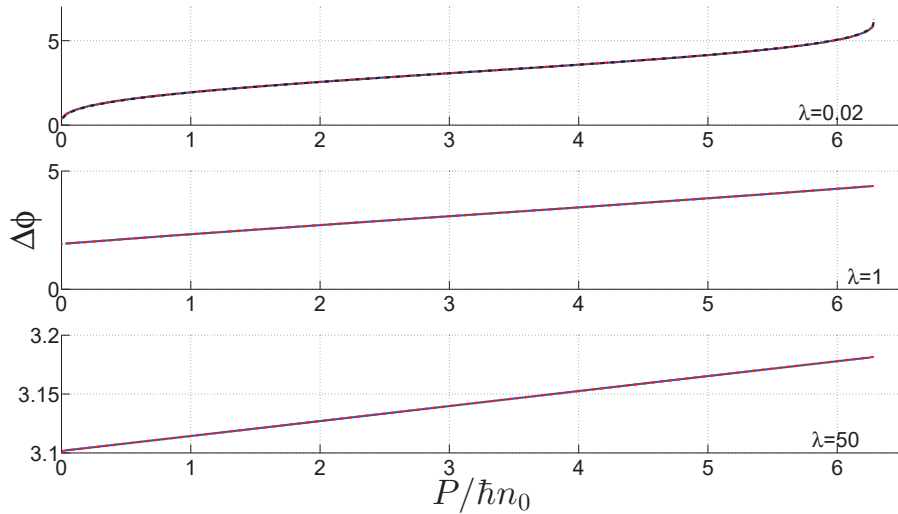
For each branch, we first give details of how the Lieb-Liniger calculation of (10.1) and Campbell's formulae (10.24)-(10.25) are to be modified, and then test the latter

---

<sup>3</sup>Note that the -1 on the right-hand side of (10.24) is missing in the thesis [192], which we believe to be a simple typographical error.



(a)



(b)

Figure 10.1: Missing particle number (a) and phase step (b) for type-II excitations in the Lieb-Liniger model (single boson holes in the  $\gamma \rightarrow \infty$  limit). Top panels:  $\lambda = 0.02, \gamma = 0.0015325$ , middle panels:  $\lambda = 1, \gamma = 1.7254$ , bottom panels:  $\lambda = 50, \gamma = 155.08$ . Direct evaluation of (10.1) yields the results plotted as solid blue lines, while those from Campbell's formula are shown as dashed red lines. The top panels of each subfigure also show the missing particle number and phase step of Gross-Pitaevskii dark solitons, plotted as black dash-dotted lines.

against the former. Knowing the nature of the excitations in the limiting cases of  $\gamma \rightarrow 0$  and  $\gamma \rightarrow \pm\infty$ , and armed with our experience with the Tonks-Girardeau limit of the Lieb-Liniger model, we expect  $N_d$  to be equal to negative the number of fermions involved in the hole excitations in both Tonks-Girardeau limits, independent of momentum. We shall see that this is exactly what the calculation returns. Moreover, we will find that Campbell's formulae are valid in all cases except for the spin-flip branch in the attractive case where the structure of the excitation differs from the Lieb-Liniger case in a non-trivial way.

The plots of  $N_d$  and  $\Delta\phi$  are shown for all branches in Figs. 10.2–10.6. Indeed we observe the correct limiting behaviour of  $N_d$  in both the non-interacting and infinitely-strongly-interacting regimes, fully consistent with the nature of the excitation.

### 10.2.2.1 Single Fermion Holes (Attractive)

The  $f$ -functions (10.3)-(10.5) are defined exactly as for the Lieb-Liniger model. The momentum is given by (10.7), while the energy is

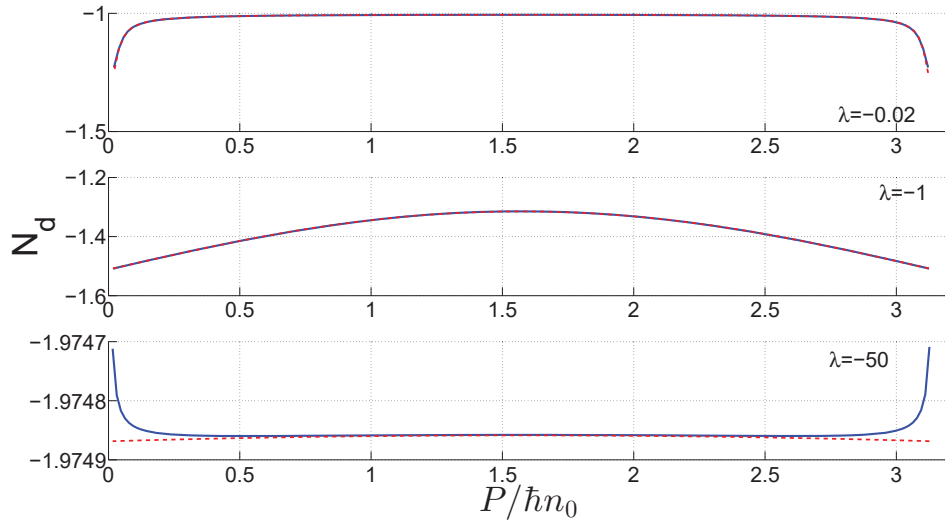
$$E = \frac{\hbar^2}{2m} \frac{n_0^2}{2f_1(\gamma)} [-q^2 + f_2(\gamma, q)] + 2\mu. \quad (10.26)$$

The velocity is given by (10.8), except that it is smaller by a factor of two. Since the momentum expression is unchanged, the derivative  $dP/dn_0$  is also given directly by (10.21), while

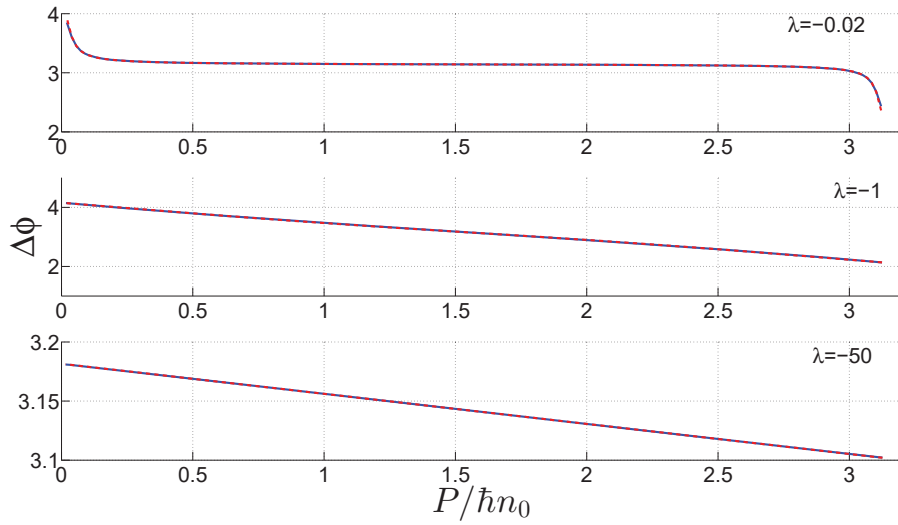
$$\frac{dE}{dn_0} = \frac{\hbar^2}{2m} \frac{2n_0 f_1 - n_0^2 \frac{df_1}{dn_0}}{2f_1^2} [-q^2 + f_2] + \frac{\hbar^2}{2m} \frac{n_0^2}{2f_1} \left( -2q \frac{dq}{dn_0} + \frac{df_2}{dn_0} \right) + 2 \frac{d\mu}{dn_0}. \quad (10.27)$$

The rest of the calculation is the same as in the Lieb-Liniger case, with the understanding that  $\tilde{v}_s$  is to be modified the same way as  $v_s$ .

Campbell's formulae are unchanged except that the -1 on the right-hand side of (10.24) is replaced by -2 and an additional factor of 2 is needed on the right-hand side of (10.25).  $N_d$  and  $\Delta\phi$  for this branch, evaluated from (10.1) and Campbell's formulae, are shown in Fig. 10.2. The two methods clearly agree for all interaction strengths, and in the limiting cases the missing particle number reflects the nature of the excitation:  $N_d = -1$  as  $\gamma \rightarrow 0$  where it is a single fermion hole and  $N_d = -2$  as  $\gamma \rightarrow -\infty$  where it becomes a dimer hole.



(a)



(b)

Figure 10.2: Missing particle number for single fermion holes in the attractive regime (referring to the excitations according to their nature in the  $\gamma \rightarrow 0$  limit), which become single dimer holes in the  $\gamma \rightarrow -\infty$  limit. Top panels:  $\lambda = -0.02, \gamma = -0.030815$ , middle panels:  $\lambda = -1, \gamma = -1.1363$ , bottom panels:  $\lambda = -50, \gamma = -39.770$ . Direct evaluation of (10.1) yields the results plotted as solid blue lines, while those from Campbell's formula are shown as dashed red lines.

### 10.2.2.2 Double Fermion Holes (Attractive)

The  $f$ -functions (10.3)-(10.5) are defined exactly as for the Lieb-Liniger model. We write the excitation energy and momentum as

$$E = \frac{\hbar^2}{2m} \frac{n_0^2}{2f_1(\gamma)} [-2q^2 + f_2(\gamma, q)] + 4\mu, \quad (10.28)$$

$$P = \hbar \frac{n_0}{\sqrt{f_1(\gamma)}} [-2q + f_3(\gamma, q)]. \quad (10.29)$$

The velocity is

$$v_s = \frac{dE}{dP} = \frac{\hbar}{2m} \frac{n_0}{2\sqrt{f_1}} \left\{ \frac{-4q + \frac{df_2}{dq}}{-2 + \frac{df_3}{dq}} \right\}. \quad (10.30)$$

Differentiating the energy and momentum, we find

$$\begin{aligned} \frac{dE}{dn_0} &= \frac{\hbar^2}{2m} \frac{2n_0 f_1 - n_0^2 \frac{df_1}{dn_0}}{2f_1^2} [-2q^2 + f_2] \\ &+ \frac{\hbar^2}{2m} \frac{n_0^2}{2f_1} \left( -4q \frac{dq}{dn_0} + \frac{df_2}{dn_0} \right) + 4 \frac{d\mu}{dn_0}, \end{aligned} \quad (10.31)$$

$$\begin{aligned} \frac{dP}{dn_0} &= \frac{\hbar}{\sqrt{f_1}} (f_3 - 2q) - \frac{\hbar n_0}{2} f_1^{-3/2} \frac{df_1}{dn_0} (f_3 - 2q) \\ &+ \frac{\hbar n_0}{\sqrt{f_1}} \left( \frac{df_3}{dn_0} - 2 \frac{dq}{dn_0} \right). \end{aligned} \quad (10.32)$$

The rest of the calculation is the same as in the Lieb-Liniger case, with the understanding that  $\tilde{v}_s$  is to be modified the same way as  $v_s$ .

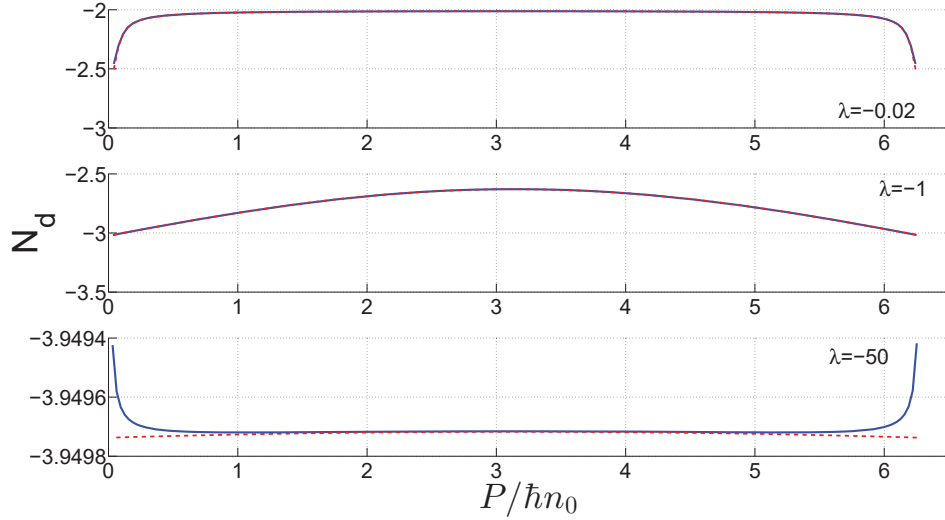
Campbell's formulae are unchanged except that the -1 on the right-hand side of (10.24) is replaced by -4 and an additional factor of 2 is needed on the right-hand side of (10.25).  $N_d$  and  $\Delta\phi$  for this branch, evaluated from (10.1) and Campbell's formulae, are shown in Fig. 10.3. The two methods clearly agree for all interaction strengths, and in the limiting cases the missing particle number reflects the nature of the excitation:  $N_d = -2$  as  $\gamma \rightarrow 0$  where it is a double fermion hole and  $N_d = -4$  as  $\gamma \rightarrow -\infty$  where it becomes a double dimer hole.

### 10.2.2.3 Spin-Flip Excitations (Attractive)

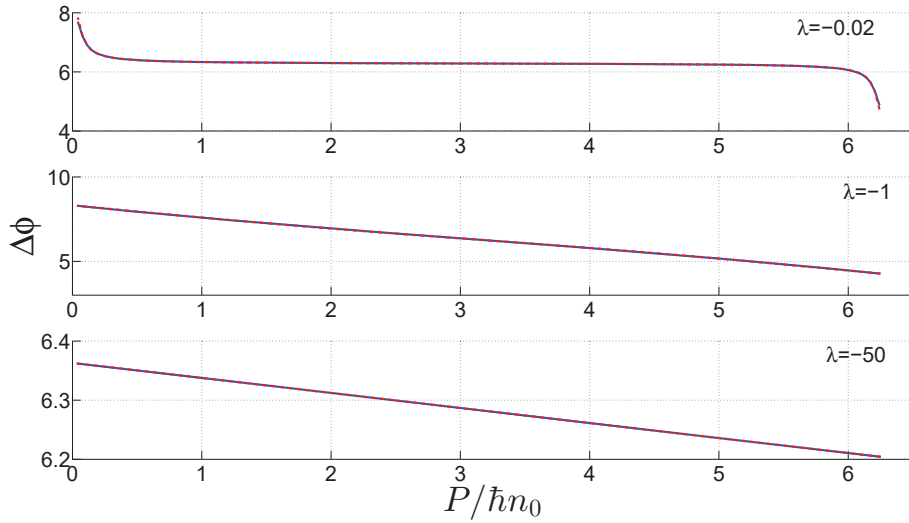
The  $f$ -functions (10.3)-(10.5) are defined exactly as for the Lieb-Liniger model. The momentum is given by (10.7), while the energy is

$$E = \frac{\hbar^2}{2m} \frac{n_0^2}{2f_1(\gamma)} [-q^2 + f_2(\gamma, q) + 1] + \frac{\hbar^2}{2m} \frac{c^2}{2}. \quad (10.33)$$

The velocity is given by (10.8), except that it is smaller by a factor of two. Since the momentum expression is unchanged, the derivative  $dP/dn_0$  is also given directly



(a)



(b)

Figure 10.3: Missing particle number for double fermion holes in the attractive regime (referring to the excitations according to their nature in the  $\gamma \rightarrow 0$  limit), which become double dimer holes in the  $\gamma \rightarrow -\infty$  limit. Top panels:  $\lambda = -0.02, \gamma = -0.030815$ , middle panels:  $\lambda = -1, \gamma = -1.1363$ , bottom panels:  $\lambda = -50, \gamma = -39.770$ . Direct evaluation of (10.1) yields the results plotted as solid blue lines, while those from Campbell's formula are shown as dashed red lines.

by (10.21), while

$$\frac{dE}{dn_0} = \frac{\hbar^2}{2m} \frac{2n_0 f_1 - n_0^2 \frac{df_1}{dn_0}}{2f_1^2} [-q^2 + f_2 + 1] + \frac{\hbar^2}{2m} \frac{n_0^2}{2f_1} \left( -2q \frac{dq}{dn_0} + \frac{df_2}{dn_0} \right). \quad (10.34)$$

The rest of the calculation is the same as in the Lieb-Liniger case, with the understanding that  $\tilde{v}_s$  is to be modified the same way as  $v_s$ .

Campbell's formulae are unchanged except that the -1 on the right-hand side of (10.24) is removed and an additional factor of 2 is needed on the right-hand side of (10.25).  $N_d$  and  $\Delta\phi$  for this branch, evaluated from (10.1) and Campbell's formulae, are shown in Fig. 10.4. The two methods clearly disagree for all interaction strengths. In the limiting cases, only the full calculation of the missing particle number from (10.1) reflects the nature of the excitation:  $N_d = -1$  as  $\gamma \rightarrow 0$  where a spin-flip is equivalent to a single fermion hole (due to the Pauli exclusion principle) and  $N_d = -2$  as  $\gamma \rightarrow -\infty$  which may be sensible if we consider the broken dimer as a hole in the dimer rapidity distribution.

#### 10.2.2.4 Single Fermion Holes (Repulsive)

The  $f$ -functions (10.3)-(10.5) are defined exactly as for the Lieb-Liniger model, except that  $x$  is replaced by  $y$ . We write the excitation energy and momentum as

$$E = \frac{\hbar^2}{2m} \frac{n_0^2}{f_1(\gamma)} f_2(\gamma, q), \quad (10.35)$$

$$P = \hbar \frac{n_0}{\sqrt{f_1(\gamma)}} f_3(\gamma, q). \quad (10.36)$$

The velocity is

$$v_s = \frac{dE}{dP} = \frac{\hbar}{2m} \frac{n_0}{\sqrt{f_1}} \left\{ \begin{array}{c} \frac{df_2}{dq} \\ \frac{df_3}{dq} \end{array} \right\}. \quad (10.37)$$

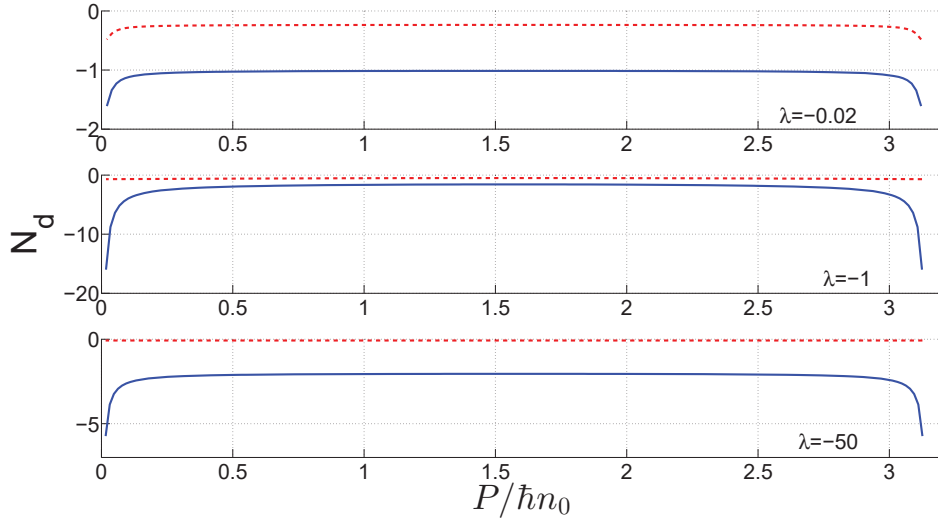
Next, differentiating the energy and momentum, we obtain

$$\frac{dE}{dn_0} = \frac{\hbar^2}{2m} \frac{2n_0 f_1 - n_0^2 \frac{df_1}{dn_0}}{f_1^2} f_2 + \frac{\hbar^2}{2m} \frac{n_0^2}{f_1} \frac{df_2}{dn_0}, \quad (10.38)$$

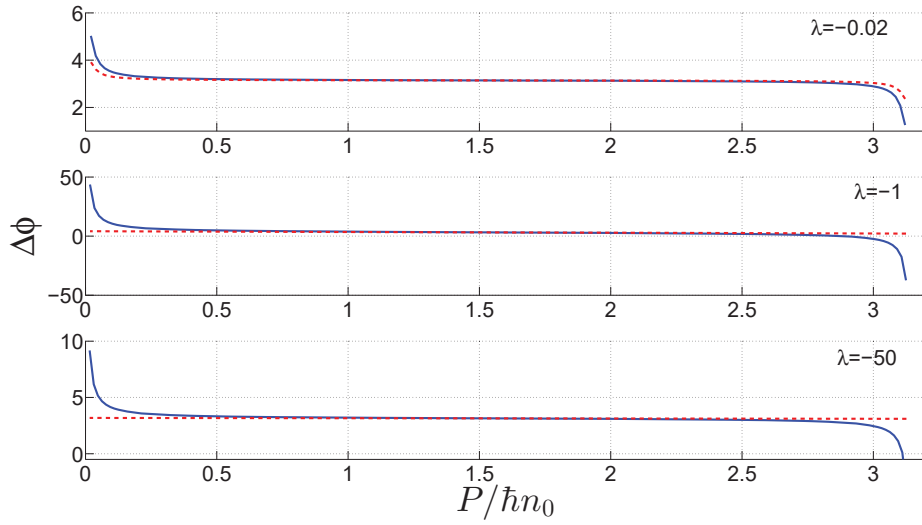
$$\frac{dP}{dn_0} = \frac{\hbar}{\sqrt{f_1}} f_3 - \frac{\hbar n_0}{2} f_1^{-3/2} \frac{df_1}{dn_0} f_3 + \frac{\hbar n_0}{\sqrt{f_1}} \frac{df_3}{dn_0}. \quad (10.39)$$

The rest of the calculation is the same as in the Lieb-Liniger case, with the understanding that  $\tilde{v}_s$  is to be modified the same way as  $v_s$ .

Campbell's formulae are unchanged except that the -1 on the right-hand side of (10.24) is removed and an additional factor of 2 is needed on the right-hand side of (10.25).  $N_d$  and  $\Delta\phi$  for this branch, evaluated from (10.1) and Campbell's formulae, are shown in Fig. 10.5. The two methods clearly agree for all interaction



(a)



(b)

Figure 10.4: Missing particle number for spin-flip excitations (attractive regime). Top panels:  $\lambda = -0.02, \gamma = -0.030815$ , middle panels:  $\lambda = -1, \gamma = -1.1363$ , bottom panels:  $\lambda = -50, \gamma = -39.770$ . Direct evaluation of (10.1) yields the results plotted as solid blue lines, while those from Campbell's formula are shown as dashed red lines.

strengths, and in the limiting cases the missing particle number reflects the nature of the excitation:  $N_d = -1$  as  $\gamma \rightarrow 0$  where it is a single fermion hole and  $N_d = 0$  as  $\gamma \rightarrow \infty$  where it becomes a system translation.

### 10.2.2.5 Double Fermion Holes (Repulsive)

The  $f$ -functions (10.3)-(10.5) are defined exactly as for the Lieb-Liniger model, except that  $x$  is replaced by  $y$ . The energy, momentum and velocity written through these functions are identical to the Lieb-Liniger case. Since the momentum and energy expressions are unchanged, the derivatives  $dE/dn_0$  and  $dP/dn_0$  are also given directly by (10.9) and (10.21). The rest of the calculation is the same as in the Lieb-Liniger case.

Campbell's formulae are unchanged except that an additional factor of 2 is needed on the right-hand side of (10.25).  $N_d$  and  $\Delta\phi$  for this branch, evaluated from (10.1) and Campbell's formulae, are shown in Fig. 10.6. The two methods clearly agree for all interaction strengths, and in the limiting cases the missing particle number reflects the nature of the excitation:  $N_d = -2$  as  $\gamma \rightarrow 0$  where it is a double fermion hole and  $N_d = -1$  as  $\gamma \rightarrow \infty$  where it becomes a single fermion hole.

### 10.2.2.6 Spin-Flip Excitations (Repulsive)

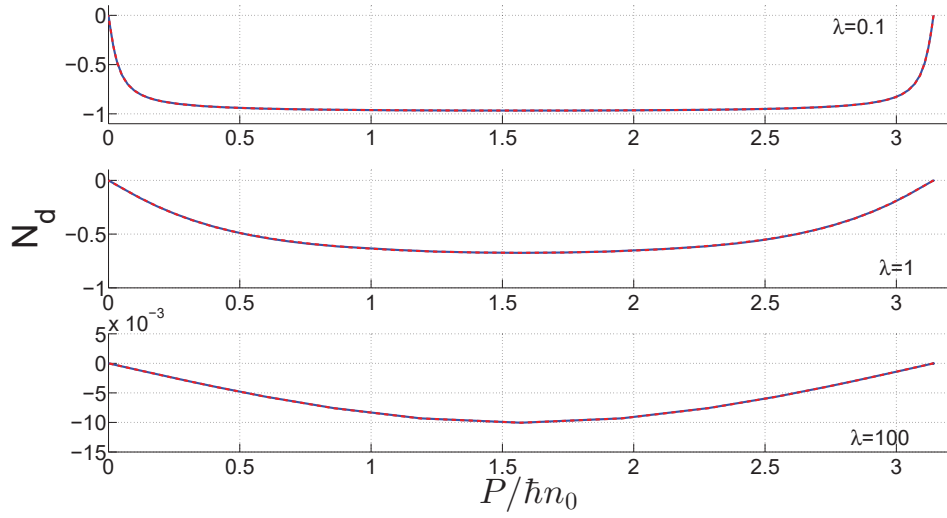
The  $f$ -functions (10.3)-(10.5) are defined exactly as for the Lieb-Liniger model, except that  $x$  is replaced by  $y$ . The energy, momentum and velocity written through these functions are identical to the single fermion holes case in section 10.2.2.4, as are  $dE/dn_0$  and  $dP/dn_0$ . The rest of the calculation is the same as in the Lieb-Liniger case, with the understanding that  $\tilde{v}_s$  is to be modified the same way as  $v_s$ .

Campbell's formulae are unchanged except that the -1 on the right-hand side of (10.24) is removed and an additional factor of 2 is needed on the right-hand side of (10.25).  $N_d$  and  $\Delta\phi$ , evaluated from (10.1) and Campbell's formulae are identical to those of the single fermion branch shown in Fig. 10.5.

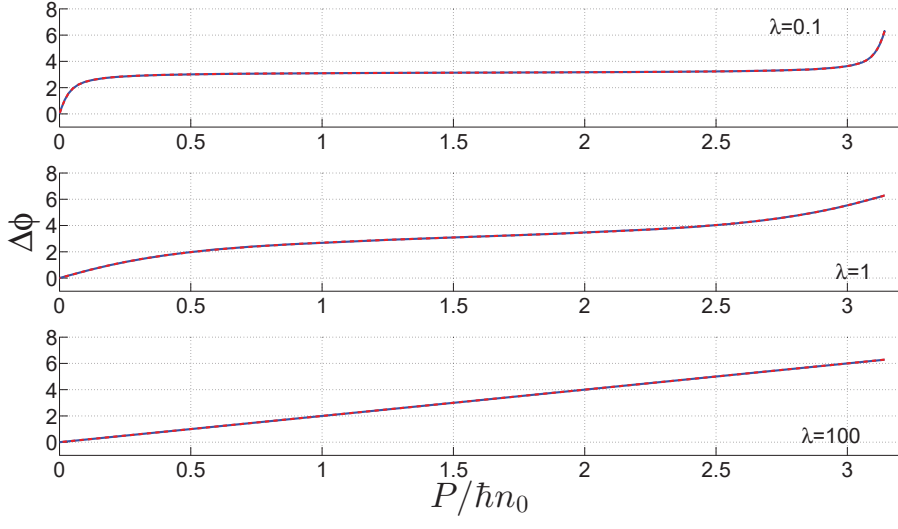
## 10.3 Physical and Inertial Masses

Having both the dispersion relation and the missing particle number at our disposal, we can easily compute the “physical mass” associated with the missing particle number (which is simply  $m_P = mN_s = mN_d$  at zero velocity) and the “inertial mass”, which captures the response of the quasi-particles to applied forces. Recall that the inertial mass is given by

$$m_I = \frac{dP}{dv_s} = 2 \frac{dE}{d(v_s^2)} = \left( \frac{d^2E}{dP^2} \right)^{-1}, \quad (10.40)$$

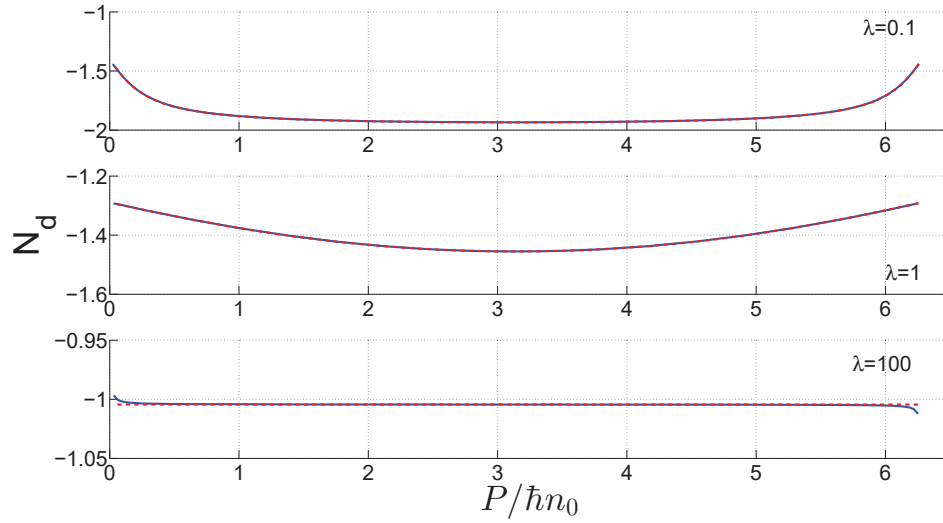


(a)

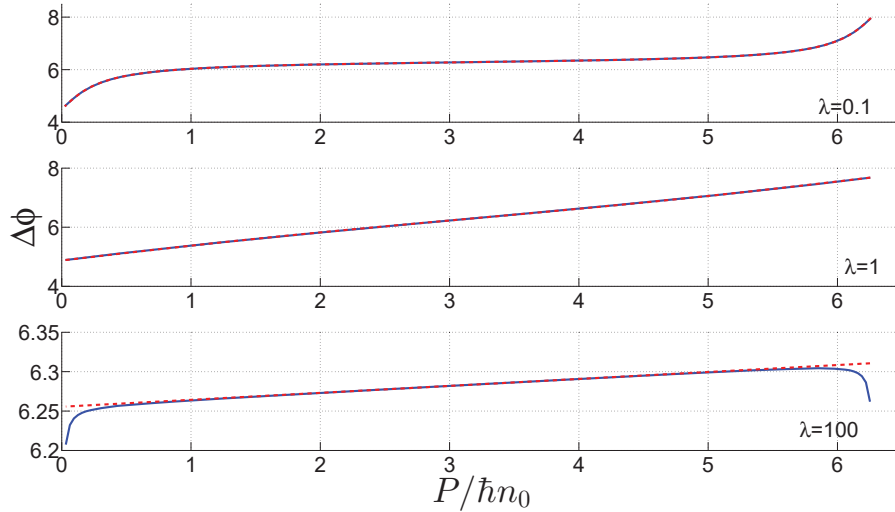


(b)

Figure 10.5: Missing particle number for single fermion holes in the repulsive regime (referring to the excitations according to their nature in the  $\gamma \rightarrow 0$  limit), which become a global system translation excitation in the  $\gamma \rightarrow \infty$  limit. Top panels:  $\lambda = 0.1, \gamma = 0.16886$ , middle panels:  $\lambda = 1, \gamma = 2.2491$ , bottom panels:  $\lambda = 100, \gamma = 312.773$ . Direct evaluation of (10.1) yields the results plotted as solid blue lines, while those from Campbell's formula are shown as dashed red lines. The plots shown here are identical to those that are obtained for the spin-flip branch.



(a)



(b)

Figure 10.6: Missing particle number for double fermion holes in the repulsive regime (referring to the excitations according to their nature in the  $\gamma \rightarrow 0$  limit) which become one fermion holes in the  $\gamma \rightarrow \infty$  limit. Top panels:  $\lambda = 0.1, \gamma = 0.16886$ , middle panels:  $\lambda = 1, \gamma = 2.2491$ , bottom panels:  $\lambda = 100, \gamma = 312.773$ . Direct evaluation of (10.1) yields the results plotted as solid blue lines, while those from Campbell's formula are shown as dashed red lines.

where the derivatives should be evaluated at the extrema of the dispersion relation (i.e. at zero velocity).

Moreover, in [109], it is shown that  $\frac{m_I}{m_P} = \left(\frac{T_s}{T_t}\right)^2$ , where  $T_s$  is the oscillation period of a solitonic excitation in a harmonic trap with period  $T_t$  (for small amplitude oscillations under the local density approximation), so the ratio of the inertial-to-physical masses has direct relevance to experiments. In this section we compute  $m_I, m_P$  and  $m_I/m_P$  at the center of the dispersion relation for all branches as a function of coupling strength.

Figures 10.7–10.12 show the physical and inertial masses and their ratio as a function of interaction strength. Once again, the plots for the repulsive spin-flip branch are identical to those for the single fermion hole branch (Fig. 10.11) and are thus not shown separately. For the Lieb-Liniger model, in the weak-coupling regime the type-II masses are in agreement with those of the Gross-Pitaevskii dark soliton (chapter 2), which is hardly surprising as both the dispersion relation and the missing particle number coincide in this regime. For arbitrary coupling, we recover the results found in [148] as  $N_s = N_d$  at  $v_s = 0$ .

With the exception of the Lieb-Liniger type-II excitations at small coupling,  $m_P$  for all branches remains of order unity (or less) for all interaction strengths. The same is true for  $m_I$ , except for single fermion holes and spin-flip excitations in the repulsive Yang-Gaudin system, where  $m_I$  diverges to  $-\infty$  as  $\gamma \rightarrow \infty$  since the dispersion relation becomes a flat line at zero energy. Seeing that for these last two branches  $m_P \rightarrow 0$  and  $m_I \rightarrow -\infty$  as  $\gamma \rightarrow \infty$ , the ratio  $m_I/m_P$  diverges to  $\infty$  in this limit very quickly indeed.

Moreover, we notice that for repulsive interactions in both the Lieb-Liniger and Yang-Gaudin models,  $m_I/m_P > 1$ , implying that the soliton (if it exists) would oscillate slower than the trap frequency. On the other hand, for attractive interactions, the Yang-Gaudin type-II branches have  $m_I/m_P < 1$ , so the hypothesized solitons would oscillate faster than the trap frequency.

## 10.4 Discussion and Conclusions

The main result of our work here is the application of the formula (10.1), which allows one to extract the missing particle number from the dispersion relation of a solitonic excitation, to type-II elementary excitations in the Lieb-Liniger and Yang-Gaudin models. Apart from illustrating the general formalism, we have also tested and confirmed Campbell's formulae as equivalent (and much simpler) in all cases except for spin-flip excitations in the attractive Yang-Gaudin model. We saw that the missing particle number reflected perfectly the previously-known nature of all type-II branches in the limiting cases of weak and strong interactions.

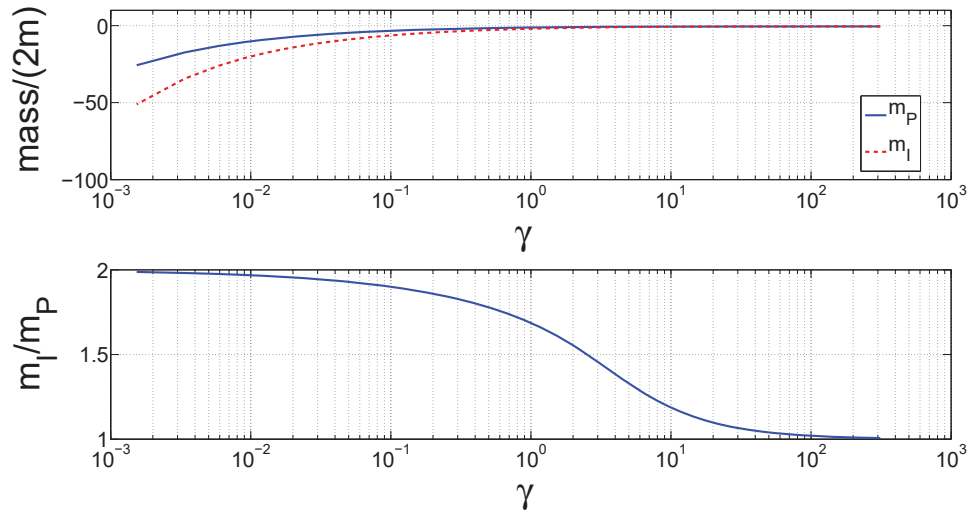


Figure 10.7: Physical and inertial masses (a) and their ratio (b) for type-II excitations in the Lieb-Liniger model (single boson holes in the  $\gamma \rightarrow \infty$  limit).

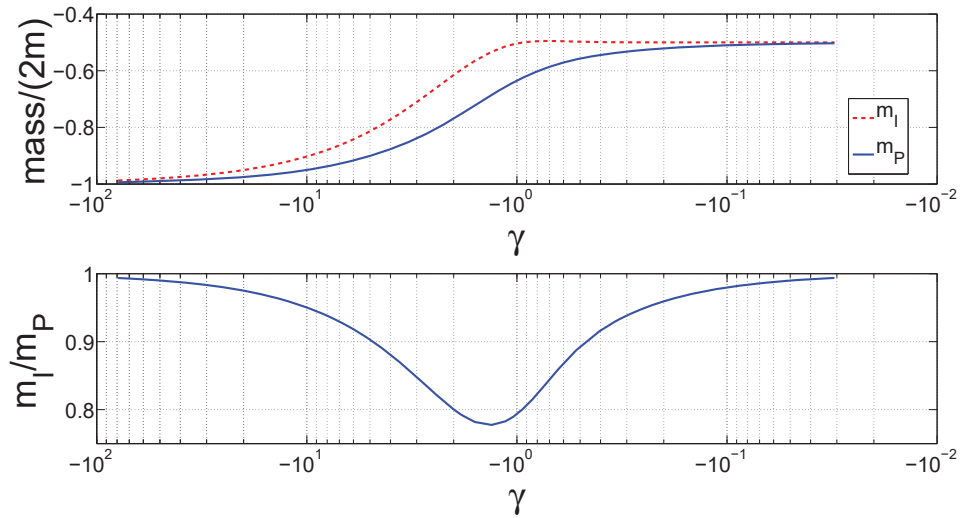


Figure 10.8: Physical and inertial masses (a) and their ratio (b) for single fermion holes (referring to the excitations according to their nature in the  $\gamma \rightarrow 0$  limit), which become single dimer holes in the  $\gamma \rightarrow -\infty$  limit.

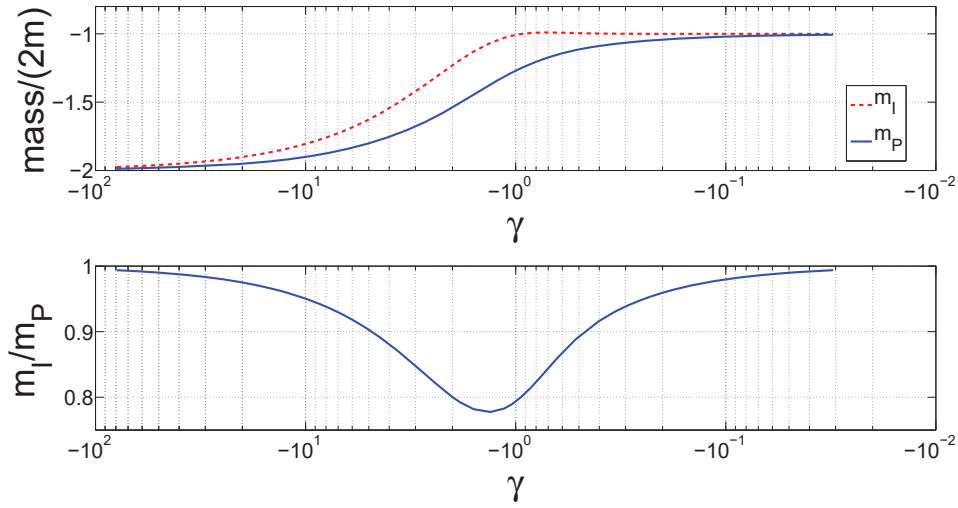


Figure 10.9: Physical and inertial masses (a) and their ratio (b) for double fermion holes (referring to the excitations according to their nature in the  $\gamma \rightarrow 0$  limit), which become double dimer holes in the  $\gamma \rightarrow -\infty$  limit.

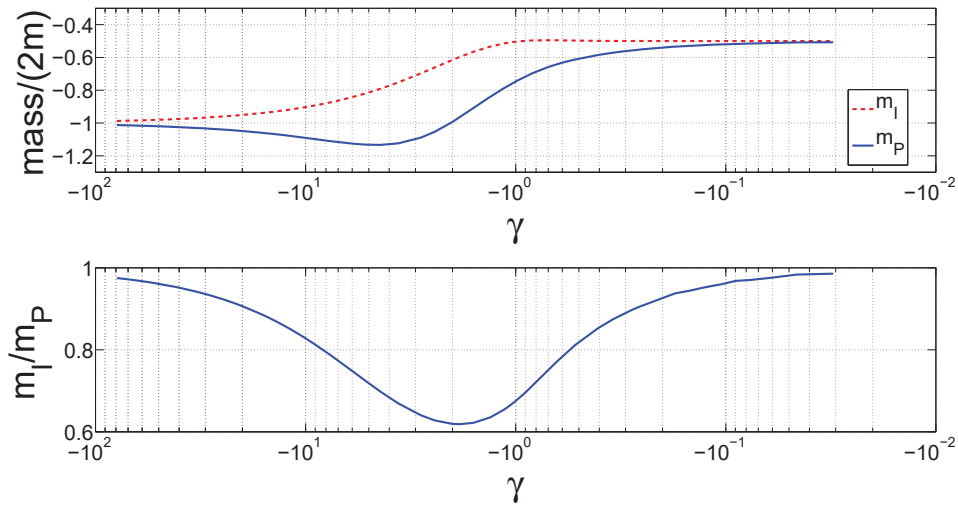


Figure 10.10: Physical and inertial masses (a) and their ratio (b) for spin-flip excitations.

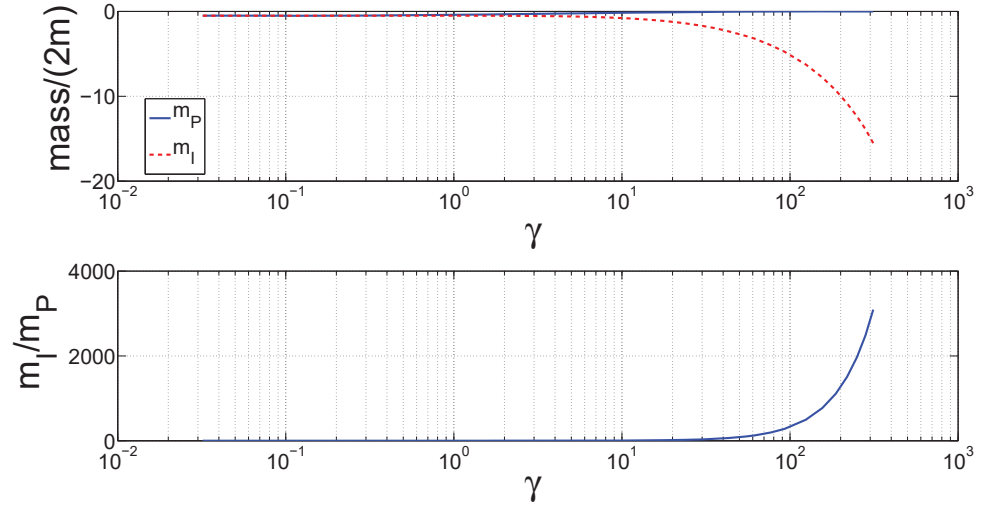


Figure 10.11: Physical and inertial masses (a) and their ratio (b) for single fermion holes (referring to the excitations according to their nature in the  $\gamma \rightarrow 0$  limit), which become a global system translation excitation in the  $\gamma \rightarrow \infty$  limit. The plots shown here are identical to those that are obtained for the spin-flip branch.

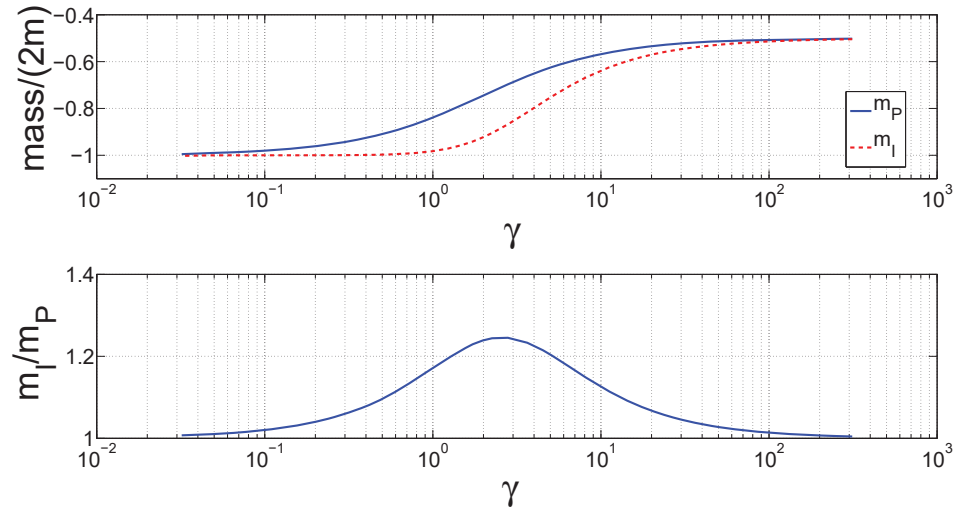


Figure 10.12: Physical and inertial masses (a) and their ratio (b) for double fermion holes (referring to the excitations according to their nature in the  $\gamma \rightarrow 0$  limit) which become one fermion holes in the  $\gamma \rightarrow \infty$  limit.

However, despite some clear indications that the calculation returned reasonable results, we must question the precise physical meaning of a missing particle number for eigenstates that are spatially uniform and a phase step for an uncondensed gas. This matter is resolved in chapter 12.

We also point out that in chapter 11 we will develop an approximation to the dispersion relation of a solitonic excitation in a finite-system based fully on thermodynamic limit results. We will successfully apply the derived formulae to Lieb-Liniger type-II excitations, heavily using  $N_d$  and  $\Delta\phi$  as calculated in the present chapter. This suggests that the missing particle number, the phase step, and the solitonic interpretation of type-II states are physically-sound concepts.

In fact, if these excitations were to be created in the laboratory, it is possible that measurements would reveal a dark soliton profile [65, 66]. According to our calculations, however, the physical mass of all elementary type-II excitations in the Yang-Gaudin model remains of order unity or less for  $-\infty < \gamma < \infty$ . It is likely that detecting such a small missing particle number will be experimentally problematic, so a different method – perhaps based on the phase profile instead of the density – will need to be developed.

# Appendix

## 10.A Approximate Analytical Solutions

In this appendix we give a summary of analytical results in the limits of  $\gamma \rightarrow \pm\infty$  and  $\gamma \rightarrow 0$ . All results for the Yang-Gaudin model specifically assume  $N = 2M$ . The mathematical description of excitations in the Yang-Gaudin model is quite complicated, with the exception of the limit  $\gamma \rightarrow -\infty$  which is the only case for which we will present explicit results. In the two remaining limits,  $\gamma \rightarrow +\infty$  and  $\gamma \rightarrow 0$ , there are no currently-known methods to obtain approximate solutions for excitations.

### 10.A.1 Repulsive Lieb-Liniger Model

For the Lieb-Liniger model, all limits can be successfully tackled. We begin from the strong-coupling limit, where for the ground state equation, we neglect  $(x - x')^2$  compared to  $\lambda^2$  in the kernel. This immediately leads to a constant solution,  $g = \frac{1}{2}(\pi - 2/\lambda)^{-1}$ . It is then simple to derive the ground state properties

$$K = n_0 \frac{\pi\lambda - 2}{\lambda}, \quad (10.41)$$

$$\gamma = 2 \left( \frac{\pi\lambda}{2} - 1 \right), \quad (10.42)$$

$$e = \frac{1}{3} \left( \pi - \frac{2}{\lambda} \right)^2, \quad (10.43)$$

$$\mu = \frac{\hbar^2 n_0^2}{2m} \left[ \pi^2 - \frac{16\pi}{3\lambda} \right]. \quad (10.44)$$

For the single boson hole excitations, expanding the inhomogeneous term in the integral equation to first order about zero, naturally leads to a linear ansatz:  $h(x) = \alpha(\lambda, q) + \beta(\lambda, q)x$ . Upon substitution, we find  $\alpha(\lambda, q) = \frac{\pi\lambda - 2q}{2(\pi\lambda - 2)}$  and  $\beta(\lambda) = \frac{1}{\pi\lambda}$ . The excitation energy and momentum can then be computed, and eliminating  $q$ , the dispersion relation can be expressed as

$$E = \frac{P\pi}{m\hbar n_0} \left( 1 - \frac{P}{2\hbar\pi n_0} \right) \left( \frac{\gamma}{2 + \gamma} \right)^2. \quad (10.45)$$

From Campbell's formulae, we further obtain

$$N_d = -1 - \frac{2}{\gamma}, \quad (10.46)$$

$$\Delta\phi = \pi \left[ 1 + \left( \frac{P}{\pi\hbar n_0} - 1 \right) (1 + \gamma/2)^{-1} \right]. \quad (10.47)$$

Finally, the masses and their ratio are given by

$$m_P = -m \frac{\gamma + 2}{\gamma}, \quad (10.48)$$

$$m_I = -m \left( \frac{\gamma + 2}{\gamma} \right)^2, \quad (10.49)$$

$$\frac{m_I}{m_P} = \frac{\gamma + 2}{\gamma}. \quad (10.50)$$

In the weak coupling limit, the integral equations are much harder to solve. Lieb and Liniger [46] suggest the leading order term in the ground state solution as a semi-circle (which compares quite well indeed to the exact numerical result):

$$g(x) = \frac{1}{2\pi\lambda} \sqrt{1 - x^2}, \quad (10.51)$$

$$K = 2n_0\sqrt{\gamma}, \quad (10.52)$$

$$\gamma = (2\lambda)^2, \quad (10.53)$$

$$e = \gamma, \quad (10.54)$$

$$\mu = \frac{\hbar^2 n_0^2}{m} \gamma. \quad (10.55)$$

As for single boson holes, a solution is suggested in [60]:

$$h(x) = \frac{1}{\lambda} \left\{ \frac{1}{2\pi} (x - q) \ln \left( \frac{1 - qx + \sqrt{1 - q^2} \sqrt{1 - x^2}}{1 - qx - \sqrt{1 - q^2} \sqrt{1 - x^2}} \right) + \left( \frac{1}{2} - \frac{1}{\pi} \sin^{-1}(q) \right) \sqrt{1 - x^2} \right\}. \quad (10.56)$$

Using the above solution  $h(x)$  and the Lieb-Liniger expressions for  $E$  and  $P$ , we get:

$$E = \frac{\hbar^2 n_0^2}{2m} 16\lambda^2 \left[ -q^2 + \frac{1}{3\lambda} (1 - q^2)^{3/2} \right] + \frac{\hbar^2 n_0^2}{m} 4\lambda^2, \quad (10.57)$$

$$P = 4\hbar n_0 \lambda \left[ -q - \frac{1}{2\lambda} q \sqrt{1 - q^2} + \frac{\pi}{4\lambda} - \frac{1}{2\lambda} \sin^{-1}(q) \right]. \quad (10.58)$$

Now, we can find  $v_s$  and  $v_c$  (the speed of sound) in the small  $\lambda$  limit, both from the ground state and from the dispersion relation. From the ground state we obtain  $v_c = \sqrt{\mu/m}$ . From the dispersion relation we get the same  $v_c$  (if we use  $\lambda \ll 1$  first,

and then take  $q \rightarrow 1$ ), and

$$v_s \approx \frac{\hbar}{2m} 4\lambda\rho q, \quad (10.59)$$

so  $q = s \equiv v_s/v_c$ . Now, the Gross-Pitaevskii expressions for energy and momentum are (chapter 2)

$$E_{GP} = \frac{4\mu^{3/2}\sqrt{m}}{3\hbar c} (1-s^2)^{3/2}, \quad (10.60)$$

$$P_{GP} = \frac{2m\mu}{\hbar c} \left[ \cos^{-1}(s) - s\sqrt{1-s^2} \right], \quad (10.61)$$

and the full expressions for the Lieb-Liniger quantities can then be written as

$$E = E_{GP} + \mu - 2mv_s^2, \quad (10.62)$$

$$P = P_{GP} - 2mv_s. \quad (10.63)$$

However, comparing to exact numerical results we find that the Gross-Pitaevskii expressions alone perform much better. Therefore, we proceed with the Gross-Pitaevskii energy and momentum.

Next, computing  $N_d$  and  $\Delta\phi$  from Campbell's formulae returns identically zero (a limits issue), so we must use the derivative formula (10.1). Since both the ground and excited state properties are best described by Gross-Pitaevskii results, the outcome of the calculation is the Gross-Pitaevskii missing particle number (chapter 2):

$$N_d = -\frac{2\sqrt{m\mu}}{\hbar c} \sqrt{1-s^2}. \quad (10.64)$$

Computing the phase step, we again obviously recover the Gross-Pitaevskii result

$$\Delta\phi = 2 \cos^{-1}(s). \quad (10.65)$$

Note that since the relation between momentum and velocity is not linear, it is not possible to eliminate  $s$  and express everything in terms of  $P$ . For the masses, we find

$$m_P = -m \frac{2\sqrt{m\mu}}{\hbar c}, \quad (10.66)$$

$$m_I = -\frac{4\sqrt{\mu}m^{3/2}}{\hbar c}, \quad (10.67)$$

$$\frac{m_I}{m_P} = 2. \quad (10.68)$$

Thus in the limit  $\gamma \rightarrow 0$ , the Lieb-Liniger ground state is best described by the Gross-Pitaevskii background solution, while single boson holes have the same properties as dark solitons of the Gross-Pitaevskii equation [148].

## 10.A.2 Attractive Yang-Gaudin Model

Once again, the simplest limit is  $\gamma \rightarrow -\infty$ , where exactly the same approach as for the Lieb-Liniger model yields the following ground state properties:

$$g = (\pi - 2/\lambda)^{-1}, \quad (10.69)$$

$$b = n_0 \frac{\pi\lambda - 2}{4\lambda}, \quad (10.70)$$

$$\gamma = \frac{1}{2} \left( \frac{\pi\lambda}{2} - 1 \right), \quad (10.71)$$

$$e = \frac{1}{48} \left( \pi - \frac{2}{\lambda} \right)^2, \quad (10.72)$$

$$\mu = \frac{\hbar^2 n_0^2}{2m} \left[ \frac{\pi^2}{16} - \frac{\pi}{3\lambda} \right]. \quad (10.73)$$

Single fermion hole excitations have  $h(x) = \alpha(\lambda, q) + \beta(\lambda, q)x$  with  $\alpha(\lambda, q) = \frac{\pi\lambda - 2q}{2(\pi\lambda - 2)}$  and  $\beta(\lambda) = \frac{1}{\pi\lambda}$ , the dispersion relation

$$E = \frac{P\pi}{4m\hbar n_0} \left( 1 - \frac{P}{\hbar\pi n_0} \right) \left( \frac{2\gamma}{1 + 2\gamma} \right)^2, \quad (10.74)$$

missing particle number and phase step

$$N_d = -2 - \frac{1}{\gamma}, \quad (10.75)$$

$$\Delta\phi = \pi \left[ 1 + \left( \frac{2P}{\pi\hbar n_0} - 1 \right) (1 + 2\gamma)^{-1} \right], \quad (10.76)$$

and masses

$$m_P = -2m \frac{2\gamma + 1}{2\gamma}, \quad (10.77)$$

$$m_I = -2m \left( \frac{2\gamma + 1}{2\gamma} \right)^2, \quad (10.78)$$

$$\frac{m_I}{m_P} = \frac{2\gamma + 1}{2\gamma}. \quad (10.79)$$

Double fermion holes have  $h(x) = \alpha(\lambda, q) + \beta(\lambda, q)x$  with  $\alpha(\lambda, q) = 2 \frac{\pi\lambda - 2q}{2(\pi\lambda - 2)}$  and  $\beta(\lambda) = \frac{2}{\pi\lambda}$ . The other properties are

$$E = \frac{P\pi}{4m\hbar n_0} \left( 1 - \frac{P}{2\hbar\pi n_0} \right) \left( \frac{2\gamma}{1 + 2\gamma} \right)^2, \quad (10.80)$$

$$N_d = -4 - \frac{2}{\gamma}, \quad (10.81)$$

$$(10.82)$$

$$\Delta\phi = 2\pi \left[ 1 + \left( \frac{P}{\pi\hbar n_0} - 1 \right) (1 + 2\gamma)^{-1} \right], \quad (10.83)$$

$$m_P = -2m \frac{2\gamma + 1}{\gamma}, \quad (10.84)$$

$$m_I = -4m \left( \frac{2\gamma + 1}{2\gamma} \right)^2, \quad (10.85)$$

$$\frac{m_I}{m_P} = \frac{2\gamma + 1}{2\gamma}. \quad (10.86)$$

Finally, spin-flip excitations have  $h(x) = \alpha(\lambda, q) + \beta(\lambda, q)x$  with  $\alpha(\lambda, q) = \frac{\pi\lambda - 2q}{2(\pi\lambda - 2)}$  and  $\beta(\lambda) = -\frac{3}{\pi\lambda + 2}$ , and dispersion relation

$$E = \frac{\hbar^2 n_0^2 \gamma^2}{4m} \left\{ \frac{\pi^2}{(1 + 2\gamma)^2} \left[ -\frac{1}{1 + \gamma} + \frac{4P}{\hbar n_0 \pi} - \frac{4P^2}{\hbar^2 n_0^2 \pi^2} \right] + 1 \right\}. \quad (10.87)$$

The missing particle number must be computed from (10.1) as Campbell's formulae fail in this case. We get

$$N_d = \frac{-\frac{\gamma^2}{(1+2\gamma)^2} \left\{ -\frac{\gamma(5+6\gamma)}{4(1+2\gamma)(1+\gamma)^2} + \frac{1}{1+2\gamma} \left[ \frac{P(2\gamma-1)}{\pi\hbar n_0} + \frac{2P^2}{(\hbar n_0 \pi)^2} \right] + \frac{P}{\pi\hbar n_0} \left( 1 - \frac{2P}{\pi\hbar n_0} \right) \right\}}{\frac{1}{16} - \frac{1}{6(1+2\gamma)} - \frac{\gamma^4}{(1+2\gamma)^4} \left[ 1 - \frac{2P}{\pi\hbar n_0} \right]^2}, \quad (10.88)$$

$$v_s = \frac{\hbar n_0 \pi \gamma^2}{m(1 + 2\gamma)^2} \left( 1 - \frac{2P}{\hbar n_0 \pi} \right), \quad (10.89)$$

$$\Delta\phi = \frac{2(P - mN_d v_s)}{\hbar n_0}. \quad (10.90)$$

The masses read

$$m_P = \frac{-\frac{m\gamma^3}{(1+2\gamma)^3} \left( 1 - \frac{5+6\gamma}{4(1+\gamma)^2} \right)}{\frac{1}{16} - \frac{1}{6(1+2\gamma)}}, \quad (10.91)$$

$$m_I = -\frac{m(1 + 2\gamma)^2}{2\gamma^2}, \quad (10.92)$$

$$\frac{m_I}{m_P} = \frac{(1 + 2\gamma)^5 \frac{1}{16} - \frac{1}{6(1+2\gamma)}}{2\gamma^5 \left( 1 - \frac{5+6\gamma}{4(1+\gamma)^2} \right)}. \quad (10.93)$$

In the opposite limit of  $\gamma \rightarrow 0$ , only the ground state solution is known [189]. Its properties are

$$g(x) = \frac{1}{\pi} + \frac{1}{2\pi^2} \left[ \tan^{-1} \left( \frac{2(x+1)}{\lambda} \right) - \tan^{-1} \left( \frac{2(x-1)}{\lambda} \right) \right], \quad (10.94)$$

$$b = \frac{2\pi^2 n_0}{8\pi + 8 \tan^{-1}(4/\lambda) + \lambda \ln \left( \frac{\lambda^2}{16 + \lambda^2} \right)}, \quad (10.95)$$

$$\gamma = \frac{2\pi^2\lambda}{8\pi + 8\tan^{-1}(4/\lambda) + \lambda \ln(\frac{\lambda^2}{16+\lambda^2})}, \quad (10.96)$$

$$e = \frac{\pi^2}{12} + \frac{\gamma}{2}, \quad (10.97)$$

$$\mu = \frac{\hbar^2 n_0^2}{2m} \left( \frac{\pi^2}{4} + \gamma \right). \quad (10.98)$$

No results are available to date on excited state equations.

### 10.A.3 Repulsive Yang-Gaudin Model

The ground state properties in the limit  $\gamma \rightarrow \infty$  have been derived in [189]:

$$g(y) = \frac{\lambda}{2\pi\lambda - 4\ln(2)}, \quad (10.99)$$

$$a = \frac{n_0}{2g}, \quad (10.100)$$

$$\gamma = \frac{\lambda}{2g}, \quad (10.101)$$

$$e = \frac{1}{3(2g)^2}, \quad (10.102)$$

$$\mu = \frac{\hbar^2 n_0^2}{2m} \frac{1}{g^2} \left( \frac{1}{4} - \frac{\ln(2)}{6\pi\gamma g} \right). \quad (10.103)$$

As for excited states, the problem is no simpler than in the weak-coupling limit (where no solutions are available). We note that the integral bounds in the integral equations for  $f(x)$  diverge in this limit, i.e.,  $b/a \rightarrow \infty$  [189]. This implies that  $(x - x')^2$  [or  $(x - y)^2$  etc.] cannot be considered small compared to  $\lambda^2$  since  $x \in [-b/a, b/a]$  and  $b/a$  grows even faster than  $\lambda$ . Thus, no useful approximations can be made.

In the limit  $\gamma \rightarrow 0$ , only ground state results are known [189]:

$$g(y) = \frac{1}{\pi} - \frac{1}{2\pi^2} \left[ \tan^{-1} \left( \frac{\lambda}{y+1} \right) + \tan^{-1} \left( \frac{\lambda}{1-y} \right) \right], \quad (10.104)$$

$$a = \frac{2\pi^2 n_0}{3\pi + 2\tan^{-1}(\frac{2}{\lambda}) - 2\tan^{-1}(\frac{\lambda}{2}) - \lambda \ln(1 + \frac{4}{\lambda^2})}, \quad (10.105)$$

$$\gamma = \frac{2\pi^2\lambda}{3\pi + 2\tan^{-1}(\frac{2}{\lambda}) - 2\tan^{-1}(\frac{\lambda}{2}) - \lambda \ln(1 + \frac{4}{\lambda^2})}, \quad (10.106)$$

$$e = \frac{\pi^2}{12} + \frac{\gamma}{2}, \quad (10.107)$$

$$\mu = \frac{\hbar^2 n_0^2}{2m} \left( \frac{\pi^2}{4} + \gamma \right). \quad (10.108)$$

No approach has been proposed to tackle the excited state equations.

# Chapter 11

## Finite-System Approximation

In this chapter we will use concepts appropriate for dark solitons to obtain a simple approximation of the finite-system dispersion relation from the thermodynamic limit one. We test the derived formulae on Gross-Pitaevskii dark solitons and on Lieb-Liniger type-II excitations, finding excellent agreement in both cases. This serves as further evidence for the solitonic interpretation of type-II states. In the process, we also find an approximate Gross-Pitaevskii wavefunction for a dark soliton on a finite ring which is very accurate as long as the soliton is well-localised and much simpler mathematically than the exact result. Furthermore, the ability to correct thermodynamic limit quantities (such as the missing particle number) for finite-size effects will be invaluable to our work in chapter 12.

### 11.1 Introduction

Solitons and other nonlinear collective excitations in (quasi-)one-dimensional systems have been of rising interest over the recent years, particularly in cold-atom systems which provide an excellent platform to study such excitations because of the high precision and control that they offer [80]. The number of condensed atoms in the trap and the trap length (along the axial direction) in experiments are usually quite large, so that a thermodynamic limit description is appropriate [16, 21, 22, 72, 73]. Finite-size effects can be non-negligible, though (as smaller systems are beginning to be explored [56, 79]) and one may wish to account for them in some quick and easy way, without necessarily solving the full many-body system or the finite-size mean-field problem (as appropriate).

A key characteristic of any excitation is its dispersion relation, the excitation energy as a function of excitation momentum, which allows one to make various experimental predictions and extract useful information (such as the inertial mass [109]). Here we use simple arguments, starting from translational invariance, to derive an approximation to the finite-system dispersion relation based fully on thermodynamic limit results. We assume that the excitation is solitonic in nature, i.e. that it has a localized dip in the density profile and a phase step across the excitation. Furthermore, we assume that the soliton feature is well-localized and heals

to the constant background density to a reasonable degree within the constraints of the finite system.

Our derivation yields three different levels of approximation: the first produces an excellent approximation of both the dispersion relation and other properties of the excited state but requires more computational effort than the others. The second is the poorest approximation and has no advantages over the other two, while the third, being considerably simpler to evaluate than the first, performs just as well as the first for the dispersion relation approximation but is unable to correctly capture any other properties of the soliton.

The chapter is organized as follows: in section 11.2 we present the main derivation, while in sections 11.3 and 11.4 we apply the derived equations to Gross-Pitaevskii dark soliton and type-II hole excitations in the Lieb-Liniger model, respectively. In these sections we compare and contrast the three levels of approximation in a parameter regime where small differences between them can be seen. We also compare to the exact finite-system results which are available for both models. Finally, in section 11.5, we summarize the results.

## 11.2 The Derivation

We wish to find an approximation to the dispersion relation of a solitonic excitation in a finite system with  $N$  particles on a one-dimensional ring (i.e. with periodic boundary conditions) of length  $L$ . The formalism here is quite similar to that used in chapter 5. Consider a mean-field system described by a non-linear Schrödinger equation such as

$$0 = -i\hbar v_s \partial_z \psi + \frac{\hbar^2}{2m} \partial_{zz} \psi + \mu \psi - g [|\psi|^2] \psi, \quad (11.1)$$

where the only time-dependence of the solution is assumed to be translation at a constant speed  $v_s$  and the equation is written in the co-moving frame with  $z = x - v_s t$ . Furthermore,  $m$  is the mass of the constituent particles,  $\mu$  the chemical potential, and  $g [|\psi|^2]$  is some arbitrary function of the order parameter mod-squared (the non-linearity in the model stems from this term).

The grand canonical energy associated with this non-linear Schrödinger equation is

$$W[\psi] = \int \frac{\hbar^2}{2m} |\partial_z \psi|^2 - \mu |\psi|^2 + u[\psi] dz, \quad (11.2)$$

where  $u[\psi]$  is such that the functional-derivative of  $\int u[\psi] dz$  is  $g [|\psi|^2] \psi$ .  $W$  is linked to the canonical ensemble energy operator  $H$  through  $W = H - \mu N$ .

Let us assume we have some non-uniform, exact solution to this equation with open boundary conditions,  $\psi_s(z)$ . This solution is assumed to be solitonic in nature,

and in particular, it translates at constant velocity without changing shape, exhibits a localized dip in the density profile and has a phase step across the excitation.

It is possible to construct a periodic boundary condition wavefunction,  $\psi_{pbc}(z)$ , from  $\psi_s(z)$  at the expense of the solution becoming only accurate to order  $1/L$ :

$$\psi_{pbc} = \exp(i\Delta\phi z/L)\psi_s, \quad (11.3)$$

where  $\Delta\phi = -\arg[\psi_s(+\infty)] + \arg[\psi_s(-\infty)]$  is the phase step across the excitation. The additional phase factor guarantees that the phase is continuous and smooth across the boundaries.

When  $\psi_s$  is replaced by  $\psi_{pbc}$  in the energy functional of equation (11.2),  $W[\psi_{pbc}]$  gains two new terms not present in  $W[\psi_s]$ :  $v_{cf}P_s$  and  $\frac{1}{2}mv_{cf}^2\langle N\rangle_s$ , where  $P_s$  is the momentum in the state  $\psi_s$ ,  $v_{cf} = \frac{\hbar\Delta\phi}{mL}$  is the counter-flow velocity of the background superfluid, and  $\langle N\rangle_s$  is the number of particles in the state  $\psi_s$ . In fact, these are precisely the terms one would obtain by simply Galilean-boosting the system by  $v_{cf}$ .

For a soliton in an infinite system, the momentum functional,

$$P[\psi] = \int -\frac{i\hbar}{2}(\psi^*\partial_z\psi - \psi\partial_z\psi^*) dz, \quad (11.4)$$

evaluated at  $\psi_{pbc}$ , yields  $P_c = P_s + \hbar n_0\Delta\phi$  where  $n_0$  is the background density to which the soliton density heals far from the excitation.

Now, in the grand canonical ensemble one compares excited states (denoted below by subscript  $s$ ) to a background state (subscript  $BG$ ) at the same  $\mu$  (subscript  $\mu$ ), and in the canonical ensemble, to a ground state with the same  $N$  (subscript  $N$ ). We now turn to consider a finite system of length  $L$  with  $N$  particles.

Thus we want to construct  $\langle H\rangle_{s,N} - \langle H\rangle_{BG,N}$  (the canonical energy difference of an excited state and the ground state, both with  $N$  particles) starting from  $E_s = \langle W\rangle_{s,\mu} - \langle W\rangle_{BG,\mu} = \langle H\rangle_{s,\mu} - \mu\langle N\rangle_{s,\mu} - \langle H\rangle_{BG,\mu} + \mu\langle N\rangle_{BG,\mu} = \langle H\rangle_{s,\mu} - \langle H\rangle_{BG,\mu} - \mu N_d$ . Here,  $E_s$  is the grand canonical energy difference between an excited state and a background state, both at the same chemical potential  $\mu$ . Meantime,  $N_d$  is defined as the difference in particle number keeping  $\mu$  constant:  $N_d = \langle N\rangle_{s,\mu} - \langle N\rangle_{BG,\mu}$ . Note that we assume  $L$  is large enough for the density dip to heal to the background density to a reasonable degree, i.e. our solitonic excitation is well-localized in the finite system.

We associate  $\langle H\rangle_{s,\mu} + v_{cf}P_s + \frac{1}{2}mv_{cf}^2\langle N\rangle_{s,\mu}$  with  $\langle H\rangle_{s,N}$ . By virtue of this association, the excited state in the infinite system must have  $N$  particles when cut down to size  $L$ , so when  $\mu$  is kept constant, it is compared to a background state of density  $\frac{N-N_d}{L}$ . This means that when we evaluate  $E_s$ ,  $v_{cf}$ ,  $P_s$  and  $N_d$  for our energy approximation [see (11.5)], we need to calculate these four thermodynamic limit

quantities at a density which consistently solves  $\rho = \frac{N - N_d(\rho)}{L}$  where  $\rho$  is the required density, in general different from  $n_0 = N/L$ . Furthermore,  $\rho$  will be different at each point along the dispersion relation because  $N_d$  depends on the momentum.

Thus, we can write the finite-system energy approximation as

$$\begin{aligned} E_F &\equiv \langle H \rangle_{s,N} - \langle H \rangle_{BG,N} \approx E_s(\rho) + v_{cf}(\rho)P_s(\rho) \\ &+ \frac{1}{2}mv_{cf}^2(\rho)N + \langle H \rangle_{BG,\mu} - \langle H \rangle_{BG,N} + \mu(\rho)N_d(\rho). \end{aligned} \quad (11.5)$$

Let us see what the last three terms on the right-hand side above evaluate to.  $\langle H \rangle_{BG,N}$  has  $N$  particles and a uniform density of  $\frac{N}{L}$  while  $\langle H \rangle_{BG,\mu}$  has  $N - N_d(\rho)$  particles and a uniform density of  $\frac{N - N_d(\rho)}{L}$ . Furthermore, in the last term  $\mu(\rho)N_d(\rho)$ ,  $\mu$  is the chemical potential at the background density  $\rho = \frac{N - N_d(\rho)}{L}$ .

Since  $N_d(\rho)/L$  goes to zero in the thermodynamic limit, we can expand the ground state energy and chemical potential at density  $\rho$  as a Taylor expansion in the density about  $n_0$ . The energy needs to be expanded to second order while the chemical potential, to first.

We start from the energy:

$$\begin{aligned} \langle H \rangle_{BG,\mu} - \langle H \rangle_{BG,N} &= E_{GS}(\rho) - E_{GS}(n_0) \\ &\approx E_{GS}(n_0) + \left. \frac{dE_{GS}}{dn_0} \right|_{n_0} \times \left( \frac{-N_d(\rho)}{L} \right) + \frac{1}{2} \left. \frac{d^2E_{GS}}{dn_0^2} \right|_{n_0} \times \left( \frac{-N_d(\rho)}{L} \right)^2 - E_{GS}(n_0) \\ &= \left. \frac{dE_{GS}}{dN} \right|_{n_0} L \left( \frac{-N_d(\rho)}{L} \right) + \frac{1}{2} L \left. \frac{d\mu}{dn_0} \right|_{n_0} \left( \frac{-N_d(\rho)}{L} \right)^2 \\ &= -\mu(n_0)N_d(\rho) + \frac{N_d^2(\rho)}{2L} \left. \frac{d\mu}{dn_0} \right|_{n_0}. \end{aligned} \quad (11.6)$$

In the last two lines we use the definitions  $\frac{dE_{GS}}{dN} = \mu$  and  $n_0 = N/L$ , which allows us to obtain  $\frac{dE_{GS}}{dn_0} = L\mu$  and  $\frac{d^2E_{GS}}{dn_0^2} = L \frac{d\mu}{dn_0}$ , where during such derivatives with respect to  $n_0$ ,  $N$  is varied while  $L$  is held fixed.

Meantime, expanding the chemical potential:

$$\mu(\rho)N_d(\rho) \approx \mu(n_0)N_d(\rho) - \left. \frac{d\mu}{dn_0} \right|_{n_0} \frac{N_d^2(\rho)}{L}. \quad (11.7)$$

Combining the results of our Taylor expansions (11.6) and (11.7), the last three terms on the right-hand side of (11.5) are simply  $-\frac{N_d^2(\rho)}{2L} \left. \frac{d\mu}{dn_0} \right|_{n_0}$ . This allows us to write (11.5) as

$$E_F \approx E_s(\rho) + v_{cf}(\rho)P_s(\rho) + \frac{1}{2}mv_{cf}^2(\rho)N - \frac{N_d^2(\rho)}{2L} \left. \frac{d\mu}{dn_0} \right|_{n_0}. \quad (11.8)$$

As for the total momentum, we compute

$$P_F \approx mv_s(\rho)N_d(\rho) + n_0\hbar\Delta\phi(\rho). \quad (11.9)$$

Notice that the density in the second (counterflow) term is  $n_0$  and *not*  $\rho$ , because it is the momentum of the superflow in the excited state with  $N$  particles,  $mNv_{cf}$ .

Equations (11.8) and (11.9) constitute an approximation to the dispersion relation of the finite system which is fully based on thermodynamic limit results. However, in order to evaluate these expressions, one has to solve the consistency equation  $\rho = \frac{N-N_d(\rho)}{L}$  at each point along the dispersion relation. If simple, analytical thermodynamic limit results are available,  $\rho$  can be readily determined, but that is rarely the case. If the thermodynamic limit equations need to be solved numerically, solving for  $\rho$  introduces extra computational effort which, as we shall see, can be avoided.

On the other hand, the current level of approximation captures the real finite excited state quite well and such quantities as  $N_d$  and  $\Delta\phi$  (and even the density and phase profiles of the soliton,  $n_s(z)$  and  $\phi_s(z)$ ), are approximated well. In what follows, we find a simpler approximation for the dispersion relation, but not for the other properties of the excitation, for which one should turn to the full  $\rho$ -dependent quantities, as above.

Seeking a simpler expression for the dispersion relation, since we only need our approximation to be accurate to  $\mathcal{O}(\frac{1}{L})$ , we can expand all the thermodynamic limit quantities that are evaluated at  $\rho$  to first order about  $n_0$ . Firstly, the last three terms on the right-hand side of (11.8) are all  $\mathcal{O}(\frac{1}{L})$ , so only zeroth order terms in the expansions are kept, simply yielding  $v_{cf}(n_0)P_s(n_0) + \frac{1}{2}mv_{cf}^2(n_0)N - \frac{N_d^2(n_0)}{2L} \frac{d\mu}{dn_0} \Big|_{n_0}$ .

We start by expanding all the terms in the expression for the finite-system momentum:

$$\begin{aligned} P_F &\approx mv_s(n_0)N_d(n_0) + n_0\hbar\Delta\phi(n_0) - \frac{N_d(n_0)}{L}x(n_0) \\ &= P_c(n_0) - \frac{N_d(n_0)}{L}x(n_0) \end{aligned} \quad (11.10)$$

where  $N_d(\rho)$  is already replaced by  $N_d(n_0)$  since this term is proportional to  $1/L$  and

$$x(n_0) = mN_d(n_0) \frac{dv_s}{dn_0} \Big|_{n_0} + mv_s(n_0) \frac{dN_d}{dn_0} \Big|_{n_0} + \hbar n_0 \frac{d\Delta\phi}{dn_0} \Big|_{n_0}. \quad (11.11)$$

Note that  $x$  can be more concisely written as

$$x(n_0) = \frac{dP_c}{dn_0} \Big|_{n_0} - \hbar\Delta\phi(n_0). \quad (11.12)$$

In order to proceed, we also require a result obtained in chapter 5, which states that

$$N_d = \frac{-\left.\frac{dE_s}{d\mu}\right|_{v_s} + v_s \left.\frac{dP_c}{d\mu}\right|_{v_s} - \frac{v_s}{n_0} \frac{dn_0}{d\mu} P_c}{1 - \frac{mv_s^2}{n_0} \frac{dn_0}{d\mu}}. \quad (11.13)$$

The subscripts on the right of the derivatives now indicate which variables are to be held constant during differentiation. This equation can be rearranged for  $\left.\frac{dE_s}{d\mu}\right|_{v_s}$ , which we now need. Moreover, we point out that since  $\left.\frac{dE_s}{dP_c}\right|_{n_0} = v_s$ , it is clear that  $\left.\frac{dE_s}{dv_s}\right|_{n_0} = v_s \left.\frac{dP_c}{dv_s}\right|_{n_0}$ . Expanding  $E_s$  we find

$$\begin{aligned} E_s(\rho) &\approx E_s(n_0) - \frac{N_d(n_0)}{L} \left\{ -N_d \frac{d\mu}{dn_0} + \frac{mv_s^2 N_d}{n_0} \right. \\ &+ \left. v_s \left.\frac{dP_c}{dn_0}\right|_{v_s} - \frac{v_s P_c}{n_0} + v_s \left.\frac{dP_c}{dv_s}\right|_{n_0} \frac{dv_s}{dn_0} \right\} \\ &= E_s(n_0) + \frac{N_d^2(n_0)}{L} \frac{d\mu}{dn_0} - \frac{N_d(n_0)}{L} v_s x(n_0). \end{aligned} \quad (11.14)$$

Inserting this into (11.8) gives the finite-system energy as

$$E_F \approx E_s(n_0) + v_{cf}(n_0) P_s(n_0) + \frac{1}{2} m v_{cf}^2(n_0) N + \frac{N_d^2(n_0)}{2L} \left.\frac{d\mu}{dn_0}\right|_{n_0} - \frac{N_d(n_0)}{L} v_s x(n_0). \quad (11.15)$$

Since absolutely everything in (11.10) and (11.15) is now evaluated at  $n_0$ , we may drop the explicit dependence on  $n_0$  of all terms and define  $v_x = -x/(mL)$  so that  $P_F, E_F$  become

$$P_F \approx P_c + m v_x N_d, \quad (11.16)$$

$$E_F \approx E_s + v_x P_s + v_{cf} P_s + \frac{1}{2} m v_{cf}^2 N + \frac{N_d^2}{2L} \frac{d\mu}{dn_0}. \quad (11.17)$$

In the current form,  $P_F$  and  $E_F$  only differ from their  $\rho$ -dependent counterparts in terms of order  $1/L^2$ . We have succeeded in removing the need to compute  $\rho$  along the dispersion relation, but the current form still features  $v_x$ , a combination of rather cumbersome derivatives. In fact, it is possible to avoid the computation of  $v_x$  all together.

It is clear that the  $v_x$ -terms are  $\mathcal{O}(1/L)$  and as such, cannot be neglected on the basis of the accuracy of the expansion. Indeed,  $v_x$  itself is generally non-zero, neither is it always negligibly small. The  $v_x$ -terms make a non-negligible contribution to each of  $P_F$  and  $E_F$ . However, remarkably,  $E_F(P_F)$  is affected very little by the inclusion or exclusion of the  $x$ -terms. We now demonstrate how this comes about.

We notice that all the terms on the right-hand sides of (11.16) & (11.17) can be

thought of as functions of  $P_c$ , the thermodynamic limit momentum. We wish to eliminate the parameter  $P_c$  and directly express the finite-system dispersion relation as  $E_F(P_F)$ . Knowing that  $P_c = P_F - mv_x N_d$ , we can expand  $E_s(P_c)$  in momentum about  $E_s(P_F)$ :

$$E_s(P_c) \approx E_s(P_F) + \left. \frac{dE_s}{dP_c} \right|_{P_c} (-mv_x N_d), \quad (11.18)$$

where the derivative is already evaluated at  $P_c$  seeing as  $v_x \propto 1/L$ . In this manner we find

$$E_s(P_c) \approx E_s(P_F) - v_s m v_x N_d = E_s(P_F) - v_x P_s. \quad (11.19)$$

Substituting this into  $E_F$  leads to

$$E_F(P_F) \approx E_s(P_F) + v_{cf}(P_F)P_s(P_F) + \frac{1}{2}mv_{cf}^2(P_F)N + \frac{N_d^2(P_F)}{2L} \frac{d\mu}{dn_0}. \quad (11.20)$$

The last three terms in  $E_F$  are  $\mathcal{O}(1/L)$ , so we may freely change from evaluating them at  $P_c$  to evaluating them at  $P_F$ , since the differences are  $\mathcal{O}(1/L^2)$ .

Equation (11.20) shows that the energy of the finite system as a function of the total momentum does not feature the  $v_x$ -term. Now, since physically, the finite-system momentum must be confined to the same range as  $P_c$  in the thermodynamic limit, for convenience we may parametrize  $P_F$  as  $P_c$ , the thermodynamic limit momentum.

This means that the finite-system approximate dispersion relation,  $E_F(P_F)$ , can be found by computing

$$P_F \approx P_c, \quad (11.21)$$

$$E_F \approx E_s + v_{cf}P_s + \frac{1}{2}mv_{cf}^2N + \frac{N_d^2}{2L} \frac{d\mu}{dn_0}, \quad (11.22)$$

where  $P_c, E_s, v_{cf}, P_s, N_d$  are to be calculated in the thermodynamic limit at a fixed density  $n_0$ , and  $\frac{d\mu}{dn_0}$  is found for the ground state of the thermodynamic limit system, also at  $n_0$ .

This final result is an enormous simplification compared both to the approximation of equations (11.8) & (11.9), and to that of equations (11.16) & (11.17). It merely requires the thermodynamic limit equation of state [that is,  $\mu(n_0)$ ] and the thermodynamic limit excited-state properties  $P_c, E_s, \Delta\phi$  and  $N_d$ .

### 11.3 Gross-Pitaevskii Dark Solitons

An excellent test-case for the derived approximation is the Gross-Pitaevskii dark soliton, because an exact analytical solution of both the infinite case with open boundary conditions (keeping  $\mu$  constant) [59] and the finite case with periodic boundary conditions (keeping  $N$  constant) [105–108] is available. As such, we can

use the thermodynamic limit results to compute the approximation to the finite-system dark soliton dispersion relation and explicitly compare it to the exact result. Moreover, we can calculate the approximate dispersion relation at all three levels of approximation – at each stage of the general derivation of the previous section. This demonstration will serve to clarify the procedure and illustrate the success of the final result.

Dark solitons of the one-dimensional Gross-Pitaevskii equation [i.e. equation (11.1) with  $g(|\psi|^2) = g|\psi|^2$ ] on the infinite line have the following properties (chapter 2):

$$E_s = \frac{4\hbar\mu^{3/2}}{3g\sqrt{m}}(1-s^2)^{3/2}, \quad (11.23)$$

$$N_d = -\frac{2\hbar}{g}\sqrt{\frac{\mu}{m}}\sqrt{1-s^2}, \quad (11.24)$$

$$P_s = mv_s N_d = -\frac{2\mu\hbar}{g}s\sqrt{1-s^2}, \quad (11.25)$$

$$\Delta\phi = 2\cos^{-1}(s), \quad (11.26)$$

$$v_{cf} = \frac{\hbar\Delta\phi}{mL} = \frac{\hbar}{mL}2\cos^{-1}(s), \quad (11.27)$$

$$v_s = \sqrt{\frac{\mu}{m}}s, \quad (11.28)$$

$$\mu = n_0g, \quad (11.29)$$

$$\frac{d\mu}{dn_0} = g. \quad (11.30)$$

First, we wish to use equations (11.8) & (11.9), where  $E_s, v_{cf}, P_s, N_d$  are evaluated at  $\rho$ . Writing out the self-consistent condition for  $\rho$ ,

$$\rho = \frac{N + \frac{2\hbar}{g}\sqrt{\frac{\rho g}{m}}\sqrt{1-s^2}}{L}, \quad (11.31)$$

leads to the solution (choosing the positive sign in the quadratic formula)

$$\sqrt{\rho} = \frac{y + \sqrt{y^2 + LN}}{L}, \quad (11.32)$$

$$y = \frac{\hbar\sqrt{1-s^2}}{\sqrt{gm}}. \quad (11.33)$$

The thermodynamic limit quantities necessary for (11.8) & (11.9) are found by replacing  $\mu(n_0)$  in (11.23)-(11.28) by  $\mu(\rho) = g\rho$ .

We remark that the approximate finite momentum of equation (11.9) necessarily begins at 0 ( $s = 1$ ) and ends at  $2\pi\hbar n_0$  ( $s = -1$ ). This is guaranteed because  $N_d$  vanishes at  $s = \pm 1$ , and so  $\rho(s = \pm 1) = n_0$ . However,  $P_F$  is not restricted to this

range: it “overshoots” the end points (at some  $|s| < 1$ ) and then returns to the correct end points at  $s = \pm 1$ . This manifests as “folding” of the dispersion relation near the edges, and the affected region can be estimated by studying the zero-crossing of  $P_F$ . We find that the dispersion relation is approximated well (without unphysical folding) for

$$\frac{3}{N\sqrt{\gamma}} < \cos^{-1}(s) < \pi - \frac{3}{N\sqrt{\gamma}}, \quad (11.34)$$

where the soliton is localized sufficiently well. Here,  $\gamma = mg/\hbar^2 n_0$  is the Lieb-Liniger dimensionless interaction constant. The folding of the dispersion relation occurs over such a small momentum range for the parameters used in Fig. 11.1 that it is completely unresolvable on the scale of the plot.

Next, we will utilize expressions (11.16) & (11.17) which do not require the use of  $\rho$  but do involve the  $v_x$ -terms. For the dark soliton,  $x$  evaluates to  $x = -2\hbar s\sqrt{1-s^2}$ .

Finally, we can apply (11.21) & (11.22), the simplest formulae for which we only need the direct thermodynamic limit quantities listed in (11.23)-(11.28).

All three levels of approximation are plotted in Fig. 11.1 (a) (numbered consecutively from one to three in the order of derivation) for a specific set of parameters. We choose  $mg/n_0\hbar^2 = 2$  and  $N = 10$  because with these parameters, the soliton is fairly well-localized in the finite system, but not so small compared to the system size so that no difference between the three stages of approximation is visible.

The exact finite-system dispersion relation is also plotted in Fig. 11.1 according to the prescription of Refs. [107, 108] and [105, 106] (see appendix 2.A).

With reference to Fig. 11.1 (a), we see that the dispersion relation at the first – and thus most exact, as it involves the smallest number of approximations – level of approximation is indistinguishable from the exact result. The third level – the simplest to compute – is also excellent, only slightly under-estimating the exact energy. The second level is by far the worst, although increasing  $mg/n_0\hbar^2$  to 20 or  $N$  to 20 makes all three approximations overlap, so it is simply a question of degree of localization. It is remarkable that the third level approximation reproduces the correct shape of the dispersion relation better than the second.

In panel (b), we compare the exact dispersion relation to the approximation derived in section IV B of [105], starting from the general exact result and taking the limit of large rings. It is clear that this approximation is far less accurate when compared to ours: while it reproduces the central region of the dispersion relation well, towards the edges it merges with the system translation parabola and curves away from the true dispersion relation. Moreover, it is far more complicated to compute than our formulae (at either level). It is also numerically less robust: at the modest parameters of  $mg/n_0\hbar^2 = 2, N = 10$ , for a significant number of the

points that are meant to lie on the soliton dispersion relation, the procedure actually returns excited states of the uniform background – simple superflow, a translation of the constant density solution – resulting in points that lie on the translation parabola and not on the dark soliton dispersion relation.

To conclude the section, we emphasize that the first level approximation can be used to approximate all other properties of the excited state, not just the dispersion relation. For example, the density and phase profiles of the solution can be well approximated, again based on the thermodynamic limit results. The thermodynamic limit dark soliton solution is  $\psi_s(x) = \sqrt{n_s(z)}e^{i\phi_s(z)}$  where

$$n_s(z) = n_0^2 \left[ s^2 + (1 - s^2) \tanh^2 \left( a\sqrt{1 - s^2}z \right) \right] \quad (11.35)$$

with  $a = \frac{\sqrt{mgn_0}}{\hbar}$ , while the phase is given by

$$\phi_s(z) = \tan^{-1} \left\{ \frac{s}{\sqrt{1 - s^2} \tanh(a\sqrt{1 - s^2}z)} \right\}. \quad (11.36)$$

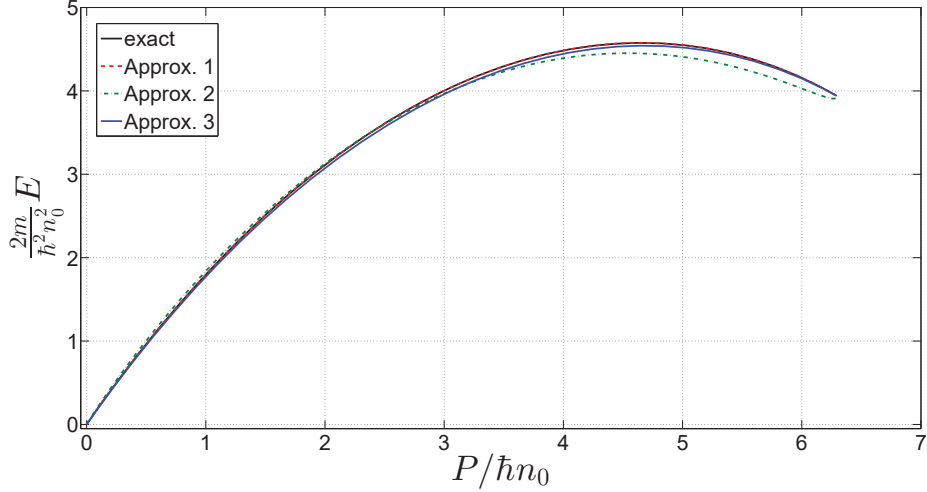
The finite-system approximation of the profiles is obtained by replacing  $n_0$  by  $\rho$  and adding the counter-flow term to the phase:  $\frac{\Delta\phi z}{L}$  [recall that  $\psi_{pb} = \exp(i\Delta\phi z/L)\psi_s$ ].

These approximate equations compare well to the exact profiles, all along the dispersion relation. This is shown in Fig. 11.2, where we give two examples: one close at the edge, at  $P_c = 0.5\hbar n_0$ , and the other close to the center, at  $P_c = 4\hbar n_0$ . In both cases, the approximation is superb. Consequently, if we define the missing particle number  $N_d$  in a finite system with  $N$  particles as  $N - n_{max}L$  where  $n_{max}$  is the maximal density in the soliton state, then we would expect  $N_d(\rho)$  from the first level approximation to match extremely closely with the exact result. A direct comparison is shown in Fig. 11.3: we see that the approximate  $N_d$  is indeed close, but lies lower (at more negative values) than the exact result near the edges of the dispersion relation. This occurs because the finite soliton density does not fully heal to the background –  $L$  is not large enough. This leads to  $n_{max} < n_0$  and causes the visible difference in Fig. 11.3, while the density profile itself is reproduced perfectly.

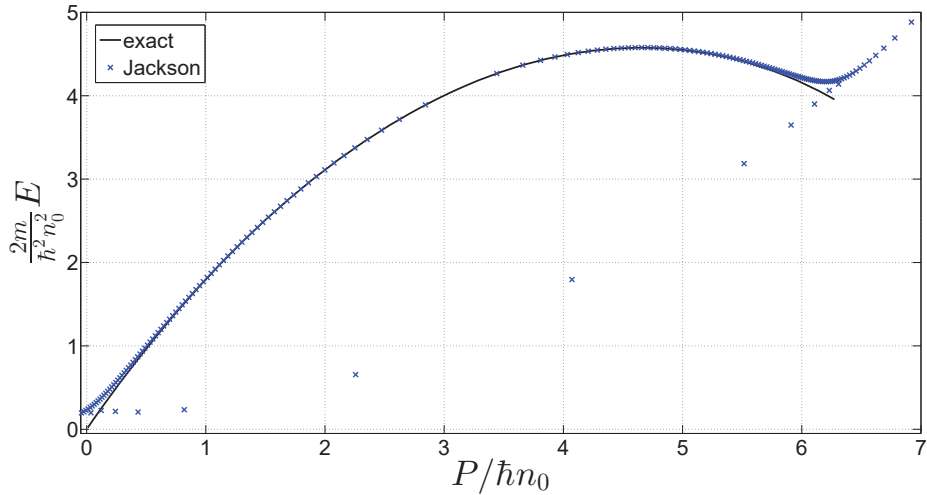
As a final note, we point out that this approximation of the finite dark soliton wavefunction is used in chapter 12 to perform an analytical calculation which would be impractical using the exact solution.

## 11.4 Lieb-Liniger Type-II Excitations

The second example we present is type-II excitations in the Lieb-Liniger model [46, 47]. As we have seen, it is exactly solvable by the Bethe ansatz, both for finite systems and in the thermodynamic limit. Type-II states have long been associated



(a)



(b)

Figure 11.1: Dispersion relation for dark solitons in the one-dimensional Gross-Pitaevskii equation with  $mg/n_0\hbar^2 = 2$ ,  $N = 10$ . Plotted as a black solid line (on both panels) is the exact result, calculated according to Refs. [107, 108] and [105, 106]. In (a), we show all three levels of approximation as derived in section 11.2: using (11.8) & (11.9) – red dashed line, using (11.16) & (11.17) – green dash-dotted line, and using (11.21) & (11.22) – blue dashed line. The first level of approximation is the most accurate and is indistinguishable from the exact result. The third level is very close to the exact dispersion relation and has the correct shape, only slightly under-estimating the energy. The second level is furthest from the true dispersion relation, and has a visibly incorrect shape. This is alleviated at higher values of  $mg/n_0\hbar^2$  &  $N$  where no difference between the three levels of approximation can be seen. In (b), we compare the exact result to a previously published approximation of the dark soliton finite-system dispersion relation in the limit of large rings (see [105], section IV B). This recipe performs well near the middle of the dispersion relation but near the edges, deviates from the exact result considerably, instead merging into the system translation parabola – a translated uniform superfluid state.

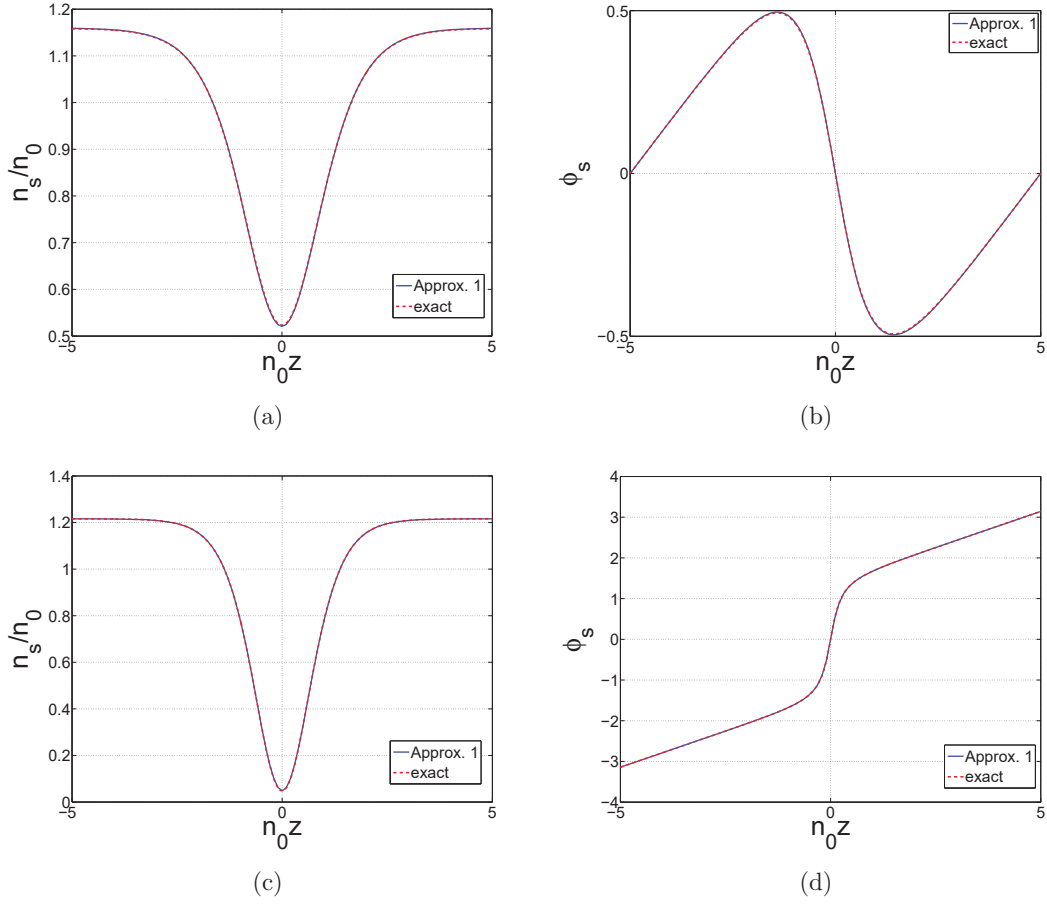


Figure 11.2: Density and phase profiles for dark solitons in the one-dimensional Gross-Pitaevskii equation with  $mg/n_0 \hbar^2 = 2$ ,  $N = 10$ . (a) & (b) are plotted at  $P_c = 0.5 \hbar n_0$ , while (c) & (d) at  $P_c = 4 \hbar n_0$ . The blue solid line shows the approximation, while the red dashed line shows the exact result, calculated according to Refs. [107, 108] and [105, 106]. The agreement is essentially perfect in both cases.

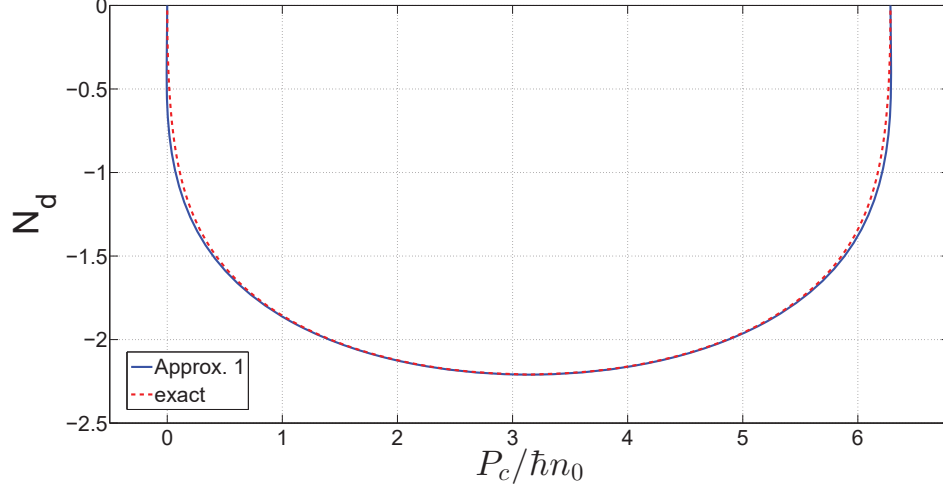


Figure 11.3: The missing particle number  $N_d$  for dark solitons in the one-dimensional Gross-Pitaevskii equation with  $mg/n_0\hbar^2 = 2$ ,  $N = 10$ .  $N_d(\rho)$  is plotted as a blue solid line, while the red dashed line shows the “exact result” [105–108], defined in a finite system as  $N - n_{max}L$  where  $n_{max}$  is the maximal density in the soliton state. The small discrepancy visible on either side of the center point is fully due to the fact that in a finite system of length  $L$ , the dark soliton density does not heal all the way to  $n_0$  at  $\pm L/2$ , and therefore,  $n_{max} < n_0$ .

with dark solitons, and have an extremely similar dispersion relation [60]. This motivates us to apply our finite-system approximation to these excitations and examine how closely the finite-system dispersion relation is reproduced. After all, the derivation of section 11.2 is strongly based on the *solitonic* nature of the excited state, so a successful approximation would indicate that the assumptions are, at least to some degree, justified. In a way, this complements our work in chapter 12.

The finite Bethe ansatz equations and quantum numbers for the ground state and type-II excitations can be found in chapter 7 while the thermodynamic limit is reviewed in chapter 9. Moreover, in chapter 10, details are also given as to how one can compute  $N_d$  and  $\Delta\phi$  (all at a constant background density,  $n_0$ ). Armed with these key quantities, we can find  $P_s = mv_s N_d$  and  $v_{cf} = \frac{\hbar\Delta\phi}{mL}$  and easily evaluate the third level of approximation, equations (11.21) & (11.22).

To obtain the second level of approximation, we simply need to calculate  $v_x$ , necessary for (11.16) & (11.17). In the Lieb-Liniger model the natural dimensionless parameter that parametrizes the excitation is  $q$  – see chapter 9 for details. In the notation of chapter 10,  $x$  can be calculated as

$$x = \frac{dP_c}{dn_0} - \hbar\Delta\phi = \frac{1}{\sqrt{f_1}}(f_3 - q) \left( 1 + \frac{\gamma}{2f_1} \frac{df_1}{d\gamma} \right) - \frac{\gamma}{\sqrt{f_1}} \frac{df_3}{d\gamma} - \hbar\Delta\phi. \quad (11.37)$$

Finally, to compute the first level of approximation with a changing background density  $\rho$ , the following is done: we choose  $c$  and  $n_0$  and find the appropriate  $\lambda$  that yields  $\gamma = c/n_0$ . This is achieved with the Matlab function `fminsearch.m` (an implementation of the simplex search algorithm), which is used for optimization throughout the first level approximation procedure. At this  $\lambda(n_0)$ , we calculate  $\frac{d\mu}{dn_0}$ . Then at each  $q \in [-1, 1]$ , we use functional minimization to calculate the  $\lambda$  that gives  $\rho(\lambda)$  which solves the consistency condition for  $\rho$ . During this optimization,  $N_d$  is calculated using Campbell's formula, which only requires the ground- and excited-state integral equations to be solved once for each iteration over  $\lambda$ .

Once the optimal  $\lambda(\rho)$  is found at a given fixed  $q$ , we solve the ground- and excited-state integral equations at this  $\lambda(\rho)$  and  $q$ , and calculate  $P, E, N_d, \Delta\phi$ , (the latter two according to Campbell's formulae, which are far more numerically efficient). The velocity is evaluated as

$$v_s = \frac{n_0}{\sqrt{f_1}} \left\{ \begin{array}{l} -2q + \frac{df_2}{dq} \\ -1 + \frac{df_3}{dq} \end{array} \right\}, \quad (11.38)$$

which requires the excited-state to be solved for twice more, on either side of  $q$ , to allow for the numerical evaluation of the derivatives with respect to  $q$  (during which  $\lambda$  is clearly held constant).

This procedure yields all the necessary quantities for equations (11.8) & (11.9), with the association  $E_s = E$  the thermodynamic limit excitation energy of the type-II state in the canonical ensemble<sup>1</sup>. Numerically, such a calculation is fairly efficient on a standard desktop machine, taking perhaps 30 seconds to compute.

The comparison of our approximations to the exact dispersion relation is shown in Fig. 11.4 for  $\gamma = 1, N = 10$  and the result is very encouraging indeed. The close agreement suggests that our approximation is not restricted to truly superfluid systems, and is further evidence that type-II excitations *can* be interpreted as dark solitons (see chapter 12 for details). The simplest, third level approximation underestimates the energy somewhat, while the first over-estimates it (in contrast to the Gross-Pitaevskii dark soliton example above where it yields perfect agreement). The intermediate, second level approximation is once again the worst, with deviations in the form of the curve very similar to what we have seen for the dark soliton.

It is immediately obvious that the momentum range at level one (with a varying background density  $\rho$ ) and two (with the  $x$ -terms included) is incorrect. The approximate finite-system momentum of (11.9) & (11.16) extends to either side beyond the physical range of  $[0, 2\pi]\hbar n_0$ . This occurs because  $N_d$  of type-II excitations does not vanish at the edges of the dispersion relation (see chapter 10) and so we do not get

---

<sup>1</sup>Recall equations (5.40) & (5.41), showing that the two are interchangeable up to terms  $\mathcal{O}(1/L^2)$ .

$\rho = n_0$  at the edges, as we do for dark solitons. However, with this understanding, the appropriate dispersion relation, restricted to the correct momentum range, is in close agreement with the exact result.

Once again we stress that the parameters used for the illustration of Fig. 11.4 were chosen so that our approximation is applicable, and yet visible differences exist between the three levels of approximation and the exact result. Increasing either one of  $\gamma$  or  $N$  improves the agreement between all data sets shown until they are indistinguishable.

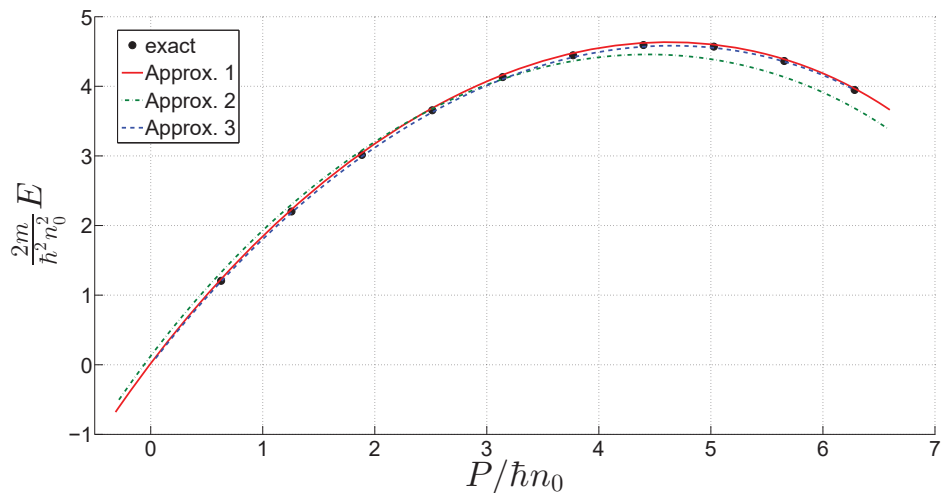


Figure 11.4: Dispersion relation for type-II excitations in the Lieb-Liniger model with  $\gamma = 1$ ,  $N = 10$ . Black circles show the exact finite dispersion relation, red solid line – equations (11.8) & (11.9), green dash-dotted line – equations (11.16) & (11.17), and blue dashed line – results of (11.21) & (11.22). Once again, the third level of approximation is very close to the exact dispersion relation, only slightly under-estimating the energy, while the first level over-estimates the energy. The second level is furthest from the true dispersion relation, falling considerably short of the real energy for higher momenta, in the same way as for Gross-Pitaevskii dark solitons. The approximations agree much better with each other and the exact result for higher  $\gamma, N$  in this case, too. In the first and second levels of approximation, the momentum range is larger than physically allowed because  $N_d$  is non-zero at  $q = \pm 1$  (the edges of the dispersion relation) and therefore we do not get  $\rho = n_0$  at these points, thus extending the momentum range.

As a final note, all three levels of approximation can be computed analytically in the Tonks-Girardeau limit, as well as the exact finite-system dispersion relation. The Tonks-Girardeau gas is equivalent to a (single-component) gas of free fermions, so the properties of the ground state and hole excitations are readily computed. Remarkably, both the first and third level approximations reproduce the finite dispersion exactly.

## 11.5 Discussion and Conclusions

Our derivation was carried out for a general superfluid system in one dimension, respecting Galilean invariance. For a localized excitation with solitonic properties (a density dip and a phase jump), we were able to reconstruct the finite-system dispersion relation (holding  $N$  constant) from the thermodynamic limit dispersion relation (holding  $\mu$  constant). Largely, this was possible due to the assumption that  $L$  is larger than the healing length of the soliton and thus the density in the excited state heals to the background  $n_0$  at the boundaries. In broad terms, the energy has to be corrected by adding the contribution of the counterflow, present due to periodic boundary conditions and finite  $L$ , as well as a term that can be thought of as a correction to the ground state energy. The momentum expression, on the other hand, is of the same form as in the thermodynamic limit since the counterflow momentum is finite even in an infinite system.

We note that it is not necessary to assume the system obeys the non-linear Schrödinger equation, (11.1). In fact, it is sufficient to assume superfluidity, so that the order parameter has a coherent phase the spatial derivative of which gives rise to super-currents, and translational/Galilean invariance. The contribution to the energy from the counterflow can be simply obtained by performing a Galilean boost to velocity  $v_{cf}$ , as mentioned earlier, leaving the rest of the derivation unaffected. Moreover, the logic is not constrained to pure one-dimensional systems. The arguments can easily be generalized to an elongated three-dimensional geometry as long as the density vanishes far from the longitudinal axis and translational invariance is maintained in the longitudinal direction. In the three-dimensional case, the only point of difference is that the one-dimensional density is replaced by a linear density, given by the three-dimensional density integrated over the radial and azimuthal directions.

Our principal argument has led to equations (11.8) and (11.9), which we consequently referred to as the first level approximation. While simple in form, they require one to solve for  $\rho$ , the self-consistent, modified background density, at each point along the dispersion relation. The advantage of this approximation is that, as we have shown in section 11.3, it allows one to accurately obtain other properties of the excitation, such as the density and phase profiles, as well as  $N_d$  and  $\Delta\phi$ .

Equations (11.21) and (11.22) are the final, simplest expressions referred to as the third level of approximation. These have a form as simple as those at the first level, but conveniently are evaluated at the constant background density  $n_0$ , which is a significant simplification. In terms of reproducing the correct dispersion relation, the third level equations are practically as accurate as the first – so much so that in most cases, the additional computational cost of the first level approximation is

hardly justified.

The intermediate, second level equations (11.16) and (11.17) have shown the poorest performance out of all three levels. These are also evaluated at  $n_0$  but have additional terms that are difficult to compute and, as we have shown, unnecessary. It is remarkable that the third level equations yield better results than the second (on which they are based) for larger healing-length-to-system-size ratios, thus solidifying the conclusion that in order to approximate the dispersion relation, the third and simplest set of equations is best used. Finally, we confirmed that when the size of the soliton compared to system size decreases, all three approximations become equivalent.

We have used one-dimensional Gross-Pitaevskii dark solitons and Lieb-Liniger type-II excitations (solved by the Bethe ansatz) to illustrate how the approximations are to be computed, and evaluated their performance by comparing to exact results. In so doing, Refs. [105–108] were incredibly useful as they have found exact dark soliton solutions of the one-dimensional Gross-Pitaevskii equation, and our work in chapter 10 provided the necessary technical details to easily evaluate the approximations for the Lieb-Liniger model. The success of the approximation in the Lieb-Liniger model for states that technically satisfy none of the assumptions on which the derivation is based shows the potential of our result as an investigative tool: if the physical nature of some excitation is unknown, the level of accuracy of our approximation can shed light on the matter, while requiring only “global” measurements or calculations.

# Chapter 12

## Quantum Dark Solitons

In this chapter we finally address the main research question of the thesis – the connection of Lieb-Liniger type-II states to Gross-Pitaevskii dark solitons. So far, we have seen that the two types of excitations have very similar dispersion relations – in the thermodynamic limit & for finite systems with small particle numbers, with weak to intermediate interactions. Furthermore, the missing particle number and phase step of type-II excitations approached the Gross-Pitaevskii dark soliton quantities in the limit as  $\gamma \rightarrow 0$ . In addition, the finite-system approximation, derived for well-localized dark solitons in a superfluid, performed superbly for Lieb-Liniger type-II states. All these observations constitute evidence for a fundamental relation between dark solitons and type-II states, underlining their many common properties. We now turn to search for this link.

### 12.1 Introduction

Recall that dark solitons are nonlinear solutions of the one-dimensional Gross-Pitaevskii equation, characterized by a density dip and a phase step across the excitation (chapter 2), observed experimentally [16, 21, 22] in ultra-cold atomic Bose-Einstein condensates [12, 13]. In addition to dark solitons in an infinite system [20], solutions on finite rings are also analytically known [105–108, 113]. Dark solitons are dynamically stable in a one-dimensional configuration (in three dimensions they decay via the snaking instability [110, 154]) and can be observed for experimentally long periods of time [111, 193] as they propagate (on a uniform background) at constant speed and without changing shape. Moreover, in a spinless one-dimensional system, they constitute the lowest energy excitations of the Gross-Pitaevskii equation, and as such, have attracted much attention.

Now, the one-dimensional Bose gas with repulsive contact interactions and periodic boundary conditions is described by the Lieb-Liniger model [46, 47], and can be solved exactly with the Bethe ansatz [52]. The weak-coupling limit of the Lieb-Liniger model is well captured by Gross-Pitaevskii physics, while the strong-coupling limit is the Tonks-Girardeau gas (mappable to a free Fermi system), realized experimentally in [74, 75]. The Lieb-Liniger model famously features two types

of elementary excitations – type-I (particles) and type-II (holes), which have been recently probed through their dynamical response functions [56]. A theoretical proposal to access the type-II states directly is also available [194]. These elementary excitations are eigenstates of the momentum operator (which commutes with the Hamiltonian) and are thus necessarily spatially uniform. Type-I excitations have been interpreted as the Bogoliubov phonon branch, while the nature of the type-II states has (initially) been more illusive.

Ishikawa and Takayama [60] were the first to suggest a connection between type-II excitations of the Lieb-Liniger model and dark solitons of the Gross-Pitaevskii equation: they showed that the dispersion relations (excitation energy versus momentum) become identical as the coupling strength vanishes. Not long after, the closely-related bright-soliton case (relevant for attractive interactions) was considered: [195] has analytically shown that the order parameter of the Gross-Pitaevskii equation is the large-particle-number limit of the matrix element of the field operator between superposition states of Bethe ansatz eigenstates with particle number differing by one. Meanwhile [174, 175] have argued that quantum soliton states are constructed by either making a product state of the mean-field soliton solution (Hartree approximation) or taking a superposition of the Bethe ansatz eigenstates of different momentum and particle density. A very recent paper on quantum bright solitons is [173] where the single-particle density matrix is computed, and bright solitons are identified as superpositions of string states [170].

Returning to dark solitons, there have been numerous works illuminating the connection to type-II states by various approaches. As an example, [196, 197] compare statistical distributions at high temperatures and show that the number of dark solitons and type-II excitations at a given momentum match. Astrakharchic and Pitaevskii [148] compute solitonic properties for type-II excitations, notably the effective missing particle number, which is certainly motivated by the solitonic interpretation of these states. A series of papers [61–63, 198–200] address the greying of the density notch of a dark soliton when evolved under the full quantum-mechanical Hamiltonian and explain the effect as filling with depleted atoms. Moreover, a strong case is made for the idea that the theoretical tools used to predict the greying are simply reporting on an ensemble average of many realizations, and that in any given run of the experiment, the soliton will not fill up but be found at random positions along the ring.

Crucially, this line of argument culminated in two remarkable studies: [64] has used time-evolving block decimation to demonstrate that indeed, while the single-particle density shows the solitonic dip filling up, individual trajectories find the soliton shape unaltered, but its position shifted around the ring. The distribution of the soliton’s position around the ring is found to be Gaussian, and the width of

the Gaussian grows quadratically in time. The second study of particular interest is [65, 66], which uses the Bethe ansatz to model a position measurement performed on a type-II state, and finds that a dark soliton profile emerges at random positions around the ring. In other words, one can think of type-II states as being constructed from dark solitons, translated all around the ring, restoring spatial symmetry.

In parallel, a different group has been pursuing the idea that dark solitons can be constructed as superpositions of type-II states [201–204], making use of the algebraic Bethe ansatz [96, 97, 205–207] to obtain convenient formulae for matrix elements of the density and field operators. We believe that the definition of the dark soliton (and in particular, the expansion coefficients) adopted in these papers are incorrect, and provide the appropriate expressions in the present chapter.

Meanwhile, there have been endeavours to find dark solitons in Fermi condensates [14, 15, 72, 73], which is in some ways quite relevant to the problem addressed here because a simple mean-field description is usually not possible for fermions (it is only applicable in the strongly-bound case when the dimers can be thought of as a Bose-Einstein condensate – see [82, 186–188]). In particular, at unitarity where the scattering length diverges, there is no known good theory to describe the three-dimensional gas. As a result, several initiatives have been taken: [208] uses the local density approximation, [155, 209, 210] solve the three-dimensional Bogoliubov de-Gennes equations numerically, and approximate analytical studies of the three-dimensional case (complimented by full numerical Bogoliubov de-Gennes simulations) are done in [109, 147]. In one dimension, [68] analytically solves the mean-field Bogoliubov de-Gennes equations, while [67] employs the Bethe ansatz to identify dark solitons with lowest-energy type-II excitations in the Yang-Gaudin model [48, 49].

In this chapter, then, we continue two prominent lines of investigation, the first of which is the idea that dark solitons may be constructed as superpositions of type-II states. The authors of [201–204] express a dark soliton as a superposition of all type-II states in the momentum interval  $[0, 2\pi n_0 \hbar]$  with equal weights. There is a clear problem with this proposition: such a momentum distribution has a mean value of  $\pi \hbar n_0$ , and so at best, this could only (possibly) correspond to a stationary soliton. We will see that localized momentum distributions (e.g. Gaussians) for the expansion coefficients allow us to create objects which behave much like solitons at any momentum value. In fact, in the weakly-interacting regime, we will use the Gross-Pitaevskii dark soliton wavefunction to extract these distributions and show that the correct dark soliton is reproduced by this construction.

The second idea we will pursue is related to [64]. Taking inspiration from work on bright solitons [175] (specifically, equation (3.8) of this paper) and [211], we hypothesize that the density profiles of the various localized momentum-space su-

perpositions evolved to any arbitrary time, can be described by the convolution of some fundamental solitonic density profile with a center-of-mass of the missing particles Gaussian density. This concept is, of course, fully consistent with the findings of [64]. Furthermore, [211] demonstrates that for bright solitons, this convolution model is always applicable as long as the Hamiltonian separates into center-of-mass and relative-motion parts, and that the variance of the single-particle density is the sum of the variances of the convolutants. Since the center-of-mass density obeys analytically predictable spreading, and since the data follows the predicted trends very closely, these assumptions allow for the direct extraction of the width of the fundamental, underlining quantum dark soliton.

Now, the ideas of the previous two paragraphs are closely intertwined: if dark solitons are localized momentum-space superpositions of uniform type-II states, and type-II states are uniform superpositions of dark solitons shifted around the ring, it follows that perhaps dark soliton-like objects can be formed by a localized spatial superposition of some fundamental dark soliton translated around the ring. This is equivalent to saying that dark soliton-like density profiles resulting from localized type-II superpositions can be modelled by the convolution of a localized distribution in physical space with an underlying solitonic density.

The chapter is structured as follows. We begin by recalling the Lieb-Liniger Hamiltonian in section 12.2, together with the Bethe ansatz equations necessary to find type-II excitations. In section 12.3 we introduce the idea of constructing a superposition of type-II states with arbitrary coefficients and show how the density and phase profiles of this state can be computed. Moreover, we give an approximate method of obtaining the current, from which the phase step across the soliton may be extracted. Then, in 12.3.1 we show the specific formulae for the matrix elements necessary for evaluation of the density and phase from the algebraic Bethe ansatz. In 12.3.2 we specialize to Gaussian expansion coefficients and in 12.3.2.1 compute the corresponding density profile (approximately) in the Tonks-Girardeau limit. Next, in 12.3.3 we derive the expansion coefficients necessary to produce Gross-Pitaevskii dark solitons and study the behaviour of this distribution with changing parameters. The main results are presented in sections 12.4 and 12.5, exploring various properties of the superposition states and the length scale of the quantum dark soliton, respectively. Discussion and conclusions are given in section 12.6.

## 12.2 Lieb-Liniger Model

Recall that the Lieb-Liniger model describes a system of  $N$  spinless bosons on a ring of length  $L$ , interacting via a repulsive two-body contact potential. The Hamiltonian is given by (6.1). As always, define the dimensionless interaction parameter  $\gamma = \frac{c}{n_0}$ ,

where  $n_0 = N/L$  is the one-dimensional density.

Hamiltonian (6.1) can be diagonalized by the Bethe ansatz, culminating in a set of nonlinear coupled equations for  $N$  rapidities,  $\{k_j\}$ , initially-unknown quasimomenta that feature in the ansatz for the wavefunction (chapter 6). For a finite system, these can be found in chapter 7, together with the quantum numbers corresponding to the ground state and type-II excitations. The energy of Bethe ansatz states is denoted by  $E$  and the momentum by  $p$ .

### 12.3 Superpositions of Type-II States

Consider some arbitrary superposition of type-II eigenstates of the Lieb-Liniger model with  $N$  particles, which we may write as

$$|S_{p_0}, N\rangle = \sum_p C_{p,N}^{p_0} |p, N\rangle, \quad (12.1)$$

where  $|p, N\rangle$  is a type-II state with momentum  $p$  and energy  $E_p$ , and  $C_{p,N}^{p_0}$  are coefficients centred at  $p_0$ . In order for the superposition state to be normalized, we need

$$\sum_p |C_{p,N}^{p_0}|^2 = 1. \quad (12.2)$$

The single-particle density of this state can be found from

$$\begin{aligned} \langle S_{p_0}, N | \rho(x, t) | S_{p_0}, N \rangle &= \sum_{p,p'} C_{p',N}^{p_0*} C_{p,N}^{p_0} \langle p' | \rho(0, 0) | p \rangle \\ &\exp [i(p - p')(x - x_0)/\hbar - i(E_p - E_{p'})t/\hbar], \end{aligned} \quad (12.3)$$

where  $\rho = \psi^\dagger \psi$  is the density operator. If we wish to associate a phase with this state, then one possible choice is the phase of the matrix element of  $\psi(x)$ , taken between states with particle number differing by one. The matrix element of the field operator is

$$\begin{aligned} \langle S_{p_0}, N - 1 | \psi(x) | S_{p_0}, N \rangle &= \sum_p \sum_{p'}^{N-1} C_{p',N-1}^{p_0*} C_{p,N}^{p_0} \\ &\exp [i(p - p')(x - x_0)/\hbar] \langle p', N - 1 | \psi(0) | p, N \rangle. \end{aligned} \quad (12.4)$$

Note that in contrast to the density, the time evolution of (12.4) is not trivially known. Thus one can take the phase of the superposition state (12.1) as the phase of the matrix element (12.4). If such a correspondence is to be trusted, then one would hope that  $|\langle S_{p_0}, N - 1 | \psi(x) | S_{p_0}, N \rangle|^2$  would closely match the density profile,

$\langle S_{p_0}, N | \rho(x, t) | S_{p_0}, N \rangle$ . One could define

$$r_p = \int dx |\langle S_{p_0}, N - 1 | \psi(x) | S_{p_0}, N \rangle|^2, \quad (12.5)$$

so that the saturation ratio  $r_p/N < 1$  would quantify the consistency of the calculation: if the saturation is close to unity, we can have confidence in the results, and *vice versa*.

Once the phase profile is obtained, we can extract the phase step across the soliton,  $\Delta\phi$ , which in infinite systems with open boundary conditions is defined as  $\Delta\phi = \phi_s(-\infty) - \phi_s(\infty)$ , where  $\phi_s(x)$  is the phase profile. In a finite system  $\Delta\phi$  can be extracted from gradient of the phase far from the location of the soliton: we assume that the infinite-system phase is related to the finite-system phase by the addition of a linear function in position,  $\Delta\phi x/L$ . This is fully justified when the soliton is well localized in the ring (see chapter 11).

There is another possible method of computing the phase step. Let us write

$$\begin{aligned} \langle S_{p_0}, N | \psi^\dagger(x)\psi(x') | S_{p_0}, N \rangle &= \sum_{\nu} \langle S_{p_0}, N | \psi^\dagger(x) | \nu, N - 1 \rangle \\ &\langle \nu, N - 1 | \psi(x') | S_{p_0}, N \rangle, \end{aligned} \quad (12.6)$$

where we have inserted an identity expanded over the kets  $|\nu, N - 1\rangle$ , comprising a complete basis for the  $(N - 1)$ -particle Hilbert space. Unfortunately, the exact evaluation of the single-particle density matrix is very computationally intensive [55], but if we make the approximation of only including the type-II Bethe ansatz states in the expansion of the identity, the resulting expression is easily computed. Substituting (12.1) into (12.6), we obtain

$$\begin{aligned} \langle S_{p_0}, N | \psi^\dagger(x)\psi(x') | S_{p_0}, N \rangle &\approx \sum_{p, p', k} C_{p, N}^{p_0*} C_{p', N}^{p_0} \exp[-i(p - k)(x - x_0)/\hbar] \\ &\exp[i(p' - k)(x' - x_0)/\hbar] \langle p, N | \psi^\dagger(0) | k, N - 1 \rangle \langle k, N - 1 | \psi(0) | p', N \rangle. \end{aligned} \quad (12.7)$$

Setting  $x = x'$  yields another approximation to the density profile. Similarly to (12.5), we can define  $r_j$  as the integral over  $x$  of this approximate density and the saturation  $r_j/N < 1$  once again acts as an indicator of the quality of the approximation.

The single-particle density matrix can also be used to calculate the current:

$$\langle j(x) \rangle = \frac{\hbar}{2mi} \left\{ \partial_{x'} \langle \psi^\dagger(x)\psi(x') \rangle \Big|_{x'=x} - \partial_x \langle \psi^\dagger(x)\psi(x') \rangle \Big|_{x'=x} \right\}, \quad (12.8)$$

where the expectation value is taken with respect to (12.1). Once the current is

obtained, the phase step can be calculated as

$$\Delta\phi = \frac{j_0 m L}{n_0 \hbar}, \quad (12.9)$$

since far from the soliton the only contributor to the current is the backflow of the entire fluid at velocity  $v_{cf} = \frac{\hbar \Delta\phi}{mL}$ , present due to periodic boundary conditions. In the above,  $j_0$  is the current far from the soliton.

Finally, for future reference, let us also define

$$R = \int dx m \langle j(x) \rangle, \quad (12.10)$$

which is the momentum carried by the current.

### 12.3.1 Algebraic Bethe Ansatz

In order to evaluate the density and field operator expressions (12.3) & (12.4), we need to compute the matrix elements of  $\rho(0, 0)$  and  $\psi(0)$  appearing on the right-hand sides. This can be done with the help of formulae that emerge from the algebraic Bethe ansatz [201, 202].

We begin with the density. Let the set of quasi-momenta  $\{k\}$  correspond to state label  $p$  and  $\{k'\}$  to  $p'$ . Then

$$\begin{aligned} \langle p' | \rho(0, 0) | p \rangle &= (-1)^{\frac{N(N+1)}{2}} \frac{p - p'}{\hbar} \left( \prod_{j,\ell=1}^N \frac{1}{k'_j - k_\ell} \right) \\ &\left( \prod_{j>\ell}^N (k_j - k_\ell)(k'_j - k'_\ell) \sqrt{\frac{(k_j - k_\ell)^2 + c^2}{(k'_j - k'_\ell)^2 + c^2}} \right) \frac{\det U(k, k')}{\sqrt{\det G(k) \det G(k')}}. \end{aligned} \quad (12.11)$$

In the above formula, we have two matrices with the following entries:

$$G(k)_{j,\ell} = \delta_{j,\ell} \left[ L + \sum_{m=1}^N \frac{2c}{(k_j - k_m)^2 + c^2} \right] - \frac{2c}{(k_j - k_\ell)^2 + c^2}, \quad (12.12)$$

$$\begin{aligned} U(k, k')_{j,\ell} &= 2\delta_{j,\ell} \operatorname{Im} \left[ \prod_{a=1}^N \frac{k'_a - k_j + ic}{k_a - k_j + ic} \right] + \frac{\prod_{a=1}^N (k'_a - k_j)}{\prod_{a=1}^N (k_a - k_j)} \times \\ &\times \left[ \frac{2c}{(k_j - k_\ell)^2 + c^2} - \frac{2c}{(k_N - k_\ell)^2 + c^2} \right], \end{aligned} \quad (12.13)$$

where, after constructing the  $N \times N$  matrix  $U$ , the last ( $N^{\text{th}}$ ) row and column must be deleted to produce an  $(N - 1) \times (N - 1)$  matrix.  $G$  remains an  $N \times N$  matrix.

Now, the expressions for the field operator are similar:

$$\begin{aligned}
\langle p', N-1 | \psi(0) | p, N \rangle &= (-1)^{\frac{N(N+1)}{2}+1} \left( \prod_{j=1}^{N-1} \prod_{\ell=1}^N \frac{1}{k'_j - k_\ell} \right) \\
&\left( \prod_{j>\ell}^N (k_j - k_\ell) \sqrt{(k_j - k_\ell)^2 + c^2} \right) \left( \prod_{j>\ell}^{N-1} \frac{(k'_j - k'_\ell)}{\sqrt{(k'_j - k'_\ell)^2 + c^2}} \right) \\
&\frac{\det U(k, k')}{\sqrt{\det G(k) \det G(k')}}.
\end{aligned} \tag{12.14}$$

While the  $G$  matrix is unchanged, the  $U$  matrix is somewhat different:

$$\begin{aligned}
U(k, k')_{j,\ell} &= 2\delta_{j,\ell} \operatorname{Im} \left[ \frac{\prod_{a=1}^{N-1} k'_a - k_j + ic}{\prod_{a=1}^N k_a - k_j + ic} \right] + \frac{\prod_{a=1}^{N-1} (k'_a - k_j)}{\prod_{a \neq j}^N (k_a - k_j)} \times \\
&\times \left[ \frac{2c}{(k_j - k_\ell)^2 + c^2} - \frac{2c}{(k_N - k_\ell)^2 + c^2} \right].
\end{aligned} \tag{12.15}$$

This time,  $U$  is an intrinsically  $(N-1) \times (N-1)$  matrix while the size of  $G$  depends on the number of particles.

Note that in order to apply this algorithm to large problems (e.g.  $N \sim 100$ ) in practice, first, for-loops are to be avoided in favour of vectorized coding (in Matlab). Second, one must take the logarithm of equations (12.11) and (12.14) and numerically evaluate the *logarithm* of each factor, add them together and take the exponential of the result. Unless this is done, the numerical precision of the calculation is exceeded and one ends up with zeros and infinities, whereas the product is in fact finite.

Another important numerical issue is that during the evaluation of (12.11) and (12.14), which can be visualized as matrices with the type-II states as a basis, for weak interactions, some far off-diagonal elements are computed spuriously large. Both matrices are peaked around the main diagonal and decay rapidly away from it. Identifying and eliminating the numerical noise is then a simple task, but it must be done before proceeding with the construction of (12.3) and (12.4).

### 12.3.2 Gaussian Momentum Distribution

We shall be making heavy use of a Gaussian distribution for the expansion coefficients:

$$C_{p,N}^{p_0} = \sqrt{A} \exp \left( -\frac{(p - p_0)^2}{2\sigma_p^2} \right), \tag{12.16}$$

where  $A$  is a normalization constant to ensure (12.2).

### 12.3.2.1 Tonks-Girardeau Limit

The Tonks-Girardeau gas is the limit of the Lieb-Liniger model when  $c \rightarrow \infty$ , and is by far the simplest regime since the system is then mappable onto free fermions. In this trivial limit it becomes possible to approximately evaluate the density profile (12.3) with Gaussian coefficients (12.16) analytically.

As  $c \rightarrow \infty$ , the matrix elements (12.11) become very simple:  $\langle p' | \rho(0, 0) | p \rangle = \pm 1/L$ , with a positive (negative) sign if  $p - p'$  is an odd (even) multiple of  $2\pi\hbar/L$ , and  $\langle p' | \rho(0, 0) | p \rangle = n_0$  if  $p = p'$ . Meanwhile, the energy of type-II excitations in the Tonks-Girardeau limit is given by (chapter 7 & [212])

$$E(p) = \frac{p}{2m} \left[ 2\pi\hbar n_0 \left( 1 + \frac{1}{N} \right) - p \right]. \quad (12.17)$$

Going to the (continuous) thermodynamic limit where  $N, L \rightarrow \infty$  with  $n_0$  remaining constant, we can replace the two sums in (12.3) by integrals. Taking into account the integration step (momentum is quantized in steps of  $2\pi\hbar/L$ ), the integrals need to be divided by  $(2\pi\hbar/L)^2$  to approximate the sums.

Now, if we think of the density operator  $\rho(0, 0)$  as a matrix in the type-II momentum basis, then on the main diagonal all entries are  $n_0$ , and as we move out from the main diagonal, the value of the density operator alternates along the diagonals as  $+1/L, -1/L, +1/L$ , etc. Clearly, as long as we do not actually take  $L \rightarrow \infty$  (which would eliminate all the interesting features), we have a discontinuous integrand. To overcome this difficulty, we can approximate the density operator using an oscillating function which takes on the correct values at its extrema. In particular, we choose

$$\langle p' | \rho(0, 0) | p \rangle = \delta_{p,p'} (n_0 + 1/L) - 1/L \cos(Lp/2\hbar) \cos(Lp'/2\hbar). \quad (12.18)$$

This leads to the final result:

$$\begin{aligned} \langle S_{p_0}, N | \rho(x, t) | S_{p_0}, N \rangle &= n_0 + \frac{1}{L} - \frac{\sigma_p}{\sqrt{\pi\hbar}} (1 + 4\tilde{t}\tilde{\sigma}_p^4)^{-1/2} \exp(-\tilde{p}_0^2/\tilde{\sigma}_p^2) \\ &\left| \exp \left[ \frac{i(-2i\tilde{p}_0 + \tilde{\sigma}_p^2(-1 + 2\alpha))^2}{8\tilde{\sigma}_p^2(-i + 2\tilde{\sigma}_p^2\tilde{t})} \right] + \exp \left[ \frac{i(-2i\tilde{p}_0 + \tilde{\sigma}_p^2(1 + 2\alpha))^2}{8\tilde{\sigma}_p^2(-i + 2\tilde{\sigma}_p^2\tilde{t})} \right] \right|^2, \end{aligned} \quad (12.19)$$

with the scaled variables  $p_0 = \hbar\tilde{p}_0/L$ ,  $\sigma_p = \hbar\tilde{\sigma}_p/L$ ,  $x = L\tilde{x}$ ,  $x_0 = L\tilde{x}_0$ ,  $t = 2mL^2\tilde{t}/\hbar$ , and  $\alpha = 2(N + 1)\pi\tilde{t} - \tilde{x} + \tilde{x}_0$ . This expression captures the full numerical profile extremely closely, as long as the  $C_{p,N}^{p_0}$  distribution does not significantly “spill over” outside the fundamental interval  $[0, 2\pi\hbar n_0]$ , which is a requirement we shall

be imposing based on physical arguments later (see section 12.4).

### 12.3.3 Momentum Distribution of Gross-Pitaevskii Dark Solitons

So far, we have introduced Gaussian superpositions of type-II states, localized around some momentum value. Such a wavepacket is certainly physically sensible, but one can go further and attempt to compute the coefficients  $C_{p,N}^{p_0}$  in the weak-coupling regime corresponding to Gross-Pitaevskii dark solitons. In other words, we attempt to extract the momentum-eigenstates distribution (weighting) contributing to Gross-Pitaevskii dark soliton states.

Now, for this calculation, we will require the dark soliton wavefunction on a finite ring. An exact, analytical result is available [105–108], but the expressions are quite cumbersome and difficult to evaluate numerically. An alternative approximate expression was developed in chapter 11, which is based on a first-order finite-size correction of the infinite-system result. This approximation is excellent as long as the soliton is well-localized in the ring. Since faster-moving solitons have a larger healing-length [59], we will see that close to the edges of the dispersion relation the approximation breaks down, necessitating the use of the exact result.

Thus, the finite-system approximation of a Gross-Pitaevskii soliton (centred at position  $x_0$  and with momentum  $p_0$ ) is:

$$\begin{aligned}
\psi_{x_0,p_0}^{GP}(x) &= \sqrt{n_s} e^{i\phi_s}, \\
n_s(x) &= \rho \left\{ s^2 + (1 - s^2) \tanh^2 \left[ a\sqrt{1 - s^2} (x - x_0) \right] \right\}, \\
\phi_s(x) &= \tan^{-1} \left\{ \frac{s}{\sqrt{1 - s^2} \tanh \left[ a\sqrt{1 - s^2} (x - x_0) \right]} \right\} + \frac{2 \cos^{-1}(s)(x - x_0)}{L}, \\
a &= \frac{\sqrt{mg\rho}}{\hbar}, \quad \sqrt{\rho} = \frac{y + \sqrt{y^2 + LN}}{L}, \quad y = \frac{\hbar\sqrt{1 - s^2}}{\sqrt{gm}}, \quad n_0 = \frac{N}{L}, \\
p_0 &= -2\hbar\rho s\sqrt{1 - s^2} + 2\hbar n_0 \cos^{-1}(s).
\end{aligned} \tag{12.20}$$

Here,  $s = v_s/v_c$  is the speed of the soliton in the infinite system scaled by the speed of sound, and varies from  $-1$  to  $1$ . These equations specify the initial wavefunction, and since a soliton simply translates at constant speed, the profiles at any time  $t$  may be found by substituting  $x \rightarrow x - (v_s + v_{cf})t$ , where the counter-flow velocity is  $v_{cf} = \frac{\hbar\Delta\phi}{mL}$  and  $\Delta\phi = 2 \cos^{-1}(s)$  is the phase step across the soliton in the infinite system.

We can now write down the  $N$ -particle Gross-Pitaevskii ket:

$$|S_{x_0, p_0}^{GP}\rangle = \frac{1}{\sqrt{N!}} a_{x_0, p_0}^{\dagger N} |0\rangle, \quad (12.21)$$

$$a_{x_0, p_0}^{\dagger} = \int_{-L/2}^{L/2} dx \frac{\psi_{0, p_0}^{GP}(x)}{\sqrt{N}} \hat{\psi}^{\dagger}(x + x_0), \quad (12.22)$$

where  $|0\rangle$  is the vacuum state. Note that the Gross-Pitaevskii wavefunction is normalized to  $N$  particles, while the norm of the Gross-Pitaevskii ket is 1.

It is convenient to also introduce a momentum expansion of the Gross-Pitaevskii ket in the Bethe ansatz basis:

$$|S_{0, p_0}^{GP}\rangle = \sum_{p, n} c_{p, n}^{p_0} |p_n\rangle, \quad (12.23)$$

where  $n$  is a degeneracy index: all the  $|p_n\rangle$  states have the same momentum eigenvalue  $p$ , but different energy eigenvalues (as mentioned previously, since  $\hat{H}$  and  $\hat{P}$  commute, they have common eigenstates, which are precisely those found via the Bethe ansatz).

We will also need the translation operator,  $\hat{T}(x_0)$ , fundamentally defined by its action on position eigenkets:

$$\hat{T}(x_0) = \exp\left(-\frac{i}{\hbar} \hat{P} x_0\right), \quad (12.24)$$

$$\hat{T}(x_0)|x\rangle = |x + x_0\rangle. \quad (12.25)$$

Due to the second equation, the translation operator acts on field operators in the following way:

$$\hat{T}(x_0)\hat{\psi}(x)\hat{T}^{\dagger}(x_0) = \hat{T}(x_0)\hat{\psi}(x)\hat{T}(-x_0) = \hat{\psi}(x + x_0). \quad (12.26)$$

The above equation also holds if  $\hat{\psi}(x)$  is replaced by  $\hat{\psi}^{\dagger}(x)$ .

We can now construct a momentum eigenstate out of the Gross-Pitaevskii ket:

$$\begin{aligned} |p_{p_0}^{SP}\rangle &= \frac{1}{\sqrt{N_{p_0}(p)}} \frac{1}{L} \int_{-L/2}^{L/2} dx \hat{T}(x) |S_{0, p_0}^{GP}\rangle e^{ipx/\hbar} \\ &= \frac{1}{\sqrt{N_{p_0}(p)}} \sum_n c_{p, n}^{p_0} |p_n\rangle. \end{aligned} \quad (12.27)$$

To go from the first line to the second, we expand the Gross-Pitaevskii ket through momentum eigenstates as in (12.23). In this representation the effect of the trans-

lation operator becomes a multiplication by a phase (i.e. the momentum operator is replaced by its eigenvalue), and we use the identity

$$\frac{1}{L} \int_{-L/2}^{L/2} dx \exp \left[ \frac{i}{\hbar} (p - p') x \right] = \delta_{p,p'}. \quad (12.28)$$

By requiring  $|p_{p_0}^{SP}\rangle$  to be normalized to unity, we get

$$N_{p_0}(p) = \sum_n |c_{p,n}^{p_0}|^2. \quad (12.29)$$

We now turn to calculating  $N_{p_0}(p)$ , once again by requiring the normalization of  $|p_{p_0}^{SP}\rangle$ :

$$N_{p_0}(p) = \frac{1}{L^2} \int_{-L/2}^{L/2} dx' \int_{-L/2}^{L/2} dx \langle S_{x',p_0}^{GP} | S_{x,p_0}^{GP} \rangle \exp \left[ \frac{ip}{\hbar} (x - x') \right]. \quad (12.30)$$

Let us simplify the inner product first:

$$\langle S_{x',p_0}^{GP} | S_{x,p_0}^{GP} \rangle = \frac{1}{N!} \langle 0 | a_{x',p_0}^N a_{x,p_0}^{\dagger N} | 0 \rangle. \quad (12.31)$$

We need the commutator

$$\begin{aligned} \Omega(x - x', p_0) &\equiv [a_{x',p_0}, a_{x,p_0}^\dagger] = \\ &= \frac{1}{N} \int_{-L/2+x'}^{L/2+x'} dy' \int_{-L/2+x}^{L/2+x} dy \psi_{0,p_0}^{GP*}(y' - x') \psi_{0,p_0}^{GP}(y - x) \delta(y - y') = \\ &= \frac{1}{N} \int_{-L/2}^{L/2} dz \psi_{0,p_0}^{GP*}(z + x - x') \psi_{0,p_0}^{GP}(z). \end{aligned} \quad (12.32)$$

It is then possible to show that the inner product of (12.31) is simply  $\Omega(x - x', p_0)^N$ . Since  $\Omega$  is only a function of  $x - x'$ , for further calculations, it is convenient to change variables:

$$u = x + x', \quad (12.33)$$

$$v = x - x'. \quad (12.34)$$

Note that the wavefunction has periodic boundary conditions, which must be carefully accounted for when computing the overlap integral in (12.32). This can be easily done numerically for both the exact and approximate wavefunctions, and

in the latter case, an analytical piecewise expression can also be derived (where  $r = \sqrt{1 - s^2}$ ):

$$\Omega(v = 0, p_0) = \frac{\rho}{n_0} \left( 1 - \frac{2r}{aL} \tanh \left[ \frac{aLr}{2} \right] \right), \quad (12.35)$$

$$\begin{aligned} \Omega(v > 0, p_0) &= \frac{\rho}{n_0} \exp(-2v \cosh^{-1}(s)/L) \left\{ 1 + \frac{v}{L} \left( e^{2 \cosh^{-1}(s)} - 1 \right) \right. \\ &+ \log \left[ \frac{1 + \cosh[ar(L - 2v)]}{1 + \cosh(aLr)} \right] \left[ \frac{is}{aL} \left( e^{2 \cosh^{-1}(s)} - 1 \right) \right. \\ &\left. \left. + \frac{r}{aL} \left( e^{2 \cosh^{-1}(s)} \coth(ar(L - v)) + \coth(arv) \right) \right] \right\}, \end{aligned} \quad (12.36)$$

and to obtain  $\Omega(v < 0, p_0)$ , take  $\Omega(v > 0, p_0)$  and replace  $v \rightarrow v + L$ .

Returning to (12.30), we express the region of integration over  $x$  and  $x'$  in terms of  $u$  and  $v$ : as  $v$  ranges from  $-L$  to  $L$ ,  $u$  is confined to the area bounded by  $u = -v - L$  &  $u = v + L$  if  $v < 0$ , and  $u = v - L$  &  $u = -v + L$  if  $v > 0$ . Integrating in (12.30) over  $u$  contributes an additional factor of  $\left(1 - \frac{|v|}{L}\right)$  to the remaining  $v$ -integrand. Moreover, the absolute value of the determinant of the Jacobian matrix for the transformation from  $x, x'$  to  $u, v$  is  $1/2$ . Substituting  $\Omega$  into (12.30), gives

$$N_{p_0}(p) = \frac{1}{L} \int_{-L}^L dv \left( 1 - \frac{|v|}{L} \right) \exp \left[ \frac{i}{\hbar} pv \right] \Omega(v, p_0)^N. \quad (12.37)$$

This final integral cannot be done analytically (even for the approximate wavefunction), but its numerical evaluation is straightforward. However, it is crucial to take the integration step sufficiently small (precisely how small depends on the parameters): one must always check the convergence of the integral with step size directly. Thus, we can calculate  $N_{p_0}(p)$  using either the exact or approximate dark soliton wavefunction.

What requirements do we have of  $N_{p_0}(p)$ ? Firstly, it should be dimensionless, which can easily be confirmed from (12.37). Recalling equation (12.29),  $N_{p_0}(p)$  must be real and bounded between 0 and 1. Moreover, by virtue of (12.29) and (12.23), we must have  $\sum_p N_{p_0}(p) = 1$ . In our treatment of the problem,  $p$  is a continuous variable, however we are trying to approximate a full quantum-mechanical many-body system in which momentum is quantized in multiples of  $2\pi\hbar/L$ . Therefore the function  $N_{p_0}(p)$  must be evaluated at this discrete set of  $p$ 's before the sum is taken. If any of these properties are not satisfied, it is very likely that the approximate wavefunction is failing and one should use the exact expression.

Note that, in principle, the  $N_{p_0}(p)$  distribution is defined on  $p \in (-\infty, \infty)$ . There is no *a priori* restriction to the fundamental momentum interval  $[0, 2\pi\hbar n_0]$ .

Moreover, at the very edge of the dispersion relation, the dark soliton solution

simplifies to a uniform background state. In this case  $N_{p_0}(p)$  can be computed analytically, and we find

$$N_{p_0=0}(p) = \frac{2\hbar^2}{L^2 p^2} \left[ 1 - \cos\left(\frac{Lp}{\hbar}\right) \right]. \quad (12.38)$$

We can now examine the  $N_{p_0}(p)$  distribution and study its dependence on the parameters – several examples are shown in Fig. 12.1. Overall, the distribution is localized about  $p_0$  (as expected), and gets narrower with increasing soliton speed (i.e. as  $p_0 \rightarrow 0, 2\pi\hbar n_0$ ). There are pronounced oscillations on top of an approximate bell-shaped curve (these oscillations arise due to the periodic boundary conditions on the wavefunction), which are attenuated as either  $c$  or  $N, L$  are increased. For fairly large  $N, L$ , the dependence on  $L$  becomes dominantly a scaling by  $1/L$  (also see below). Increasing  $c$  makes the distribution visibly wider, and vice versa: decreasing  $c$  makes  $N_{p_0}(p)$  narrower. There is a direct inverse correlation between the width of  $N_{p_0}(p)$  and that of the Gross-Pitaevskii dark soliton. It is clear, however, that as  $p_0 \rightarrow 0, 2\pi\hbar n_0$  at finite  $N, L, c$ , the distribution retains a finite width.

Let us now consider the thermodynamic limit. As  $N, L$  are increased and we go to the continuous limit, the condition  $\sum_p N_{p_0}(p) = 1$  must be replaced by  $\int N_{p_0}(p) dp = 1$ . Taking into account the integral step size,  $2\pi\hbar/L$ , we expect the quantity  $N_{p_0}(p)L/2\pi\hbar$  to have a well-defined thermodynamic limit, and this is indeed the case. Simply increasing the system size at a finite  $c$  leads to converged distributions with non-zero widths. It is only when we take  $c \rightarrow 0$  and approach the Gross-Pitaevskii limit, that the width decreases and eventually (we expect), the distribution tends to a  $\delta$ -function. As such, only one type-II state is then required, which is consistent with the fact that the dark soliton becomes infinitely-wide in this regime, matching the uniform density profile of a single type-II state. This implies that in the true Gross-Pitaevskii regime,  $N_{p_0}(p)$  will not extend beyond the fundamental momentum interval, as for example does the green dash-dotted curve in Fig. 12.1.

Notice that in the absence of a soliton, the sinc-like distribution  $N_{p_0=0}(p)$  of equation (12.38) has an  $L$ -dependent width. As we increase  $N, L$  keeping  $c$  constant and finite,  $N_{p_0=0}(p)$  narrows and approaches the  $\delta$ -function.

## 12.4 Physical Properties of Superposition States

In this section we will examine the properties of superpositions of type-II states, in general given by (12.1), with either Gaussian coefficients (12.16), or with the coefficients determined from the  $N_{p_0}(p)$  Gross-Pitaevskii dark soliton distribution. Indeed, if we suppose that the only momentum eigenstates contributing to (12.23)

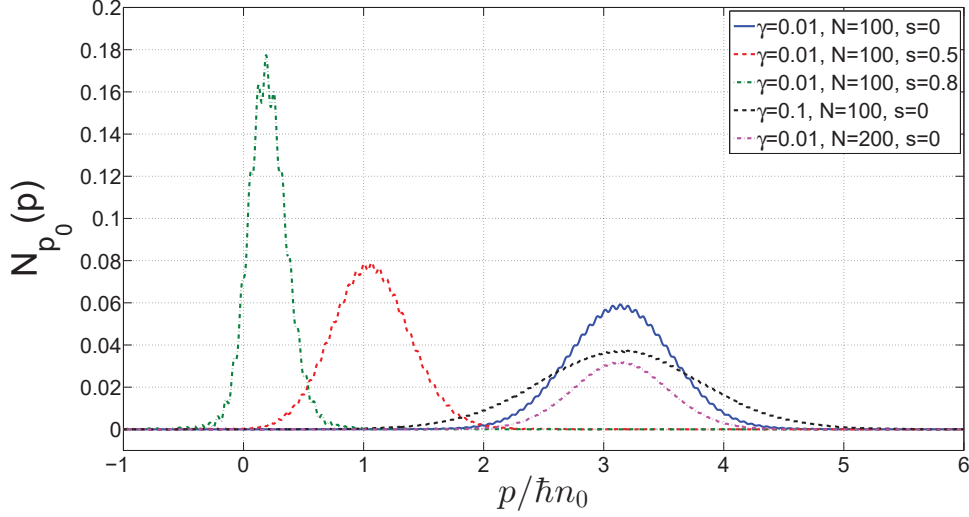


Figure 12.1: The momentum distribution of Gross-Pitaevskii dark solitons,  $N_{p_0}(p)$ , for various parameters. Blue solid line:  $N = 100$ ,  $\gamma = 0.01$ ,  $s = 0$ , red dashed line:  $N = 100$ ,  $\gamma = 0.01$ ,  $s = 0.5$ , green dash-dotted line:  $N = 100$ ,  $\gamma = 0.01$ ,  $s = 0.8$ , black dashed line:  $N = 100$ ,  $\gamma = 0.1$ ,  $s = 0$ , magenta dash-dotted line:  $N = 200$ ,  $\gamma = 0.01$ ,  $s = 0$ . All curves except for the green dash-dotted line are calculated using the approximate dark soliton wavefunction. When  $s = 0.8$ , however, the soliton is so wide that the approximation breaks down and we resort to the exact result.

are the lowest-energy eigenstates of the Bethe ansatz, i.e. type-II states, then in (12.23), only the  $n = 1$  terms are non-zero. The summation is no longer necessary in equation (12.29), then, which leads to  $C_{p,N}^{p_0} = \sqrt{N_{p_0}(p)}$ . This assumption is justified by the fact that the momentum and energy of the superposition state involving only type-II states in the expansion will equal those of the type-II state on which the superposition state is centred, simply due to the averaging process. Recall that both the dark soliton solutions of the Gross-Pitaevskii equation and the type-II excitations of the Lieb-Liniger model are the lowest energy excitations at a given momentum value of their respective models. If any higher energy states were involved, the energy of the superposition state would greatly exceed that of the type-II branch, and as we already know, the dispersion relations of dark solitons and type-II excitations practically overlap in this regime, so this is highly unlikely. Ultimately, so may test this hypothesis by constructing superpositions with  $C_{p,N}^{p_0} = \sqrt{N_{p_0}(p)}$  and comparing the results to the known Gross-Pitaevskii dark solitons in the small coupling regime.

Precisely such a comparison is made in Fig. 12.2. The three panels in each sub-figure correspond to the blue, red and green curves in Fig. 12.1, in that order. Both the density profile,  $n_s$ , and the phase profile,  $\phi_s$ , are shown. Each panel quotes  $s$ ,

the dimensionless velocity appearing in the approximate dark soliton wavefunction, and  $p_0$ , the corresponding canonical momentum. Each panel displays three curves: the exact profile, the approximate one, and that of the reconstructed dark soliton, obtained as a superposition of type-II states with expansion coefficients given by  $C_{p,N}^{p_0} = \sqrt{N_{p_0}(p)}$ . Once again, only for the highest velocity was it necessary to use the exact wavefunction in the calculation of  $N_{p_0}(p)$ , and small differences visible between the exact and approximate curves justify this decision. It is also vitally important to note that since the  $N_{p_0}(p)$  distribution for this case extends beyond the fundamental momentum interval, we used an extended type-II state basis, spanning the interval  $[-2\pi, 4\pi]\hbar n_0$ . In all cases, the reconstructed profiles overlap very closely with the known Gross-Pitaevskii dark soliton profiles, which justifies our hypothesis that only type-II states contribute to the make-up of dark solitons.

In Fig. 12.2 we have examined solitons whose momentum distributions  $N_{p_0}(p)$  are predominantly localized in  $[0, 2\pi\hbar n_0]$ . One may then ask what happens as  $p_0 \rightarrow 0$  and whether the agreement between the known Gross-Pitaevskii solitons and reconstructed profiles remains of such high fidelity. This question is addressed in Fig. 12.3, where we choose an extremely small  $p_0 = 0.0095\hbar n_0$ . The top panel shows the  $N_{p_0}(p)$  distributions: that obtained from the exact dark soliton solution, the approximate, and the analytical formula at  $p_0 = 0$  given by (12.38). It is clear that by this stage the approximation is quite poor and that the  $N_{p_0}(p)$  distribution tends to the symmetric black dash-dotted line as  $p_0 \rightarrow 0$ . The bottom panel presents the density profiles associated with these distributions. Five curves are shown: the direct plots of the exact and approximate  $n_s$ , the reconstructed density profiles using the corresponding distributions as the coefficients, and the density profile obtained using the zero momentum distribution (12.38). None of the curves overlap, and most importantly, the exact dark soliton density and the reconstructed density based on the exact momentum distribution are quite different. This suggests that very close to the edges of the fundamental interval,  $c$  needs to be much smaller to see agreement, or alternatively, at finite  $c > 0$ , higher energy states contribute to the momentum composition of the dark soliton.

Given that we will always work with a finite  $c > 0$ , a natural question arises: is it sensible to construct superpositions with coefficients that extend beyond the fundamental interval and expect such a wavepacket to behave as a dark soliton? After all, the group velocity of type-II states on either side of (for instance)  $p = 0$  is very different (the dispersion relation has a cusp at each umklapp point), so it is unlikely that the resulting object will translate at constant speed without changing shape. This matter is investigated in Fig. 12.4, where density profiles are shown at  $t = 0$  and  $t = 100 \times 2m/n_0^2\hbar$  for a Gaussian superposition that extends beyond the fundamental interval. We see a significant deformation of the profile in addition

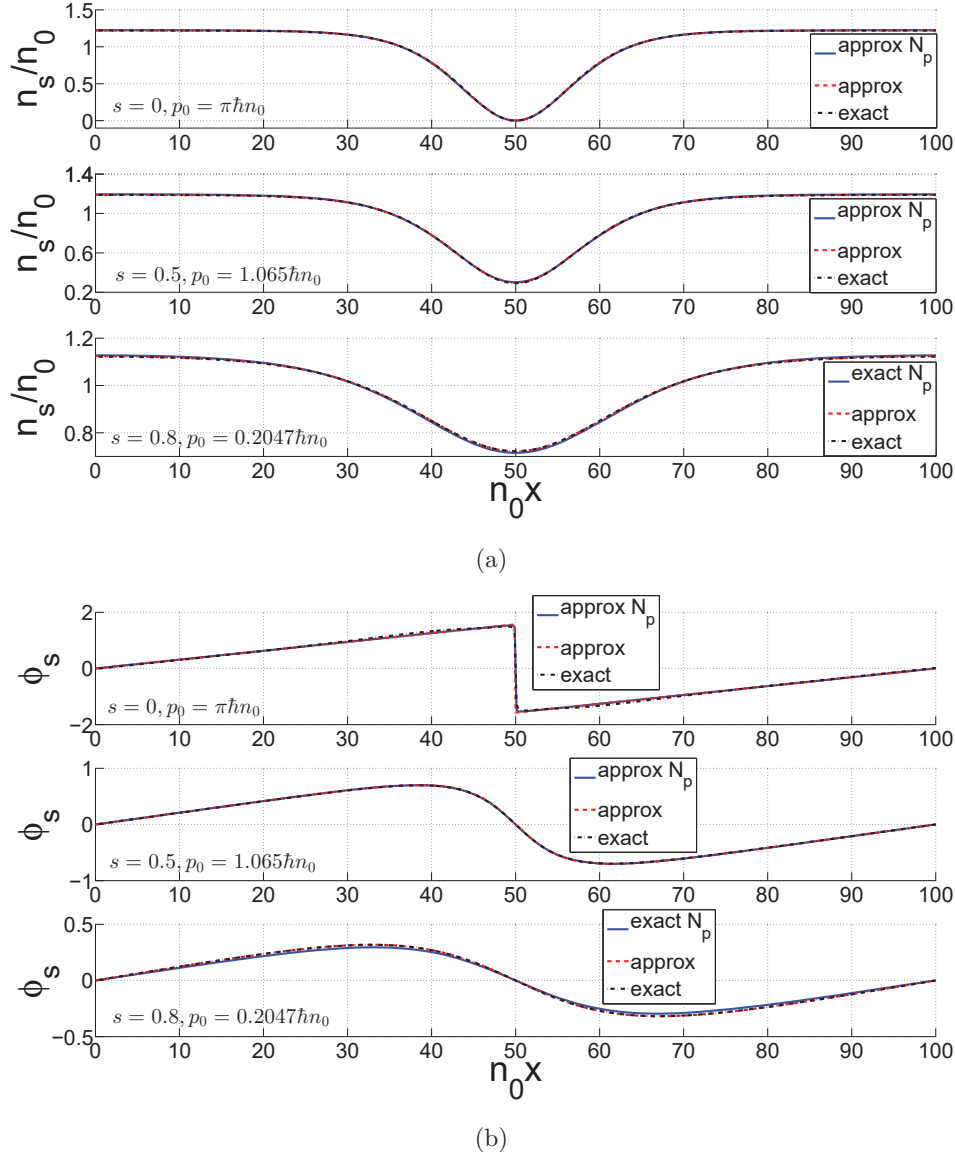


Figure 12.2: Density (a) and phase (b) profiles of dark solitons in a system with  $\gamma = 0.01, N = 100$ . In each subfigure, the panels going from top to bottom correspond to a soliton of a different velocity, in particular:  $s = 0, p_0 = \pi \hbar n_0$ ,  $s = 0.5, p_0 = 1.065 \hbar n_0$  and  $s = 0.8, p_0 = 0.2047 \hbar n_0$ , in that order. Each panel shows three curves: the solid blue line is the reconstructed soliton, made up of type-II states with coefficients given by the  $N_{p_0}(p)$  distribution. Only in the case of  $s = 0.8$  is  $N_{p_0}(p)$  computed based on the exact dark soliton wavefunction. The red dashed line displays the approximate profile, while black dash-dotted shows the exact. The superb agreement between the known dark soliton profiles and the reconstructed profiles via a superposition of type-II states suggests that indeed dark solitons do not have a meaningful contribution from higher energy momentum eigenstates, but only from type-II excitations.

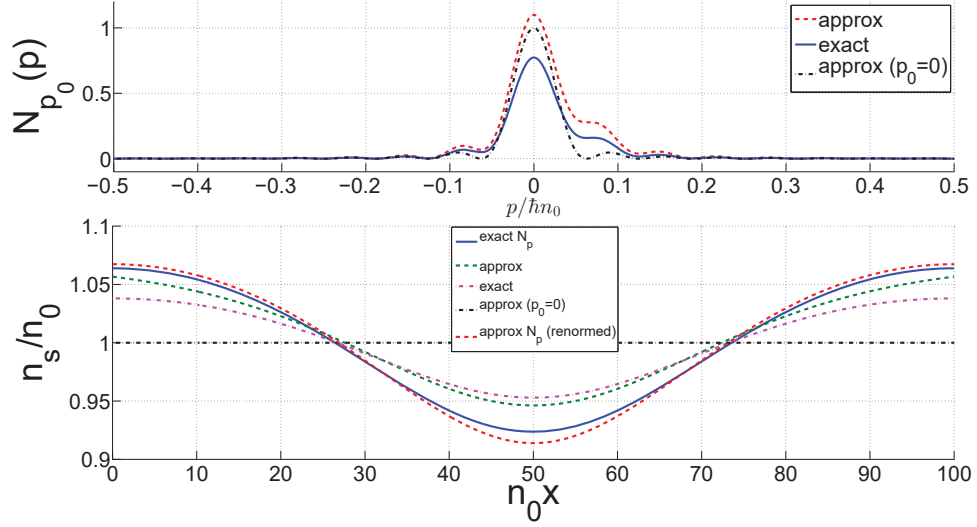


Figure 12.3: Momentum distribution (a) and associated density profiles (b) for a system with  $\gamma = 0.01$ ,  $N = 100$  and a dark soliton with  $p_0 = 0.0095\hbar n_0$  ( $s = 0.9402$ ). (a) The  $N_{p_0}(p)$  distribution obtained from the exact dark soliton solution (solid blue line), the approximate (dashed red line), and the analytical formula at  $p_0 = 0$  given by (12.38) (black dash-dotted line). (b) The density profiles associated with the distributions from (a). Magenta dash-dotted line: direct plot of the exact density, green dashed line: direct plot of the approximate  $n_s$ , solid blue line: reconstructed density profile using the exact distribution for coefficients, red dashed line: reconstructed density profile using the approximate distribution for coefficients (with  $C_{p,N}^{p_0}$  renormalized after the calculation of  $N_{p_0}(p)$  as the approximation is so poor by this stage that the norm of  $N_{p_0}(p)$  is considerably different from one), black dash-dotted line: reconstructed density profile obtained using the zero momentum distribution (12.38). The disagreement between the exact density plotted directly and that of the reconstructed soliton using exact  $N_{p_0}(p)$  coefficients implies that higher momentum eigenstates must contribute to the dark soliton at non-zero  $c$ 's and close to  $p_0 = 0$ .

to translation: while a larger part of the dip translates to the right, a smaller dip forms and breaks off, moving to the left. This sort of effect is always seen when we include states outside of  $[0, 2\pi\hbar n_0]$  with non-vanishing coefficients, and the larger the weight of the states outside of the fundamental interval, the larger the secondary dip moving in the opposite direction. Thus, it becomes clear that if one wishes to construct an object that will behave as a dark soliton should, one must ensure the  $C_{p,N}^{p_0}$  coefficients decay sufficiently in the fundamental momentum interval<sup>1</sup>.

Now, even if we are careful to ensure the expansion coefficients decay within the fundamental interval, evolution over time causes minor deformations of the density profile (skewness), but slight distortions aside, the major changes in the density with

<sup>1</sup>Recall that  $N_{p_0}(p)$  becomes narrower as  $c \rightarrow 0$ , so in the Gross-Pitaevskii regime, this will not be a problem.

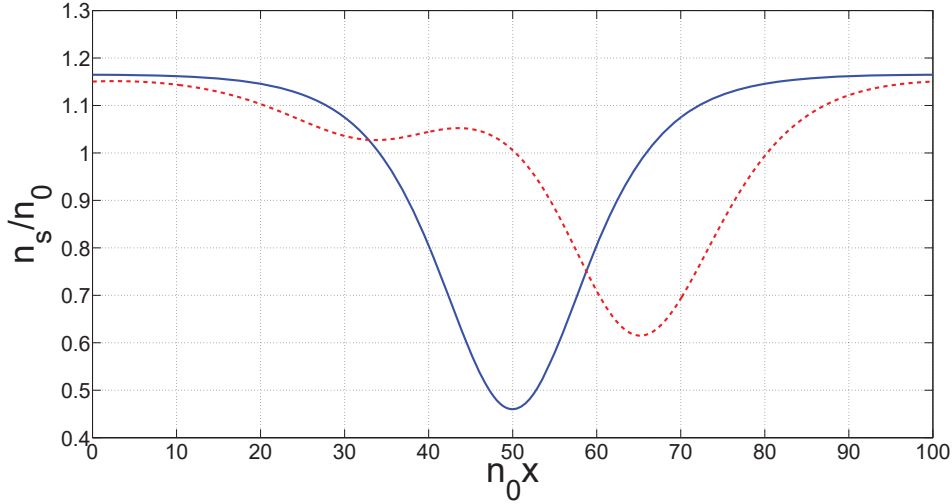


Figure 12.4: Density profiles at  $t = 0$  (blue solid line) and  $t = 100 \times 2m/n_0^2\hbar$  (red dashed line), for a system with  $\gamma = 0.01$ ,  $N = 100$  and a Gaussian superposition with  $p_0 = 0.5\hbar n_0$ ,  $\sigma_p = 1\hbar n_0$ . The small density dip moving to the left is a direct consequence of the fact that the momentum distribution that makes up the wavepacket overfills into the region  $p < 0$  where the group velocity differs from that immediately beyond  $p = 0$  as the dispersion relation has a cusp at each umklapp point.

time are a translation at a constant speed of  $v_s + v_{cf}$ , and a gradual filling-up of the density notch. In order to visualize the effects of time evolution, let us define several useful quantities:

$$N_d = \int n_s(x) - \max[n_s(x)] dx, \quad (12.39)$$

$$\Delta p = \sqrt{\langle p^2 \rangle - \langle p \rangle^2}, \quad (12.40)$$

$$\Delta x = \sqrt{\langle x^2 \rangle - \langle x \rangle^2}, \quad (12.41)$$

where the “expectation-value” integrals are to be done with respect to the following distributions: for momentum,  $C_{p,N}^{p_0^2} / \int C_{p,N}^{p_0^2} dp$  and for position  $(n_s(x) - \max[n_s(x)]) / N_d$ . Note that  $N_d$  is the missing particle number – the number of atoms removed from a uniform, homogeneous state to create the dark soliton, while  $\Delta x$  and  $\Delta p$  are measures of the width of the density dip and momentum distribution, respectively. For Gaussian  $C_{p,N}^{p_0}$  coefficients,  $\Delta p = \sigma_p / \sqrt{2}$ . Next, care must be taken when it comes to computing  $\Delta x$  for moving solitons. Since the wavefunction has periodic boundary conditions, when the soliton arrives at  $L$  it simply reappears at  $0$ , so for a segment of time during each trip around the ring, the soliton density dip is split and located around the edges of the interval  $[0, L]$ . While usually the

absolute position of the distribution does not affect its width, such splitting can be shown to be non-trivial: it causes  $\Delta x$  to increase strongly for a clearly artificial reason. Therefore, we manually center all density profiles prior to calculating  $\Delta x$ .

Figure 12.5 shows the time-evolution of  $\Delta x$  and  $N_d$  for superposition states with  $p_0 = \pi\hbar n_0$  (solid blue lines) and  $p_0 = \pi\hbar n_0/2$  (dashed red lines) at three different coupling strengths:  $\gamma = 0.01$  (top panels),  $\gamma = 1$  (middle panels), and  $\gamma = 100$  (bottom panels). In the small coupling regime we use the  $N_{p_0}(p)$  distribution to create the superpositions, but for larger  $\gamma$  values, we use Gaussian distributions of the same width as  $N_{p_0}(p)$  at  $\gamma = 0.01$ . The total evolution time in each coupling regime is set by the rate of expansion and filling of the density dip. We see that  $\Delta x$  initially disperses quadratically but then the spreading of the wavepacket becomes linear in time. The dispersion rate certainly grows strongly with increasing  $c$  (approximately as a power law) – in other words, initially localized density features retain their shape far longer in the weakly-interacting regime. Meanwhile,  $N_d$  initially stays fairly constant, but after some time begins increasing, tending to 0, the  $N_d$  value associated with a flat profile. This process begins when the density dip becomes so wide that it is no longer well-localized in the finite ring, and therefore the definition of  $N_d$  becomes inapplicable.

We can also examine the dependence of  $\Delta x$  and  $N_d$  on the width of the momentum distribution used to create the wavepacket,  $\Delta p$ . This is shown in Fig. 12.6, where each subfigure corresponds to a different interaction strength:  $\gamma = 0.01, 1, 100$  for (a)-(c), respectively. Gaussian coefficients of various  $\sigma_p$  are used to create superpositions, the properties of which are shown as blue lines. The left columns in each subfigure have  $p_0 = \pi\hbar n_0$ , while the right columns have superpositions with  $p_0 = \pi\hbar n_0/2$ . Top panels in each subfigure show  $\Delta x$  and the bottom panels,  $N_d$ . The range of  $\Delta p$  used is determined by the largest width of the Gaussian distribution which still fits well into the fundamental interval  $[0, 2\pi\hbar n_0]$ . In the Gross-Pitaevskii regime (a), we also add a data point corresponding to the  $N_{p_0}(p)$  superposition as a green square.

Magenta stars on the  $N_d$  plots at  $\Delta p = 0$  are the finite-system approximation of the missing particle number associated with the type-II states themselves (not their superpositions), the detailed calculation of which may be found in chapter 11. Briefly, this calculation extracts  $N_d$  of type-II states from the dispersion relation computed under the first level of approximation, using Campbell's formula (chapter 10). Essentially, this adds first-order finite-system corrections to the thermodynamic limit properties. The resulting values are truly remarkable: they seem to correspond to the limit as  $\Delta p \rightarrow 0$  of  $N_d$  computed from actual density dips of superposition states. More will be said about this observation below.

Several comments are in order. Firstly,  $\Delta x$  decreases with  $\Delta p$  while  $N_d$  increases.

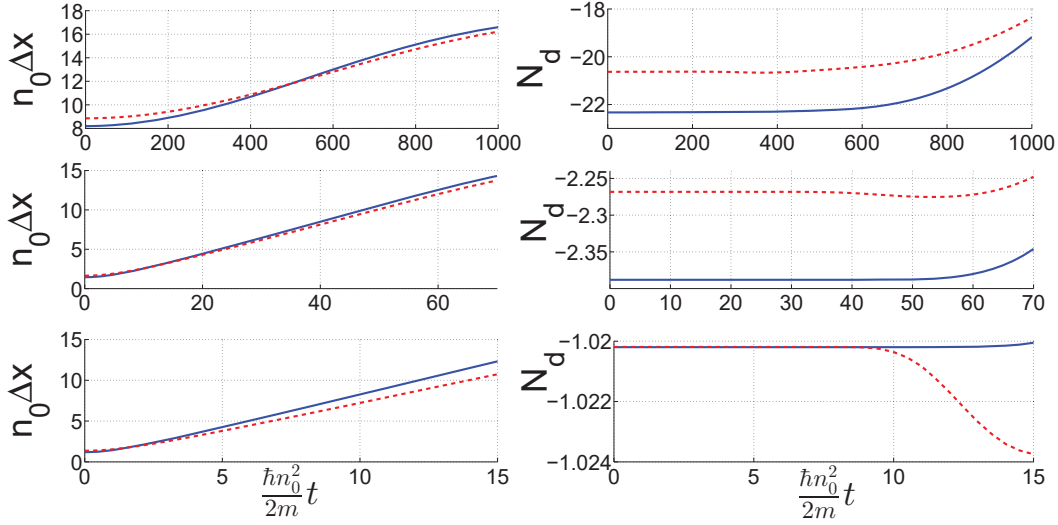


Figure 12.5: Width of the density dip ( $\Delta x$ , left column) and missing particle number ( $N_d$ , right column) for three coupling strengths:  $\gamma = 0.01$  (top panels),  $\gamma = 1$  (middle panels) and  $\gamma = 100$  (bottom panels) in a system with  $N = 100$ . Each panel shows two curves: the blue solid line corresponds to a momentum distribution with  $p_0 = \pi \hbar n_0$  (and  $s = 0$  for  $\gamma = 0.01$ ), and the red dashed line to  $p_0 = \pi \hbar n_0 / 2$  (and  $s = 0.36625$  for  $\gamma = 0.01$ ). When  $\gamma = 0.01$  (top panels) we use the Gross-Pitaevskii dark soliton  $N_{p_0}(p)$  distributions, while for the other cases, Gaussian distributions of the same width  $\Delta p$  as  $N_{p_0}(p)$  has at  $\gamma = 0.01$  are used (in particular,  $\sigma_p = 0.601995 \hbar n_0$  for the stationary soliton and  $\sigma_p = 0.521788 \hbar n_0$  for the moving soliton).

Second, in the Tonks-Girardeau limit  $N_d$  becomes essentially independent of  $\Delta p$ . While we expect  $N_d = -1$  in this limit, for large but finite  $\gamma$  we have  $N_d = -1 - 2/\gamma$  [see equation (10.46)]. Finally, in the Gross-Pitaevskii regime, physical properties of the  $N_{p_0}(p)$  superposition are practically indistinguishable from those of a Gaussian superposition of the same  $\Delta p$  (including their time evolution).

We now return to the connection of the  $N_d$  computed from the single-particle density of superpositions of type-II states, and the  $N_d$  extracted from the type-II dispersion relation in the thermodynamic limit and then corrected for finite-system effects (chapter 11). As can be seen in Fig. 12.6, the pure type-II  $N_d$  value seems to be the limit as  $\Delta p \rightarrow 0$  of the Gaussian superpositions data. However, it is clear that if we gradually reduce the number of type-II states involved in the superposition, eventually reaching one, that the density profile will become flat and  $N_d$  will vanish. This is indeed the case: if we take thinner momentum distributions than those shown in Fig. 12.6, we observe  $N_d$  increasing to zero extremely rapidly. In fact, the beginning of this rise to zero is already seen in panel (a). It is natural to then assume that the rapid plunge of  $N_d$  to zero is a finite-system effect, and as the system size

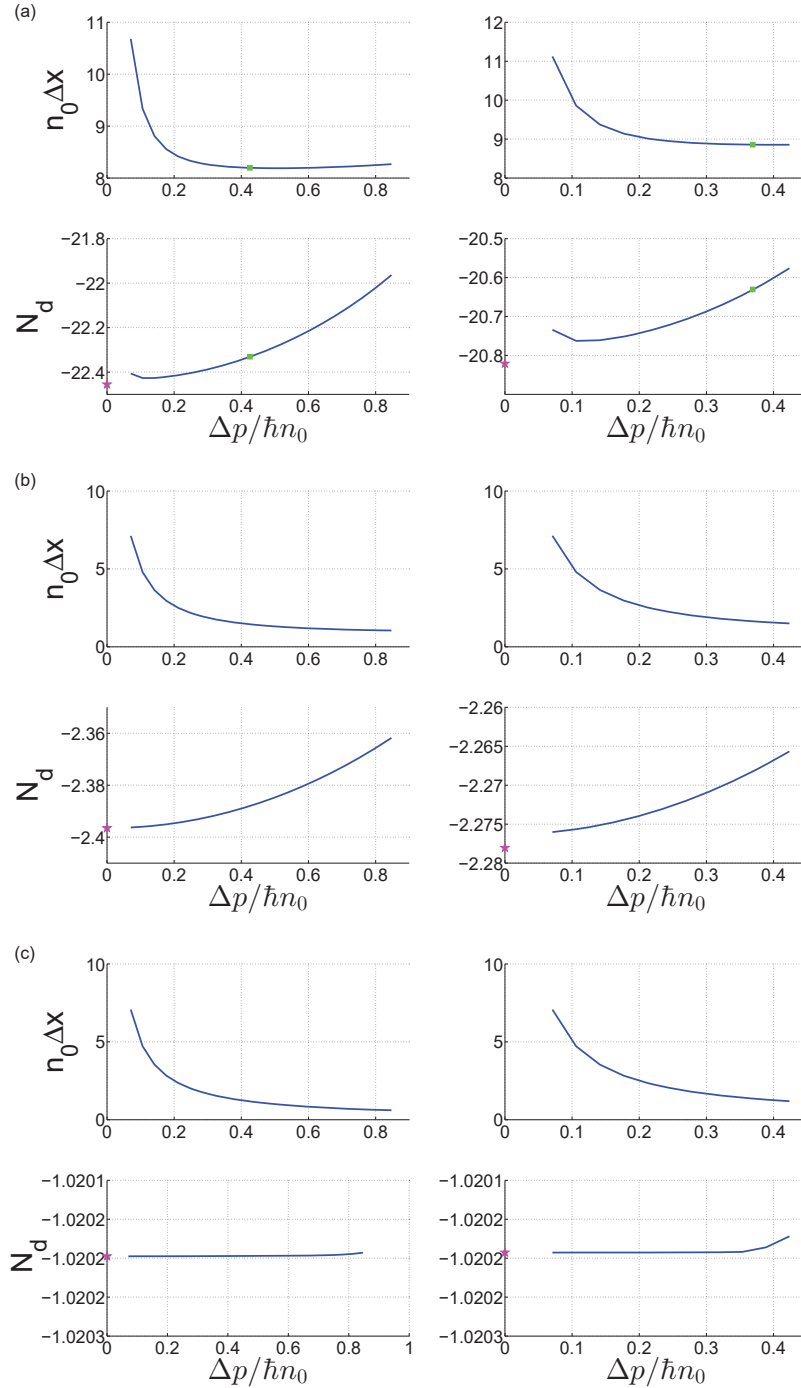


Figure 12.6: Width of the density dip ( $\Delta x$ , top panels) and missing particle number ( $N_d$ , bottom panels) for three coupling strengths:  $\gamma = 0.01$  (a),  $\gamma = 1$  (b) and  $\gamma = 100$  (c) in a system with  $N = 100$ . In each subfigure, left columns correspond to superpositions with  $p_0 = \pi\hbar n_0$  and right columns to  $p_0 = \pi\hbar n_0/2$ . Data shown as blue lines are properties of Gaussians superpositions, green squares are Gross-Pitaevskii dark soliton  $N_{p_0}(p)$  distributions (only added for small  $\gamma$ ) and magenta stars show the missing particle number of type-II states in the finite-system approximation (chapter 11).

increases,  $N_d$  would stay (roughly) constant for smaller  $\Delta p$ 's, thus giving the  $N_d$  associated with type-II states a clear physical meaning. We test this hypothesis in Fig. 12.7, where the system size is increased by a factor of two compared to that used in Fig. 12.6 (a). The increase of  $N_d$  as  $\Delta p \rightarrow 0$  is eliminated and the limit of the Gaussian data can be clearly seen to coincide with the type-II data point.

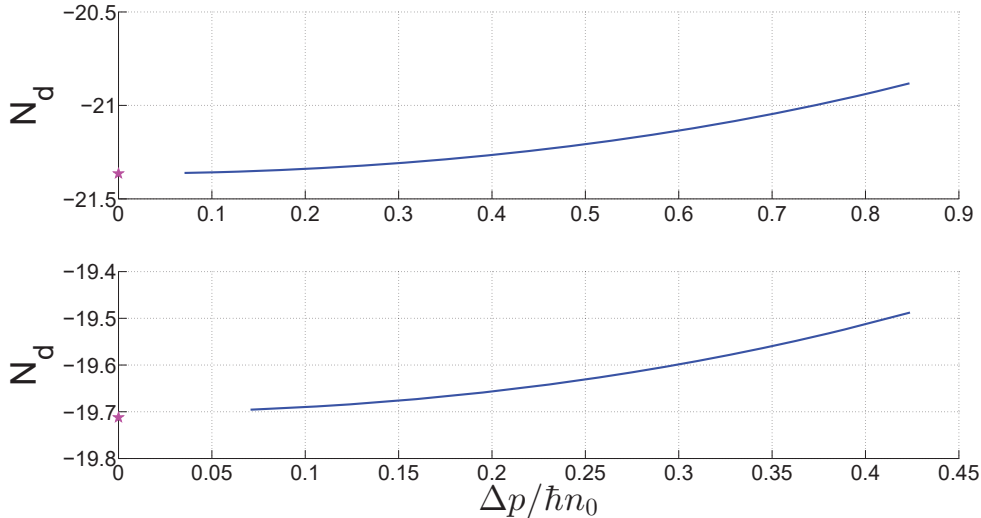


Figure 12.7: Missing particle number in a system with  $\gamma = 0.01$  and  $N = 200$ . Data from Gaussian superpositions is shown as blue solid lines, while magenta stars correspond to  $N_d$  extracted from the type-II dispersion relation in the thermodynamic limit and corrected for finite-system effects (chapter 11). In the top panel,  $p_0 = \pi \hbar n_0$  and in the bottom,  $p_0 = \pi \hbar n_0 / 2$ . The  $N_d$  value of type-II states is clearly the limit of  $N_d$  computed from superposition states as  $\Delta p \rightarrow 0$ .

One would hope that a similar argument could be drawn for the phase step across the soliton,  $\Delta\phi$ . However, before we can examine the dependence of the phase step  $\Delta\phi$  on  $\Delta p$ , we must test whether the proposed methods for computing  $\Delta\phi$  of section 12.3 are sensible. We begin by comparing the approximate density profiles – the modulus-squared of (12.4) and the special case of  $x = x'$  in equation (12.7) – to the exact, (12.3). This is shown in Fig. 12.8. For small  $\gamma$ , the two approximations closely follow the exact profile, instilling confidence in the subsequent phase calculations. However, for stronger interactions, the saturation drops rapidly and the density profile is captured poorly by both approximations, which moreover differ amongst themselves around the position of the soliton. This suggests caution is needed when examining the phase results to follow.

Next, we may study the current profiles associated with the examples shown in Fig. 12.8 – these are presented in Fig. 12.9. Again for stronger interactions, the momentum saturation drops rapidly. In fact, it is essentially equal to the density

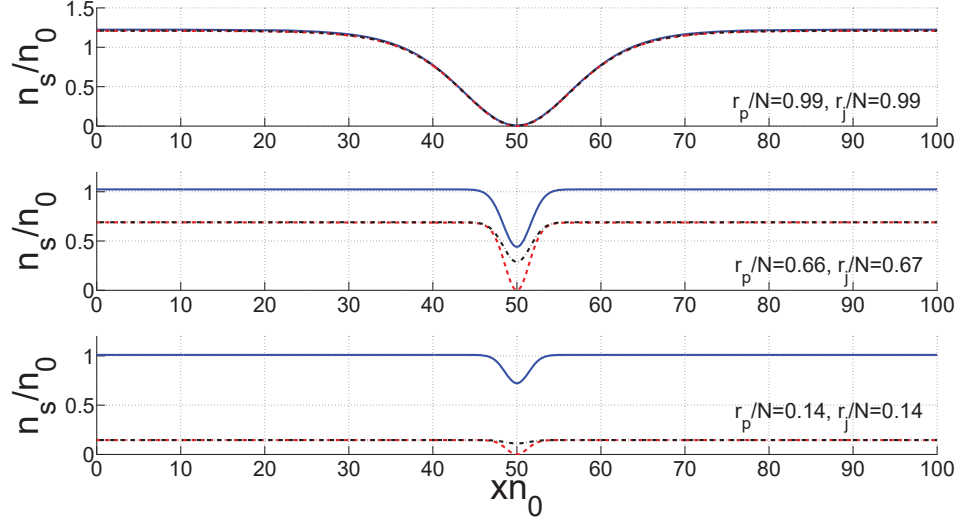


Figure 12.8: The density profiles in a system with  $N = 100$ , using a Gaussian superposition with  $p_0 = \pi\hbar n_0$  and  $\sigma_p = 0.5\hbar n_0$ . The panels, top to bottom, correspond to  $\gamma = 0.01, 1, 100$ . Blue solid lines show the exact density, equation (12.3), red dashed lines show the modulus-squared of the matrix element of  $\psi$  given by (12.4), and black dash-dotted lines depict the diagonal of the single-particle density matrix, equation (12.7). The saturation ratio for both approximations is quoted in each panel and is very similar despite the clear differences around the solitonic notch at stronger interactions. Both approximations become progressively poorer as  $\gamma$  increases.

saturation for the same parameters, implying that the entire fluid carries the total momentum, but the approximate density and current calculations only capture part of the gas – seemingly the same fraction. This suggests that if equation (12.9) is to yield reasonable results, we cannot use  $n_0 = N/L$ , but must use the maximal density attained by the diagonal of the approximate single-particle density matrix. We proceed precisely this way.

Despite the saturation issues discussed above, it is instructive to extract and study the phase step. Figure 12.10 shows  $\Delta\phi$  of Gaussian superpositions, using both methods of obtaining the phase step: from the phase profile (blue solid lines) and from the current (red dashed lines). Magenta stars display the type-II finite-system result which, like  $N_d$ , can also be extracted from the dispersion relation. Not only do the two calculations give quite consistent results, but once again it is clear that the type-II result is the limit of the Gaussian superpositions as  $\Delta p \rightarrow 0$ .

It appears the phase step of the superposition states is a meaningful result at all interactions (despite the saturation problem), since it is essentially equal to the type-II value, the significance of which is reinforced by the success of the finite system corrections to the dispersion relation (chapter 11) that are largely based on it.

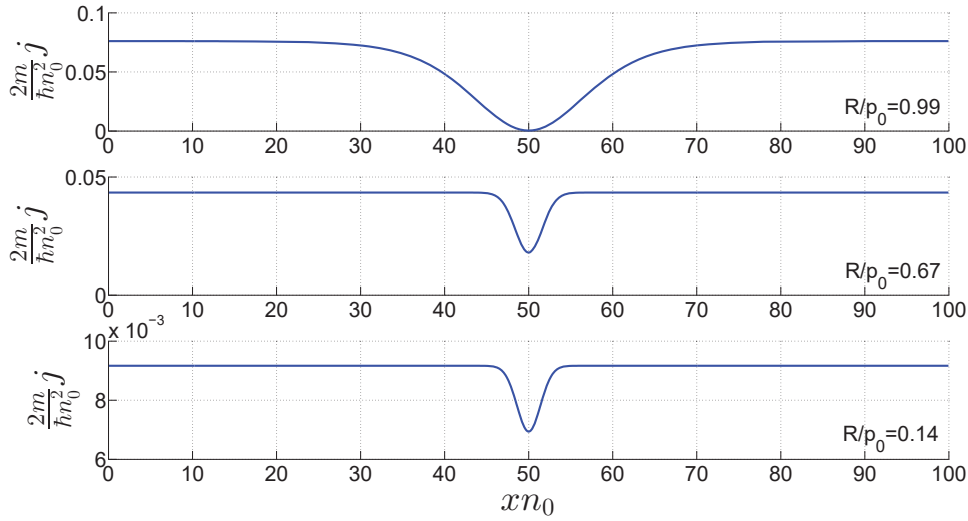


Figure 12.9: The current profiles in a system with  $N = 100$ , using a Gaussian superposition with  $p_0 = \pi\hbar n_0$  and  $\sigma_p = 0.5\hbar n_0$ . The panels, top to bottom, correspond to  $\gamma = 0.01, 1, 100$ . The momentum saturation ratio is quoted in each panel and is very similar to the density saturation ratio in each case (see Fig. 12.8). The momentum saturation decreases significantly with increasing  $\gamma$ .

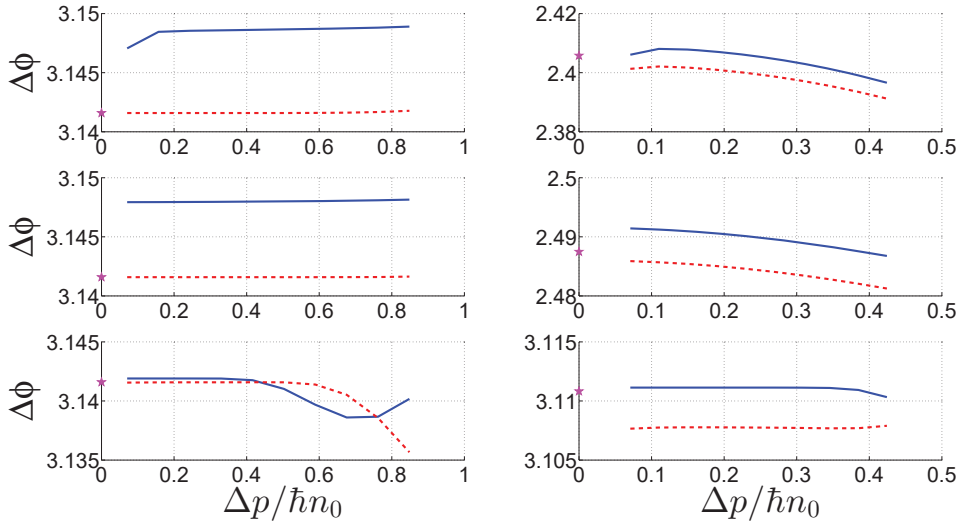


Figure 12.10: The phase step  $\Delta\phi$  in a system with  $N = 100$ . Data from Gaussian superpositions is shown as lines:  $\Delta\phi$  extracted from the phase profile is plotted with blue solid lines and from the current as red dashed lines. The magenta stars show the finite-system  $\Delta\phi$  of type-II states. Top panels corresponds to  $\gamma = 0.01$ , middle to  $\gamma = 1$  and bottom to  $\gamma = 100$ . The left panels correspond to superpositions with  $p_0 = \pi\hbar n_0$  and the right panels to  $p_0 = \pi\hbar n_0/2$ . The  $\Delta\phi$  value of type-II states is clearly the limit of  $\Delta\phi$  computed from superposition states as  $\Delta p \rightarrow 0$ .

## 12.5 Length Scale of the Quantum Dark Soliton

In the previous sections we considered localized superpositions of type-II states and studied their soliton-like properties. In the Gross-Pitaevskii regime we were able to compute the coefficients necessary to create Gross-Pitaevskii dark solitons, but of course a similar calculation is not possible for larger  $\gamma$ 's. Upon examining the physical properties of the various superpositions, we found that, in general, there was no “optimal” superposition that would give, for example, the narrowest density dip or the largest missing particle number. How then can we define a “quantum dark soliton” at any given  $c$  and  $p_0$ ? In particular, is there some unique, fundamental dark soliton-like object at each  $c$  and  $p_0$  that would underlie all the superposition states we can construct?

Let us turn to the bright soliton case (of which there is already some understanding in the literature) for inspiration. In the paper [175] by Haus and Lai, equation (3.8) gives a formula for the expectation value of the field operator in the soliton state as a sum over densities (i.e. over  $n_0 = N/L$ ) of a convolution of the classical bright soliton wavefunction with a Gaussian. In our case it makes little sense to combine several  $n_0$  values, but the convolution idea can be investigated further.

In fact, the recent article on quantum dark solitons [65, 66] demonstrates that a measurement of position performed on a type-II state reveals a solitonic density dip at a random position around the ring for any value of the interaction strength, while [64] shows that the single-particle density of dark solitons in the Gross-Pitaevskii regime can be viewed as a “superposition” of the Gross-Pitaevskii dark soliton located at various positions around the ring, with a Gaussian distribution of the coefficients.

Moreover, crucial progress has been made in Ref. [211] (appendix E), considering bright solitons, where several key results are derived. It is shown that if the Hamiltonian of an  $N$ -particle system separates into center-of-mass and relative-motion parts, the single-particle density is given by a convolution of the center-of-mass density and a function which relates to the relative-motion part of the wavefunction. Furthermore, it is shown that the variance of the single-particle density is the sum of the variances of the center-of-mass density and the relative-motion function appearing in the convolution.

In light of this evidence, it is logical to hypothesize that the single-particle density  $n_s(x)$  may be given by a convolution of some fundamental dark soliton density profile  $F(x)$  with a Gaussian center-of-mass of the missing particles density  $G(x)$ :

$$n_s(x) = (G * F)(x), \tag{12.42}$$

where  $*$  denotes convolution. Consequently, we should have

$$\Delta x^2 = \Delta x_{FS}^2 + \Delta x_{COM}^2(t), \quad (12.43)$$

where  $\Delta x^2$  is the variance of the density of a Gaussian superposition state,  $\Delta x_{FS}^2$  is the variance of the fundamental quantum dark soliton density, and  $\Delta x_{COM}^2$  the variance of the center-of-mass density. All the time dependence is assumed to be in the center-of-mass part, which disperses quadratically in time according to the usual formula

$$\Delta x_{COM}^2 = \Delta x_0^2 \left[ 1 + \left( \frac{\hbar t}{2M^* \Delta x_0^2} \right)^2 \right], \quad (12.44)$$

where  $\Delta x_0^2$  is the initial width of the Gaussian wavepacket. In particular, it is given by

$$\Delta x_0^2 = \frac{\hbar^2}{4\Delta p^2} = \text{var} \left[ \int_{-\infty}^{\infty} C_{p,N}^{p_0} e^{-ipx/\hbar} dp \right]^2, \quad (12.45)$$

for Gaussian coefficients defined by (12.16). Moreover,  $M^*$  is a quantity with the dimensions of mass, which could be expected to be related to the inertial mass,

$$m_I = \frac{dp}{d\tilde{v}_s} = 2 \frac{dE}{d\tilde{v}_s} = \left( \frac{d^2 E}{dp^2} \right)^{-1}, \quad (12.46)$$

where  $\tilde{v}_s = dE/dp$  is the derivative of the finite-system dispersion relation with periodic boundary conditions.

Equations (12.43)-(12.45) constitute a very strong statement – their assumption allows for the extraction of two key parameters – the width of the fundamental dark soliton,  $\Delta x_{FS}^2$ , and the mass associated with the center-of-mass wavefunction,  $M^*$ , which can then be compared to  $m_I$ . In more detail, the equations predict that

$$\Delta x^2(t=0) = \Delta x_{FS}^2 + \frac{\hbar^2}{4\Delta p^2}, \quad (12.47)$$

so if we plot  $n_0^2 \Delta x^2$  at  $t=0$  versus  $\frac{n_0^2 \hbar^2}{\Delta p^2}$  and find a linear relationship, we can fit the data constraining the gradient to  $1/4$ , and obtain the intercept  $n_0^2 \Delta x_{FS}^2$ . We have indeed carried out this procedure across the range of interactions ( $\gamma = 0.05 - 10$ ) and for several momenta,  $p_0$ , across the dispersion relation. Good quality linear fits with a slope of  $1/4$  were always possible. At each value of  $p_0$  we used 12 Gaussian superpositions with  $\sigma_p/\hbar n_0$  ranging from 0.1 to a  $p_0$ -dependent maximum, selected to ensure that the coefficients remain within the fundamental interval  $[0, 2\pi\hbar n_0]$ . In some examples, nonlinearity (caused by finite-size effects) became significant for higher  $\Delta p$ . Whenever this occurred, the affected data points were excluded from the

fit and the maximal  $\Delta p$  for which linear behaviour is observed was noted. Several examples of fits are shown in the left panels of Fig. 12.11. Thus  $\Delta x_{FS}^2$  can be readily extracted.

Next, from equations (12.43)-(12.45), we see that if we plot  $n_0^2 \Delta x^2$  versus  $\frac{(\hbar n_0^2)^2 t^2}{(2m)^2}$ , we expect a linear relationship with intercept  $n_0^2 \Delta x_{FS}^2 + \frac{\hbar^2 n_0^2}{4\Delta p^2}$ , and gradient  $\frac{\Delta p^2}{\hbar^2 n_0^2} \frac{(2m)^2}{M^{*2}}$ . Since the intercept is now fully known we may fit only for the gradient and extract  $M^*$ . We have systematically examined the data across the range of parameters according to this prescription and found that high-quality fits were always possible, thus confirming the assumed relations. For each  $\gamma$  and  $p_0$ , we have repeated the procedure for several  $\Delta p$  values, being careful to remain in the linear regime discussed in the previous paragraph. The time interval was covered in 12 points, ranging from zero to a maximal value, chosen such that nonlinear regimes are excluded (these occur at long times when the wavepacket has dispersed strongly and boundary effects come into play). However, the maximal time must not be too small – the accuracy of the fit is increased if the majority of the linear regime is used. We observed that  $M^*$  remained convincingly independent of  $\Delta p$ , and to reduce numerical error, averaged  $M^*$  over the different  $\Delta p$  simulations. Example fits are presented in the right panels of Fig. 12.11.

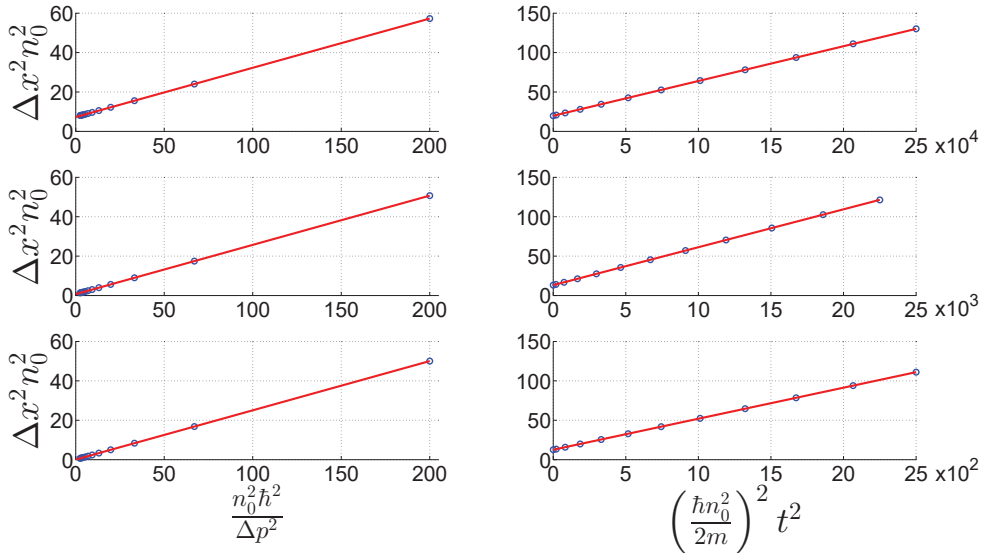


Figure 12.11: Examples of the data and linear fits used to extract the width of the fundamental dark soliton,  $\Delta x_{FS}^2$ , and the mass associated with the center-of-mass wavefunction,  $M^*$ . For all panels,  $p_0 = \pi \hbar n_0$ . Top panels use  $\gamma = 0.1$ , middle panels  $\gamma = 1$ , and bottom panels  $\gamma = 10$ . For the left-hand side panels,  $\Delta x^2$  is taken at time  $t = 0$ . For the right-hand side panels, we use  $\sigma_p = 0.2 \hbar n_0$ .

Before examining the results, it is instructive to consider what we might expect to find for the variance of the quantum dark soliton. Let us begin from Gross-Pitaevskii dark solitons in an infinite system. The variance of the density profile

$n_s(x)$  of equation (12.20) with all finite size corrections removed (i.e. replacing  $\rho$  by  $n_0$ ) can be expressed through the missing particle number of the Gross-Pitaevskii dark soliton,  $N_d$ , as

$$\Delta x_{DS}^2 = \frac{\pi^2 \hbar^4}{3g^2 m^2 N_d^2}, \quad (12.48)$$

where  $g$  is the interaction strength appearing in the one-dimensional Gross-Pitaevskii equation and

$$N_d = -\frac{2\hbar}{g} \sqrt{\frac{\mu}{m}} \sqrt{1 - s^2}. \quad (12.49)$$

The equation of state for the Gross-Pitaevskii equation is  $\mu = gn_0$ . In terms of dimensionless quantities, (12.48) can be recast as

$$\Delta x_{DS}^2 n_0^2 = \frac{\pi^2}{3\gamma^2 N_d^2}. \quad (12.50)$$

Meanwhile, the variance of the Hartree-Fock bright soliton is given by [211]

$$\Delta x_{BS}^2 = \frac{\pi^2 \hbar^4}{3g^2 m^2 (N - 1)^2}, \quad (12.51)$$

where  $N$  is the number of particles in the bound state. It is immediately clear that the bright- and dark-soliton formulae are practically identical, with only  $N$  being replaced by  $N - 1$ , caused by the difference between the Gross-Pitaevskii and Hartree-Fock formulations. The Hartree-Fock formula (12.51) diverges when  $N \rightarrow 1$ , which is an unphysical prediction. From intuition, one would expect  $\Delta x_{BS}^2$  to vanish in this limit, as with only one particle in the system, there are no interactions and we would expect the total variance to be equal to the center-of-mass variance. By virtue of (12.43), this implies that the width of the underlining soliton must vanish. Incidentally, the same is expected in the Tonks-Girardeau regime of the Lieb-Liniger model where the system becomes mappable on to non-interacting fermions.

Based on these mean-field results, we may hypothesise that for the quantum dark soliton,

$$\Delta x_{FS}^2 = \frac{\pi^2 \hbar^4}{3g^2 m^2} f(N_d), \quad (12.52)$$

or equivalently,

$$\Delta x_{FS}^2 n_0^2 = \frac{\pi^2}{3\gamma^2} f(N_d), \quad (12.53)$$

where  $f(N_d) \sim 1/N_d^2$  for large  $|N_d|$ . In fact, one may hope that  $f$  is the same function which describes the variance of quantum *bright* solitons, so that the dark soliton could be interpreted as a bound state of  $|N_d|$  bare holes, held together by repulsive  $\delta$ -function interactions, as the bright soliton is bound by attractive  $\delta$ -function interactions. Fortunately, results for exact many-body bright soliton solutions are

available in the literature. In the two-particle case, one has [211]

$$\Delta x_{BS}^2 = \frac{2\hbar^4}{g^2 m^2}, \quad (12.54)$$

and in the general  $N$ -particle case, the variance of the density can be computed from equation (6) of Ref. [213] as

$$\Delta x_{BS}^2 = \frac{16}{N^3} \frac{N-1}{g^2} {}_4F_3([1, 1, 1, 2-N]; [2, 2, N+1]; 1), \quad (12.55)$$

where  ${}_pF_q$  is the generalized hypergeometric function. This equation reduces to (12.54) for  $N = 2$ . Note that (12.55) vanishes when  $N = 1$ , as expected.

With the goal of testing (12.53) we compute the missing particle number  $N_d$  of type-II states, extracted from the dispersion relation with finite size corrections, at the same  $\gamma$  and  $p_0$  as the Gaussian superposition states studied. Figure 12.12 shows (as symbols) a plot of  $\Delta x_{FS}^2 n_0^2 \gamma^2$  extracted from the widths of Gaussian superposition states versus  $N_d$  of the type-II states. The data spans five different  $p_0$  values across the dispersion relation and a  $\gamma$  range from 0.05 to 10. In accordance with the hypothesis (12.53), all points fall on to a single curve. In the Gross-Pitaevskii regime (where  $|N_d|$  is large) the data approaches the Gross-Pitaevskii dark soliton formula, (12.50), shown as a green solid line. For comparison, we have also added the quantum bright soliton result of equation (12.55) as a blue dashed line, replacing  $N$  with  $|N_d|$ , but it is clear that in the Tonks-Girardeau regime (where  $|N_d| \rightarrow 1$ ) this function behaves completely differently to the quantum dark soliton data. In fact, in the Tonks-Girardeau regime we have confirmed that the width of the quantum dark soliton  $\Delta x_{FS}^2 n_0^2$  indeed tends to zero, as expected. This can be further corroborated by an analytical calculation of the variance of the density profile (12.19) which leads to  $\Delta x_{FS} = 0$  (for large  $N$ ). The apparent divergence on Fig. 12.12 is completely due to the  $\gamma^2$  factor.

Next, we can test whether the mass  $M^*$  which determines the dispersion rate of the center-of-mass density is indeed related to  $m_I$ . This may be expected intuitively, as the dispersion of wavepackets is related to the second derivative of the dispersion relation – essentially  $m_I$  [see equation (12.46)]. Therefore we extract the inertial mass from the finite-size corrected type-II dispersion for comparison. Figure 12.13 shows the ratio  $m_I/M^*$ , which is extremely close to one, with scatter in the data of the order of a percent. Again, five different  $p_0$  values and a large  $\gamma$  range were investigated, and the result holds throughout. We conclude that  $M^* = m_I$ .

A final, but highly important observation is in order. The convolution model (12.42) predicts that if  $n_s$  and  $F$  are both normalized to  $N$  particles, then the missing particle number of  $F * G$  is equal to that of  $F(x)$ . Therefore, we can expect  $N_d$  of

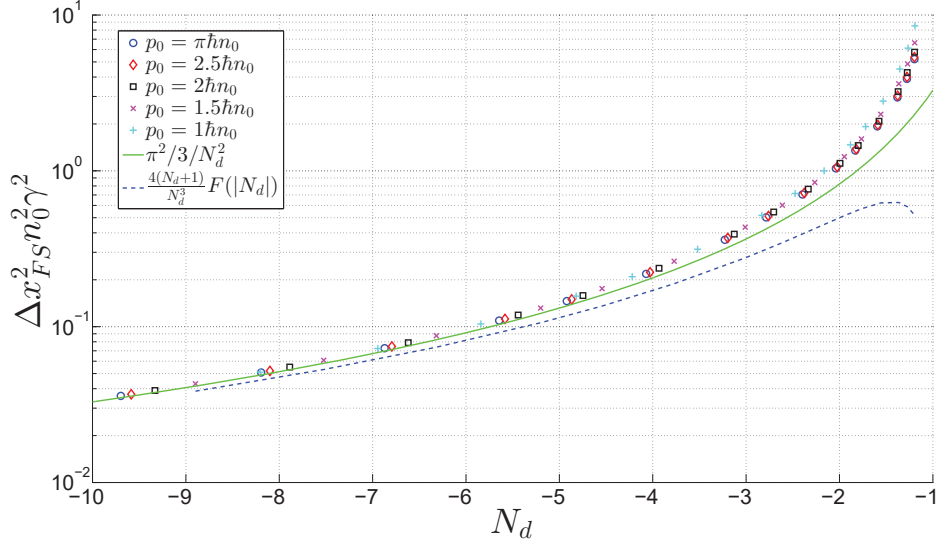


Figure 12.12: The variance of the quantum dark soliton as a function of the missing particle number. Symbols show  $\Delta x_{FS}^2 n_0^2 \gamma^2$  extracted from the widths of Gaussian superposition states versus  $N_d$  of the type-II states obtained from the dispersion relation with finite size corrections. The different symbols correspond to five different momenta  $p_0$  (see legend), and the data is taken over the range  $\gamma \in [0.05, 10]$ . The green solid line is a plot of (12.50) on the given axes, which amounts to  $\pi^2/3N_d^2$ , and the blue dashed line is a plot of equation (12.55) with  $N$  replaced by  $|N_d|$ . In the legend,  $F(|N_d|)$  is a short-hand notation for  ${}_4F_3([1, 1, 1, 2 - |N_d|]; [2, 2, |N_d| + 1]; 1)$ .

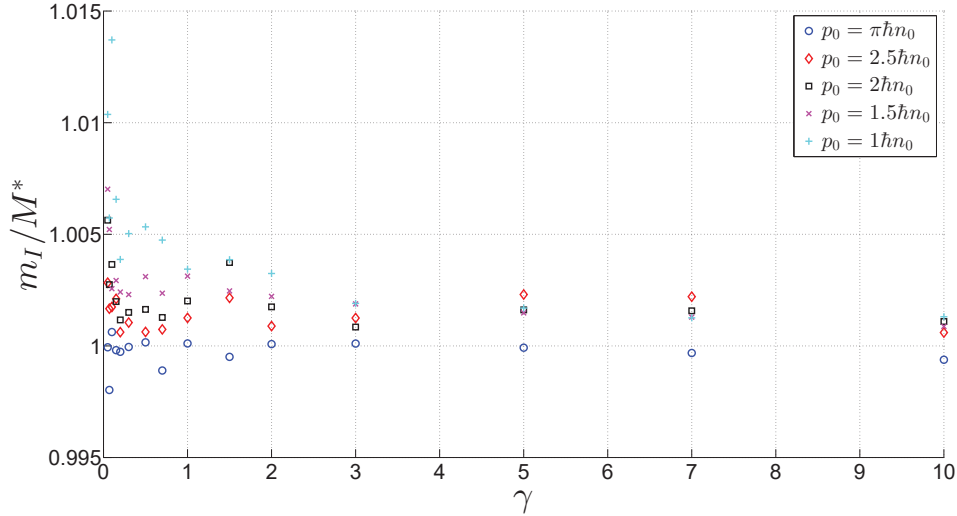


Figure 12.13: Ratio of the inertial mass to the mass appearing in the center-of-mass dispersion formula, (12.44), as a function of  $\gamma$  for five momenta  $p_0$  (see legend). There is a 1% scatter in the data about  $m_I/M^* = 1$ , regardless of parameters, which suggests that  $M^* = m_I$ .

type-II states (extracted from the dispersion relation corrected for a finite system) to be equal to  $N_d$  of  $F(x)$ , and  $N_d(\Delta p)$  of the various Gaussian superpositions shown in Fig. 12.6 to be independent of  $\Delta p$ .

Let us examine the bottom panels of all the subfigures in Fig. 12.6 with this in mind. The variation in the Gaussian superpositions data shown as blue lines is always less than 2% – these variations are clearly a small effect which is outside the scope of the convolution model. We may conclude, therefore, that within the accuracy of the convolution model,  $N_d$  of the fundamental dark soliton can be extracted directly from the type-II dispersion relation, corrected for finite-system effects (chapter 11).

Note also that since according to the convolution model,  $N_d$  of  $F(x)$  is equal to that of  $(F*G)(x)$ , the missing particle number of the various Gaussian superpositions is expected to stay constant in time. This is precisely what is seen in Fig. 12.5, up to the point when the size of the density notch becomes comparable to the size of the box,  $L$ , and the calculation of  $N_d$  becomes ambiguous.

## 12.6 Discussion and Conclusions

In this chapter we have investigated the long-standing question of the connection between type-II excitations of the Lieb-Liniger model and dark soliton solutions of the Gross-Pitaevskii equation. Physically very different objects, type-II excitations are spatially-uniform momentum eigenstates while dark solitons have prominent features in both the density and phase profiles. We solved the Bethe ansatz equations for large but finite systems, and were able to make use of the machinery of the algebraic Bethe ansatz to compute matrix elements of the field and density operators.

We expanded on the idea of Sato et al. [201–204] of constructing superpositions of type-II states, but instead of using uniform (in momentum) expansion coefficients, we used localized distributions. Moreover, in the small  $\gamma$  regime, we were able to explicitly compute the momentum distribution contributing to the Gross-Pitaevskii dark solitons, and demonstrated that the resulting superpositions matched the mean-field solutions. We then studied the physical properties of superpositions constructed with Gaussian coefficients of various widths, which, among other things, shed light on a previously-available result. In particular, in chapter 11 we have corrected the missing particle number and phase step of type-II states that can be extracted out of the thermodynamic limit dispersion relation for finite system effects. These values correspond to the limit of infinitesimally-thin Gaussian wavepackets, and as such have a clear physical meaning.

Furthermore, we assumed that there exists a fundamental solitonic density such that the density profiles of Gaussian superpositions can be described by a convo-

lution of this fundamental density with the Gaussian center-of-mass of the missing particles density. This is in line with the bright soliton case [175, 211] and is consistent with recent results [64–66] which demonstrate that the greying of a soliton (over time) seen in the single-particle density can be explained by a model where a fundamental soliton (which is not changing in time) is delocalized over the ring with a Gaussian distribution of its position.

The center-of-mass density could be predicted analytically, and accounts for all of the dependence on  $\Delta p$  and time – in fact, it obeys the textbook quadratic Gaussian spreading of single-particle quantum mechanics with the single-particle mass replaced by the inertial mass of the type-II state. The initial width of the center-of-mass density can be obtained by Fourier-transforming the Gaussian coefficients of the superposition in momentum space, and is inversely proportional to the width of the later. All fitting of the numerical data to the assumed equations was convincing and therefore supported the proposed relations.

Resorting to a further result from [211] that the variances add in convolution, we were able to use the variances of the single-particle density of Gaussian superpositions to reliably extract the width of the fundamental quantum dark soliton for various momenta and interaction strengths. We found that it is possible to scale out the dependence on  $\gamma$  and  $p_0$ , so that  $\Delta x_{FS}^2 \gamma^2 n_0^2$  was a unique function of the missing particle number  $N_d$ . This relation was compared to the Gross-Pitaevskii prediction and the quantum bright soliton variance, but neither captured the quantum dark soliton width well in the Tonks-Girardeau regime.

Another important question that is answered as a result of our investigation is why the finite-system approximation of chapter 11 is so successful for the type-II excitations when, as it would seem, none of the physical assumptions that are required for the derivation are satisfied (a localized excitation with a density dip and a phase step). While superfluidity is not guaranteed, we are now able to state that there exist solitonic objects with all the required physical properties that have the same momentum, excitation energy, missing particle number and phase step as the type-II excitations: any fairly-localized superposition of type-II states centred at some momentum  $p_0$  would have momentum  $p_0$  and excitation energy  $E(p_0)$  (where  $E$  is the type-II excitation energy), simply due to the averaging process. We have also discovered that the  $N_d$  and  $\Delta\phi$  we extract from the Lieb-Liniger dispersion relation (with a finite system correction) correspond to the  $N_d$  and  $\Delta\phi$  of all the superposition states evolved to any time  $t$  (as long as the soliton remains sufficiently well-localized), since by virtue of the convolution model these quantities are independent of  $\Delta p$  &  $t$ , and are thus equal to their values at  $\Delta p = 0$ .

The experimental detection of dark solitons in one-dimensional cold atom systems should not be very difficult. One would start from the Bose-Einstein condensate

limit where dark solitons have already been observed, created via phase imprinting [16, 21, 22]. Then the coupling strength needs to be ramped up adiabatically (using Feshbach resonances) [72, 73], which would hopefully leave the system in either the type-II state or a superposition of type-II states about the momentum of the original excitation in the weakly-coupled regime. Alternatively, it may be possible to create the soliton directly in the strongly interacting regime. For example, the seminal paper [214] exactly models the creation of dark solitons in the Tonks-Girardeau regime by imposing either a density notch or a phase step on top of the uniform ground state. Finally, detection would be possible through the density depletion, which would require resolution on the single atom level (since the soliton size and missing particle number drop considerably as  $c$  increases), but this is possible using so called quantum-gas microscopes [1, 215].

# Chapter 13

## Physics of the Yang-Gaudin Model

In this chapter we will discuss the physical implications of the Bethe ansatz calculations presented in chapters 8, 9 & 10. First we will discuss dark solitons in the spin-1/2 Fermi gas, making connections to our work on the Lieb-Liniger model (in particular, chapters 11 & 12). Then we expand on the low-energy spin excitations in the repulsive regime of the Yang-Gaudin model and consider their detection through the Hess-Fairbank effect. Two different super Tonks-Girardeau limits are considered briefly.

### 13.1 Dark Solitons

It is trivially obvious that the Bethe ansatz equations (both finite-system and thermodynamic limit) for single fermion holes in the attractive regime of the Yang-Gaudin model under the string hypothesis are almost identical to the equations for single boson holes in the Lieb-Liniger model. This is perfectly sensible, as we know that when  $\gamma$  falls below zero sufficiently, the single fermion holes become single dimer holes, taken out of a fully dimerized ground state distribution. Once the string hypothesis becomes applicable, the Fermi gas consists of tightly bound bosonic dimers, and unless a dimer is purposefully broken, the underlining fermionic nature is not apparent. Therefore, it is natural that the mathematical description be identical to single boson holes, up to the factor of two which accounts for the mass of the dimer being  $2m$ .

This insight allows us to translate much of what we have learned for boson holes in the Lieb-Liniger model to dimer holes in the Yang-Gaudin model. In particular, the connection of type-II states to quantum dark solitons established in chapter 12 can almost certainly be taken over directly into the fermionic gas<sup>1</sup>. The properties we have computed for the single (and double – see below) fermion hole branch, such as the dispersion relation, missing particle number, phase step, and inertial & physical masses, can be taken as the properties of dark solitons in the Fermi gas, because as we have shown in the previous chapter, the underlining quantum dark

---

<sup>1</sup>Unfortunately, the algebraic Bethe ansatz for nested systems (with multiple spin components of particles) is not yet as advanced as that for spinless bosons, and therefore a parallel study in the fermionic case is not currently possible.

soliton object shares all these properties with the type-II excitations.

Therefore, by performing Bethe ansatz calculations for type-II states in the Yang-Gaudin model, we have predicted the properties of dark solitons in the attractive one-dimensional spin-1/2 Fermi gas. There has not been an experimental observation of solitons in truly one-dimensional attractive fermionic systems, but a theoretical study [68] attempted to predict their properties in the weakly-interacting regime using one-dimensional Bogoliubov de-Gennes theory. Our Bethe ansatz-based results differ from the mean-field results [68] significantly, in particular in terms of the prediction of the masses and their ratio. We found that  $m_{I,P} \rightarrow m$  as  $\gamma \rightarrow 0^-$  (in accordance with the physical nature of the excitations), whereas Bogoliubov de-Gennes theory predicted  $m_I \rightarrow -\infty$  and  $m_P \rightarrow 0^-$  as  $\gamma \rightarrow 0^-$ . This discrepancy is due to the fact that the use of mean-field theory in one dimension is questionable, as outlined in chapter 2.

Of course, double fermion holes become double dimer holes as  $\gamma \rightarrow -\infty$ , and as such are analogous to two-boson holes in the Lieb-Liniger model. In this limit, they are not elementary excitations, but composite ones, and as such we did not study these in the Lieb-Liniger model. However, it has been shown by other authors [65, 66] that double boson holes in the Lieb-Liniger model correspond to states with two dark soliton excitations, in accordance with intuition. Thus, we expect the double fermion hole branch of the Yang-Gaudin model to correspond to two-soliton excitations of the attractive Fermi gas.

Now, with this in mind, we can apply the finite system approximation developed in chapter 11 to the various Yang-Gaudin branches and inspect the quality of the approximation. The details and results are presented in appendix 13.A. Using the third-level equations, we have tested all three elementary type-II branches in the attractive and repulsive regimes, and found that the approximation is only valid for single fermion holes in the attractive regime after the string hypothesis comes into play, and for double fermion holes for any  $\gamma$ , positive or negative. For these branches, the quality of the approximation is excellent. These are therefore the only two excitations that may be associated with dark solitons, at least in the sense used so far, i.e. solitons in a single-component (possibly composite) bosonic superfluid.

Note that this allows us to identify potential dark solitons also in the repulsive regime. For  $\gamma > 0$ , the double fermion holes are the lowest excitations of the *charge* sector (which decouples from the *spin* sector – see the next section) and become single fermion holes in the Tonks-Girardeau limit, in analogy to single boson holes in the Lieb-Liniger model. Even though the Bethe ansatz equations look quite different, the spin degree of freedom decouples in the strongly-repulsive limit, leaving a Tonks-Girardeau spectrum for the charge sector, in which hole excitations – the double fermion hole branch – may again be understood as dark solitons.

This is an interesting result in light of the fact that a mechanism for pairing is not obvious for repulsive interactions. In order to address this question directly we would require the two-particle (pairing) density matrix, which at the moment is theoretically inaccessible<sup>2</sup>. A dark soliton in the classical sense (e.g. in the Gross-Pitaevskii equation) certainly requires a superfluid with a coherent phase. In this thesis, we have been able to relax this condition to one-dimensional quasi-condensates with fluctuating phases, generalising the concept of dark solitons into the strongly-interacting regime. Nonetheless, intuitively, it is somewhat reassuring that the Lieb-Liniger and attractive Yang-Gaudin models have a limit where, at least in higher dimensions, one would expect superfluidity. By that we mean a Bose-Einstein condensate in the former case, and a Bardeen-Cooper-Schrieffer state in the latter case, both found in the weakly-interacting limit. For a repulsive Fermi gas, there is no regime where one would expect (conventional) superfluidity or condensation, even if we were to remove the one-dimensional constraint. As such, a prediction of dark solitons is non-trivial and perhaps questionable.

However, we cannot deny the success and consistency of our “solitonic” calculations for this branch. The Yang-Gaudin equations (without the string hypothesis) are in general very different from the Lieb-Liniger ones, and it is not trivial that computations that give reasonable results for the bosonic case should make sense also for fermions. Thus, perhaps our work here can be viewed as an indirect way of probing the pairing question in the one-dimensional Fermi gas: the success of the calculations implies that some sort of superfluidity and phase coherence should exist, which is a surprising but potentially powerful statement.

From the point of view of the Bethe ansatz and our experience in linking type-II states to dark solitons, the fact that double fermion holes seem to be solitonic is actually intuitive. The underlying fermionic nature of the gas is “hidden” for the double fermion holes: for weak repulsion, while there are still correlations between spin-up and spin-down particles, the excitation is a double-fermion hole, treating a pair as a single whole, thus leaving the spin degree of freedom untouched. For strong repulsion, the excitation is a single fermion hole, but since the two spin components become equivalent in the Tonks-Girardeau limit (at least as far as charge excitations are concerned), the spin degree of freedom is once again irrelevant.

Moreover, double fermion holes can be understood as solitonic also for weak attractive interactions, where the finite-system approximation for the single fermion holes fails. The underlying fermionic nature of the particles is hardly truly “invisible” in this limit, as the dimers are weakly bound and pair correlations are weak. Nevertheless, a pure charge excitation such as the double fermion hole still behaves

---

<sup>2</sup>Some approximate calculations are available [183], but at this stage they yield little physical insight.

very much as a (double) dark soliton and one would not hesitate to interpret it as such. The sign of the interactions in the vicinity of  $\gamma \approx 0$  then seems of little importance in such an argument.

For the other branches, the approximation is very different from the exact dispersion relation and increasing the system size does not improve the quality. Since we have no reason to expect the other branches to be solitonic, this is not surprising. Illustrative figures and further details can be found in appendix 13.A.

### 13.1.1 Dimer Super Tonks-Girardeau

Recall the concept of the super Tonks-Girardeau gas, introduced in chapter 7: the Lieb-Liniger model is taken to the Tonks-Girardeau regime, and then  $\gamma$  passes through  $\pm\infty$  ( $1/\gamma$  passes through zero). The Tonks-Girardeau solutions can be followed to the other side of the resonance, but now they are highly excited states. The bosonic super Tonks-Girardeau gas is described by the ordinary Lieb-Liniger Bethe ansatz equations with  $c < 0$ . Since these equations are practically the same (up to a factor of two) as the Yang-Gaudin dimerized equations under the string hypothesis, the results we found in the  $\gamma \rightarrow -\infty$  limit for the Yang-Gaudin model apply equally to the super Tonks-Girardeau limit of the Lieb-Liniger model [216]. In other words, we predict the existence of dark solitons as excitations of the super Tonks-Girardeau ground state. This is remarkable, as in the attractive Lieb-Liniger model one usually studies *bright* solitons – in fact the true ground state is a bright soliton – and yet there also exist highly excited dark soliton solutions.

## 13.2 Spin Waves

In chapter 8 we found two branches that approached the system translation parabola as  $\gamma \rightarrow \infty$ : these were the spin-flip excitations and single fermion holes. We solved the Bethe ansatz equations approximately in this limit and saw that it is the presence of the spin rapidities that accounts for the limiting behaviour of these branches. In other words, the system translation parabola becomes accessible at all values of the quantized momentum because of the spin degree of freedom. One might wonder if the same occurs for a two-component Bose gas, and indeed this is the case, as can be shown by approximately solving the Bethe ansatz equations with periodic boundary conditions (see appendix 13.B), given in [159]. So how may these spin excitations be interpreted?

In fact, the behaviour we uncovered with the help of the Bethe ansatz can be understood through Haldane’s Luttinger liquid theory [89, 217, 218], which shows that the “charge” sector fully decouples from the “spin” sector – the Hamiltonian is written as two identical, non-interacting parts, one for each kind of excitation. This

is known as “spin-charge separation”. The parameters entering the Hamiltonian, in particular the speeds of sound of the two sectors, are determined phenomenologically – i.e. the theory does not predict them. It is interesting that this Luttinger liquid theory can be applied to both bosons and fermions, via a technique called bosonisation, and the predictions are universal to one-dimensional gases.

Now, what is meant by “charge” and “spin” waves, terms that feature heavily in the Luttinger liquid formulation? During the reduction of the Hamiltonian to the Luttinger-liquid form, one defines the charge density as the total (bosonized) particle density and the spin density as the relative, that is, the difference between the (bosonized) densities of the two components. Charge and spin waves are then literally longitudinal and transverse waves, respectively, in these two densities, travelling at different speeds.

How can our three elementary type-II excitations be categorized under such a description? Usually, when classifying Bethe ansatz states into the Luttinger liquid phenomenology, one reasons as follows: the nature of the excitation depends on which rapidity density is perturbed in the thermodynamic limit to create it. In our case, to excite double fermion holes the charge rapidity density  $\rho(k)$  is perturbed by the removal of a  $k$  – therefore these are charge waves. For single fermion holes and spin-flips, it is the spin rapidity density that is perturbed: in the first case by the replacement of two  $\alpha$ 's by an  $A$  and in the second, by the removal of an  $\alpha$ . Therefore, both branches are spin waves. Of course this classification is not based on the direct definition of the two kinds of Luttinger liquid excitations, but the Bethe ansatz does not furnish us with sufficient information for this task and at least *a posteriori* the classification above is consistent with expectations.

Luttinger liquid theory has been used in the literature to describe one-dimensional fluids quite extensively. For example, [219] considers a one-dimensional Fermi gas in a harmonic trap, and deduces the existence of a lower dipole oscillation (“sloshing” motion of the entire cloud) frequency as a result of spin excitations being present. The authors present formulae for the Luttinger parameters for both sectors for weak interactions, and use the Bethe ansatz to compute the parameters in the Tonks-Girardeau regime. They correctly point out that the charge spectrum is that of a free Fermi gas (tying in with our nomenclature, double fermion holes belong to the charge spectrum and are the hole excitations of a single component Fermi gas with  $N$  particles). Equation (10) of [219] gives the spectrum of spin waves, which is linear in momentum due to the fact that it is derived under Luttinger liquid theory which is fundamentally linearised.

In addition, [220] look at a two-component repulsive Bose gas, the ground state of which is ferromagnetic so that a spin flip introduces one spin-up particle into a spin-down sea (i.e. essentially a polaron). The authors find a quadratic dispersion

relation for the spin-flip branch, and the effective mass associated with it approaches that of the entire system in the Tonks-Girardeau limit, in accordance with our own findings. This is also discussed in [178], where it is mentioned that the polaron effective mass is  $m$  in the  $\gamma \ll 1$  limit (clearly consistent with our results) and  $Nm$  in the Tonks-Girardeau limit.

In the review article [183], section IIIC, a collection of results for the speeds of sound for the two sectors are given, in both the strongly- and weakly-repulsive regimes, including first order corrections in  $\gamma$ . In the Tonks-Girardeau limit, the charge sector velocity approaches the Fermi velocity while the spin velocity vanishes. These results can also be found in [179]. This is fully consistent with our findings, identifying double fermion holes as charge excitations and the other two branches as spin waves (in the thermodynamic limit, the system translation parabola hugs the momentum axis).

Finally, note that Schlottmann [184] uses his formulation of the thermodynamic limit Bethe ansatz to study, among other things, spin flip excitations in the Yang-Gaudin model. His description of their behaviour in the Tonks-Girardeau limit is fully consistent with our results from chapter 9.

To summarize, the low energy spin excitations<sup>3</sup> that we found in chapter 8 decouple from the charge excitations (double fermion holes) as  $\gamma \rightarrow \infty$  and become “soft”, that is, their dispersion relation vanishes in the thermodynamic limit. At first this is quite surprising as the infinitely repulsive spin-1/2 Fermi gas is often said to be equivalent to a single component of free fermions which certainly does not feature such excitations. However, we learned that it is only the charge sector that becomes a Tonks-Girardeau gas of  $N$  particles, while the system translation parabola excitations are spin-waves that are present due to the dual-component nature of the system. This behaviour is known and understood in the literature, both in the context of Luttinger liquid theory as well as from independent Bethe ansatz calculations.

The next question we must ask is can these translatory excitations be observed in present-day experiments? In particular, are periodic boundary conditions essential, as truly one-dimensional toroidal traps are currently unavailable. First of all, we note that the original work by Haldane [89, 217] predicting spin-charge separation is done for a periodic system, but a generalization to Dirichlet boundary conditions exists [221]. In this latter paper, the authors show that spin-charge separation still occurs, but since the parameters are determined phenomenologically, there is nothing to guarantee that the spin velocity is not equal to the charge velocity.

On the other hand, it is possible to derive the Bethe ansatz equations for  $\delta$ -

---

<sup>3</sup>As explained previously, in the strongly interacting regime, single fermion holes also become spin excitations as in the string hypothesis the  $\alpha$ 's are perturbed.

interacting particles with hard-wall boundary conditions [159], for both two-component fermions and bosons. Solving the Bethe ansatz equation to first order in the infinitely repulsive regime (see appendix 13.C) we see that indeed the  $\alpha_m$ 's no longer contribute to the  $k_j$ 's. However, with hard-wall boundary conditions the total momentum is not conserved because translational symmetry is lost, so thinking in terms of dispersion relations is no longer sensible. The only observation we can make is that the energy spectrum in the Tonks-Girardeau regime is identical to that of a single spin component of free fermions, i.e. low energy spin waves are not present. This implies that periodic boundary conditions are indeed essential for the observation of these excitations.

### 13.3 Hess-Fairbank Effect

We now move on to describe in detail the possible detection of spin-waves in the repulsive Fermi gas.

#### 13.3.1 Introduction

Experiments in ultra cold atom physics have recently begun probing one-dimensional Fermi gases with two [57, 76–78] or a variable number [79] of spin components and a small particle number ( $N \sim 10$ ). One possible approach to probe the low-energy properties of a superfluid is through the Hess-Fairbank experiment [222], where the ring trap is externally rotated and the angular momentum of the ground state of the rotating gas is measured. Since superfluids have a non-classical rotational inertia, the fluid does not rotate with the container, allowing one to witness the quantisation of circulation. Originally introduced for superfluid Helium, the concept was more recently applied to bright solitons in the attractive boson gas [223–225]. In terms of repulsive multicomponent gases, as we have seen, in the strongly interacting regime spin-waves become soft and the classical parabolic dispersion relation is recovered [219, 220]. Clearly, such excitations are not present in the non-interacting limit of a Fermi system, so it is natural to inquire how this transition occurs and what would be the observable consequences in terms of the Hess-Fairbank effect.

Here we approach this question via the Bethe ansatz [52], which allows one to exactly solve the Yang-Gaudin model [48, 49] of spin-1/2 fermions in one dimension with contact interactions and periodic boundary conditions. The dispersion relations of various low energy excitations can be easily obtained, and thus the Hess-Fairbank diagram can be constructed. Experimentally, one-dimensional linear traps for Fermi condensates already exist [57, 76–78], while ring traps should become accessible in the near future, since such traps for Bose-Einstein condensates have already been realised [70, 226–228].

We find that for moderate interactions, the Yang-Gaudin model exhibits a fractionalisation of the angular momentum of the rotating ground state: rotation is quantised differently than in a single-component repulsive Bose gas [164], with fractions of the unit angular momentum ( $L_0 = N\hbar$  where  $N$  is the number of particles) appearing in the Hess-Fairbank scenario. As interactions increase, at first only half-integer multiples of  $L_0$  are accessible, indicating the creation of half-vortices [229–232] in the ground state of the rotating system. This regime is separated from the multi-step phase where some, but not all, multiples of  $L_0/N$  are available by a straight line marking the quantum phase transition. At stronger repulsion still, we find another linear phase boundary, past which all multiples of  $L_0/N$  can be accessed through system rotation.

### 13.3.2 The Model

Let us rewrite the Yang-Gaudin Hamiltonian in terms of angular quantities and in a rotating frame at  $\omega_r$ :

$$H = \sum_{j=1}^N \left[ -\frac{\hbar^2}{2mr^2} \frac{d^2}{d\theta_j^2} + i\hbar\omega_r \frac{d}{d\theta_j} \right] + \frac{\hbar^2 c}{rm} \sum_{\langle i,j \rangle} \delta(\theta_i - \theta_j). \quad (13.1)$$

Here,  $\theta_j$  are the angular coordinates of the particles,  $m$  is the mass, and  $r$  is the radius of the ring. There are  $N$  fermions in total,  $M \leq N/2$  of which are spin-down and the rest are spin-up. As always, the one-dimensional density is  $n_0 = N/2\pi r$ , and the dimensionless coupling parameter is  $\gamma = c/n_0$ . A schematic of the system is illustrated in Fig. 13.1.

When  $\omega_r = 0$ , Hamiltonian (13.1) can be exactly diagonalized by the Bethe ansatz, as was done in chapter 8. The total angular momentum and energy of the system can be found (upon solving the Bethe ansatz equations) from

$$L = r\hbar \sum_{j=1}^N k_j, \quad E = \frac{\hbar^2}{2m} \sum_{j=1}^N k_j^2. \quad (13.2)$$

Recall that the lowest energy excitations at a given momentum in the repulsive regime are the spin-flip excitations, often discussed as an elementary spin-wave [184] in the parlance of Luttinger-liquid theory [89, 217]. In chapter 8 we listed the quantum numbers necessary to create spin-flip excited states from  $L = 0$  to  $L = L_0/2$ , where we define  $L_0 = 2\pi r\hbar n_0$ . In order to complete the branch and reach  $L_0$  we again begin from the ground state quantum numbers and set  $n_1 \rightarrow n_N + 1$  – this gives the umklapp point ( $L = L_0$ ). To compute the rest, we further subtract  $1/2$  from all the  $n_j$ 's, add  $1/2$  to all the  $\ell_m$ 's, and delete each of the  $\ell_m$ 's in turn, from  $m = 1$  to  $m = M - 1$ .

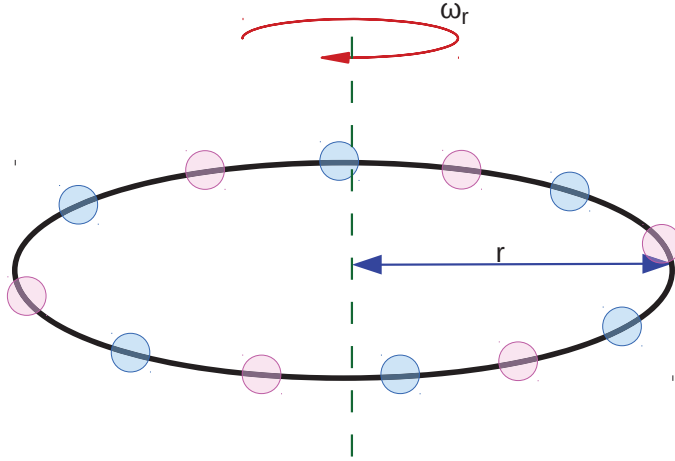


Figure 13.1: An illustration of the Yang-Gaudin model and the Hess-Fairbank set-up. The blue and pink circles represent spin-1/2 fermions,  $M$  of each spin component, so that the total number of particles in the balanced system is  $N = 2M$ . The particles are confined to a one-dimensional ring with radius  $r$ , which is externally rotated at  $\omega_r$ . The fermions experience contact repulsive interactions with dimensionless coupling strength  $\gamma$ .

### 13.3.3 Results

The Hess-Fairbank diagram depicts the angular momentum of the ground state ( $L_m$ ) of a system rotated at a certain angular velocity ( $\omega_r$ ). In order to construct it, one must compute the lowest energy dispersion relation of the stationary system,  $E(L)$ , and the energy of the rotating system,  $E' = E - \omega_r L$ . Then at each value of  $\omega_r$  we find the minimum of  $E'$  and its corresponding angular momentum value,  $L_m$ . Finally, one simply plots  $L_m$  as a function of  $\omega_r$ .

First consider the case of  $N$  free fermions, or equivalently, the bosonic Tonks-Girardeau gas. The lowest energy dispersion relation is that of holes (see chapter 7): it consists of convex curve segments with cusps at the umklapp points (at  $L_\ell = \ell L_0$ ,  $E(L_\ell) = L_\ell^2/2mNr^2$  for integer  $\ell$ ), which correspond to Galilean boosts of the ground state. Likewise, all states on the hole dispersion relation beyond the first umklapp point are simply boosted versions of their counterparts in the angular momentum interval  $[0, L_0]$ . Thus it is sufficient to compute  $E(L)$  on  $[0, L_0]$ , and obtain the  $\ell^{\text{th}}$  segment of the dispersion relation by adding  $\ell L_0$  to  $L$  and  $2\ell\hbar L/r^2 + 2\pi\ell^2\hbar^2 n_0/r$  to  $E$ . Note that at the  $\ell^{\text{th}}$  umklapp point, the system can be thought of as having  $\ell$  vortices at the center of the ring, as each vortex contributes a phase winding of  $\Delta\phi = 2\pi$  and  $L = r\hbar n_0\Delta\phi$ .

It is clear that the Hess-Fairbank diagram will have a step structure, as each of the umklapp cusps in turn becomes the ground state in the rotating frame. Moreover,

the plateaus will have angular momentum values  $L_\ell$ . The  $\ell^{\text{th}}$  plateau will start when  $E'(L_\ell)$  drops below  $E'(L_{\ell-1})$ . As the umklapp points lie on the translation parabola  $E = L^2/2mNr^2$ , setting  $E'(L_\ell) = E'(L_{\ell-1})$  gives us the condition for  $\omega_r$  of the transitions<sup>4</sup>,  $\omega_\ell = \frac{\pi n_0 \hbar (2\ell-1)}{rmN}$ . Thus the length of each plateau is  $\omega_0 = \frac{2\pi n_0 \hbar}{mNr}$ . Such a Hess-Fairbank diagram corresponds to the normal superfluid case.

If, on the other hand, we have a classical liquid with the lowest dispersion relation given by  $E = L^2/2mNr^2$ , the Hess-Fairbank diagram is a straight line passing through the set of points  $(\omega_\ell = \ell\omega_0, L_\ell = \ell L_0)$ , that is, through the middle of the steps present in the normal superfluid case. If the momentum is quantised, then one finds  $N$  small steps oscillating about the straight line of the continuous limit.

Returning to the Yang-Gaudin model, Fig. 13.2 shows the dispersion relation of the spin-flip excitations for several  $\gamma$  values (a) and the corresponding Hess-Fairbank diagrams (b). We see that when  $\gamma \ll 1$  the dispersion relation is that of a single fermion hole, expelled from the Fermi sea of its spin component due to Pauli exclusion. As interactions increase, the dispersion relation falls and in the Tonks-Girardeau limit, hugs the center of mass translation parabola.

The Hess-Fairbank diagram for  $\gamma \rightarrow 0$  is that of a normal superfluid, with additional points at  $(\omega_\ell, L_\ell/2)$ , as can be readily shown analytically using the fact that the half-umklapp points (at  $L = L_\ell/2$ ) lie on the translational dispersion relation for only one of the two spin components,  $E = L^2/mNr^2$ . These points (which later grow in to steps of finite length) can be interpreted as *half*-vortices in the center of the ring. Half vortices have been recently studied in, e.g., two-dimensional exciton-polariton condensates [231, 232], superfluid Helium-3 [230] and spinor Bose-Einstein condensates [229].

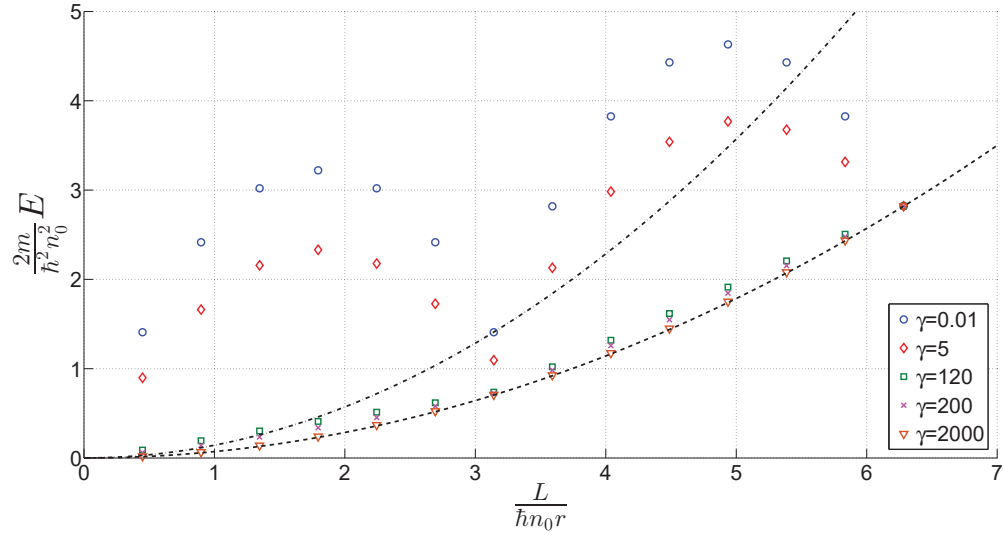
As  $\gamma$  increases, the length of this “half-way” step grows (at the expense of the original steps shrinking) due to the fact that the mid-point of the dispersion relation (at  $L = L_0/2$ ) falls gradually lower. We numerically extracted the length of the half-way step for various values of  $\gamma$  and  $N$  – the data is shown in Fig. 13.3, where we see that  $N$  can be effectively scaled out and all the points lie on a single curve (small deviations are present for very small  $N$ ). There is a clear horizontal asymptote at  $\omega_r/\omega_0 = 1/2$ , reflecting the fact that plateaus cannot overlap. In the limit of small  $\gamma$ , an analytical expression for the dispersion relation can be derived from the approximate solutions of the Bethe ansatz equations (chapter 8):

$$E(\gamma \ll 1) = \frac{\hbar^2 n_0^2}{2m} \left[ -\frac{2\gamma}{N} - \frac{L^2}{r^2 n_0^2 \hbar^2} + \frac{2L\pi(M+1)}{rn_0 \hbar N} \right], \quad (13.3)$$

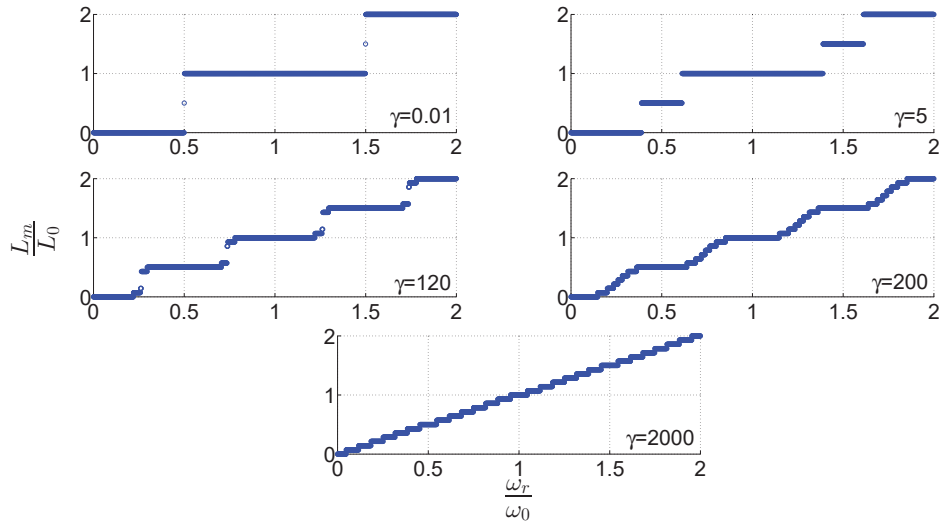
which enables us to extract the limiting behaviour of the step-length as  $\omega_r/\omega_0 =$

---

<sup>4</sup>The -1 appearing in  $\omega_\ell$  is to be omitted for even  $M$ ; in the rest of the chapter we report results for odd  $M$  but the even  $M$  case may be easily recovered by a simple shift.



(a)



(b)

Figure 13.2: Dispersion relation for spin-flip excitations of the Yang-Gaudin model with  $N = 14$ ,  $M = 7$  for several values of  $\gamma$  (a), and the corresponding Hess-Fairbank diagrams (b). The black dashed line in (a) is the system translation parabola,  $E = L^2/2mNr^2$ , while the dash-dotted line is the translational dispersion relation for only one of the two spin components,  $E = L^2/mNr^2$ .

$\gamma/\pi^2$ . In the opposite limit, as mentioned in chapter 8, the approximate dispersion relation does not include any correction terms in  $\gamma$ , so a similar calculation is not possible. An analysis of the numerical data suggests an asymptotic behaviour as  $\gamma \rightarrow \infty$  of  $\omega_r/\omega_0 = 1/2 - \pi/\gamma$ .

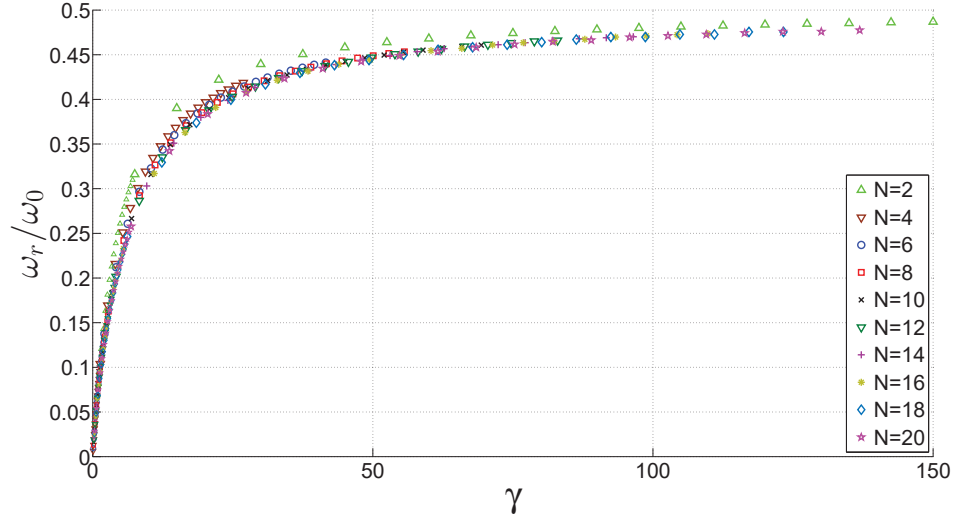


Figure 13.3: The length of the half-way step for systems of various  $N$  and across a large range of interaction strengths. For  $N > 2$  the range of the data is limited by the appearance of the mini steps (see text). For  $\gamma \ll 1$ , the asymptotic behaviour is  $\omega_r/\omega_0 = \gamma/\pi^2$ , and for  $\gamma \rightarrow \infty$ , it appears to be consistent with  $\omega_r/\omega_0 = 1/2 - \pi/\gamma$ .

Returning to Fig. 13.2 (b), the next phase of the transition is the gradual appearance of  $M - 1$  “mini” steps at integer multiples of  $L_\ell/N$  between the original and half-way plateaus, which can be thought of as fractional vortices. This is a result of the changing concavity of the dispersion relation at large  $\gamma$  values (see Fig. 13.2 (a)). In particular, the discrete  $(L, E)$  points fall non-uniformly below the straight line connecting the origin to the half-umklapp point. The mini steps appear one by one, starting off as a single point, alternatively closer to the bottom and top plateaus; their length and number grows at the expense of the original and half-way plateaus.

We can map-out this multi-step region by noting the  $\gamma$  values at which the first and last of the mini steps appear as a function of system size,  $N$ . This is shown in Fig. 13.4 – we find that the boundaries of the multi-step region are linear in  $N$ . In this “discontinuous rotation” phase, some multiples of  $L_\ell/N$  are forbidden, so the Hess-Fairbank diagram still exhibits jumps in angular momentum bigger than the quantization step.

Once all  $M - 1$  mini steps are in place, the Hess-Fairbank diagram is as continuous as it can be for a finite system – that is, as  $\omega_r$  is increased, all states on the spin-flip dispersion relation become the ground state of the rotating system in turn, with none

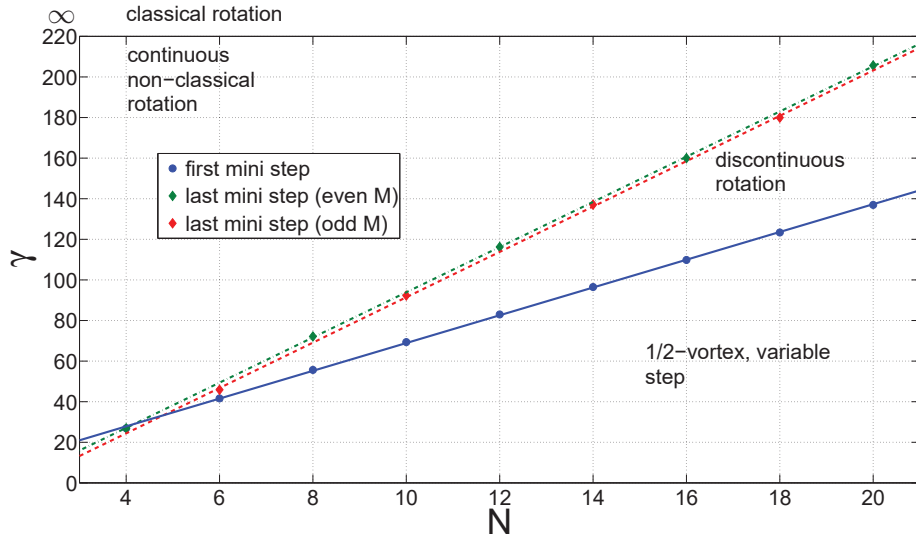


Figure 13.4: The values of  $\gamma$  as a function of number of particles  $N$  where the first and last of the mini steps appear. Since there is a small visible difference for the last mini step between even and odd  $M$ , the two data sets are treated separately. The lines are linear fits to the data: the blue solid line is given by  $\gamma = 6.8417N + 0.46011$ , the red dashed line by  $\gamma = 11.174N - 20.299$  and the green dash-dotted line by  $\gamma = 11.133N - 17.435$ .

skipped. This regime can be described as continuous non-classical rotation, because despite the fact that the jumps in the Hess-Fairbank diagram are now simply the momentum quantization step, the gas still clearly does not rotate with the container, as it would classically. Next the mini steps and the remnants of the original and half-way steps reach roughly equal size, oscillating about the continuous straight line of the classical fluid, as is shown in the final panel of Fig. 13.2 (b). In this limit we obtain a classical rotational inertia, which finally completes the quantum-to-classical fluid transition.

We remark that a spin-flipping mechanism is not essential for the potential experimental observation of these predictions. The single fermion hole branch is spin-conserving, and its dispersion relation is extremely close to the spin-flip excitations (but slightly higher in energy) throughout the repulsive regime.

In conclusion, we have predicted non-trivial, multi-phase Hess-Fairbank diagrams for spin-1/2 fermions in a one-dimensional ring trap. There are three distinct phases: half-vortices, discontinuous rotation, and continuous non-classical rotation, separated by linear boundaries.

## 13.4 Fermionic Super Tonks-Girardeau

If one takes the limit as  $\gamma \rightarrow \infty$  in the Yang-Gaudin model and enters the fermionic Tonks-Girardeau regime, it is possible to follow in  $1/\gamma$  through zero such that  $\gamma$  changes from  $+\infty$  to  $-\infty$ . Then one enters the fermionic super Tonks-Girardeau regime, the fermion counter-part of the super Tonks-Girardeau gas of the Lieb-Liniger model. This concept was introduced in [216, 233], and then further studied in [234]. In the ordinary repulsive regime, the ground state of a spin-balanced system is one with  $S = 0$  and  $S_z = 0$ , the ground state we studied via the Bethe ansatz in chapter 8. The other spin states, inaccessible through the Bethe ansatz equations derived in chapter 6, lie higher in energy. However, as  $\gamma \rightarrow \infty$ , the spin label of the particles ceases to matter as infinite contact repulsion and Pauli exclusion make interactions between like- and unlike-particles indistinguishable. All the spin states become degenerate at the point when  $1/\gamma = 0$ , and as we pass into the super Tonks-Girardeau regime, the energy levels cross so that the higher  $S$  spin states have lower energy. The true ground state of the super Tonks-Girardeau manifold is then ferromagnetic with  $S = N/2$ . This is discussed in detail, e.g., in Refs. [216, 233–238]. However, as pointed out in [234], the  $S = 0$  state can be followed into the super Tonks-Girardeau regime successfully as long as there are no spin-changing terms in the Hamiltonian (although small coupling terms would cause a transition into the ferromagnetic state).

Assuming no spin-mixing terms are present, the system will remain in the singlet “ground state” (of the excited super Tonks-Girardeau manifold). As in the bosonic case, decay into the true ground state of paired dimers (studied in chapter 8 in the attractive regime) is suppressed due to the large energy which cannot be disposed of easily. An additional advantage of the fermionic system over the bosonic one is that when we move further out of the super Tonks-Girardeau regime (i.e.  $\gamma$  increases from  $-\infty$  to  $0^-$ ), the system is far more stable against three-body loss due to Pauli exclusion, which prevents collisions of three spin-1/2 fermions. Therefore, we may theoretically consider following the system in  $\gamma$  further: from the non-interacting limit to the Tonks-Girardeau regime ( $\gamma = 0^+ \rightarrow +\infty$ ), then from the Tonks-Girardeau into the super Tonks-Girardeau ( $\gamma = +\infty \rightarrow -\infty$ ), back towards the next non-interacting limit ( $\gamma = -\infty \rightarrow 0^-$ ), crossing back into repulsive interactions ( $\gamma = 0^- \rightarrow 0^+$ ) and back to the next Tonks-Girardeau regime ( $\gamma = 0^+ \rightarrow +\infty$ ).

By following the singlet ground state through this range of interaction strengths, one can realize exotic states of the free Fermi gas, characterized by a Fermi sea of  $N$  particles with a regular pattern of holes, which we term the “holey Fermi sea”. In particular, the ground state can be followed using the logarithmic Bethe ansatz

equations with the quantum numbers given in chapter 8 from  $\gamma = 0^+ \rightarrow +\infty \rightarrow -\infty \rightarrow 0^-$ . Since the limit  $\gamma \rightarrow 0^-$  is again a free Fermi system, the charge rapidities are multiples of  $2\pi/L$  but there is now a hole following every two  $k_j$ 's occupying adjacent momenta slots. The spin rapidities fill the holes in the charge-rapidity distribution.

Next, in order to follow the ground state from  $\gamma = 0^-$  to  $\gamma = 0^+$  new quantum numbers need to be computed (by reverse-solving the Bethe ansatz equations, using the solutions at  $\gamma = 0^-$  for the rapidities, a small positive  $\gamma$ , and solving for the quantum numbers). Thus continuing onwards to the next Tonks-Girardeau regime, we find a double holey sea: the holes between pairs of occupied  $2\pi/L$  slots become double.

Two technical comments are in order. First, note that the  $\alpha_m$ 's diverge linearly with  $c$ , as can be seen from equation (8.35) (even though this equation is quantitatively inaccurate, the qualitative linear dependence on  $c$  is correct). When we cross the resonance ( $1/\gamma = 0$ ), all the  $\alpha_m$ 's swap signs, but since in the ground state they are symmetrically arranged about zero, the set of  $\alpha_m$ 's does not change. Past the resonance, as  $\gamma$  changes from  $-\infty$  to  $0^-$ , the  $\alpha_m$ 's move back in towards the origin, and they move back out again as we go to the next Tonks-Girardeau limit. Second, the ground state thermodynamic limit Bethe ansatz equations for the repulsive Yang-Gaudin model (chapter 9) cannot be solved with  $\gamma < 0$ . This is due to the ‘‘holey’’ nature of the ground state, which contradicts the assumption that the rapidities are compactly and symmetrically arranged about zero (made during the derivation). Thus the thermodynamic limit of the super Tonks-Girardeau regime cannot be captured with the same equations.

## 13.5 Conclusion

To summarise, in this chapter we have discussed the physical implications of our calculations for the Yang-Gaudin model. In particular, we have predicted the existence and properties of dark solitons in the attractive Fermi gas (likewise applicable to the bosonic super Tonks-Girardeau gas), and discovered an excitation branch that appears solitonic also in the repulsive regime. Then we discussed the low-energy translatory excitations found with repulsive interactions in the context of spin-waves in Luttinger liquid theory, and investigated their effect on the Hess-Fairbank diagrams, proposing a method for direct experimental detection of these excitations. Finally, we considered the fermionic super Tonks-Girardeau regime, and found that curious states could be realised, characterised by a Fermi sphere with regular hole patterns.

# Appendix

## 13.A Finite-System Approximate Dispersion Relations

In this appendix we present the (third-level) finite system dispersion relation approximation of chapter 11, computed for all the branches of the Yang-Gaudin model (as well as the Lieb-Liniger model for comparison), shown in Figs. 13.5–13.11. This is done in order to easily identify the solitonic branches in a one-dimensional Fermi gas. Beginning from boson holes in the Lieb-Liniger model (Fig. 13.5), we see that the approximation works well (as we already know from chapter 11), as long as the soliton is well localized on the ring (this assumption breaks down in the Gross-Pitaevskii limit where the dark soliton becomes macroscopic). Similarly, single fermion holes for  $\gamma < 0$  (Fig. 13.6) show excellent agreement as long as we are in a regime where the string hypothesis is valid. Thus, for  $|\gamma| \ll 1$  it is the complicated nature of the true rapidities that causes the approximation to perform poorly, as is illustrated in the top panel of Fig. 13.6 by repeating the finite Bethe ansatz calculation using the string hypothesis equations. Therefore, we may conclude that for sufficiently large  $|\gamma|$  or  $N$  this branch is dark soliton-like.

Double fermion holes (Figs. 13.7 & 13.10) show excellent agreement across the entire range of  $\gamma$ 's, positive and negative, indicating that they may always be interpreted as dark solitons. In the strongly repulsive regime they are clearly the only soliton-like excitation, judging from the shape of the dispersion relation and the “hole” nature of the state. An interesting feature is that as  $\gamma \rightarrow 0$ , in contrast to the Lieb-Liniger case, the approximation is still very good. This is because in the Yang-Gaudin model,  $N_d$  of the single- and double-fermion holes never becomes macroscopic (1 or 2 fermions for small coupling), which suggests that the excitations are still very well localized.

The cases when the approximation does not perform well include spin flips (for any  $\gamma$ ) and single fermion holes (for positive  $\gamma$ ). In Figs. 13.8, 13.11 & 13.9 we show the results for  $N = 10$  and  $N = 22$ , in order to demonstrate that increasing the system size does not improve the quality of the approximation (the relative error does not decrease). This implies that the nature of these branches is actually not solitonic, which is hardly surprising due to our understanding that spin flips and single fermion holes in the repulsive regime are spin-excitations.

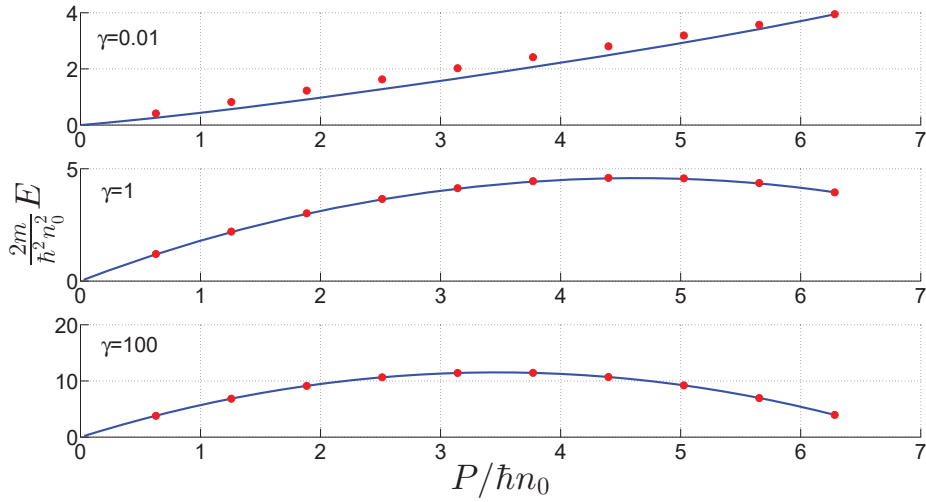


Figure 13.5: Dispersion relation of type-II Lieb-Liniger excitations in a system with  $N = 10$  and  $\gamma = 0.01$  (top),  $\gamma = 1$  (middle),  $\gamma = 100$  (bottom). Blue lines depict the third level approximation based on thermodynamic limit calculations and red circles show exact finite Bethe ansatz results.

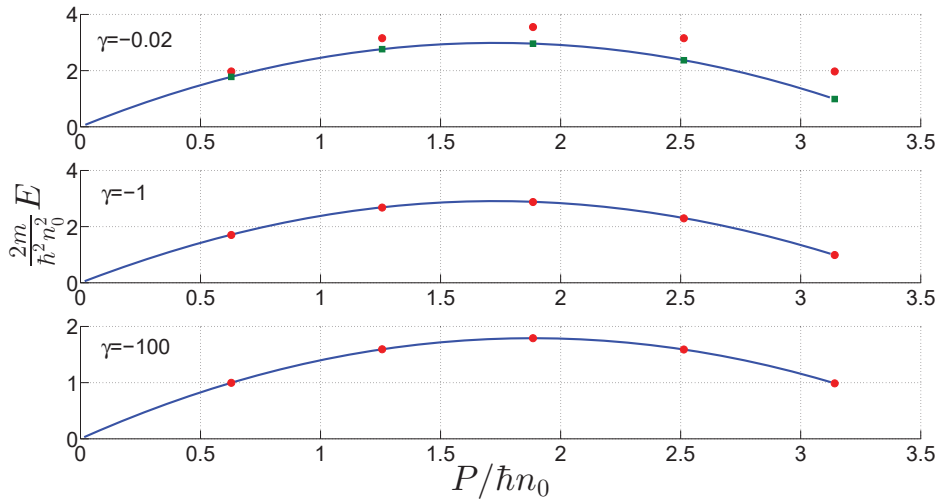


Figure 13.6: Dispersion relation of single fermion hole excitations of the attractive Yang-Gaudin model in a system with  $N = 10$  and  $\gamma = -0.02$  (top),  $\gamma = -1$  (middle),  $\gamma = -100$  (bottom). Blue lines depict the third level approximation based on thermodynamic limit calculations and red circles show exact finite Bethe ansatz results. Green squares in the upper panel show the dispersion relation obtained under the string hypothesis, even though it is completely invalid in this regime.

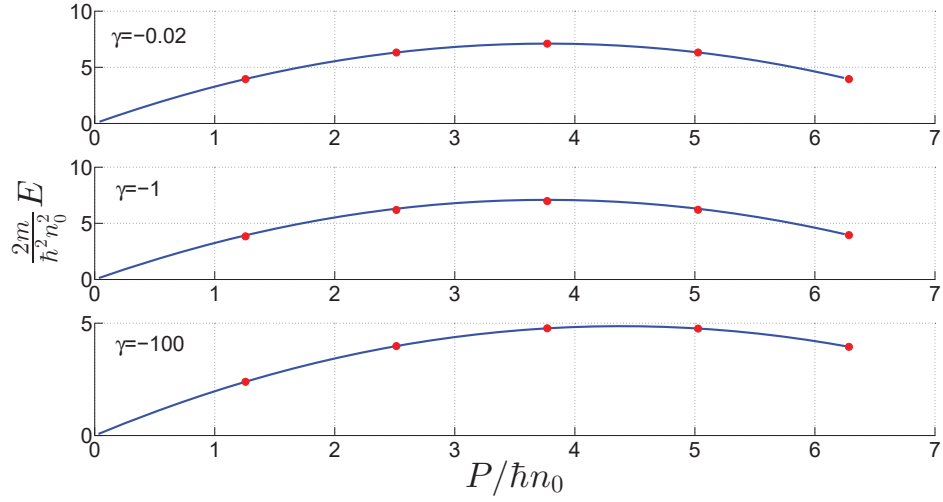


Figure 13.7: Dispersion relation of double fermion hole excitations of the attractive Yang-Gaudin model in a system with  $N = 10$  and  $\gamma = -0.02$  (top),  $\gamma = -1$  (middle),  $\gamma = -100$  (bottom). Blue lines depict the third level approximation based on thermodynamic limit calculations and red circles show exact finite Bethe ansatz results.

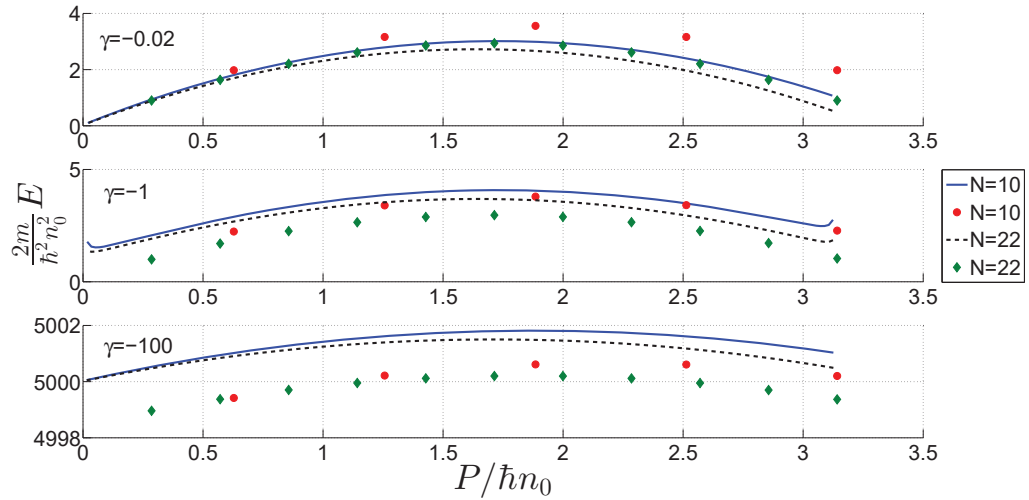


Figure 13.8: Dispersion relation of spin flip excitations of the attractive Yang-Gaudin model in a finite system with  $\gamma = -0.02$  (top),  $\gamma = -1$  (middle),  $\gamma = -100$  (bottom). Blue solid (black dashed) lines depict the third level approximation based on thermodynamic limit calculations and red circles (green diamonds) show exact finite Bethe ansatz results for  $N = 10$  ( $N = 22$ ).

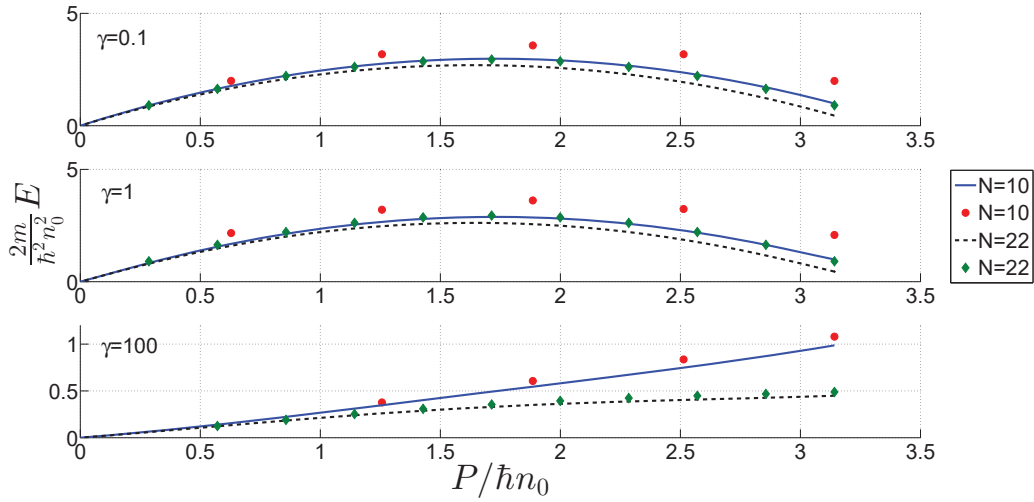


Figure 13.9: Dispersion relation of single fermion hole excitations of the repulsive Yang-Gaudin model in a finite system with  $\gamma = 0.1$  (top),  $\gamma = 1$  (middle),  $\gamma = 100$  (bottom). Blue solid (black dashed) lines depict the third level approximation based on thermodynamic limit calculations and red circles (green diamonds) show exact finite Bethe ansatz results for  $N = 10$  ( $N = 22$ ).

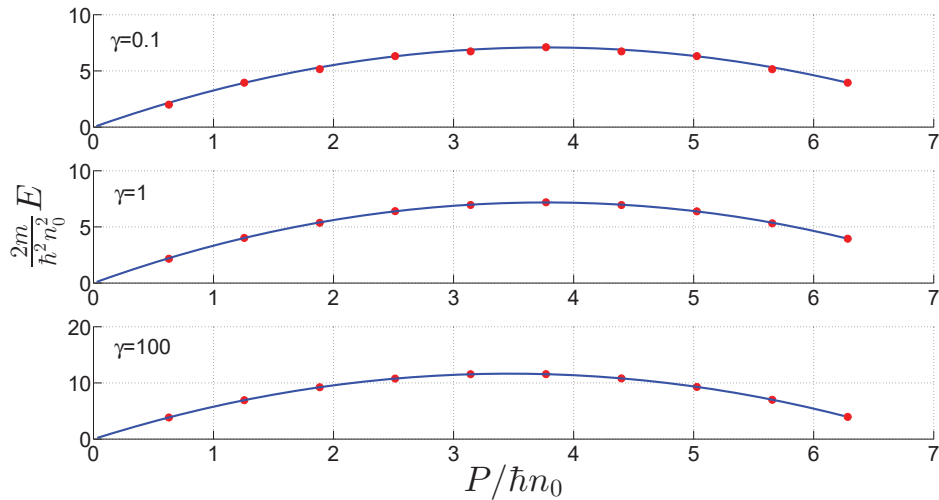


Figure 13.10: Dispersion relation of double fermion hole excitations of the repulsive Yang-Gaudin model in a system with  $N = 10$  and  $\gamma = 0.1$  (top),  $\gamma = 1$  (middle),  $\gamma = 100$  (bottom). Blue lines depict the third level approximation based on thermodynamic limit calculations and red circles show exact finite Bethe ansatz results.

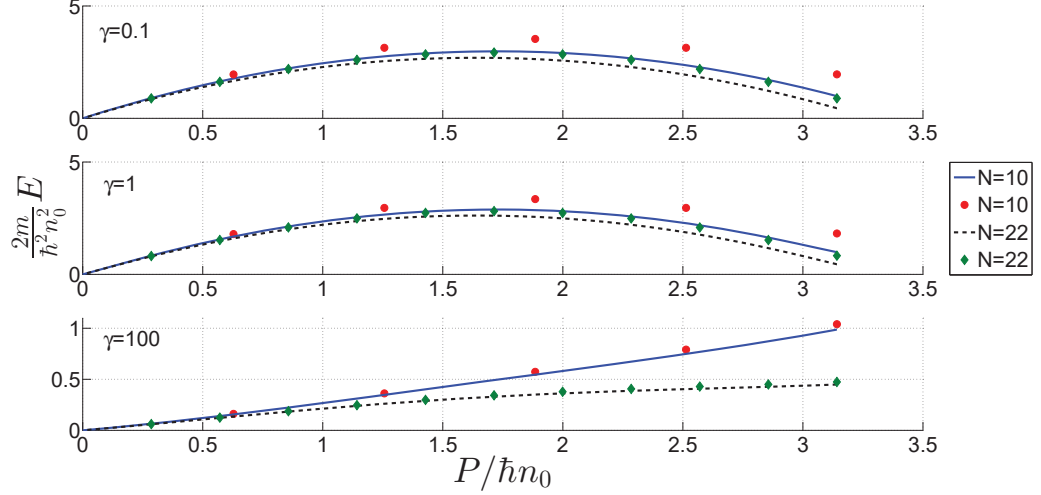


Figure 13.11: Dispersion relation of spin flip excitations of the repulsive Yang-Gaudin model in a finite system with  $\gamma = 0.1$  (top),  $\gamma = 1$  (middle),  $\gamma = 100$  (bottom). Blue solid (black dashed) lines depict the third level approximation based on thermodynamic limit calculations and red circles (green diamonds) show exact finite Bethe ansatz results for  $N = 10$  ( $N = 22$ ).

## 13.B Repulsive Two-Component Bose Gas

In this appendix we present the Bethe ansatz equations for a repulsive two-component Bose gas with periodic boundary conditions [159], and give their first order solution in the Tonks-Girardeau limit. The exponential equations are

$$\exp(ik_j L) = - \prod_{n=1}^M \frac{k_j - \alpha_n - ic/2}{k_j - \alpha_n + ic/2} \prod_{\ell=1}^N \frac{k_j - k_\ell + ic}{k_j - k_\ell - ic}, \quad (13.4)$$

$$\prod_{j=1}^N \frac{\alpha_m - k_j + ic/2}{\alpha_m - k_j - ic/2} = - \prod_{n=1}^M \frac{\alpha_m - \alpha_n + ic}{\alpha_m - \alpha_n - ic}, \quad (13.5)$$

or in logarithmic form:

$$k_j L = 2\pi n_j + \sum_{\ell=1}^N \theta(k_j - k_\ell) - \sum_{m=1}^M \theta[2(k_j - \alpha_m)], \quad (13.6)$$

$$0 = 2\pi \ell_m - \sum_{n=1}^M \theta(\alpha_m - \alpha_n) + \sum_{j=1}^N \theta[2(\alpha_m - k_j)]. \quad (13.7)$$

Going through the calculation as was done in section 8.6.4, we arrive at the following equations:

$$k_j L = 2\pi n_j + \frac{2k_j}{c}(2M - N) + \left(\frac{4\pi}{cL} - \frac{8\pi M}{NcL}\right) \sum_j n_j + \left(-\frac{4\pi}{cL} - \frac{2\pi}{N} + \frac{8\pi M}{NcL}\right) \sum_n \ell_m, \quad (13.8)$$

$$0 = 2\pi \ell_m + \frac{2\alpha_m}{c}(M - 2N) + \left(\frac{8\pi}{cL} - \frac{4\pi M}{NcL}\right) \sum_j n_j + \left(-\frac{8\pi}{cL} - \frac{\pi}{N} + \frac{4\pi M}{NcL}\right) \sum_n \ell_m. \quad (13.9)$$

Since these are already decoupled, we may focus on the first one (for the charge rapidities). Assuming  $N = 2M$  (which is an unnecessary limitation – spin flips could be involved and then this condition would not hold, but let us see how it simplifies if it *does* hold), the first equation easily reduces to

$$k_j L = 2\pi n_j - \frac{2\pi}{N} \sum_m \ell_m, \quad (13.10)$$

which is precisely what we found in the fermionic case, too. If the sum over  $\ell_m$  is an integer (which it is highly likely to be), then we recover the translation excitations.

## 13.C Box Boundary Conditions

In this appendix we present the Bethe ansatz equations for two-component repulsive fermions with box (Dirichlet) boundary conditions, requiring the wavefunction to vanish at the edges. The exponential Bethe ansatz equations are [159]

$$\exp(2ik_j L) = \prod_{n=1}^M \frac{k_j - \alpha_n + ic/2}{k_j - \alpha_n - ic/2} \frac{k_j + \alpha_n + ic/2}{k_j + \alpha_n - ic/2}, \quad (13.11)$$

$$\prod_{j=1}^N \frac{\alpha_m - k_j + ic/2}{\alpha_m - k_j - ic/2} \frac{\alpha_m + k_j + ic/2}{\alpha_m + k_j - ic/2} = \prod_{\substack{n=1, \\ n \neq m}}^M \frac{\alpha_m - \alpha_n + ic}{\alpha_m - \alpha_n - ic} \frac{\alpha_m + \alpha_n + ic}{\alpha_m + \alpha_n - ic}. \quad (13.12)$$

In logarithmic form, these become<sup>5</sup>

$$2k_j L = 2\pi n_j + \sum_{m=1}^M \{\theta[2(k_j - \alpha_m)] + \theta[2(k_j + \alpha_m)]\}, \quad (13.13)$$

$$0 = 2\pi \ell_m + \sum_{\substack{n=1, \\ n \neq m}}^M \{\theta(\alpha_m - \alpha_n) + \theta(\alpha_m + \alpha_n)\} \\ + \sum_{j=1}^N \{\theta[2(\alpha_m - k_j)] + \theta[2(\alpha_m + k_j)]\}. \quad (13.14)$$

Expanding the  $\theta$  functions to first order about zero (in order to find the approximate solutions in the Tonks-Girardeau regime) leads to very simple, decoupled, linear equations for the rapidities. The solutions are

$$k_j = \frac{2\pi n_j}{2L + 8M/c}, \quad (13.15)$$

$$\alpha_m = \frac{\pi \ell_m c}{2(M-1) + 4N}. \quad (13.16)$$

Comparing these to the rapidities of a single-component free Fermi gas described by  $\exp(2ik_j L) = 1$ , or  $2k_j L = 2\pi n_j$ , we see that since  $n_j \in \mathbb{N}$  in both cases, clearly the same  $k_j$ 's are possible.

---

<sup>5</sup>Note that Ref. [159] have a typographical error: the sign for the first sum in the second equation is wrong.



**MASSEY UNIVERSITY**  
GRADUATE RESEARCH SCHOOL

**STATEMENT OF CONTRIBUTION  
TO DOCTORAL THESIS CONTAINING PUBLICATIONS**

(To appear at the end of each thesis chapter/section/appendix submitted as an article/paper or collected as an appendix at the end of the thesis)

We, the candidate and the candidate's Principal Supervisor, certify that all co-authors have consented to their work being included in the thesis and they have accepted the candidate's contribution as indicated below in the *Statement of Originality*.

**Name of Candidate:** Samira Sophie Shamailov

**Name/Title of Principal Supervisor:** Professor Joachim Brand

**Name of Published Research Output and full reference:**

Dark-soliton-like excitations in the Yang-Gaudin gas of attractively interacting fermions,  
S. S. Shamailov and J. Brand, New Journal of Physics 18, 075004 (2016).

**In which Chapter is the Published Work:** 8,9,10,13

Please indicate either:

- The percentage of the Published Work that was contributed by the candidate:  
and / or
- Describe the contribution that the candidate has made to the Published Work:  
The candidate has performed all the numerical and analytical calculations and wrote the first draft of the paper. The supervisor initiated the main ideas and the understanding and interpretation of the results were developed jointly by the candidate and the supervisor. Both authors revised the manuscript.

*s.sha*

Candidate's Signature

*31/7/2017*

Date

*Joachim Brand*

Principal Supervisor's signature

*28-7-2017*

Date

# Chapter 14

## Summary, Conclusions & Outlook

In this thesis, we have been primarily concerned with the quantum-mechanical interpretation of dark solitons in one-dimensional ultra-cold gases. We began by reviewing condensation in three dimensions and the crucial effect of dimensionality, followed by the Gross-Pitaevskii equation in one dimension, focusing on its dark soliton solutions. In the process, we encountered the quasi-particle equation of motion for a solitonic excitation in a trap under the local density approximation, and met the inertial and physical masses that enter this equation. The physical mass was proportional to the effective missing particle number, which was expressed as a derivative of the excitation energy.

Then we proceeded to solve the system of two coupled one-dimensional Gross-Pitaevskii equations, modelling two Bose-Einstein condensate strands with coherent tunnelling. We numerically solved the time-independent Gross-Pitaevskii equations for moving Josephson vortices as well as a new excitation branch (the staggered solitons). Some limiting cases were solved analytically. We found a critical tunnelling value at which the inertial mass of the Josephson vortex diverged, compared the Gross-Pitaevskii model to the sine-Gordon model in the weak-tunnelling limit, and discovered a parameter regime in which dark solitons and Josephson vortices are bistable.

Next, we simulated two types of experiments that allow for the detection of Josephson vortices: interference of the two Bose-Einstein condensate strands resulting in a fringe pattern and the oscillatory trajectory of a Josephson vortex in a harmonic trap, the latter necessitating a time-dependent solution of the Gross-Pitaevskii equations. Furthermore, we confirmed that it is indeed the effective, and not the actual, missing particle number that enters the physical mass in the quasi-particle equation of motion, using the trapped Josephson vortex as a test-case.

We then presented an alternative derivation for the extraction of the actual missing particle number from the dispersion relation for a solitonic excitation in a superfluid, Lagrangian system. We briefly examined the conditions for the effective and actual missing particle numbers to be equal and presented illustrative examples.

In chapter 6 we moved away from mean-field problems, and introduced the Bethe ansatz technique, using it to exactly solve the Lieb-Liniger & Yang-Gaudin models.

The finite Lieb-Liniger model was then reviewed, introducing many key concepts, focusing on the ground state and type-II excitations (single boson holes). At this point we compared the dispersion relations of dark solitons and type-II excitations in finite systems and found excellent agreement, from the mean-field regime to small systems with intermediate repulsion. Next we carried out a careful and methodical study of the ground state and three elementary type-II branches of the Yang-Gaudin model. We tracked all three branches across the entire range of positive and negative interactions, identifying the limiting behaviour.

We went on to present the thermodynamic limit of the Bethe ansatz equations for the ground state and all type-II branches of interest in the Lieb-Liniger & Yang-Gaudin models, with a special emphasis on the dispersion relations. We also checked that the dispersion relations of dark solitons and type-II Lieb-Liniger excitations matched in the thermodynamic limit for weak interactions. These results were then used to extract the missing particle number, phase step, and the inertial & physical masses for all these type-II branches, as a “diagnostic” calculation the results of which shed light on the physical nature of the states examined. We found that in the weakly-interacting limit, not only the dispersion relation, but also the missing particle number & phase step of Lieb-Liniger type-II excitations tend to the Gross-Pitaevskii dark soliton values, which served as further evidence for the connection between these states.

Armed with solitonic properties of type-II states of the Lieb-Liniger model, we derived a finite-system approximation of the dispersion relation based on thermodynamic limit results, and applied it to Gross-Pitaevskii dark solitons as well as to Lieb-Liniger type-II states, finding excellent agreement in both cases. This indicated an underlying solitonic interpretation of type-II states, as both the missing particle number formula and the approximate dispersion relation were derived under the assumption that a density dip and a phase step exist. This work also allowed us to get finite-system corrections for the missing particle number and phase step extracted from the thermodynamic limit dispersion relation.

Finally, we addressed our main research question directly in chapter 12, showing that in the Gross-Pitaevskii limit, classical dark solitons can be constructed as superpositions of type-II states, and computed the expansion coefficients. In general, the quantum dark soliton may be defined as an underlying fundamental object such that its convolution with the center of mass (of the missing particles) density produces the single-particle density. We extracted the length scale of the quantum dark soliton as a function of momentum and interaction strength, and found that the dependence on both parameters can be easily scaled out, leaving the length scale as a single function of the missing particle number. In the weakly interacting regime, this function approaches the Gross-Pitaevskii dark soliton variance, while

for strong interactions it is not well-captured by the variance of the quantum bright soliton, as was initially hoped.

While the single-particle density disperses as a function of time (the larger  $\gamma$ , the faster the wavepacket disperses), a single measurement of the density will reveal the fundamental quantum dark soliton profile, centred at a random position, with the probability of detecting the soliton at a given position being a Gaussian [64].

In the course of the investigation, we uncovered the physical meaning of the missing particle number and phase step of type-II states, and understood why the finite-system dispersion relation approximation performs so well for type-II states.

Next, we turned our attention to the Yang-Gaudin model, and discussed the existence of dark solitons, identifying them as the single- and double- fermion hole branches for attractive interactions (corresponding to a single and double dark soliton state) and double-fermion holes for repulsive interactions (corresponding to single dark soliton states). We made a case for the idea that the solitonic properties of these type-II states correspond to those of the fermionic dark solitons, thus predicting properties of dark solitons in a one-dimensional Fermi gas via the Bethe ansatz. We confirmed that the finite system dispersion relation approximation performed superbly for the single- and double-fermion holes, the former only for sufficiently negative  $\gamma$ .

For repulsive interactions, the success and consistency of all our calculations assuming solitonic excitations suggests strongly that dark-soliton like states do exist, despite the fact that there is currently no information on a pairing mechanism and superfluidity for repulsive fermions in one dimension. In a way, we were able to obtain indirect evidence that implies some sort of quasi long range order may exist.

We also investigated the low-energy spin excitations in the repulsive regime, making a connection to spin-waves of Luttinger liquid theory and establishing the importance of periodic boundary conditions. We analysed the Hess-Fairbank diagrams as the lowest energy dispersion relation changed from the usual type-II concave-down shape to the concave-up system translation parabola, and found non-trivial multi-phase Hess-Fairbank diagrams, corresponding to a rotating ground state with fractional vortices. Three phases were identified all together, separated from each other by linear phase boundaries. The length of the half-vortex plateau in the Hess-Fairbank diagrams was analysed as a function of the repulsion, and we saw that the number of particles could be scaled out, leaving a single monotonic curve.

We then considered continuing the ground state of the repulsive gas into the fermionic super Tonks-Girardeau regime, and found that exotic states could thus be prepared, characterised by a “holey Fermi sea”.

## 14.1 Future Work

It would be desirable to find the physical conditions under which the effective and actual missing particle numbers become equal. We have found a general mathematical condition to this effect, however it gives little physical insight.

For completeness, one could derive the Lieb-Liniger & Yang-Gaudin Bethe ansatz equations using the algebraic, not the coordinate, Bethe ansatz. Although this method requires more background knowledge, it would give us a general proof of the validity of the Yang-Gaudin model.

As already mentioned, once the algebraic Bethe ansatz is generalized to nested systems, it would be useful to repeat the calculations of chapter 12 for the branches we identified as solitonic in the Yang-Gaudin model to confirm this statement directly. Moreover, if form factors are found in closed form for the Yang-Gaudin model, we would be able to examine the two-particle (pairing) density matrix and get conclusive results regarding pairing and superfluidity for the repulsive regime.

We have seen that only the  $S = N - M/2$ ,  $S_z = N - M/2$  states of the Yang-Gaudin model are accessible through the Bethe ansatz equations that we have derived. Is it practical to derive alternative equations that allow one to solve for the other spin-states? For example, when considering the fermionic super Tonks-Girardeau regime, it would be useful to inspect the structure of the  $S = N/2$ ,  $S_z = 0$  state, had it been easily accessible.

# Bibliography

- [1] W. S. Bakr, J. I. Gillen, A. Peng, S. Folling, and M. Greiner, *Nature* **462**, 74 (2009).
- [2] L. Pitaevskii and S. Stringari, *Journal of Low Temperature Physics* **85**, 377 (1991).
- [3] S. Bose, *Zeitschrift für Physik* **26**, 178 (1924).
- [4] A. Pais, *Subtle is the Lord: the Science and Life of Albert Einstein* (Oxford University Press, 1982) pp. 423–439.
- [5] P. Kapitza, *Nature* **141**, 74 (1938).
- [6] J. Allen and A. Meisner, *Nature* **142**, 643 (1938).
- [7] L. Landau, *Phys. Rev.* **60**, 356 (1941).
- [8] D. van Delft and P. Kes, *Physics Today* **63**, 38 (2010).
- [9] V. Ginzburg and L. Landau, *Zhurnal Eksperimental'noi i Teoreticheskoi Fiziki* **20**, 1064 (1950).
- [10] J. Bardeen, L. N. Cooper, and J. R. Schrieffer, *Phys. Rev.* **106**, 162 (1957).
- [11] J. Bardeen, L. N. Cooper, and J. R. Schrieffer, *Phys. Rev.* **108**, 1175 (1957).
- [12] M. H. Anderson, J. R. Ensher, M. R. Matthews, C. E. Wieman, and E. A. Cornell, *Science* **269**, 198 (1995).
- [13] K. B. Davis, M. O. Mewes, M. R. Andrews, N. J. van Druten, D. S. Durfee, D. M. Kurn, and W. Ketterle, *Phys. Rev. Lett.* **75**, 3969 (1995).
- [14] C. A. Regal, M. Greiner, and D. S. Jin, *Phys. Rev. Lett.* **92**, 040403 (2004).
- [15] M. W. Zwierlein, C. A. Stan, C. H. Schunck, S. M. F. Raupach, A. J. Kerman, and W. Ketterle, *Phys. Rev. Lett.* **92**, 120403 (2004).
- [16] S. Burger, K. Bongs, S. Dettmer, W. Ertmer, K. Sengstock, A. Sanpera, G. V. Shlyapnikov, and M. Lewenstein, *Phys. Rev. Lett.* **83**, 5198 (1999).
- [17] E. P. Gross, *Il Nuovo Cimento* (1955-1965) **20**, 454 (1961).

- [18] L. Pitaevskii, Zhurnal Eksperimental'noi i Teoreticheskoi Fiziki **40**, 646 (1961).
- [19] T. Tsuzuki, Journal of Low Temperature Physics **4**, 441 (1971).
- [20] V. Zakharov and A. Shabat, Journal of Experimental and Theoretical Physics **34**, 62 (1972).
- [21] J. Denschlag, J. E. Simsarian, D. L. Feder, C. W. Clark, L. A. Collins, J. Cubizolles, L. Deng, E. W. Hagley, K. Helmerson, W. P. Reinhardt, S. L. Rolston, B. I. Schneider, and W. D. Phillips, Science **287**, 97 (2000).
- [22] D. L. Feder, M. S. Pindzola, L. A. Collins, B. I. Schneider, and C. W. Clark, Phys. Rev. A **62**, 053606 (2000).
- [23] L. Onsager, Nuovo Cimento Suppl. **6**, 261 (1949).
- [24] R. Feynman, *Chapter II: Application of Quantum Mechanics to Liquid Helium*, in *Progress in Low Temperature Physics Vol. 1*, edited by C. Gorter (Elsevier, 1955) pp. 17–53.
- [25] A. Abrikosov, Zhurnal Eksperimental'noi i Teoreticheskoi Fiziki **32**, 1442 (1957).
- [26] B. P. Anderson, P. C. Haljan, C. A. Regal, D. L. Feder, L. A. Collins, C. W. Clark, and E. A. Cornell, Phys. Rev. Lett. **86**, 2926 (2001).
- [27] Z. Dutton, M. Budde, C. Slowe, and L. V. Hau, Science **293**, 663 (2001).
- [28] A. L. Fetter and A. A. Svidzinsky, Journal of Physics: Condensed Matter **13**, R135 (2001).
- [29] R. Donnelly, *Quantized Vortices in Helium II*, Cambridge Studies in Low Temperature Physics, Vol. 3 (Cambridge University Press, 1991).
- [30] L. Shubnikov *et al.*, Zhurnal Eksperimental'noi i Teoreticheskoi Fiziki **7**, 221 (1937).
- [31] D. Cribier, B. Jacrot, L. Madhav Rao, and B. Farnoux, Physics Letters **9**, 106 (1964).
- [32] U. Essmann and H. Träuble, Physics Letters A **24**, 526 (1967).
- [33] A. Barone and G. Paterno, *Physics and Applications of the Josephson Effect* (John Wiley & Sons, Inc., 2005).
- [34] A. Wallraff, A. Lukashenko, J. Lisenfeld, A. Kemp, M. Fistul, Y. Koval, and A. Ustinov, Nature **425**, 155 (2003).

- [35] T. Schweigler, V. Kasper, S. Erne, I. Mazets, B. Rauer, F. Cattalini, T. Langen, T. Gasenzer, J. Berges, and J. Schmiedmayer, *Nature* **545**, 323 (2017).
- [36] J. Brand, T. J. Haigh, and U. Zülicke, *Phys. Rev. A* **80**, 011602 (2009).
- [37] S. Russell, in *14th Meeting of the British Association for the Advancement of Science* (1844) pp. 311–390.
- [38] D. Korteweg and G. de Vries, *Philosophical Magazine Series 5* **39**, 422 (1895).
- [39] N. J. Zabusky and M. D. Kruskal, *Phys. Rev. Lett.* **15**, 240 (1965).
- [40] C. S. Gardner, J. M. Greene, M. D. Kruskal, and R. M. Miura, *Phys. Rev. Lett.* **19**, 1095 (1967).
- [41] L. Mollenauer and J. Gordon, *Solitons in Optical Fibers: Fundamentals and Applications* (Elsevier Academic Press, 2006).
- [42] H. Bethe, *Zeitschrift für Physik* **71**, 205 (1931).
- [43] M. Girardeau, *Journal of Mathematical Physics* **1**, 516 (1960).
- [44] J. B. McGuire, *Journal of Mathematical Physics* **5**, 622 (1964).
- [45] J. B. McGuire, *Journal of Mathematical Physics* **6**, 432 (1965).
- [46] E. H. Lieb and W. Liniger, *Phys. Rev.* **130**, 1605 (1963).
- [47] E. H. Lieb, *Phys. Rev.* **130**, 1616 (1963).
- [48] C. N. Yang, *Phys. Rev. Lett.* **19**, 1312 (1967).
- [49] M. Gaudin, *Physics Letters A* **24**, 55 (1967).
- [50] M. Gaudin, “Etude d’un modèle à une dimension pour un système de fermions en interaction,” (1968).
- [51] B. Sutherland, *Phys. Rev. Lett.* **20**, 98 (1968).
- [52] B. Sutherland, *Beautiful Models: 70 Years of Exactly Solved Quantum Many-Body Problems* (World Scientific Pub Co Inc, 2004).
- [53] Y. Wang, W.-L. Yang, J. Cao, and K. Shi, *Off-Diagonal Bethe Ansatz for Exactly Solvable Models* (Springer-Verlag, 2015).
- [54] V. Korepin, N. Bogoliubov, and A. Izergin, *Quantum Inverse Scattering Method and Correlation Functions*, Cambridge Monographs on Mathematical Physics (Cambridge University Press, 1993).

- [55] J.-S. Caux, *Journal of Mathematical Physics* **50**, 095214 (2009).
- [56] N. Fabbri, M. Panfil, D. Clément, L. Fallani, M. Inguscio, C. Fort, and J.-S. Caux, *Phys. Rev. A* **91**, 043617 (2015).
- [57] A. N. Wenz, G. Zrn, S. Murmann, I. Brouzos, T. Lompe, and S. Jochim, *Science* **342**, 457 (2013).
- [58] E. Lieb, R. Seiringer, J. Solovej, and J. Yngvason, “The mathematics of the bose gas and its condensation,” *arXiv:cond-mat/0610117* (2006).
- [59] L. Pitaevskii and S. Stringari, *Bose-Einstein Condensation*, International Series of Monographs on Physics (Clarendon Press, 2003).
- [60] M. Ishikawa and H. Takayama, *Journal of the Physical Society of Japan* **49**, 1242 (1980).
- [61] J. Dziarmaga, *Phys. Rev. A* **70**, 063616 (2004).
- [62] J. Dziarmaga and K. Sacha, *Phys. Rev. A* **66**, 043620 (2002).
- [63] J. Dziarmaga, Z. P. Karkuszewski, and K. Sacha, *Phys. Rev. A* **66**, 043615 (2002).
- [64] D. Delande and K. Sacha, *Phys. Rev. Lett.* **112**, 040402 (2014).
- [65] A. Syrwid and K. Sacha, *Phys. Rev. A* **92**, 032110 (2015).
- [66] A. Syrwid, M. Brewczyk, M. Gajda, and K. Sacha, *Phys. Rev. A* **94**, 023623 (2016).
- [67] S. S. Shmailov and J. Brand, *New Journal of Physics* **18**, 075004 (2016).
- [68] D. K. Efimkin and V. Galitski, *Phys. Rev. A* **91**, 023616 (2015).
- [69] J. H. Denschlag, J. E. Simsarian, H. Häffner, C. McKenzie, A. Browaeys, D. Cho, K. Helmerson, S. L. Rolston, and W. D. Phillips, *Journal of Physics B: Atomic, Molecular and Optical Physics* **35**, 3095 (2002).
- [70] A. Ramanathan, K. C. Wright, S. R. Muniz, M. Zelan, W. T. Hill, C. J. Lobb, K. Helmerson, W. D. Phillips, and G. K. Campbell, *Phys. Rev. Lett.* **106**, 130401 (2011).
- [71] C. Ryu, C. Henderson, and M. Boshier, *New Journal of Physics* **16**, 013046 (2014).

- [72] T. Yefsah, A. T. Sommer, M. J. H. Ku, L. W. Cheuk, W. Ji, W. S. Bakr, and M. W. Zwierlein, *Nature* **499**, 426 (2013).
- [73] M. J. H. Ku, W. Ji, B. Mukherjee, E. Guardado-Sanchez, L. W. Cheuk, T. Yefsah, and M. W. Zwierlein, *Phys. Rev. Lett.* **113**, 065301 (2014).
- [74] T. Kinoshita, T. Wenger, and D. S. Weiss, *Science* **305**, 1125 (2004).
- [75] B. Paredes, V. Murg, O. Mandel, S. Folling, I. Cirac, G. V. Shlyapnikov, T. W. Hansch, and I. Bloch, *Nature* **429**, 277 (2004).
- [76] F. Serwane, G. Zürn, T. Lompe, T. B. Ottenstein, A. N. Wenz, and S. Jochim, *Science* **332**, 336 (2011).
- [77] G. Zürn, F. Serwane, T. Lompe, A. N. Wenz, M. G. Ries, J. E. Bohn, and S. Jochim, *Phys. Rev. Lett.* **108**, 075303 (2012).
- [78] G. Zürn, A. N. Wenz, S. Murmann, A. Bergschneider, T. Lompe, and S. Jochim, *Phys. Rev. Lett.* **111**, 175302 (2013).
- [79] G. Pagano, M. Mancini, G. Cappellini, P. Lombardi, F. Schafer, H. Hu, X.-J. Liu, J. Catani, C. Sias, M. Inguscio, and L. Fallani, *Nat. Phys.* **10**, 198 (2014).
- [80] P. Kevrekidis, D. Franzeskakis, and R. Carretero-Gonzalez, eds., *Emergent nonlinear phenomena in Bose-Einstein condensates: theory and experiment*, Springer series on atomic, optical and plasma physics (Springer-Verlag, 2008).
- [81] N. P. Proukakis and B. Jackson, *Journal of Physics B: Atomic, Molecular and Optical Physics* **41**, 203002 (2008).
- [82] H. Moritz, T. Stöferle, K. Günter, M. Köhl, and T. Esslinger, *Phys. Rev. Lett.* **94**, 210401 (2005).
- [83] K. Huang, *Statistical Mechanics*, 2nd ed. (Jon Wiley & Sons, 1987).
- [84] N. D. Mermin and H. Wagner, *Phys. Rev. Lett.* **17**, 1133 (1966).
- [85] P. C. Hohenberg, *Phys. Rev.* **158**, 383 (1967).
- [86] J. W. Kane and L. P. Kadanoff, *Phys. Rev.* **155**, 80 (1967).
- [87] S. Coleman, *Communications in Mathematical Physics* **31**, 259 (1973).
- [88] M. Schwartz, *Phys. Rev. B* **15**, 1399 (1977).
- [89] F. D. M. Haldane, *Phys. Rev. Lett.* **47**, 1840 (1981).

- [90] A. Lenard, *Journal of Mathematical Physics* **7**, 1268 (1966).
- [91] C. N. Yang and C. P. Yang, *Journal of Mathematical Physics* **10**, 1115 (1969).
- [92] L. Reatto and G. V. Chester, *Phys. Rev.* **155**, 88 (1967).
- [93] A. Lenard, *Journal of Mathematical Physics* **5**, 930 (1964).
- [94] H. G. Vaidya and C. A. Tracy, *Phys. Rev. Lett.* **43**, 1540 (1979).
- [95] T. D. Schultz, *Journal of Mathematical Physics* **4**, 666 (1963).
- [96] J.-S. Caux and P. Calabrese, *Phys. Rev. A* **74**, 031605 (2006).
- [97] J.-S. Caux, P. Calabrese, and N. A. Slavnov, *Journal of Statistical Mechanics: Theory and Experiment* **2007**, P01008 (2007).
- [98] G. E. Astrakharchik and S. Giorgini, *Phys. Rev. A* **68**, 031602 (2003).
- [99] G. Astrakharchik and S. Giorgini, *Journal of Physics B: Atomic, Molecular and Optical Physics* **39**, S1 (2006).
- [100] D. S. Petrov, G. V. Shlyapnikov, and J. T. M. Walraven, *Phys. Rev. Lett.* **85**, 3745 (2000).
- [101] W. Xu and M. Rigol, *Phys. Rev. A* **92**, 063623 (2015).
- [102] M. D. Girardeau, E. M. Wright, and J. M. Triscari, *Phys. Rev. A* **63**, 033601 (2001).
- [103] M. Olshanii, *Phys. Rev. Lett.* **81**, 938 (1998).
- [104] I. Bouchoule, “1d bose gases and cold atoms experiments: some notes for lectures given at the tu vienna and at cqt singapore,” (2011).
- [105] J. Smyrnakis, M. Magiropoulos, G. M. Kavoulakis, and A. D. Jackson, *Phys. Rev. A* **82**, 023604 (2010).
- [106] A. Jackson, J. Smyrnakis, M. Magiropoulos, and G. Kavoulakis, *EPL (Europhysics Letters)* **95**, 30002 (2011).
- [107] R. Kanamoto, L. D. Carr, and M. Ueda, *Phys. Rev. Lett.* **100**, 060401 (2008).
- [108] R. Kanamoto, L. D. Carr, and M. Ueda, *Phys. Rev. A* **79**, 063616 (2009).
- [109] R. G. Scott, F. Dalfovo, L. P. Pitaevskii, and S. Stringari, *Phys. Rev. Lett.* **106**, 185301 (2011).

- [110] A. Muñoz Mateo and J. Brand, *New Journal of Physics* **17**, 125013 (2015).
- [111] C. Becker, S. Stellmer, P. Soltan-Panahi, S. Dorschner, M. Baumert, E.-M. Richter, J. Kronjager, K. Bongs, and K. Sengstock, *Nature Physics* **4**, 496 (2008).
- [112] A. Weller, J. P. Ronzheimer, C. Gross, J. Esteve, M. K. Oberthaler, D. J. Frantzeskakis, G. Theocharis, and P. G. Kevrekidis, *Phys. Rev. Lett.* **101**, 130401 (2008).
- [113] L. D. Carr, C. W. Clark, and W. P. Reinhardt, *Phys. Rev. A* **62**, 063610 (2000).
- [114] M. Ueda, *Fundamentals and New Frontiers of Bose-Einstein Condensation* (World Scientific, 2010).
- [115] S. Hofferberth, I. Lesanovsky, B. Fischer, T. Schumm, and J. Schmiedmayer, *Nature* **449**, 324 (2007).
- [116] T. Betz, S. Manz, R. Bücker, T. Berrada, C. Koller, G. Kazakov, I. E. Mazets, H.-P. Stimming, A. Perrin, T. Schumm, and J. Schmiedmayer, *Phys. Rev. Lett.* **106**, 020407 (2011).
- [117] E. Nicklas, H. Strobel, T. Zibold, C. Gross, B. A. Malomed, P. G. Kevrekidis, and M. K. Oberthaler, *Phys. Rev. Lett.* **107**, 193001 (2011).
- [118] E. Nicklas, W. Muessel, H. Strobel, P. G. Kevrekidis, and M. K. Oberthaler, *Phys. Rev. A* **92**, 053614 (2015).
- [119] J. Brand, T. J. Haigh, and U. Zülicke, *Phys. Rev. A* **80**, 011602 (2009).
- [120] D. T. Son and M. A. Stephanov, *Phys. Rev. A* **65**, 063621 (2002).
- [121] T. W. A. Montgomery, W. Li, and T. M. Fromhold, *Phys. Rev. Lett.* **111**, 105302 (2013).
- [122] V. Gritsev, A. Polkovnikov, and E. Demler, *Phys. Rev. B* **75**, 174511 (2007).
- [123] C. Neuenhahn, A. Polkovnikov, and F. Marquardt, *Phys. Rev. Lett.* **109**, 085304 (2012).
- [124] B. Opanchuk, R. Polkinghorne, O. Fialko, J. Brand, and P. D. Drummond, *Annalen der Physik* **525**, 866 (2013).
- [125] S.-W. Su, S.-C. Gou, A. Bradley, O. Fialko, and J. Brand, *Phys. Rev. Lett.* **110**, 215302 (2013).

- [126] O. Fialko, B. Opanchuk, A. Sidorov, P. Drummond, and J. Brand, EPL (Europhysics Letters) **110**, 56001 (2015).
- [127] V. M. Kaurov and A. B. Kuklov, Phys. Rev. A **71**, 011601 (2005).
- [128] V. M. Kaurov and A. B. Kuklov, Phys. Rev. A **73**, 013627 (2006).
- [129] M. Qadir, H. Susanto, and P. Matthews, Journal of Physics B: Atomic, Molecular and Optical Physics **45**, 035004 (2012).
- [130] S.-W. Su, S.-C. Gou, I.-K. Liu, A. S. Bradley, O. Fialko, and J. Brand, Phys. Rev. A **91**, 023631 (2015).
- [131] O. Fialko, J. Brand, and U. Zülicke, Phys. Rev. A **85**, 051605 (2012).
- [132] T. Dauxois and M. Peyrard, *Physics of Solitons* (Cambridge University Press, 2006).
- [133] C. Qu, M. Tylutki, S. Stringari, and L. P. Pitaevskii, Phys. Rev. A **95**, 033614 (2017).
- [134] N. Rosen and P. M. Morse, Phys. Rev. **42**, 210 (1932).
- [135] B. Josephson, Physics Letters **1**, 251 (1962).
- [136] P. de Gennes, Rev. Mod. Phys. **36**, 225 (1964).
- [137] M. Albiez, R. Gati, J. Fölling, S. Hunsmann, M. Cristiani, and M. K. Oberthaler, Phys. Rev. Lett. **95**, 010402 (2005).
- [138] M. Kuhnert, R. Geiger, T. Langen, M. Gring, B. Rauer, T. Kitagawa, E. Demler, D. Adu Smith, and J. Schmiedmayer, Phys. Rev. Lett. **110**, 090405 (2013).
- [139] T. Schumm, S. Hofferberth, L. M. Andersson, S. Wildermuth, S. Groth, I. Bar-Joseph, J. Schmiedmayer, and P. Kruger, Nature Physics **1**, 57 (2005).
- [140] M. R. Andrews, C. G. Townsend, H.-J. Miesner, D. S. Durfee, D. M. Kurn, and W. Ketterle, Science **275**, 637 (1997).
- [141] J. Javanainen and S. M. Yoo, Phys. Rev. Lett. **76**, 161 (1996).
- [142] Y. Castin and J. Dalibard, Phys. Rev. A **55**, 4330 (1997).
- [143] M. Naraschewski, H. Wallis, A. Schenzle, J. I. Cirac, and P. Zoller, Phys. Rev. A **54**, 2185 (1996).
- [144] R. A. Hegstrom, Chemical Physics Letters **288**, 248 (1998).

- [145] A. Röhrl, M. Naraschewski, A. Schenzle, and H. Wallis, *Phys. Rev. Lett.* **78**, 4143 (1997).
- [146] V. V. Konotop and L. Pitaevskii, *Phys. Rev. Lett.* **93**, 240403 (2004).
- [147] R. Liao and J. Brand, *Phys. Rev. A* **83**, 041604 (2011).
- [148] G. Astrakharchik and L. Pitaevskii, *EPL (Europhysics Letters)* **102**, 30004 (2013).
- [149] D. C. Wadkin-Snaith and D. M. Gangardt, *Phys. Rev. Lett.* **108**, 085301 (2012).
- [150] D. K. Efimkin and V. Galitski, *Phys. Rev. A* **91**, 023616 (2015).
- [151] L. Toikka and J. Brand, *New Journal of Physics* **19**, 023029 (2017).
- [152] M. Schechter, D. Gangardt, and A. Kamenev, *Annals of Physics* **327**, 639 (2012).
- [153] V. N. Popov, *Functional Integrals and Collective Excitations*, Cambridge Monographs on Mathematical Physics (Cambridge University Press, 1991).
- [154] A. Muñoz Mateo and J. Brand, *Phys. Rev. Lett.* **113**, 255302 (2014).
- [155] A. Cetoli, J. Brand, R. G. Scott, F. Dalfovo, and L. P. Pitaevskii, *Phys. Rev. A* **88**, 043639 (2013).
- [156] S. Shamilov, A. Muñoz Mateo, and J. Brand, “Particle number depletion of a solitary wave excitation,” (to be published).
- [157] A. Chabchoub, O. Kimmoun, H. Branger, N. Hoffmann, D. Proment, M. Onorato, and N. Akhmediev, *Phys. Rev. Lett.* **110**, 124101 (2013).
- [158] L. Pitaevskii, *Physics-Uspekhi* **59**, 1028 (2016).
- [159] N. Oelkers, M. Batchelor, M. Bortz, and X. Guan, *Journal of Physics A: Mathematical and General* **39**, 1073 (2006).
- [160] M. K. Fung, *Journal of Mathematical Physics* **22**, 2017 (1981).
- [161] J. Sakurai, *Modern Quantum Mechanics* (Addison-Wesley Publishing Company, 1994).
- [162] M. Gaudin, *The Bethe Wavefunction* (Cambridge University Press, 2014) translated by J.S. Caux.

- [163] J. Yu-Zhu, C. Yang-Yang, and G. Xi-Wen, Chinese Physics B **24**, 050311 (2015).
- [164] A. Y. Cherny, J.-S. Caux, and J. Brand, Journal of Siberian Federal University (Mathematics & Physics) **3**, 289 (2010).
- [165] A. Y. Cherny, J.-S. Caux, and J. Brand, Frontiers of Physics **7**, 54 (2012).
- [166] G. E. Astrakharchik, J. Boronat, J. Casulleras, and S. Giorgini, Phys. Rev. Lett. **95**, 190407 (2005).
- [167] M. Batchelor, M. Bortz, X. Guan, and N. Oelkers, Journal of Statistical Mechanics: Theory and Experiment **2005**, L10001 (2005).
- [168] A. S. Campbell, D. M. Gangardt, and K. V. Kheruntsyan, Phys. Rev. Lett. **114**, 125302 (2015).
- [169] K. Sakmann, A. I. Streltsov, O. E. Alon, and L. S. Cederbaum, Phys. Rev. A **72**, 033613 (2005).
- [170] A. G. Sykes, P. D. Drummond, and M. J. Davis, Phys. Rev. A **76**, 063620 (2007).
- [171] V. Yukalov and M. Girardeau, Laser Physics Letters **2**, 375 (2005).
- [172] J. B. McGuire, Journal of Mathematical Physics **5**, 622 (1964).
- [173] A. Ayet and J. Brand, Journal of Statistical Mechanics: Theory and Experiment **2017**, 023103 (2017).
- [174] Y. Lai and H. A. Haus, Phys. Rev. A **40**, 844 (1989).
- [175] Y. Lai and H. A. Haus, Phys. Rev. A **40**, 854 (1989).
- [176] E. Haller, M. Gustavsson, M. J. Mark, J. G. Danzl, R. Hart, G. Pupillo, and H.-C. Nägerl, Science **325**, 1224 (2009).
- [177] Y.-Q. Li, S.-J. Gu, Z.-J. Ying, and U. Eckern, EPL (Europhysics Letters) **61**, 368 (2003).
- [178] M. Batchelor, M. Bortz, X. Guan, and N. Oelkers, Journal of Statistical Mechanics: Theory and Experiment **2006**, P03016 (2006).
- [179] M. Batchelor, M. Bortz, X. Guan, and N. Oelkers, Journal of Physics: Conference Series **42**, 5 (2006).

- [180] L. Zhou, C. Yu Xu, and Y. Li Ma, *Journal of Statistical Mechanics: Theory and Experiment* **2012**, L03002 (2012).
- [181] V. Krivnov and A. Ovchinnikov, *Soviet Journal of Experimental and Theoretical Physics* **40**, 781 (1975).
- [182] X.-W. Guan, *Frontiers of Physics* **7**, 8 (2012).
- [183] X.-W. Guan, M. T. Batchelor, and C. Lee, *Rev. Mod. Phys.* **85**, 1633 (2013).
- [184] P. Schlottmann, *Journal of Physics: Condensed Matter* **6**, 1359 (1994).
- [185] M. Zvonarev, “Correlations in 1d boson and fermion systems: exact results,” Copenhagen University (2005).
- [186] I. V. Tokatly, *Phys. Rev. Lett.* **93**, 090405 (2004).
- [187] G. E. Astrakharchik, D. Blume, S. Giorgini, and L. P. Pitaevskii, *Phys. Rev. Lett.* **93**, 050402 (2004).
- [188] J. N. Fuchs, A. Recati, and W. Zwerger, *Phys. Rev. Lett.* **93**, 090408 (2004).
- [189] X.-W. Guan and Z.-Q. Ma, *Phys. Rev. A* **85**, 033632 (2012).
- [190] K. Atkinson and L. Shampine, “Fredholm integral equations,” <http://www.mathworks.com/matlabcentral/fileexchange/19456-fredholm-integral-equations> (2008).
- [191] C. Qu, L. P. Pitaevskii, and S. Stringari, *Phys. Rev. Lett.* **116**, 160402 (2016).
- [192] A. S. Campbell, “Mobile impurities in one-dimensional quantum liquids,” University of Birmingham (2013).
- [193] K. E. Strecker, G. B. Partridge, A. G. Truscott, and R. G. Hulet, *Nature* **417**, 150 (2002).
- [194] O. Fialko, M.-C. Delattre, J. Brand, and A. R. Kolovsky, *Phys. Rev. Lett.* **108**, 250402 (2012).
- [195] M. Wadachi and M. Sakagami, *Journal of the Physical Society of Japan* **53**, 1933 (1984).
- [196] T. Karpiuk, P. Deuar, P. Bienias, E. Witkowska, K. Pawłowski, M. Gajda, K. Rzazewski, and M. Brewczyk, *Phys. Rev. Lett.* **109**, 205302 (2012).
- [197] T. Karpiuk, T. Sowinski, G. Mariusz, K. Rzazewski, and M. Brewczyk, *Phys. Rev. A* **91**, 013621 (2015).

- [198] J. Dziarmaga, Z. P. Karkuszewski, and K. Sacha, *Journal of Physics B: Atomic, Molecular and Optical Physics* **36**, 1217 (2003).
- [199] R. V. Mishmash and L. D. Carr, *Phys. Rev. Lett.* **103**, 140403 (2009).
- [200] J. Dziarmaga, P. Deuar, and K. Sacha, *Phys. Rev. Lett.* **105**, 018903 (2010).
- [201] J. Sato, R. Kanamoto, E. Kaminishi, and T. Deguchi, “Quantum dark solitons in the 1d bose gas and the superfluid velocity,” arXiv:1204.3960 [cond-mat.quant-gas] (2012).
- [202] J. Sato, R. Kanamoto, E. Kaminishi, and T. Deguchi, *Phys. Rev. Lett.* **108**, 110401 (2012).
- [203] E. Kaminishi, J. Sato, and T. Deguchi, *Journal of Physics: Conference Series* **497**, 012030 (2014).
- [204] J. Sato, R. Kanamoto, E. Kaminishi, and T. Deguchi, *New Journal of Physics* **18**, 075008 (2016).
- [205] V. Korepin, *Commun. Math. Phys.* **86**, 391 (1982).
- [206] N. Slavnov, *Theor. Math. Phys.* **79**, 502 (1989).
- [207] N. Slavnov, *Theor. Math. Phys.* **82**, 273 (1990).
- [208] W. Wen and G. Huang, *Phys. Rev. A* **79**, 023605 (2009).
- [209] M. Antezza, F. Dalfovo, L. P. Pitaevskii, and S. Stringari, *Phys. Rev. A* **76**, 043610 (2007).
- [210] R. Scott, F. Dalfovo, L. Pitaevskii, S. Stringari, O. Fialko, R. Liao, and J. Brand, *New Journal of Physics* **14**, 023044 (2012).
- [211] J. G. Cosme, C. Weiss, and J. Brand, *Phys. Rev. A* **94**, 043603 (2016).
- [212] J. Brand, *Journal of Physics B: Atomic, Molecular and Optical Physics* **37**, S287 (2004).
- [213] F. Calogero and A. Degasperis, *Phys. Rev. A* **11**, 265 (1975).
- [214] M. D. Girardeau and E. M. Wright, *Phys. Rev. Lett.* **84**, 5691 (2000).
- [215] J. F. Sherson, C. Weitenberg, M. Endres, M. Cheneau, I. Bloch, and S. Kuhr, *Nature* **467**, 68 (2010).
- [216] M. D. Girardeau, *Phys. Rev. A* **82**, 011607 (2010).

- [217] F. Haldane, “bibfield journal “bibinfo journal Journal of Physics C: Solid State Physics“ “textbf “bibinfo volume 14,“ “bibinfo pages 2585 (“bibinfo year 1981“natexlab).
- [218] M. A. Cazalilla, Journal of Physics B: Atomic, Molecular and Optical Physics **37**, S1 (2004).
- [219] A. Recati, P. O. Fedichev, W. Zwerger, and P. Zoller, Phys. Rev. Lett. **90**, 020401 (2003).
- [220] J. N. Fuchs, D. M. Gangardt, T. Keilmann, and G. V. Shlyapnikov, Phys. Rev. Lett. **95**, 150402 (2005).
- [221] M. Fabrizio and A. O. Gogolin, Phys. Rev. B **51**, 17827 (1995).
- [222] G. Hess and W. Fairbank, Phys. Rev. Lett. **19**, 216 (1967).
- [223] M. Ueda and A. J. Leggett, Phys. Rev. Lett. **83**, 1489 (1999).
- [224] R. Kanamoto, H. Saito, M. Tsubota, and M. Ueda, Journal of Low Temperature Physics **138**, 681 (2005).
- [225] R. Kanamoto, H. Saito, and M. Ueda, Phys. Rev. Lett. **94**, 090404 (2005).
- [226] K. Henderson, C. Ryu, C. MacCormick, and M. Boshier, New Journal of Physics **11**, 043030 (2009).
- [227] C. Ryu, K. Henderson, and M. Boshier, New Journal of Physics **16**, 013046 (2014).
- [228] B. E. Sherlock, M. Gildemeister, E. Owen, E. Nugent, and C. J. Foot, Phys. Rev. A **83**, 043408 (2011).
- [229] S. W. Seo, S. Kang, W. J. Kwon, and Y.-i. Shin, Phys. Rev. Lett. **115**, 015301 (2015).
- [230] V. Mineev, Low Temperature Physics **39**, 818 (2013).
- [231] K. G. Lagoudakis, T. Ostatnický, A. V. Kavokin, Y. G. Rubo, R. André, and B. Deveaud-Plédran, Science **326**, 974 (2009).
- [232] L. Dominici, G. Dagvadorj, J. M. Fellows, D. Ballarini, M. De Giorgi, F. M. Marchetti, B. Piccirillo, L. Marrucci, A. Bramati, G. Gigli, M. H. Szymańska, and D. Sanvitto, Science Advances **1** (2015).
- [233] L. Guan and S. Chen, Phys. Rev. Lett. **105**, 175301 (2010).

- [234] X. Cui and T.-L. Ho, Phys. Rev. A **89**, 023611 (2014).
- [235] L. Yang, L. Guan, and H. Pu, Phys. Rev. A **91**, 043634 (2015).
- [236] F. Deuretzbacher, K. Fredenhagen, D. Becker, K. Bongs, K. Sengstock, and D. Pfannkuche, Phys. Rev. Lett. **100**, 160405 (2008).
- [237] A. G. Volosniev, D. V. Fedorov, A. S. Jensen, M. Valiente, and N. T. Zinner, Nature Communications **5**, 5300 (2014).
- [238] L. Guan, S. Chen, Y. Wang, and Z.-Q. Ma, Phys. Rev. Lett. **102**, 160402 (2009).